SCUOLA DI DOTTORATO

UNIVERSITÀ DEGLI STUDI DI MILANO-BICOCCA

Department of Biotechnology and Biosciences

PhD program in Converging Technologies for Biomolecular Systems (TeCSBi)

Cycle XXXV

Selective SERCA2a stimulation:

a new promising therapeutic approach for heart failure treatment

Surname Arici

Name Martina

Registration n° 772225

Tutor: Prof. Marcella Rocchetti

Coordinator: Prof. Paola Branduardi

ACADEMIC YEAR 2021/2022

Contents:

Thesis Abstract:

Heart failure (HF) is one of the leading causes of sudden death in developed countries and it is known that failing hearts are characterized by reduced contractile properties caused by impaired Ca^{2+} cycling between the sarcoplasm and sarcoplasmic reticulum (SR). In this field, istaroxime is a small-molecule drug under phase 2 clinical trial that, combining inhibition of Na^+/K^+ ATPase and SERCA2a stimulation, shows an interesting profile for acute HF treatment. However, istaroxime use is restricted to acute i.v. infusion because of its plasma half-life of about 1 hour in humans and its extensive hepatic metabolism to a molecule, named PST3093.

The first aim of my thesis project dealt with the investigation whether PST3093, the main metabolite of istaroxime, may, on its own, be endowed with pharmacological activity and at least partially explain in vivo istaroxime effects. In light of the results, the second aim was to develop PST3093 analogues with metabolically stable groups, with the purpose to generate orally administrable SERCA2a stimulators. *In vivo* and *in vitro* effects of PST3093 follow-on compounds were evaluated by using streptozotocin (STZ)-treated rats developing diabetic cardiomyopathy with diastolic dysfunction associated to SERCA2a downregulation.

Firstly, we characterized PST3093 effects on SERCA2a and Na^+/K^+ ATPase activities, intracellular Ca^{2+} dynamics in isolated ventricular myocytes and in vivo hemodynamic effects in STZ rats. At variance with its parent compound, PST3093 is a “selective” (i.e. devoid of Na^+/K^+ ATPase inhibition) SERCA2a stimulator, showing a safer profile than istaroxime. It is active at nanomolar concentrations in cardiac preparations from normal guinea pig and STZ rats and, similarly to istaroxime, it stimulates SERCA2a only in the presence of phospholamban (PLN), thus relieving its inhibitory activity on SERCA2a. In-vivo PST3093 i.v. infusion (acute effects) in STZ rats improved overall cardiac performance and reversed most STZ-induced abnormalities.

Thanks to a collaboration with chemists of our Department, we synthesized a panel of PST3093 derivatives devoid of Na^+/K^+ ATPase inhibitory activity to develop a class of compounds suitable for chronic (oral) HF treatment. Most of them retained SERCA2a stimulatory action with nanomolar potency. Two selected PST3093 analogues, compound **5** and compound **8**, were further characterized in isolated cardiomyocytes

and their acute in vivo effects were firstly evaluated after i.v. infusion in STZ rats. Both compounds, stimulating SERCA2a, improved intracellular Ca^{2+} handling (promoting SR Ca^{2+} compartmentalization) and restored diastolic function following acute i.v. infusion in STZ rats.

Finally, we evaluated chronic in vivo effects of compound **8** in STZ rats after oral administration at two dosages (40 or 80 mg/kg) at 1 or 4 daily doses to evaluate potential dose-dependent effects and to indirectly explore its pharmacokinetic in rats. Compound **8** dose-dependently ameliorated STZ-induced diastolic dysfunction and its pharmacokinetic was comparable to that of PST3093, i.e., longer than istaroxime one. Off-target effects of compound **8** were excluded based on the analysis of its molecular interaction with a panel of 50 ligands. Acute toxicity in mice was finally evaluated, showing a safer profile of compound **8** than PST3093 and istaroxime.

In conclusion, PST3093 and its derivatives act as “selective” SERCA2a stimulators. While PST3093 is suitable to prolong the cardiac beneficial effect of istaroxime infusion, PST3093 derivatives can be considered the prototype of a novel pharmacodynamic class for the ino-lusitropic approach of HF. In particular, compound 8 seems to be a favorable drug candidate for chronic HF therapy.

Chapter 1

Introduction:

Role of SERCA2a in intracellular Ca^{2+} dynamics

1.1 CARDIAC EXCITATION-CONTRACTION COUPLING

The sarcoplasmic reticulum (SR) is an intracellular membrane network in cardiac cells that plays an essential role in excitation-contraction coupling (ECC), the process from electrical excitation of the myocyte to the contraction of the heart[1]. SR main function is the storage and distribution of Ca^{2+} ions that initiates cardiac contraction and relaxation[2]; the importance of Ca^{2+} signaling is highlighted by the precise nature by which Ca^{2+} ions are extensively regulated within cells[3].

During systole, the action potential facilitates a minor Ca^{2+} influx through sarcolemmal L-type Ca^{2+} channels (LCCT), depolarization-activated Ca^{2+} channels which contribute to action potential plateau. This, in turn, induces a major Ca^{2+} release from the SR stores through the Ca^{2+} release channels (ryanodine receptor 2, RyR2), leading to the defined Ca^{2+}-induced Ca^{2+} release (CICR) ECC system. The combination of Ca^{2+} influx and release raises the free intracellular Ca^{2+} concentration $[Ca^{2+}]_i$ from $\sim$100 nM to $\sim$ 1µM, allowing Ca^{2+} to bind to the myofilament protein troponin C, which then switches on the contractile machinery and initiates the cross-bridge movement of the myofilaments[1] (Figure 1).

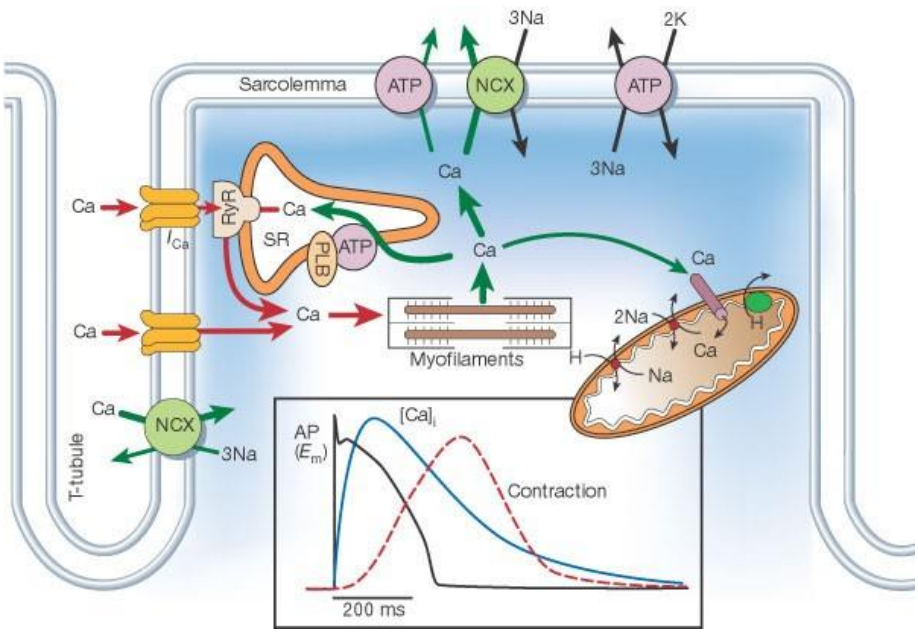

Figure 1. Ca^{2+} transport in ventricular myocytes. Inset shows the time course of an action potential, Ca^{2+} transient and contraction measured in a rabbit ventricular myocyte at 37 °C. NCX, Na^+/Ca^{2+} exchange; ATP, ATPase; PLB, phospholamban; SR, sarcoplasmic reticulum *(from [1])*.

The quick removal of Ca^{2+} either into the SR, or the extracellular lumen, is essential for cardiac relaxation (i.e. to $[Ca^{2+}]_i$ ~ 100 nM). In human, rabbit, ferret and cat hearts, this Ca^{2+} sequestration during diastole is mainly facilitated by the Sarco-Endoplasmic Reticulum Ca^{2+}-ATPase (SERCA, 70%) and to a lesser extent by the sarcolemmal Na^+/Ca^{2+} exchanger (NCX, 28%)[1]. Other systems, such as the slow Ca^{2+} removal systems, i.e. the plasma membrane Ca^{2+}-ATPase (PMCA), the mitochondrial Na^+/Ca^{2+} exchanger (mitNCX) and the mitochondria Ca^{2+} uniporter (MCU), play minor roles in intracellular Ca^{2+} handling during dynamic activity (~ 2%). In contrast, in both rat and mouse myocardium, SERCA plays a predominant role with an approximately 92% contribution to the sequestration of Ca^{2+} (NCX: 7% of Ca^{2+} sequestration, slow Ca^{2+} removal systems: ~ 1%)[1]. Upon SR sequestration, Ca^{2+} binds mainly to the SR Ca^{2+}-storage protein, calsequestrin (CASQ)[4] and to other Ca^{2+}-binding proteins, such as calreticulin (CARL)[5] and the histidine-rich calcium binding protein (HRC)[6].

1.2 SERCA

As mentioned above, SERCA is the main protein involved in the re-uptake of Ca^{2+} and serves a dual function: (1) to cause muscle relaxation by lowering the cytosolic Ca^{2+}, and at the same time (2) to restore SR Ca^{2+} necessary for muscle contraction[7].

SERCA belongs to the family of P-type ATPase, and it is a single polypeptide of molecular mass ~110 kDa with three cytoplasmic domains joined to a set of 10 transmembrane helices by a narrow extramembrane pentahelical stalk[7] (Figure 2).

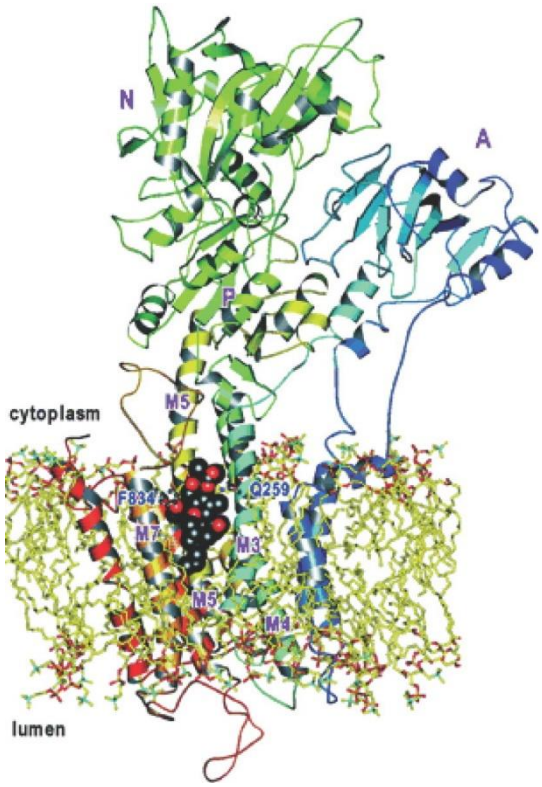

Figure 2. Ca^{2+}-ATPase embedded in the lipid bilayer based on crystal structure with its antagonist Tapsigargin (*in black*) *(from [7]).*

A notable feature of P-type ATPases is the transfer of terminal phosphate from ATP to an aspartate residue in the catalytic domain, resulting in a reversible conformational change. P-type ATPases couple the hydrolysis of ATP to the movement of ions across a biological membrane, in particular, two Ca^{2+} ions are transported for each molecule of ATP hydrolyzed[7].

In vertebrates there are three distinct genes ATP2A1, ATP2A2 and ATP2A3 encoding SERCA1, 2, and 3 respectively that are known to produce more than 10 isoforms, mainly through alternative splicing.

SERCA1 is expressed in fast-twitch skeletal muscle and is alternatively spliced to encode SERCA1a (994 aa, adult) and 1b (1011 aa, fetal)[8,9].

SERCA2, that is the predominant variant of all SERCA isoforms and phylogenetically the oldest, encodes SERCA2a (997 aa), which is expressed predominantly in cardiac and slow-twitch skeletal muscle[10,11]. SERCA2b (1042 aa) is expressed in all tissues at low levels, including muscle and non-muscle cells[12]. Recently, a third isoform, SERCA2c (999 aa), has been reported in cardiac muscle. The latter was only detected in a confined area of cardiomyocytes, in close proximity to the sarcolemma[13].

SERCA3 isoforms are expressed in several non-muscle tissues but appear to be a minor form in muscle. In humans, SERCA3 is known to encode for six isoforms, 3a–3f (~999–1052 aa) at the mRNA level and it is expressed in multiple tissues and cell types. At the protein level, there are data only for the 3a, b and c isoforms which are expressed at high levels in the hematopoietic cell lineages, platelets, epithelial cells, fibroblasts, and endothelial cells[14] (Table 1).

Table 1. Distribution of SERCA isoforms in mammalian tissues *(from [7])*.

Table 1. Distribution of SERCA isoforms in mammalian tissues.

	Skeletal muscle							
	Fast twitch		Slow twitch		Cardiac muscle		Smooth muscle	Non-muscle cells
SERCA isoform	Fetal	Adult	Fetal	Adult	Fetal	Adult		
SERCA 1a	–	+++++	–	–	–	–	–	–
SERCA 1b	+++	–	–	–	–	–	–	–
SERCA 2a	+	–	+	+++	+	++++	+	–
SERCA 2b	+	+	+	+	+	+	+	+
SERCA 3a	–	–	–	–	–	–	–	+
SERCA 3b	–	–	–	–	–	–	–	+
SERCA 3c	–	–	–	–	–	–	–	+

A notable feature of SERCA isoforms is that their primary structure is highly conserved. In particular, SERCA1 shows 84% similarity to SERCA2a and 75% to SERCA3. Because of their similar structures, it has been predicted that all SERCA isoforms might have similar native transmembrane arrangements and tertiary conformations, and hence, their sensitivity to Ca^{2+} and enzyme activity should be equivalent. In particular,

the muscle isoforms SERCA1 and SERCA2a have enzymatic properties that are almost identical[15]. The exception is the ubiquitous SERCA2b isoform, which is a unique structural and functional splice variant containing a 11th transmembrane helix and a C-terminal extension that resides in the ER lumen[16,17]. This unique modification of SERCA2b imparts the highest Ca^{2+} affinity between the SERCA isoforms[18] and provides a potential point for regulation from within the ER lumen. Instead, SERCA2c showed a lower apparent affinity for cytosolic Ca^{2+} than the other SERCA2 isoforms and a catalytic turnover rate similar to SERCA2b[13].

Due to the similarity between the isoforms, currently, there are no pharmacological tools to specifically modulate the different isoforms of SERCA.

1.3 SERCA2a

SERCA2a is the cardiac isoform, and its enzymatic activity is controlled by the inhibitory peptide phospholamban (PLN).

Structurally, SERCA2a has two key domains: one is the region between amino acids 336 and 412 in the phosphorylation (P) domain, which responds to the action of PLN; the other is the region between amino acids 467 and 762 in the nucleotide-binding (N) domain, which mainly determines the strength of SERCA2 for Ca^{2+} affinity[19]. As for the other isoforms, the A domain serves as the transduction element that couples ATP hydrolysis with active Ca^{2+} transport in the catalytic cycle of the pump (Figure 3).

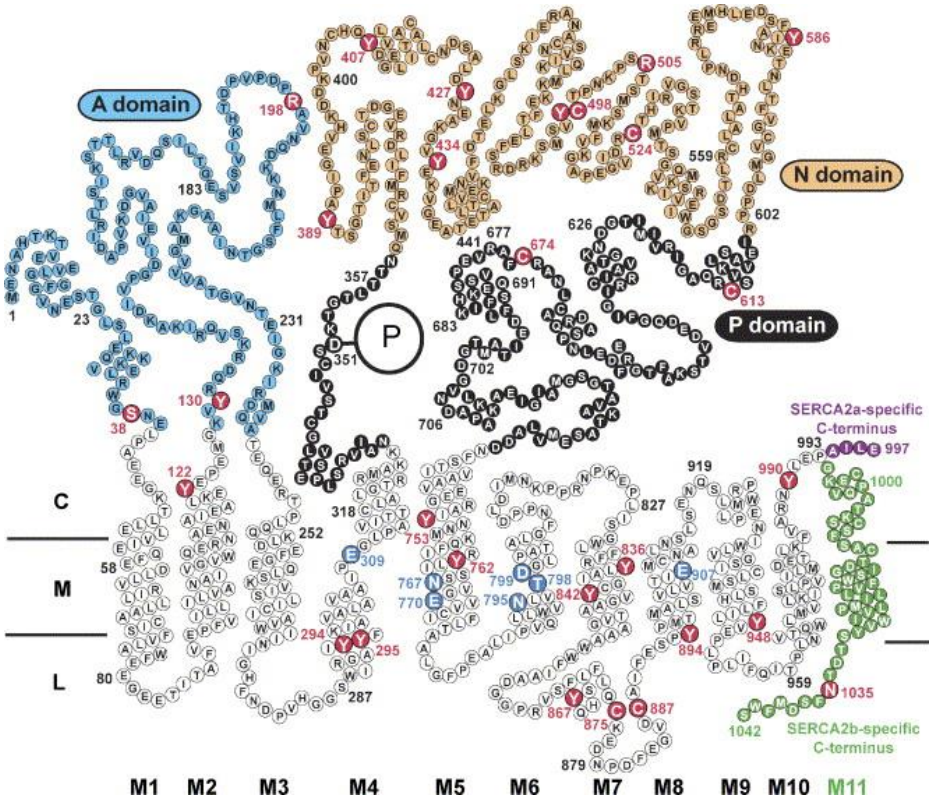

Figure 3. Planar model of the primary and putative secondary structure of the human SERCA2 isoforms. Each circle corresponds to an amino acid residue indicated by the single-letter code inside the circle, α-helical structures are shown as stacked diagonal rows of three or four residues,

β-strands are displayed as ladder-type residue arrangements and linear sections represent loops. M1–M10 denote the membrane-spanning helices in SERCA2a. Essential amino acid residues participating in Ca^{2+} binding are shown as blue circles with white letters in M4, M5, M6 and M8. A domain, actuator domain (azure circles); P domain, phosphorylation domain (inverted color black circles); N domain, nucleotide-binding domain (orange circles); C, cytosol; M, membrane; L, lumen (from[20]).

The process of Ca^{2+} reuptake involves the mutual transformation of the two conformations of the SERCA2a protein: E1 and E2 (Figure 4). The E1 conformation of SERCA2a has a higher affinity for Ca^{2+}, and the binding site is exposed to the cytosol. The E2 conformation has a lower affinity for Ca^{2+} and is located on the lumen of the SR. After relaxation of cardiomyocytes, Ca^{2+} is released from troponin into the cytosol and binds to E1 (the binding site is at the aspartic acid residue Asp351, conserved in all P-type ATPases[21]), after which phosphorylation of E1 occurs with the participation of ATP (Ca^{2+}-E1-P), forming high-energy phospho-intermediate[22] that causes a conformational change from E1 to E2 (Ca^{2+}-E2-P), and the E2 conformations becomes an ADP insensitive intermediate[23,24]. This process results in the localization of the Ca^{2+} binding site in the SR. Due to the low affinity of E2 for Ca^{2+}, Ca^{2+} is released into the SR after uncoupling with E2, followed by the release of inorganic phosphate molecule[25] and accompanied by E2 converted to E1 and re-entering the next cycle.

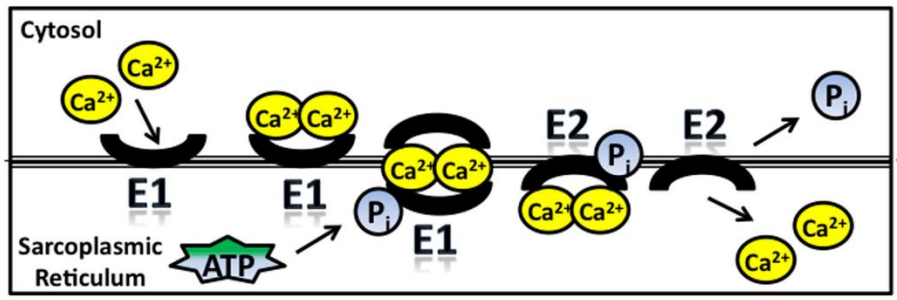

Figure 4. Ca^{2+} recycling during contraction–relaxation cycle in the cardiac muscle. Note the cyclic changes that occur for SERCA2 in order to deliver Ca^{2+} from the cytosol into the lumen of the SR against the concentration gradient hydrolyzing one ATP molecule for each 2 Ca^{2+} in diastolic phase of the cardiomyocyte *(modified from*[22]).

1.3.1 Post translational modifications (PTMs)

PTM refers to the covalent attachment of chemical small molecule groups to the amino acid side chain of a protein, significantly increasing the complexity and diversity of the protein. A number of studies have demonstrated that SERCA2a is capable of PTMs and different types of PTMs occur at different sites, which affects SR function (Figure 5). Acting on PTMs may be a promising direction in clinical or experimental settings to improve reduced activity in heart failure (HF)[19]. Thus, a brief description of main SERCA2a PMTs are described below.

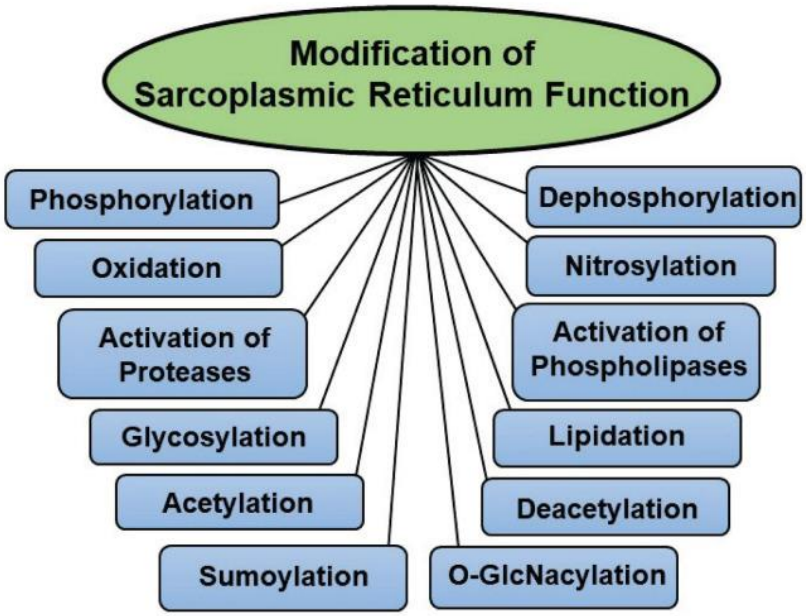

Figure 5. Modification of cardiac sarcoplasmic reticulum function by some post-translational events *(From [26]).*

1.3.1.1 SUMOylation

SUMOylation is a PTM mediated by SUMO1 (Small ubiquitin-like modifier type 1), a protein of the family of peptides that alter the function of other proteins in cells[27]. Despite their similarity with the structure of ubiquitin, SUMO family is widely involved in cellular activities such as protein structural stability, nuclear translocation, and

regulation of transcriptional activity through the process of reversible covalent linking of SUMO to the target protein[28]. In the heart, SUMOylation has a crucial impact on normal cardiac development and function[29], as well as adaptation of the heart to pathological stress[30].

Kho and colleagues[31] showed that SERCA2a is SUMOylated at two lysine residues (lys480 and lys585) and this SUMOylation is essential for preserving the activity and stability of SERCA2a[32]. It was also reported that the levels of both SERCA2a itself and SERCA2a SUMOylation were significantly reduced in failing hearts and seems that this PTM has cardioprotective properties. This reduction in SUMOylation correlated with reduced ATPase activity and decreased SERCA2a stability. It is possible that SUMOylation may induce a conformational change within SERCA2a or may provide an additional interface for ATP binding, leading to increase ATPase activity[31] (Figure 6). However, increased levels of unSUMOylated SERCA2a due to low SUMO1 protein pools triggers impaired SERCA2a activity and induces cardiac dysfunction under pathophysiological conditions[31].

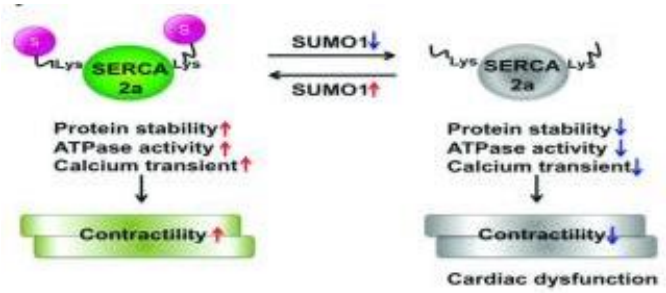

Figure 6. A working model for the regulation of SERCA2a function by SUMOylation. Under basal conditions, SUMOylation enhances SERCA2a's protein stability and its Ca^{2+} pump function to regulate cardiac contractility. However, increased levels of unSUMOylated SERCA2a due to low SUMO1 protein pools triggers impaired SERCA2a activity and induces cardiac dysfunction under pathophysiological conditions *(from [31])*.

Previous work indicated that SUMOs targeting the proteins contribute to a number of human cardiovascular disease, such as valvular abnormalities, ischemic heart disease, cardiac hypertrophy, and idiopathic cardiomyopathy[33]. In animals subjected to heart I/R, SUMO1 conjugations were shown to be inactivated[34].

More details regarding SUMOylation are reported below, in 1.6.1.1.3 paragraph.

1.3.1.2 Nitration and Glutathiolation

Nitric oxide (NO) is a signal molecule with pleiotropic effects, and it is a physiological regulator that stimulates SERCA2a accelerating the reduction of intracellular Ca^{2+} concentration[19].

On the contrary, the appearance of increased nitration, the process that involve the adding of one or more NO_2 groups, and the partial inactivation of SERCA2a in several types of muscle under conditions of chronic oxidative stress suggests that a common functional response to nitrative stress of the muscle involves prolongation of the Ca^{2+} transient with slower contraction and relaxation times of the muscle (40% loss in SERCA activity)[35]. It has also been reported that nitration of SERCA2a occurs through polyol pathway and it is believed that nitration of certain tyrosine residues may cause distortion in helical interactions and thus restricts the coordinated movement of membrane helices, which is required for optimal SERCA function.

Furthermore, NO-derived intermediates can also play a role in protein modification, such as S-Glutathiolation[36]. It is noteworthy that both oxidative stress and nitrosative stress are known to adversely affect the process of glutathionylation where disulphide bonds are formed between cysteine and glutathione in SR proteins, and this PTM induce an increase of SERCA activity and boost Ca^{2+} uptake[19,26].

1.3.1.3 Glycosylation and O-GlcNAc modification

In diabetes, when glucose levels are high, an increase in SERCA2a glycosylation occur, and this rise causes a significant decrease in SERCA2a activity[26]. A substantial decrease in both SERCA2a mRNA and proteins as well as a considerable increase in PLN have been attributed to the increase in glycosylation.

A non-canonical glycosylation involves the attachment of single O-linked N-acetylglucosamine (O-GlcNAc) moieties to Ser and Thr residues of cytoplasmic, nuclear and mitochondrial proteins[37]. This is involved in the regulation of many important biological processes in cells, and application in human diseases and treatment. When O-GlcNAc is incorporated into threonine or serine residues of SERCA2a, the levels of

the protein are altered and result in the disruption of Ca^{2+} cycling[26]. In addition, O-GlcNAc can also modify SERCA2a activity by regulating phosphorylation of PLN. So, O-GlcNAc regulates the activity of SERCA2a either directly or indirectly[19].

1.3.1.4 Acetylation

The acetylation is the transfer of the acetyl group of the donor to the amino acid residue of the protein of interest by an enzymatic or spontaneous reaction, which modulates the function of the target protein[19].

It was proposed that acetylation and deacetylation play a role in the acute modification of SERCA2a activity[32]. In a recent study from humans, pigs and mice, was found a significant increase in the level of acetylation of SERCA2a in failing hearts, a phenomenon attributed to a decrease in the level of SIRT1 (a class III histone deacetylase) that promotes the enzymatic dysfunction. The increase in acetylation of SERCA2a significantly reduced the activity of the pump, which caused a decrease in the uptake of Ca^{2+} and impaired cardiac function[38].

1.3.1.5 Phosphorylation

Phosphorylation of proteins is the most widely studied PTM and it is involved in the regulation of various important molecular activities and functions. Striated muscle-specific protein kinase (SPEG), as a member of the myosin light chain kinase (MLCK) subgroup of the CaMK Ser/Thr protein kinase family, is closely related to the phosphorylation of SERCA2a[19].

Quick and colleagues[39] used proteomics to discover that SERCA2a interacts with SPEG; the second kinase domain of SPEG acts on SERCA2a directly phosphorylating the Thr484 site, thereby enhancing the oligomerization of SERCA2a and increasing the Ca^{2+} transport capacity of the pump.

1.4 PHOSPHOLAMBAN (PLN)

PLN has proven to be the major regulator of SERCA2a activity and so far, it is the only SERCA2a-associated protein directly involved in cardiac disease development, including (HF). It is expressed mainly in cardiac muscle and, to a lesser extent, in slow-twitch skeletal, smooth muscles and endothelial cells[2].

PLN is a small membrane-spanning protein, comprising 52 amino acid residues and it is in dynamic equilibrium between monomeric and oligomeric states (Figure 7)[27]. The secondary and tertiary structure of the protein can be subdivided into two main domains: domain I is hydrophilic and contains the cytoplasmic region (amino acids 1-30), whereas domain II includes the hydrophobic SR membrane-spanning part of the protein with a probable α-helical structure (amino acid residues 31-52). Domain I contains two further motifs: domain Ia (residues 1-20) presumably forming an α-helical structure, and domain Ib (residues 21- 30), which is likely to exist as a random coil[40].

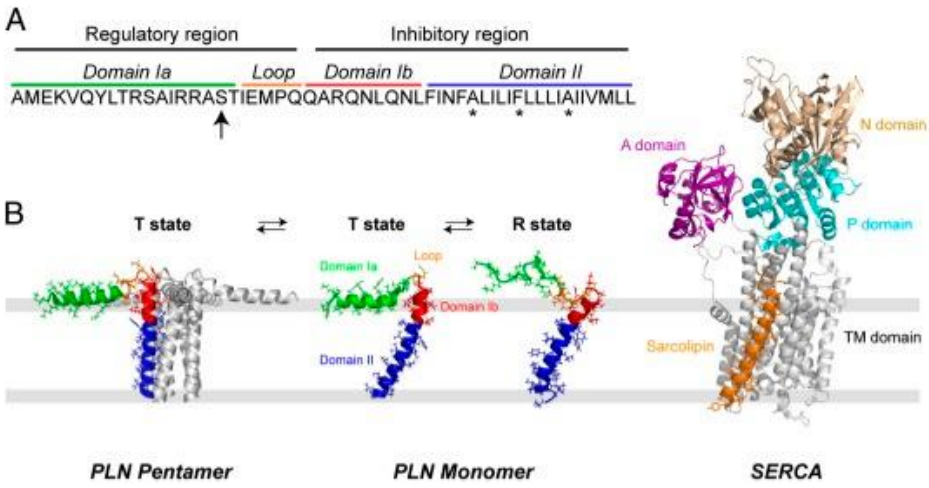

Figure 7: Structures of PLN and SERCA. (A) Primary sequence and domains of PLN^{AFA}. The S16 phosphorylation site is marked with an arrow, and mutation sites (AFA: C36A, C41F, C46A) are indicated with asterisks. (B) 3D structures of PLN pentamer [Protein Data Bank (PDB) ID code 2KYV], PLN^{AFA} monomer in the T (PDB ID code 2KB7) and R states (PDB ID code 2LPF), and SERCA in complex with sarcolipin (PDB ID code 3W5A). SERCA includes 10 TM helices and three cytoplasmic domains: nucleotide binding (N domain), actuator (A domain), and phosphorylation (P domain) *(From [41])*.

In vitro studies with purified SR membranes have demonstrated that PLN can be phosphorylated at three distinct sites in domain I: 1) Ser16 by cAMP-dependent protein kinase A (PKA); 2) Thr17 by Ca^{2+} calmodulin-dependent protein kinase (CAMKII); and 3) Ser10 by Ca^{2+} phospholipid-dependent protein kinase (PKC)[2].

The region of PLN interacting with SERCA2 may involve amino acids 2–18 and PLN inhibits the apparent affinity of SERCA for Ca^{2+} in its dephosphorylated form. Upon phosphorylation of PLN through β-adrenergic stimulation and enhanced PKA activity, the inhibitory effect of PLN on SERCA is relieved, due to the positive charges of the cytosolic domain partially neutralized by the phosphate moiety in this vicinity[2]. This leads to increased initial rates of SR Ca^{2+} uptake, accelerated relaxation and enhanced SR Ca^{2+} load, which is available for release through the RyR2, resulting in enhanced relaxation. The inhibitory effects of PLN are restored through dephosphorylation by an SR-associated phosphatase[42] (Figure 8).

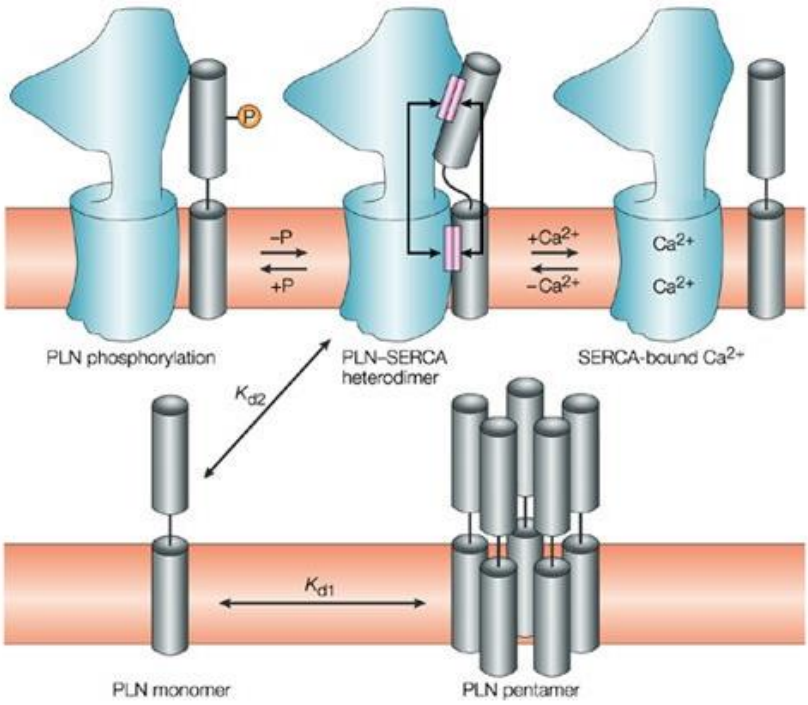

Figure 8. Reversible inhibition of sarco(endo)plasmic reticulum Ca^{2+}-ATPase (SERCA) activity by phospholamban (PLN). Two steps can be dissected: first, the association/dissociation of pentameric PLN (K_{d1}), and second, the association/dissociation of monomeric PLN and SERCA

(K_{d2}). The phosphorylation of PLN and Ca^{2+} binding to SERCA are driving forces for the dissociation of the PLN–SERCA complex, thereby activating SERCA. Phosphorylation of PLN dissociates functional interactions, but is less effective than Ca^{2+} binding to SERCA in breaking up physical interaction (*from*[4])

The initial model for SERCA inhibition involved reversible binding of monomeric PLN and dynamic equilibrium of the monomer between the SERCA-bound and pentameric states[43]. In this scenario, the pentamer was considered an inactive storage form of PLN. However, active roles have been proposed for the PLN pentamer, including the modulation of SR Ca^{2+} homeostasis and PKA-mediated phosphorylation, at least less active than monomeric isoform. The PLN pentamer has also been found to stimulate the V_{max} of SERCA, which depends on the SERCA-PLN molar ratio and density in the membrane. Providing a context for this latter effect was the finding that PLN pentamers associate with SERCA[44]. In particular, PLN pentamer spontaneously associates with SERCA at a site distinct from the inhibitory groove (M2, M6, and M9 of SERCA) and the interaction provides an explanation for the stimulation of SERCA's maximal activity[44] (Figure 9).

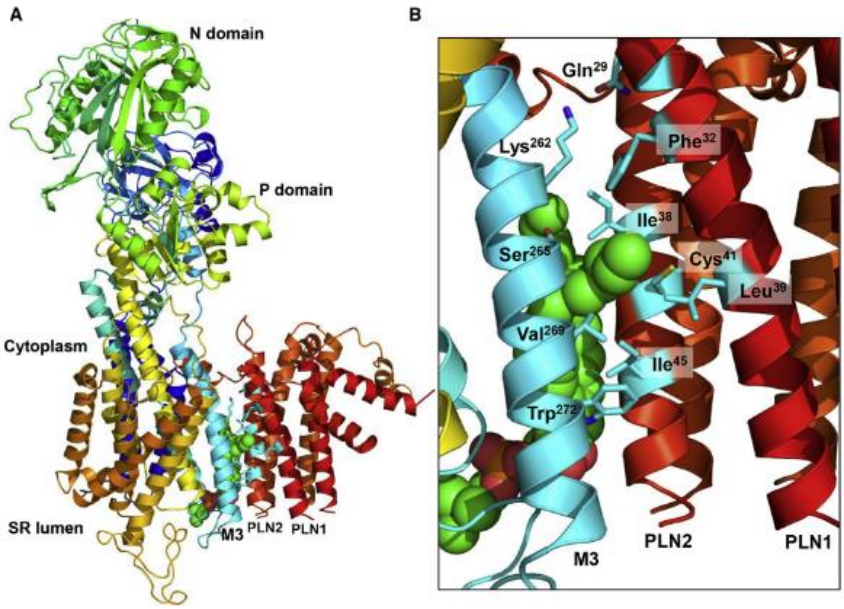

Figure 9. (A) Interaction interface between SERCA and the pentameric form of PLN. SERCA and PLN are shown in ribbon representation, with PLN in orange to red and SERCA in spectrum from blue at the N-terminus to orange at the C-terminus. (B) The interface between transmembrane

segment M3 of SERCA (cyan) and two PLN molecules in the pentamer (red) is shown. The cytoplasmic end of M3 interacts with the transmembrane domain of one PLN molecule (PLN1), whereas the luminal end of M3 interacts with the transmembrane domain of a second PLN molecule (PLN2). Lys262 of M3 interacts with Gln29 and Phe32 of PLN1, and Trp262 of M3 interacts with Ile45 of PLN2. In between these regions, a lipid acyl chain (green spheres) inserts into the SERCA-PLN interface and interacts with a number of residues from M3 (Ser265 and Val269), PLN1 (Leu39), and PLN2 (Cys41 and Ile38).

1.5 OTHER SERCA2a BINDING PARTERS and REGULATORS

Together with PLN, SERCA2a is strictly regulated by several micropeptides and proteins.

1.5.1 Micropeptides

The widespread regulation of SERCA activity by small transmembrane micropeptides represents a conserved and ancient mechanism to control Ca^{2+} handling in muscles, which alter the affinity of SERCA for Ca^{2+} and modify the rate of Ca^{2+} reuptake into the SR[3]. In the heart, a homologous protein of PLN, sarcolipin (SLN), inhibits the activity of SERCA2a; moreover, other 2 micropeptides that directly bind SERCA in muscle, myoregulin (MLN) and dwarf open reading frame (DWORF), were identified[3]. Finally, Anderson and colleagues[3] found either another-regulin (ALN) and endoregulin (ELN) that share key amino acids with their muscle-specific counterparts and function as direct inhibitors of SERCA pump activity with a widespread expression (Figure 9-10).

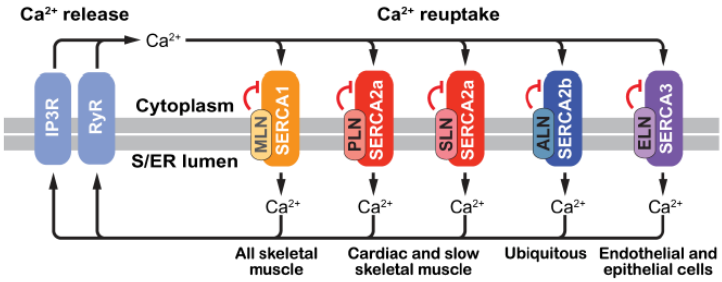

Figure 9: Family of SERCA-inhibiting micropeptides. Model depicting the expression patterns of the predominant SERCA and micropeptide inhibitors across different muscle and non-muscle tissues in vertebrates. The discovery of ELN and ALN suggests that the regulation of SERCA activity by SERCA-inhibiting micropeptides represents a general mechanism to control Ca^{2+} handling across diverse cell types *(From [3])*.

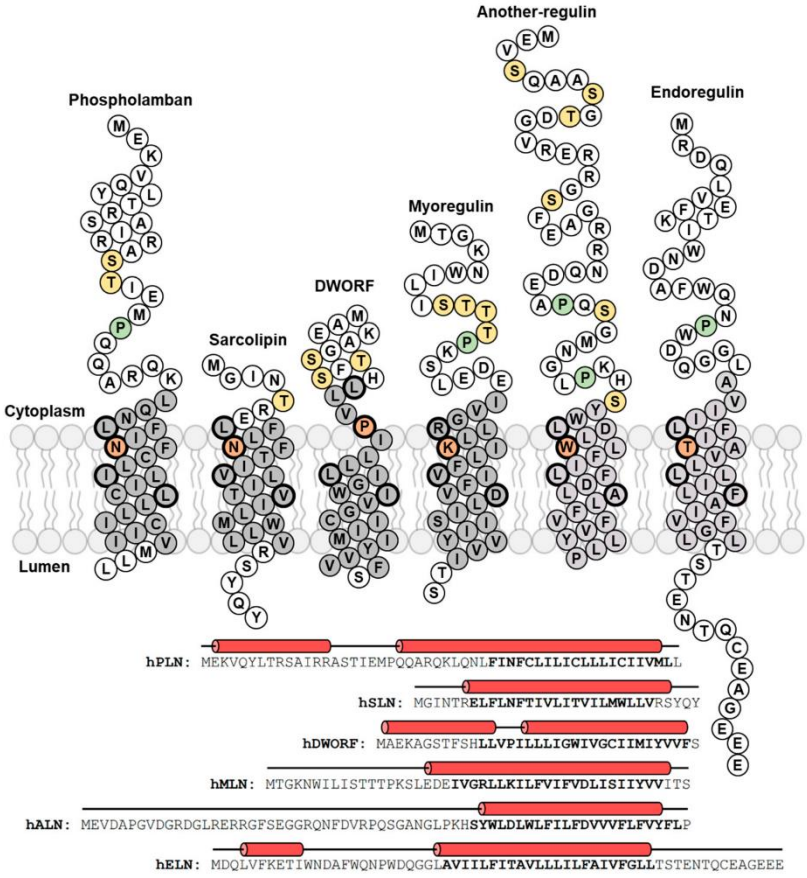

Figure 10. Topology models and sequence alignments for the regulin family of small transmembrane peptides. For the topology models, the transmembrane domains are highlighted in gray, Asn34 in PLN and Asn11 in SLN are highlighted in orange. Polar residues in MLN, ALN, and ALN that align with Asn34 of PLN and Asn11 of SLN are also highlighted in orange. Potential phosphorylation sites (yellow) and proline residues (green) are indicated. Pro15 of DWORF aligns with Asn34 of PLN and Asn11 of SLN and is colored as an essential residue (orange). For the sequence alignments, the predicted transmembrane domains are in bold and predicted helical regions are indicated as red cylinders *(from* [45]*)*.

1.5.1.1 Sarcolipin (SLN)

In skeletal and atrial muscle, SERCA is regulated by SLN, a 31-residue tail-anchored integral membrane protein that resides in the SR membrane and it is homologous to PLN[46]. However, the structure of SLN is quite distinct, with a short cytoplasmic domain

(residues 1–7), a transmembrane α-helix (residues 8–26), and a unique luminal tail (residues 27–31). Like PLN, SLN alters the apparent Ca^{2+} affinity of SERCA, yet there are substantial differences in the mechanism[47]. The inhibitory properties of SLN are strongly dependent on the highly conserved C-terminal tail (Arg27-Ser-Tyr-Gln-Tyr31 or RSYQY sequence), whereas the inhibitory properties of PLN are encoded in its transmembrane domain. In addition, SLN appears to remain associated with SERCA throughout the Ca^{2+} transport cycle. Several studies have since shown that SLN can form a mixture of oligomeric species including a pentamer that appeared to be a complex of an SLN dimer and an SLN trimer, with complementary hydrophobic interfaces that stabilize the dimer and trimer[46]. Moreover, studies in literature reported that SLN can bind PLN forming a complex and this interaction seems to prevent the polymerization of PLN[48].

1.5.1.2 DWORF

DWORF is a 34–amino acids peptide that can replace PLN and SLN, thereby enhancing the activity of SERCA2a. DWORF is primarily expressed in ventricular and slow-twitch skeletal muscles[49] and has a higher affinity for SERCA than PLN competing with it. Overexpression of DWORF significantly improved cardiac function in dilated heart disease mice and improved dysregulated Ca^{2+} circulation[50].

The binding of DWORF to SERCA2a depends entirely on the TM domain of DWORF and, moreover, DWORF is also able to activate SERCA2a directly in the absence of PLN[51].

1.5.1.3 MLN/ELN/ALN

The C-terminal transmembrane helix of ELN, ALN, and MLN is similar to PLN and SLN (Figure 10), suggesting that these new transmembrane micropeptides are a conserved mechanism for Ca^{2+} regulation. Currently, enough evidence is unavailable concerning whether these new micropeptides have similar effects on SERCA2a like PLN and SLN[19].

1.5.2 Proteins

The existence of such a protein complex in the regulation of SR Ca^{2+} uptake it is well establish and, in particular, SERCA2a has been found to interact with proteins of the SR lumen, such as Histidine-Rich Calcium binding protein (HRC)[6] and calreticulin, while its cytosolic region has been shown to bind to S100A1[52].

Furthermore, there are many proteins involved in the regulation of PLN/SERCA activity, such as HS-1 Associated protein X-1 (HAX-1), Protein Phosphatase 1 (PP1) and Heat Shock Protein 20 (Hsp20) (Figure 11).

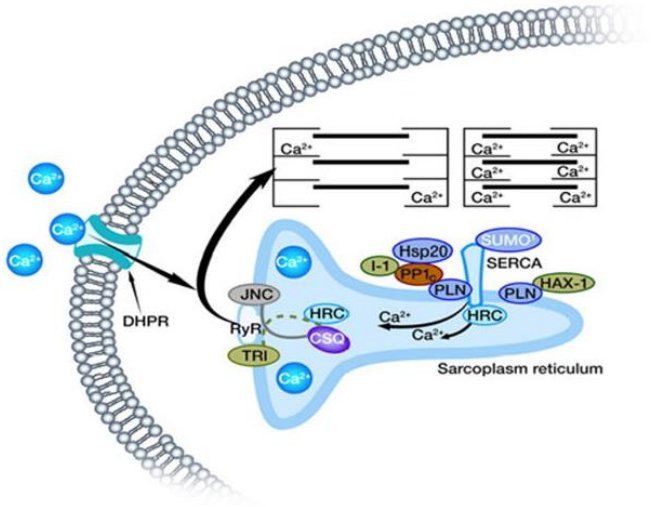

Figure 11: Regulation of SR Ca-transport by a multimeric protein complex. SERCA2a activity is regulated by its reversible inhibitor PLN, SUMO and the histidine rich Ca-binding protein (HRC). Phosphorylation of PLN is mediated by cAMP-dependent or Ca-CAM-dependent PKs and dephosphorylation occurs by protein phosphatase 1 (PP1). The activity of PP1 is regulated by inhibitor-1 (I-1) *(from [27])*.

1.5.2.1 Histidine-Rich Calcium binding protein (HRC)

HRC is a low-affinity, high capacity Ca^{2+}-binding protein located in the cardiac SR lumen. HRC is a regulator of SERCA2a activity, and the interactions may be regulated in a Ca^{2+}-dependent manner during the cardiac cycle. In particular, the binding of HRC to SERCA2 was attenuated upon increased Ca^{2+} levels[53].

Overall, HRC have a critical role in maintaining Ca^{2+} homeostasis in the SR by regulating Ca^{2+} storage, release and uptake[27].

1.5.2.2 S100A1

S100A1 is specifically and highly expressed in the human heart and alterations in the expression of this protein are associated with an impaired Ca^{2+}-handling in HF.

The S100A1 contains two EF-hand calcium-binding motifs and is highly prevalent in cardiac cells, localizing at the SR, the myofilaments, and the mitochondria. The target protein interaction is mediated by the C-terminal part and the central hinge region of S100A1 that exhibits a conformational change upon Ca^{2+}-binding and exposes hydrophobic residues on the protein surface[52].

Previous reports suggested that S100A1 interacts with SERCA2a and PLN and may be affecting SERCA due to its potent molecular chaperone character, functioning predominantly as a Ca^{2+}-sensor rather than a Ca^{2+}-storage protein[27].

1.5.2.3 HS-1 associated protein X-1 (HAX-1)

HAX-1 has a MW of ~35 kDa and is ubiquitously expressed in mitochondria and was originally identified as an intracellular protein with antiapoptotic function. Interestingly, more recent studies have revealed that HAX-1 also localizes to the SR, and it is an important regulator of Ca^{2+} cycling and cardiac contractility. These effects are primarily mediated through its interaction with PLN abolishing its phosphorylation and to a lesser extent through direct SERCA2a modulation[54].

1.5.2.4 Protein Phosphatase 1 (PP1)

The major phosphatase dephosphorylating PLN is PP1, a holoenzyme comprised of catalytic domain, which possesses its phosphatase activity, complexed with as many as 100 established or putative regulatory subunits[27].

Upon stimulation of the β-adrenergic axis, PKA phosphorylates Inhibitor-1 (I-1, an endogenous inhibitor of PP1), resulting in PP1 inhibition and allowing increase in the SERCA2a activity[55].

1.5.2.5 Heat Shock Protein 20 (Hsp20)

It is now widely acknowledged that the induction of heat shock proteins is cytoprotective, which is attributed at least partly, to chaperone activities of these "stress proteins". Several studies have focused on elucidating the role of Hsp20 and interestingly, it has been suggested that Hsp20 regulates myocardial contraction via regulation of the PP1/PLN axis. In particular, Hsp20 is able to inhibit the PP1 leading to augmented PLN phosphorylation and consequently to amplified SR Ca^{2+} cycling by SERCA2a increased activity[56].

1.6 SERCA2a in CARDIAC DISEASES

Changes in Ca^{2+} homeostasis after partial depletion of SR Ca^{2+}, impairment of Ca^{2+} channels, Ca^{2+} leaks or reduced expression of SERCA2 occur in major cardiac diseases, including ischemic heart disease (IHD), hypertrophic (HCM) and dilated cardiomyopathies (DCM), which often progress to HF. Although alteration of SERCA2 expression and function may not always be the initial cause of heart disease, it clearly contributes to the deterioration of cardiac function after injury[57]. There is also evidence that chronic up-regulation of SERCA2 leads to cardiac hypertrophy and congestive HF[58].

In particular, HF is one of the leading causes of sudden death in developed countries and is defined as the inability of the heart to meet the metabolic demand of peripheral organs. The normal response of the body to this event is then triggered with the activation of the neuro-hormonal response resulting in cardiac hypertrophy and an increase in left ventricular (LV) volume. Under chronic conditions, the heart starts an irreversible degeneration process that brings about a loss of contractile function, progressively severe disability and death[59].

Failing hearts are characterized by reduced contractile properties caused by impaired Ca^{2+} cycling between the sarcoplasm and SR. This could be attributable to the expression of SERCA2a, that is decreased at the transcript level and the protein level[32]. Moreover, the SERCA2a:PLN ratio is reduced in patients with advanced HF, with a relative increase in the unphosphorylated PLN fraction allowing PLN to inhibit SERCA2a[60]. This diminished phosphorylation of PLN can be attributed to an attenuation of β-adrenergic cascade due to receptor desensitization, receptor down-regulation and uncoupling, which occur during disease progression[61]. Furthermore, decreases in the protein level of HAX-1 and I-1 as well as PKA-phosphorylation of I-1 have been observed in failing hearts, which are expected to further contribute to the depressed SR Ca^{2+}-cycling homeostasis[27].

For this reason, restoration of reduced SERCA2a levels and/or activity is a potential treatment option for HF.

1.6.1 SERCA2a-PLN complex as therapeutic target for heart failure

Different therapeutics approaches that activate SERCA2a or inhibit PLN have been implemented in the last years[62](Figure 12).

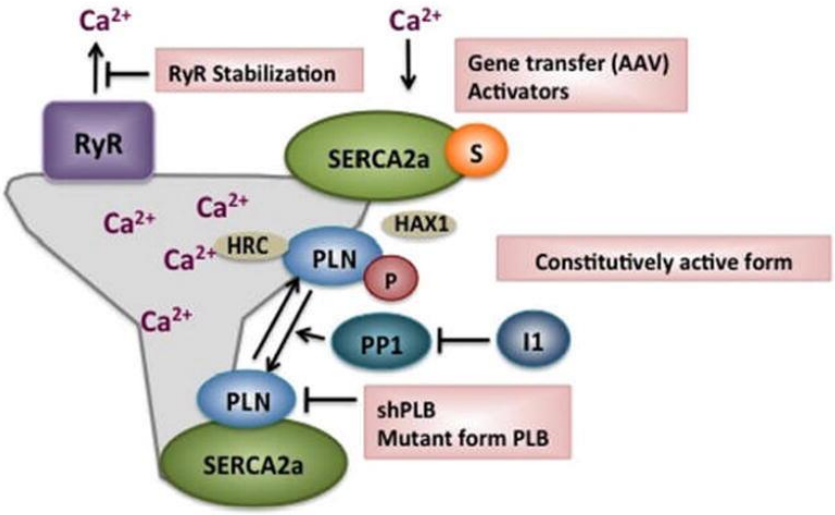

Figure 12. Strategies of improving Ca^{2+} handling and SR Ca-content in HF. These strategies have focused pharmacologically on inhibiting the Na^+/K^+ ATPase which results in increased intracellular Ca^{2+} and more recently on stabilizing the Ryanodine Receptor in resulting in decreased SR Ca^{2+} leak. Gene editing techniques have focused on enhancing SERCA2a's activity by either increasing the level of SERCA2a or altering the expression of its partners.

1.6.1.1 SERCA stimulation or overexpression

The use of therapeutic approaches that increase SERCA2 expression or function has been suggested as effective strategies to alleviate the loss of contractile function that develops with HF[22]. In this field, several approaches have been proposed, such as the use of drugs, gene therapy or SERCA2a SUMOylation.

1.6.1.1.1 Drugs

Drugs that prevent the reduction or assist in restoring SERCA2a expression or activity, are considered as good potential therapeutic tools to improve Ca^{2+}

homeostasis. These drugs can be divided into two groups: those which affect SERCA2a expression and those which modulate its function (Table 2)[22].

Table 2. List of drugs that alter cardiac SERCA2a/b expression and function *(Modified from [22])*

SERCA2a/b expression		SERCA2a/b function	
↑		↑	
Name	**Reference**	**Name**	**Reference**
Enalapril	Guo et al. (2003)	**Etomoxir**	Greene et al. (2000)
Losartan	Guo et al. (2003)	**Enalapril**	Guo et al. (2003)
Carvedilol	Koitabashi et al. (2005)	**Losartan**	Guo et al. (2003)
Phenylephrine	Anwar et al. (2005)	**Carvedilol**	Koitabashi et al. (2005)
Candesartan	Soga et al. (2006)	**Astragaloside IV**	Xu et al. (2008)
Insulin-like growth factor I	Byrne et al. (2009)	**Ivabradine**	Maczewski and Mackiewicz (2008)
Astragaloside IV	Xu et al. (2008)	**Istaroxime**	Khan et al. (2009), Micheletti et al. (2007)
Metoprolol	Bridges et al. (2005), Kubo et al. (2001)	**Heparin-derived oligosaccharides**	Hughes et al. (2010)
Resveratrol	Sulaiman et al. (2010)	**Hydralazine**	Kao et al. (2011)
Hydralazine	Kao et al. (2011)	**Oxymatrine**	Gwathmey et al. (2011)
Oxymatrine	Gwathmey et al. (2011)	**Glucocorticoids**	Pearl et al. (2011)

Despite significant advances with the use of pharmacological drugs such as inotropic agents in the treatment of HF, the use of these drugs remains controversial mostly due to their pleiotropic effects.

So, it has been suggested that a targeted approach could be more effective.

In this field, Kaneko and colleagues[62] proposed a new compound, that was able to selectively stimulate SERCA2a, without affecting SERCA1, through the binding and inhibition of PLN, but further improvement of *in vivo* activity and pharmacokinetic properties are required.

Istaroxime is a first-in-class original luso-inotropic agent, shown to be highly effective and safe in patients[63], thanks to its stimulatory action on SERCA2a. A detailed description of istaroxime is reported below.

1.6.1.1.2 Gene Therapy

Recently, gene therapy has received increasing attention as a targeted delivery approach to reverse depressed contractile function. SERCA2a viral-mediated gene transfer used in animal models and in human failing cardiomyocytes has shown some beneficial effects on cardiac performances. Among the many vector systems examined so far, recombinant viral vectors have the highest gene transfer efficiency and are associated with an increased long-term transgenic expression[64]. Among them, adenoviral vectors (AV) and adeno-associated viral vectors (AAV) are the most commonly used vectors in cardiac disease[65].

Based on the extensive evidence that SERCA2a induces beneficial effects in multiple models of HF, in 2007 started the first clinical trial of gene therapy in advanced HF patients named CUPID (Calcium Up-Regulation by Percutaneous Administration of Gene Therapy in Cardiac Disease). It was used an AAV1.SERCA2a vector consisting of an AAV1 capsid and the human SERCA2a cDNA flanked by inverted terminal repeats. Despite promising results after the first 3-years study, in the followed trials CUPID-2, at the end, AAV1.SERCA2a at the dose tested did not improve the clinical course of patients with HF and reduced ejection fraction. Insufficient SERCA2a expression was considered as a cause for the failure of this clinical study[66].

CUPID has paved the way for other clinical trials of SERCA2a gene therapy, such as SERCA-LVAD in UK, where AAV1.SERCA2a was infused in patient who have received a LVAD (Left Ventricular Assistant Device) for chronic HF, and AGENT-HF trial in France[60]. Regarding the first, after 3 years from the treatment, the absolute levels of detectable transgene DNA were low, and no functional benefit was observed[67], while in AGENT-HF trial, any improvement in ventricular remodeling in response to AAV1.SERCA2a was assessed at the dose studied[68]. Both of these trials terminated prematurely due the neutral results of the CUPID-2 outcome trial.

So, further research into the use of gene therapy to treat patients with HF are necessary.

1.6.1.1.3 SUMOylation

The levels of cytoplasmic SUMO1 are regulated in parallel to the levels and activity of SERCA2a and SUMOylation of SERCA2a increases its stability increasing its lifetime and activity. Laboratory studies have demonstrated that SUMOylation of SERCA2a is reduced in HF and targeting it for therapeutic benefits to the heart may be possible[31].

Gene therapy with AAV9.SUMO1 vector to increase SUMO1 expression in an animal model of HF led to markedly improved cardiac function, comparable to SERCA2a gene delivery[31], and it was additive when dual AAV9.SERCA and AAV9.SUMO was applied to the failing heart in vivo[60].

Moreover, it was reported that some drugs could increasing cardiac contractility promoting SERCA2a SUMOylation. In fact, Maning and coworkers[69] reported that carvedilol, a well-known β-blocker used in the treatment of hypertension and HF, stimulates βarrestin2-mediated SERCA2a SUMOylation and activity through the β_1 adrenergic receptor (AR) in cardiac myocytes, translating into direct positive inotropy. However, this unique βarrestin2-dependent pro-contractile effect of carvedilol may be opposed or masked by carvedilol-bound β_2AR subtype signaling.

1.6.1.2 PLN silencing or modulation

PLN is considered as another attractive target for improving SERCA2a activity in HF. During cardiac failure, the level of PLN is often unaffected, but PLN phosphorylation is lower, which causes further loss of SERCA2a activity[32].

Cardiac-specific overexpression of PLN inhibited SR Ca^{2+} uptake and reduced systolic Ca^{2+} levels, contractile parameters, and basal systolic function in mice[70]. In contrast, PLN knockout (KO) mice exhibited enhanced Ca^{2+} cycling and myocardial contractility with no gross developmental abnormalities. The elevated contractile parameters are associated with increased affinity of SERCA2a for Ca^{2+}. These findings suggest that the PLN level may determine the parallel outcomes in SR function and cardiac contractility in mice[32].

Several approaches have been explored including the use of PLN-mimicking antibodies, antisense sequences, and mutated forms of the molecule[71–74].

1.6.1.2.1 PLN inactivation

Ablation of PLN is the most extreme modification of PLN–SERCA interaction and it is impractical for therapeutic purposes and has recently even been identified as a cause for DCM in humans[75].

Differently, in human cardiomyocytes, AAV-mediated overexpression of a mutant non-functional form of PLN improved contraction and relaxation velocities similar to the benefit seen with gene transfer of SERCA2a[71]. Similar findings were observed also in hamsters[73], rats[76] and sheeps[77].

As an alternative to conventional gene therapy, RNA interference (RNAi) therapy was used for the first time in a rat model of HF to suppress PLN expression. Both adenoviral and AAV vectors were used to generate small hairpin RNA to silence PLN, and this resulted in suppressed PLN protein expression. As a consequence, SERCA2a activity increased, resulting in improved systolic and diastolic cardiac function[78].

A more novel approach, avoiding mutations in PLN, is the use of an antibody specifically targeted to the cytoplasmic portion of the protein. In a recent study, it was described a recombinant antibody-based protein (PLN-Ab) that binds to the cytoplasmic domain of phospholamban, mimicking the effects of PLN phosphorylation. PLN-Ab accelerated the decay of the calcium transient when expressed in neonatal rat and adult mouse ventricular cardiac myocytes. In addition, direct injection of adenovirus encoding PLN-Ab into the diabetic mouse heart enhanced contractility when measured in vivo by echocardiography and in ex vivo Langendorff perfused hearts[79].

Furthermore, Dieterle and colleagues[72] described the effects on cardiac function in vivo of a recombinant single chain antibody, developed from avian heavy and light chain IgY chains, that specifically targets the cytoplasmic portion of PLN named PLN-antibody derived protein (PLADP). They demonstrated that expression of PLADP in cardiac myocytes improved cardiac function with enhanced contractility and relaxation in vivo and improved contractility in isolated cardiac myocytes from cardiomyopathic hamster.

These results should be treated cautiously, however, when translating this animal work of PLN inhibition into a potential treatment for HF in humans. A naturally

occurring mutation of PLN in the human population is not associated with improved cardiac function; conversely, it leads to a severe HF phenotype[75].

1.6.1.2.2 Targeting PP1 and I-1

Decreased phosphorylation of PLN in failing hearts is mainly caused by increased PP1 activity, so inhibiting PP1-mediated dephosphorylation of PLN can be another strategy to activate SERCA2a. However, this may have limitations as PP1 is involved in a variety of biological processes in many organs, thus, careful arrangements for targeted inhibition of PP1 specifically in hearts are needed[32]. For this reason, acting on its inhibitor I-1 could be an alternative approach. Different studies reported the efficacy of ablation or adenoviral-mediated expression of a truncated form of I-1 (I-1 c) enhanced contractile parameters and also enhanced Ca^{2+} kinetics of human failing cardiomyocytes[80]. Collectively, overexpression of I-1 may be valuable therapy for the treatment of HF.

1.7 ISTAROXIME

Istaroxime [(E,Z)-3-((2-Aminoethoxy)imino)androstane-6,17-dione Hydrochloride] (or PST2744, Figure 13) is a small-molecule drug under phase 2 of clinical trial with an interesting profile for the treatment of acute HF.

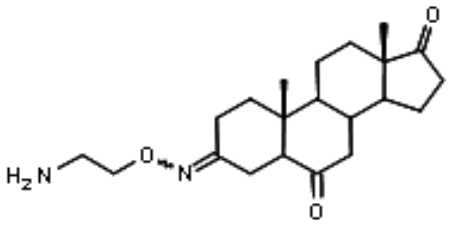

Figure 13: Chemical structure of istaroxime *(from [81])*

Istaroxime is the first-in-class original luso-inotropic agent, shown to be highly effective and safe in patients[63]. Istaroxime is a steroidal compound not related to cardiac glycosides with a double mechanism of action that consists in the ability to inhibit Na^+/K^+ ATPase and enhance SERCA2a ATPase activity[82], this last obtained through the relief of PLN inhibitory effect on SERCA2a[83], without inducing spontaneous Ca^{2+} release (SCR) from SR[82,84]. In fact, as reported in literature, isolated stimulation of SERCA by itself can increase the intra-SR Ca^{2+} threshold for Ca^{2+} wave generation, limiting the generation and propagation of these events. This implies a negative feedback which results in a mitigation of the Ca^{2+} related arrhythmogenicity[85]. Thus, istaroxime increases overall cell Ca^{2+} content while promoting rapid Ca^{2+} sequestration into the SR. Moreover, the lack of CaMKII activation is an additional mechanism underlying the low arrhythmogenicity of this drug[86].

The peculiar combination of targets seems to confer istaroxime a better safety profile compared with other Na^+/K^+ ATPase inhibitors, like digitalis that has been extensively used as a therapy for patients suffering HF because of its positive inotropic effect[87]. However, in the past decades, the use of digitalis compounds like digoxin was strongly reduced because of their associated toxicity, which includes life-threatening arrhythmias and clinical trials not providing evidence of reduced mortality[88].

Studies on istaroxime in healthy and failing animal models started about 20 years ago. In brief, in 2005 we identified the association of the favorable inotropy-to-toxicity ratio previously described for istaroxime[81] with direct SERCA2a stimulation[82]. This

unique characteristic of istaroxime was then proved by testing its efficacy in failing hearts. In 2007 Micheletti and coworkers[89] showed for the first time that istaroxime i.v. infusion significantly increased both contraction and relaxation indexes in failing guinea pig (pressure overload HF). We then characterized at the cellular level istaroxime ability to restore intracellular Ca^{2+} abnormalities in failing guinea pig myocytes stimulating SERCA2a and favoring SR Ca^{2+} compartmentalization[90], thus reducing the toxicity associated with Na^+/K^+ pump blockade[84].

In addition, Sabbah and colleagues[91] in 2007 reported the effect of acute i.v. administration of istaroxime in dogs with advanced HF. In this model, istaroxime elicited potent positive luso-inotropic effects and, unlike classic cyclic adenosine monophospate–dependent positive inotropic agents, istaroxime induced its benefits without increasing myocardial oxygen consumption or heart rate. Lack of the proarrhythmic effect (expected from Na^+/K^+ inhibition) is likely due to SERCA2a stimulation. So, it is logical to predict that a pure SERCA2a activator may exert substantial antiarrhythmic effects, at least under common conditions characterized by SR instability, like HF. In line with this, our group reported that istaroxime at concentration that marginally affects Na^+/K^+ ATPase, was able to improve intracellular Ca^{2+} handling and diastolic function in a model of diabetic cardiomyopathy[92], indicating that selective SERCA2a stimulation can be considered a promising therapeutic approach for diastolic dysfunction treatment.

Istaroxime was also shown enhancing LV performance even in the context of acute myocardial infarction in dogs[93].

A more recent study published in 2021[94] explored the effect of istaroxime in PLN p.Arg14del zebrafish model. This mutation was widely characterized in the last years since was found in patients with dilated or arrhythmogenic cardiomyopathy[95]. In particular, p.Arg14del causes cardiac contractile dysfunction and arrhythmogenesis by affecting intracellular Ca^{2+} dynamics. Istaroxime treatment ameliorates the in vivo Ca^{2+} dysregulation while it improves cardiac relaxation in zebrafish embryos and rescues the cellular action potential duration alternans in isolated ventricular myocytes from adult zebrafish.

Animal studies were translated into clinical trials. A phase 1-2 clinical trial in humans with chronic stable HF was the first evaluation of istaroxime in humans[96], suggested that this molecule is potentially useful in the treatment of HF and may offer a unique

treatment for systolic and/or diastolic dysfunction. The first phase 2, randomized, double-blind, placebo-controlled, multicenter dose escalation exploratory study comparing 3 different doses of istaroxime to placebo was carried out in patients with LV systolic dysfunction (LV ejection fraction ≤35%) admitted to the hospital with worsening HF (HORIZON-HF study)[63,97,98]. Six hours istaroxime infusion resulted in improvements of both left ventricular diastolic and systolic function, with a slight increase in systolic blood pressure and reduction in HR. Recently, Carubelli and coworkers[99] assessed the effects of a 24 h infusion of istaroxime in patients hospitalised for acute HF, showing again improved parameters of diastolic and systolic cardiac function without major cardiac adverse effects. Lastly, in a phase 2a study of patients with acute HF related pre-cardiogenic shock (pre-CS), istaroxime improved blood pressure and some echocardiography measures related to HF[100].

Chronic effects of istaroxime were evaluated after oral treatment of Bio TO.2 Syrian hamsters, which represent a reproducible model of progressive cardiac hypertrophy, dilation and failure, that exhibits features resembling those of dilated cardiomyopathy in human. These hamsters show a reduced heart rate variability (HRV) due to a shift towards increased sympathetic and decreased parasympathetic tones[101], and it could be considered predictive for cardiovascular disease. A similar shift was reported in patients[102–104]. Improvement of cardiac function and HRV was observed after chronic treatment, in fact, istaroxime-treated hamsters sympathetic drive was enhanced and that the higher HRV indexes found are mainly due to a preserved parasympathetic activity[101].

Even though the compound demonstrated good tolerability in a phase I/II safety study, symptoms related to the gastro-intestinal tract and pain at the injection site were reported as the most frequent side effects. A drug delivery system was designed to encapsulate istaroxime and minimize the pain perceived upon administration[105].

Overall, in spite of the clear benefits induced by istaroxime i.v. infusion in human and animal failing models, its use in chronic HF therapy is generally limited by its short plasma half-life (less than 1 hour in humans), because of extensive hepatic metabolism to a molecule, named PST3093[98,99]; this restricts istaroxime usage to acute intravenous therapy.

Starting from this, new istaroxime follow-on compounds, chemically stable and thus suitable for chronic HF therapy have been developed by our group.

1.8 REFERENCES

(1) Bers, D. M. Cardiac Excitation–Contraction Coupling. *Nature* **2002**, *415*, 198–205.

(2) Frank, K.; Kranias, E. G. Phospholamban and Cardiac Contractility. *Ann Med* **2000**, *32* (8), 572–578. https://doi.org/10.3109/07853890008998837.

(3) Anderson, D. M.; Makarewich, C. A.; Anderson, K. M.; Shelton, J. M.; Bezprozvannaya, S.; Bassel-Duby, R.; Olson, E. N. Widespread Control of Calcium Signaling by a Family of SERCA-Inhibiting Micropeptides. *Sci Signal* **2016**, *9* (457). https://doi.org/10.1126/scisignal.aaj1460.

(4) MacLennan, D. H.; Kranias, E. G. Phospholamban: A Crucial Regulator of Cardiac Contractility. *Nature Reviews in Molecular Cell Biology* **2003**, *4*, 566–577. https://doi.org/10.1038/nrm1151.

(5) Michalak, M.; Corbett, E. F.; Mesaeli, N.; Nakamura, K.; Opas, M. Calreticulin: One Protein, One Gene, Many Functions. *Biochemical Journal* **1999**, *344*, 281–292.

(6) Suk, J. Y.; Kim, Y. S.; Park, W. J. HRC (Histidine-Rich Ca2+ Binding Protein) Resides in the Lumen of Sarcoplasmic Reticulum as a Multimer. *Biochem Biophys Res Commun* **1999**, *263*, 667–671.

(7) Periasamy, M.; Kalyanasundaram, A. SERCA Pump Isoforms: Their Role in Calcium Transport and Disease. *Muscle and Nerve*. April 2007, pp 430–442. https://doi.org/10.1002/mus.20745.

(8) Brandls, C. J.; Deleon, S.; Martin, D. R.; Maclennan, D. H. Adult Forms of the Ca2+ATPase of Sarcoplasmic Reticulum. Expression in Developing Skeletal Muscle. *J Biol Chem* **1987**, *262* (8), 3768–3774.

(9) Brandl, C. J.; Green, N. M.; Korczak, B.; Maclennan, D. H. *Two Ca2+ ATPase Genes: Homologies and Mechanistic Implications of Deduced Amino Acid Sequences*; 1986; Vol. 44.

(10) MacLennan, D. H.; Brandl, C. J.; Korczak, B.; Michael Greent, N. Amino-Acid Sequence of a Ca2+ + Mg2+-Dependent ATPase from Rabbit Muscle Sarcoplasmic Reticulum, Deduced from Its Complementary DNA Sequence. *Nature* **1985**, *316*, 696–700.

(11) Zarain-Herzbergs, A.; Maclennangll, D. H.; Periasamyll, M. Characterization of Rabbit Cardiac Sarco(Endo)Plasmic Reticulum Ca2+-ATPase Gene. *J Biol Chem* **1990**, *265* (8), 4670–4677.

(12) Gunteski-Hamblin, A.-M.; Greeb, J.; Shull, G. E. A Novel Ca2+ Pump Expressed in Brain, Kidney, and Stomach Is Encoded by an Alternative Transcript of the Slow-Twitch Muscle Sarcoplasmic Reticulum Ca-ATPase Gene. *J Biol Chem* **1988**, *263* (29), 15032–15040.

(13) Dally, S.; Bredoux, R.; Corvazier, E.; Andersen, J. P.; Clausen, J. D.; Dode, L.; Fanchaouy, M.; Gelebart, P.; Monceau, V.; del Monte, F.; Gwathmey, J. K.; Hajjar, R.; Chaabane, C.; Bobe, R.; Raies, A.; Enouf, J. Ca2+-ATPases in Non-Failing and Failing Heart: Evidence for a Novel Cardiac Sarco/Endoplasmic Reticulum Ca 2+-ATPase 2 Isoform (SERCA2c). *Biochemical Journal* **2006**, *395*, 249–258. https://doi.org/10.1042/BJ20051427.

(14) Anger, M.; Samuel, J.-L.; Marotte, F.; Wuytack, F.; Rappaport, L.; Lompr6, A.-M. The Sarco(Endo)Plasmic Reticulum Ca2+-ATPase MRNA Isoform, SERCA 3, Is Expressed in Endothelial and Epithelial Cells in Various Organs. *FEBS letter* **1993**, *334* (1), 45–48. https://doi.org/10.1016/0014-5793(93)81677-R.

(15) Xu, H.; van Remmen, H. The SarcoEndoplasmic Reticulum Calcium ATPase (SERCA) Pump: A Potential Target for Intervention in Aging and Skeletal Muscle Pathologies. *Skeletal Muscle*. BioMed Central Ltd December 1, 2021. https://doi.org/10.1186/s13395-021-00280-7.

(16) Vandecaetsbeek, I.; Trekels, M.; de Maeyer, M.; Ceulemans, H.; Lescrinier, E.; Raeymaekers, L.; Wuytack, F.; Vangheluwe, P. Structural Basis for the High Ca2+ Affinity of the Ubiquitous SERCA2b Ca2+ Pump. *The Proceedings of the National Academy of Sciences* **2009**, *106* (44), 18533–18538.

(17) Zhang, Y.; Inoue, M.; Tsutsumi, A.; Watanabe, S.; Nishizawa, T.; Nagata, K.; Kikkawa, M.; Inaba, K. Cryo-EM Structures of SERCA2b Reveal the Mechanism of Regulation by the Luminal Extension Tail. *Sci Adv* **2020**, *6*, 147–159.

(18) Dode, L.; Andersen, J. P.; Leslie, N.; Dhitavat, J.; Vilsen, B.; Hovnanian, A. Dissection of the Functional Differences between Sarco(Endo)Plasmic Reticulum Ca2+ -ATPase (SERCA) 1 and 2 Isoforms and Characterization of Darier Disease (SERCA2) Mutants by Steady-State and Transient Kinetic Analyses. *Journal of Biological Chemistry* **2003**, *278* (48), 47877–47889. https://doi.org/10.1074/jbc.M306784200.

(19) Zhihao, L.; Jingyu, N.; Lan, L.; Michael, S.; Rui, G.; Xiyun, B.; Xiaozhi, L.; Guanwei, F. SERCA2a: A Key Protein in the Ca2+ Cycle of the Heart Failure. *Heart Failure Reviews*. Springer May 1, 2020, pp 523–535. https://doi.org/10.1007/s10741-019-09873-3.

(20) Vangheluwe, P.; Raeymaekers, L.; Dode, L.; Wuytack, F. Modulating Sarco(Endo)Plasmic Reticulum Ca2+ ATPase 2 (SERCA2) Activity: Cell Biological Implications. *Cell Calcium* **2005**, *38* (3-4 SPEC. ISS.), 291–302. https://doi.org/10.1016/j.ceca.2005.06.033.

(21) McIntosh, D. B.; Woolley, D. G.; MacLennan, D. H.; Vilsen, B.; Andersen, J. P. Interaction of Nucleotides with Asp351 and the Conserved Phosphorylation Loop of Sarcoplasmic Reticulum Ca2+-ATPase. *Journal of Biological Chemistry* **1999**, *274* (36), 25227–25236. https://doi.org/10.1074/jbc.274.36.25227.

(22) Shareef, M. A.; Anwer, L. A.; Poizat, C. Cardiac SERCA2A/B: Therapeutic Targets for Heart Failure. *European Journal of Pharmacology*. February 5, 2014, pp 1–8. https://doi.org/10.1016/j.ejphar.2013.12.018.

(23) Toyoshima, C.; Iwasawa, S.; Ogawa, H.; Hirata, A.; Tsueda, J.; Inesi, G. Crystal Structures of the Calcium Pump and Sarcolipin in the Mg 21-Bound E1 State. *Nature* **2013**, *495*, 260–264. https://doi.org/10.1038/nature11899.

(24) Winther, A.-M. L.; Bublitz, M.; Karlsen, J. L.; Møller, J. v; Hansen, J. B.; Nissen, P.; Buch-Pedersen, M. J. The Sarcolipin-Bound Calcium Pump Stabilizes Calcium Sites Exposed to the Cytoplasm. *Nature* **2013**, *495*, 265–269. https://doi.org/10.1038/nature11900.

(25) Li, X.; Li, W.; Gao, Z.; Li, H. Association of Cardiac Injury with Iron-Increased Oxidative and Nitrative Modifications of the SERCA2a Isoform of Sarcoplasmic Reticulum Ca2+-ATPase in Diabetic Rats. *Biochimie* **2016**, *127*, 144–152. https://doi.org/10.1016/j.biochi.2016.05.011.

(26) Nusier, M.; Shah, A. K.; Dhalla, N. S. Structure-Function Relationships and Modifications of Cardiac Sarcoplasmic Reticulum Ca2+-Transport. *Physiol Res* **2021**, *70*, 443–470. https://doi.org/10.33549/physiolres.934805.

(27) Kranias, E. G.; Hajjar, R. J. Modulation of Cardiac Contractility by the Phopholamban/SERCA2a Regulatome. *Circ Res* **2012**, *110* (12), 1646–1660. https://doi.org/10.1161/CIRCRESAHA.111.259754.

(28) Schwartz, R. J.; Yeh, E. T.; Aruni Bhatnagar, by; Marian, A. J. Weighing in on Heart Failure: The Role of SERCA2a SUMOylation SUMO1-Dependent Modulation of

SERCA2a in Heart Failure. *Circ Res* **2012**, *110*, 198–199. https://doi.org/10.1161/RES.0b013e318246f187.

(29) Kim, E. Y.; Zhang, Y.; Beketaev, I.; Segura, A. M.; Yu, W.; Xi, Y.; Chang, J.; Wang, J. SENP5, a SUMO Isopeptidase, Induces Apoptosis and Cardiomyopathy. *J Mol Cell Cardiol* **2015**, *78*, 154–164. https://doi.org/10.1016/j.yjmcc.2014.08.003.

(30) Shimizu, Y.; Lambert, J. P.; Nicholson, C. K.; Kim, J. J.; Wolfson, D. W.; Cho, H. C.; Husain, A.; Naqvi, N.; Chin, L. S.; Li, L.; Calvert, J. W. DJ-1 Protects the Heart against Ischemia-Reperfusion Injury by Regulating Mitochondrial Fission. *J Mol Cell Cardiol* **2016**, *97*, 56–66. https://doi.org/10.1016/j.yjmcc.2016.04.008.

(31) Kho, C.; Lee, A.; Jeong, D.; Oh, J. G.; Chaanine, A. H.; Kizana, E.; Park, W. J.; Hajjar, R. J. SUMO1-Dependent Modulation of SERCA2a in Heart Failure. *Nature* **2011**, *477* (7366), 601–606. https://doi.org/10.1038/nature10407.

(32) Park, J.; Oh, J. G. SERCA2a: A Prime Target for Modulation of Cardiac Contractility during Heart Failure. *BMB Rep* **2013**, *46*, 237–243.

(33) Mendler, L.; Braun, T.; Müller, S. The Ubiquitin-Like SUMO System and Heart Function: From Development to Disease. *Circulation Research*. Lippincott Williams and Wilkins January 8, 2016, pp 132–144. https://doi.org/10.1161/CIRCRESAHA.115.307730.

(34) Du, Y.; Liu, P.; Xu, T.; Pan, D.; Zhu, H.; Zhai, N.; Zhang, Y.; Li, D. Luteolin Modulates SERCA2a Leading to Attenuation of Myocardial Ischemia/Reperfusion Injury via Sumoylation at Lysine 585 in Mice. *Cellular Physiology and Biochemistry* **2018**, *45* (3), 883–898. https://doi.org/10.1159/000487283.

(35) Knyushko, T. v.; Sharov, V. S.; Williams, T. D.; Schöneich, C.; Bigelow, D. J. 3-Nitrotyrosine Modification of SERCA2a in the Aging Heart: A Distinct Signature of the Cellular Redox Environment. *Biochemistry* **2005**, *44* (39), 13071–13081. https://doi.org/10.1021/bi051226n.

(36) Lancel, S.; Zhang, J.; Evangelista, A.; Trucillo, M. P.; Tong, X.; Siwik, D. A.; Cohen, R. A.; Colucci, W. S. Nitroxyl Activates SERCA in Cardiac Myocytes via Glutathiolation of Cysteine 674 Results and Discussion HNO Activation of SERCA Involves Reversible, Oxidative Thiol Modification. *Circ Res* **2009**, *104* (6), 720–723. https://doi.org/10.1161/CIRCRESAHA.108.188441.

(37) Yang, X.; Qian, K. Protein O-GlcNAcylation: Emerging Mechanisms and Functions. *Nature* **2017**, *18*, 452–465. https://doi.org/10.1038/nrm.2017.22.

(38) Gorski, P. A.; Jang, S. P.; Jeong, D.; Lee, A.; Lee, P.; Oh, J. G.; Chepurko, V.; Yang, D. K.; Kwak, T. H.; Eom, S. H.; Park, Z.-Y.; Yoo, Y. J.; Kim, D. H.; Kook, H.; Sunagawa, Y.; Morimoto, T.; Hasegawa, K.; Sadoshima, J.; Vangheluwe, P.; Hajjar, R. J.; Park, W. J.; Kho, C. Role of SIRT1 in Modulating Acetylation of the Sarco-Endoplasmic Reticulum Ca2+-ATPase in Heart Failure. *Circ Res* **2019**, *124*, 63–80. https://doi.org/10.1161/CIRCRESAHA.118.313865.

(39) Quick, A. P.; Wang, Q.; Philippen, L. E.; Barreto-Torres, G.; Chiang, D. Y.; Beavers, D.; Wang, G.; Khalid, M.; Reynolds, J. O.; Campbell, H. H. T.; Showell, J.; McCauley, M. D.; Scholten, A.; Wehrens, X. H. T. SPEG (Striated Muscle Preferentially Expressed Protein Kinase) Is Essential for Cardiac Function by Regulating Junctional Membrane Complex Activity. *Circ Res* **2016**, *120*, 110–119. https://doi.org/10.1161/CIRCRESAHA.116.309977.

(40) Simmerman, H. K. B.; Jones, L. R. Phospholamban: Protein Structure, Mechanism of Action, and Role in Cardiac Function. *Physiol Rev* **1998**, *78* (4).

(41) Gustavsson, M.; Verardi, R.; Mullen, D. G.; Mote, K. R.; Traaseth, N. J.; Gopinath, T.; Veglia, G. Allosteric Regulation of SERCA by Phosphorylation Mediated Conformational Shift of Phospholamban. *Proc Natl Acad Sci U S A* **2013**, *110* (43), 17338–17343. https://doi.org/10.1073/pnas.1303006110.

(42) Kranias, E. G. Regulation of Calcium Transport by Protein Phosphatase Activity Associated with Cardiac Sarcoplasmic Reticulum. *J Biol Chem* **1985**, *260* (20), 11006–11010.

(43) Kimura, Y.; Kurzydlowski, K.; Tada, M.; MacLennan, D. H. Phospholamban Inhibitory Function Is Activated by Depolymerization. *J Biol Chem* **1997**, *272* (24), 15061–15064.

(44) Glaves, J. P.; Primeau, J. O.; Espinoza-Fonseca, L. M.; Lemieux, M. J.; Young, H. S. The Phospholamban Pentamer Alters Function of the Sarcoplasmic Reticulum Calcium Pump SERCA. *Biophys J* **2019**, *116* (4), 633–647. https://doi.org/10.1016/j.bpj.2019.01.013.

(45) Rathod, N.; Bak, J. J.; Primeau, J. O.; Fisher, L. E.; Michel Espinoza-Fonseca, L.; Joanne Lemieux, M.; Young, H. S.; Zanotti, G.; Calì, T. Nothing Regular about the Regulins: Distinct Functional Properties of SERCA Transmembrane Peptide Regulatory Subunits. *Journal of Molecular Sciences* **2021**, 22. https://doi.org/10.3390/ijms22168891.

(46) Glaves, J. P.; Primeau, J. O.; Gorski, P. A.; Espinoza-Fonseca, L. M.; Lemieux, M. J.; Young, H. S. Interaction of a Sarcolipin Pentamer and Monomer with the Sarcoplasmic Reticulum Calcium Pump, SERCA. *Biophys J* **2020**, *118* (2), 518–531. https://doi.org/10.1016/j.bpj.2019.11.3385.

(47) Gorski, P. A.; Glaves, J. P.; Vangheluwe, P.; Young, H. S. Sarco(Endo)Plasmic Reticulum Calcium ATPase (SERCA) Inhibition by Sarcolipin Is Encoded in Its Luminal Tail. *Journal of Biological Chemistry* **2013**, *288* (12), 8456–8467. https://doi.org/10.1074/jbc.M112.446161.

(48) Asahi, M.; Sugita, Y.; Kurzydlowski, K.; de Leon, S.; Tada, M.; Toyoshima, C.; MacLennan, D. H. Sarcolipin Regulates Sarco(Endo)Plasmic Reticulum-ATPase (SERCA) by Binding to Transmembrane Alone or in Association with Phospholamban. *The Proceeding of the National Academy of Sciences* **2003**, *100* (9), 5040–5045.

(49) Nelson, B. R.; Makarewich, C. A.; Anderson, D. M.; Winders, B. R.; Troupes, C. D.; Wu, F.; Reese, A. L.; McAnally, J. R.; Chen, X.; Kavalali, E. T.; Cannon, S. C.; Houser, S. R.; Bassel-Duby, R.; Olson, E. N. A Peptide Encoded by a Transcriptannotated as Long Noncoding RNAenhances SERCA Activity in Muscle. *Science (1979)* **2016**, *351*, 271–275. https://doi.org/10.1126/science.aad3023.

(50) Makarewich, C. A.; Munir, A. Z.; Schiattarella, G. G.; Bezprozvannaya, S.; Raguimova, O. N.; Cho, E. E.; Vidal, A. H.; Robia, S. L.; Bassel-Duby, R.; Olson, E. N. The DWORF Micropeptide Enhances Contractility and Prevents Heart Failure in a Mouse Model of Dilated Cardiomyopathy. *Elife* **2018**, *7*. https://doi.org/10.7554/eLife.38319.001.

(51) Li, A.; Yuen, S. L.; Stroik, D. R.; Kleinboehl, E.; Cornea, R. L.; Thomas, D. D. The Transmembrane Peptide DWORF Activates SERCA2a via Dual Mechanisms. *Journal of Biological Chemistry* **2021**, *296*. https://doi.org/10.1016/j.jbc.2021.100412.

(52) Kiewitz, R.; Acklin, C.; Schäfer, B. W.; Maco, B.; Uhrík, B.; Wuytack, F.; Erne, P.; Heizmann, C. W. Ca2+-Dependent Interaction of S100A1 with the Sarcoplasmic Reticulum Ca2+-ATPase2a and Phospholamban in the Human Heart. *Biochem Biophys Res Commun* **2003**, *306* (2), 550–557. https://doi.org/10.1016/S0006-291X(03)00987-2.

(53) Arvanitis, D. A.; Vafiadaki, E.; Fan, G. C.; Mitton, B. A.; Gregory, K. N.; del Monte, F.; Kontrogianni-Konstantopoulos, A.; Sanoudou, D.; Kranias, E. G. Histidine-Rich Ca-Binding Protein Interacts with Sarcoplasmic Reticulum Ca-ATPase. *Am J*

Physiol Heart Circ Physiol **2007**, *293* (3). https://doi.org/10.1152/ajpheart.00278.2007.

(54) Zhao, W.; Waggoner, J. R.; Zhang, Z.-G.; Lam, C. K.; Han, P.; Qian, J.; Schroder, P. M.; Mitton, B.; Kontrogianni-Konstantopoulos, A.; Robia, S. L.; Kranias, E. G. The Anti-Apoptotic Protein HAX-1 Is a Regulator of Cardiac Function. *The Proceedings of the National Academy of Sciences* **2009**, *106* (49), 20776–20781.

(55) Pathak, A.; del Monte, F.; Zhao, W.; Schultz, J.-E.; Lorenz, J. N.; Bodi, I.; Weiser, D.; Hahn, H.; Carr, A. N.; Syed, F.; Mavila, N.; Jha, L.; Qian, J.; Marreez, Y.; Chen, G.; Mcgraw, D. W.; Kevin Heist, E.; Guerrero, J. L.; Depaoli-Roach, A. A.; Hajjar, R. J.; Kranias, E. G. Enhancement of Cardiac Function and Suppression of Heart Failure Progression By Inhibition of Protein Phosphatase 1. *Circ Res* **2005**, *96*, 756–766. https://doi.org/10.1161/01.RES.0000161256.85833.fa.

(56) Qian, J.; Vafiadaki, E.; Florea, S. M.; Singh, V. P.; Song, W.; Lam, C. K.; Wang, Y.; Yuan, Q.; Pritchard, T. J.; Cai, W.; Haghighi, K.; Rodriguez, P.; Wang, H.-S.; Sanoudou, D.; Fan, G.-C.; Kranias, E. G. Small Heat Shock Protein 20 Interacts With Protein Phosphatase-1 and Enhances Sarcoplasmic Reticulum Calcium Cycling. *Circ Res* **2011**, *108*, 1429–1438. https://doi.org/10.1161/CIRCRESAHA.110.237644.

(57) Hasenfuss, G.; Meyer, M.; Schillinger, W.; Preuss, M.; Pieske, B.; Just, H.; Meyer, (~) -M. Calcium Handling Proteins in the Failing Human Heart. *Basic Res Cardiol* **1997**, *92*, 87–93.

(58) Vangheluwe, P.; Sipido, K. R.; Raeymaekers, L.; Wuytack, F. New Perspectives on the Role of SERCA2's Ca2+ Affinity in Cardiac Function. *Biochimica et Biophysica Acta - Molecular Cell Research*. November 2006, pp 1216–1228. https://doi.org/10.1016/j.bbamcr.2006.08.025.

(59) Gianni, D.; Chan, J.; Gwathmey, J. K.; del Monte, F.; Hajjar, R. J. SERCA2a in Heart Failure: Role and Therapeutic Prospects. *Journal of Bioenergetics and Biomembranes*. December 2005, pp 375–380. https://doi.org/10.1007/s10863-005-9474-z.

(60) Hayward, C.; Patel, H.; Lyon, A. Gene Therapy in Heart Failure. SERCA2a as a Therapeutic Target. *Circulation journal : official journal of the Japanese Circulation Society*. 2014, pp 2577–2587. https://doi.org/10.1253/circj.CJ-14-1053.

(61) Barki-Harrington, L.; Perrino, C.; Rockman, H. A. Network Integration of the Adrenergic System in Cardiac Hypertrophy. *Cardiovasc Res* **2004**, *63*, 391–402. https://doi.org/10.1016/j.cardiores.2004.03.011.

(62) Kaneko, M.; Yamamoto, H.; Sakai, H.; Kamada, Y.; Tanaka, T.; Fujiwara, S.; Yamamoto, S.; Takahagi, H.; Igawa, H.; Kasai, S.; Noda, M.; Inui, M.; Nishimoto, T. A Pyridone Derivative Activates SERCA2a by Attenuating the Inhibitory Effect of Phospholamban. *Eur J Pharmacol* **2017**, *814*, 1–8. https://doi.org/10.1016/j.ejphar.2017.07.035.

(63) Shah, S. J.; Blair, J. E. A.; Filippatos, G. S.; MacArie, C.; Ruzyllo, W.; Korewicki, J.; Bubenek-Turconi, S. I.; Ceracchi, M.; Bianchetti, M.; Carminati, P.; Kremastinos, D.; Grzybowski, J.; Valentini, G.; Sabbah, H. N.; Gheorghiade, M. Effects of Istaroxime on Diastolic Stiffness in Acute Heart Failure Syndromes: Results from the Hemodynamic, Echocardiographic, and Neurohormonal Effects of Istaroxime, a Novel Intravenous Inotropic and Lusitropic Agent: A Randomized Controlled Trial in Patients Hospitalized with Heart Failure (HORIZON-HF) Trial. *Am Heart J* **2009**, *157* (6), 1035–1041. https://doi.org/10.1016/j.ahj.2009.03.007.

(64) Tilemann, L.; Ishikawa, K.; Weber, T.; Hajjar, R. J. Gene Therapy for Heart Failure. *Circ Res* **2012**, *110*, 777–793. https://doi.org/10.1161/CIRCRESAHA.111.252981.

(65) Gwathmey, J. K.; Yerevanian, A. I.; Hajjar, R. J. Cardiac Gene Therapy with SERCA2a: From Bench to Bedside. *Journal of Molecular and Cellular Cardiology*. May 2011, pp 803–812. https://doi.org/10.1016/j.yjmcc.2010.11.011.

(66) Greenberg, B.; Butler, J.; Felker, G. M.; Ponikowski, P.; Voors, A. A.; Desai, A. S.; Barnard, D.; Bouchard, A.; Jaski, B.; Lyon, A. R.; Pogoda, J. M.; Rudy, J. J.; Zsebo, K. M. Calcium Upregulation by Percutaneous Administration of Gene Therapy in Patients with Cardiac Disease (CUPID 2): A Randomised, Multinational, Double-Blind, Placebo-Controlled, Phase 2b Trial. *The Lancet* **2016**, *387* (10024), 1178–1186. https://doi.org/10.1016/S0140-6736(16)00082-9.

(67) Lyon, A. R.; Babalis, D.; Morley-Smith, A. C.; Hedger, M.; Suarez Barrientos, A.; Foldes, G.; Couch, L. S.; Chowdhury, R. A.; Tzortzis, K. N.; Peters, N. S.; Rog-Zielinska, E. A.; Yang, H.; Welch, S.; Bowles, C. T.; Rahman Haley, S.; Bell, A. R.; Rice, A.; Sasikaran, T.; Johnson, N. A.; Falaschetti, E.; Parameshwar, J.; Lewis, C.; Tsui, S.; Simon, A.; Pepper, J.; Rudy, J. J.; Zsebo, K. M.; Macleod, K. T.; Terracciano, C. M.; Hajjar, R. J.; Banner, N.; Harding, S. E. Investigation of the Safety and Feasibility of AAV1/SERCA2a Gene Transfer in Patients with Chronic

Heart Failure Supported with a Left Ventricular Assist Device Â€“ the SERCA-LVAD TRIAL. *Gene Ther* **2020**, *27*, 579–590. https://doi.org/10.1038/s41434-020-0171-7.

(68) Hulot, J.-S.; Salem, J.-E.; Redheuil, A.; Collet, J.-P.; Varnous, S.; Jourdain, P.; Logeart, D.; Gandjbakhch, E.; Bernard, C.; Hatem, S. N.; Isnard, R.; Cluzel, P.; le Feuvre, C.; Leprince, P.; Hammoudi, N.; Lemoine, F. M.; Klatzmann, D.; Vicaut, E.; Komajda, M.; Montalescot, G.; Lompré, A.-M.; Hajjar, R. J. Effect of Intracoronary Administration of AAV1/SERCA2a on Ventricular Remodelling in Patients with Advanced Systolic Heart Failure: Results from the AGENT-HF Randomized Phase 2 Trial. *Eur J Heart Fail* **2017**, *19*, 1534–1541. https://doi.org/10.1002/ejhf.826.

(69) Maning, J.; Desimine, V. L.; Pollard, C. M.; Ghandour, J.; Lymperopoulos, A. Carvedilol Selectively Stimulates BArrestin2-Dependent SERCA2a Activity in Cardiomyocytes to Augment Contractility. *Int J Mol Sci* **2022**, *23* (19). https://doi.org/10.3390/ijms231911315.

(70) Limas, C. J.; Olivari, M.-T.; Goldenberg, I. F.; Levine, B.; Benditt, D. G.; Simon, A. *Calcium Uptake by Cardiac Sarcoplasmic Reticulum in Human Dilated Cardiomyopathy*; 1987; Vol. 21. https://academic.oup.com/cardiovascres/article/21/8/601/316843.

(71) del Monte, F.; Sian, H. E.; Dec, W. G.; Gwathmey, J. K.; Hajjar, R. J. Targeting Phospholamban by Gene Transfer in Human Heart Failure. *Circulation* **2002**, *105*, 904–907. https://doi.org/10.1161/hc0802.105564.

(72) Dieterle, T.; Meyer, M.; Gu, Y.; Belke, D. D.; Swanson, E.; Iwatate, M.; Hollander, J.; Peterson, K. L.; Ross, J.; Dillmann, W. H. Gene Transfer of a Phospholamban-Targeted Antibody Improves Calcium Handling and Cardiac Function in Heart Failure. *Cardiovasc Res* **2005**, *67*, 678–688. https://doi.org/10.1016/j.cardiores.2005.04.029.

(73) Hoshijima, M.; Ikeda, Y.; Iwanaga, Y.; Minamisawa, S.; Date, M.; Gu, Y.; Iwatate, M.; Li, M.; Wang, L.; Wilson, J. M.; Wang, Y.; Ross, J. J.; Chien, K. R. Chronic Suppression of Heart-Failure Progression by a Pseudophosphorylated Mutant of Phospholamban via in Vivo Cardiac RAAV Gene Delivery. *Nat Med* **2002**, *8* (8), 864–871. https://doi.org/10.1038/nm739.

(74) Ziolo, M. T.; Martin, J. L.; Bossuyt, J.; Bers, D. M.; Pogwizd, S. M. Adenoviral Gene Transfer of Mutant Phospholamban Rescues Contractile Dysfunction in Failing Rabbit Myocytes With Relatively Preserved SERCA Function Materials and

Methods Rabbit Heart Failure Model and Cardiac Myocyte Isolation. *Circ Res* **2005**, *96*, 815–817. https://doi.org/10.1161/01.RES.0000163981.97262.3b.

(75) Haghighi, K.; Schmidt, A. G.; Hoit, B. D.; Brittsan, A. G.; Yatani, A.; Lester, J. W.; Zhai, J.; Kimura, Y.; Dorn, G. W.; MacLennan, D. H.; Kranias, E. G. Superinhibition of Sarcoplasmic Reticulum Function by Phospholamban Induces Cardiac Contractile Failure. *Journal of Biological Chemistry* **2001**, *276* (26), 24145–24152. https://doi.org/10.1074/jbc.M102403200.

(76) Iwanaga, Y.; Hoshijima, M.; Gu, Y.; Iwatate, M.; Dieterle, T.; Ikeda, Y.; Date, M.; Chrast, J.; Matsuzaki, M.; Peterson, K. L.; Chien, K. R.; Ross, J. J. Chronic Phospholamban Inhibition Prevents Progressive Cardiac Dysfunction and Pathological Remodeling after Infarction in Rats. *The Journal of Clinical Investigation* **2004**, *113* (5), 727–736. https://doi.org/10.1172/JCI200418716.

(77) Kaye, D. M.; Preovolos, A.; Marshall, T.; Byrne, M.; Hoshijima, M.; Hajjar, R.; Mariani, J. A.; Pepe, S.; Chien, K. R.; Power, J. M. Percutaneous Cardiac Recirculation-Mediated Gene Transfer of an Inhibitory Phospholamban Peptide Reverses Advanced Heart Failure in Large Animals. *J Am Coll Cardiol* **2007**, *50* (3), 253–260. https://doi.org/10.1016/j.jacc.2007.03.047.

(78) Suckau, L.; Fechner, H.; Chemaly, E.; Krohn, S.; Hadri, L.; Kockskämper, J.; Westermann, D.; Bisping, E.; Ly, H.; Wang, X.; Kawase, Y.; Chen, J.; Liang, L.; Sipo, I.; Vetter, R.; Weger, S.; Kurreck, J.; Erdmann, V.; Tschope, C.; Pieske, B.; Lebeche, D.; Schultheiss, H.-P.; Hajjar, R. J.; Poller, W. C. Long-Term Cardiac-Targeted RNA Interference for the Treatment of Heart Failure Restores Cardiac Function and Reduces Pathological Hypertrophy. *Circulation* **2009**, *119*, 1241–1252. https://doi.org/10.1161/CIRCULATIONAHA.108.783852.

(79) Meyer, M.; Belke, D. D.; Trost, S. U.; Swanson, E.; Dieterle, T.; Scott, B.; Cary, S. P.; Ho, P.; Bluhm, W. F.; Mcdonough, P. M.; Silverman, G. J.; Dillmann, W. H.; Dillmann, W. H. A Recombinant Antibody Increases Cardiac Contractility by Mimicking Phospholamban Phosphorylation; A Recombinant Antibody Increases Cardiac Contractility by Mimicking Phospholamban Phosphorylation. *The FASEB Journal* **2004**. https://doi.org/10.1096/fj.03-1231fje.

(80) Carr, A. N.; Schmidt, A. G.; Suzuki, Y.; del Monte, F.; Sato, Y.; Lanner, C.; Breeden, K.; Jing, S.-L.; Allen, P. B.; Greengard, P.; Yatani, A.; Hoit, B. D.; Grupp, I. L.; Hajjar, R. J.; DePaoli-Roach, A. A.; Kranias, E. G. Type 1 Phosphatase, a Negative Regulator of Cardiac Function. *Mol Cell Biol* **2002**, *22* (12), 4124–4135. https://doi.org/10.1128/mcb.22.12.4124-4135.2002.

(81) Micheletti, R.; Mattera, G. G.; Rocchetti, M.; Schiavone, A.; Loi, M. F.; Zaza, A.; Gagnol, R. J. P.; de Munari, S.; Melloni, P.; Carminati, P.; Bianchi, G.; Ferrari, P. Pharmacological Profile of the Novel Inotropic Agent (E,Z)-3-((2-Aminoethoxy)Imino)Androstane-6,17-Dione Hydrochloride (PST2744). *J Pharmacol Exp Ther* **2002**, *303*, 592–600. https://doi.org/10.1124/jpet.102.038331.

(82) Rocchetti, M.; Besana, A.; Mostacciuolo, G.; Micheletti, R.; Ferrari, P.; Sarkozi, S.; Szegedi, C.; Jona, I.; Zaza, A. Modulation of Sarcoplasmic Reticulum Function by Na/K Pump Inhibitors with Different Toxicity: Digoxin and PST2744 [(E,Z)-3-((2-Aminoethoxy)Imino)Androstane-6,17-Dione Hydrochloride]. *J Pharmacol Exp Ther* **2005**, *313*, 207–215. https://doi.org/10.1124/jpet.104.077933.

(83) Ferrandi, M.; Barassi, P.; Tadini-Buoninsegni, F.; Bartolommei, G.; Molinari, I.; Tripodi, M. G.; Reina, C.; Moncelli, M. R.; Bianchi, G.; Ferrari, P. Istaroxime Stimulates SERCA2a and Accelerates Calcium Cycling in Heart Failure by Relieving Phospholamban Inhibition. *Br J Pharmacol* **2013**, *169*, 1849–1861. https://doi.org/10.1111/bph.12288.

(84) Alemanni, M.; Rocchetti, M.; Re, D.; Zaza, A. Role and Mechanism of Subcellular Ca2+ Distribution in the Action of Two Inotropic Agents with Different Toxicity. *J Mol Cell Cardiol* **2011**, *50* (5), 910–918. https://doi.org/10.1016/j.yjmcc.2011.02.008.

(85) Fernandez-Tenorio, M.; Niggli, E. Stabilization of Ca2+ Signaling in Cardiac Muscle by Stimulation of SERCA. *J Mol Cell Cardiol* **2018**, *119*, 87–95. https://doi.org/10.1016/j.yjmcc.2018.04.015.

(86) Racioppi, M. F.; Burgos, J. I.; Morell, M.; Gonano, L. A.; Petroff, M. V. Cellular Mechanisms Underlying the Low Cardiotoxicity of Istaroxime. *J Am Heart Assoc* **2021**, *10* (14). https://doi.org/10.1161/JAHA.120.018833.

(87) Maack, C.; Eschenhagen, T.; Hamdani, N.; Heinze, F. R.; Lyon, A. R.; Manstein, D. J.; Metzger, J.; Papp, Z.; Tocchetti, C. G.; Yilmaz, M. B.; Anker, S. D.; Balligand, J. L.; Bauersachs, J.; Brutsaert, D.; Carrier, L.; Chlopicki, S.; Cleland, J. G.; de Boer, R. A.; Dietl, A.; Fischmeister, R.; Harjola, V. P.; Heymans, S.; Hilfiker-Kleiner, D.; Holzmeister, J.; de Keulenaer, G.; Limongelli, G.; Linke, W. A.; Lund, L. H.; Masip, J.; Metra, M.; Mueller, C.; Pieske, B.; Ponikowski, P.; Risti, A.; Ruschitzka, F.; Seferovi, P. M.; Skouri, H.; Zimmermann, W. H.; Mebazaa, A. Treatments Targeting Inotropy. *Eur Heart J* **2019**, *40* (44), 3626-3640D. https://doi.org/10.1093/eurheartj/ehy600.

(88) The Digitalis Investigation Group. The Effect of Digoxin on Mortality and Morbidity in Patients with Heart Failure. *N Engl J Med* **1997**, *336* (8), 525–533.

(89) Micheletti, R.; Palazzo, F.; Barassi, P.; Giacalone, G.; Ferrandi, M.; Schiavone, A.; Moro, B.; Parodi, O.; Ferrari, P.; Bianchi, G. Istaroxime, a Stimulator of Sarcoplasmic Reticulum Calcium Adenosine Triphosphatase Isoform 2a Activity, as a Novel Therapeutic Approach to Heart Failure. *American Journal of Cardiology* **2007**, *99* (2 SUPPL.). https://doi.org/10.1016/j.amjcard.2006.09.003.

(90) Rocchetti, M.; Alemanni, M.; Mostacciuolo, G.; Barassi, P.; Altomare, C.; Chisci, R.; Micheletti, R.; Ferrari, P.; Zaza, A. Modulation of Sarcoplasmic Reticulum Function by PST2744 [Istaroxime; (E,Z)-3-((2-Aminoethoxy)Imino) Androstane-6,17-Dione Hydrochloride] in a Pressure-Overload Heart Failure Model. *Journal of Pharmacology and Experimental Therapeutics* **2008**, *326* (3), 957–965. https://doi.org/10.1124/jpet.108.138701.

(91) Sabbah, H. N.; Imai, M.; Cowart, D.; Amato, A.; Carminati, P.; Gheorghiade, M. Hemodynamic Properties of a New-Generation Positive Luso-Inotropic Agent for the Acute Treatment of Advanced Heart Failure. *American Journal of Cardiology* **2007**, *99* (2 SUPPL.). https://doi.org/10.1016/j.amjcard.2006.09.005.

(92) Torre, E.; Arici, M.; Lodrini, A. M.; Ferrandi, M.; Barassi, P.; Hsu, S.-C.; Chang, G.-J.; Boz, E.; Sala, E.; Vagni, S.; Altomare, C.; Mostacciuolo, G.; Bussadori, C.; Ferrari, P.; Bianchi, G.; Rocchetti, M. SERCA2a Stimulation by Istaroxime Improves Intracellular Ca2+ Handling and Diastolic Dysfunction in a Model of Diabetic Cardiomyopathy. *Cardiovasc Res* **2022**, *118*, 1020–1032. https://doi.org/10.1093/cvr/cvab123.

(93) Mattera, G. G.; Vanoli, E.; Gagnol, J.-P.; Maria, F.; Loi, P.; Borsini, F.; Carminati, P. Sympathomimetic Inefficiency in Restoring Contractility in the Acute or Chronic β-Blocker-Treated Ischaemic Heart: Comparison with a New Agent. *The European Journal of Heart Failure* **2008**, *10*, 990–996. https://doi.org/10.1016/j.ejheart.2008.07.007.

(94) Kamel, S. M.; M van Opbergen, C. J.; Koopman, C. D.; Verkerk, A. O.; D Boukens, B. J.; de Jonge, B.; Onderwater, Y. L.; van Alebeek, E.; Chocron, S.; Polidoro Pontalti, C.; Weuring, W. J.; Vos, M. A.; de Boer, T. P.; B van Veen, T. A.; Bakkers, J. Istaroxime Treatment Ameliorates Calcium Dysregulation in a Zebrafish Model of Phospholamban R14del Cardiomyopathy. *Nat Commun* **2021**, *12*, 7151. https://doi.org/10.1038/s41467-021-27461-8.

(95) Hof, I. E.; van der Heijden, J. F.; Kranias, · E G; Sanoudou, · D; de Boer, R. A.; van Tintelen, J. P.; van der Zwaag, P. A.; Doevendans, P. A.; Kranias, E. G.; Sanoudou,

D. Point of View Prevalence and Cardiac Phenotype of Patients with a Phospholamban Mutation. *Netherlands Heart Journal* **2018**. https://doi.org/10.1007/s12471-018-1211-4.

(96) Ghali, J. K.; Smith, W. B.; Torre-Amione, G.; Haynos, W.; Rayburn, B. K.; Amato, A.; Zhang, D.; Cowart, D.; Valentini, G.; Carminati, P.; Gheorghiade, M. A Phase 1-2 Dose-Escalating Study Evaluating the Safety and Tolerability of Istaroxime and Specific Effects on Electrocardiographic and Hemodynamic Parameters in Patients with Chronic Heart Failure with Reduced Systolic Function. *American Journal of Cardiology* **2007**, *99* (2 SUPPL.). https://doi.org/10.1016/j.amjcard.2006.09.006.

(97) Blair, J. E. A.; Macarie, C.; Ruzyllo, W.; Bacchieri, A.; Valentini, G.; Bianchetti, M.; Pang, P. S.; Harinstein, M. E.; Sabbah, H. N.; Filippatos, G. S.; Gheorghiade, M. Rationale and Design of the Hemodynamic, Echocardiographic and Neurohormonal Effects of Istaroxime, a Novel Intravenous Inotropic and Lusitropic Agent: A Randomized Controlled Trial in Patients Hospitalized With Heart Failure (HORIZON-HF) Trial. *Am J Ther* **2008**, *15*, 231–240.

(98) Gheorghiade, M.; Blair, J. E. A.; Filippatos, G. S.; Macarie, C.; Ruzyllo, W.; Korewicki, J.; Bubenek-Turconi, S. I.; Ceracchi, M.; Bianchetti, M.; Carminati, P.; Kremastinos, D.; Valentini, G.; Sabbah, H. N. Hemodynamic, Echocardiographic, and Neurohormonal Effects of Istaroxime, a Novel Intravenous Inotropic and Lusitropic Agent: A Randomized Controlled Trial in Patients Hospitalized With Heart Failure. *J Am Coll Cardiol* **2008**, *51* (23), 2276–2285. https://doi.org/10.1016/J.JACC.2008.03.015.

(99) Carubelli, V.; Zhang, Y.; Metra, M.; Lombardi, C.; Michael Felker, G.; Filippatos, G.; O, C. M.; Teerlink, J. R.; Simmons, P.; Segal, R.; Malfatto, G.; Teresa La Rovere, M.; Li, D.; Han, X.; Yuan, Z.; Yao, Y.; Li, B.; Fui Lau, L.; Bianchi, G.; Zhang, J. Treatment with 24 Hour Istaroxime Infusion in Patients Hospitalised for Acute Heart Failure: A Randomised, Placebo-Controlled Trial. *Eur J Heart Fail* **2020**, *22*, 1684–1693. https://doi.org/10.1002/ejhf.1743.

(100) Metra, M.; Chioncel, O.; Cotter, G.; Davison, B.; Filippatos, G.; Mebazaa, A.; Novosadova, M.; Ponikowski, P.; Simmons, P.; Soffer, J.; Simonson, S. Safety and Efficacy of Istaroxime in Patients with Acute Heart Failure-Related Pre-Cardiogenic Shock – a Multicentre, Randomized, Double-Blind, Placebo-Controlled, Parallel Group Study (SEISMiC). *Eur J Heart Fail* **2022**. https://doi.org/10.1002/ejhf.2629.

(101) lo Giudice, P.; Mattera, G. G.; Gagnol, J.-P.; Borsini, F. Chronic Istaroxime Improves Cardiac Function and Heart Rate Variability in Cardiomyopathic Hamsters. *Cardiovasc Drugs Ther* **2011**, *25*, 133–138. https://doi.org/10.1007/s10557-011-6283-y.

(102) Binkley, P. F.; Nunziata, E.; Haas, G. J.; Nelson, S. D.; Cody, R. J.; Ohio, C. *Parasympathetic Withdrawal Is an Integral Component of Autonomic Imbalance in Congestive Heart Failure : Demonstration In Human Subjects and Verification in a Paced Canine Model Of Ventricular Failure*; 1991.

(103) Szabò, B. M.; van Veldhuisen, D. J.; Brouwer, J.; Haaksma, J.; Lie, K. I. Relation between Severity of Disease and Impairment of Heart Rate Variability Parameters in Patients with Chronic Congestive Heart Failure Secondary to Coronary Artery Disease. *Am J Cardiol* **1995**, *76*, 713–716.

(104) Stefenelli, T. H.; Bergler-Klein, J.; Gl6bits, S.; Pacher, ^r; Glogar, D. *Heart Rate Behaviour at Different Stages of Congestive Heart Failure*; 1992; Vol. 13.

(105) Luciani, P.; Fevre, M.; Leroux, J. C. Development and Physico-Chemical Characterization of a Liposomal Formulation of Istaroxime. *European Journal of Pharmaceutics and Biopharmaceutics* **2011**, *79* (2), 285–293. https://doi.org/10.1016/j.ejpb.2011.04.013.

Chapter 2

Materials & Methods

2.1 ANIMAL MODELS

The animal study protocols were approved by the Institutional Review Board of Milano Bicocca (29C09.26 and 29C09.N.YRR protocol codes approved in January 2021 and June 2018 respectively) and Chang Gung (CGU107-068 protocol code approved In June 2018) Universities in accordance with the Guide for the Care and Use of Laboratory Animals as adopted and promulgated by the U.S. National Institutes of Health.

Female Dunkin-Hartley guinea pigs (175-200 g) were used for cardiac and skeletal preparations (male 450-500 g) and myocytes isolation and, male Albino Swiss CD1 mice (30 g) were used for *in vivo* toxicity.

Streptozotocin (STZ)-induced diabetes was selected as a pathological model to test compounds *in vivo* and *in vitro* because of its association with reduced SERCA2a function[1–3] and relevance to diastolic dysfunction[4], for which a lusitropic action may be more relevant.

Diabetes was induced in Sprague Dawley (SD) male rats (150-175 g) by a single STZ (50 mg/kg in citrate buffer) i.v. injection (STZ group) in the tail vein. Control (healthy group) rats received STZ vehicle (citrate buffer). Fasting glycaemia was measured after 1 week and rats with values >290 mg/dL were considered diabetic[1]. Rats were euthanized by cervical dislocation under anesthesia with ketamine/xylazine (130-7.5 mg/kg i.p) 9 weeks after STZ injection.

2.2 CHEMICALS

All reagents and solvents were purchased from commercial sources and used without further purifications, unless stated otherwise.

Istaroxime {PST2744: [E,Z]-3-[(2-aminoethoxy)imino]-androstane-6,17-dione hydrochloride} and its metabolite PST3093 {(E,Z)-[(6-beta-hydroxy-17-oxoandrostan-3-ylidene)amino]oxyacetic acid} were synthesized and produced at Prassis Research Institute and Sigma-Tau Pharmaceutical Company and then by CVie Therapeutics Limited and WindTree Therapeutics. The batch of PST3093 utilized for *in vitro* and *in vivo* studies was a 1:1 mixture of oxime E:Z isomers. It was synthesized according to standard procedures, characterized by NMR spectroscopy and its purity (about 95%) was assessed by HPLC (Figure S1 in Supporting information of Chapter 3). Digoxin was

purchased from Sigma-Aldrich. Istaroxime (PubChem CID: 9841834); digoxin (PubChem CID: 2724385).

For the synthesis of the new compounds, reactions were carried out under an argon atmosphere unless otherwise noted and were monitored by thin-layer chromatography performed over silica gel 60 F_{254} plates (Merck), revealed using UV light or with molybdate staining [molybdate phosphorus acid and Ce(IV) sulfate in 4% H_2SO_4]. Flash chromatography purifications were performed on silica gel 60 (40−63 μm) purchased from commercial sources. Purity of final compounds was about 95% as assessed by high-performance liquid chromatography analysis.

Reaction conditions and complete compounds characterization are reported in the Supporting Information of Chapter 4 (see paragraph 4.9).

New compounds were patented (EP19202257.2 application “New androstane derivatives with activity as pure or predominantly pure stimulators of SERCA2a for the treatment of heart failure”).

2.3 PHARMACOKINETICS in HUMANS

Pharmacokinetics (PKs) of istaroxime and its metabolite PST3093 were assessed in 30 HF patients infused for 6 hours with istaroxime at 1.0 μg/kg/min (secondary analysis of the HORIZON-HF study, NCT00616161)[5]. Blood samples were taken before, during, and up to 18 hours after starting the infusion. The lowest concentration resolved by the technique was 2.6 ng/mL for istaroxime and 2.9 ng/mL for PST3093, lower values were considered as zero. PKs parameters were estimated using the dedicated software Kinetica (version 4.4, Thermo Electron Corp., Waltham, Massachusetts). Samples were excluded from the analysis if contamination was suspected, or ≥ 2 consecutive samples were missing. The following PKs parameters were estimated: maximum observed concentration (C_{max}), the time of maximum observed concentration (T_{max}), the elimination half lifetime ($T_{0.5}$) and the area under the concentration curve from the start of istaroxime administration to the time of final sampling (AUC_{last}).

2.4 SERCA and Na^+/K^+ ATPase ACTIVITIES in CELL-FREE PREPARATIONS

2.4.1 Renal Na^+/K^+ ATPase purification and activity

The inhibitory effect of compounds on Na^+/K^+ ATPase activities was tested, at multiple concentrations, on suspensions of the enzyme α1 isoform from dog kidney. The purification of renal Na^+/K^+ ATPase was performed according to the method of Jørgensen[6]. Briefly, frozen kidneys from 1-3 years-old male beagle dogs were obtained from the General Pharmacology Department of Sigma-tau, Pomezia, Italy. Kidneys were sliced and the outer medulla was dissected, pooled and suspended in a sucrose-histidine solution (1g in 10 mL), containing 250 mM sucrose, 30 mM histidine and 5 mM EDTA, pH 7.2 and homogenized. The homogenate was centrifuged at 6,000 g for 15 min, the supernatant was decanted and centrifuged at 48,000 g for 30 min. The pellet was suspended in the sucrose-histidine buffer and incubated for 20 min with a sodium-dodecyl-sulphate (SDS) solution, dissolved in a gradient buffer, containing 25 mM imidazole and 1 mM EDTA, pH 7.5. The sample was layered on the top of a sucrose discontinuous gradient (10, 15 and 29.4%) and centrifuged at 60,000 g for 115 min. The final pellet was suspended in the gradient buffer.

Na^+/K^+ ATPase activity was assayed by measuring the rate of ^{32}P-ATP hydrolysis (µmol/min) at 37°C, as previously described[7]. Increasing concentrations of the standard ouabain, or tested compound, were incubated with 0.3 µg of purified dog kidney enzyme for 10 min at 37°C in 120 µL final volume of a medium, containing 140 mM NaCl, 3 mM $MgCl_2$, 50 mM Hepes-Tris, 3 mM ATP, pH 7.5. Then, 10 µL of incubation solution containing 10 mM KCl and 20 nCi of ^{32}P-ATP (3-10 Ci/mmol, Perkin Elmer) were added, the reaction continued for 15 min at 37°C and was stopped by acidification with 20% ice-cold perchloric acid. ^{32}P was separated by centrifugation with activated charcoal (Norit A, Serva) and the radioactivity was measured. Effects of increasing concentrations of the test compound were compared to ouabain, as positive standard, and to vehicle (control) at 37°C. The inhibitory activity was expressed as percent of activity in control.

Na^+/K^+ ATPase activity was identified as the ouabain (1 mM)-sensitive component of total one; compound efficacy was expressed as the concentration exerting 50%

inhibition (IC_{50}) calculated by non-linear fitting of data points (KaleidagraphTM, Sinergy Software).

2.4.2 SERCA ATPase activity

To preserve interaction with proteins of the macromolecular complex within the native membrane lipid environment, SERCA activity was measured in whole tissue homogenates (rat) or in cardiac SR enriched microsomes (guinea pig). As verified by Western blot, cardiac preparations included SERCA2a and PLN[1] and skeletal muscle ones included SERCA1 only.

Briefly, LV were dissected from rat and guinea pig of healthy and failing preparations and frozen until use. Tissues were homogenized, subjected to centrifugation to obtain SR-enriched microsomes and sarcomeric proteins were extracted, as previously described[8].

In the case of rat hearts, cardiac homogenates were used in order to have sufficient material to replicate the experiments within a single animal. LV tissues from healthy and STZ rats were homogenized in a medium containing 300 mM sucrose, 50 mM K-phosphate, 10 mM NaF, 0.3 mM PMSF, 0.5 mM DTT (pH 7) and centrifuged at 35,000 g for 30 min. The final pellet was resuspended in the same buffer.

In the case of guinea pig hearts, LV tissues were homogenized in 4 volumes of 10 mM $NaHCO_3$, 1 mM PMSF, 10 µg/mL aprotinin and leupeptin (pH 7) and centrifuged at 12,000g for 15 minutes. Supernatants were filtered and centrifuged at 100,000 g for 30 min. Contractile proteins were extracted by suspending the pellets with 0.6 M KCl, 30 mM histidine, pH 7 and further centrifugation at 100,000 g for 30 min. Final pellets were reconstituted with 0.3 M sucrose, 30 mM histidine, pH 7, to obtain SR-enriched microsomes.

SERCA2a ATPase activity was measured as the rate of ^{32}P-ATP release at multiple Ca^{2+} concentrations in the absence and presence of test compounds, as previously described[8]. Increasing concentrations of each compound were pre-incubated with 2 µg of cardiac preparations for 5 min at 4° C in 80 µL of a solution containing 100 mM KCl, 5 mM $MgCl_2$, 1 µM A23187, 20 mM Tris, pH 7.5. Then, 20 µL of 5 mM Tris-ATP containing 50 nCi of ^{32}P-ATP (3-10 Ci/mmol, Perkin Elmer) were added. The ATP hydrolysis was continued for 15 min at 37°C and the reaction was stopped by

acidification with 100 µL of 20% ice-cold perchloric acid. ^{32}P was separated by centrifugation with activated charcoal (Norit A, Serva) and the radioactivity was measured.

The SERCA component was identified as the cyclopiazonic acid (CPA, 10 µM)-sensitive one. Ca^{2+} dose-response curves were fitted by nonlinear regression (KaleidographTM, Sinergy Software) to estimate SERCA maximal hydrolytic velocity (V_{max}, µmol/min/mg protein) and Ca^{2+} dissociation constant (K_dCa, nM). Either an increase of V_{max}, or a decrease of K_dCa (increased Ca^{2+} affinity) stand for enhancement of SERCA function.

2.4.3 Reconstitution of SERCA1 with PLN_{1-32} synthetic fragment.

To test for PLN involvement in the effect of compounds, SERCA1 activity was also measured in PLN-free microsomes (from guinea-pig skeletal muscle) before and after reconstitution with the PLN_{1-32} inhibitory fragment. Adult healthy guinea pigs were used to prepare SERCA1-enriched SR microsomes from fast-twitch hind leg muscles. Microsomes were prepared as described for SERCA2a preparations. For reconstitution experiments, SERCA1 (PLN-free) was pre-incubated with synthetic PLN_{1-32} fragment (canine sequence, Biomatik Corporation, Canada) in 20 mM imidazole, pH 7, at 1:300 SERCA1:PLN ratio for 30 min at room temperature. After preincubation, SERCA1 (PLN-free) alone, or reconstituted with PLN_{1-32} fragment, was utilized for SERCA activity measurement by using ^{32}P-ATP hydrolysis method at different Ca^{2+} concentrations in the absence and presence of increasing concentrations of tested compounds, as described for SERCA2a ATPase activity.

2.5 OFF-TARGET ACTIONS

To predict potential off-target actions of PST3093 and Compound **8**, their interaction with a panel of 50 ligands, potentially relevant to off-target effects, was carried out by Eurofins (Taiwan) on crude membrane preparations according to Eurofins described procedures. The assays are partly based on radioligand displacement (e.g. for receptors) and partly on spectrophotometric detection of change in function (e.g. for enzymes). Results were compared to appropriate reference standards; a >50% change

in affinity was considered as a positive hit (interaction present). Compounds were tested at the concentration of 10 µM.

2.6 Na^+/K^+ ATPase CURRENT (I_{Nak}) and INTRACELLULAR Ca^{2+} DYNAMICS in HEALTHY and DISEASED MYOCYTES

Rat and guinea pig LV ventricular myocytes were isolated by using a retrograde coronary perfusion method previously published[9] with minor modifications. Rod-shaped, Ca^{2+}- tolerant myocytes were used within 12 h from dissociation. LV myocytes were clamped in the whole-cell configuration (Axopatch 200A, Axon Instruments Inc., Union City, CA). During measurements, myocytes were superfused at 2 ml/min with Tyrode's solution containing 154 mM NaCl, 4 mM KCl, 2 mM $CaCl_2$, 1 mM $MgCl_2$, 5 mM HEPES/NaOH, and 5.5 mM D-glucose, adjusted to pH 7.35. A thermo-stated manifold, allowing for fast (electronically timed) solution switch, was used for cell superfusion. All measurements were performed at 35°C. The pipette solution contained 110 mM K^+-aspartate, 23 mM KCl, 0.2 mM $CaCl_2$ (10^{-7} M calculated free-Ca^{2+} concentration), 3 mM $MgCl_2$, 5 mM HEPES-KOH, 0.5 mM EGTA-KOH, 0.4 mM GTP-Na^+ salt, 5 mM ATP-Na^+ salt, and 5 mM creatine phosphate Na^+ salt, pH 7.3. Membrane capacitance and series resistance were measured in every cell but left un-compensated. Current signals were filtered at 2 KHz and digitized at 5 KHz (Axon Digidata 1200). Trace acquisition and analysis was controlled by dedicated software (Axon pClamp 8.0).

To ensure stabilization of drug effect, isolated myocytes were analyzed after incubation with compounds or vehicle (control) for at least 30 min. Difference between means was thus tested by group comparison.

2.6.1 Na^+/K^+ ATPase current (I_{NaK}) measurements

Na^+/K^+ ATPase current (I_{NaK}) was recorded (V-clamp) in isolated rat left ventricular (LV) myocytes as the holding current at -40 mV under conditions enhancing I_{NaK} and minimizing contamination by other conductances[1,9]. Briefly, the current was measured in the presence of Ni^{2+} (5 mM), nifedipine (5 µM), Ba^{2+} (1 mM) and 4-aminopyridine (2 mM) to minimize contamination by changes in Na^+/Ca^{2+} exchanger (NCX), Ca^{2+} and K^+ currents, respectively. Tetraethylammonium-Cl (20 mM) and EGTA (5 mM) were added to the pipette solution and intracellular K^+ was replaced by Cs^+. To optimize the

recording conditions, I_{NaK} was enhanced by increasing intracellular Na^+ (10 mM) and extracellular K^+ (5.4 mM). All drugs were dissolved in dimethyl sulfoxide (DMSO). Control and test solutions contained maximum 1:100 DMSO.

I_{NaK} inhibition by the compounds was expressed as percent reduction of ouabain (1 mM)-sensitive current; efficacy was expressed as the compound concentration exerting 50% inhibition (IC_{50}) effect.

2.6.2 Intracellular Ca^{2+} dynamics in field stimulated and V-clamped myocytes

LV myocytes were incubated in Tyrode's solution for 30 min with the membrane-permeant form of the dye, Fluo4-AM (10 µM), and then washed for 15 min to allow dye de-esterification. Fluo4 emission was collected through a 535 nm band pass filter, converted to voltage, low-pass filtered (100 Hz) and digitized at 2 kHz after further low-pass digital filtering (FFT, 50 Hz). After subtraction of background luminescence, a reference fluorescence (F_0) value was used for signal normalization (F/F_0).

Properties of voltage-induced Ca^{2+} transients (Ca_T, amplitude and decay kinetics) and caffeine-induced ones (estimating total SR Ca^{2+} content, Ca_{SR}) were assessed in intact myocytes, field-stimulated at 2 Hz. To highlight the ability of SR to uptake Ca^{2+} at resting (SERCA2a function) a post-rest potentiation protocol was applied (Figure 1). Briefly, Ca_T were evocated at 2 Hz and steady state (ss) Ca_T were interrupted by increasing resting pauses (1-5-10-20 s). The amplitude of 1st Ca_T evocated following each resting pause was then normalized to the amplitude of the pre-pause $ssCa_T$ to evaluate SR Ca^{2+} compartmentalization during rest intervals. Ca_{SR} was estimated by measuring caffeine (10 mM)-induced Ca_T amplitude, electronically evocated 0.5s (Ca_{SR} 0.5s) and 20s (Ca_{SR} 20s) post train pulses. The ratio between Ca_{SR} 20s /Ca_{SR} 0.5s was calculated to evaluate post-rest SR Ca^{2+} compartmentalization at resting. Resting Ca^{2+} (Ca_{rest}) 20s following pacing train was used as reference fluorescence (F_0) for signal normalization (F/F_0).

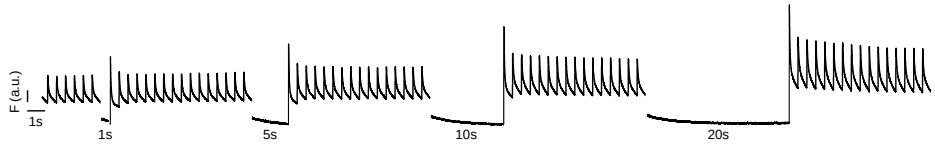

Figure 1. Post-rest potentiation protocol to evaluate SR Ca^{2+} uptake ability at resting in field stimulated myocytes. Ca^{2+} transients (Ca_T) were evocated at 2 Hz and steady state Ca_T were interrupted by increasing resting pauses (1-5-10-20 s). The amplitude of the 1st Ca_T increased at increasing resting pause, indicating SR Ca^{2+} uptake at resting through SERCA2a.

Unlike Ca^{2+} dynamics measurements in field stimulated cells, measurements in patch-clamped myocytes allows to control membrane potential and highlight differences between experimental groups directly related to changes in EC-coupling proteins function. In particular, SR Ca^{2+} uptake rate was evaluated through a "SR loading" voltage protocol, specifically devised to examine the system at multiple levels of SR Ca^{2+} loading and to rule out Na^+/Ca^{2+} exchanger (NCX) contribution[10]. Membrane current, whose time-dependent component mainly reflected the sarcolemmal Ca^{2+} current (I_{CaL}), was simultaneously recorded to FLUO4 fluorescent signal. The protocol (Figure 2) consisted in emptying the SR by a brief caffeine (10 mM) pulse and then progressively refilling it by 7-10 voltage steps (-35 to 0 mV) activating Ca^{2+} influx through I_{CaL}. NCX was blocked by omission of Na^+ from intracellular and extracellular (replaced by equimolar Li^+ and 1 mM EGTA) solutions. The procedure agrees with published methods, with minor modifications[1,10,11]. Multiple parameters, suitable to quantify SR Ca^{2+} uptake, can be extracted from Ca^{2+} and I_{CaL} response to the protocol: the time constant (τ) of cytosolic Ca^{2+} decay within each V-step largely reflects net Ca^{2+} flux across the SR membrane (the faster SR Ca^{2+} uptake, the smaller τ decay). Because of the steep dependency of Ca_T amplitude on SR Ca^{2+} content, the rate at which Ca_T amplitude increases across the subsequent pulses of the protocol reflects the rate at which the SR refills. To rule out the potential contribution of changes in I_{CaL}, in each loading step, Ca_T amplitude was normalized to Ca^{2+} influx (estimated from I_{CaL} integral up to Ca_T peak) to obtain excitation-release (ER) gain. As expected from its strong dependency on SR Ca^{2+} content, this parameter progressively increases during the loading protocol. Diastolic Ca^{2+} of the first step was used as F_0 for signal normalization (F/F_0). Specificity of the "loading protocol" parameters in detecting SERCA2a activation

is supported by the observation that they did not detect any effect of digoxin, an inotropic agent blocking the Na^+/K^+ pump and devoid of SERCA2a stimulating effect[10,11].

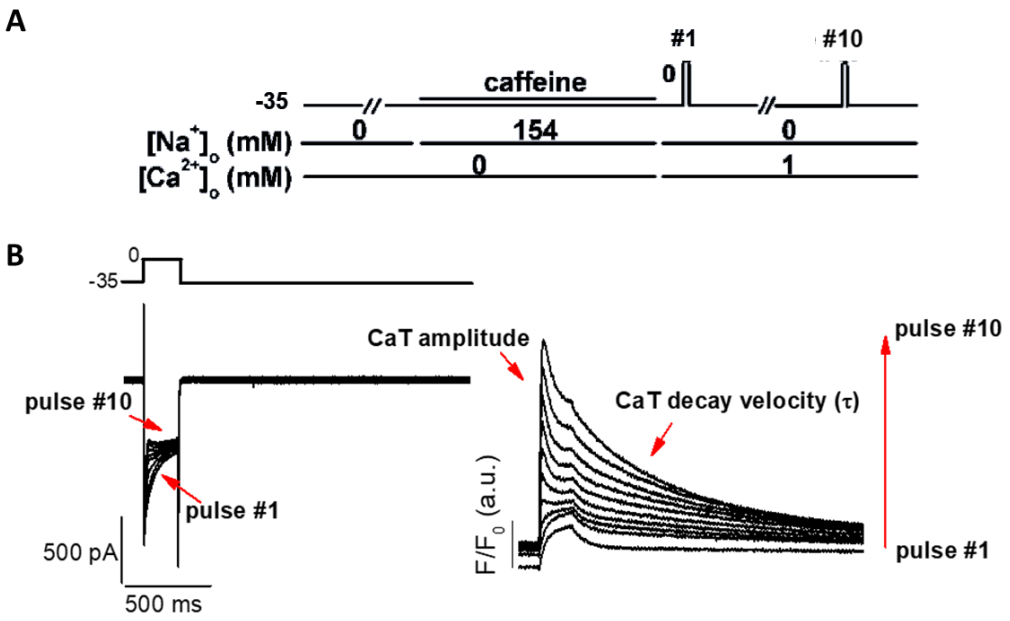

Figure 2. Protocol to evaluate intracellular Ca^{2+} dynamics in patch-clamped cells under Na^+ free condition. A) Protocol outline. B) Transmembrane current (left) and Ca^{2+} transients (right) recordings during SR reloading after caffeine-induced SR depletion in patch-clamped cells.

2.7 ELECTRICAL ACTIVITY in HEALTHY MYOCYTES

Action potentials (APs) were recorded by patch-clamp (I-clamp) from isolated guinea pig LV myocytes, selected because of the AP similarity to the human one[12], under Tyrode superfusion. AP duration at 50% and 90% repolarization (APD_{50} and APD_{90}) and diastolic potential (E_{diast}) were measured 1) during steady state pacing at several rates; 2) dynamically upon stepping between two rates (APD_{90} adaptation). During steady state pacing, short-term APD_{90} variability (STV) was calculated from 20-30 subsequent APD_{90} values according to Eq. 1[13]:

$$STV = \Sigma(|APD(n+1) - APDn|)/[nbeats * \sqrt{2}] \quad \text{(Eq. 1)}$$

The kinetics of APD_{90} adaptation was quantified by the time constant (τ) of exponential data fitting.

2.8 *IN VIVO* HEMODYNAMICS of DISEASED HEARTS

Healthy and STZ rats were studied by transthoracic echocardiographic under urethane anesthesia (1.25 g/kg i.p., for acute i.v. treatment) or ketamine/pentobarbital anesthesia (60-37.5 mg/kg i.p., for chronic oral treatment) by means of a Mindray M9 ultrasound machine (Mindray Co, Shen Zhen, China) equipped with a P10-4s phased ultrasound transducer. Left-ventricular end-diastolic (LVEDD) and end-systolic (LVESD) diameter, posterior wall (PWT) and interventricular septal (IVST) thickness were measured according to the American Society of Echocardiography guidelines[14]. The Teichholz formula (7/ (2.4+ D) × D^3, D = LVESD or LVEDD) was used to calculate LV end-diastolic volume (EDV) and end-systolic volume (ESV). Stroke volume (SV) was calculated as the difference between EDV and ESV. LV ejection fraction (EF) was calculated as SV/EDV and expressed in %[15]. Fractional shortening was calculated as FS = (LVEDD-LVESD)/LVEDD and expressed in %. Trans-mitral flow velocity was measured (pulsed Doppler) to obtain early and late filling velocities (E, A waves) and E wave deceleration time (DT). DT was also normalized to E wave amplitude (DT/E ratio). Peak myocardial systolic (s') and diastolic velocities (e' and a'), were measured at the mitral annulus by Tissue Doppler Imaging (TDI). Two-dimensional LV mass and its relative index to body weight, were estimated in healthy and STZ rats.

Compounds were i.v. infused in STZ rats through a polyethylene 50 cannula insert into a jugular vein at 0.2 mg/kg/min (0.16 ml/min) under urethane anesthesia. Echocardiography started 13 min and 27 min after the beginning of drug infusion, when a total cumulative dose of 2.6 and 5.4 mg/kg was infused. Echocardiography lasted on average 3.5 min, therefore at the last interrogation (always TDI), a total dose of approximately 6 mg/kg was infused. Overall, echocardiographic parameters were measured before (basal), at 15 and 30 min during drug infusion and 10 min after drug discontinuation. Istaroxime (0.22 mg/kg) and digoxin (0.11 mg/kg), both infused for 15 min, were used as comparators. At the end of the echocardiography, animals were sacrificed by i.v. administration of KCl. A previous study in the same setting demonstrated that neither urethane anesthesia, nor the infusion volumes per se affected echocardiographic parameters[1]. Compound **8** was also studied after 1 and 4 once daily administration at 40 or 80 mg/kg (5 ml/kg body weight) compared with a

control group receiving vehicle (saline) only (Figure 3). Briefly, at day 1 rats were randomly split in control and drug-treated groups; all the animals received an oral bolus of saline and 60 min following treatment they were subjected to basal echocardiography. At day 5, rats were orally treated with saline (control group) or compound **8** (40 mg/kg or 80 mg/kg) and 60 min following treatment they were subjected to echocardiography. From day 6 to day 8, each group of rats was orally treated once daily with saline or compound **8** and at day 8 each rat was subjected to echocardiography 60 min following treatment. Echo measurements were performed under ketamine/pentobarbital anesthesia.

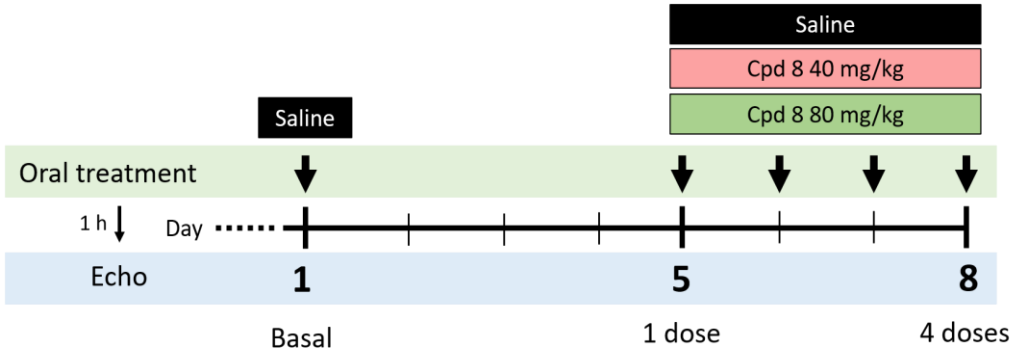

Figure 3: Protocol for oral administration. Rats were treated on day 1 with saline and 60 min after the treatment were subjected to echocardiographic measurements (basal). At day 5 rats were treated once daily with saline, 40 mg/kg or 80 mg/kg of compound **8**. Echocardiographic measurements were repeated on day 5 and day 8.

2.9 *IN VIVO* ACUTE TOXICITY

Acute toxicity of the compounds was preliminarily evaluated in male Albino Swiss CD-1 mice by identifying the dose causing 50% mortality (LD_{50}, mg/kg body weight) at 24 hours after i.v. injection or oral treatment.

PST3093 was dissolved in DMSO and injected at 50, 100, 200, and 250 mg/kg (4 animals for each group). Higher PST3093 dose levels were not tested due to the solubility limit of the compound. Furthermore, PST3093 was orally tested at 200 mg/kg (four animals for each group). Control animals received the vehicle only (DMSO).

Compound **5** and compound **8** were dissolved in saline solution and i.v. injected at 50, 100, 200, 250, 275, and/or 300 mg/kg (1−4 animals for each group) or orally administered at 100, 200, 400, 600, 700 and/or 800 mg/kg (4 animals for each group). Control animals received the vehicle only (saline solution).

Acute toxicity of istaroxime was also evaluated for comparison. Istaroxime was i.v. injected at 15, 22, 27 and 33 mg/kg (5 animals for each group) and orally administered at 30, 100, and 300 mg/kg (4 animals for each group).

2.10 STATISTICAL ANALYSIS

Individual means were compared by paired or unpaired Student's t-test; multiple means were compared by one or two-way ANOVA for repeated measurements (RM) plus post-hoc Tukey's multiple comparisons; drug-induced changes in overall curve steepness were defined according to significance of the "factor X group" interaction. Data are reported as mean ± SEM; $p<0.05$ defined statistical significance of differences in all comparisons. Number of animals (N) and/or cells (n) are shown in each figure legend.

2.11 ABBREVIATIONS

2D-COSY, two-dimension homonuclear correlation spectroscopy; 2D-HSQC, two-dimension heteronuclear correlation spectroscopy; 2D-NOESY, two-dimension nuclear Overhauser effect spectroscopy; a', peak late diastolic tissue velocity; A, late diastolic transmitral flow velocity; AHF, acute heart failure; AP, action potential; APD, action potential duration; APD_{50}, AP duration at 50% of repolarization; APD_{90}, AP duration at

90% of repolarization; APT, attached proton test; AUC_{last}, the area under the curve from the start of drug administration to the time of final sampling; Ca_{rest}, resting Ca^{2+} at 20s pause end; Ca_{SR}, sarcoplasmic reticulum Ca^{2+} content; Ca_T, Ca^{2+} transient; C_{max}, maximum observed concentration; CO, cardiac output; CPA, cyclopiazonic acid; Cpd, compound; DMF, dimethylformamide; DMSO, dimethylsulfoxide; DT, deceleration time; e', peak early diastolic tissue velocity; E, early diastolic transmitral flow velocity; E_{diast}, diastolic potential; EDC, N-ethyl-N'-(3-dimethylaminopropyl)carbodiimide; EDV, end diastolic volume; EF, ejection fraction; ER, excitation-release; ESV, end systolic volume; EtOAc, ethyl acetate; EtOH, ethanol; F_0, reference fluorescence; FS, fractional shortening; HF, heart failure; HR, heart rate; HPLC, high-performance liquid chromatography; I_{CaL}, L type Ca^{2+} current; I_{NaK}, Na^+/K^+ ATPase current; i.p., intraperitoneal administration; i.v., intravenous administration; IVSTd or IVSTs, interventricular septum thickness in diastole or systole; K_dCa, Ca^{2+} dissociation constant, LiHMDS, lithium bis(trimethylsilyl)amide; LD_{50}, in vivo dose causing 50% mortality; LV, left ventricle; LVEDD or LVESD, LV end-diastolic or systolic diameter; N, number of animal; n, number of cells; NCX, Na^+/Ca^{2+} exchanger; PK, pharmacokinetic; PLN, phospholamban; PWTd or PWTs, posterior wall thickness in diastole or systole; QSAR, quantitative structure-activity relationship; RM, repeated measurements; s', peak systolic tissue velocity; SERCA, sarcoplasmic reticulum Ca^{2+} ATPase; SR, sarcoplasmic reticulum; STV, short term variability; STZ, streptozotocin; SV, stroke volume; SW, septal diastolic wall thickness; $t_{0.5}$, Ca^{2+} transient decay half-time or elimination half life time; τ_{decay}, time-constant of Ca^{2+} decay; TDI, Tissue Doppler Imaging; THF, tetrahydrofuran; TLC, thin-layer chromatography; T_{max}, the time of maximum observed concentration; V_{max}, maximal hydrolytic velocity.

2.12 REFERENCES

(1) Torre, E.; Arici, M.; Lodrini, A. M.; Ferrandi, M.; Barassi, P.; Hsu, S.-C.; Chang, G.-J.; Boz, E.; Sala, E.; Vagni, S.; Altomare, C.; Mostacciuolo, G.; Bussadori, C.; Ferrari, P.; Bianchi, G.; Rocchetti, M. SERCA2a Stimulation by Istaroxime Improves Intracellular Ca2+ Handling and Diastolic Dysfunction in a Model of Diabetic Cardiomyopathy. *Cardiovasc Res* **2022**, *118*, 1020–1032. https://doi.org/10.1093/cvr/cvab123.

(2) Choi, K. M.; Zhong, Y.; Hoit, B. D.; Grupp, I. L.; Hahn, H.; Dilly, K. W.; Guatimosim, S.; Lederer, W. J.; Matlib, M. A.; Guatimo-Sim, S. Defective Intracellular Ca2+ Signaling Contributes to Cardiomyopathy in Type 1 Diabetic Rats. *Am J Physiol Heart Circ Physiol* **2002**, *283*, H1398–H1408. https://doi.org/10.1152/ajpheart.00313.2002.-The.

(3) Vasanji, Z.; Dhalla, N. S.; Netticadan, T. Increased Inhibition of SERCA2 by Phospholamban in the Type I Diabetic Heart. *Mol Cell Biochem* **2004**, 1–5.

(4) Valero-Muñoz, M.; Backman, W.; Sam, F. Murine Models of Heart Failure With Preserved Ejection Fraction A "Fishing Expedition." *Journal of American College of Cardiology: Basic to Translational Science* **2017**, *2*, 770–789.

(5) Gheorghiade, M.; Blair, J. E. A.; Filippatos, G. S.; Macarie, C.; Ruzyllo, W.; Korewicki, J.; Bubenek-Turconi, S. I.; Ceracchi, M.; Bianchetti, M.; Carminati, P.; Kremastinos, D.; Valentini, G.; Sabbah, H. N. Hemodynamic, Echocardiographic, and Neurohormonal Effects of Istaroxime, a Novel Intravenous Inotropic and Lusitropic Agent: A Randomized Controlled Trial in Patients Hospitalized With Heart Failure. *J Am Coll Cardiol* **2008**, *51* (23), 2276–2285. https://doi.org/10.1016/J.JACC.2008.03.015.

(6) Jørgensen, P. L. Purification of Na+,K+-ATPase: Enzyme Sources, Preparative Problems, and Preparation from Mammalian Kidney. *Methods Enzymol* **1988**, *156*, 29–43.

(7) Ferrandi, M.; Tripodi, G.; Salardi, S.; Florio, M.; Modica, R.; Barassi, P.; Parenti, P.; Shainskaya, A.; Karlish, S.; Bianchi, G.; Ferrari, P. Renal Na,K-ATPase in Genetic Hypertension. *Hypertension* **1996**, *28* (6), 1018–1025. https://doi.org/10.1161/01.HYP.28.6.1018.

(8) Micheletti, R.; Palazzo, F.; Barassi, P.; Giacalone, G.; Ferrandi, M.; Schiavone, A.; Moro, B.; Parodi, O.; Ferrari, P.; Bianchi, G. Istaroxime, a Stimulator of Sarcoplasmic Reticulum Calcium Adenosine Triphosphatase Isoform 2a Activity, as a Novel Therapeutic Approach to Heart Failure. *American Journal of Cardiology* **2007**, *99* (2 SUPPL.). https://doi.org/10.1016/j.amjcard.2006.09.003.

(9) Rocchetti, M.; Besana, A.; Mostacciuolo, G.; Ferrari, P.; Micheletti, R.; Zaza, A. Diverse Toxicity Associated with Cardiac Na+/K+ Pump Inhibition: Evaluation of Electrophysiological Mechanisms. *Journal of Pharmacology and Experimental Therapeutics* **2003**, *305* (2), 765–771. https://doi.org/10.1124/jpet.102.047696.

(10) Rocchetti, M.; Besana, A.; Mostacciuolo, G.; Micheletti, R.; Ferrari, P.; Sarkozi, S.; Szegedi, C.; Jona, I.; Zaza, A. Modulation of Sarcoplasmic Reticulum Function by Na/K Pump Inhibitors with Different Toxicity: Digoxin and PST2744 [(E,Z)-3-((2-Aminoethoxy)Imino)Androstane-6,17-Dione Hydrochloride]. *J Pharmacol Exp Ther* **2005**, *313*, 207–215. https://doi.org/10.1124/jpet.104.077933.

(11) Alemanni, M.; Rocchetti, M.; Re, D.; Zaza, A. Role and Mechanism of Subcellular Ca2+ Distribution in the Action of Two Inotropic Agents with Different Toxicity. *J Mol Cell Cardiol* **2011**, *50* (5), 910–918. https://doi.org/10.1016/j.yjmcc.2011.02.008.

(12) Odening, K. E.; Gomez, A.-M.; Dobrev, D.; Fabritz, L.; Heinzel, F. R.; Mangoni, M. E.; Molina, C. E.; Sacconi, L.; Smith, G.; Stengl, M.; Thomas, D.; Zaza, A.; Remme, C. A.; Heijman, J. ESC Working Group on Cardiac Cellular Electrophysiology Position Paper: Relevance, Opportunities, and Limitations of Experimental Models for Cardiac Electrophysiology Research. *Europace* **2021**, *23*, 1795–1814. https://doi.org/10.1093/europace/euab142.

(13) Altomare, C.; Bartolucci, C.; Sala, L.; Bernardi, J.; Mostacciuolo, G.; Rocchetti, M.; Severi, S.; Zaza, A. IKr Impact on Repolarization and Its Variability Assessed by Dynamic Cla mp. *Circulation: Arrhytmia and Electrophysiology* **2015**, *8*, 1265–1275. https://doi.org/10.1161/CIRCEP.114.002572.

(14) Lang, R. M.; Bierig, M.; Devereux, R. B.; Flachskampf, F. A.; Foster, E.; Pellikka, P. A.; Picard, M. H.; Roman, M. J.; Seward, J.; Shanewise, J.; Solomon, S.; Spencer, K. T.; St John Sutton, M.; Stewart, W. Recommendations for Chamber Quantification. *European Journal of Echocardiography* **2006**, *7*, 79–108. https://doi.org/10.1016/j.euje.2005.12.014.

(15) Tournoux, F.; Petersen, B.; Thibault, H.; Zou, L.; Raher, M. J.; Kurtz, B.; Halpern, E. F.; Chaput, M.; Chao, W.; Picard, M. H.; Scherrer-Crosbie, M. Validation of Noninvasive Measurements of Cardiac Output in Mice Using Echocardiography. *Journal of the American Society of Echocardiography* **2011**, *24* (4), 465–470. https://doi.org/10.1016/J.ECHO.2010.12.019.

Chapter 3

Istaroxime Metabolite PST3093 Selectively Stimulates SERCA2a and Reverses Disease-Induced Changes in Cardiac Function

Martina Arici[1#], Mara Ferrandi[2#], Paolo Barassi[2], Shih-Che Hsu[3], Eleonora Torre[1], Andrea Luraghi[1], Carlotta Ronchi[1], Gwo-Jyh Chang[4], Francesco Peri[1], Patrizia Ferrari[2], Giuseppe Bianchi[2,5], Marcella Rocchetti[1*] and Antonio Zaza[1*]

[1]Department of Biotechnology and Biosciences, Università degli Studi di Milano-Bicocca, 20126 Milan, Italy.
[2]Windtree Therapeutics Inc., Warrington, Pennsylvania, 18976, USA.
[3]CVie Therapeutics Limited, Taipei, 11047 Taiwan.
[4]Chang Gung University, Tao-Yuan, 333323 Taiwan.
[5]Università Vita-Salute San Raffaele, 20132 Milan, Italy.

#MA and MF contributed equally as first authors to the article
*MR and AZ contributed equally as senior authors to the article

PUBLISHED ON

J Pharmacol Exp Ther. 2023 Jan; 384 (1) 231-244.

doi: 10.1124/jpet.122.001335.

Viewpoint on this work have been published

J Pharmacol Exp Ther. 2023 Jan;384 (1) 227-230.

doi: 10.1124/jpet.122.001446.

3.1. ABSTRACT

Heart failure (HF) therapeutic toolkit would strongly benefit from the availability of ino-lusitropic agents with a favorable pharmacodynamics and safety profile. Istaroxime is a promising agent, which combines Na^+/K^+ pump inhibition with sarcoplasmic reticulum Ca^{2+} ATPase (SERCA2a) stimulation; however, it has a very short half-life and extensive metabolism to a molecule named PST3093. The present work aims to investigate whether PST3093 still retains the pharmacodynamic and pharmacokinetic properties of its parent compound. We studied PST3093 for its effects on SERCA2a and Na^+/K^+ ATPase activities, Ca^{2+} dynamics in isolated myocytes and hemodynamic effects in an in vivo rat model of diabetic [streptozotocin (STZ)-induced] cardiomyopathy. Istaroxime infusion in HF patients led to accumulation of PST3093 in the plasma; clearance was substantially slower for PST3093 than for istaroxime. In cardiac rat preparations, PST3093 did not inhibit the Na^+/K^+ ATPase activity but retained SERCA2a stimulatory activity. In in vivo echocardiographic assessment, PST3093 improved overall cardiac performance and reversed most STZ-induced abnormalities. PST3093 intravenous toxicity was considerably lower than that of istaroxime, and it failed to significantly interact with 50 off-targets. Overall, PST3093 is a “selective” SERCA2a activator, the prototype of a novel pharmacodynamic category with a potential in the ino-lusitropic approach to HF with prevailing diastolic dysfunction. Its pharmacodynamics is peculiar, and its pharmacokinetics are suitable to prolong the cardiac beneficial effect of istaroxime infusion.

3.2. GRAPHICAL ABSTRACT

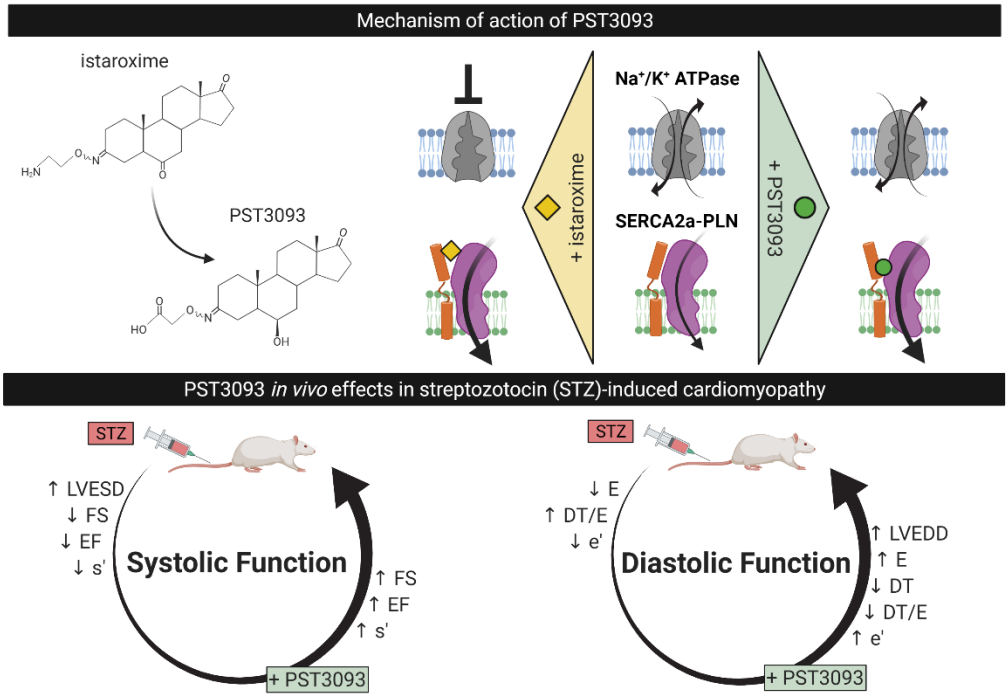

3.3. SIGNIFICANCE STATEMENT

Heart failure (HF) treatment would benefit from the availability of ino-lusitropic agents with favorable profiles. PST3093 is the main metabolite of istaroxime, a promising agent combining Na^+/K^+ pump inhibition and sarcoplasmic reticulum Ca^{2+} ATPase2a (SERCA2a) stimulation. PST3093 shows a longer half-life in human circulation compared to istaroxime, selectively activates SERCA2a, and improves cardiac performance in a model of diabetic cardiomyopathy. Overall, PST3093 as selective SERCA2a activator can be considered the prototype of a novel pharmacodynamic category for HF treatment.

3.4. INTRODUCTION

Heart failure (HF) is characterized by abnormal Ca^{2+} distribution among subcellular compartments, which contributes to impaired contractility and relaxation[1], facilitates arrhythmias[2], and, in the long run, contributes to myocardial remodeling[3]. Evidence of a deficient sarcoplasmic reticulum Ca^{2+} ATPase2a (SERCA2a) activity in HF dates to the 1970s[4,5]. Since then, many studies confirmed this finding[6–8] showing that the impaired SERCA2a activity can often result from an over-inhibition by phospholamban (PLN)[9,10]. Loss of SERCA2a function accounts for abnormal distribution of intracellular Ca^{2+}, with numerous detrimental consequences. Interventions currently available to modulate myocyte Ca^{2+} handling (e.g., amines, PDE inhibitors etc.) stimulate SERCA2a, but they do so in the context of a multitarget action, thus resulting in untoward effects. Selective SERCA2a enhancement would afford inotropic and lusitropic effects without the drawbacks of the multitarget action[2]. Accordingly, the use of SERCA2a stimulation in HF therapy is receiving considerable attention, and many attempts to selectively stimulate SERCA2a activity with gene therapy or "small molecule" agents have been reported[11–13]. Nonetheless, for reasons other than refutation of the principle, none of these attempts has been successfully translated into the clinic. The only exception is istaroxime, a small-molecule drug, identified as SERCA2a enhancer by our group[14] and currently under clinical development for the treatment of acute HF[15,16]. Istaroxime has a double mechanism of action: it inhibits the Na^+/K^+ pump[17] and activates SERCA2a[14]. Thus, istaroxime increases overall cell Ca^{2+} content while promoting rapid Ca^{2+} sequestration into the sarcoplasmic reticulum (SR). Notably, at variance with Na^+/K^+ pump blockade alone, this neither facilitates spontaneous Ca^{2+} release from the SR[18] nor increases myocardial oxygen demand[19]. Thus, istaroxime may improve systolic and diastolic performance[15] without promoting arrhythmia or ischemia[16,20]. However, istaroxime has a plasma half-life of less than 1 hour because of extensive hepatic metabolism to a molecule named PST3093[16,20]; this restricts istaroxime usage to acute intravenous therapy.

The present work aims to investigate whether PST3093 may, on its own, be endowed with pharmacological activity. To this end, PST3093 has been synthesized and compared to istaroxime and digoxin (as reference compounds) in experimental setups

at different levels of biological organization and in the context of disease-induced dysfunction.

The data here reported indicate that PST3093 shows a longer half-life in human circulation compared to parent drug; it stimulates SERCA2a activity, but, at variance with istaroxime, it does not inhibit the Na^+/K^+ ATPase. This pharmacodynamic profile translates to positive inotropy and lusitropy in an in vivo disease model characterized by SERCA2a downregulation. Therefore, PST3093 qualifies as a “pure” SERCA2a activator, able to improve cardiac mechanical performance in vivo.

Table 1: Synopsis of the studies

Evaluation	Experimental model	Scope
Pharmacokinetics in humans.	Human blood samples from the clinical HORIZON-HF study on istaroxime [23].	To assess compatibility of pharmacokinetics with chronic usage.
Effects on SERCA2a and Na^+/K^+ ATPase activities in cell-free preparations (enzymatic assays).	Tissue homogenates/microsomes from: dog kidney (Na^+/K^+ ATPase); rat and guinea pig ventricle (SERCA2a); guinea pig skeletal muscle (SERCA1).	To assess efficacy and selectivity in modulating the ATPase proteins relevant to the ino-lusitropic effect. Demonstration of PLN-SERCA2a interaction as the molecular target.
In vitro effects for ligands potentially accounting for off-target actions.	High-throughput in vitro ligation to a panel of 50 molecular ligands.	To screen for a wide range of interactors potentially involved in off-target effects.
Effects on Na^+/K^+ ATPase current and intracellular Ca^{2+} dynamics in healthy and diseased myocytes.	Ventricular myocytes isolated from healthy and diseased rats with known SERCA2a dysfunction (STZ-diabetic rats).	To assess in isolated cells efficacy in restoring the SR function in diseased cardiac myocytes.
Effects on electrical activity of healthy myocytes.	Ventricular myocytes isolated from guinea pigs, a species with human-like repolarization.	To test for potential off-target effects of proarrhythmic relevance.
Effects on in vivo hemodynamics of diseased hearts.	Healthy and STZ-diabetic rats; echocardiographic evaluation before and during drug infusion.	To assess efficacy in reversing disease-induced hemodynamic abnormalities in vivo.
In vivo acute toxicity.	Healthy mice, evaluation of LD_{50}.	To assess drug toxicity in vivo.

3.5. RESULTS

3.5.1 Chemical Structure of PST3093

PST3093 is the final metabolite of istaroxime[20]; its chemical structure is shown in Fig. 1A. Compared to istaroxime, PST3093 retains the oxime moiety at position 3 with the amino-chain oxidized into a carboxylic chain, while the 6-keto group of istaroxime is stereo selectively reduced to a 6β-hydroxyl group.

3.5.2 Pharmacokinetics

Fig. 1B shows istaroxime and PST3093 plasma levels over a 6-hours istaroxime infusion at 1 μg/kg/min and up to 12 hours after discontinuation of infusion in HF patients[20]. All patients showed measurable istaroxime levels until 10 min after stopping the infusion; drug levels decreased rapidly thereafter, and just one patient had a quantifiable istaroxime level 2 hours after the end of the infusion. PST3093 plasma levels increased with a lag from the start of istaroxime infusion (as expected for a metabolite) being detectable in all patients from 1 hour after the start of infusion. Plasma PST3093 levels remained detectable long after discontinuation of the infusion, up to the last sample at 12 hours after wash out. The data suggest that, if istaroxime infusion had continued beyond 6 hours, the metabolite would have accumulated further.

In quantitative terms, PST3093 had a $T_{0.5}$ of about 9 hours, i.e., substantially longer than that of istaroxime (less than 1 hour), leading to a huge enhancement of the AUC_{last} index for PST3093; although the C_{max} of PST3093 was similar to istaroxime one at this infusion rate, the T_{max} was longer for PST3093 in comparison to istaroxime (Fig. 1C).

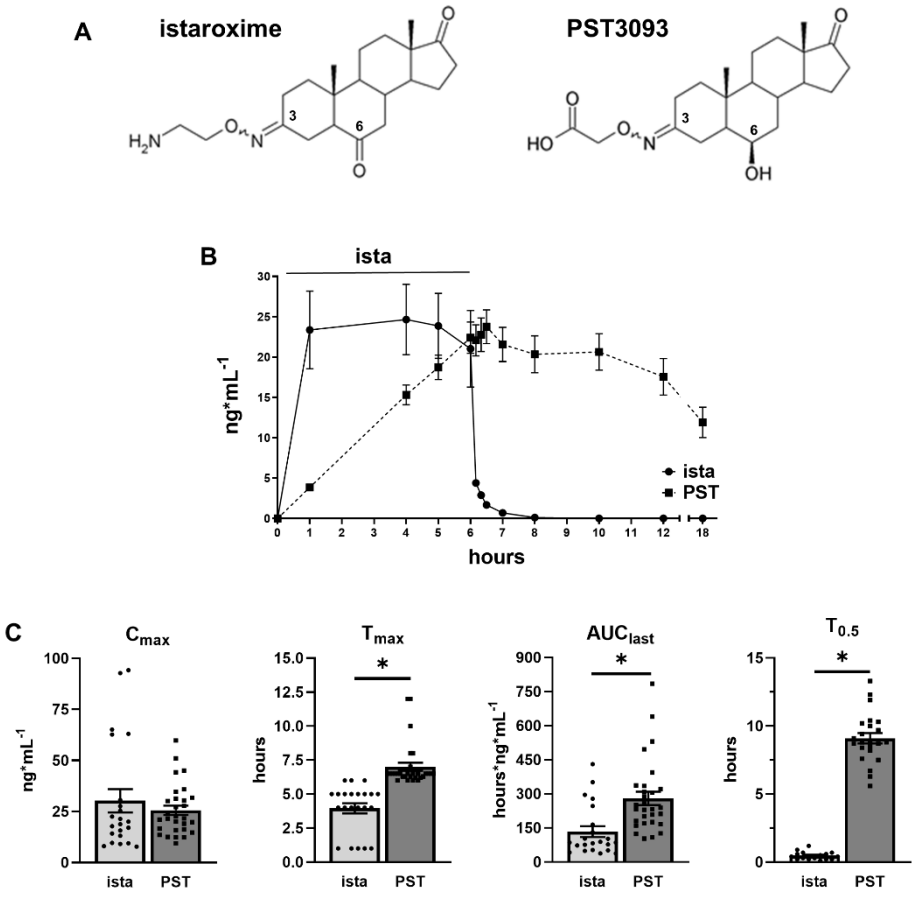

Fig. 1. Chemical structure of istaroxime and its metabolite PST3093 (A) and PKs in humans (B and C). (A) The main metabolic pathways of istaroxime are reduction of the carbonyl in position 6 catalyzed by carbonyl reductases and oxidative deamination of the primary amino group catalyzed by monoamine oxidases or tissue-bound semicarbazide-sensitive amine oxidase. (B) Istaroxime (N=22) and PST3093 (N=29) plasma levels evaluated over 6 hours istaroxime infusion in HF patients at 1 µg/kg per minute and up to 12 hours after discontinuation of infusion (from HORIZON-HF study, #NCT00616161). (C) Statistics of C_{max}, T_{max}, AUC_{last}, and $T_{0.5}$; *P<0.05 versus istaroxime (unpaired *t* test). Data are the mean ± S.E.M. ista, istaroxime; PST, PST3093.

3.5.3 Effect of PST3093 on Na^+/K^+ ATPase

Istaroxime and PST3093 effects on Na^+/K^+ ATPase activity were tested in a range of concentrations from 10^{-9} to 10^{-4} M (Fig. 2A). Na^+/K^+ ATPase from dog kidney had a specific baseline activity of 14 µmol/min/mg protein. The reference compound istaroxime inhibited Na^+/K^+ ATPase activity with IC_{50} of 0.14 ± 0.02 µM in dog kidney (Fig. 2A), which corresponds to a higher affinity as compared with that observed in rat renal preparations [IC_{50} of 55 ± 19 µM from [21]]. PST3093 did not inhibit the Na^+/K^+ ATPase activity up to 100 µM, the maximal tested concentration (Fig. 2A).

PST3093 effects on I_{NaK} were furtherly evaluated in rat LV myocytes in comparison with istaroxime (Fig. 2B). The estimated IC_{50} for I_{NaK} inhibition by istaroxime was 32 ± 4 µM, [from [21]]; for PST3093, a barely detectable inhibition (9.2 ± 1.1%) was observed at the limit concentration for solubility (100 µM), an effect that can be considered insignificant.

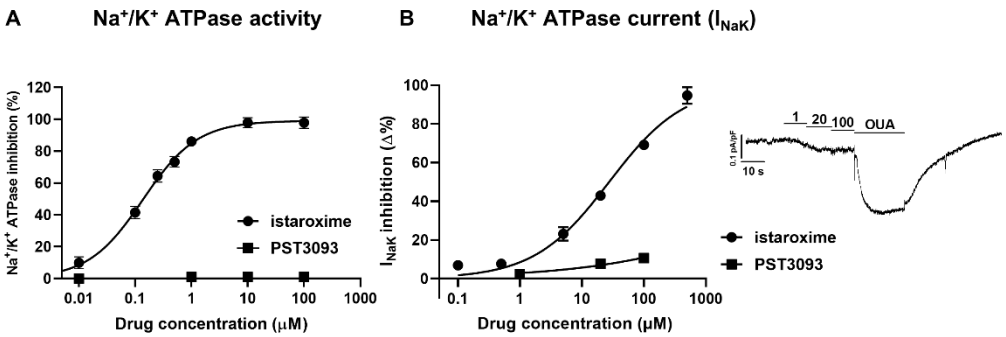

Fig. 2. Modulation of Na^+/K^+ ATPase activity. (A) inhibition of Na^+/K^+ ATPase activity by istaroxime and PST3093 in dog renal preparations (N=3). (B) Concentration-response curves for I_{NaK} inhibition by PST3093 (n=15) and istaroxime (modified from [21]; this work is available under a CC-BY-NC license) in rat LV myocytes; I_{NaK} recording under increasing concentrations of PST3093 and finally to ouabain (OUA as reference) is shown on the right. Data are the mean ± S.E.M.

3.5.4 Effect of PST3093 on SERCA ATPase Activity

3.5.4.1 Effects on SERCA2a Activity in Normal and Diseased Myocardial Preparations

In STZ rat preparations (N=30), baseline SERCA2a V_{max} was lower (by -27%) than in healthy ones (N=29) (0.199 ± 0.01 versus 0.272 ± 0.01 µmol/min/mg protein, P<0.05), with no difference in K_dCa (448 ± 35 vs 393 ± 22 nM, NS), similarly to what reported recently in the same setting [21]. As also reported previously[22], the response of enzyme kinetics parameters to modulation was species specific: whereas in rat preparations both PST3093 and istaroxime (Fig. 3) increased V_{max}, in guinea pig ones the compounds decreased K_dCa instead (Supplemental Table 1).

Over the whole range of concentration tested (0.1 - 1µM), PST3093 and istaroxime failed to affect ATPase Ca^{2+}-dependency in healthy rat preparations (Fig. 3, A and C) but similarly increased V_{max} in STZ ones (e.g., + 22% and + 20%, respectively, at 300 nM) with thresholds at 100 nM and 300 nM for PST3093 and istaroxime, respectively (Fig. 3, B and D); SERCA2a K_dCa in rat preparations was affected by neither istaroxime nor PST3093. Thus, PST3093 and istaroxime displayed similar potency in ameliorating disease-induced depression of SERCA2a ATPase activity.

PST3093 and istaroxime effect was also detected in preparations from normal guinea pig hearts, where they both reduced the SERCA2a K_dCa value by about 20% at 100 nM (Supplemental Table 1).

To summarize, PST3093 and istaroxime equally stimulated SERCA2a ATPase activity in preparations including PLN. Regardless of the kinetic parameter affected, a stimulatory effect was present in healthy guinea pig microsomes and in rat homogenates from the STZ disease model.

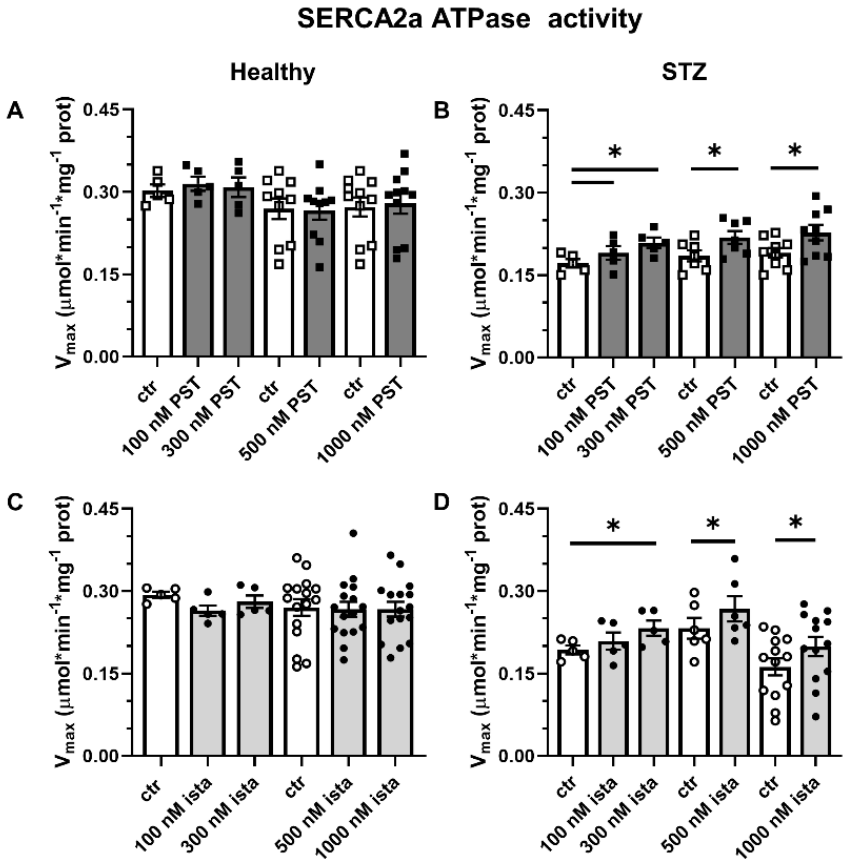

Fig. 3. Modulation of SERCA2a ATPase activity in healthy and diseased (STZ) preparations. Effect of PST3093 (N=5-11) (A and B) and istaroxime (N=5-16) (C and D) on SERCA2a V_{max} estimated from Ca^{2+}-dose response curves in cardiac homogenates from healthy and diabetic (STZ) rats. Internal controls (ctr) are provided. Data are the mean ± S.E.M. * P<0.05 vs ctr (RM one-way ANOVA plus post-hoc Tukey's multiple comparisons test or paired *t* test).

3.5.4.2 Dependency of SERCA Stimulation on PLN

In a range of concentrations from 30 to 1000 nM, PST3093 and istaroxime failed to affect SERCA1 activity in the absence of PLN in skeletal muscle preparations (Fig. 4, A and C). Reconstitution with the PLN_{1-32} fragment markedly reduced SERCA1 affinity for Ca^{2+} (K_dCa increased by 23-26%) (Fig. 4, B and D). Under this condition, both PST3093 (Fig. 4B) and istaroxime (Fig. 4D) dose-dependently reversed PLN-induced shift in K_dCa with an EC_{50} of 39 nM and 40 nM, respectively.

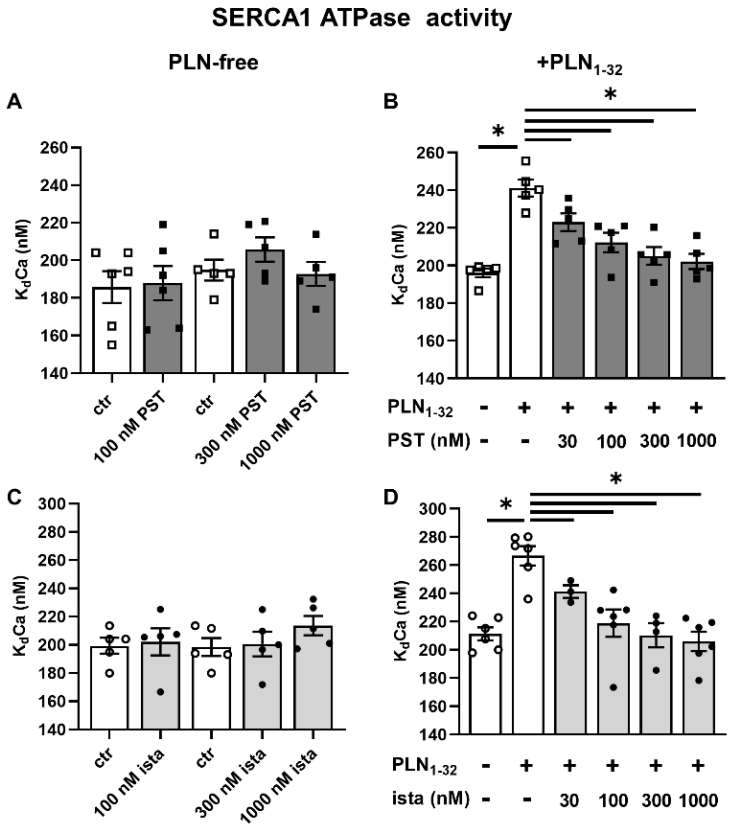

Fig. 4. Modulation of SERCA1 ATPase activity. Concentration dependency of PST3093 and istaroxime modulation of SERCA1 K_dCa in guinea pig skeletal muscle microsomes containing SERCA1 alone (A and C) (N=5-6) and after reconstitution with the PLN_{1-32} fragment (B and D) (N=5-6). Data are the mean ± S.E.M. *P<0.05 (RM or mixed model one-way ANOVA plus post hoc Tukey's multiple comparisons).

3.5.5 PST3093 Interaction with Targets other than SERCA

The targets panel (50 items) included membrane receptors, key enzymes, ion channels, and transporters relevant to potential off-target cardiac and extracardiac effects (list in Supplemental Table 2); PST3093 was tested at the concentration of 10 µM. None among the 50 items met criteria for significance of interaction. Thus, at least for the ligands shown in Supplemental Table 2, no off-target action of PST3093 is expected.

3.5.6 Effects of PST3093 on Intracellular Ca^{2+} Dynamics in Cardiac Myocytes

3.5.6.1 Global Effects in Field Stimulated Myocytes

Ca^{2+} dynamics were analyzed in field-stimulated (2 Hz, Fig. 5) rat LV myocytes isolated from healthy or STZ rats.

STZ myocytes had a lower Ca_{SR} and a slower Ca_T decay than healthy ones; however, Ca_T amplitude remained unchanged. These changes are compatible with reduced SERCA2a function, possibly compensated by APD prolongation, known to increase cell Ca^{2+} content[21]. Whereas in healthy myocytes, 1 µM PST3093 failed to affect any of the Ca^{2+} dynamics parameters, in STZ myocytes PST3093 reduced the quiescence Ca^{2+} (Ca_{rest}) prior to caffeine application and partially restored Ca_{SR} and Ca_T decay. Moreover, PST3093 restored in STZ myocytes the distribution of Ca_{SR} values peculiar of healthy ones. Comparable results have been obtained with istaroxime at a concentration marginally affecting Na^+/K^+ ATPase[21]. Taken together, this observation suggests that PST3093 improved Ca^{2+} sequestration into the SR during the post-train quiescence period.

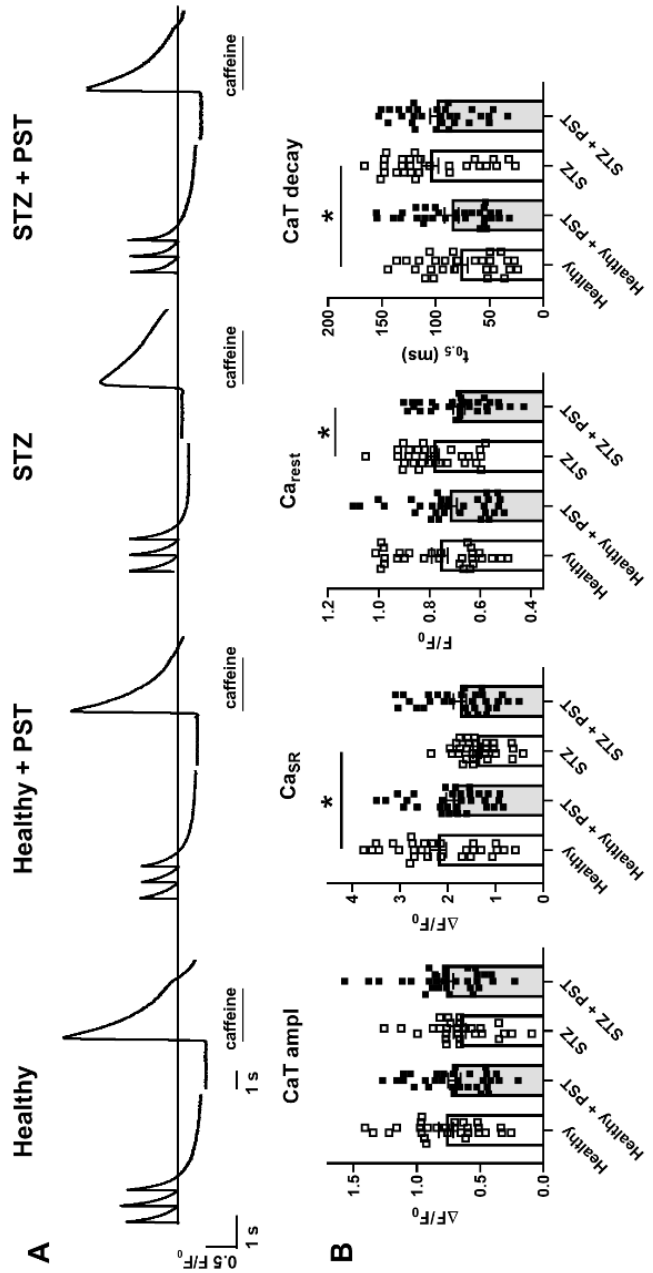

Fig. 5. Modulation of intracellular Ca^{2+} handling in field-stimulated myocytes from healthy and diseased (STZ) hearts. (A) Representative recordings of Ca_T triggered by steady-state electrical stimulation at 2Hz in intact cells, followed after 20 seconds by caffeine-induced Ca^{2+} release measuring Ca_{SR}. PST3093 (1 µM) was tested in normal (healthy) and STZ myocytes. (B) Statistics for Ca_T amplitude (ampl), Ca_{SR}, Ca_{rest}, and time for 50% Ca_T decay ($t_{0.5}$). CTR N=3 (n=28 without PST3093, n=31 with PST3093), STZ N=4 (n=28 without PST3093, n=30 with PST3093). *P<0.05 (one-way ANOVA plus post hoc Tukey's multiple comparisons).

3.5.6.2 Effects on SR Ca^{2+} Uptake Function under NCX Inhibition

STZ-induced changes in repolarization affect Ca^{2+} handling in a direction masking SERCA2a downregulation[21]. Thus, the "SR loading" protocol (see Paragraph 2.6.2 and Fig. 2 in Chapter 2) was performed under V-clamp and used to assess SR Ca^{2+} uptake under conditions emphasizing SERCA2a role (NCX inhibition). In STZ myocytes, as compared to healthy ones, SR reloading was significantly depressed (both in terms of Ca_T amplitude and ER gain), and Ca_T decay was slower at all timepoints during reloading (Fig. 6A). These changes are compatible with depressed SERCA2a function[21]. PST3093 (1 µM) was tested in STZ myocytes (Fig. 6B), where it sharply accelerated Ca_T decay, restoring the profile observed in healthy myocytes. Albeit less evident, drug-induced changes in Ca_T and ER gain pointed in the same direction. Comparable results have been obtained with istaroxime at a concentration marginally affecting Na^+/K^+ ATPase[21].

Overall, PST3093 restored SR function in diseased myocytes, i.e., the context of the pathological cellular environment, most likely through SERCA2a enhancement.

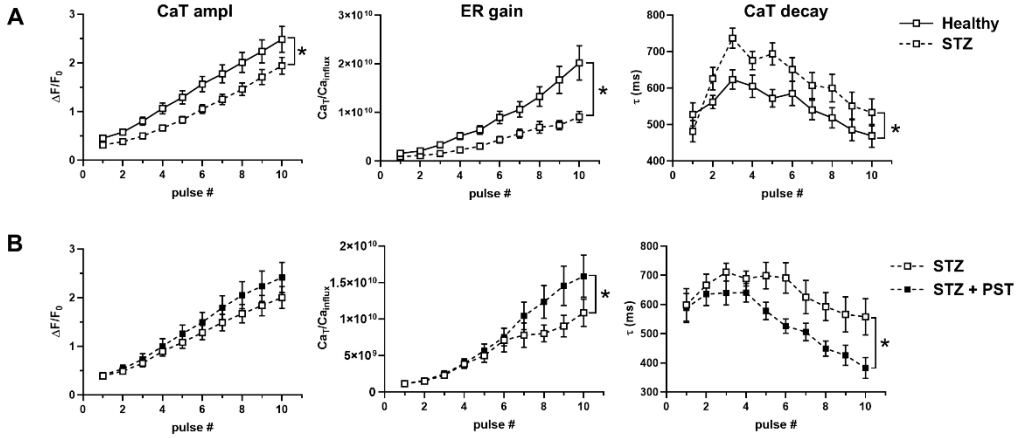

Fig. 6. Modulation of SR Ca^{2+} uptake under NCX inhibition in V-clamped myocytes from STZ hearts. (A) Disease (STZ) effect on SR Ca^{2+} loading in patch-clamped myocytes. SR Ca^{2+} loading by a train of V-clamp pulses was initiated after caffeine-induced SR depletion; NCX was blocked by Na^+ substitution to identify SERCA2a-specific effects (see paragraph 2.6.2 and Fig. 2 in Chapter 2); myocytes from healthy (N=9, n=32) and diseased hearts (STZ, N=6, n=31) are compared. (B) PST3093 effect in STZ myocytes (N=4; without PST3093 n=18, with PST3093 n=19). Panels from left to right: Ca_T amplitude, ER gain (the ratio between Ca_T amplitude and Ca^{2+} influx through I_{CaL}), and τ of Ca_T decay. *P<0.05 for the "interaction factor" in RM two-way ANOVA, indicating a different steepness of curves.

3.5.7 Effects of PST3093 on Cellular Electrical Activity

To assess the electrophysiological safety of PST3093, its effects on AP of LV myocytes were investigated. Guinea pig myocytes were used instead of rat ones because their AP is closer to the human one.

PST3093 (100 nM) marginally reduced APD_{50} at all pacing rates, leaving the other AP parameters unchanged (Fig. 7, A and B). Notably, also APD rate dependency at steady-state and the kinetics of APD adaptation following a step change in rate were unaffected by the agent (Fig. 7C). STV of APD_{90}, a reporter of repolarization stability, was also unaffected by PST3093 at all pacing rates (Fig. 7, D and E). Except for the absence of APD_{50} reduction, similar results were obtained with PST3093 at 1 μM (Supplemental Fig. 2).

The paucity of PST3093 effects on the AP is consistent with the absence of hits in the analysis of PST3093 interaction (up to 10 μM) with molecular targets other than SERCA2a, among them ion channels and transporters (Supplemental Table 2).

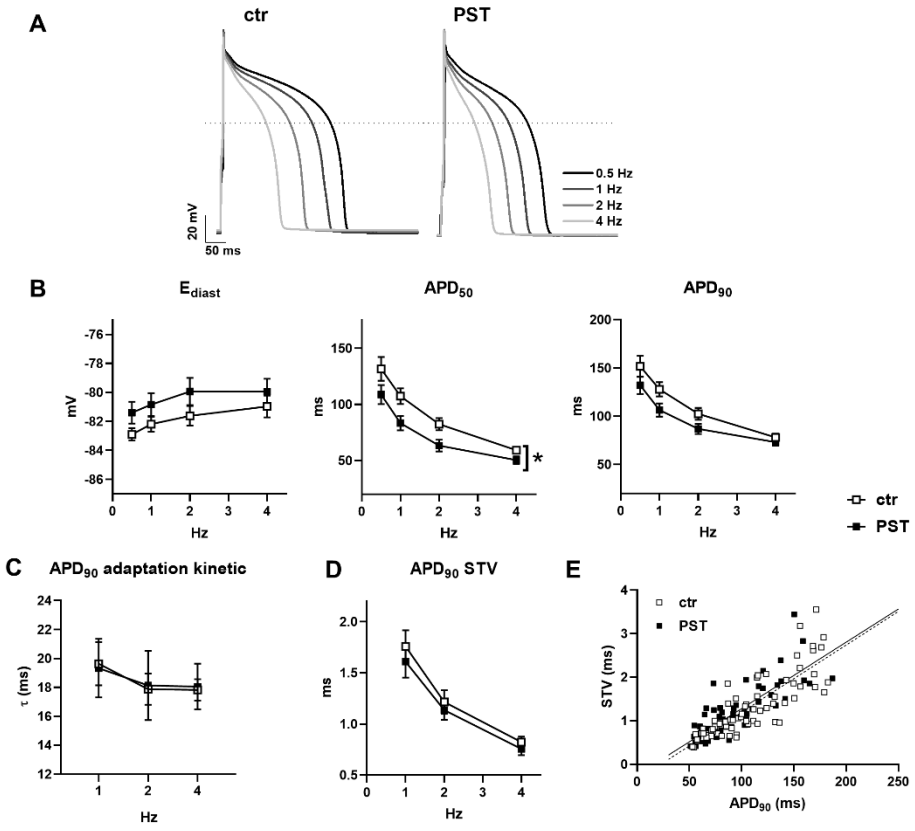

Fig. 7. Modulation of electrical activity in guinea pig myocytes. The effect of 100 nM PST3093 was tested on AP parameters and their steady-state rate dependency in guinea pig myocytes (N=5). (A) representative APs recorded at 0.5, 1, 2, 4 Hz in control (left) and with 100 nM PST3093 (right). (B) Effect on the rate dependency of diastolic potential (E_{diast}) and AP duration (APD_{50}, APD_{90}) (n≥24 without PST3093, n≥22 with PST3093). (C) Effect on the τ of APD_{90} adaptation following a step change in rate (n≥22 without PST3093, n≥16 with PST3093). (D) Effect on the rate dependency of APD_{90} STV (n≥24 without PST3093, n≥20 with PST3093). (E) Effect on the correlation between STV of APD_{90} and APD_{90} values; data from 1, 2, 4 Hz were pooled. *P<0.05 for the "interaction factor" of RM two-way ANOVA. The effect of PST3093 at a higher concentration (1 μM) is reported in Supplemental Fig. 2.

3.5.8 In Vivo Acute Toxicity in Mice

In vivo toxicity after intravenous injection was investigated in mice for PST3093 and istaroxime. PST3093 was well tolerated and did not cause death up to 250 mg/kg. The LD_{50} was not calculated since no deaths occurred at the maximal usable dose (limited by solubility). The LD_{50} for istaroxime was 23.06 mg/kg. The main signs of toxicity were prostration, gasping and convulsions. In most of the animals, death occurred within 5 min after istaroxime administration. Post-mortem examination revealed pulmonary edema and/or hemorrhages and generalized organ congestion. No remarkable alterations were found in the surviving animals.

Therefore, when intravenously administered, PST3093 was far less toxic than istaroxime, a result ascribable to its lack of effects on the Na^+/K^+ ATPase.

3.5.9 Modulation of Cardiac Function in Vivo in Rats with Diabetic Cardiomyopathy

In vivo cardiac function was evaluated by echocardiography. In light of the uncertainty inherent to the mechanistic interpretation of drug effect on individual echo indexes, this set of experiments was designed to test whether PST3093 was able to reverse the derangements peculiar of the STZ disease model. To this end, the STZ model had to be first characterized.

3.5.9.1 Features of the Disease Model

Fasting hyperglycemia, polydipsia, polyuria and polyphagia ensued 1 week after STZ injection; none of these symptoms was observed in healthy rats. Eight weeks after STZ, total body weight was substantially lower in STZ rats; LV mass (by echo) was reduced in absolute value but, when normalized to body weight, was not significantly different in STZ rats (Supplemental Table 3). The STZ model was largely characterized in a previous work of ours[21].

In this study a comprehensive echocardiographic analysis of STZ rats in comparison to healthy ones was performed. Figure 8 compares some echo indexes in STZ versus healthy rats; Supplemental Table 4 lists all the measured echo parameters in the two

groups. Heart rate (HR) was lower in STZ rats (-20%; P<0.05) and SV was unchanged; nonetheless, differences in cardiac output (CO) between the two groups did not achieve significance. *Systolic indexes*: in STZ rats, LVESD was larger, and the EF reduced; FS and systolic tissue velocity (s') were depressed. *Diastolic indexes*: in STZ rats, LVEDD tended to be larger; peak E-wave velocity (E) was slightly smaller, and A-wave velocity (A) was unchanged (E/A unchanged); E-wave DT was unchanged in absolute, but the DT/E ratio was increased. Changes in early (e') and late (a') diastolic tissue velocities paralleled those in E and A waves; therefore, the e'/a' and E/e' ratios did not differ between STZ and healthy rats.

To summarize, in STZ rat, echocardiographic abnormalities were rather subtle; nonetheless, 11 out of 21 indexes were significantly affected, indicating derangements in both systolic and diastolic function.

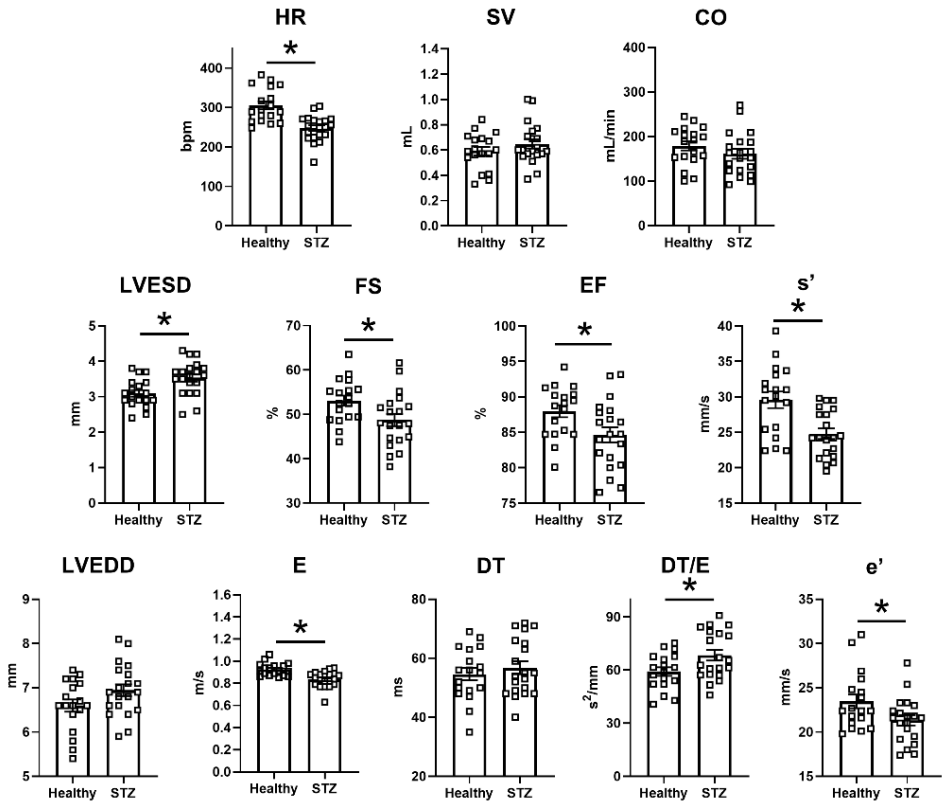

Fig. 8. Disease (STZ) effects on in vivo echocardiographic parameters. Echocardiographic parameters are compared between healthy rats (N=18) and 8 weeks after STZ treatment (N=20). Top row, global function parameters; mid row, systolic function parameters; bottom row, diastolic function parameters. *P<0.05 (unpaired *t* test).

3.5.9.2 Drug Effects in the Disease Model

The in vivo acute effect of PST3093 (0.22 mg/kg/min) on echo indexes of STZ rats was investigated at 15 and 30 minutes of infusion (Fig. 9). Data at 15 min were also obtained with istaroxime (0.22 mg/kg/min) and digoxin (0.11 mg/kg/min) (Table 2). Overall, PST3093 increased SV volume and CO, without changing HR (Fig. 9). *Systolic indexes*: PST3093 tended to decrease LVESD and increased FS, EF and s'. *Diastolic indexes*: PST3093 increased LVEDD, E, A (at 30 minutes), and e' (E/A and E/e' unchanged, Table 2); DT and DT/E were reduced. PST3093 effect was almost complete at 15 min of infusion; only minor increments were observed at 30 min (Fig. 9). Collectively, PST3093 improved overall cardiac function, both systolic and diastolic, beyond simple recovery of STZ-induced derangements. As shown in Fig. 9, PST3093 "reversed" STZ-induced changes in 7 out of 11 indexes; moreover, five additional indexes, unaffected by STZ, were changed by PST3093 in a direction compatible with positive inotropy/lusitropy (Table 2).

PST3093 effects were only partially shared by istaroxime at the same infusion rate (Table 2). Istaroxime failed to increase SV and systolic indexes (SV, FS, EF, s'); it increased CO, but, at variance with PST3093, this was because HR increased. Similar to PST3093, istaroxime shortened DT and DT/E and increased e', a' and A; however, it did not change E, thus reducing E/e'. Digoxin (Table 2), as expected from its inotropic effect, increased systolic indexes (FS, EF and s'); however, at variance with PST3093, it did not affect SV or CO. Notably, also digoxin improved diastolic function to some extent: E/A, DT and DT/E were reduced, and e' was increased.

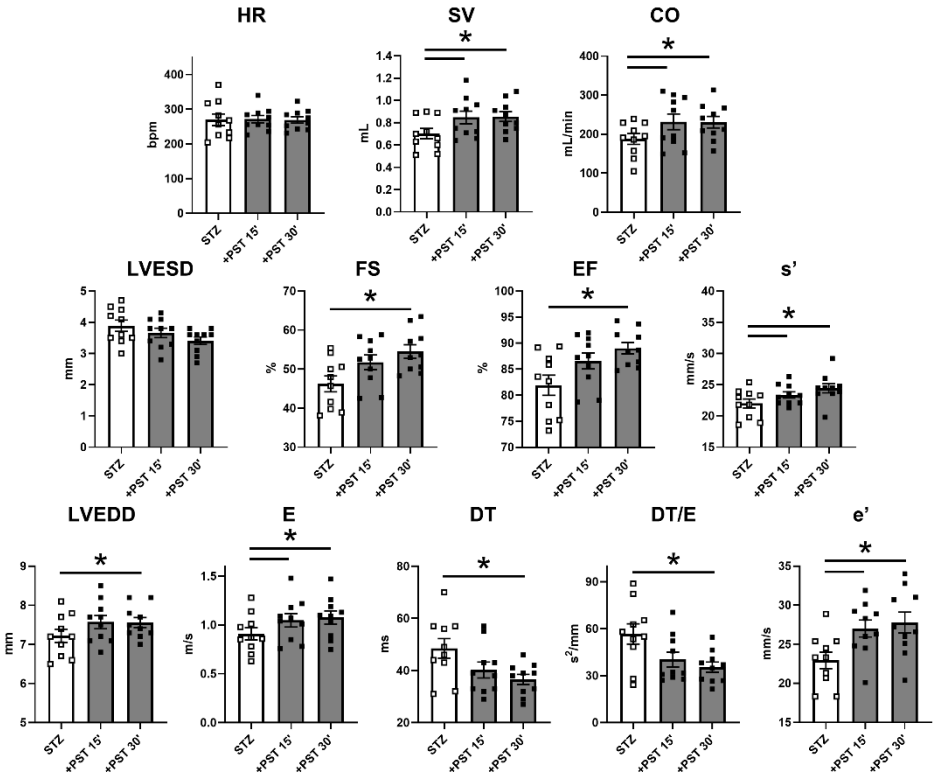

Fig. 9. PST3093 effects on in vivo echocardiographic parameters in diseased (STZ) rats. PST3093 was intravenously infused (0.22 mg/kg/min) in rats 8 weeks after STZ treatment. Echocardiographic parameters were measured before and at 15 and 30 minutes during drug infusion. Rows and symbols as in Fig. 8; N=10 rats. Data are the mean ± S.E.M. *P<0.05 (RM one-way ANOVA plus post-hoc Tukey's multiple comparisons). Effects of PST3093 on all echocardiographic parameters at 15 minutes of infusion in STZ rats in comparison to istaroxime and digoxin are reported in Table 2.

Table 2. Effects of PST3093 (0.22 mg/kg/min), istaroxime (0.22 mg/kg/min) and digoxin (0.11 mg/kg/min) on echo indexes of STZ rats at 15 minutes of infusion. Data are the mean ± S.E.M. #P<0.05 vs before drug infusion (paired *t* test).

		Istaroxime		PST3093		Digoxin	
Echo Parameters		Before	At 15 Min	Before	At 15 Min	Before	At 15 Min
Morphometric Parameters	IVSTd (mm)	1.91 ± 0.09	1.97 ± 0.16	1.89 ± 0.09	1.86 ± 0.11	1.79 ± 0.07	1.81 ± 0.04
	PWTd (mm)	1.6 ± 0.07	1.68 ± 0.09	1.46 ± 0.05	1.47 ± 0.07	1.71 ± 0.08	1.66 ± 0.1
	LVEDD (mm)	7.25 ± 0.15	7.1 ± 0.2	7.22 ± 0.17	7.57 ± 0.17	6.76 ± 0.15	6.67 ± 0.15
	IVSTs (mm)	2.4 ± 0.1	2.45 ± 0.12	2.16 ± 0.11	2.31 ± 0.13	2.25 ± 0.14	2.31 ± 0.1
	PWTs (mm)	2.33 ± 0.16	2.42 ± 0.15	2.43 ± 0.12	2.62 ± 0.14	2.47 ± 0.16	2.68 ± 0.14
	LVESD (mm)	3.82 ± 0.21	3.8 ± 0.2	3.89 ± 0.18	3.66 ± 0.15	3.53 ± 0.17	3.14 ± 0.14[a]
Systolic Parameters	FS (%)	47.21 ± 2.4	46.72 ± 2.1	46.2 ± 2.02	51.8 ± 1.89[a]	47.62 ± 1.9	53.09 ± 1.8[a]
	s′ (mm/s)	23.37 ± 0.9	23.05 ± 0.7	22.0 ± 0.72	23.4 ± 0.5[a]	23.5 ± 0.9	26 ± 1.5[a]
	EF (%)	83 ± 2	82 ± 62	82 ± 1.9	87 ± 1.5[a]	84 ± 1.5	88 ± 1.3[a]
Diastolic Parameters	E (mm/s)	0.91 ± 0.04	0.94 ± 0.04	0.91 ± 0.06	1.05 ± 0.07[a]	0.831 ± 0.03	0.924 ± 0.06
	A (mm/s)	0.66 ± 0.04	0.78 ± 0.05[a]	0.79 ± 0.08	0.87 ± 0.07	0.59 ± 0.05	0.79 ± 0.05[a]
	E/A	1.39 ± 0.06	1.22 ± 0.08	1.18 ± 0.05	1.22 ± 0.04	1.48 ± 0.11	1.2 ± 0.06[a]
	DT (ms)	46.62 ± 4.1	34.12 ± 2.5[a]	48.5 ± 3.8	40.2 ± 3.0	53.4 ± 3.8	44.1 ± 3.2[a]
	DT/E	51.91 ± 4.9	36.66 ± 3.3[a]	56.7 ± 6.5	40.39 ± 4.8[a]	65.21 ± 5.3	50.18 ± 5.4[a]
	E/DT	21.28 ± 3.2	28.98 ± 2.8[a]	20.61 ± 3.0	27.51 ± 2.6[a]	16.53 ± 1.7	22.66 ± 3.0
	e′ (mm/s)	21.23 ± 0.99	24.73 ± 0.61[a]	22.94 ± 1.0	27.01 ± 1.1[a]	20.9 ± 0.5	23.8 ± 0.9[a]
	a′ (mm/s)	27.61 ± 1.9	31.35 ± 1.5[a]	28.72 ± 2.2	31.06 ± 1.5	25.9 ± 1.9	29.8 ± 1.9
	e′/a′	0.78 ± 0.04	0.79 ± 0.03	0.83 ± 0.06	0.88 ± 0.04	0.85 ± 0.06	0.82 ± 0.04
	E/e′	43.6 ± 2.6	38.29 ± 1.6[a]	39.5 ± 1.7	38.61 ± 1.5	39.64 ± 0.9	38.95 ± 2.3
Cardiac Function	HR (bpm)	266.2 ± 9.8	316.2 ± 7.5[a]	270 ± 17	271 ± 10	236 ± 12	257 ± 11
	SV (ml)	0.71 ± 0.04	0.67 ± 0.05	0.702 ± 0.05	0.847 ± 0.06[a]	0.589 ± 0.03	0.601 ± 0.04
	CO (ml/min)	188.8 ± 10.5	211.2 ± 13.2[a]	187.7 ± 13.7	231.7 ± 20.2[a]	138.5 ± 11.2	155.6 ± 14.4
	N	8	8	10	10	10	10

[a] $P < 0.05$ versus before drug infusion (paired t test).

3.6. DISCUSSION

In the present study, we have investigated effects of the istaroxime metabolite PST3093 at molecular, cellular, and in vivo levels. The interest in this molecule is motivated by 1) the possibility that it may actually contribute to (i.e., be endowed with) the unique mechanism of action and interesting therapeutic profile of istaroxime (inotropy and lusitropy at low proarrhythmic risk, confirmed in phase 2 clinical trials)[15,16,19,20] and 2) the possibility it would afford to test the clinical benefit associated specifically with the rescue of SERCA2a depression, which is widely recognized as the basis for many among HF abnormalities.

PST3093 effect has been tested in three experimental settings with incremental level of biological organization, including in vivo measurements from diseased hearts. The consistency of effects across these three sets of experiments confers robustness to the findings.

The results of molecular studies indicate that PST3093 differs from istaroxime because it is devoid of any inhibitory activity on the Na^+/K^+ ATPase while retaining SERCA2a stimulatory action. This identifies PST3093 as a "selective" SERCA2a activator. The results also indicate that, similar to istaroxime[22], PST3093 may act by weakening SERCA-PLN interaction. In rat preparations, PST3093 (and istaroxime) increased SERCA2a V_{max}. Although this apparently conflicts with the notion that interference with PLN should decrease the K_dCa instead[24], the same pattern coexisted with evidence, by several independent approaches, of istaroxime antagonism of SERCA2a-PLN interaction[22]. The reason for this apparent discrepancy is unclear; the observation that PST3093 effect on SR Ca^{2+} uptake was present in rat cardiac myocytes (i.e., at physiologic Ca^{2+} concentrations) suggests that it may reside in specificities of the microsomal preparation.

Investigations in intact ventricular myocytes confirm a negligible effect of PST3093 on Na^+/K^+ pump function. Furthermore, PST3093 abolished STZ-induced intracellular Ca^{2+} abnormalities likely dependent on SERCA2a downregulation. Although PST3093 clearly affected several Ca^{2+} cycling parameters under V-clamp conditions (Fig. 6), its effects in field-stimulated cells were apparently small (Fig. 5). As we have previously shown in this experimental model[21], evaluation of Ca^{2+} handling without controlling

membrane potential (field stimulation) and without disabling competing mechanisms (NCX) may be unsuitable to detect SERCA2a activation.

This is why we also performed experiments under V-clamp and with disabled NCX function, shown in Fig. 6. Field-stimulation experiments are nonetheless informative because they better represent drug effects at the cell level under "physiological" conditions. In particular, the reduction in Ca_{rest} indicates that PST3093 allows the other Ca^{2+} cycling parameters to be preserved (or even showing a trend to improve) at a lower cytosolic Ca^{2+} level. Considering that all Ca^{2+} homeostatic mechanisms are in place in this setting, this is precisely what should be expected from pure SERCA2a activation[2,18], i.e., improved subcellular Ca^{2+} compartmentalization. That this apparently small change in myocyte physiology has an impact on I -vivo cardiac performance is shown by the in vivo echo measurements (Fig. 9).

The present in vivo studies were conducted by echocardiography in a disease model characterized by impairment of SERCA2a function[21,25]. In this model, PST3093 infusion improved overall cardiac performance (SV and CO); both systolic and diastolic indexes were positively affected by the agent. Mechanistic interpretation of echocardiographic indexes is often ambiguous. For instance, both DT prolongation and shortening have been associated with deterioration of diastolic function[19,26]. These puzzling observations can be interpreted by considering the contribution to DT of opposing factors, each prevailing in a specific condition[27]. At any rate, whenever HF was associated with DT shortening, istaroxime (having PST3093 as a metabolite) prolonged it[15,19]. A further difficulty may arise from the expectation that ino-lusitropy may increase atrial contraction (A amplitude) and ventricular relaxation (E amplitude) at the same time, thus conceivably making their ratio (E/A) unable to detect drug effects on diastolic function. A similar consideration applies to the E/e' index. An approach to the interpretation of drug effects, independent of mechanistic models, is to check whether the drug counters disease-induced abnormalities. In the case of PST3093, this was true for the majority of indexes (7 out of 11), the most notable exception being a small further increase in LVEDD. Although increments in LVEDD are usually associated with deterioration of systolic function, PST3093 tended to decrease LVESD instead. The LVEDD increment was indeed associated with increased SV and EF, to which it likely contributed.

With the exception of guinea pigs, PST3093 efficacy on SERCA2a function in the diseased condition consistently contrasted with the lack of effect in healthy preparations (Figs. 3 and 5). This suggests that SERCA2a function, while not strictly limiting in health, may become so whenever its "reserve" is diminished. This view may not clash with the clear-cut effect of PLN knockout in healthy murine myocytes; indeed, SERCA2a modulation by PST3093 may be, albeit functionally significant, subtler than complete PLN ablation.

Although failing to increase the amplitude of Ca_T, PST3093 improved echo indexes of systolic function. Mechanisms at two levels may account for this observation: at the intracellular level, increased compartmentation of Ca^{2+} within the SR may improve the energetic efficiency of Ca^{2+} cycling[28]; at the organ level, improved relaxation may increase preload, with its well known impact on systolic force[29]. Indeed, normalization of diastolic function in HF patients with preserved EF, may restore CO irrespective of changes in the latter[30]. On the other hand, digoxin, whose mechanism of action is purely inotropic, accelerated early relaxation (DT shortening and e' increase). This is consistent with systo-diastolic coupling, i.e., the contribution to early relaxation of elastic restitution (recoil) of systolic force[31].

Beside affording inotropy and lusitropy, SERCA2a stimulation may improve intracellular Ca^{2+} compartmentalization, with potential long-term effects on energetic efficiency and biology of cardiac myocytes[2].

PST3093 is remarkably less toxic than istaroxime which, in turn, has a lower proarrhythmic risk as compared to digoxin[17]. We speculate that the low PST3093 toxicity, relative to istaroxime, may be due its failure to inhibit the Na^+/K^+ pump. The absence of interaction with 50 cardiac and noncardiac targets commonly involved in drug toxicity provides at least a first-level evidence of PST3093 suitability as a therapeutic agent.

3.6.1 Limitations

Whereas, in the in vivo experiments PST3093 effects generally achieved a maximum at 30 minutes of infusion, the istaroxime infusion period was limited to 15 minutes. Our previous study[21] indicates that a 15-minutes infusion is sufficient for modulation of diastolic parameters by istaroxime. This timepoint was selected in the present study to minimize metabolism to PST3093, thus allowing it to differentiate istaroxime's own effect from that of its metabolite. Nonetheless, istaroxime effects reported here might differ from the steady-state ones described in previous studies[15,16,19], to which PST3093 (the metabolite) might actually contribute.

Echo parameters are sensitive to changes in blood pressure, which was not directly measured. Nonetheless, previous in vivo studies ruled out the effect of infused istaroxime, and, implicitly, of PST3093 on pulmonary and peripheral resistances[20].

Translation of the present in vivo results to human therapy has to consider differences between clinical HF and the STZ rat model, which has specific hemodynamic features[32]. However, consistency of the istaroxime effect reported here with that described in HF patients[16] supports this translation.

3.6.2 Therapeutic Relevance and Perspective

The results of this study identify PST3093 as a prototype "selective" (i.e., devoid of Na^+/K^+ pump inhibition) SERCA2a activator. This may entail significant differences from the already characterized pharmacodynamic profile of istaroxime.

In the case of istaroxime, lack of the proarrhythmic effect [expected from Na^+/K^+ ATPase inhibition[14]] is likely due to SERCA2a stimulation. Indeed, the latter may reduce the occurrence of "Ca^{2+} waves" and the resulting "triggered activity"[2,33,34]. It is logical to predict that a pure SERCA2a activator may exert substantial antiarrhythmic effects, at least under the common conditions characterized by SR instability (e.g., HF). On the other hand, Na^+/K^+ pump inhibition may contribute to inotropy; thus, at least theoretically, PST3093 should increase systolic force less than istaroxime. The present results argue for a PST3093 effect on global cardiac function, including positive inotropy. Moreover, compared to istaroxime, PST3093 has a much longer half-life that, per se, may also prolong the beneficial hemodynamic effect of istaroxime infusion.

Overall, PST3093 acting as “selective” SERCA2a activator can be considered the prototype of a novel pharmacodynamic class for the ino-lusitropic approach of HF. After more than 50 years from the suggestion of the involvement of a reduced SERCA2a function as a cause of the depressed cardiac function and the increased arrhythmias in HF, we may have the possibility to prove this hypothesis and provide a “causal” and selective therapy for HF patients.

3.7. AUTHOR CONTRIBUTION

Participated in research design: Rocchetti, Zaza, Peri, Ferrari and Bianchi.
Conducted experiments: Arici, Ferrandi, Barassi, Hsu and Chang.
Performed data analysis: Arici, Ferrandi, Torre, Luraghi and Ronchi.
Wrote or contributed to the writing of the manuscript: Rocchetti and Zaza.

3.8. REFERENCES

(1) Bers, D. M.; Despa, S.; Bossuyt, J. Regulation of Ca2+ and Na+ in Normal and Failing Cardiac Myocytes. *Annals of the New York Academy Sciences* **2006**, *1080*, 165–177. https://doi.org/10.1196/annals.1380.015.

(2) Zaza, A.; Rocchetti, M. *Calcium Store Stability as an Antiarrhythmic Endpoint*; 2015; Vol. 21.

(3) Nakayama, H.; Chen, X.; Baines, C. P.; Klevitsky, R.; Zhang, X.; Zhang, H.; Jaleel, N.; Chua, B. H. L.; Hewett, T. E.; Robbins, J.; Houser, S. R.; Molkentin, J. D.; Quillen, J. H. Ca2+-and Mitochondrial-Dependent Cardiomyocyte Necrosis as a Primary Mediator of Heart Failure. *J Clin Invest* **2007**, *117*. https://doi.org/10.1172/JCI31060.

(4) Suko, J.; Vogel, J. H. K.; Chidsey, C. A. Intracellular Calcium and Myocardial Contractility. *Circ Res* **1970**, *27*, 235–247.

(5) Sulakhe, P. v; Dhalla, N. S. Excitation-Contraction Coupling in Heart. *J Clin Invest* **1971**, *50*, 1019–1027.

(6) Gwathmey, J. K.; Copelas, L.; Mackinnon, R.; Schoen, F. J.; Feldman, M. D.; Grossman, W.; Morgan, J. P. Abnormal Intracellular Calcium Handling in Myocardium From Patients With End-Stage Heart Failure. *Circ Res* **1987**, *61*, 70–76.

(7) Arai, M.; Alpert, N. R.; Maclennan, D. H.; Barton, P.; Periasamy, M.; Periasamy, M. *Alterations in Sarcoplasmic Reticulum Gene Expression in Human Heart Failure: A Possible Mechanism for Alterations in Systolic and Diastolic Properties of the Failing Myocardium*; 1993; Vol. 72.

(8) Kranias, E. G.; Hajjar, R. J. Modulation of Cardiac Contractility by the Phopholamban/SERCA2a Regulatome. *Circ Res* **2012**, *110* (12), 1646–1660. https://doi.org/10.1161/CIRCRESAHA.111.259754.

(9) Haghighi, K.; Schmidt, A. G.; Hoit, B. D.; Brittsan, A. G.; Yatani, A.; Lester, J. W.; Zhai, J.; Kimura, Y.; Dorn, G. W.; MacLennan, D. H.; Kranias, E. G. Superinhibition of Sarcoplasmic Reticulum Function by Phospholamban Induces Cardiac Contractile Failure. *Journal of Biological Chemistry* **2001**, *276* (26), 24145–24152. https://doi.org/10.1074/jbc.M102403200.

(10) del Monte, F.; Sian, H. E.; Dec, W. G.; Gwathmey, J. K.; Hajjar, R. J. Targeting Phospholamban by Gene Transfer in Human Heart Failure. *Circulation* **2002**, *105*, 904–907. https://doi.org/10.1161/hc0802.105564.

(11) Kho, C.; Lee, A.; Jeong, D.; Oh, J. G.; Chaanine, A. H.; Kizana, E.; Park, W. J.; Hajjar, R. J. SUMO1-Dependent Modulation of SERCA2a in Heart Failure. *Nature* **2011**, *477* (7366), 601–606. https://doi.org/10.1038/nature10407.

(12) Kaneko, M.; Yamamoto, H.; Sakai, H.; Kamada, Y.; Tanaka, T.; Fujiwara, S.; Yamamoto, S.; Takahagi, H.; Igawa, H.; Kasai, S.; Noda, M.; Inui, M.; Nishimoto, T. A Pyridone Derivative Activates SERCA2a by Attenuating the Inhibitory Effect of Phospholamban. *Eur J Pharmacol* **2017**, *814*, 1–8. https://doi.org/10.1016/j.ejphar.2017.07.035.

(13) Schaaf, T. M.; Kleinboehl, E.; Yuen, S. L.; Roelike, L. N.; Svensson, B.; Thompson, A. R.; Cornea, R. L.; Thomas, D. D. Live-Cell Cardiac-Specific High-Throughput Screening Platform for Drug-Like Molecules That Enhance Ca2+ Transport. *Cells* **2020**, *9* (5). https://doi.org/10.3390/cells9051170.

(14) Rocchetti, M.; Besana, A.; Mostacciuolo, G.; Micheletti, R.; Ferrari, P.; Sarkozi, S.; Szegedi, C.; Jona, I.; Zaza, A. Modulation of Sarcoplasmic Reticulum Function by Na/K Pump Inhibitors with Different Toxicity: Digoxin and PST2744 [(E,Z)-3-((2-Aminoethoxy)Imino)Androstane-6,17-Dione Hydrochloride]. *J Pharmacol Exp Ther* **2005**, *313*, 207–215. https://doi.org/10.1124/jpet.104.077933.

(15) Shah, S. J.; Blair, J. E. A.; Filippatos, G. S.; MacArie, C.; Ruzyllo, W.; Korewicki, J.; Bubenek-Turconi, S. I.; Ceracchi, M.; Bianchetti, M.; Carminati, P.; Kremastinos, D.; Grzybowski, J.; Valentini, G.; Sabbah, H. N.; Gheorghiade, M. Effects of Istaroxime on Diastolic Stiffness in Acute Heart Failure Syndromes: Results from the Hemodynamic, Echocardiographic, and Neurohormonal Effects of Istaroxime, a Novel Intravenous Inotropic and Lusitropic Agent: A Randomized Controlled Trial in Patients Hospitalized with Heart Failure (HORIZON-HF) Trial. *Am Heart J* **2009**, *157* (6), 1035–1041. https://doi.org/10.1016/j.ahj.2009.03.007.

(16) Carubelli, V.; Zhang, Y.; Metra, M.; Lombardi, C.; Michael Felker, G.; Filippatos, G.; O, C. M.; Teerlink, J. R.; Simmons, P.; Segal, R.; Malfatto, G.; Teresa La Rovere, M.; Li, D.; Han, X.; Yuan, Z.; Yao, Y.; Li, B.; Fui Lau, L.; Bianchi, G.; Zhang, J. Treatment with 24 Hour Istaroxime Infusion in Patients Hospitalised for Acute Heart Failure: A Randomised, Placebo-Controlled Trial Aim Methods and Results. *Eur J Heart Fail* **2020**, *22*, 1684–1693. https://doi.org/10.1002/ejhf.1743.

(17) Micheletti, R.; Mattera, G. G.; Rocchetti, M.; Schiavone, A.; Loi, M. F.; Zaza, A.; Gagnol, R. J. P.; de Munari, S.; Melloni, P.; Carminati, P.; Bianchi, G.; Ferrari, P. Pharmacological Profile of the Novel Inotropic Agent (E,Z)-3-((2-Aminoethoxy)Imino)Androstane-6,17-Dione Hydrochloride (PST2744). *J Pharmacol Exp Ther* **2002**, *303*, 592–600. https://doi.org/10.1124/jpet.102.038331.

(18) Alemanni, M.; Rocchetti, M.; Re, D.; Zaza, A. Role and Mechanism of Subcellular Ca2+ Distribution in the Action of Two Inotropic Agents with Different Toxicity. *J Mol Cell Cardiol* **2011**, *50* (5), 910–918. https://doi.org/10.1016/j.yjmcc.2011.02.008.

(19) Sabbah, H. N.; Imai, M.; Cowart, D.; Amato, A.; Carminati, P.; Gheorghiade, M. Hemodynamic Properties of a New-Generation Positive Luso-Inotropic Agent for the Acute Treatment of Advanced Heart Failure. *American Journal of Cardiology* **2007**, *99* (2 SUPPL.). https://doi.org/10.1016/j.amjcard.2006.09.005.

(20) Gheorghiade, M.; Blair, J. E. A.; Filippatos, G. S.; Macarie, C.; Ruzyllo, W.; Korewicki, J.; Bubenek-Turconi, S. I.; Ceracchi, M.; Bianchetti, M.; Carminati, P.; Kremastinos, D.; Valentini, G.; Sabbah, H. N. Hemodynamic, Echocardiographic, and Neurohormonal Effects of Istaroxime, a Novel Intravenous Inotropic and Lusitropic Agent: A Randomized Controlled Trial in Patients Hospitalized With Heart Failure. *J Am Coll Cardiol* **2008**, *51* (23), 2276–2285. https://doi.org/10.1016/J.JACC.2008.03.015.

(21) Torre, E.; Arici, M.; Lodrini, A. M.; Ferrandi, M.; Barassi, P.; Hsu, S.-C.; Chang, G.-J.; Boz, E.; Sala, E.; Vagni, S.; Altomare, C.; Mostacciuolo, G.; Bussadori, C.; Ferrari, P.; Bianchi, G.; Rocchetti, M. SERCA2a Stimulation by Istaroxime Improves Intracellular Ca2+ Handling and Diastolic Dysfunction in a Model of Diabetic Cardiomyopathy. *Cardiovasc Res* **2022**, *118*, 1020–1032. https://doi.org/10.1093/cvr/cvab123.

(22) Ferrandi, M.; Barassi, P.; Tadini-Buoninsegni, F.; Bartolommei, G.; Molinari, I.; Tripodi, M. G.; Reina, C.; Moncelli, M. R.; Bianchi, G.; Ferrari, P. Istaroxime Stimulates SERCA2a and Accelerates Calcium Cycling in Heart Failure by Relieving Phospholamban Inhibition Correspondence. *Br J Pharmacol* **2013**, *169*, 1849–1861. https://doi.org/10.1111/bph.12288.

(23) Gheorghiade, M.; Blair, J. E. A.; Filippatos, G. S.; Macarie, C.; Ruzyllo, W.; Korewicki, J.; Bubenek-Turconi, S. I.; Ceracchi, M.; Bianchetti, M.; Carminati, P.; Kremastinos, D.; Valentini, G.; Sabbah, H. N. Hemodynamic, Echocardiographic, and Neurohormonal Effects of Istaroxime, a Novel Intravenous Inotropic and Lusitropic Agent. A Randomized Controlled Trial in Patients Hospitalized With Heart Failure. *J Am Coll Cardiol* **2008**, *51*, 2276–2285. https://doi.org/10.1016/j.jacc.2008.03.015.

(24) Brittsan, A. G.; Ginsburg, K. S.; Chu, G.; Yatani, A.; Wolska, B. M.; Schmidt, A. G.; Asahi, M.; Maclennan, D. H.; Bers, D. M.; Kranias, E. G. Chronic SR Ca 2+-ATPase Inhibition Causes Adaptive Changes in Cellular Ca 2+ Transport. *Circ Res* **2003**, *92*, 769–776. https://doi.org/10.1161/01.RES.0000066661.49920.59.

(25) Choi, K. M.; Zhong, Y.; Hoit, B. D.; Grupp, I. L.; Hahn, H.; Dilly, K. W.; Guatimosim, S.; Lederer, W. J.; Matlib, M. A.; Guatimo-Sim, S. Defective Intracellular Ca2+ Signaling Contributes to Cardiomyopathy in Type 1 Diabetic Rats. *Am J Physiol Heart Circ Physiol* **2002**, *283*, H1398–H1408. https://doi.org/10.1152/ajpheart.00313.2002.-The.

(26) Eren, M.; Gorgulu, S.; Uslu, N.; Celik, S.; Dagdeviren, B.; Tezel, T.; Gorgulu, S. Relation between Aortic Stiffness and Left Ventricular Diastolic Function in Patients with Hypertension, Diabetes, or Both. *Heart* **2004**, *90*, 37–43. https://doi.org/10.1136/heart.90.1.37.

(27) Mossahebi, S.; Zhu, S.; Kovàcs, S. J. Fractionating E-Wave Deceleration Time Into Its Stiffness and Relaxation Components Dis tinguishes Pseudonormal From Normal Filling. *Circ Cardiovasc Imaging* **2015**, *8*. https://doi.org/10.1161/CIRCIMAGING.114.002177.

(28) Shannon, T. R.; Chu, G.; Kranias, E. G.; Bers, D. M. Phospholamban Decreases the Energetic Efficiency of the Sarcoplasmic Reticulum Ca Pump. *Journal of Biological Chemistry* **2001**, *276* (10), 7195–7201. https://doi.org/10.1074/jbc.M007085200.

(29) Shiels, H. A.; White, E. The Frank–Starling Mechanism in Vertebrate Cardiac Myocytes. *J Exp Biol* **2008**. https://doi.org/10.1242/jeb.003145.

(30) Tobushi, T.; Nakano, M.; Hosokawa, K.; Koga, H.; Yamada, A. Improved Diastolic Function Is Associated With Higher Cardiac Output in Patients With Heart Failure Irrespective of Left Ventricular Ejection Fraction. *J Am Heart Assoc* **2017**, *6*. https://doi.org/10.1161/JAHA.116.003389.

(31) Burns, A. T.; Gerche, A. la; Prior, D. L.; Macisaac, A. I. Left Ventricular Untwisting Is an Important Determinant of Early Diastolic Function. *The Journal of American College of Cardiology: Cardiovascular Imaging* **2009**, *2* (6), 709–716.

(32) Mihm, M. J.; Seifert, J. L.; Coyle, C. M.; Bauer, J. A.; Bauer, J. A. *Diabetes Related Cardiomyopathy Time Dependent Echocardiographic Evaluation in an Experimental Rat Model*; 2001; Vol. 69.

(33) Bai, Y.; Jones, P. P.; Guo, J.; Zhong, X.; Clark, R. B.; Zhou, Q.; Wang, R.; Vallmitjana, A.; Benitez, R.; Hove-Madsen, L.; Semeniuk, L.; Guo, A.; Song, L.-S.; Duff, H. J.; Chen, S. R. W. Phospholamban Knockout Breaks Arrhythmogenic Ca2+ Waves and Suppresses Catecholaminergic Polymorphic Ventricular Tachycardia in Mice. *Circ Res* **2013**, *113*, 517–526. https://doi.org/10.1161/CIRCRESAHA.113.301678.

(34) Fernandez-Tenorio, M.; Niggli, E. Stabilization of Ca2+ Signaling in Cardiac Muscle by Stimulation of SERCA. *J Mol Cell Cardiol* **2018**, *119*, 87–95. https://doi.org/10.1016/j.yjmcc.2018.04.015.

3.9. FOOTNOTES

This research was supported by CVie Therapeutics Limited (Taipei, Taiwan), WindTree Therapeutics (Warrington, USA) and University of Milano Bicocca. This work received no external funding.

3.10. CONFLICT of INTEREST

MF and PB are Windtree employees, PF and GB are Windtree consultants, S-CH is an employee of CVie Therapeutics Limited. All the other Authors declare no conflict of interest.

3.11. SUPPORTING INFORMATION

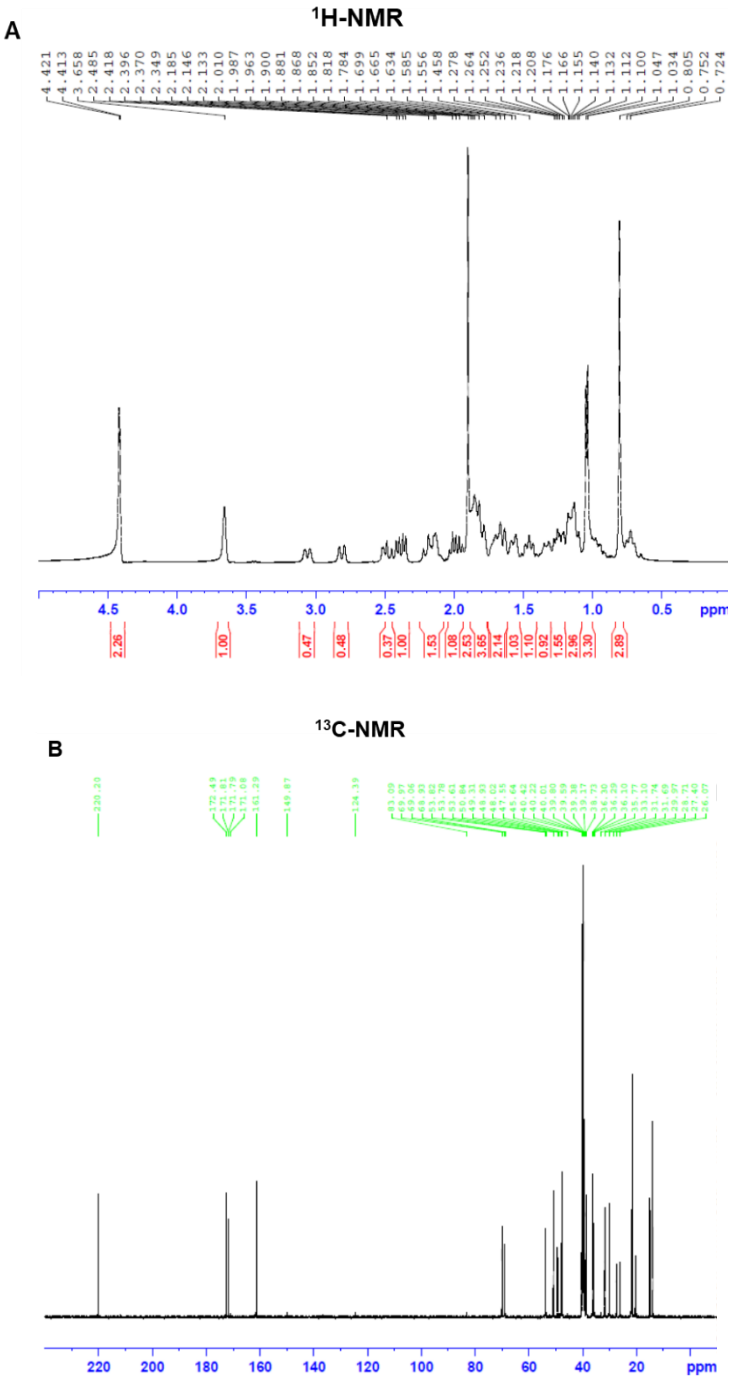

C

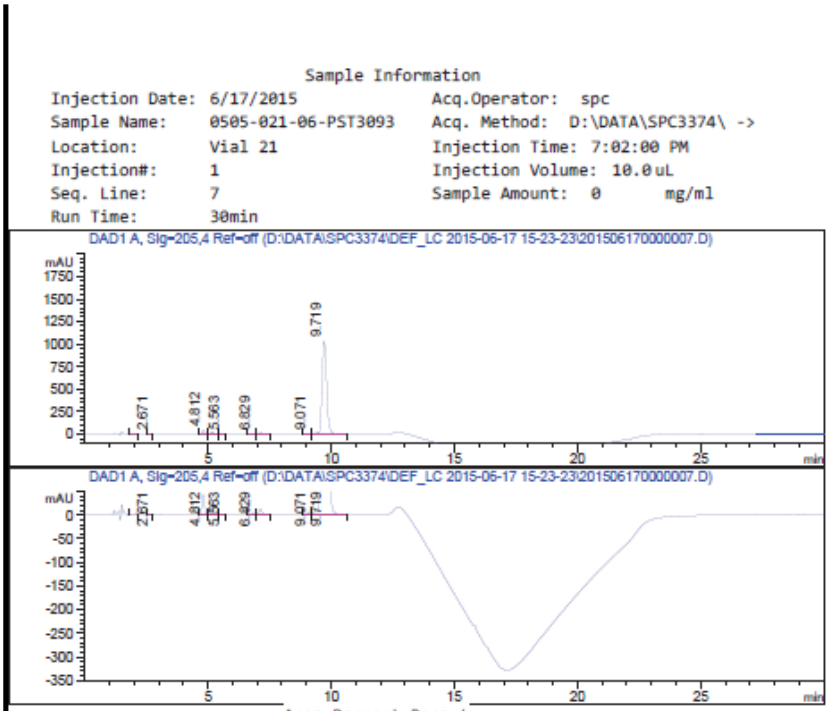

Sample Information

Injection Date:	6/17/2015	Acq.Operator:	spc
Sample Name:	0505-021-06-PST3093	Acq. Method:	D:\DATA\SPC3374\ ->
Location:	Vial 21	Injection Time:	7:02:00 PM
Injection#:	1	Injection Volume:	10.0 uL
Seq. Line:	7	Sample Amount:	0 mg/ml
Run Time:	30min		

Area Percent Report

Signal: DAD1 A, Sig=205,4 Ref=off

#	Compound Name	Meas. R	Peak T	Width	Area	Height	Area %
1		2.081	MM	0.116	29.910	4.293	0.211
2		2.671	BV	0.085	5.830	1.052	0.041
3		4.812	BV	0.121	338.417	43.471	2.384
4		5.164	VV	0.118	174.666	22.747	1.231
5		5.563	VB	0.122	9.090	1.176	0.064
6		6.829	BV	0.142	31.993	3.441	0.225
7		7.133	VB	0.151	125.430	12.685	0.884
8		9.071	BV	0.165	52.584	4.919	0.371
9		9.719	VB	0.201	13424.721	1.034e3	94.589

*** End of Report ***

Operator: Review:

Figure S1. Analytical characterization of PST3093. A) ^{1}H-NMR in DMSO (400 MHz, Bruker), B) ^{13}C-NMR in DMSO (100 MHz, Bruker), C) HPLC profile (about 95% purity).

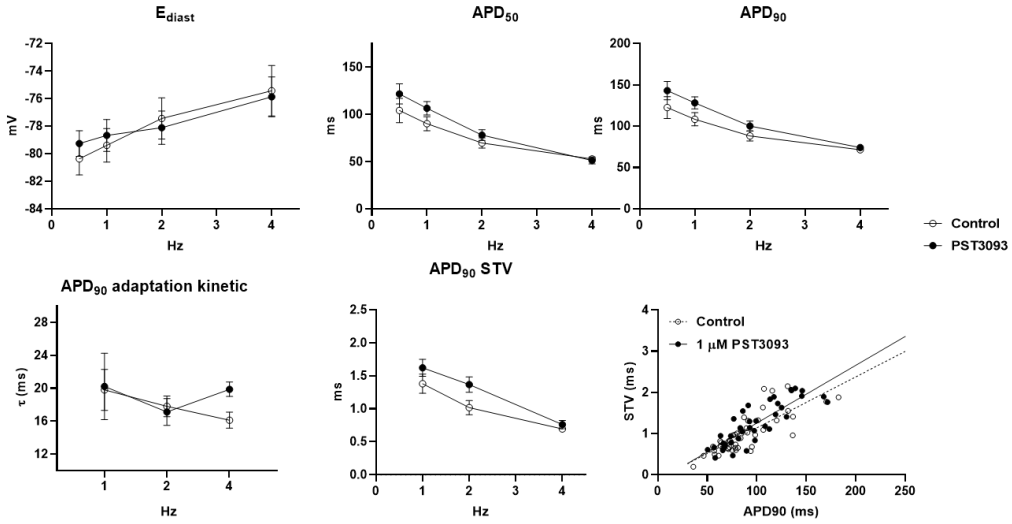

Figure S2. Effects of 1 µM PST3093 on electrical activity in guinea pig myocytes. Rate dependency of AP parameters (Ediast, APD50, APD90), APD90 adaptation kinetics and APD90 short term variability (STV) with or w/o 1 µM PST3093; N=3 (n=16 w/o PST3093, n=18 with PST3093). Bottom right: linear correlation between STV of APD90 and APD90 values with or w/o PST3093; data from 1, 2, 4 Hz were pooled (w/o PST3093 slope = 0.012, with PST3093 slope = 0.014, NS).

Supplemental Table 1. Effect of PST3093 and istaroxime on SERCA2a kinetic parameters in cardiac preparations from healthy guinea pigs. Data are mean ± SEM; N indicates the number of experiments. *p<0.05 vs control (RM one-way ANOVA with post-hoc Tukey's multiple comparisons test or paired *t* test).

Guinea pigs						
[nM]	**N**	**control**	**PST3093**	**N**	**control**	**istaroxime**
V_{max} (µmol/min/mg)						
1	9	2,28±0,17	2,16±0,18	9	2,51±0,08	2,50±0,04
10			2,15±0,15			2,47±0,06
100	11	2,38±0,16	2,34±0,16			2,49±0,07
K_dCa (nM)						
1	9	567±12	504±23*	9	584±22	524±19
10			501±17*			485±16*
100	11	557±12	445±30*			478±19*

Supplemental Table 2. Effect of PST3093 (10 μM) on the panel of molecular targets (Eurofins, Taiwan).

	Cat #	Assay name	Batch	Species	PST3093 effect (%)
1	107480	ATPase, Ca^{2+}, skeletal muscle	438642	pig	-18
2	118040	CYP450, 19	438644	human	12
3	124010	HMG-CoA Reductase	438610	human	-2
4	140010	Monoamine Oxidase MAO-A	438645	human	2
5	140120	Monoamine Oxidase MAO-B	438647	human	-3
6	143000	Nitric Oxide Synthase, Endothelial (eNOS)	438568	bovine	2
7	107300	Peptidase, Angiotensin Converting Enzyme	438641	rabbit	3
8	164610	Peptidase, Renin	438648	human	6
9	152000	Phosphodiesterase PDE3	438611	human	-3
10	171601	Protein Tyrosine Kinase, ABL1	438612	human	3
11	176810	Protein Tyrosine Kinase, Src	438613	human	-1
12	200510	Adenosine A1	438614	human	-2
13	200610	Adenosine A2A	438614	human	-6
14	203100	Adrenergic α1A	438615	rat	2
15	203200	Adrenergic α1B	438615	rat	0
16	203630	Adrenergic α2A	438616	human	-5
17	204010	Adrenergic β1	438652	human	-4
18	204110	Adrenergic β2	438571	human	7
19	204600	Aldosterone	438617	rat	5
20	206000	Androgen (Testosterone)	438618	human	3
21	210030	Angiotensin AT1	438653	human	-1
22	210120	Angiotensin AT2	438653	human	7

23	214600	Calcium Channel L-type, Dihydropyridine	438620	rat	-8
24	219500	Dopamine D1	438660	human	3
25	219700	Dopamine D2s	439024	human	26
26	219800	Dopamine D3	438660	human	1
27	226010	Estrogen ERα	438622	human	-6
28	226050	Estrogen ERβ	438622	human	7
29	226600	$GABA_A$, Flunitrazepam, Central	438624	rat	4
30	226500	$GABA_A$, Muscimol, Central	438623	rat	9
31	232030	Glucocorticoid	438626	human	8
32	233000	Glutamate, NMDA, Phencyclidine	438627	rat	-8
33	239610	Histamine H1	438628	human	-3
34	241000	Imidazoline I2, Central	438629	rat	5
35	243000	Insulin	438654	rat	6
36	252710	Muscarinic M2	438621	human	-7
37	252810	Muscarinic M3	438661	human	4
38	253010	Muscarinic M5	438661	human	5
39	258730	Nicotinic Acetylcholine α3β4	438656	human	1
40	260410	Opiate μ (OP3, MOP)	438616	human	-5
41	264500	Phorbol Ester	438624	mouse	-7
42	265600	Potassium Channel (K_{ATP})	438632	hamster	-8
43	265900	Potassium Channel hERG	438633	human	10
44	299005	Progesterone PR-B	438638	human	-15
45	270300	Ryanodine RyR3	438634	rat	2
46	271010	Serotonin (5-Hydroxytryptamine) 5-HT1, non-selective	438668	rat	0
47	299007	Sigma σ2	438662	human	12

48	278110	Sigma σ1	438636	human	7
49	279510	Sodium Channel, Site 2	438637	rat	2
50	204410	Transporter, Norepinephrine (NET)	438597	human	4

Supplemental Table 3. Characterization of the STZ diabetic rat model. Parameters were measured after 1 or 8 weeks (wk) from STZ injection. Data are mean ± SEM. N represents the number of rats for each group. *p<0.05 vs healthy rats (unpaired *t* test).

	Healthy		**STZ**	
Parameters	**1 wk after vehicle**	**8 wk after vehicle**	**1 wk after STZ**	**8 wk after STZ**
BW (g)	201±4.7	449±11.8	193±4.2	305±12.9*****
Glycaemia (mg/dL)	130±6.6	nd	398±16*****	nd
LV mass (mm^3)	nd	985±34	nd	781±40*****
LV mass index (mm^3/g)	nd	2,23±0,1	nd	2,66±0,2
N	18	18	20	20

Supplemental Table 4. Echocardiographic parameters in healthy and STZ diabetic rats. Data are mean ± SEM. N represents the number of rats for each group. *p<0.05 vs healthy rats (unpaired *t* test).

Echo parameters		Healthy	STZ
Morphometric parameters	IVSTd (mm)	2,22±0,07	1,73±0,1 *
	PWTd (mm)	1,87±0,09	1,54±0,05 *
	LVEDD (mm)	6,6±0,14	6,95±0,13
	IVSTs (mm)	2,46±0,07	2,26±0,1
	PWTs (mm)	2,96±0,09	2,47±0,11 *
	LVESD (mm)	3,09±0,09	3,54±0,1 *
Systolic parameters	FS (%)	53,08±1,17	48,73±1,37 *
	s' (mm/s)	29,59±1,15	24,8±0,75 *
	EF (%)	88 ± 0,8	85 ±1,08 *
Diastolic parameters	E (mm/s)	0,93±0,01	0,84±0,02 *
	A (mm/s)	0,65±0,04	0,63±0,03
	E/A	1,50±0,08	1,38±0,07
	DT (ms)	54,61±2,1	56,8±2,16
	DT/E	59,23±2,4	68,37±3,0 *
	E/DT	17,41±0,77	15,18±0,67 *
	e' (mm/s)	23,46±0,77	21,34±0,58 *
	a' (mm/s)	24,54±1,38	24,3±1,13
	e'/a'	1,01±0,06	0,91±0,04
	E/e'	40,1±1,33	39,64±1,0
Overall cardiac function	HR (bpm)	306±10	248±7,4 *
	LV EDV (mL)	0.67±0.04	0.77±0.04

	LV ESV (mL)	0.08±0.01	0.12±0.01 *
	SV (ml)	0,59±0,03	0,65±0,04
	CO (ml/min)	178,9±10,2	161,1±10,9
	N	18	20

Chapter 4

Highly Selective SERCA2a Activators: Preclinical Development of a Congeneric Group of First-in-Class Drug Leads against Heart Failure

Andrea Luraghi[1], Mara Ferrandi[2], Paolo Barassi[2], Martina Arici[1], Shih-Che Hsu[3], Eleonora Torre[1], Carlotta Ronchi[1], Alessio Romerio[1], Gwo-Jyh Chang[4], Patrizia Ferrari[2], Giuseppe Bianchi[2,5], Antonio Zaza[1]*, Marcella Rocchetti[1]*, and Francesco Peri[1]*

[1]Department of Biotechnology and Biosciences, Università degli Studi di Milano-Bicocca, 20126 Milan, Italy.
[2]Windtree Therapeutics Inc., Warrington, Pennsylvania, 18976, USA.
[3]CVie Therapeutics Limited, Taipei, 11047 Taiwan
[4]Chang Gung University, Tao-Yuan, 333323 Taiwan.
[5]Università Vita-Salute San Raffaele, 20132 Milan, Italy.

*Contributed equally as senior authors to the article

PUBLISHED ON:

J Med Chem. 2022 May 26;65(10):7324-7333.

doi: 10.1021/acs.jmedchem.2c00347. Epub 2022 May 17.

4.1. ABSTRACT

The stimulation of sarcoplasmic reticulum calcium ATPase SERCA2a emerged as a novel therapeutic strategy to efficiently improve overall cardiac function in heart failure (HF) with reduced arrhythmogenic risk. Istaroxime is a clinical-phase IIb compound with a double mechanism of action, Na^+/K^+ ATPase inhibition and SERCA2a stimulation. Starting from the observation that istaroxime metabolite PST3093 does not inhibit Na^+/K^+ ATPase while stimulates SERCA2a, we synthesized a series of bioisosteric PST3093 analogues devoid of Na^+/K^+ ATPase inhibitory activity. Most of them retained SERCA2a stimulatory action with nanomolar potency in cardiac preparations from healthy guinea pigs and streptozotocin (STZ)-treated rats. One compound was further characterized in isolated cardiomyocytes, confirming SERCA2a stimulation and in vivo showing a safety profile and improvement of cardiac performance following acute infusion in STZ rats. We identified a new class of selective SERCA2a activators as first-in-class drug candidates for HF treatment.

4.2. GRAPHICAL ABSTRACT

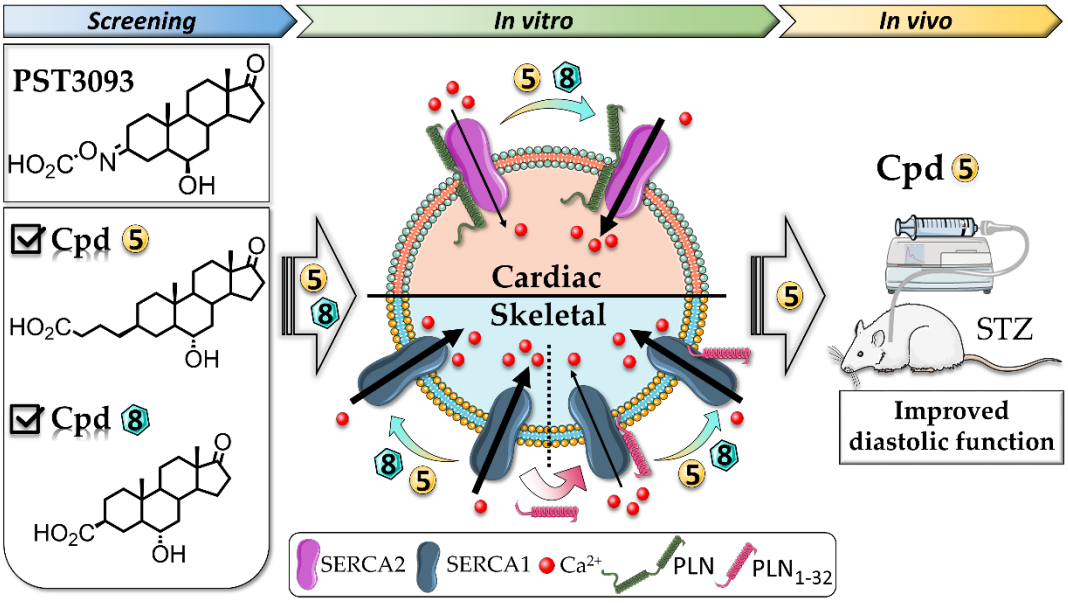

4.3. INTRODUCTION

Heart failure (HF) is a life-threatening syndrome characterized by an inability of the heart to meet the metabolic demands of the body. It is age-dependent, ranging from less than 2% of people younger than 60 years to more than 10% of individuals older than 75 years. Most patients with HF have a history of hypertension, coronary artery disease, cardiomyopathies, valve disease, or a combination of these disorders[1]. The calculated lifetime risk of developing HF is expected to increase, and those with hypertension are at higher risk[2]. Clinical symptoms in HF are caused by a cardiac double pathological feature that consists of diminished systolic emptying (systolic dysfunction) and impaired ability of the ventricles to receive blood from the venous system (diastolic dysfunction). The impaired contractility and relaxation are also caused by an abnormal distribution of intracellular Ca^{2+}, resulting from reduced Ca^{2+} uptake by the sarcoplasmic reticulum (SR)[3]. SR Ca^{2+} uptake is operated by the SR Ca^{2+} ATPase, SERCA2a, a 110 kDa membrane protein. During ion transport across the membrane, SERCA2a undergoes large conformational changes switching between Ca^{2+}-bound E1 and Ca^{2+}-free E2 states[4]. SERCA2a activity is physiologically inhibited by the interaction with phospholamban (PLN), a small protein[5,6] that stabilizes the E2 state, incompatible with Ca^{2+} binding[7]. SERCA2a inhibition by PLN is normally relieved by PLN phosphorylation with protein kinase A, a signaling pathway severely depressed as a consequence of myocardial remodeling[8]. SERCA2a activators are therefore promising drugs that might improve overall cardiac function in HF with reduced arrhythmogenic risk.

Various therapeutic approaches that increase SERCA2a function have been recently investigated[9–13]. Small-molecule SERCA2a activators have been recently discovered. Among them, a pyridone derivative directly binds to PLN displacing it from SERCA2a[14] and a small molecule activates SERCA2a by promoting its SUMOylation [small ubiquitin-related modifier (SUMO)][15]. Overall, new SERCA2a activators might be very useful in HF treatment together with the first line of therapeutic agents, β-blockers, and angiotensin-converting enzyme (ACE) inhibitors.

The work of our laboratory led to the successful completion of phase IIb clinical trials of the steroid derivative istaroxime[16], which is endowed with a double mechanism of action, that is, Na^+/K^+ ATPase inhibition[17] and SERCA2a activation[18]. Istaroxime is an

inotropic/lusitropic agent, which is capable of improving both systolic and diastolic functions (HORIZON study)[19] with a much lower proarrhythmic effect than digoxin, a pure Na^+/K^+ ATPase inhibitor[18]. This suggests that, by improving Ca^{2+} clearance from the cytosol[20], SERCA2a stimulation may minimize the proarrhythmic effect of Na^+/K^+ ATPase blockade[18,19,21] while preserving its inotropic effect.

Although having an excellent pharmacodynamic profile, istaroxime is not optimal for chronic administration because of its poor gastrointestinal absorption, high clearance rate, and extensive metabolic transformation[19] which leads to the formation of a final metabolite, named PST3093. A recent study from our laboratory[22] indicates that PST3093 behaves as a selective SERCA2a activator showing a longer half-life than istaroxime and it is likely to account for the lusitropic effect of istaroxime in patients; nonetheless, the presence of the oxime function may still limit the chronic usage of PST3093. The main aim of this work has been the rational design and synthesis of bioisosteric PST3093 analogues with metabolically stable groups replacing the oxime function, with the purpose to maintain the selective activity on SERCA2a. We present here the ligand-based rational design, the synthesis, and the biochemical and pharmacological in vitro and in vivo characterization of a new class of alkene-based PST3093 derivatives that turned out to have selective activity on SERCA2a.

4.4. RESULTS

4.4.1 Ligand-based rational design and synthesis of PST3093-derived compounds

The metabolite PST3093 (Figure 1A) possesses a 17-androstanone core of istaroxime with two main structural differences: a carboxylic acid group instead of amino group on the C3-oxime linker and a hydroxyl group with R configuration (or β-configuration) at C6 instead of istaroxime's carbonyl. A series of PST3093 variants (compounds **1–12**, Figure 1B) has been designed by a ligand-based approach to carry a carboxylic group (acid or ethyl ester) attached through a linker to the C3 position of the 6-hydroxy-17-oxo androstane core. Although structural information and quantitative structure−activity relationship data allowed the identification of the pharmacophore of istaroxime derivatives that binds to Na^+/K^+ ATPase[16,23], no structural information is available on the interaction between compound PST3093 and SERCA2a and/or PLN. The ligand-based design of compounds **1–12** involved the selective variation of substituents at positions C3 and C6, allowing the pharmacophore identification. The 12 compounds presented here belong to a larger library of synthetic androstane derivatives that were screened for their SERCA2a activity. The need to replace the oxime function with a bioisosteric group guided the design of all derivatives. Namely, the oxime double bond in steroid C3 was replaced with an alkene in compounds **1–4** (in the Z or E configuration) and a saturated C−C bond in the β configuration in compounds **5–12**. The single or double carbon−carbon bonds in C3 would ensure a greater metabolic stability in all compounds compared to PST3093. The length of the C3 linker was also varied: a four-atom linker is present in compounds **1–7** exactly reproducing the PST3093 structure, while a shorter two atom linker is present in compounds **8**, **9** and **10**, and a longer six-atom linker is present in compounds **11** and **12**. All synthetic compounds have a hydroxyl group at C6 as in PST3093: compounds **3**, **4**, **6**, and **9** are in the (R) configuration as PST3093, all the others are in the (S) configuration.

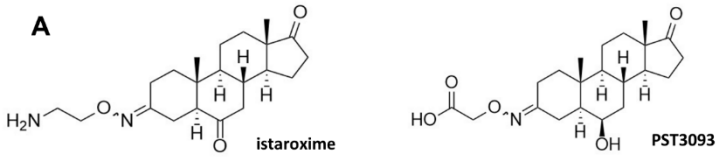

B

Cpd	3	6	n	R
1	*E*	*S*	2	H
2	*Z*	*S*	2	H
3	*E*	*R*	2	H
4	*Z*	*R*	2	H
5	*S*	*S*	2	H
6	*S*	*R*	2	H
7	*S*	*S*	2	Et
8	*S*	*S*	0	H
9	*S*	*R*	0	H
10	*S*	*S*	0	Et
11	*S*	*S*	4	H
12	*S*	*S*	4	Et

Figure 1. Chemical structure of (A) istaroxime and its metabolite PST3093, and (B) PST3093 synthetic variants 1-12.

Compounds **1–12** were synthesized through the synthetic strategy depicted in Scheme 1. Compounds **13** and **14**, 6R and 6S-hydroxyandrostane-3,17-dione, respectively, were prepared as described from the commercially available prasterone (3β-hydroxyandrost-5-en-17-one)[16]. The lower reactivity of C17 carbonyl compared to that of C3 allowed for the regioselective reaction of the C3 ketones in Wittig or Horner−Emmons reactions, obtaining the insertion of the carboxylic acid or ester functionalities at position C3.

Compounds **1** and **3** were synthesized by reacting compounds **13** and **14**, respectively, with (3-carboxypropyl)-triphenylphosphonium bromide and sodium hydride in dry dimethylsulfoxide (DMSO), giving the corresponding carboxylic acids (mixture of E + Z isomers 1:2 at C3 alkene) as products of the Wittig reaction that were converted into methyl esters by dissolving in methanol and treating with N-(3-dimethylaminopropyl)-N-ethylcarbodiimide (EDC) and 4-(dimethylamino)pyridine. The E and Z isomers of esters were separated by chromatography, giving compounds **15** and **17**, respectively. Ethyl ester hydrolysis with aqueous lithium hydroxide in tetrahydrofuran (THF) afforded compounds **1** and **3**. The same Wittig reaction using (3-carboxypentyl)-triphenylphosphonium bromide followed by ethanol esterification gave compound **19** as a mixture of E + Z isomers.

Although the use of sodium hydride as a base for the Wittig reaction gave a mixture of E + Z isomers, by reacting **13** and **14** with the same phosphonium salt in the presence of lithium bis(trimethylsilyl)amide (LiHMDS) in THF, it was possible to obtain stereoselectively only the Z olefins, compounds **2** and **4**.

The reaction of **13** and **14** with triethylphosphonoacetate in the presence of sodium hydride (Horner−Wadsworth−Emmons reaction) gave the esters **20** and **21** (E + Z mixture).

The catalytic hydrogenation (H2, Pd/C) of compounds **15**, **17**, **19**, **20**, and **21** afforded compounds **7**, **22**, **12**, **10**, and **23**, respectively (Scheme 1). Interestingly, the hydrogenation at the C3 carbon−carbon double bond was found to be completely stereoselective for all derivatives, affording only the β (S) isomers. This is very likely due to the steric hindrance of the C19 methyl group on the upper face of the androstane A ring. Hydrolysis of the esters **7**, **22**, **12**, **10**, and **23** by treatment with aqueous lithium hydroxide in THF gave final carboxylic acids **5**, **6**, **11**, **8**, and **9**, respectively.

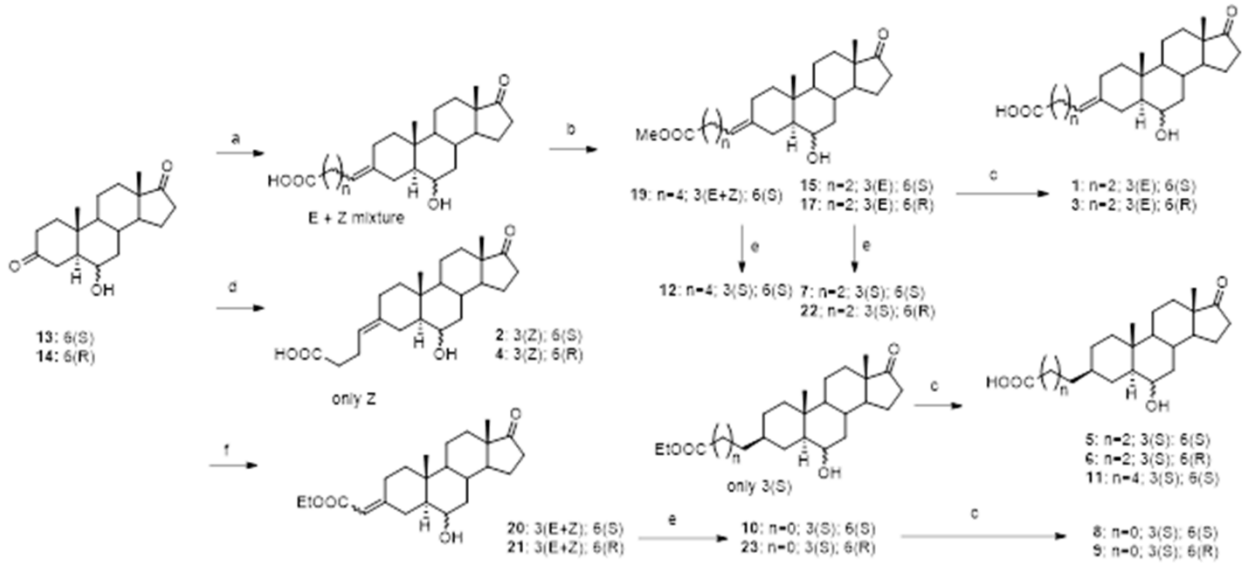

Scheme 1. Synthesis of Compound 1-12 from the Common Precursors 13 and 14 (Reagents and conditions: (a) NaH, (3-carboxypropyl)triphenylphosphonium or (3-carboxypentyl)triphenylphosphonium bromide, DMSO. (b) EDC, EtOH. *E*/*Z* 1:2. (c) aq LiOH 1 M, THF. (d) LiHMDS, (3-carboxypropyl)triphenylphosphonium bromide, THF. (e) H_2/Pd–C, EtOAc. (f) triethylphosphonoacetate, NaH, dimethylformamide.

4.4.2 New synthetic compounds do not affect Na^+/K^+ ATPase and stimulate SERCA2a in a PLN-dependent way

It has been recently shown that although istaroxime inhibits the Na^+/K^+ ATPase activity (IC_{50} 0.14 µM in dog renal preparations), its metabolite PST3093 is inactive against Na^+/K^+ ATPase. In contrast, both molecules improve disease induced SERCA2a depression with a similar potency[22]. To assess whether the new PST3093 derivatives retain the pharmacological activity of the parent compound, Na^+/K^+ ATPase and SERCA2a activities were evaluated in in vitro assays.

Compounds were tested in a concentration range from 10^{-9} to 10^{-4} M on a purified renal Na^+/K^+ ATPase preparation with a specific activity of 14 µmol/min/mg protein. None of the tested molecules inhibited Na^+/K^+ ATPase activity up to 10^{-4} M (Figure 2), similar to PST3093[22].

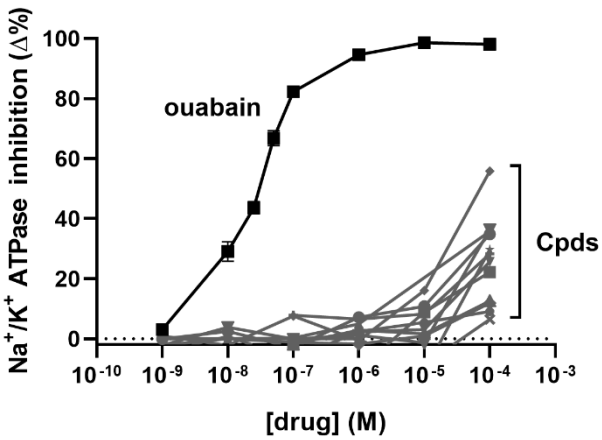

Figure 2. Na^+/K^+ ATPase activity inhibition in a dog purified enzyme preparation. All compounds were tested in a concentration range from 10^{-9} to 10^{-4} M in comparison to ouabain. (•) Cpd 9 (−62% at 10^{-4} M), (⧫) Cpd 3 (−55% at 10^{-4} M), and all the other compounds showed <40% inhibition at 10^{-4} M (*N* = 2).

SERCA2a ATPase activity was assessed in SR preparations from healthy guinea pig hearts. Ca^{2+} dependency of ATPase activity was measured, and kinetic parameters (K_dCa and V_{max}) were estimated at compound concentrations of 10 and 100 nM.

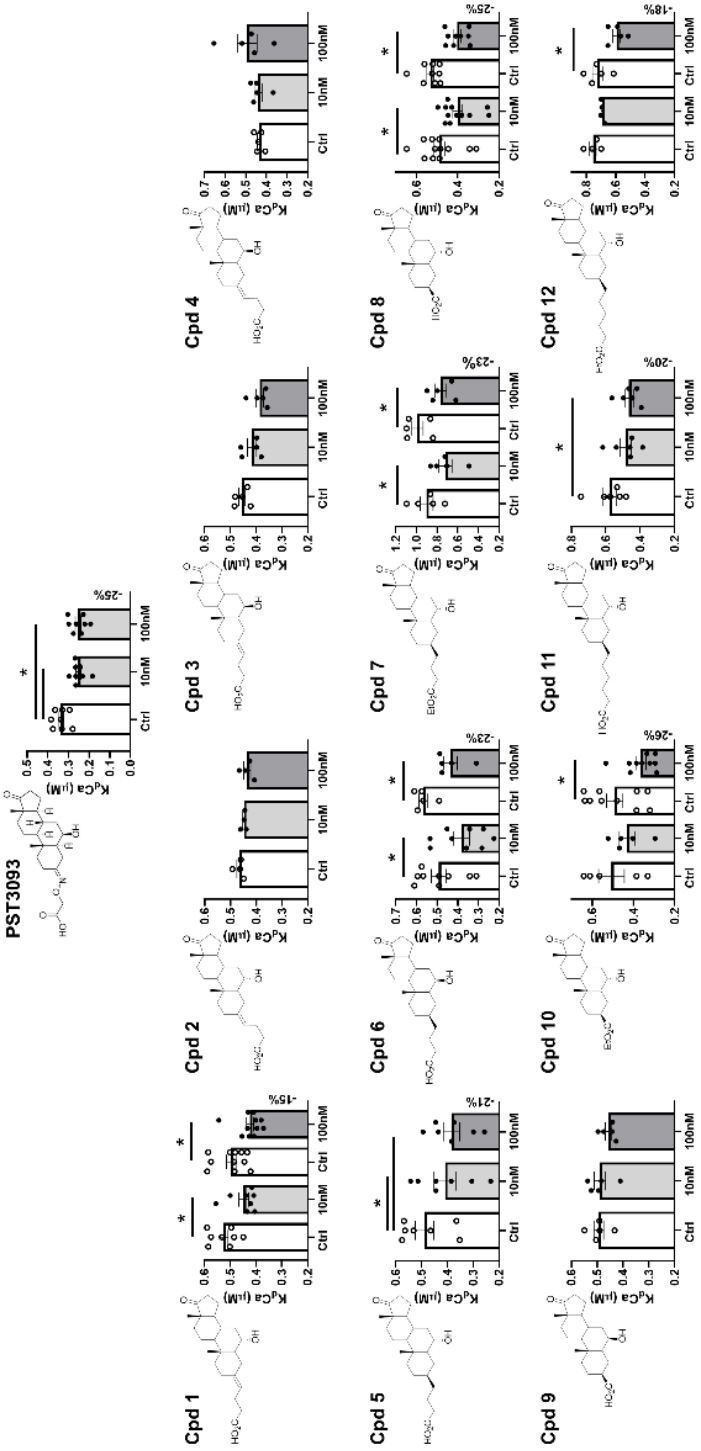

Figure 3. Screening of the compounds by testing their activity on SERCA2a Ca^{2+} dependency in guinea pig microsomal preparations. Concentration dependency of SERCA2a Ca^{2+} affinity (K_dCa) modulation by all compounds and PST3093 (N = 4–11). All compounds were tested at the concentrations of 10 and 100 nM. PST3093, compounds **5** and **8** were also tested at 1 nM (see text). Data are the mean ± SEM. *$p < 0.05$ (one-way RM ANOVA plus post hoc Tukey's multiple comparisons or paired t-test).

Four compounds (**2**, **3**, **4**, and **9**) were inactive, while the other eight compounds significantly increased SERCA2a−Ca^{2+} affinity (decreased K_dCa) at nanomolar concentrations (Figure 3). The maximal effect of compounds on K_dCa reached −26% at 100 nM, close to that of PST3093 (−25% at 100 nM). No compound affected SERCA2a Vmax activity in healthy guinea pig SR preparations.

Compounds **5–8** and **10** had similar potencies in increasing SERCA2a−Ca^{2+} affinity (i.e., in stimulating SERCA2a). The activity of compounds **5** and **8** on SERCA2a was further investigated at 1 nM in comparison to PST3093. Also, at these concentrations from 30 to 1000 nM, compounds **5** and **8** failed to affect skeletal SERCA1 activity in the absence of PLN (Figure 4A). As expected, reconstitution with the $PLN_{1–32}$ fragment markedly reduced SERCA1 affinity for Ca^{2+} (K_dCa increased by 23−25%), without affecting V_{max}. Under this condition, compounds **5** and **8** dose-dependently reversed the PLN-induced shift in K_dCa, leaving SERCA1 V_{max} unchanged, as previously reported for istaroxime[22,24] and PST3093[22]. The present results indicate that in the absence of PLN, SERCA1 is insensitive to compounds **5** and **8**; however, sensitivity is restored after reconstitution of SERCA1 with PLN, suggesting that the compounds act by weakening SERCA−PLN interaction, similar to istaroxime[24] and PST3093[22].

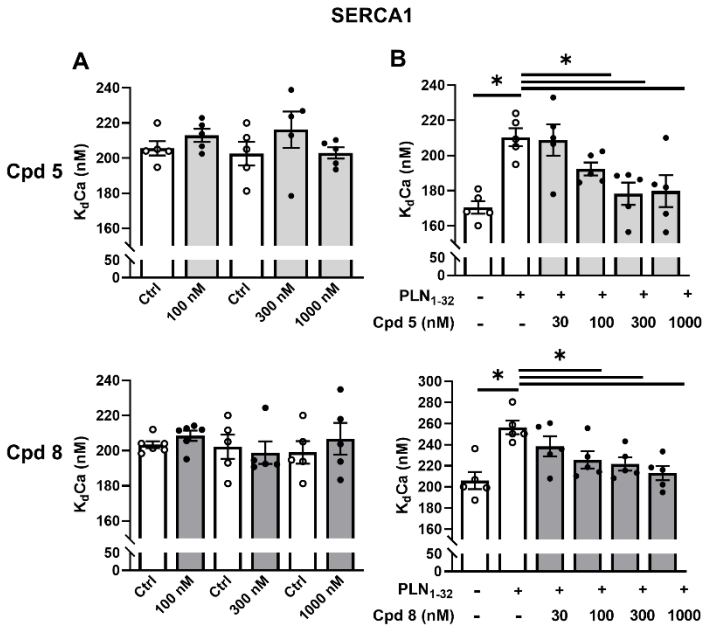

Figure 4. Effects of compounds 5 and 8 on SERCA1 ATPase activity and its PLN dependency in guinea pig microsomal preparations. Concentration dependency of SERCA1–Ca^{2+} affinity (K_dCa) modulation with compounds 5 and 8 in skeletal muscle microsomes containing SERCA1 alone (A) and after reconstitution with $PLN_{1–32}$ fragments (B) (N = 5). Data are the mean ± SEM. *p < 0.05 (one-way RM ANOVA plus post hoc Tukey's multiple comparisons or paired t-test).

Compounds **5** and **8** were further characterized by testing their effects in cardiac preparations from a diabetic rat model [streptozotocin (STZ)-induced] with impaired SERCA2a function[22,25].

Consistent with our previous reports[22,25], baseline SERCA2a V_{max} activity was 30% lower in STZ (0.239 ± 0.012 µmol/min/mg protein, N = 9) than in healthy rats (0.343 ± 0.02 µmol/min/mg protein, N = 8, p < 0.05); SERCA2a K_dCa was instead unchanged in STZ rats (healthy 259 ± 22 nM, STZ 293 ± 23 nM, NS). Thus, as previously reported[22,25], V_{max} may represent a better readout of SERCA2a activity in this species. Over the whole range of concentrations tested, compounds **5** and **8** increased SERCA2a V_{max} in STZ rats (+26% and +25%, +17% and +28%, at 300 and 500 nM, respectively) (Figure 5), thus reversing STZ-induced SERCA2a depression. SERCA2a K_dCa was unchanged by all compounds. Both compounds failed to affect ATPase Ca^{2+} dependency in healthy rats in terms of both parameters K_dCa and V_{max} (Table S1).

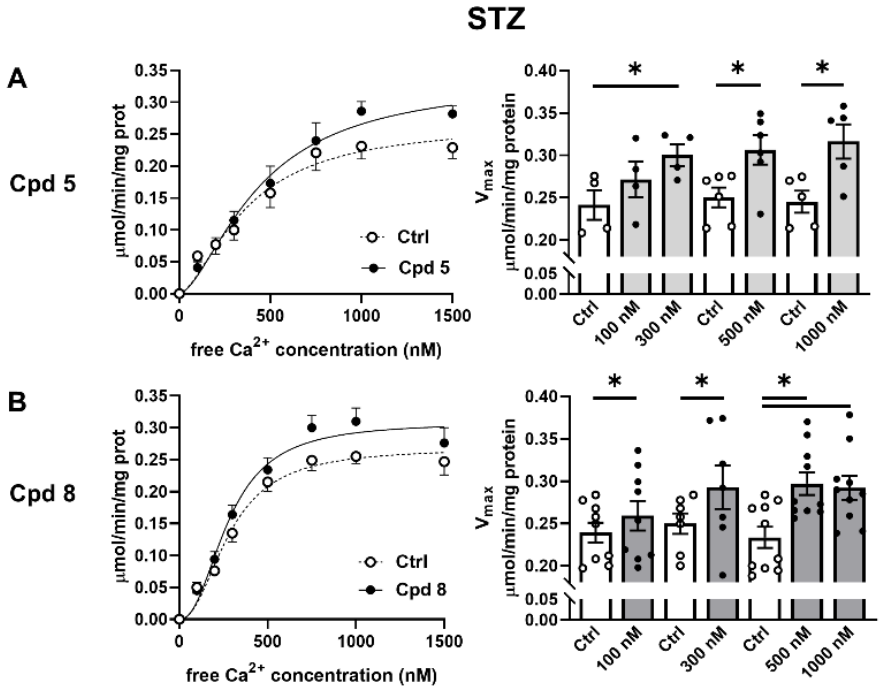

Figure 5. Modulation of SERCA2a ATPase activity in diseased cardiac preparations. Effect of compounds 5 (A) and 8 (B) (concentration range from 100 to 1000 nM) on SERCA2a maximal activity (V_{max}) in cardiac homogenates from diabetic (STZ) rats (N = 4–10). Data are the mean ± SEM. *p < 0.05 (one-way RM ANOVA or paired t-test).

In summary, compounds **5** and **8** displayed similar potency in recovering disease-induced depression of SERCA2a ATPase activity in STZ rats, as previously shown for istaroxime[25] and PST3093[22]. The absence of effects on Na^+/K^+ ATPase implies that compounds **5** and **8** may represent new selective SERCA2a activators, similar to their precursor PST3093. Compound **5** was selected for further in vitro and in vivo effects.

4.4.3 Compound 5 stimulates SR Ca^{2+} uptake in isolated STZ cardiomyocytes

Proof-of-principle evidence that compound **5** stimulates SERCA2a was provided by testing its effects on SR Ca^{2+} uptake function in isolated STZ cardiomyocytes through the "SR loading" protocol. This protocol (see paragraph 2.6.2 and Figure 2 in Chapter 2 and refs [22,25]) is suitable to assess SR Ca^{2+} uptake kinetics following caffeine induced SR depletion under conditions emphasizing the SERCA2a role, that is, in the absence of the Na^+/Ca^+ exchanger (NCX) function. In particular, through this protocol, we recently showed[22] that voltage-induced SR Ca^{2+} reloading is significantly depressed in STZ myocytes, a functional readout of the depressed SERCA2a function in this model.

Cells were incubated for at least 30 min with compound **5** at 1 µM, a concentration not affecting Na^+/K^+ ATPase. Indeed, as shown in Figure 6A, in isolated rat cardiomyocytes, a detectable inhibition of the Na^+/K^+ ATPase current (I_{NaK}) was observed at concentrations higher than 20 µM (−19.8 ± 3.1% at 100 µM, N = 22), likely for PST3093[22].

In STZ myocytes, compound **5** (1 µM) sharply accelerated Ca^{2+} transient (Ca_T) decay (reducing the Ca_T decay time constant) and increased excitation release (ER) gain at each pulse of the reloading protocol; Ca_T amplitude was not significantly affected by the drug (Figure 6B). Comparable results have been obtained with 1 µM PST3093[22].

Overall, compound **5** stimulates SR function in diseased myocytes, most likely through SERCA2a enhancement, within the context of an intact cellular environment.

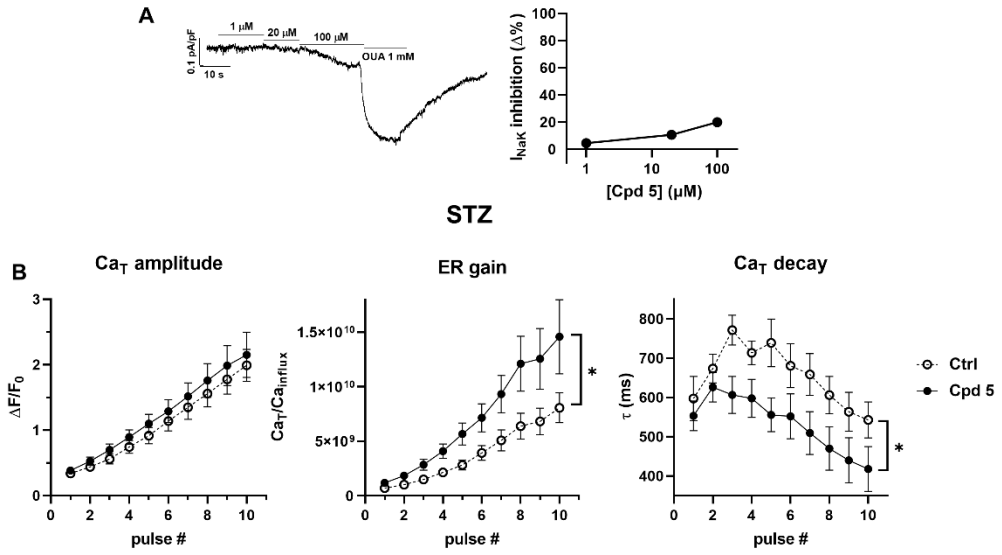

Figure 6. Modulation of SR Ca^{2+} uptake under NCX inhibition in V-clamped myocytes from STZ hearts. (A) Na^+/K^+ ATPase current (I_{NaK}) inhibition by compound **5** (n = 22) in rat LV myocytes; I_{NaK} recording at increasing concentrations of compound **5** and finally to ouabain (OUA as reference) is shown on the left. Data are the mean ± SEM. (B) Effect of compound **5** on SR Ca^{2+} loading in patch-clamped STZ myocytes. SR Ca^{2+} loading by a train of V-clamp pulses was initiated after caffeine-induced SR depletion; NCX was blocked by Na^+ substitution to identify SERCA2a-specific effects (see paragraph 2.6.2 and Figure 2 of Chapter 2); N = 3, ctrl n = 14, with compound **5**, n = 11. Panels from left to right: Ca_T amplitude, ER gain (the ratio between Ca_T amplitude and Ca^{2+} influx through I_{CaL}), and the time constant (τ) of Ca_T decay. *$p \leq 0.05$ for the "interaction factor" in RM two-way ANOVA, indicating a different steepness of curves.

4.4.4 *In vivo* administration of compound 5 is safe and improves STZ-induced diastolic dysfunction.

Toxicity. Compound **5** was selected to evaluate in vivo effects of the new class. Acute toxicity (LD_{50}) was preliminarily evaluated in mice following i.v. and oral drug administration. For i.v. administration, compound **5** had an LD_{50} of 300 mg/kg; for comparison, the LD_{50} of PST3093 and istaroxime was >250[22] and 23 mg/kg[22], respectively. Oral toxicity of compound **5** was >800 mg/kg, as compared to >200 and 200 mg/kg for PST3093 and istaroxime, respectively. The main signs of toxicity were prostration, gasping, and convulsions. No overt signs of acute toxicity were observed in

the surviving animals. Collectively, the present data indicate low toxicity of compound **5**, particularly as compared to i.v. istaroxime. This is likely due to lack of inhibitory activity on the Na^+/K^+ pump, which also applies to istaroxime after its first-pass conversion to PST3093 in the case of oral administration.

In vivo hemodynamics. Features of the STZ-induced diabetic cardiomyopathy have been previously assessed by comparing morphometric, echocardiographic, and cellular parameters between healthy and STZ-treated rats under urethane anesthesia[22]. Echo measurements in STZ rats indicated primarily an impairment of diastolic function, evidenced by decreased early filling velocity (E), increased E wave deceleration time over the E ratio (DT/E), and decreased protodiastolic TDI relaxation velocity (e'). The systolic function was moderately altered, as shown by larger LV end-systolic diameter (LVESD), reduced ejection fraction, depressed fractional shortening (FS) and systolic tissue velocity (s')[22].

Compound **5** was i.v. infused in STZ rats at a rate of 0.2 mg/kg/min, and the effects on echo parameters were investigated at 15 and 30 min of infusion and 10 min after discontinuation (Figure 7 and Table S2 for all echo parameters). Compound **5** positively affected transmitral Doppler flow indexes by increasing E and A waves; it shortened the DT, reduced the DT/E ratio, and increased both protodiastolic (e') and telediastolic (a') TDI relaxation velocities. Compound **5** increased CO, without significantly affecting HR or systolic indexes, such as FS, systolic TDI velocity (s'), or LVESD. Drug effects reached a plateau at 15 min of infusion; 10 min after discontinuation of the infusion, most echo indexes affected by the compound returned to the basal level.

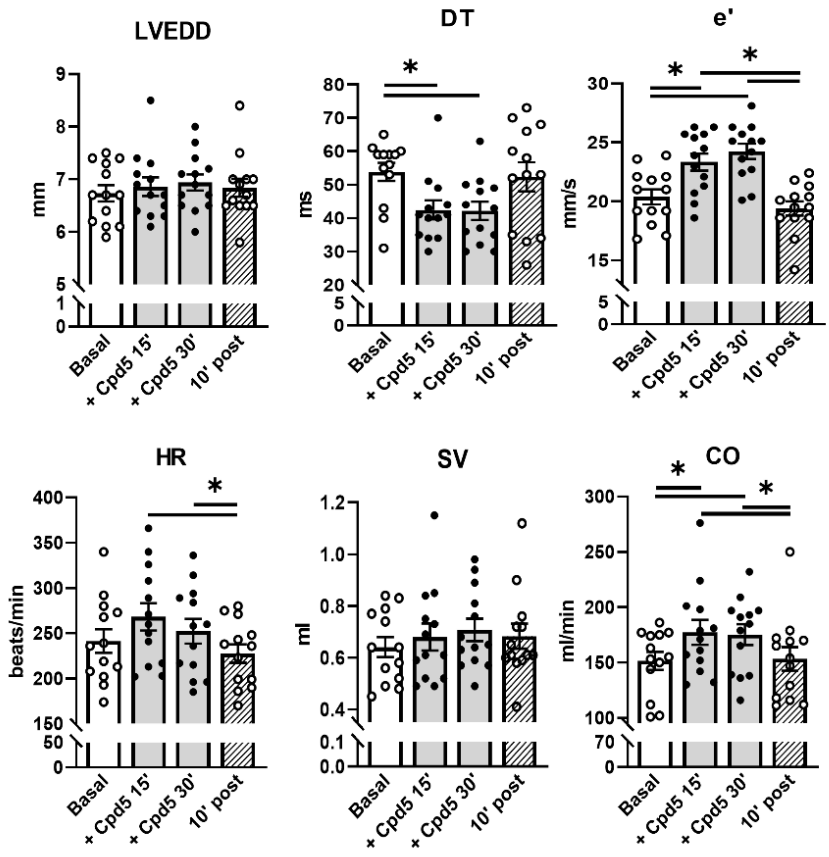

Figure 7. Effect of compound 5 on in vivo echocardiographic parameters in STZ diabetic rats. Compound 5 was i.v. infused (0.2 mg/kg/min) in rats 8 weeks after STZ treatment. Echocardiographic parameters were measured before (basal) and at 15 and 30 min during drug infusion and 10 min after drug interruption under urethane anesthesia. Data are the mean ± SEM; all the results of echocardiographic indexes are summarized in Table S2; $N = 13$; $*p < 0.05$ (one-way RM ANOVA).

To summarize, *in vivo* hemodynamic data indicate a specific lusitropic effect of compound **5** in STZ rats, compatible with rescue of SERCA2a function and largely comparable to the in vivo effect of the parent drug PST3093[22].

4.5. DISCUSSION and CONCLUSION

In spite of the intense research targeting the discovery of small molecules or gene therapy aimed at selectively activating SERCA2a, recognized to be depressed in HF, no promising clinical outcomes have been reached so far. Therefore, there is still a compelling medical need for a compound with positive lusitropic activity. In this context, we successfully developed a new class of derivatives of PST3093 (the long-lasting metabolite of istaroxime)[22] with a selective stimulatory action on SERCA2a but devoid of inhibitory activity on Na^+/K^+ ATPase. This was achieved by replacing the metabolically unstable oxime of PST3093 with more stable saturated and unsaturated carbon−carbon bonds, without altering the molecular geometry. Biological effects of the new compounds have been investigated by *in vitro* and *in vivo* assays.

The in vitro tests on SERCA2a clearly point out that replacing the C=N group of PST3093 with an alkene C=C, the activity on SERCA2a is partially retained in the case of E isomers (Figure 3). Indeed, although compound 1 (100 nM), carrying the alkene bond in the E configuration, reduced SERCA2a K_dCa by 15%, compound **2** with the same bond in the Z configuration was inactive. However, albeit in the E configuration, compound **3** was less active than compound **1**, that is, it showed only a trend to SERCA2a K_dCa reduction.

For comparison, PST3093 (100 nM) reduced SERCA2a K_dCa by 25% in the same guinea pig preparation. The fact that compounds with C=C in the E configuration are active while Z isomers are inactive parallels the observation that the oxime isomer E is the most active in istaroxime[16]. The replacement of oxime with a saturated C−C bond in C3 in the beta configuration led to compounds **5–12**. Compounds **5–8** and **10**, in which the C3 linker is two- and four-carbon atom long, have similar activities. Compounds **11** and **12** with a six-carbon linker are slightly less active.

Among the compounds with significant SERCA2a stimulatory activity, compounds **5** and **8**, had the best balance between potency and efficiency of chemical synthesis; thus, they were selected as leads for further evaluations. At nanomolar concentrations, the new compounds enhanced in vitro SERCA2a activity in healthy guinea pig preparations and in diseased (STZ) rat preparations; furthermore, the stimulatory effect on SERCA2a depended on the presence of PLN. This pattern is superimposable on that previously reported for the parent compound PST3093 and suggests that the

new compounds may also act by partially relieving SERCA2a from PLN-induced inhibition[22].

SR Ca^{2+} uptake function in diseased (STZ) myocytes was stimulated by compound **5** at a concentration not affecting Na^+/K^+ ATPase. According to the protocol specificity, this effect is surely attributable to SERCA2a stimulation under conditions of depressed function (STZ-induced SERCA2a downregulation). The parent compound PST3093 also in this case shows similar effects[22].

In vivo studies investigated the effects of compound **5** on cardiac function in STZ diabetic rats, a disease model characterized by diastolic dysfunction, as assessed by echocardiography[22]. Compound **5** i.v. infusion at a single dose improved diastolic echo indexes and, because of a small increase in the heart rate, cardiac output; however, it did not affect systolic function significantly (Table S2). Although improvement of diastolic indexes mimics the effect of the parent compound, PST3093 also improved systolic indexes[22].

Similar to compound **5**, PST3093 does not inhibit the Na^+/K^+ pump; therefore, the reason for this difference remains to be verified.

Evaluation of *in vivo* acute toxicity after i.v. administration yielded an LD_{50} of compound **5** comparable to that of PST3093 whereas the oral one was higher, indicating a lower toxicity. The difference between i.v. and oral toxicity may result from the absence of enteric transit/absorption and first-pass hepatic metabolism, which characterize the former administration route. The remarkable reduction of istaroxime toxicity when orally administered can be accounted for by its fast conversion to PST3093, missing Na^+/K^+ pump inhibition.

Overall, the new PST3093 derivatives provide a tool for pharmacological enhancement of SERCA2a function, leading to improvement of in vivo diastolic function. With respect to PST3093, its derivatives are devoid of the oxime function and thus suitable for chronic usage and have a lower acute oral toxicity. They further differ from istaroxime, the progenitor of “PLN antagonists” already tested for clinical use because of lack of Na^+/K^+ pump inhibition. Considering the proarrhythmic potential of the latter, this may represent a substantial advantage in terms of safety; nonetheless, at variance with istaroxime, the new compounds should be seen as purely “lusitropic” agents, that is, devoid of “inotropic” effects beyond that expected from systo−diastolic coupling.

Although the mechanism of action of PST3093 and synthetic analogues has still to be investigated, the reversal of electrostatic properties from cationic ammonium for istaroxime to anionic carboxylate for PST3093 and analogues could account for the inactivity toward Na^+/K^+ ATPase.

Because PST3093 has a half-life (~10 h) much longer than that of istaroxime (~1 h)[22] and its derivatives have been obtained by introducing groups with higher chemical stability, pharmacokinetics of the new compounds is likely compatible with chronic oral dosing. Nonetheless, suitability of the new compounds for chronic therapy, their natural destination, remains to be directly tested.

4.6. ACKNOWLEDGMENTS

This research was supported by CVie Therapeutics Limited (Taipei, Taiwan), WindTree Therapeutics (Warrington, USA), and the University of Milano Bicocca. We thank Dr Alberto Cerri, sadly passed away, for his valuable contribution to the structural design of the new compounds. Alberto, you'll always be in our hearts.

4.7. AUTHOR CONTRIBUTION

F.P., M.R., and A.Z. contributed equally as senior authors to the article. A.L. and A.R. conducted chemical assays; M.F. and P.B. conducted biochemical assays; M.A. and E.T. conducted functional measurements in isolated myocytes; S.-C.H. carried out in vivo measurements; C.R. carried out formal analysis; G.-J.C. supervised in vivo measurements; P.F. and G.B. supervised biochemical measurements; A.Z., M.R., and F.P. revised and supervised the study and wrote the article.

The authors declare the following competing financial interest(s): MF and PB are Windtree employees, PF and GB are Windtree consultants, S-CH is an employee of CVie Therapeutics Limited. All the other Authors declare no conflict of interest.

4.8. REFERENCES

(1) Metra, M.; Teerlink, J. R. Heart Failure. *The Lancet* **2017**, *390* (10106), 1981–1995. https://doi.org/10.1016/S0140-6736(17)31071-1.

(2) Lloyd-Jones, D. M.; Larson, M. G.; Leip, E. P.; Beiser, A.; D, R. B.; Kannel, W. B.; Murabito, J. M.; Vasan, R. S.; Benjamin, E. J.; Levy, D. Lifetime Risk for Developing Congestive Heart Failure The Framingham Heart Study. *Circulation* **2002**, *106*, 3068–3072. https://doi.org/10.1161/01.CIR.0000039105.49749.6F.

(3) Bers, D. M.; Despa, S.; Bossuyt, J. Regulation of Ca2+ and Na+ in Normal and Failing Cardiac Myocytes. *Annals of the New York Academy Sciences* **2006**, *1080*, 165–177. https://doi.org/10.1196/annals.1380.015.

(4) Sitsel, A.; de Raeymaecker, J.; Drachmann, N. D.; Derua, R.; Smaardijk, S.; Andersen, J. L.; Vandecaetsbeek, I.; Chen, J.; de Maeyer, M.; Waelkens, E.; Olesen, C.; Vangheluwe, P.; Nissen, P. Structures of the Heart Specific SERCA 2a Ca2+ - ATP Ase. *EMBO J* **2019**, *38* (5). https://doi.org/10.15252/embj.2018100020.

(5) Bers, D. M. Calcium Cycling and Signaling in Cardiac Myocytes. *Annu Rev Physiol* **2008**, *70*, 23–49. https://doi.org/10.1146/annurev.physiol.70.113006.100455.

(6) MacLennan, D. H.; Kranias, E. G. Phospholamban: A Crucial Regulator of Cardiac Contractility. *Nature Reviews in Molecular Cell Biology* **2003**, *4*, 566–577. https://doi.org/10.1038/nrm1151.

(7) Akin, B. L.; Hurley, T. D.; Chen, Z.; Jones, L. R. The Structural Basis for Phospholamban Inhibition of the Calcium Pump in Sarcoplasmic Reticulum. *Journal of Biological Chemistry* **2013**, *288* (42), 30181–30191. https://doi.org/10.1074/jbc.M113.501585.

(8) Liu, Y.; Chen, J.; Fontes, S. K.; Bautista, E. N.; Cheng, Z. Physiological and Pathological Roles of Protein Kinase A in the Heart. *Cardiovasc Res* **2021**, *118*, 386–398. https://doi.org/10.1093/cvr/cvab008.

(9) Byrne, M. J.; Power, J. M.; Preovolos, A.; Mariani, J. A.; Hajjar, R. J.; Kaye, D. M. Recirculating Cardiac Delivery of AAV2/1SERCA2a Improves Myocardial Function in an Experimental Model of Heart Failure in Large Animals. *Gene Ther* **2008**, *15* (23), 1550–1557. https://doi.org/10.1038/gt.2008.120.

(10) Hoshijima, M.; Ikeda, Y.; Iwanaga, Y.; Minamisawa, S.; Date, M.; Gu, Y.; Iwatate, M.; Li, M.; Wang, L.; Wilson, J. M.; Wang, Y.; Ross, J. J.; Chien, K. R. Chronic Suppression of Heart-Failure Progression by a Pseudophosphorylated Mutant of Phospholamban via in Vivo Cardiac RAAV Gene Delivery. *Nat Med* **2002**, *8* (8), 864–871. https://doi.org/10.1038/nm739.

(11) Iwanaga, Y.; Hoshijima, M.; Gu, Y.; Iwatate, M.; Dieterle, T.; Ikeda, Y.; Date, M.; Chrast, J.; Matsuzaki, M.; Peterson, K. L.; Chien, K. R.; Ross, J. J. Chronic Phospholamban Inhibition Prevents Progressive Cardiac Dysfunction and Pathological Remodeling after Infarction in Rats. *The Journal of Clinical Investigation* **2004**, *113* (5), 727–736. https://doi.org/10.1172/JCI200418716.

(12) Suckau, L.; Fechner, H.; Chemaly, E.; Krohn, S.; Hadri, L.; Kockskämper, J.; Westermann, D.; Bisping, E.; Ly, H.; Wang, X.; Kawase, Y.; Chen, J.; Liang, L.; Sipo, I.; Vetter, R.; Weger, S.; Kurreck, J.; Erdmann, V.; Tschope, C.; Pieske, B.; Lebeche, D.; Schultheiss, H.-P.; Hajjar, R. J.; Poller, W. C. Long-Term Cardiac-Targeted RNA Interference for the Treatment of Heart Failure Restores Cardiac Function and Reduces Pathological Hypertrophy. *Circulation* **2009**, *119*, 1241–1252. https://doi.org/10.1161/CIRCULATIONAHA.108.783852.

(13) Größl, T.; Hammer, E.; Bien-Möller, S.; Geisler, A.; Pinkert, S.; Röger, C.; Poller, W.; Kurreck, J.; Völker, U.; Vetter, R.; Fechner, H. A Novel Artificial MicroRNA Expressing AAV Vector ForPhospholamban Silencing in Cardiomyocytes ImprovesCa2+ Uptake into the Sarcoplasmic Reticulum. *PLoS One* **2014**, *9* (3). https://doi.org/10.1371/journal.pone.0092188.

(14) Kaneko, M.; Yamamoto, H.; Sakai, H.; Kamada, Y.; Tanaka, T.; Fujiwara, S.; Yamamoto, S.; Takahagi, H.; Igawa, H.; Kasai, S.; Noda, M.; Inui, M.; Nishimoto, T. A Pyridone Derivative Activates SERCA2a by Attenuating the Inhibitory Effect of Phospholamban. *Eur J Pharmacol* **2017**, *814*, 1–8. https://doi.org/10.1016/j.ejphar.2017.07.035.

(15) Kho, C.; Lee, A.; Jeong, D.; Oh, J. G.; Gorski, P. A.; Fish, K.; Sanchez, R.; Devita, R. J.; Christensen, G.; Dahl, R.; Hajjar, R. J. Small-Molecule Activation of SERCA2a SUMOylation for the Treatment of Heart Failure. *Nature Communication* **2015**, *6*. https://doi.org/10.1038/ncomms8229.

(16) de Munari, S.; Cerri, A.; Gobbini, M.; Almirante, N.; Banfi, L.; Carzana, G.; Ferrari, P.; Marazzi, G.; Micheletti, R.; Schiavone, A.; Sputore, S.; Torri, M.; Zappavigna, M. P.; Melloni, P. Structure-Based Design and Synthesis of Novel Potent Na+ ,K+-ATPase Inhibitors Derived from a 5r,14r-Androstane Scaffold as Positive Inotropic Compounds. *The Journal of Medicinal Chemistry* **2003**, *46*, 3644–3654. https://doi.org/10.1021/jm030830y.

(17) Micheletti, R.; Mattera, G. G.; Rocchetti, M.; Schiavone, A.; Loi, M. F.; Zaza, A.; Gagnol, R. J. P.; de Munari, S.; Melloni, P.; Carminati, P.; Bianchi, G.; Ferrari, P. Pharmacological Profile of the Novel Inotropic Agent (E,Z)-3-((2-Aminoethoxy)Imino)Androstane-6,17-Dione Hydrochloride (PST2744). *J Pharmacol Exp Ther* **2002**, *303*, 592–600. https://doi.org/10.1124/jpet.102.038331.

(18) Rocchetti, M.; Besana, A.; Mostacciuolo, G.; Micheletti, R.; Ferrari, P.; Sarkozi, S.; Szegedi, C.; Jona, I.; Zaza, A. Modulation of Sarcoplasmic Reticulum Function by Na/K Pump Inhibitors with Different Toxicity: Digoxin and PST2744 [(E,Z)-3-((2-Aminoethoxy)Imino)Androstane-6,17-Dione Hydrochloride]. *J Pharmacol Exp Ther* **2005**, *313*, 207–215. https://doi.org/10.1124/jpet.104.077933.

(19) Gheorghiade, M.; Blair, J. E. A.; Filippatos, G. S.; Macarie, C.; Ruzyllo, W.; Korewicki, J.; Bubenek-Turconi, S. I.; Ceracchi, M.; Bianchetti, M.; Carminati, P.; Kremastinos, D.; Valentini, G.; Sabbah, H. N. Hemodynamic, Echocardiographic, and Neurohormonal Effects of Istaroxime, a Novel Intravenous Inotropic and Lusitropic Agent: A Randomized Controlled Trial in Patients Hospitalized With Heart Failure. *J Am Coll Cardiol* **2008**, *51* (23), 2276–2285. https://doi.org/10.1016/J.JACC.2008.03.015.

(20) Alemanni, M.; Rocchetti, M.; Re, D.; Zaza, A. Role and Mechanism of Subcellular Ca2+ Distribution in the Action of Two Inotropic Agents with Different Toxicity. *J Mol Cell Cardiol* **2011**, *50* (5), 910–918. https://doi.org/10.1016/j.yjmcc.2011.02.008.

(21) Zaza, A.; Rocchetti, M. *Calcium Store Stability as an Antiarrhythmic Endpoint*; 2015; Vol. 21.

(22) Arici, M.; Ferrandi, M.; Barassi, P.; Hsu, S.-C.; Torre, E.; Luraghi, A.; Ronchi, C.; Chang, G.-J.; Peri, F.; Ferrari, P.; Bianchi, G.; Rocchetti, M.; Zaza, A. Istaroxime Metabolite PST3093 Selectively Stimulates SERCA2a and Reverses Disease-Induced Changes in Cardiac Function Running Title: PST3093 Stimulates SERCA2a and Improves Cardiac Function. *Journal of Pharmacology and Experimental Therapeutics* **2022**. https://doi.org/10.1124/jpet.122.001335.

(23) Gobbini, M.; Armaroli, S.; Banfi, L.; Benicchio, A.; Carzana, G.; Ferrari, P.; Giacalone, G.; Marazzi, G.; Moro, B.; Micheletti, R.; Sputore, S.; Torri, M.; Zappavigna, M. P.; Cerri, A. Novel Analogues of Istaroxime, a Potent Inhibitor of Na+,K+-ATPase: Synthesis, Structure-Activity Relationship and 3D-Quantitative Structure-Activity Relationship of Derivatives at Position 6 on the Androstane Scaffold. *Bioorg Med Chem* **2010**, *18* (12), 4275–4299. https://doi.org/10.1016/j.bmc.2010.04.095.

(24) Ferrandi, M.; Barassi, P.; Tadini-Buoninsegni, F.; Bartolommei, G.; Molinari, I.; Tripodi, M. G.; Reina, C.; Moncelli, M. R.; Bianchi, G.; Ferrari, P. Istaroxime Stimulates SERCA2a and Accelerates Calcium Cycling in Heart Failure by Relieving Phospholamban Inhibition. *Br J Pharmacol* **2013**, *169*, 1849–1861. https://doi.org/10.1111/bph.12288.

(25) Torre, E.; Arici, M.; Lodrini, A. M.; Ferrandi, M.; Barassi, P.; Hsu, S.-C.; Chang, G.-J.; Boz, E.; Sala, E.; Vagni, S.; Altomare, C.; Mostacciuolo, G.; Bussadori, C.;

Ferrari, P.; Bianchi, G.; Rocchetti, M. SERCA2a Stimulation by Istaroxime Improves Intracellular Ca2+ Handling and Diastolic Dysfunction in a Model of Diabetic Cardiomyopathy. *Cardiovasc Res* **2022**, *118*, 1020–1032. https://doi.org/10.1093/cvr/cvab123.

4.9. SUPPORTING INFORMATION

Complete information regarding the synthesis and the experimental spectra of the compounds are reported in the online supplemental materials.

https://www.ncbi.nlm.nih.gov/pmc/articles/PMC9150102/

4.9.1 HPLC analysis

Column: InfinityLab Poroshell 120 EC- C18; 2.7 µm, 3.0 x 150 mm. Flow rate: 0.8 mL/min. Detection:292 nm.

Mobile phase	Start	End
H_2O+0.01 HCOOH	95%	5%
ACN+0,01 HCOOH	5%	95%

Compound 5

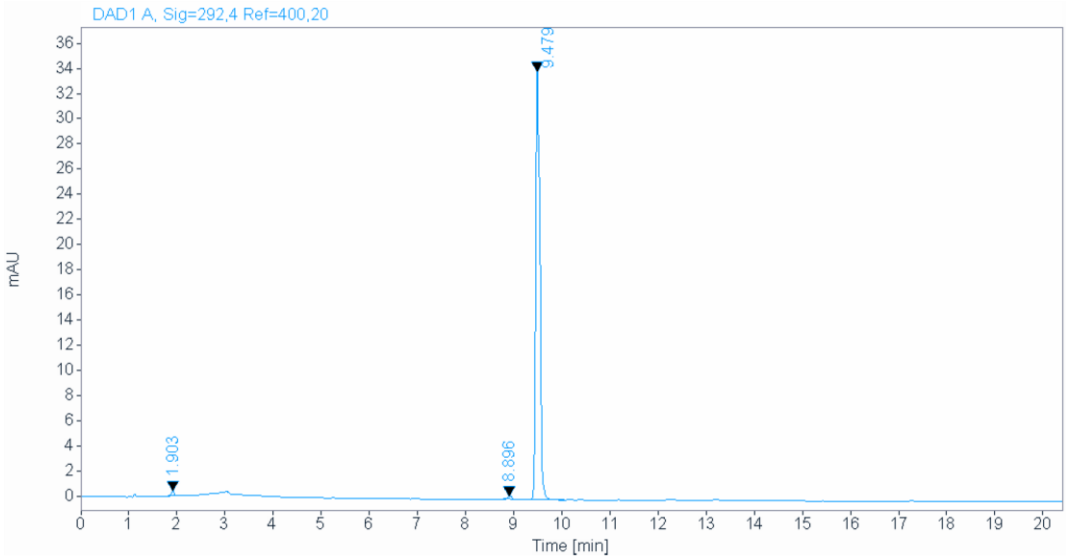

Compound 8

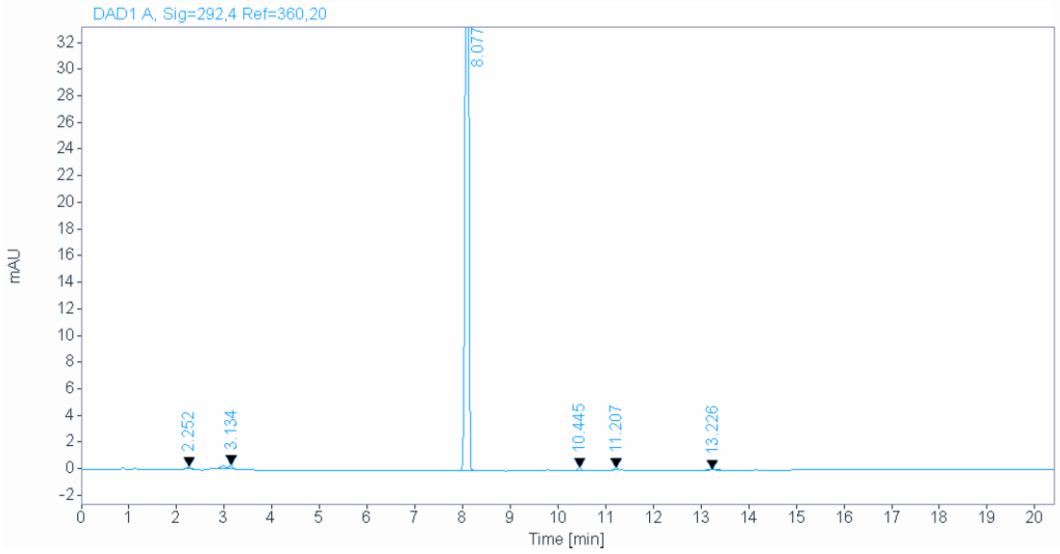

Table S1. Effect of compounds 5 and 8 on SERCA2a activity in cardiac SR homogenates from healthy rats. Data are expressed as mean ± SEM, N = number of experiments.

SERCA2a						
			KdCa (nM)		V_{max} (µmol/min/mg)	
Cpd	**Concentration nM**	**N**	**control**	**Cpd**	**control**	**Cpd**
5	100	6	224 ± 25	221 ± 24	0,379 ± 0,023	0,371 ± 0,021
	300			221 ± 21		0,384 ± 0,023
	500	6	208 ± 30	220 ± 24	0,370 ± 0,023	0,374 ± 0,031
	1000			219 ± 32		0,377 ± 0,029
8	100	5	231 ± 18	214 ± 17	0,364 ± 0,025	0,344 ± 0,038
	300			210 ± 13		0,366 ± 0,027
	500	5	282 ± 29	260 ± 35	0,314 ± 0,021	0,313 ± 0,028
	1000			273 ± 32		0,320 ± 0,020

Table S2. Effect of compound 5 on echocardiographic and tissue Doppler parameters in STZ rats after intravenous infusion at the dose of 0.2 mg/kg/min. Echo parameters were measured at 15 and 30 min after infusion start and 10 min after drug interruption under urethane anesthesia. Data are mean ± SEM. *p<0.05 vs basal (one-way ANOVA for repeated measurements).

		STZ			
		basal	**after 15 min Cpd 5**	**after 30 min Cpd 5**	**after 10 min stop**
Morphometric parameters	**IVSTd, mm**	1,68±0,09	1,81±0,08	1,71±0,1	1,68 ± 0,07
	PWTd, mm	1,22±0,07	1,16±0,07	1,22±0,07	1,17 ± 0,07
	LVEDD, mm	6,73±0,15	6,86±0,17	6,94±0,15	6,84 ± 0,17
	IVSTs, mm	2,31±0,14	2,34±0,10	2,55±0,13	2,55 ± 0,10
	PWTs, mm	2,5±0,09	2,59±0,09	2,53±0,10	2,42 ± 0,10
	LVESD, mm	2,84±0,17	2,87±0,18	2,73±0,18	2,64 ± 0,17
Systolic function	**FS, %**	57,9±2,01	58,1±2,38	60,7±2,31	61,3±2,05
	s', mm/s	21,3±0,59	22,4±0,86	21,8±0,78	20,6±0,53
	EF, %	90,85±1,25	90,68±1,4	92,19±1,18	92,66±1,05
Diastolic function	**E, mm/s**	0,78±0,031	0,88±0,04*	0,91±0,05*	0,78±0,03
	A, mm/s	0,55±0,034	0,65±0,04*	0,69±0,032*	0,58±0,02
	E/A	1,46±0,10	1,36±0,05	1,34±0,06	1,37±0,06
	DT, ms	53,8±2,72	42,46±2,83*	42,15±2,74*	52,4±4,36
	DT/E, s2/mm	71,4±5,31	49,52±3,44*	48,51±4,56*	68,2±6,13
	E/DT, m/s2	15,14±1,4	21,49±1,61*	23,18±2,32*	16,5±1,78
	e', mm/s	20,38±0,64	23,33±0,73*	24,24±0,65*	19,4±0,60
	a', mm/s	22,99±1,57	29,13±1,82*	28,94±1,47*	26,22±1,31*
	e'/a'	0,95±0,09	0,84±0,07	0,86±0,05	0,76±0,047*
	E/e'	38,03±0,99	37,49±1,2	37,45±1,24	40,22±0,82
Overall cardiac function	**HR, bpm**	241±13	268±15	252±14	228±10
	SV, ml	0,64±0,04	0,68±0,05	0,71±0,04	0,68±0,05
	CO, ml/min	151,5±8,13	177,2±11,27*	175,15±9,4*	153,2±10,67
	N	13			

Chapter 5

Selective SERCA2a Activator as Candidate for Oral Heart Failure Therapy

Martina Arici[1#], Shih-Che Hsu[2#], Mara Ferrandi[3], Paolo Barassi[3], Carlotta Ronchi[1], Eleonora Torre[1], Gwo-Jyh Chang[4], Francesco Peri[1], Patrizia Ferrari[3], Giuseppe Bianchi[3,5], Antonio Zaza[1*], Marcella Rocchetti[1*]

[1]Department of Biotechnology and Biosciences, Università degli Studi di Milano-Bicocca, 20126 Milan, Italy.
[2]CVie Therapeutics Limited, Taipei, 11047 Taiwan
[3]Windtree Therapeutics Inc., Warrington, Pennsylvania, 18976, USA.
[4]Chang Gung University, Tao-Yuan, 333323 Taiwan.
[5]Università Vita-Salute San Raffaele, 20132 Milan, Italy.

# Contributed equally as first authors to the article

*Contributed equally as senior authors to the article

5.1. ABSTRACT

The pathological features of diastolic dysfunction in heart failure (HF) are strongly associated with sarcoplasmic reticulum (SR) Ca^{2+} ATPase (SERCA2a) depression, suggesting that SERCA2a is an interesting therapeutic target. Istaroxime is an inolusitropic drug that combines the ability to inhibit the Na^{+}/K^{+} ATPase and stimulate SERCA2a activity in failing animal models and in patients with acute HF. Novel SERCA2a activators have been synthetized as PST3093 derivatives, the main metabolite of istaroxime showing a more favourable pharmacokinetic profile than the parent drug. PST3093 and its derivatives are selective SERCA2a stimulators. Compound **8** was selected and here furtherly characterized to be a promising drug candidate for oral (chronic) HF therapy. Effects were evaluated in a context of SERCA2a depression, by using streptozotocin (STZ)-treated rats, a well-known model of diastolic dysfunction. The impact of SERCA2a stimulation by compound **8** was assessed both at the cellular level ad in vivo following i.v. infusion (acute effects) or oral administration (chronic effects). Stimulating SERCA2a, compound **8** induced SR Ca^{2+} compartmentalization at resting in STZ myocytes. Echocardiographic analysis during i.v. infusion and especially after oral treatment with single or repeated doses of compound **8**, showed STZ-induced diastolic dysfunction improvement. Moreover, compound **8** did not affect electrical activity of healthy guinea pig myocytes, in line with the absence of off-target effects. Finally, compound **8** was well tolerated in mice with no evidence of acute toxicity.

Overall, the pharmacological evaluation of compound **8** indicates that it is a safe and selective SERCA2a stimulator and a favourable drug candidate for chronic HF therapy.

5.2. GRAPHICAL ABSTRACT

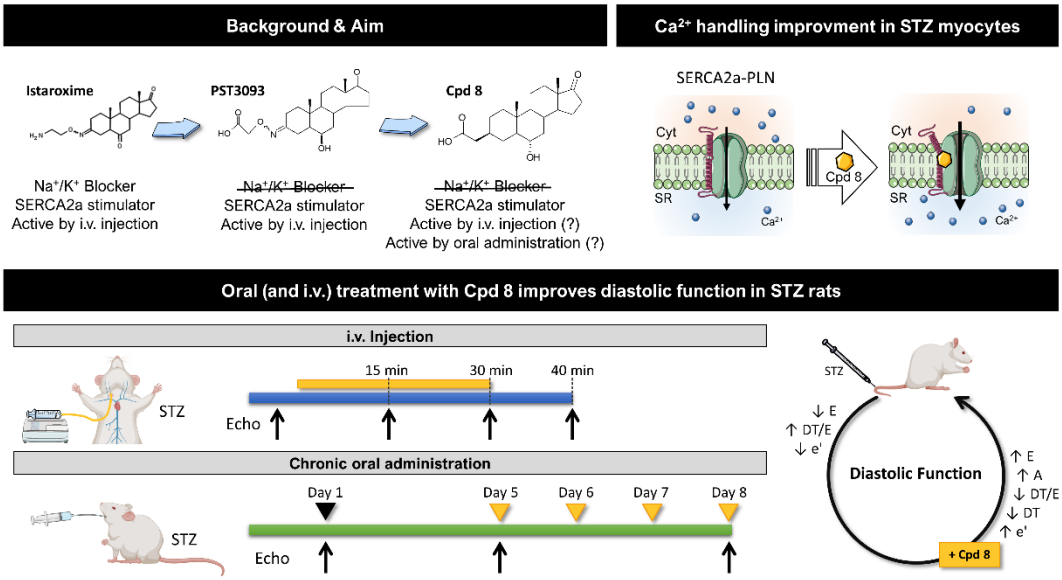

5.3. INTRODUCTION

Heart failure (HF) has become a global public health burden which affects people worldwide with increasing in prevalence and high hospitalization and mortality rate. The limited efficacy and the long-term safety concerns of the existing therapy of HF indicate that there is still a critical medical need for the development of drugs that may improve patient outcomes, without increasing untoward effects, including arrythmias, and the mortality risk[1].

Pathological features of HF refer to the inability of the failing heart to accomplish the systolic and diastolic function with diminished contraction and relaxation activity. The abnormality in cardiac compliance is strongly influenced by Ca^{2+} fluxes. Sarcoplasmic reticulum (SR) SERCA2a ATPase is an enzyme involved in Ca^{2+} homeostasis, a fundamental process in the myocardial contraction-relaxation cycle. The specific inhibition of SERCA2a transport activity, or a reduction in its expression, causes changes in contractile function, whereas SERCA2a administration via the lentiviral vector improves contraction in damaged cardiac tissues[2]. This suggests that SERCA2a is one of the most important pathophysiological substrates for HF and makes it a particularly interesting therapeutic target. Several SERCA2a activators as therapeutic approach to HF have been explored, however no beneficial agent successfully reached the clinic.

Istaroxime is an innovative and unique ino-lusitropic drug that combines the ability to inhibit the Na^+/K^+ ATPase and stimulate SERCA2a activity, resulting in improvement of the failing heart function[3,4]. SERCA2a stimulation by istaroxime is dependent on the relief of phospholamban (PLN) inhibitory effect on SERCA2a, without inducing spontaneous Ca2+ release from the SR[5]. In healthy and failing animal models and in patients with acute heart failure syndrome (Phase IIb clinical trials), istaroxime improves the systolic and diastolic performance and the efficiency of cardiac contraction with a low oxygen consumption, minimizing the risk of arrhythmias and ischemia[6–8]. Although endowed of an excellent pharmacodynamic profile, pharmacokinetic studies have indicated that istaroxime has a short plasma half-life (less than 1h)[6], its plasma levels decrease quickly after drug infusion interruption due to its extensive metabolization to a long-lasting metabolite, PST3093[9]. PST3093 retains the ability to stimulate SERCA2a, it does not inhibit Na^+/K^+ ATPase[9] and may participate

to istaroxime beneficial effects on cardiac relaxation-contraction coupling, as shown in pre-clinical settings[10]. However, istaroxime extensive metabolization and its weak gastrointestinal absorption limit the chronic use of the compound.

This let us to approach a rational design for novel SERCA2a activators as PST3093 derivatives, devoid of inhibitory activity on Na^+/K^+ ATPase, orally absorbed and thus suitable for a chronic treatment[11]. Among the developed PST3093 derivates, compound **8** was one of the two selected compounds furtherly characterized through *in vitro* assays, reporting its ability to recover streptozotocin (STZ)-induced SERCA2a activity depression in a PLN-dependent manner, analogously to its parent compound PST3093[11]. We present here the further pharmacological evaluation of compound **8** that proves to be a safe and selective SERCA2a stimulator and a favourable drug candidate for oral HF therapy.

5.4. RESULTS

5.4.1 Chemical structure of compound 8

The chemical structure of compound **8** is shown in Figure 1A in comparison to that of PST3093 and istaroxime; the chemical synthesis of compound **8** has been extensively described elsewhere[11]. Compound **8** is a novel PST3093 derivative with a saturated bond in position 3 which ensures a greater metabolic stability compared to the progenitor molecules. In compound **8**, the length of the C3 linker is reduced to 2 carbon atoms and the hydroxyl group in C6 is in the α-configuration[11].

5.4.2 Compound 8 is a selective SERCA2a activator

Compound **8** has been previously characterized[11] for its stimulatory action on SERCA2a activity at nanomolar concentration and its null effect on purified renal Na^+/K^+ ATPase up to 10^{-4} M, similarly to its parent compound PST3093[9]. Here, we further characterized compound **8** in isolated cardiomyocytes to highlight its SERCA2a stimulatory action in a physiological whole cell context.

Measurements of Na^+/K^+ ATPase current (I_{NaK}) in V-clamped rat ventricular myocytes confirmed the low affinity of compound **8** for the Na^+/K^+ pump, similarly to its parent compound PST3093 (Figure 1B). Indeed, at the limit concentration for solubility (100 µM), the effect of compound **8** (-21.8 ± 2%) was in the same range of PST3093 (-9.2 ± 1.1%)[9], quite different from istaroxime effect in the same experimental settings (estimated IC_{50} 32 ± 4 µM,[12]). According to this finding, measurements in isolated myocytes to analyse effects on SERCA2a were performed by testing compound **8** at 1 µM.

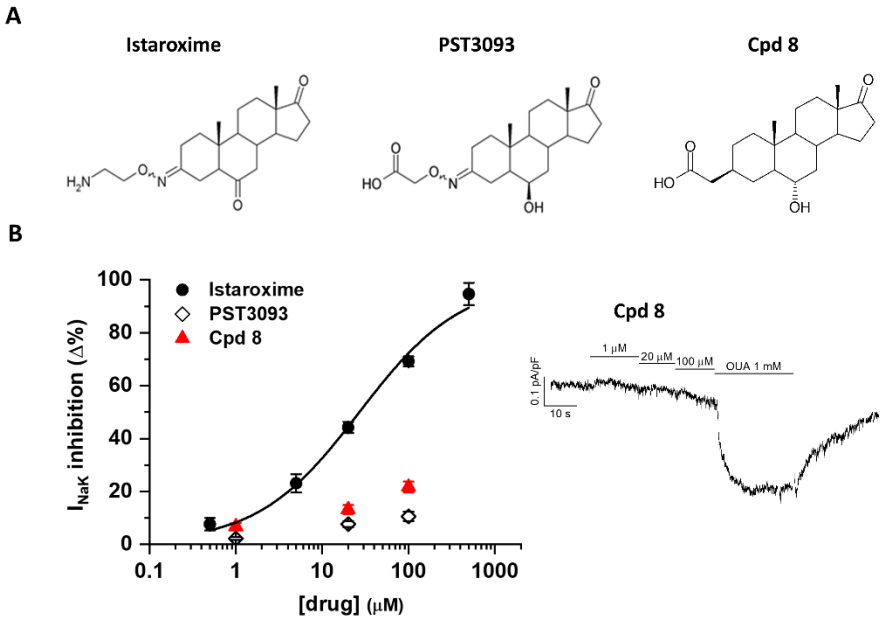

Figure 1. A) Chemical structures of compound **8** in comparison to istaroxime and its metabolite, PST3093. B) Concentration-response curve for I_{NaK} inhibition by compound **8** (N=3, n=21), in comparison to PST3093 and istaroxime (modified from [9]) in rat LV myocytes; I_{NaK} recording under increasing concentration of compound **8** and finally ouabain (OUA as reference) is shown on the right. Data are the mean ± SEM.

STZ-induced diabetes was selected as a pathological model because of its association with reduced SERCA2a function[12] and relevance to diastolic dysfunction[13]. A comprehensive in vivo and in vitro analysis of STZ model was performed in previous studies of our group[9,11,12].

To functional evaluate compound **8** effects on SERCA2a activity, we measured the SR ability to accumulate resting Ca^{2+} through a post-rest potentiation protocol in control (healthy) and STZ myocytes (see paragraph 2.6.2 and Figure 1 of Chapter 2). As shown in Figure 2A-B, following increasing resting pauses, the amplitude of the 1st Ca_T increased progressively in healthy myocytes; according to STZ-induced SERCA2a down-regulation[12], post-rest potentiation was reduced in STZ myocytes at all resting intervals. Compound **8** (1 μM) failed to affect post-rest potentiation in healthy myocytes, while it restored the ability of SR to accumulate Ca^{2+} in STZ myocytes, in agreement with its stimulatory action on SERCA2a. Accordingly, in STZ myocytes resting Ca^{2+} (Ca_{rest})

increased and compound **8** fully restored it to control values. $ssCa_T$ amplitude was not significantly affected by STZ and compound **8**, while $ssCa_T$ decay kinetic was slower in STZ myocytes in comparison to control myocytes and compound **8** failed to restore it (Figure 2C). Similar findings were observed with the parent compound PST3093 in the same experimental setting[9]. Moreover, SR Ca^{2+} content (Ca_{SR}) was evaluated by measuring caffeine-induced Ca_T amplitude evocated 0.5s and 20s following voltage pacing train in the same cell (Figure 2D-E). While, as expected in healthy myocytes Ca_{SR} increased as the pause increased, in STZ myocytes this finding was severely blunted according to SR function depression. In STZ myocytes, compound **8** stimulating SERCA2a restored Ca_{SR} pause-dependency to control level. Taken together, these results suggest that compound **8** improved Ca^{2+} sequestration into the SR during the post-train quiescence period, particularly in conditions of SERCA2a depression.

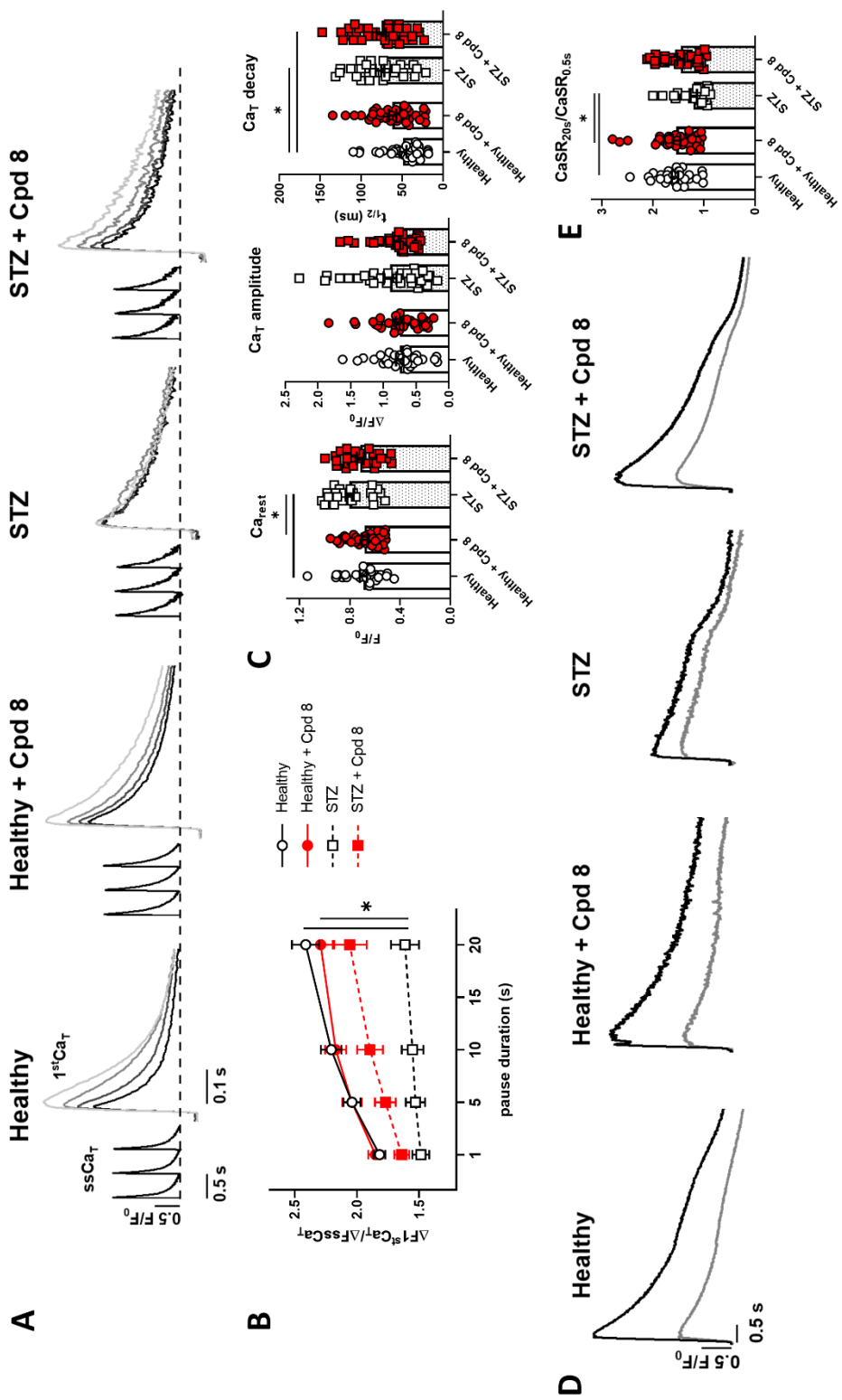
A
Healthy
Healthy + Cpd 8
STZ
STZ + Cpd 8
1st Ca_T
ssCa_T
0.5 F/F0
0.1 s
0.5 s
B
Healthy
Healthy + Cpd 8
STZ
STZ + Cpd 8
ΔF+1st Ca_T/ΔFssCa_T
pause duration (s)
C
Ca_rest
F/F0
Ca_T amplitude
ΔF/F0
Ca_T decay
t1/2 (ms)
D
Healthy
Healthy + Cpd 8
STZ
STZ + Cpd 8
0.5 F/F0
0.5 s
E
CaSR20s/CaSR0.5s

Figure 2. Modulation of SR Ca^{2+} uptake at resting in field stimulated STZ myocytes. A) Post-rest potentiation protocol in Fluo4 field stimulated (2 Hz) myocytes: steady state Ca^{2+} transients ($ssCa_T$) and superimposed first Ca^{2+} transients (1^{st} Ca_T) following increasing resting pause (1-5-10-20 s) are reported in Healthy and STZ myocytes, with or w/o 1 µM compound **8**. Traces were normalized to own diastolic Ca^{2+} level (dotted line). B) Analysis of the 1^{st} Ca_T amplitude normalized to the amplitude of the pre-pause $ssCa_T$ and its pause dependency; healthy N=3 (n=34 w/o compound **8**, n=38 with compound **8**), STZ N=3 (n=31 w/o compound **8**, n=32 with compound **8**). *p<0.05 for the "interaction factor" in RM two-way ANOVA, indicating a different steepness of curves. C) Statistics for Ca_{rest}, $ssCa_T$ amplitude and $ssCa_T$ half decay time ($t_{1/2}$); healthy N=3 (n=28 w/o compound **8**, n=35 with compound **8**), STZ N=3 (n=24 w/o compound **8**, n=28 with compound **8**). *p<0.05 (one way ANOVA plus post-hoc Tukey's multiple comparison). D) Caffeine-induced Ca_T evocated (Ca_{SR}) in field stimulated Healthy and STZ myocytes with or w/o 1 µM compound **8** following 0.5s (in grey) or 20s (in black) resting pause. E) Statistics for $CaSR_{20s}$/$CaSR_{0.5s}$; healthy N=3 (n=28 w/o compound **8**, n=35 with compound **8**), STZ N=3 (n=23 w/o compound **8**, n=28 with compound **8**). *p<0.05 (one way ANOVA plus post-hoc Tukey's multiple comparison).

To assess SR Ca^{2+} uptake under conditions emphasizing SERCA2a role (NCX inhibition), compound **8** effects were analysed under V-clamp by using the "SR loading" protocol (see paragraph 2.6.2 and Figure 2 of Chapter 2). As previously shown[9], this protocol allows functional evaluation of SERCA2a downregulation in failing myocytes; in particular, in STZ myocytes, as compared to healthy ones, SR reloading was significantly depressed (both in terms of Ca_T amplitude and ER gain) and Ca_T decay was slower at all time-points during reloading[9]. Here we tested compound **8** (1 µM) effects in STZ myocytes (Figure 3). Compound **8** sharply accelerated Ca_T decay, Ca_T amplitude and ER-gain, restoring the profile observed in healthy myocytes[9]. Comparable results have been obtained by istaroxime at a concentration marginally affecting Na^+/K^+ ATPase[12], by its metabolite PST3093[9] and another PST3093 derivative (compound **5** in [11]).

Overall, these results are in accordance with the data observed in the cell-free system[11]. Compound **8**, as its parent compounds, restored SR function in diseased myocytes, i.e. the context of the pathological cellular environment, most likely through SERCA2a enhancement, and are suggestive of a selective ability of the compound to stimulate SERCA2a activity.

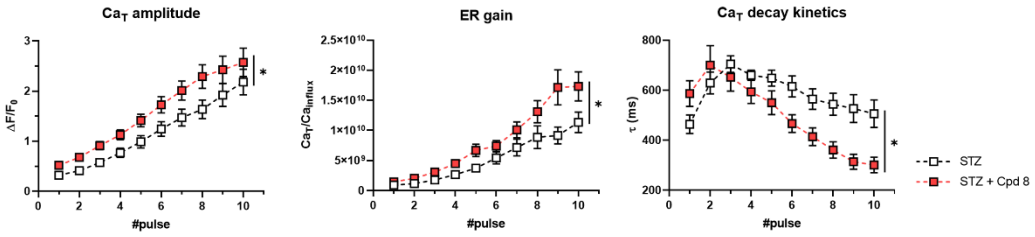

Figure 3. Modulation of SR Ca^{2+} uptake under NCX inhibition in V-clamped myocytes STZ myocytes. SR Ca^{2+} loading by a train of V-clamped pulses was initiated after caffeine-induced SR depletion; NCX was blocked by Na^+ substitution to identify SERCA2a-specific effects (see paragraph 2.6.2 of Chapter 2); myocyte from STZ w/o compound **8** are compared. Panels from left to right: Ca_T amplitude, Exitation-Release (ER) gain (the ratio between Ca_T amplitude and Ca^{2+} influx through I_{CaL}), time constant (τ) of Ca_T decay; STZ N=3 (n=18 w/o compound **8**, n=23 with compound **8**). *p<0.05 for the "interaction factor" in RM two-way ANOVA, indicating a different steepness of curves.

5.4.3 Compound 8 does not affect electrical activity in healthy myocytes

To assess the electrophysiological safety of compound **8**, its effects on AP of LV myocytes were investigated. Guinea pig myocytes were used because their AP is closer to the human one. Compound **8**, tested at the concentration of 1 μM, did not induce changes of AP parameters (APD_{90}, E_{diast}, dV/dt_{max}) (Figure 4A). Notably, also APD rate-dependency at steady-state and the kinetics of APD adaptation following a step change in rate, were unaffected by the agent (Figure 4B). STV of APD_{90}, a reporter of repolarization stability, was also unaffected by compound **8** at all pacing rates (Figure 4C). Similar results were also obtained with compound **8** at lower concentrations (data not shown).

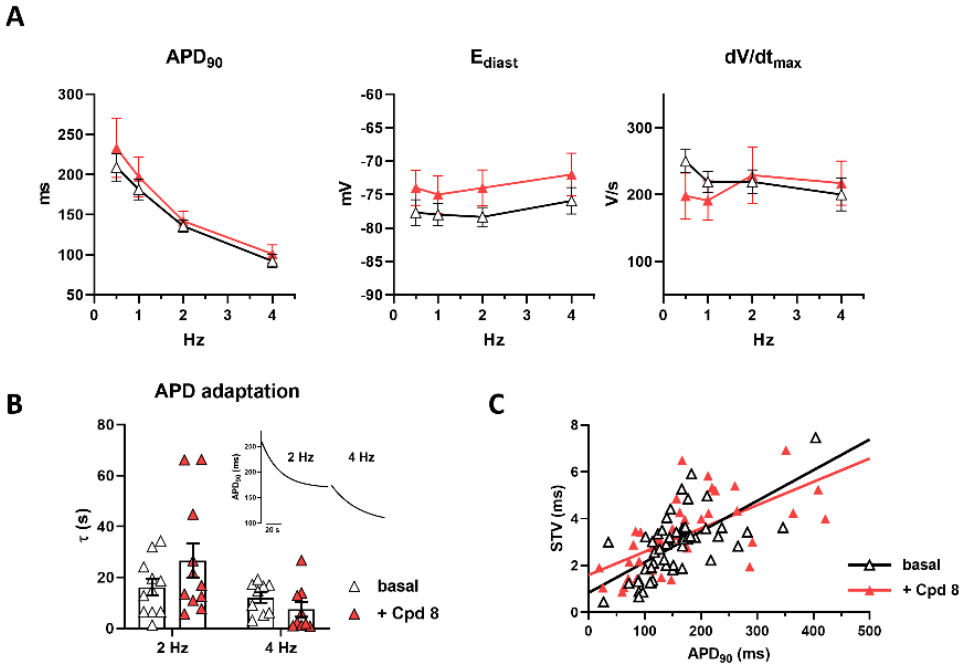

Figure 4. Modulation of electrical activity in healthy guinea pig myocytes. The effect of 1 µM compound **8** was tested on action potential (AP) parameters and their steady-state rate dependency in guinea pig myocytes. A) Effect on the rate dependency of AP duration (APD_{50} and APD_{90}), diastolic potential (E_{diast}) and maximal phase 0 velocity (dV/dt_{max}); (n=13 w/o compound **8**, n=11 with compound **8**. B) Effect on the time constant (τ) of APD_{90} adaptation following a step change in rate. 4Hz: n=9 w/o compound **8**, n=10 with compound **8**; 2 Hz: n=11 with or w/o compound **8**. C) Effect on the correlation between STV of APD_{90} and APD_{90} values on the right; data from 1, 2 and 4 Hz were pooled. *p<0.05 for the "interaction factor" of RM two-way ANOVA.

5.4.4 Off-target effects

Off-target effects of compound **8** were analysed at 10 µM. Molecular targets other than SERCA2a (50 items), including membrane receptors, key enzymes, ion channels and transporters, are shown in Table S1. None among the 50 items met criteria for significance of interaction. Thus, at least for the ligands shown in Table S1, no off-target action of compound **8** is expected. Similar findings were observed with the parent compound PST3093[9].

5.4.5 In vivo acute toxicity

Compound **8** acute toxicity was preliminarily evaluated in CD1 mice following i.v. and oral administration. The compound was well tolerated and did not cause death up to 300 mg/kg after i.v. administration, similarly to PST3093[9]. For comparison, istaroxime LD_{50} following i.v. infusion was 23 mg/kg[9]. Oral acute toxicity of compound **8** was higher than 700 mg/kg, the highest tested dose. As previously reported[11], PST3093 and istaroxime oral toxicities were higher than compound **8** (>200 mg/kg and 200 mg/kg respectively), underlying the suitable profile of compound **8** for chronic oral treatment.

5.4.6 Hemodynamic studies in STZ diabetic rats

The effect of compound **8** on echocardiographic indexes in the STZ cardiomyopathic rat model was assessed after i.v. infusion or oral administration.

For the first experimental setting (i.v. infusion), the evaluation was done under urethane anaesthesia and previous published echocardiographic data in healthy and diseased rats[9] were considered as reference for the model alterations. In comparison to healthy controls, STZ rats showed an impairment of diastolic function, with decreased early filling velocity (E), increased deceleration time (DT) and E wave deceleration time over E ratio (DT/E), decreased TDI relaxation velocity (e'), and systolic function, with decreased fractional shortening (FS), ejection fraction (EF) and TDI contraction velocity (s'); stroke volume (SV) and cardiac output (CO) were similar between STZ and healthy rats while heart rate (HR) was significantly reduced in STZ[9].

5.4.6.1 i.v. administration

Compound **8** was i.v. infused in STZ rats at the rate of 0.2 mg/kg/min and the effects on echocardiographic parameters were investigated at 15 and 30 min of infusion under urethane anaesthesia. The echo measurement was additionally evaluated 10 min after drug infusion discontinuation to establish whether the effects induced by the compound during infusion were reversible (Figure 5, Figure S1). Compound **8** positively affected transmitral Doppler flow indexes by increasing A wave, leading to a decreased

E/A ratio (Figure S1); the compound shortened the DT, reduced the DT/E ratio, enhanced the TDI relaxation velocity e' and increased LVEDD. The compound improved SV and CO, without affecting HR or systolic indexes, such as FS, systolic TDI velocity (s') and LVESD. Drug effects reached a plateau at 15 min of infusion; 10 min after infusion discontinuation, most echo indexes affected by the compound reverted to the basal level, except for LVEDD and SV that remained significantly increased over basal condition.

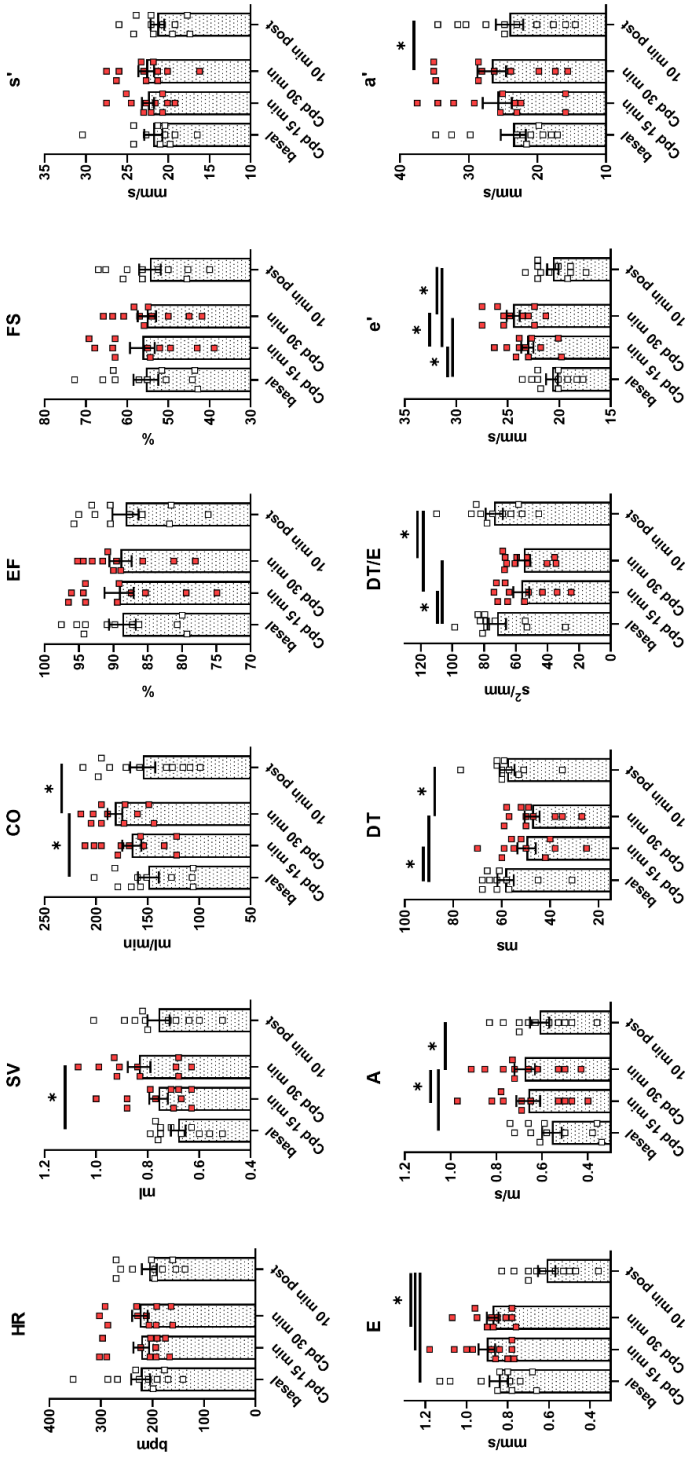

Figure 5. In vivo effects after i.v. infusion in STZ rats. Compound **8** was i.v. infused at 0.2 mg/kg/min under urethane anaesthesia, in rats 8 weeks after STZ treatment. Echocardiographic parameters (see also Figure S1) were measured under basal condition, at 15 and 30 minutes during drug infusion and 10 minutes after drug infusion interruption. Data are mean ± SEM. STZ N=11; *p<0.05 (one-way RM ANOVA plus post-hoc Tukey's multiple comparison).

5.4.6.2 Oral administration

For the oral administration protocol, STZ rats were subjected to single or repeated doses of compound **8** or saline, and urethane anaesthesia was substituted with ketamine/pentobarbital to permit the recovery of the animals after each experimental echocardiographic session. Compound **8** was orally administered at 40 and 80 mg/kg in STZ rats for 1 or 4 once daily doses and a control group of STZ rats received vehicle only (saline group) (Figure 6, Figure S2). Each echo parameter measured following 1 (day 5) and 4 (day 8) doses of drug (or saline) treatment was normalized to its basal value (day 1) to better highlight dose-dependent or cumulative drug effects. Absolute values of each echo parameter are shown in Table S2.

Saline group of STZ rats showed time dependent E wave and e' relaxation velocity reduction at day 8 vs day 1; the other echo indexes remained constant during the entire protocol.

When compared to the saline group, echo parameters following 1 single oral dose (40 mg/kg) of compound **8** were not significantly affected by the drug, excepting the drug-induced e' relaxation velocity enhancement; however, following 4 once daily oral 40 mg/kg administrations, compound **8** ameliorated several diastolic parameters, by increasing E and A waves, e' and a' relaxation velocities and decreasing DT/E ratio; on the other hand, DT (Figure 6), E/A, e'/a' and E/e' ratios (Figure S2) were not significantly affected. Compound **8** at 40 mg/kg did not affect systolic parameters, such as FS, SV and EF, while s' was slightly increased after 4 doses of compound **8** (Figure 6). Increasing in CO was mainly dependent on HR enhancement (Figure 6).

In comparison to the saline group, compound **8**, administered in STZ rats at higher dose (80 mg/kg) significantly affected several diastolic indexes following 1 single oral dose. Indeed, it increased E and A waves, reducing the DT/E ratio, and it enhanced the e' and a' TDI relaxation velocity (Figure 6). Similar effects were observed after 4 once daily oral administrations at 80 mg/kg; moreover, compound **8** furtherly ameliorated diastolic function by significantly reducing DT (Figure 6). Effects on systolic parameters and on global cardiac function (HR, SV and CO parameters) were comparable but more pronounced to those observed at the lower dose of compound.

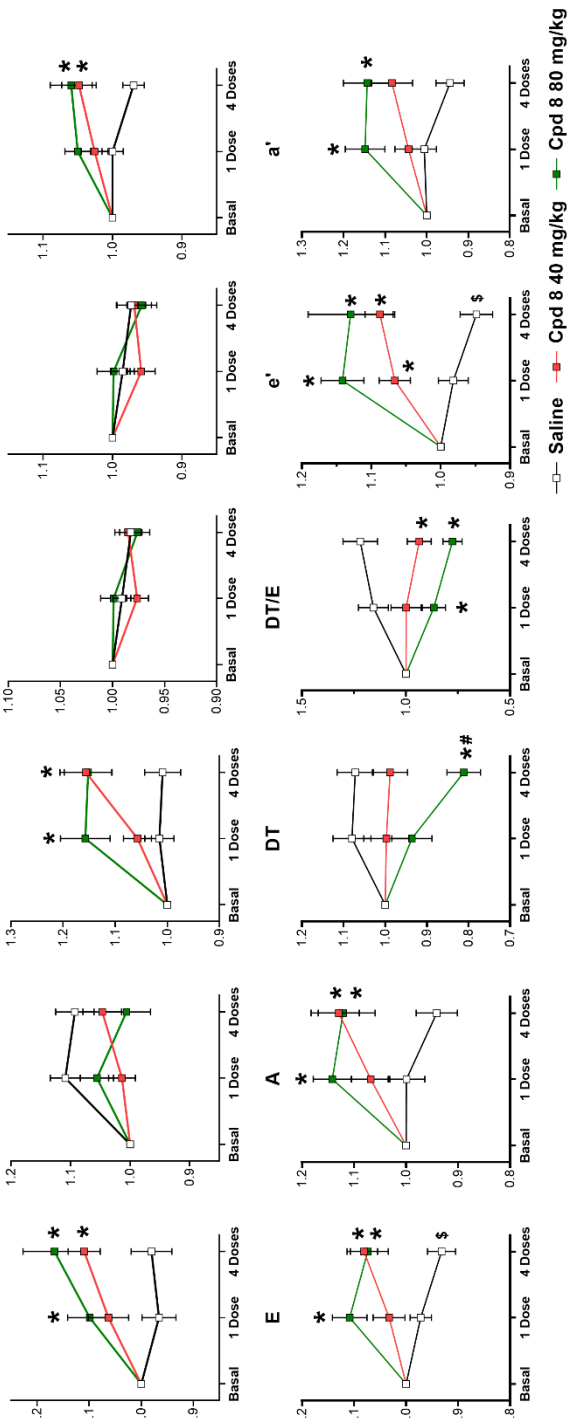

Figure 6. In vivo effects after oral treatment in STZ rats. Rats were treated with compound **8** at 40 mg/kg or 80 mg/kg or with saline (control group) for 1 to 4 once-daily doses accordingly to the protocol shown in Figure 2 of paragraph 2.6.2 in Chapter 2. Echocardiographic parameters (see also Figure S2) were measured in each group at 60-min from treatment under ketamine/pentobarbital anesthesia. Data were normalized to the basal level measured at day 1. Data are mean ± SEM; saline N=40 (animals from the 2 control groups were pooled), 40 mg/kg compound 8 N=22, 80 mg/kg compound 8 N=21. *p<0.05 vs saline group, #p<0.05 vs basal (two-way RM ANOVA plus post-hoc Tukey's multiple comparison).

Overall, chronic effects of compound **8** after oral treatment in STZ rats were comparable to those observed following acute i.v. infusion, they were dose-dependent after 1 single oral dose of compound, and they were indicative of a specific lusitropic action of the compound due to SERCA2a function rescue. Systolic function was marginally affected by the compound, probably due to the lack of inhibitory activity on the Na^+/K^+ pump.

5.5. DISCUSSION

The present study summarizes the preclinical data related to compound **8**, a derivate of istaroxime long-lasting metabolite PST3093, that has been previously selected by an *in vitro* screening, showing its ability to activate cardiac SERCA2a, being deprived of inhibitory activity on Na^+/K^+ ATPase[11]. The preclinical profile of compound **8** indicates that it has a low acute toxicity, it is highly selective, and it is active in isolated myocytes and *in vivo* in ameliorating STZ-induced cardiac function abnormalities after i.v. and oral treatment. Thus, compound **8** can be considered an example of a small molecule acting as a "pure" SERCA2a activator, suitable for chronic HF therapy.

Reliable data on compound **8** have been provided by using independent methodologies indicating that the compound displays a specific molecular mechanism as suggested by previous data in cell free systems[11] and in this study at the cellular and *in vivo* levels.

As previously shown[11], differently from istaroxime, compound **8** is devoid of any inhibitory activity on Na^+/K^+ ATPase while it is endowed of a selective SERCA2a stimulatory activity that occurs at nanomolar concentrations in cardiac preparations from normal guinea pig and diabetic (STZ) rats with impaired SERCA2a function. As shown for istaroxime[5] and PST3093[9], compound **8** stimulatory activity of SERCA2a is dependent on the presence of PLN, whose inhibitory activity on SERCA2a is dose-dependently relieved by the compound[11].

Studies in isolated myocytes (Figures 2-3) confirmed the ability of the compound to compartmentalize Ca^{2+} in the SR at resting by stimulating SERCA2a, in line with previous studies of our[9,11,12]. Effects were evident especially in myocytes isolated from STZ rats, characterized by cardiac SERCA2a down-regulation[9,12], suggesting that stimulation of SERCA2a function is easily detected whenever its "reserve" is diminished. SR Ca^{2+} compartmentalization has potential long-term effects on energetic efficiency and biology of cardiac myocytes[14]; thus, a pure SERCA2a activator might exert substantial antiarrhythmic effects, at least under the common conditions characterized by SR instability (e.g. HF). Indeed, an increase in SERCA2a activity may exert an antiarrhythmic effect due to the inhibition of Ca^{2+} waves[15]. Further studies focused on this are necessary to better characterize potential antiarrhythmic effects of SERCA2a stimulators.

The main goal of this study was to evaluate chronic in vivo effects of compound **8** after oral administration in a failing cardiac model. All in vivo data available in literature are suggestive of the high therapeutic potential of istaroxime[6–8,10], its metabolite PST3093[9] and PST3093 derivatives[11], but this is the first study evaluating chronic effects of one of these follow-on compounds through its oral administration in the STZ model. STZ rats were chosen because of their well-known diastolic dysfunction. Echocardiographic parameters were evaluated at two dosages of compound **8** and after 1 or 4 daily doses to evaluate potential dose-dependent effects and to indirectly explore its pharmacokinetic in rats. Pharmacokinetics of compound **8** are still unknown, but it is hopeful that its plasma half-life should be comparable to that of its parent compound PST3093[9]. PST3093 showed a plasma half-life of about 9 hours in humans, substantially longer than that of istaroxime (less than 1 hour)[9]. Even though species-specific differences cannot be ruled out, results obtained in the present study using the lower dosage (40 mg/kg) of compound **8** are indicative of a long plasma half-life of compound **8** in rats. Indeed, cumulative effects were detected following 4 once-daily doses at 40 mg/kg (Figure 6). The two dosages (40 and 80 mg/kg) were chosen accordingly to the absence of in vivo acute toxicity up to 700 mg/kg in mice.

Overall, compound **8** improved diastolic relaxation in STZ rats after 60 min gavage at 40 and 80 mg/kg, as 1 or 4 repeated once-daily doses versus control group receiving vehicle only. This was particularly evident after 4 oral doses at 40 mg/kg and even 1 oral dose at 80 mg/kg. Similar results on diastolic indexes were obtained following acute i.v. injection of compound **8** in STZ rats, thus strengthening the potency of compound **8** in ameliorating diastolic function in diseased condition.

At any dose (oral or i.v. administration), compound **8** failed to affect systolic indexes, except for the s' enhancement following 4 doses (at 40 or 80 mg/kg). The absence of a clear inotropic effect of compound **8** is probably due to the lack of Na^+/K^+ ATPase blockade. Similar results have been obtained with i.v. infusion with another PST3093 derivative[11]. However, the parent compound PST3093 showed either lusitropic and inotropic effects when i.v. administrated *in vivo* in STZ rats[9]. These differences might depend on differences in the progressive pathogenesis of the diabetic cardiomyopathy, starting with diastolic dysfunction (HF with preserved EF, HFpEF) that generally evolves in symptomatic systolic dysfunction (HF with reduced EF, HFrEF)[16]. Thus, it is reasonable that these compounds are able to ameliorate STZ-induced diastolic and even systolic

abnormalities when they are present. Using other HF models (i.e pressure overload HF models) with a clear systolic dysfunction might better clarify the inotropic action of SERCA2a stimulation.

Following 4 doses of 40 mg/kg or 1 single dose of 80 mg/kg compound **8** orally administrated, CO increased mainly as a consequence of HR enhancement. However, following i.v. infusion HR left unchanged, while SV and CO increased, similarly to PST3093 after i.v. infusion[9]. Differences related to different routes of administration are likely and they might suggest the presence of different compensatory mechanisms. Further studies are necessary to clarify this point.

In summary, the specific lusitropic effect of compound **8** in STZ rats detected after i.v. infusion and oral administration may be ascribed to the stimulation of SERCA2a that is downregulated in this model. The present data may be relevant in the clinical setting even though the pathophysiological differences between the STZ rats and the patients with acute HF have to be considered. In the STZ animal model, marked changes in body fluids, sympathetic nervous system, and HR, may per se affect echocardiographic parameters, independently from the changes in cellular Ca^{2+} handling and decrease of SERCA2a activity[17]. Therefore, the similarities between rats and humans may be considered as having the same underlying mechanism that is the stimulation of SERCA2a activity by compound **8**.

5.5.1 Study limitations

A limitation of the present study is the influence of different anaesthesia (urethane for i.v. infusion versus ketamine/pentobarbital for oral administration) on echocardiography parameters measured in STZ rats. The confounding effect of anaesthesia on profiles of heart function in STZ rats must be taken into consideration when commenting on the specific effects of the treatment with compound **8**.

5.6. ACKNOWLEDGMENT

We thank Dr Albero Cerri for his valuable contribution as a founder of the medicinal chemistry project.

5.7. AUTHOR CONTRIBUTION

Participated in research design: Rocchetti, Zaza, Peri, Ferrari and Bianchi. Conducted experiments: Arici, Hsu, Ferrandi, Barassi, and Chang. Performed data analysis: Arici, Hsu, Ferrandi, Ronchi and Torre. Wrote or contributed to the writing of the manuscript: Rocchetti and Zaza.

5.8. REFERENCES

(1) Chioncel, O.; Mebazaa, A.; Harjola, V.-P.; Coats, A. J.; Piepoli, M. F.; Crespo-Leiro, M. G.; Laroche, C.; Seferovic, P. M.; Anker, S. D.; Ferrari, R.; Ruschitzka, F.; Lopez-Fernandez, S.; Miani, D.; Filippatos, G.; Maggioni, A. P. Clinical Phenotypes and Outcome of Patients Hospitalized for Acute Heart Failure: The ESC Heart Failure Long-Term Registry. *Eur J Heart Fail* **2017**, *19*, 1242–1254. https://doi.org/10.1002/ejhf.890.

(2) Gwathmey, J. K.; Yerevanian, A. I.; Hajjar, R. J. Cardiac Gene Therapy with SERCA2a: From Bench to Bedside. *Journal of Molecular and Cellular Cardiology*. May 2011, pp 803–812. https://doi.org/10.1016/j.yjmcc.2010.11.011.

(3) Micheletti, R.; Mattera, G. G.; Rocchetti, M.; Schiavone, A.; Loi, M. F.; Zaza, A.; Gagnol, R. J. P.; de Munari, S.; Melloni, P.; Carminati, P.; Bianchi, G.; Ferrari, P. Pharmacological Profile of the Novel Inotropic Agent (E,Z)-3-((2-Aminoethoxy)Imino)Androstane-6,17-Dione Hydrochloride (PST2744). *J Pharmacol Exp Ther* **2002**, *303*, 592–600. https://doi.org/10.1124/jpet.102.038331.

(4) Rocchetti, M.; Besana, A.; Mostacciuolo, G.; Micheletti, R.; Ferrari, P.; Sarkozi, S.; Szegedi, C.; Jona, I.; Zaza, A. Modulation of Sarcoplasmic Reticulum Function by Na/K Pump Inhibitors with Different Toxicity: Digoxin and PST2744 [(E,Z)-3-((2-Aminoethoxy)Imino)Androstane-6,17-Dione Hydrochloride]. *J Pharmacol Exp Ther* **2005**, *313*, 207–215. https://doi.org/10.1124/jpet.104.077933.

(5) Ferrandi, M.; Barassi, P.; Tadini-Buoninsegni, F.; Bartolommei, G.; Molinari, I.; Tripodi, M. G.; Reina, C.; Moncelli, M. R.; Bianchi, G.; Ferrari, P. Istaroxime Stimulates SERCA2a and Accelerates Calcium Cycling in Heart Failure by Relieving Phospholamban Inhibition. *Br J Pharmacol* **2013**, *169*, 1849–1861. https://doi.org/10.1111/bph.12288.

(6) Gheorghiade, M.; Blair, J. E. A.; Filippatos, G. S.; Macarie, C.; Ruzyllo, W.; Korewicki, J.; Bubenek-Turconi, S. I.; Ceracchi, M.; Bianchetti, M.; Carminati, P.; Kremastinos, D.; Valentini, G.; Sabbah, H. N. Hemodynamic, Echocardiographic, and Neurohormonal Effects of Istaroxime, a Novel Intravenous Inotropic and Lusitropic Agent: A Randomized Controlled Trial in Patients Hospitalized With Heart Failure. *J Am Coll Cardiol* **2008**, *51* (23), 2276–2285. https://doi.org/10.1016/J.JACC.2008.03.015.

(7) Shah, S. J.; Blair, J. E. A.; Filippatos, G. S.; MacArie, C.; Ruzyllo, W.; Korewicki, J.; Bubenek-Turconi, S. I.; Ceracchi, M.; Bianchetti, M.; Carminati, P.; Kremastinos, D.; Grzybowski, J.; Valentini, G.; Sabbah, H. N.; Gheorghiade, M. Effects of Istaroxime on Diastolic Stiffness in Acute Heart Failure Syndromes: Results from the Hemodynamic, Echocardiographic, and Neurohormonal Effects of

Istaroxime, a Novel Intravenous Inotropic and Lusitropic Agent: A Randomized Controlled Trial in Patients Hospitalized with Heart Failure (HORIZON-HF) Trial. *Am Heart J* **2009**, *157* (6), 1035–1041. https://doi.org/10.1016/j.ahj.2009.03.007.

(8) Sabbah, H. N.; Imai, M.; Cowart, D.; Amato, A.; Carminati, P.; Gheorghiade, M. Hemodynamic Properties of a New-Generation Positive Luso-Inotropic Agent for the Acute Treatment of Advanced Heart Failure. *American Journal of Cardiology* **2007**, *99* (2 SUPPL.). https://doi.org/10.1016/j.amjcard.2006.09.005.

(9) Arici, M.; Ferrandi, M.; Barassi, P.; Hsu, S.-C.; Torre, E.; Luraghi, A.; Ronchi, C.; Chang, G.-J.; Peri, F.; Ferrari, P.; Bianchi, G.; Rocchetti, M.; Zaza, A. Istaroxime Metabolite PST3093 Selectively Stimulates SERCA2a and Reverses Disease-Induced Changes in Cardiac Function Running Title: PST3093 Stimulates SERCA2a and Improves Cardiac Function. *Journal of Pharmacology and Experimental Therapeutics* **2022**. https://doi.org/10.1124/jpet.122.001335.

(10) Carubelli, V.; Zhang, Y.; Metra, M.; Lombardi, C.; Michael Felker, G.; Filippatos, G.; O, C. M.; Teerlink, J. R.; Simmons, P.; Segal, R.; Malfatto, G.; Teresa La Rovere, M.; Li, D.; Han, X.; Yuan, Z.; Yao, Y.; Li, B.; Fui Lau, L.; Bianchi, G.; Zhang, J. Treatment with 24 Hour Istaroxime Infusion in Patients Hospitalised for Acute Heart Failure: A Randomised, Placebo-Controlled Trial. *Eur J Heart Fail* **2020**, *22*, 1684–1693. https://doi.org/10.1002/ejhf.1743.

(11) Luraghi, A.; Ferrandi, M.; Barassi, P.; Arici, M.; Hsu, S. C.; Torre, E.; Ronchi, C.; Romerio, A.; Chang, G. J.; Ferrari, P.; Bianchi, G.; Zaza, A.; Rocchetti, M.; Peri, F. Highly Selective SERCA2a Activators: Preclinical Development of a Congeneric Group of First-in-Class Drug Leads against Heart Failure. *J Med Chem* **2022**, *65* (10), 7324–7333. https://doi.org/10.1021/acs.jmedchem.2c00347.

(12) Torre, E.; Arici, M.; Lodrini, A. M.; Ferrandi, M.; Barassi, P.; Hsu, S.-C.; Chang, G.-J.; Boz, E.; Sala, E.; Vagni, S.; Altomare, C.; Mostacciuolo, G.; Bussadori, C.; Ferrari, P.; Bianchi, G.; Rocchetti, M. SERCA2a Stimulation by Istaroxime Improves Intracellular Ca2+ Handling and Diastolic Dysfunction in a Model of Diabetic Cardiomyopathy. *Cardiovasc Res* **2022**, *118*, 1020–1032. https://doi.org/10.1093/cvr/cvab123.

(13) Valero-Muñoz, M.; Backman, W.; Sam, F. Murine Models of Heart Failure With Preserved Ejection Fraction A “Fishing Expedition.” *Journal of American College of Cardiology: Basic to Translational Science* **2017**, *2*, 770–789.

(14) Zaza, A.; Rocchetti, M. *Calcium Store Stability as an Antiarrhythmic Endpoint*; 2015; Vol. 21.

(15) Fernandez-Tenorio, M.; Niggli, E. Stabilization of Ca2+ Signaling in Cardiac Muscle by Stimulation of SERCA. *J Mol Cell Cardiol* **2018**, *119*, 87–95. https://doi.org/10.1016/j.yjmcc.2018.04.015.

(16) Kang, Y.; Wang, S.; Huang, J.; Cai, L.; Keller, B. B. Right Ventricular Dysfunction and Remodeling in Diabetic Cardiomyopathy. *American Journal of Physiology-Heart and Circulatory Physiology* **2019**, *316* (1), H113–H122. https://doi.org/10.1152/ajpheart.00440.2018.

(17) Mihm, M. J.; Seifert, J. L.; Coyle, C. M.; Bauer, J. A.; Bauer, J. A. *Diabetes Related Cardiomyopathy Time Dependent Echocardiographic Evaluation in an Experimental Rat Model*; 2001; Vol. 69.

5.9. FOOTNOTES

This research was supported by CVie Therapeutics Limited (Taipei, Taiwan), WindTree Therapeutics (Warrington, USA) and University of Milano Bicocca. This work received no external funding.

5.10. CONFLICT of INTEREST

MF and PB are Windtree employees, PF and GB are Windtree consultants, S-CH is an employee of CVie Therapeutics Limited. All the other Authors declare no conflict of interest.

5.11. SUPPORTING INFORMATION

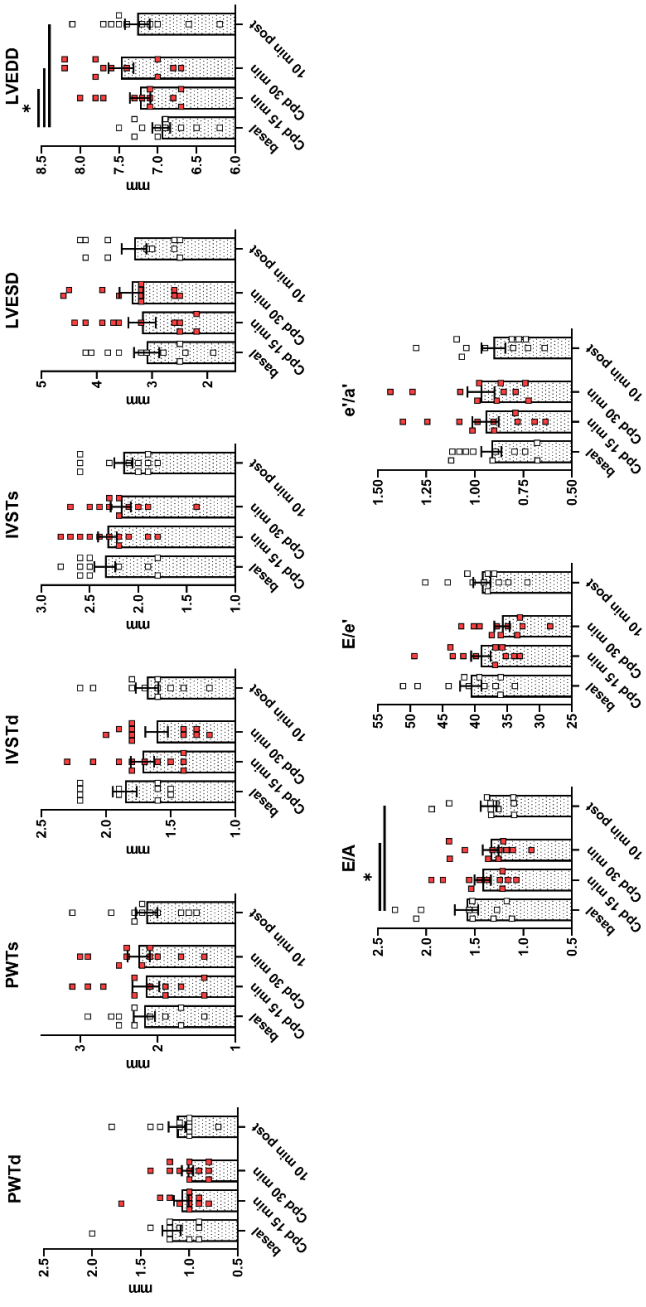

Figure S1. In vivo effects after i.v. infusion in STZ rats. Changes in echocardiographic parameters induced by acute i.v. infusion of compound **8** (0.2 mg/kg/min). See main Figure 5 for a complete analysis of echocardiographic parameters. Data are mean ± SEM. *p<0.05 (one-way RM ANOVA plus post-hoc Tukey's multiple comparison).

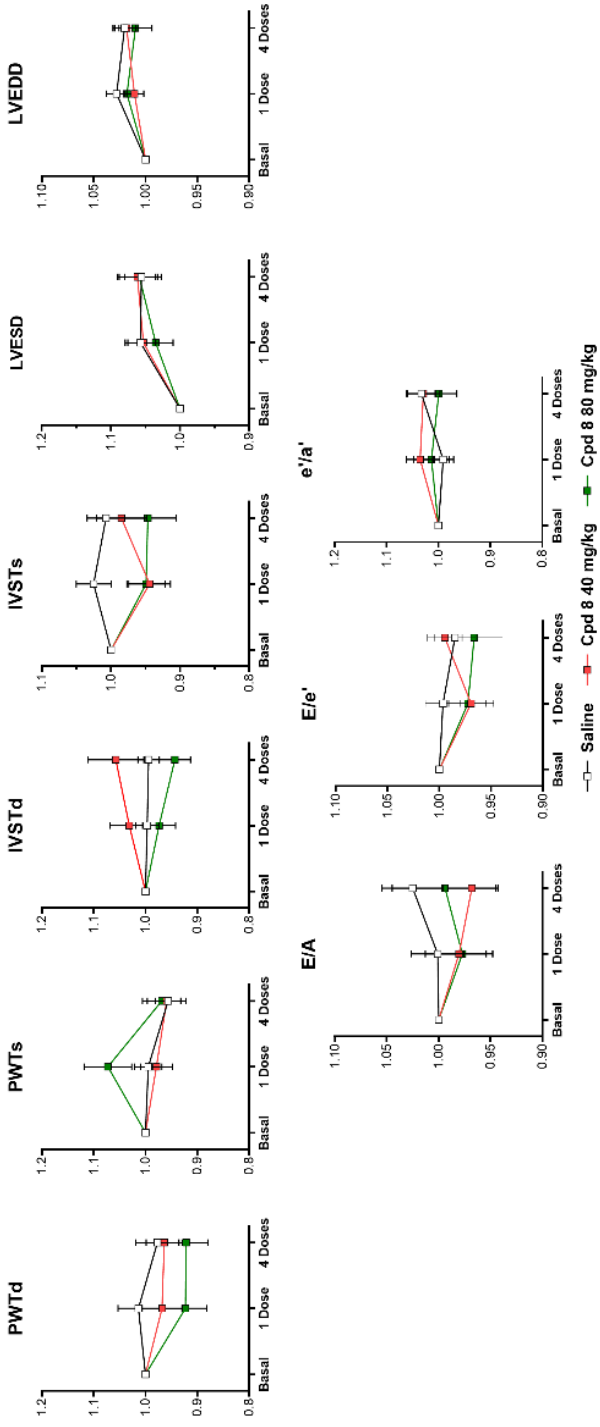

Figure S2. In vivo effects after oral treatment in STZ rats. Effect of compound **8** at 40 mg/kg and 80 mg/kg for 1 to 4 once-daily doses on echocardiographic parameters in STZ rats. Data are normalized on basal value measured at day 1. See main Figure 6 for a complete analysis of echocardiographic parameters. Data are mean ± SEM.

Table S1. Effect of compound 8 (10 µM) on a panel of molecular targets (Eurofins, Taiwan). Data are reported as Δ% effect (inhibition or activation).

Cat #	Assay name	Batch	Species	Cpd 8 effect (Δ%)
107480	ATPase, Ca^{2+}, skeletal muscle	438642	pig	-1
118040	CYP450, 19	438644	human	0
124010	HMG-CoA Reductase	438610	human	-4
140010	Monoamine Oxidase MAO-A	438645	human	1
140120	Monoamine Oxidase MAO-B	438647	human	-2
143000	Nitric Oxide Synthase, Endothelial (eNOS)	438568	bovine	2
107300	Peptidase, Angiotensin Converting Enzyme	438641	rabbit	7
164610	Peptidase, Renin	438648	human	7
152000	Phosphodiesterase PDE3	438611	human	-25
171601	Protein Tyrosine Kinase, ABL1	438612	human	13
176810	Protein Tyrosine Kinase, Src	438613	human	2
200510	Adenosine A1	438614	human	-1
200610	Adenosine A2A	438614	human	-1
203100	Adrenergic α1A	438615	rat	5
203200	Adrenergic α1B	438615	rat	6
203630	Adrenergic α2A	438616	human	-2
204010	Adrenergic β1	438652	human	2
204110	Adrenergic β2	438571	human	-6
204600	Aldosterone	438617	rat	-3
206000	Androgen (Testosterone)	438618	human	6
210030	Angiotensin AT1	438653	human	1
210120	Angiotensin AT2	438653	human	-6

214600	Calcium Channel L-type, Dihydropyridine	438620	rat	-20
219500	Dopamine D1	438660	human	13
219700	Dopamine D2s	439024	human	-4
219800	Dopamine D3	438660	human	0
226010	Estrogen ERα	438622	human	-3
226050	Estrogen ERβ	438622	hum	-6
226600	$GABA_A$, Flunitrazepam, Central	438624	rat	1
226500	$GABA_A$, Muscimol, Central	438623	rat	2
232030	Glucocorticoid	438626	human	-9
233000	Glutamate, NMDA, Phencyclidine	438627	rat	-7
239610	Histamine H1	438628	human	12
241000	Imidazoline I2, Central	438629	rat	1
243000	Insulin	438654	rat	4
252710	Muscarinic M2	438621	human	-20
252810	Muscarinic M3	438661	human	-6
253010	Muscarinic M5	438661	human	0
258730	Nicotinic Acetylcholine α3β4	438656	human	-3
260410	Opiate μ (OP3, MOP)	438616	human	11
264500	Phorbol Ester	438624	mouse	-7
265600	Potassium Channel (K_{ATP})	438632	hamster	-11
265900	Potassium Channel hERG	438633	human	0
299005	Progesterone PR-B	438638	human	1
270300	Ryanodine RyR3	438634	rat	-10
271010	Serotonin (5-Hydroxytryptamine) 5-HT1, non-selective	438668	rat	12
299007	Sigma σ2	438662	human	4

278110	Sigma σ1	438636	human	2
279510	Sodium Channel, Site 2	438637	rat	-5
204410	Transporter, Norepinephrine (NET)	438597	human	-4

Table S2. Echocardiographic and tissue Doppler parameters in STZ rats (raw data). Echo parameters were measured after 60 min from treatment start under ketamine/pentobarbital anesthesia. Basal: echo after saline at day 1; 1 dose: echo at day 5 (after saline, 40 mg/kg or 80 mg/kg compound **8**); 4 doses: echo at day 8 (after saline, 40 mg/kg or 80 mg/kg compound **8**). Data are mean ± SEM.

Echo parameters		STZ orally treated with saline or 40 mg/kg or 80 mg/kg compound 8								
		Saline			40 mg/kg			80 mg/kg		
		Basal	1 dose	4 doses	Basal	1 dose	4 doses	Basal	1 dose	4 doses
Morphometric parameters	IVSTd, mm	1,66±0,03	1,64±0,03	1,64±0,03	1,57±0,05	1,6±0,04	1,63±0,04	1,69±0,03	1,63±0,04	1,58±0,054
	PWTd, mm	1,05±0,03	1,03±0,03	1,00±0,03	1,03±0,03	0,99±0,04	0,98±0,03	1,11±0,03	1,01±0,04	1,02±0,05
	LVEDD, mm	7,98±0,09	8,18±0,09	8,12±0,09	8,30±0,11	8,38±0,09	8,42±0,11	8,38±0,12	8,52±0,10	8,43±0,15
	IVSTs, mm	2,14±0,05	2,17±0,04	2,14±0,05	2,19±0,08	2,04±0,06	2,13±0,08	2,27±0,07	2,14±0,07	2,11±0,07
	PWTs, mm	1,94±0,05	1,90±0,05	1,85±0,05	1,79±0,05	1,74±0,06	1,70±0,07	2,00±0,08	2,10±0,07	1,93±0,08
	LVESD, mm	4,17±0,09	4,36±0,08	4,36±0,10	4,44±0,10	4,65±0,09	4,67±0,10	4,48±0,11	4,60±0,09	4,67±0,15
Systolic function	FS, %	47,81±0,73	46,80±0,67	46,27±0,89	46,57±0,93	44,45±0,89	44,75±0,79	46,56±1,04	46,10±0,69	44,88±1,11
	s', mm/s	21,41±0,36	21,32±0,38	20,69±0,38	20,72±0,39	21,2±0,44	21,57±0,42	21,24±0,45	22,20±0,3	22,47±0,55
	EF, %	83,54±0,62	82,64±0,57	81,97±0,80	82,39±0,85	80,36±0,89	80,95±0,66	82,21±0,96	82,04±0,67	80,71±1,04
Diastolic function	E, mm/s	0,93±0,02	0,90±0,02	0,86±0,02	0,85±0,02	0,87±0,03	0,92±0,03	0,86±0,02	0,95±0,02	0,93±0,03
	A, mm/s	0,73±0,03	0,70±0,02	0,66±0,02	0,68±0,03	0,71±0,03	0,76±0,03	0,68±0,02	0,77±0,03	0,76±0,04
	E/A	1,31±0,03	1,30±0,02	1,32±0,03	1,28±0,04	1,24±0,03	1,23±0,03	1,29±0,02	1,26±0,03	1,27±0,06
	DT, ms	55,88±1,84	58,03±1,68	57,44±1,34	57,41±2,50	55,09±2,06	56,14±2,3	60,62±2,11	55,86±2,63	49,11±2,58
	DT/E, s^2/mm	62,29±3,04	65,83±2,26	68,48±2,21	69,03±3,84	65,0±3,58	63,12±3,66	70,52±2,26	60,21±3,52	54,60±3,70
	E/DT, mm/s^2	17,89±1,03	16,11±0,72	15,26±0,56	15,75±1,14	16,62±1,13	17,55±1,61	14,57±0,64	18,57±1,76	20,35±1,91
	e', mm/s	23,56±0,48	22,85±0,37	22,09±0,39	21,49±0,50	22,8±0,52	23,28±0,57	22,06±0,47	25,04±0,59	24,63±0,92
	a', mm/s	28,16±0,81	27,72±0,69	25,92±0,76	26,82±0,96	27,8±1,08	28,69±1,23	26,50±0,92	29,86±0,86	30,18±1,46
	e'/a'	0,85±0,02	0,84±0,02	0,87±0,02	0,81±0,02	0,84±0,03	0,83±0,03	0,84±0,02	0,85±0,02	0,83±0,02
	E/e'	39,74±0,72	39,47±0,85	38,96±0,95	39,75±0,88	38,39±0,98	39,51±0,79	39,23±0,66	38,09±0,82	37,99±1,07
Overall cardiac function	HR, bpm	241,3±8,7	226±7	228,5±6,8	221,4±9,4	232,4±8,8	240,6±9,2	229,1±9,8	248,1±10,1	262,3±11,6
	SV, ml	0,94±0,03	1,00±0,03	0,96±0,03	1,03±0,04	1,02±0,03	1,05±0,04	1,06±0,04	1,10±0,04	1,05±0,04
	CO	223±8,3	223±8,1	223±9,6	228±12,3	240,0±13,2	252,8±12,1	241±13	271±11	274±15
	n	40	40	39	22	22	21	21	21	18

Chapter 6

Additional Studies

1. Altomare C, Lodrini AM, Milano G, Biemmi V, Lazzarini E, Bolis S, Pernigoni N, Torre E, Arici M, Ferrandi M, Barile L, Rocchetti M, Vassalli G. **Structural and Electrophysiological Changes in a Model of Cardiotoxicity Induced by Anthracycline Combined With Trastuzumab**.
   Front Physiol. 2021 Apr 7;12:658790. doi: 10.3389/fphys.2021.658790.
   PMID: 33897465; PMCID: MC8058443.

2. Lazzarini E, Lodrini AM, Arici M, Bolis S, Vagni S, Panella S, Rendon-Angel A, Saibene M, Metallo A, Torre T, Vassalli G, Ameri P, Altomare C, Rocchetti M, Barile L. **Stress-induced premature senescence is associated with a prolonged QT interval and recapitulates features of cardiac aging.**
   Theranostics. 2022 Jul 4;12(11):5237-5257. doi: 10.7150/thno.70884.
   PMID: 35836799; PMCID: PMC9274748.

3. Palmioli A, Nicolini G, Tripodi F, Orsato A, Ceresa C, Donzelli E, Arici M, Coccetti P, Rocchetti M, La Ferla B, Airoldi C. **Targeting GRP receptor: Design, synthesis and preliminary biological characterization of new non-peptide antagonists of bombesin.**
   Bioorg Chem. 2021 Apr;109:104739. doi: 10.1016/j.bioorg.2021.104739.
   Epub 2021 Feb 17. PMID: 33626451.

4. Sforza A, Vigorelli V, Rurali E, Gambini E, Arici M, Rinaldi R, Fiorina P, Barbuti A, Raucci A, Rocchetti M, Pompilio G, Genovese S, Vinci MC. **Liraglutide Preserves CD34+ Stem Cells from Dysfunction Induced by High Glucose Exposure.**
   Cardiovasc Diabetol. 2022 Apr 9;21(1):51. doi: 10.1186/s12933-022-01486-9. PMID: 35397526; PMCID: PMC8994898.

5. Torre E, Arici M, Lodrini AM, Ferrandi M, Barassi P, Hsu SC, Chang GJ, Boz E, Sala E, Vagni S, Altomare C, Mostacciuolo G, Bussadori C, Ferrari P, Bianchi G, Rocchetti M. **SERCA2a stimulation by istaroxime improves intracellular Ca^{2+} handling and diastolic dysfunction in a model of diabetic cardiomyopathy**. *Cardiovasc Res.* 2022 Mar 16;118(4):1020-1032. doi: 10.1093/cvr/cvab123. PMID: 33792692; PMCID: PMC8930067.

6. Altomare C, Bartolucci C, Sala L, Balbi C, Burrello J, Pietrogiovanna N, Burrello A, Bolis S, Panella S, Arici M, Krause R, Rocchetti M, Severi S, Barile L. **A dynamic clamping approach using in silico I_{K1} current for discrimination of chamber-specific hiPSC-derived cardiomyocytes.**
   Under Revision COMMSBIO-22-1473

frontiers in Physiology

ORIGINAL RESEARCH
published: 07 April 2021
doi: 10.3389/fphys.2021.658790

Structural and Electrophysiological Changes in a Model of Cardiotoxicity Induced by Anthracycline Combined With Trastuzumab

Claudia Altomare[1], Alessandra Maria Lodrini[2,3], Giuseppina Milano[1,4], Vanessa Biemmi[3], Edoardo Lazzarini[3], Sara Bolis[1,3], Nicolò Pernigoni[1], Eleonora Torre[2], Martina Arici[2], Mara Ferrandi[5], Lucio Barile[3,6,7], Marcella Rocchetti[2†] and Giuseppe Vassalli[1,6,8*†]*

[1] *Laboratory of Cellular and Molecular Cardiology, Cardiocentro Ticino Foundation, Lugano, Switzerland,* [2] *Department of Biotechnology and Biosciences, Università degli Studi di Milano – Bicocca, Milan, Italy,* [3] *Laboratory for Cardiovascular Theranostics, Cardiocentro Ticino Foundation, Lugano, Switzerland,* [4] *Laboratory of Cardiovascular Research, Lausanne University Hospital, Lausanne, Switzerland,* [5] *Windtree Therapeutics Inc., Warrington, PA, United States,* [6] *Faculty of Biomedical Sciences, Università della Svizzera italiana, Lugano, Switzerland,* [7] *Institute of Life Science, Scuola Superiore Sant'Anna, Pisa, Italy,* [8] *Center for Molecular Cardiology, University of Zurich, Zurich, Switzerland*

OPEN ACCESS

Edited by:
Victor A. Maltsev, National Institute on Aging (NIH), United States

Reviewed by:
Dmitry Terentyev, Brown University, United States
Livia Hool, University of Western Australia, Australia

****Correspondence:***
Giuseppe Vassalli
giuseppe.vassalli@cardiocentro.org
Claudia Altomare
claudia.altomare@cardiocentro.org

† These authors have contributed equally to this work and share senior authorship

Specialty section:
This article was submitted to Cardiac Electrophysiology, a section of the journal Frontiers in Physiology

Received: *28 January 2021*
Accepted: *16 March 2021*
Published: *07 April 2021*

Citation:
Altomare C, Lodrini AM, Milano G, Biemmi V, Lazzarini E, Bolis S, Pernigoni N, Torre E, Arici M, Ferrandi M, Barile L, Rocchetti M and Vassalli G (2021) Structural and Electrophysiological Changes in a Model of Cardiotoxicity Induced by Anthracycline Combined With Trastuzumab. Front. Physiol. 12:658790. doi: 10.3389/fphys.2021.658790

Background: Combined treatment with anthracyclines (e.g., doxorubicin; Dox) and trastuzumab (Trz), a humanized anti-human epidermal growth factor receptor 2 (HER2; ErbB2) antibody, in patients with HER2-positive cancer is limited by cardiotoxicity, as manifested by contractile dysfunction and arrhythmia. The respective roles of the two agents in the cardiotoxicity of the combined therapy are incompletely understood.

Objective: To assess cardiac performance, T-tubule organization, electrophysiological changes and intracellular Ca^{2+} handling in cardiac myocytes (CMs) using an *in vivo* rat model of Dox/Trz-related cardiotoxicity.

Methods and Results: Adult rats received 6 doses of either Dox or Trz, or the two agents sequentially. Dox-mediated left ventricular (LV) dysfunction was aggravated by Trz administration. Dox treatment, but not Trz, induced T-tubule disarray. Moreover, Dox, but not Trz monotherapy, induced prolonged action potential duration (APD), increased incidence of delayed afterdepolarizations (DADs) and beat-to-beat variability of repolarization (BVR), and slower Ca^{2+} transient decay. Although APD, DADs, BVR and Ca^{2+} transient decay recovered over time after the cessation of Dox treatment, subsequent Trz administration exacerbated these abnormalities. Trz, but not Dox, reduced Ca^{2+} transient amplitude and SR Ca^{2+} content, although only Dox treatment was associated with SERCA downregulation. Finally, Dox treatment increased Ca^{2+} spark frequency, resting Ca^{2+} waves, sarcoplasmic reticulum (SR) Ca^{2+} leak, and long-lasting Ca^{2+} release events (so-called Ca^{2+} "embers"), partially reproduced by Trz treatment.

Conclusion: These results suggest that *in vivo* Dox but not Trz administration causes T-tubule disarray and pronounced changes in electrical activity of CMs. While adaptive changes may account for normal AP shape and reduced DADs late after Dox administration, subsequent Trz administration interferes with such adaptive changes.

Intracellular Ca^{2+} handling was differently affected by Dox and Trz treatment, leading to SR instability in both cases. These findings illustrate the specific roles of Dox and Trz, and their interactions in cardiotoxicity and arrhythmogenicity.

Keywords: doxorubicin, trastuzumab, cardiotoxicity, T-tubules, electrophysiology, calcium handling

INTRODUCTION

Anthracyclines (e.g., doxorubicin; Dox) are among the most efficient and frequently used chemotherapeutic agents, being prescribed to more than 40% of women with breast cancer (Giordano et al., 2012). Following anthracyclines and cyclophosphamide treatment, the human epidermal growth factor receptor 2 (HER2; ErbB2)/neu inhibitor trastuzumab (Trz), in combination with paclitaxel, improves outcomes in women with surgically removed HER2-positive breast cancer (Romond et al., 2005). However, both anthracyclines-related cardiotoxicity, including chronic congestive heart failure and Trz-related cardiotoxicity (Mor-Avi et al., 2011; Sawaya et al., 2012; Thavendiranathan et al., 2013), limit the clinical use of these agents. Because the simultaneous delivery of the two drugs results in enhanced cardiotoxicity, currently used clinical protocols involve their sequential administration. However, Dox/Trz combined therapy is still associated with a risk of left ventricular (LV) dysfunction in up to one-quarter of breast cancer patients (Ewer and Ewer, 2015; Advani et al., 2016; Ghigo et al., 2016), along with an increased risk of arrhythmia (Muraru et al., 2014; Santoro et al., 2017). In this regard, acute arrhythmogenicity of Dox administration has been reported (Steinberg et al., 1987). In a recent study from the Mayo Clinic, episodes of non-sustained ventricular tachycardia (VT), atrial fibrillation and sustained VT or ventricular fibrillation were seen respectively in 73.9, 56.6, and 30.4% of patients with anthracycline-related cardiomyopathy who had implantable cardioverter defibrillators (Mazur et al., 2017). Rare cases of malignant ventricular arrhythmias associated with Trz treatment have also been reported (Piotrowski et al., 2012). However, electrophysiological changes induced by Dox/Trz combined therapy are poorly characterized.

The underlying mechanisms of anthracyclines-induced cardiotoxicity are incompletely understood but increased oxidative stress, abnormal intracellular Ca^{2+} homeostasis and mitochondrial energetics, degradation of ultrastructural proteins, direct DNA damage via inhibition of topoisomerase 2β, and inhibition of pro-survival pathways such as neuregulin 1 (NRG) and ErbB (Dubey et al., 2016; Cappetta et al., 2017a) may be involved. In this regard, ErbB2 overexpression protected against Dox-related cardiotoxicity (Belmonte et al., 2015), whereas Trz-mediated inhibition of ErbB2 signaling interfered with the protective effects of ErbB2 and NRG, potentiating Dox-related toxicity in rat ventricular cardiac myocytes (CMs) (Sawyer et al., 2002).

The respective roles of Dox and Trz in cardiotoxicity induced by their combined administration remain to be fully elucidated. Here, we investigated these roles in T-tubule (TT) disarray, electrophysiological alterations and changes in intracellular Ca^{2+} handling using an *in vivo* rat model that mimics currently applied clinical regimens, specifically with respect to the sequential delivery of the two agents. Electrical measurements were performed at a single cell level. Dox treatment induced severe TT disarray, significant electrical abnormalities with a preserved Ca^{2+} handling. Although Trz monotherapy did not affect electrical activity and TT organization, administration of this agent following Dox pre-treatment exacerbated the abnormalities observed after the initial Dox treatment. These results suggest that CMs pre-stressed by Dox may become susceptible to Trz-mediated toxicity, especially electrical instability.

MATERIALS AND METHODS

Animal Models

The animal protocol was approved by the Committee on the Ethics of Animal Experiments of the Canton Ticino, Switzerland (TI32/18). The study was carried out in strict accordance with the recommendations in the Guide for the Care and Use of Laboratory Animals of the Directive 2010/63/EU. The study protocol is depicted schematically in **Figure 1A**. Sprague Dawley female rats (10–12 weeks old; from Charles River Laboratories) were subdivided into four groups. In the Dox group, rats were injected i.p. with 6 doses of Dox hydrochloride (Sigma-Aldrich), one dose each other day (from d1 to d11), for a cumulative dosage of 20 mg/kg, followed by six doses of phosphate-buffered saline (PBS; pH 7.4), one dose each other day (from d19 to d29), as described (Milano et al., 2014). In the Trz group, rats received 6 doses of PBS (from d1 to d11) followed by 6 doses of Trz (Roche), one dose each other day (from d19 to d29), for a cumulative dosage of 20 mg/kg. In the combined Dox/Trz group, rats received 6 doses of Dox hydrochloride (from d1 to d11) followed by 6 doses of Trz (from d19 to d29). Control (Ctrl) rats received 12 doses of PBS at the time points corresponding to drug administration in treated groups (from d1 to d11, and from d19 to d29). Notably, Trz monotherapy was started at d19 of the study protocol to match the time point of Trz administration in the combined therapy group. Trz-mediated changes in LV function at later points were measured in a separate series of experiments (**Supplementary Figure 1**).

Echocardiography

Heart function was monitored by echocardiography using a VEVO 2100 high-resolution imaging system (VisualSonics) at d0, d12, d19, d30, and d37, as described. Anesthesia was induced using 2% isoflurane mixed with 100% oxygen in an induction chamber. Rats were then placed on a heat pad in the supine position and kept at 37°C to minimize fluctuations of body temperature. Data acquisition was performed in

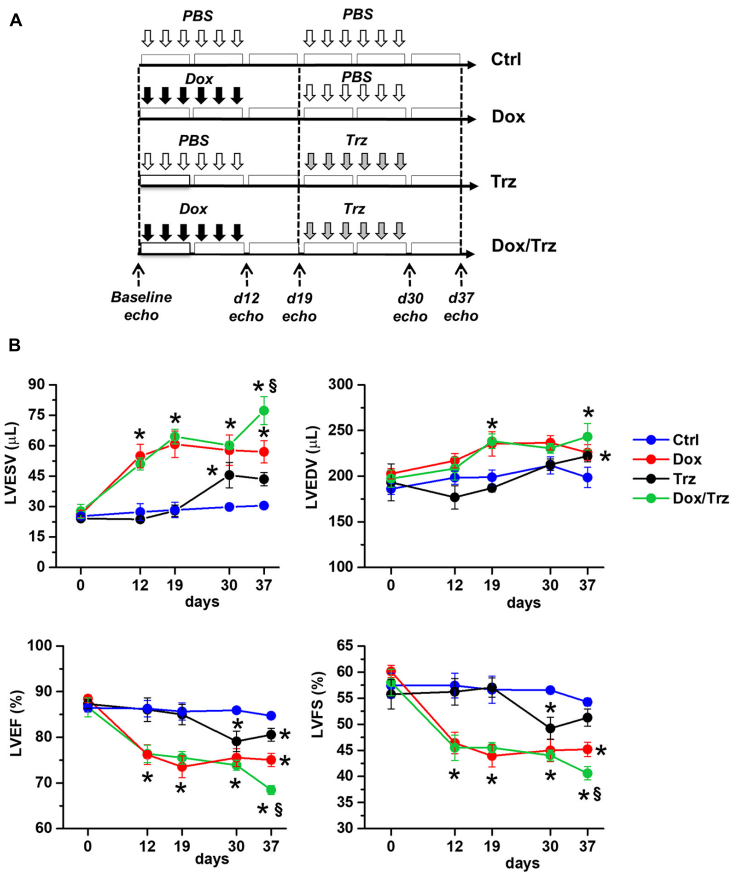

FIGURE 1 | Effects of Dox and Trz on LV function. **(A)** Schema depicting the experimental protocol. Dox and Trz were administered sequentially (from d1 to d11, and from d19 to d29, respectively). The timing of Trz administration was the same in the Dox/Trz and Trz groups. **(B)** Echocardiographic results for LV end-systolic volume (LVESV), LV end-diastolic volume (LVEDV), LV ejection fraction (LVEF), and LV fractional shortening (LVFS) in different groups at varying time points. Two-way ANOVA for multiple groups has been used. Data are mean ± SEM; $^{*}p < 0.05$ vs. Ctrl; $^{§}p < 0.05$ vs. Trz (Ctrl, $n = 5$; Dox, $n = 6$; Trz, $n = 8$; Dox/Trz, $n = 6$). Additional data generated at later time points after Trz administration are shown in **Supplementary Figure 1**.

rats lightly anesthetized with 0.5–1% isoflurane in order to maintain HR ≥ 350 bpm. Two-dimensional short-axis M-mode echocardiography was performed and LV end-systolic (LVESV) and end-diastolic (LVEDV) volumes, ejection fraction (LVEF) and fractional shortening (LVFS) were determined, as previously described (Barile et al., 2018).

Cardiac Myocyte Isolation

Isolated CMs from *in vivo* treated rats were analyzed at d19 (early Dox time point), and at d37 (late Dox time point, early Trz time point, combined Dox/Trz treatment). For CMs isolation, rats were anesthetized using a cocktail of ketamine (100 mg/kg) and xylazine (75 mg/kg) and humanly euthanized by cervical dislocation. Hearts were harvested and perfused *ex vivo* in a Langendorff mode, as previously described (Rocchetti et al., 2014). CMs were isolated separately from LV and right ventricular (RV) free walls. Rod-shaped, Ca^{2+} tolerant CMs were used for patch-clamp measurements and confocal microscopy less than 12 h after tissue dissociation.

TT Analysis

To investigate the impact of each treatment on the organization of TT, sarcolemmal membranes were marked by incubating CMs with 20 μM 3-di-ANEPPDHQ (Life Technologies, Carlsbad, CA, United States) and TT oriented transversely along z-lines were visualized (Rocchetti et al., 2014). 3-di-ANEPPDHQ was dissolved in the following solution (in mM): 40 KCl, 3 $MgCl_2$, 70 KOH, 20 KH_2PO_4, 0.5 EGTA, 50 L-Glutamic acid, 20 Taurine, 10 HEPES, 10 D-glucose (pH 7.4) for 10 min at RT (Sacconi et al., 2012). Cell contraction was prevented by adding

blebbistatin (17 μM; Sigma). CMs were washed with the same solution before confocal microscopy analysis. Images of loaded CMs were acquired by laser-scanning microscopy (images: 1,024 × 1,024 pxls, 78 μm × 78 μm) using a confocal microscope (Nikon C2 plus) with a 40× oil-immersion objective. Eight-bit gray-scaled images were analyzed by spatial Fast Fourier Transform analysis to quantify periodic components of pixel variance. To compensate for staining differences among cells, a raw power spectrum was generated with ImageJ (v.1.4) and normalized to its central peak. TT density was quantified by normalizing the area under the harmonic relative to the spatial frequency of 0.5 μm^{-1} (between 0.3 and 0.7 μm^{-1}) to the area of the entire spectrum (Rocchetti et al., 2014).

Electrical Activity

Action potentials (AP) were recorded by pacing CMs at 1 Hz in current-clamp conditions. AP duration measured at 90% and 50% of the repolarization phase (APD_{90} and APD_{50}, respectively), diastolic potential (E_{diast}) and maximal AP phase 0 depolarization velocity (dV/dt_{max}) were determined. Single cells were superfused with standard Tyrode's solution containing (in mM): 154 NaCl, 4 KCl, 2 $CaCl_2$, 1 $MgCl_2$, 5.5 D-glucose, and 5 HEPES-NaOH (pH 7.35). Experiments were carried out in whole-cell configuration; the pipette solution contained (in mM): 23 KCl, 110 KAsp, 0.4 $CaCl_2$, 3 $MgCl_2$, 5 HEPES-KOH, 1 EGTA-KOH, 0.4 NaGTP, 5 Na_2ATP, 5 Na_2PC (pH 7.3). Delayed afterdepolarizations (DADs) were defined as diastolic depolarizations with amplitude ≥1 mV. The percentage of cells exhibiting DADs was quantified. Beat-to-beat variability of repolarization (BVR) was expressed as the short-term variability (STV) of APD_{90} (i.e., the mean orthogonal deviation from the identity line (Heijman et al., 2013; Altomare et al., 2015), calculated as follows:

$$STV = \sum(|APD_{n+1} - APD_n|)/\left[n_{beats}\, x\, \sqrt{2}\right]$$

for 30 consecutive APs (n_{beats}) at steady-state level. STV data are shown using APD_n versus APD_{n+1} (Poincaré) plots.

Intracellular Ca^{2+} Handling Analyses

Cardiac myocytes were incubated in Tyrode's solution for 45 min with the membrane-permeant form of the dye, Fluo4-AM (10 μmol/L), and then washed for 30 min to allow for the de-esterification process. Fluo4 emission was collected through a 535 nm band pass filter, converted to voltage, low-pass filtered (100 Hz) and digitized at 2 kHz after further low-pass digital filtering (FFT, 50 Hz). Intact CMs were field-stimulated at 1, 2 and 4 Hz at 37°C during superfusion with standard Tyrode's solution. Ca^{2+} transient (CaT) amplitude at steady-state and the sarcoplasmic reticulum (SR) Ca^{2+} content (CaSR) estimated by an electronically timed 10 mmol/L caffeine pulse were evaluated at each cycle length. The diastolic fluorescence was used as reference (F_0) for signal normalization (F/F_0) after subtraction of background luminescence. For intergroup comparisons, Ca^{2+} handling parameters measured at each cycle length in a treated group were normalized to values measured in Ctrl. Rate-dependency of CaT decay kinetic was expressed as half-time decay ($T_{0.5}$). Na^+/Ca^{2+} exchanger (NCX) function was estimated by mono-exponential fit of caffeine-induced CaT. Frequency of resting Ca^{2+} waves was assessed under 1 min resting conditions before pacing. A Ca^{2+} wave was defined as a Ca^{2+} oscillation occurring at rest with an amplitude >3 SD over resting fluorescence levels (F_{rest}). Comparable results were obtained using amplitude cutoffs up to 5 F_{rest} SD. Frequency of spontaneous CaT occurring at rest (resting CaT) was assessed as an additional parameter of SR instability and Ca^{2+} overload.

Ca^{2+} Sparks

Spontaneous unitary Ca^{2+} release events (Ca^{2+} sparks) were recorded at RT in Fluo4-AM (10 μM)-loaded CMs under resting conditions. Tyrode bath solution contained 2 mM $CaCl_2$. Images were acquired at 60× magnification in line-scan mode (*xt*) at 0.5 kHz by confocal Nikon A1R microscope. Each cell was scanned along a longitudinal line and #10 *xt* frames (512 × 512 pxls) were acquired. Background fluorescence was measured. Confocal setting parameters were kept constant among experimental groups. Images were analyzed by SparkMaster plugin (Fiji) software (Picht et al., 2007). Automatic spark detection threshold was 3.8. Only in-focus Ca^{2+} sparks (amplitude > 0.3) were included in analyses. The following spark parameters were measured: frequency (event number/s/100 μm), amplitude ($\Delta F/F0$), full width at half-maximal amplitude (FWHM; μm), full duration at half-maximal amplitude (FDHM; ms), full width (FW; μm) and full duration (FD; ms), time-to-peak (TtP, ms), and decay time constant (τ; ms). Spark mass ($\Delta F/F_0{}^*\mu m^3$), an index of Ca^{2+} spark volume (Hollingworth et al., 2001), was calculated as spark amplitude*1.206* $FWHM^3$. Spark-mediated SR Ca^{2+} leak was calculated as the product of spark mass and frequency.

Western Blotting

Proteins from CMs extracts were separated by SDS-polyacrylamide gel electrophoresis (4–12% Bis-Tris Criterion BIO-RAD gels), blotted for 1 h, incubated with polyclonal anti-SERCA2 primary antibody (N-19; Santa Cruz Biotechnology) at 4°C overnight, followed by incubation with a specific secondary antibody labeled with fluorescent markers (Alexa Fluor or IRDye) for 1 h. Signal intensity was quantified by Odyssey Infrared Imaging System (LI-COR). SERCA2 protein levels were normalized to actin levels, as measured using polyclonal anti-actin Ab (Sigma). Data are shown as percent changes vs. Ctrl.

Statistics

Results are shown as mean ± SE. Unpaired Student's *t*-test was used to test for significant differences in two-group analyses. One-way and two-way ANOVA were used to test for significance among multiple groups, with *post hoc* comparison analyses using Bonferroni's multiple comparison test. Chi^2-test was used for comparison of categorical variables. The statistical test used in each analysis is mentioned in the respective figure legends. Statistical significance was defined as $p < 0.05$.

RESULTS

Trz Treatment Aggravates Dox-Induced LV Dysfunction

Echocardiographic results are shown in **Figure 1B**. Compared to Ctrl, Dox-treated animals showed increases in LVESV at d19, d30, and d37, and in LVEDV at d19 and d37, along with decreases in LVEF and LVFS at all time points. In the absence of Dox pre-treatment, Trz-treated animals showed an increase in LVESV at d30 (i.e., one day after administration of the last Trz dose), and decreases in LVEF and LVFS. Of note, in this study Trz was administered from d19 to d29 to mimic clinical protocols that involve the sequential administration of the two agents to attenuate toxicity. In a separate study, we evaluated the effects of Trz on LV function for up to 37 days (i.e., the same time frame used for Dox). The results are shown in **Supplementary Figure 1**. Trz induced a transient decrease in LVFS at d12 and a transient increase in LVESV at d19. Animals receiving Dox/Trz combined therapy showed increases in LVESV and LVEDV, along with decreases in LVEF and LVFS at d30 and d37. Significant differences between Trz monotherapy and the combined Dox/Trz treatment were observed for LVESV and LVEF at d37, consistent with additive toxic effects by the two agents. Body weight, tibia length, and heart weight did not significantly differ among groups (**Supplementary Table 1**).

Dox Treatment, but Not Trz, Induces TT Disarray

Representative confocal region of interest (ROI) of 3-di-ANEPPDHQ–treated CMs in the different groups are shown in **Figure 2A**. Disruption of TT architecture in the Dox and Dox/Trz groups, but not in the Trz group, can be appreciated visually. Representative spatial Fast Fourier Transform analyses of TT-power in LV and RV CMs are shown in **Figure 2B**. Quantitative analysis confirmed that Dox, but not Trz, treatment induces TT disarray (**Figure 2C**).

Trz Treatment Enhances Dox-Induced Action Potential Duration Prolongation and DADs

LV and RV CMs were analyzed separately because electrical measurements are influenced by ventricular loading conditions. AP recordings in isolated CMs from either ventricle showed increases in both APD_{50} and APD_{90} in the Dox group at d19, but not at d37 (**Figures 3A,B**), indicating negligible effects at later time points. In the absence of Dox pre-treatment, Trz did not affect APD, whereas it significantly prolonged it in Dox pre-treated rats (**Supplementary Table 2**). Depolarizing events during diastole and systole were recorded as DADs and early afterdepolarizations (EADs), respectively. The percentage of cells exhibiting DADs at 1 Hz-stimulation was increased in Dox-treated animals at d19, but not at d37. In analogy to its effect on APD, Trz increased the frequency of DADs selectively in rats pre-treated with Dox (**Figures 3C,D**). Similar changes were found for beat-to-beat variability of repolarization (BVR), which reflects APD_{90} time-variability (i.e., electrical instability) and represents a pro-arrhythmic parameter (Johnson et al., 2010). The dispersion of APD_{90} values around the identity line in Poincaré plots was increased in the Dox group at d19 and in the Dox/Trz group, but not in the Dox group at d37 neither in Trz monotherapy (**Figure 4A**). Quantitative STV data are shown in **Figure 4B**. The slope of the linear correlation between STV and APD_{90} was comparable in all groups (**Supplementary Figure 2**), indicating that increases in BVR were strictly dependent on APD prolongation. These results indicate pro-arrhythmic conditions in both the Dox and Dox/Trz groups.

Effects of Dox and Trz on Intracellular Ca^{2+} Handling

In principle, TT disarray and changes in APD, DADs, and BVR can impact intracellular Ca^{2+} handling. We analyzed evocated Ca^{2+} transients (CaT) at 1, 2 and 4 Hz in field-stimulation, as well as caffeine-induced CaT which reflects SR Ca^{2+} content (CaSR; **Supplementary Figure 3**). Trz treatment resulted in significant decreases in CaT amplitude and CaSR in LV CMs, and to a slightly lesser extent in RV CMs. Unaltered or even increased CaT amplitudes were observed in Dox and Dox/Trz CMs (**Figure 5A**). Studies of the CaT decay kinetics showed a smaller decay half-time ($T_{0.5}$) in Ctrl LV CMs compared to Ctrl RV CMs, in line with faster SR Ca^{2+} sequestration in LV CMs compared to RV CMs (Sathish et al., 2006). CaT decay in Dox d19 and to a lesser extent in Dox/Trz LV CMs was slower than in Ctrl (**Figure 5B**), suggesting Dox-induced changes in Ca^{2+} removal kinetics; a similar trend was observed in RV CMs. Accordingly, SERCA protein levels were significantly decreased in LV and RV CMs in both Dox and Dox/Trz CMs (**Figure 5C**). Trz alone did not significantly affect CaT decay kinetic and SERCA protein levels. To assess removal of intracellular Ca^{2+} through NCX, caffeine-induced CaT decay kinetic was evaluated. As shown in **Supplementary Figure 4**, rate-dependent NCX activity was observed in LV but not in RV Ctrl CMs, accordingly to previous data on chamber-specific NCX expression (Correia Pinto et al., 2006). However, rate-dependent NCX activity was absent in CMs from treated animals, particularly in the Trz group, suggesting faster NCX-dependent Ca^{2+} removal under these conditions, especially at slow pacing rates. The percentage of LV CMs exhibiting Ca^{2+} waves at resting was increased in all treated groups, with a similar increase in RV CMs from Dox d37 rats. The frequency of spontaneous CaT at resting in LV CMs was increased in both Dox and Dox/Trz groups (**Figure 5D**). These findings are in good agreement with our results on DAD frequency (**Figures 3C,D**).

To sum up, in spite of SERCA downregulation, global Ca^{2+} handling was preserved in field-stimulated CMs in Dox and Dox/Trz groups, while SR instability was observed mainly at resting. This suggests that compensative mechanisms (i.e., increased Ca^{2+} influx during prolonged APs) may take place in Dox and Dox/Trz groups. Trz alone did not affect electrical activity while directly affect intracellular Ca^{2+} handling.

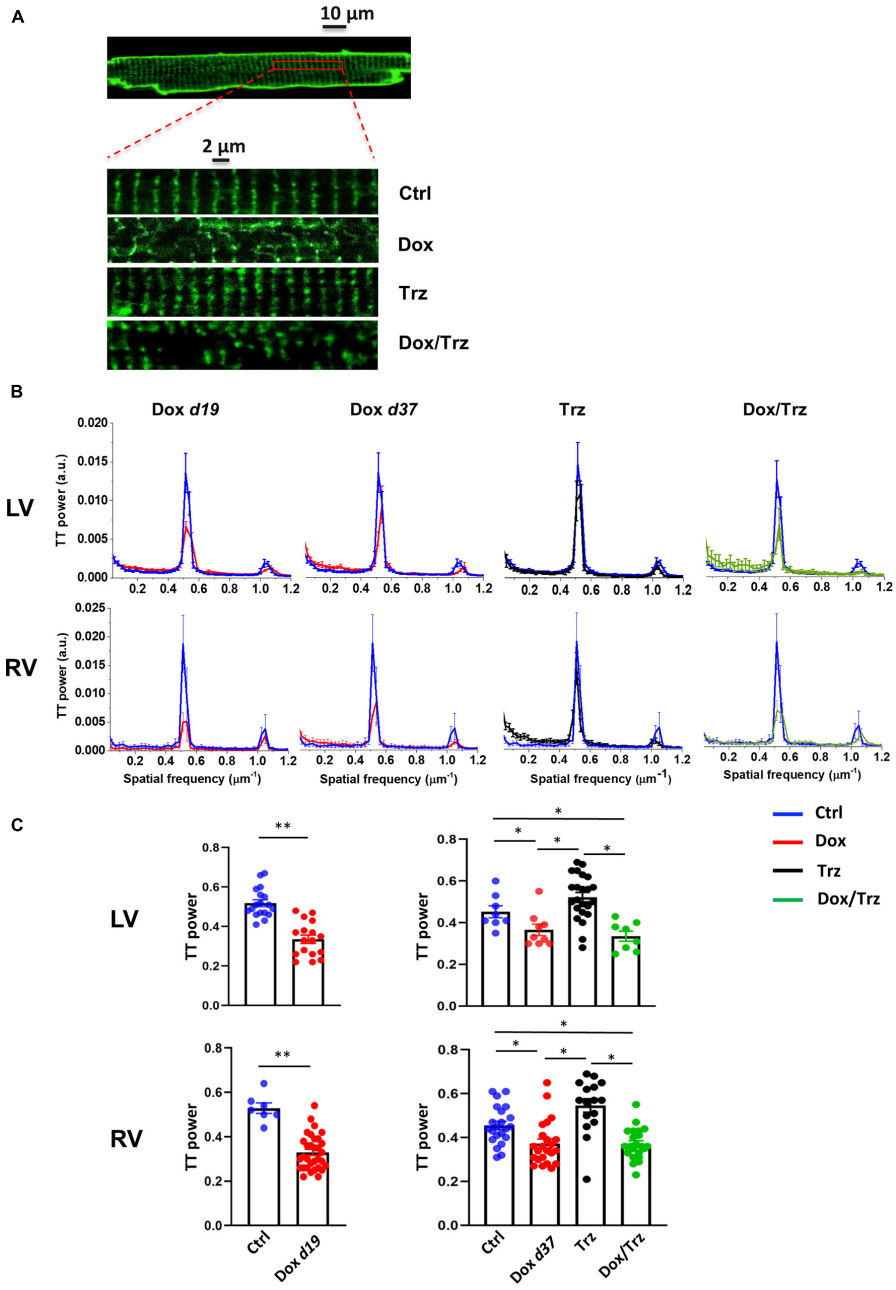

FIGURE 2 | Effects of Dox and Trz on TT organization. **(A)** Confocal regions of interest (ROI) of a 3-di-ANEPPDHQ–treated LV CM from a Ctrl rat, and representative higher-magnification LV CM confocal ROI in all groups. Disruption of TT organization in the Dox and Dox/Trz groups, but not in the Trz group, is apparent. **(B)** Mean TT power spectra in LV and RV CMs in Dox (red), Trz (black) and Dox/Trz groups (green) at the indicated time points, superimposed to those in the Ctrl group (blue). **(C)** Quantitative analysis of the TT periodic component in LV and RV CMs. Data on the Dox group is shown at d19 and at d37. Unpaired Student's *t*-test and one-way ANOVA were used to test for significant differences at d19 and d37, respectively. Bars are mean ± SEM ($n = \geq 15$ cells from ≥ 3 rats/group; $^{*}p < 0.05$; $^{**}p < 0.01$).

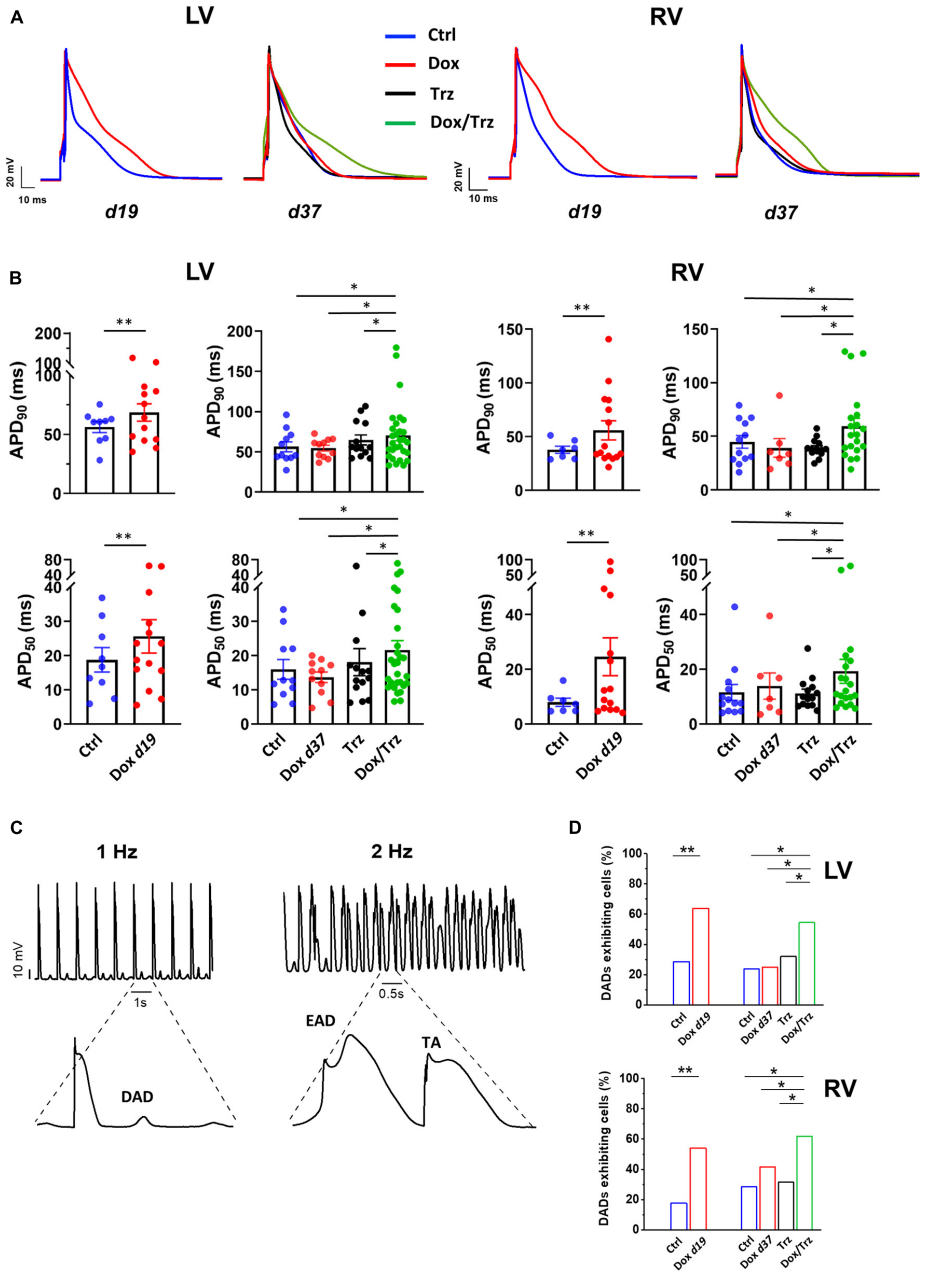

FIGURE 3 | Effects of Dox and Trz on electrical activity. **(A)** Electrical recordings of stimulated (1 Hz) APs in LV and RV CMs in all groups. Measurements were performed at d19 and at d37 (before and after Trz administration, respectively). **(B)** Quantitative analysis of APD_{50} and APD_{90} showing APD prolongation in the Dox group (at d19) and in the Dox/Trz group (at d37). **(C)** Electrical recordings showing DAD at 1 Hz-stimulation, as well as EAD and trigger activity (TA) at 2 Hz-stimulation in the Dox/Trz group. **(D)** Quantitative analysis of cells (%) exhibiting DADs at 1 Hz-stimulation. Data were acquired at d19 and at d37 (see above). Unpaired Student's *t*-test and one-way ANOVA was used to test for significant differences at d19 and d37, respectively, in panel **(B)**. Chi^2-test was used for comparison of categorical variables in panel **(D)**. Bars are mean ± SEM (n = ≥12 cells from ≥3 rats/group; $^*p < 0.05$; $^{**}p < 0.01$).

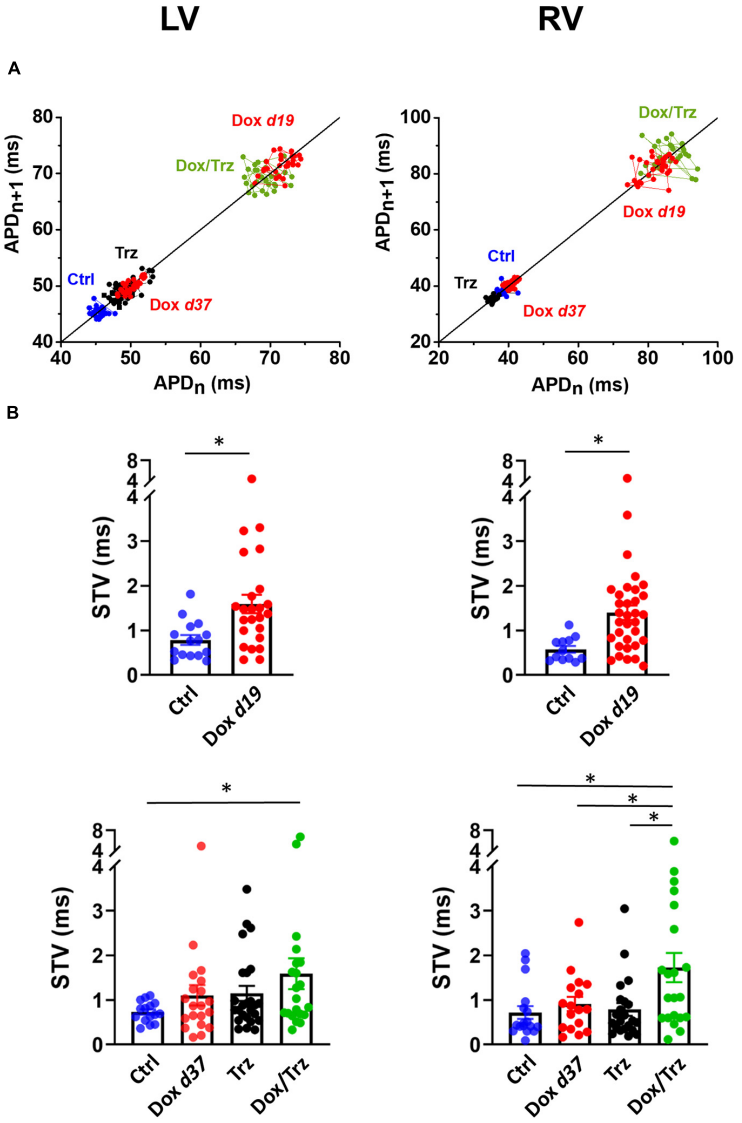

FIGURE 4 | Effects of Dox and Trz on beat-to-beat variability of repolarization (BVR). **(A)** Poincaré plots showing the dispersion of APD_{90} values around the identity line in LV and RV CMs in all groups. **(B)** Quantitative analysis of short-term variability (STV) of APD values. STV was increased in the Dox group at d19 and in the Dox/Trz group at d37. Data are shown at d19 and at d37. Unpaired Student's *t*-test and one-way ANOVA was used to test for significant differences at d19 and d37, respectively. Bars are mean ± SEM ($n = \geq 12$ from ≥ 3 rats/group; $^*p < 0.05$).

Dox, but Not Trz, Induces Ca^{2+} Sparks

The effects of Dox on Ca^{2+} waves and resting CaT led us to investigate SR stability by quantifying spontaneous SR Ca^{2+} release events visualized as Ca^{2+} sparks. Representative images of Ca^{2+} sparks in the different LV groups are shown in **Figure 6A**. A similar pattern was observed in RV CMs. Increased frequency of Ca^{2+} sparks was readily apparent in the Dox and Dox/Trz group, whereas Trz alone did not significantly impact this parameter. Spark mass was increased in LV CMs from Trz-treated animals, with similar trends in Dox-treated ones (Llach et al., 2019), but not in the Dox/Trz group. Dox, and to a lesser extent Trz, induced an increased spark-mediated SR

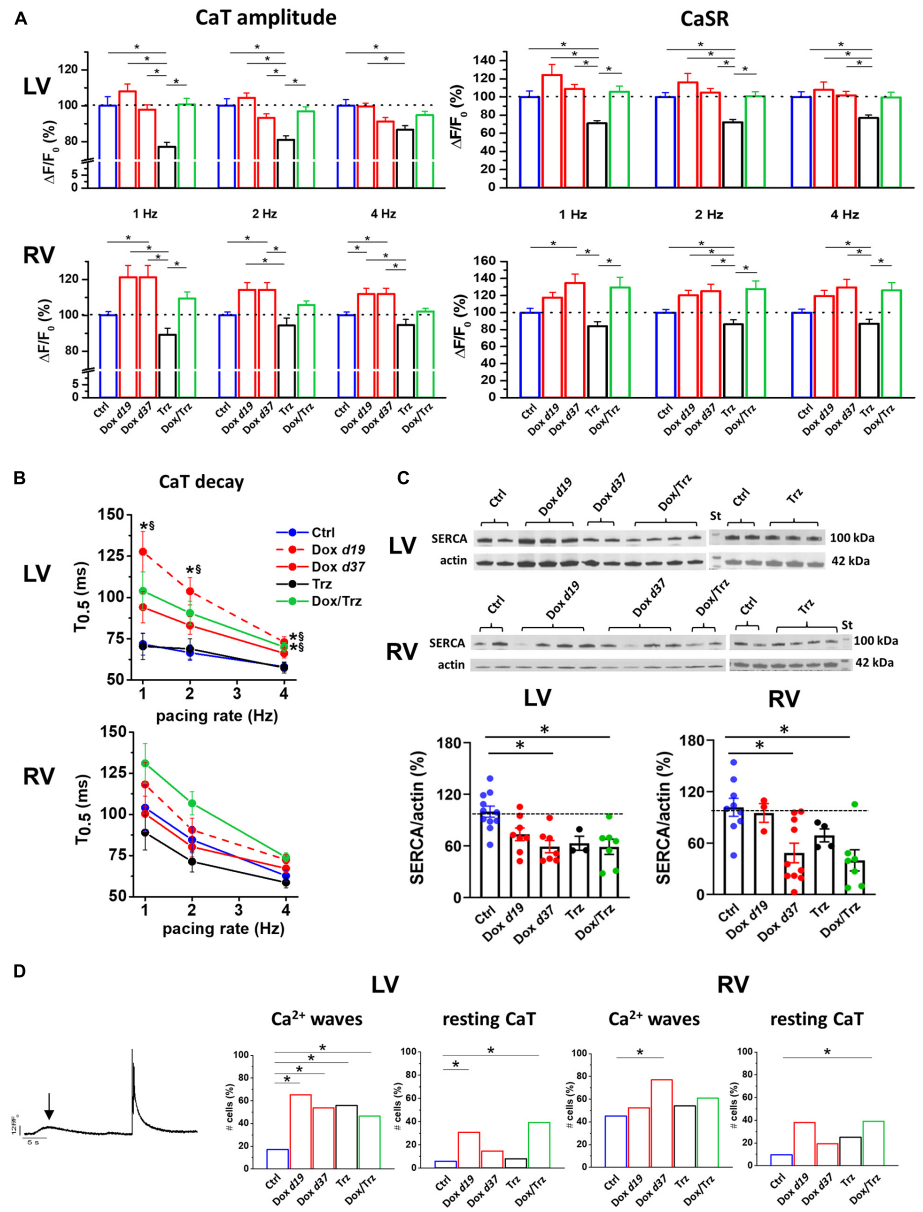

FIGURE 5 | Effects of Dox and Trz on intracellular Ca^{2+} handling. **(A)** Quantitative analysis of Ca^{2+} transient (CaT) amplitude and SR Ca^{2+} content (CaSR) estimated by a caffeine pulse at different pacing rates (1, 2, and 4 Hz) in field stimulated LV and RV CMs. Dox increased both CaT amplitude and CaSR in RV CMs but not in LV CMs, whereas Trz reduced them in both CMs. **(B)** Rate dependency of CaT decay kinetics (CaT decay half time, $T_{0.5}$) in both RV and LV CMs. LV CaT decay was slower in the Dox and Dox/Trz groups, but not in the Trz group, compared to Ctrl. $^{*}p < 0.05$ vs. Ctrl, $^{\S}p < 0.05$ vs. Trz. **(C)** Immunoblots showing SERCA protein levels (n = 2–4 rats/group; data in the Trz group and respective Ctrl were analyzed separately). Densitometric analysis. **(D)** Left panel: Example of Ca^{2+} wave (arrow) and spontaneous CaT occurring at resting. Quantitative analysis of cells (%) exhibiting spontaneous Ca^{2+} waves and resting CaT in both LV and RV CMs. Data on the Dox group are shown at d19 and at d37. One-way ANOVA was used to test for significant differences among multiple groups in panel **(A,C)**. Mixed effect model of two-way ANOVA was used in panel **(B)** for statistical evaluation of CaT decay of multiple groups vs. pacing rate. Chi^2-test was used for comparison of categorical variables in panel **(D)**. Bars are mean ± SEM ($n > 17$ cells/group; $^{*}p < 0.05$).

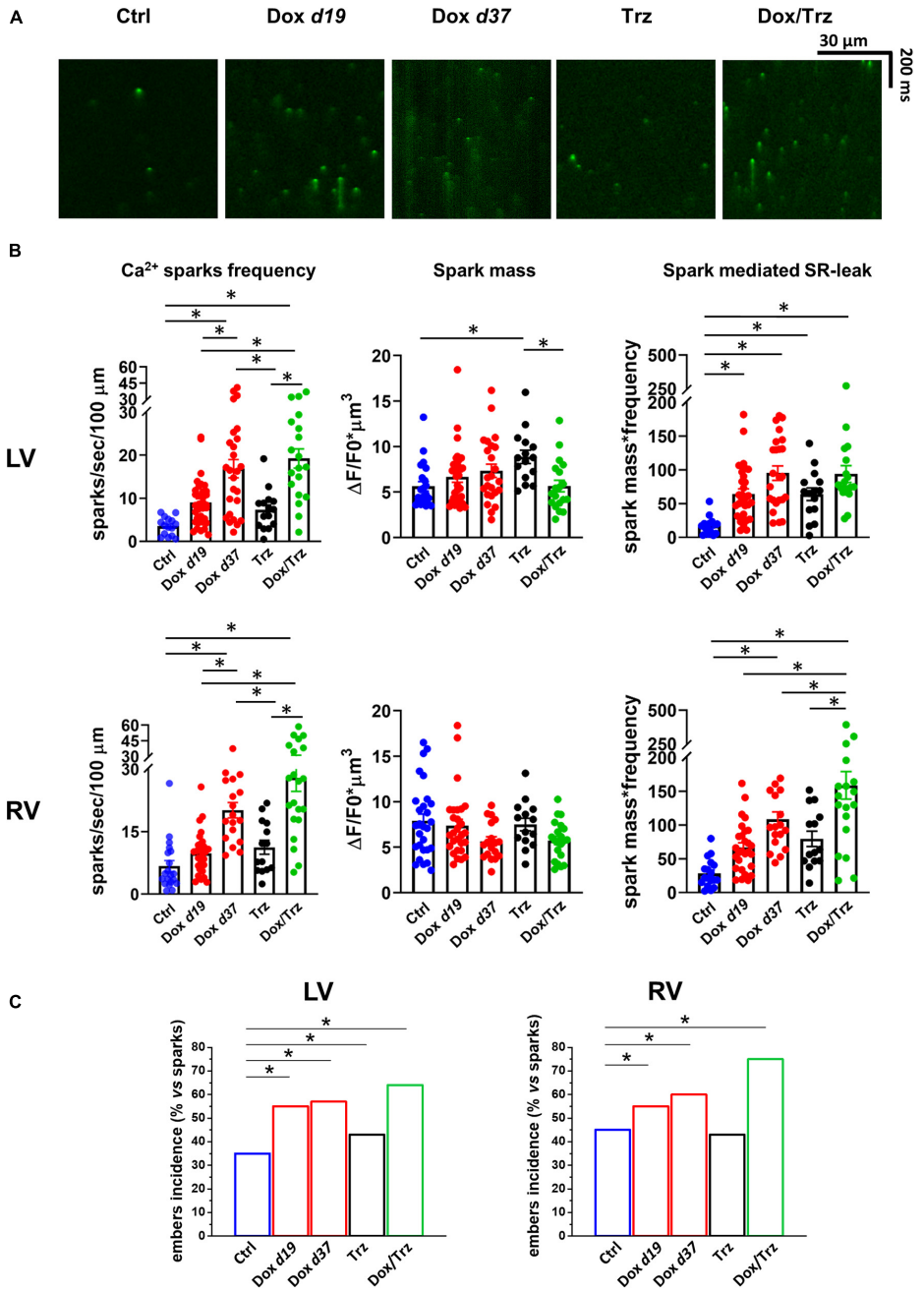

FIGURE 6 | Effects of Dox and Trz on Ca^{2+} sparks. **(A)** Confocal xt-images of FLuo4-AM loaded LV CMs in all groups. **(B)** Quantitative analyses of Ca^{2+} sparks frequency, spark mass, and sparks-mediated SR Ca^{2+} leak (n = 14–24 cells from 3 to 5 rats per group). **(C)** Quantitative analysis of Ca^{2+} "embers" (i.e., Ca^{2+} sparks with FDHM > 20 ms). One-way ANOVA was used to test for significant differences between multiple groups in panel **(B)**, and Chi^2-test was used for comparison of categorical variables in panel **(C)**. Bars are mean ± SEM (*$p < 0.05$).

Ca^{2+} leak quantified by the spark mass*spark frequency index (**Figure 6B**). Dox, and to a lesser extent Trz, increased the number of so-called Ca^{2+} "embers," defined as Ca^{2+} sparks with FDHM > 20 ms, the peak value of the FDHM distribution (Louch et al., 2013; **Figure 6C** and **Supplementary Figure 5**). Moreover, FDHM and the decay time constant (tau_{decay}), two markers of altered RyR openings, were increased in LV myocytes of Dox-treated animals (**Supplementary Table 3**), supporting Dox-induced SR instability.

DISCUSSION

Cardiotoxicity limits the application of anthracycline-based chemotherapy and anti-HER2 therapy combined regimens. Here, we investigated selected aspects of this condition including TT organization, electrophysiological changes, and intracellular Ca^{2+} handling using an *in vivo* rat model that mimics clinically used combined regimens. Dox treatment induced LV dysfunction lasting for more than 37 days. Trz monotherapy likewise impaired contractile function, albeit less severely than Dox, and for a shorter time period. The sequential administration of the two agents is reported to increase ROS levels and cardiac fibrosis, and to impair LV function to greater extents than did either agent alone, consistent with additive toxicity (Milano et al., 2014). Several mechanisms may be responsible for these findings. First, previous data in *Erb2*-mutated mice (Ozcelik et al., 2002), as well as in human induced pluripotent stem cell (hiPSC)-derived CMs suggested that pre-existing cellular stress induced by Dox may exacerbate Trz-related cardiotoxicity by inhibiting protective pathways including Erb2/4 (Tocchetti et al., 2012; Hsu et al., 2018; Kurokawa et al., 2018). It also has been shown that lapatinib, another HER2 inhibitor, potentiates Dox-related cardiotoxicity via iNOS signaling (Hsu et al., 2018).

Dox treatment, but not Trz, induced sustained TT disarray that accounted for, at least in part, LV dysfunction in this group. An association between TT disarray and heart failure of various etiologies including dilated cardiomyopathy has been reported previously in both human patients and animal models (Heinzel et al., 2008; Crocini et al., 2014; Crossman et al., 2015). Time course studies revealed that TT disruption preceded the development of heart failure, suggesting a causative role for the former in disease progression (Wei et al., 2010). In addition, altered TT structure has been shown to impair AP propagation (Crocini et al., 2017; Manfra et al., 2017). In the present study, Dox treatment resulted in APD prolongation in CMs. These results are in line with previous data on Dox-induced QT-interval prolongation in guinea pigs and reduced I_{Ks} component in stably transfected HEK293 cells (Ducroq et al., 2010). Another study reported increased I_{NaL} leading to changes in Ca^{2+} and Na^{+} handling in a model of Dox-induced LV diastolic dysfunction (Cappetta et al., 2017b). Moreover, Keung EC and coworkers (Keung et al., 1991) showed increased L-type Ca^{2+} current (I_{CaL}) density and fast decay time constant of I_{CaL} inactivation in LV CMs from Dox-treated rats, due to altered TT organization and excitation-contraction (EC)-coupling mechanisms. Thus, Dox-induced increases in I_{CaL} and I_{NaL} could potentially account for the huge drug-induced APD prolongation in treated rats. Alternatively, K^{+} channels downregulation cannot be ruled out.

In our model, Dox-mediated APD prolongation was associated with increases in the frequency of DADs as a reflection of spontaneously released Ca^{2+} being extruded by NCX, as well as in BVR as an index of arrhythmogenicity. Trz treatment did not significantly impact APD, DADs, and BVR in the absence of Dox pre-treatment. In pre-treated rats, however, it induced changes in these parameters similar to those induced by Dox itself. Of note, these Trz-induced changes in pre-treated rats were observed after a full recovery in these electrical parameters following Dox treatment, suggesting that the latter exacerbated subsequent Trz toxicity. Clinical evidence of arrhythmia in Trz-treated patients has been reported (Piotrowski et al., 2012), although infrequently.

The analysis of intracellular Ca^{2+} handling revealed a preserved global Ca^{2+} handling in paced CMs from both LV and RV. Indeed, in spite of the slower SR Ca^{2+} uptake, SERCA downregulation and SR instability, CaT amplitude and CaSR were preserved in Dox and Dox/Trz LV CMs and even increased in RV CMs. These counterintuitive findings may reflect compensative mechanisms taking place in intact field-stimulated cells. Under such conditions, evocated CaT are influenced by changes in electrical activity. Especially in Dox19 and Dox/Trz group, AP prolongation may result in an increase in Ca^{2+} influx, which may compensate changes dependent on SERCA downregulation. CaT decay was slower after Dox/Trz combined therapy, and to a lesser extent after Dox monotherapy, but not after Trz monotherapy.

Unlike Dox, Trz treatment resulted in a decrease in both the amplitude of CaT and CaSR in LV CMs. Trz treatment didn't affect APD, indicating that its effect on Ca^{2+} handling was independent on changes in electrical activity. While we did not analyze the precise mechanisms underlying Trz effects in this study, we hypothesize that the effect of this agent on Ca^{2+} handling might reflect metabolic changes, as previously described in hiPSC-derived CMs (Kitani et al., 2019). Moreover, sorafenib, a distinct tyrosine kinase inhibitor, is reported to reduce CaT amplitude and CaSR in human atrial CMs and in mouse ventricular CMs, inducing a reversible negative inotropic effect (Schneider et al., 2018).

During cell relaxation, released Ca^{2+} is recycled into the SR by the action of SERCA and extruded from the cell by NCX membrane protein, which plays a central role in the induction of Ca^{2+} waves. Dox treatment induced increases and in spontaneous Ca^{2+} waves and Ca^{2+} sparks which reflect SR instability. Previous studies have shown that low density of poorly organized TT favors de-synchronized and protracted Ca^{2+} release in failing CMs (Louch et al., 2004; Lyon et al., 2009),

which has been linked to the slowed and decreased amplitude of contraction typical of the failing heart (Bokenes et al., 2008; Mork et al., 2009). Ca^{2+} spark mass, which reflects the amount of Ca^{2+} released within an individual spark, was increased by Trz in LV CMs, with a trend in the same direction for Dox. Previous data in isolated CMs suggest that ROS-dependent activation of CAMKII pathway may result in CaMKII-dependent SR Ca^{2+} leak contributing to Dox-mediated impairment of Ca^{2+} handling (Sag et al., 2011). Accordingly, in the present study, Dox induced an increase in prolonged spontaneous Ca^{2+} events (so-called Ca^{2+} "embers") previously described in congestive heart failure (Louch et al., 2013), but not in chemotherapy-related cardiotoxicity. Ca^{2+} "embers" likely contributed to spontaneous SR Ca^{2+} leak, which was increased in all treated groups.

In conclusion, our data using an *in vivo* rat model of chemotherapy-related cardiotoxicity suggest that Dox treatment induces LV dysfunction, TT disarray, APD prolongation, electrical and SR instability, which are associated with a global preserved intracellular Ca^{2+} content regardless of SR abnormalities. Trz treatment alone induces a lesser degree of LV dysfunction, no TT disarray, no significant electrical changes. On the other hand, Trz affects intracellular Ca^{2+} handling, a finding that warrants further mechanistic characterization. However, Dox pre-treatment exacerbates Trz-related cardiotoxicity. While descriptive, our results highlight distinct yet interrelated cardiotoxic effects, including arrhythmogenicity, by the two agents when administered in combination.

DATA AVAILABILITY STATEMENT

The original contributions presented in the study are included in the article/**Supplementary Material**, further inquiries can be directed to the corresponding authors.

ETHICS STATEMENT

The animal study was reviewed and approved by the Ethics of Animal Experiments of the Canton Ticino, Switzerland (TI32/18).

AUTHOR CONTRIBUTIONS

CA, MR, LB, and GV contributed to the experimental design. GM and VB carried out the echocardiographic measurements and analysis. CA, SB, and NP performed patch-clamp experiments and data analysis. CA, NP, and LB performed confocal experiments. AL, ET, and MA carried out Ca^{2+} handling and sparks experiments with data analysis. EL evaluated the intracellular ROS. MF performed the western blot analysis. CA wrote the draft of the manuscript. LB critically revised the manuscript. GV and MR supervised the general project and wrote the manuscript. All authors read and approved the submitted version.

FUNDING

This work was supported by grants of the Swiss Cancer League, as well as of the Cecilia-Augusta Foundation and the San Salvatore Foundation (Lugano, Switzerland) to GV and Fondo Ricerca di Ateneo of University of Milano-Bicocca to MR.

SUPPLEMENTARY MATERIAL

The Supplementary Material for this article can be found online at: https://www.frontiersin.org/articles/10.3389/fphys.2021.658790/full#supplementary-material

REFERENCES

Advani, P. P., Ballman, K. V., Dockter, T. J., Colon-Otero, G., and Perez, E. A. (2016). Long-term cardiac safety analysis of NCCTG N9831 (Alliance) adjuvant Trastuzumab trial. *J. Clin. Oncol.* 34, 581–587. doi: 10.1200/JCO.2015.61.8413

Altomare, C., Bartolucci, C., Sala, L., Bernardi, J., Mostacciuolo, G., Rocchetti, M., et al. (2015). IKr impact on repolarization and its variability assessed by dynamic clamp. *Circ. Arrhythm. Electrophysiol.* 8, 1265–1275. doi: 10.1161/CIRCEP.114.002572

Barile, L., Cervio, E., Lionetti, V., Milano, G., Ciullo, A., Biemmi, V., et al. (2018). Cardioprotection by cardiac progenitor cell-secreted exosomes: role of pregnancy-associated plasma protein-A. *Cardiovasc. Res.* 114, 992–1005. doi: 10.1093/cvr/cvy055

Belmonte, F., Das, S., Sysa-Shah, P., Sivakumaran, V., Stanley, B., Guo, X., et al. (2015). ErbB2 overexpression upregulates antioxidant enzymes, reduces basal levels of reactive oxygen species, and protects against doxorubicin cardiotoxicity. *Am. J. Physiol. Heart Circ. Physiol.* 309, H1271–H1280. doi: 10.1152/ajpheart.00517.2014

Bokenes, J., Aronsen, J. M., Birkeland, J. A., Henriksen, U. L., Louch, W. E., Sjaastad, I., et al. (2008). Slow contractions characterize failing rat hearts. *Basic Res. Cardiol.* 103, 328–344. doi: 10.1007/s00395-008-0719-y

Cappetta, D., De Angelis, A., Sapio, L., Prezioso, L., Illiano, M., Quaini, F., et al. (2017a). Oxidative stress and cellular response to doxorubicin: a common factor in the complex milieu of Anthracycline Cardiotoxicity. *Oxid. Med. Cell. Longev.* 2017:1521020. doi: 10.1155/2017/1521020

Cappetta, D., Esposito, G., Coppini, R., Piegari, E., Russo, R., Ciuffreda, L. P., et al. (2017b). Effects of ranolazine in a model of doxorubicin-induced left ventricle diastolic dysfunction. *Br. J. Pharmacol.* 174, 3696–3712. doi: 10.1111/bph.13791

Correia Pinto, J., Henriques-Coelho, T., Roncon-Albuquerque, R. Jr., and Leite-Moreira, A. F. (2006). Differential right and left ventricular diastolic tolerance to acute afterload and NCX gene expression in Wistar rats. *Physiol. Res.* 55, 513–526.

Crocini, C., Coppini, R., Ferrantini, C., Yan, P., Loew, L. M., Tesi, C., et al. (2014). Defects in T-tubular electrical activity underlie local alterations of calcium release in heart failure. *Proc. Natl. Acad. Sci. U.S.A.* 111, 15196–15201. doi: 10.1073/pnas.1411557111

Crocini, C., Ferrantini, C., Coppini, R., and Sacconi, L. (2017). Electrical defects of the transverse-axial tubular system in cardiac diseases. *J. Physiol.* 595, 3815–3822. doi: 10.1113/JP273042

Crossman, D. J., Young, A. A., Ruygrok, P. N., Nason, G. P., Baddelely, D., Soeller, C., et al. (2015). T-tubule disease: relationship between t-tubule organization and regional contractile performance in human dilated cardiomyopathy. *J. Mol. Cell Cardiol.* 84, 170–178. doi: 10.1016/j.yjmcc.2015.04.022

Dubey, R., Lebensohn, A. M., Bahrami-Nejad, Z., Marceau, C., Champion, M., Gevaert, O., et al. (2016). Chromatin-remodeling complex SWI/SNF controls multidrug resistance by transcriptionally regulating the drug efflux pump ABCB1. *Cancer Res.* 76, 5810–5821. doi: 10.1158/0008-5472.CAN-16-0716

Ducroq, J., Moha ou Maati, H., Guilbot, S., Dilly, S., Laemmel, E., Pons-Himbert, C., et al. (2010). Dexrazoxane protects the heart from acute doxorubicin-induced QT prolongation: a key role for I(Ks). *Br. J. Pharmacol.* 159, 93–101. doi: 10.1111/j.1476-5381.2009.00371.x

Ewer, M. S., and Ewer, S. M. (2015). Cardiotoxicity of anticancer treatments. *Nat. Rev. Cardiol.* 12, 547–558. doi: 10.1038/nrcardio.2015.65

Ghigo, A., Li, M., and Hirsch, E. (2016). New signal transduction paradigms in anthracycline-induced cardiotoxicity. *Biochim. Biophys. Acta* 1863(7 Pt B), 1916–1925. doi: 10.1016/j.bbamcr.2016.01.021

Giordano, S. H., Lin, Y. L., Kuo, Y. F., Hortobagyi, G. N., and Goodwin, J. S. (2012). Decline in the use of anthracyclines for breast cancer. *J. Clin. Oncol.* 30, 2232–2239. doi: 10.1200/JCO.2011.40.1273

Heijman, J., Zaza, A., Johnson, D. M., Rudy, Y., Peeters, R. L., Volders, P. G., et al. (2013). Determinants of beat-to-beat variability of repolarization duration in the canine ventricular myocyte: a computational analysis. *PLoS Comput. Biol.* 9:e1003202. doi: 10.1371/journal.pcbi.1003202

Heinzel, F. R., Bito, V., Biesmans, L., Wu, M., Detre, E., von Wegner, F., et al. (2008). Remodeling of T-tubules and reduced synchrony of Ca2+ release in myocytes from chronically ischemic myocardium. *Circ. Res.* 102, 338–346. doi: 10.1161/CIRCRESAHA.107.160085

Hollingworth, S., Peet, J., Chandler, W. K., and Baylor, S. M. (2001). Calcium sparks in intact skeletal muscle fibers of the frog. *J. Gen. Physiol.* 118, 653–678. doi: 10.1085/jgp.118.6.653

Hsu, W. T., Huang, C. Y., Yen, C. Y. T., Cheng, A. L., and Hsieh, P. C. H. (2018). The HER2 inhibitor lapatinib potentiates doxorubicin-induced cardiotoxicity through iNOS signaling. *Theranostics* 8, 3176–3188. doi: 10.7150/thno.23207

Johnson, D. M., Heijman, J., Pollard, C. E., Valentin, J. P., Crijns, H. J., Abi-Gerges, N., et al. (2010). I(Ks) restricts excessive beat-to-beat variability of repolarization during beta-adrenergic receptor stimulation. *J. Mol. Cell Cardiol.* 48, 122–130. doi: 10.1016/j.yjmcc.2009.08.033

Keung, E. C., Toll, L., Ellis, M., and Jensen, R. A. (1991). L-type cardiac calcium channels in doxorubicin cardiomyopathy in rats morphological, biochemical, and functional correlations. *J. Clin. Invest.* 87, 2108–2113. doi: 10.1172/JCI115241

Kitani, T., Ong, S. G., Lam, C. K., Rhee, J. W., Zhang, J. Z., Oikonomopoulos, A., et al. (2019). Human-induced pluripotent stem cell model of trastuzumab-induced cardiac dysfunction in patients with breast cancer. *Circulation* 139, 2451–2465. doi: 10.1161/CIRCULATIONAHA.118.037357

Kurokawa, Y. K., Shang, M. R., Yin, R. T., and George, S. C. (2018). Modeling trastuzumab-related cardiotoxicity *in vitro* using human stem cell-derived cardiomyocytes. *Toxicol. Lett.* 285, 74–80. doi: 10.1016/j.toxlet.2018.01.001

Llach, A., Mazevet, M., Mateo, P., Villejouvert, O., Ridoux, A., Rucker-Martin, C., et al. (2019). Progression of excitation-contraction coupling defects in doxorubicin cardiotoxicity. *J. Mol. Cell Cardiol.* 126, 129–139. doi: 10.1016/j.yjmcc.2018.11.019

Louch, W. E., Bito, V., Heinzel, F. R., Macianskiene, R., Vanhaecke, J., Flameng, W., et al. (2004). Reduced synchrony of Ca2+ release with loss of T-tubules-a comparison to Ca2+ release in human failing cardiomyocytes. *Cardiovasc. Res.* 62, 63–73. doi: 10.1016/j.cardiores.2003.12.031

Louch, W. E., Hake, J., Mork, H. K., Hougen, K., Skrbic, B., Ursu, D., et al. (2013). Slow Ca(2)(+) sparks de-synchronize Ca(2)(+) release in failing cardiomyocytes: evidence for altered configuration of Ca(2)(+) release units? *J. Mol. Cell Cardiol.* 58, 41–52. doi: 10.1016/j.yjmcc.2013.01.014

Lyon, A. R., MacLeod, K. T., Zhang, Y., Garcia, E., Kanda, G. K., Lab, M. J., et al. (2009). Loss of T-tubules and other changes to surface topography in ventricular myocytes from failing human and rat heart. *Proc. Natl. Acad. Sci. U.S.A.* 106, 6854–6859. doi: 10.1073/pnas.0809777106

Manfra, O., Frisk, M., and Louch, W. E. (2017). Regulation of Cardiomyocyte T-tubular structure: opportunities for therapy. *Curr. Heart Fail. Rep.* 14, 167–178. doi: 10.1007/s11897-017-0329-9

Mazur, M., Wang, F., Hodge, D. O., Siontis, B. L., Beinborn, D. S., Villarraga, H. R., et al. (2017). Burden of cardiac arrhythmias in patients with anthracycline-related cardiomyopathy. *JACC Clin. Electrophysiol.* 3, 139–150. doi: 10.1016/j.jacep.2016.08.009

Milano, G., Raucci, A., Scopece, A., Daniele, R., Guerrini, U., Sironi, L., et al. (2014). Doxorubicin and trastuzumab regimen induces biventricular failure in mice. *J. Am. Soc. Echocardiogr.* 27, 568–579. doi: 10.1016/j.echo.2014.01.014

Mor-Avi, V., Lang, R. M., Badano, L. P., Belohlavek, M., Cardim, N. M., Derumeaux, G., et al. (2011). Current and evolving echocardiographic techniques for the quantitative evaluation of cardiac mechanics: ASE/EAE consensus statement on methodology and indications endorsed by the Japanese Society of Echocardiography. *J. Am. Soc. Echocardiogr.* 24, 277–313. doi: 10.1016/j.echo.2011.01.015

Mork, H. K., Sjaastad, I., Sejersted, O. M., and Louch, W. E. (2009). Slowing of cardiomyocyte Ca2+ release and contraction during heart failure progression in postinfarction mice. *Am. J. Physiol. Heart Circ. Physiol.* 296, H1069–H1079. doi: 10.1152/ajpheart.01009.2008

Muraru, D., Cucchini, U., Mihaila, S., Miglioranza, M. H., Aruta, P., Cavalli, G., et al. (2014). Left ventricular myocardial strain by three-dimensional speckle-tracking echocardiography in healthy subjects: reference values and analysis of their physiologic and technical determinants. *J. Am. Soc. Echocardiogr.* 27, 858–871.e1. doi: 10.1016/j.echo.2014.05.010

Ozcelik, C., Erdmann, B., Pilz, B., Wettschureck, N., Britsch, S., Hubner, N., et al. (2002). Conditional mutation of the ErbB2 (HER2) receptor in cardiomyocytes leads to dilated cardiomyopathy. *Proc. Natl. Acad. Sci. U.S.A.* 99, 8880–8885. doi: 10.1073/pnas.122249299

Picht, E., Zima, A. V., Blatter, L. A., and Bers, D. M. (2007). SparkMaster: automated calcium spark analysis with ImageJ. *Am. J. Physiol. Cell Physiol.* 293, C1073–C1081. doi: 10.1152/ajpcell.00586.2006

Piotrowski, G., Gawor, R., Slomka, R., Banasiak, M., Strzelecki, P., Gawor, Z., et al. (2012). [Cardioverter-defibrillator in the treatment of arrhythmia induced by trastuzumab used in the adjuvant setting in a patient with positive human epidermal growth factor receptor type-2 breast cancer]. *Kardiol. Pol.* 70, 756–757.

Rocchetti, M., Sala, L., Rizzetto, R., Staszewsky, L. I., Alemanni, M., Zambelli, V., et al. (2014). Ranolazine prevents INaL enhancement and blunts myocardial remodelling in a model of pulmonary hypertension. *Cardiovasc. Res.* 104, 37–48. doi: 10.1093/cvr/cvu188

Romond, E. H., Perez, E. A., Bryant, J., Suman, V. J., Geyer, C. E. Jr., Davidson, N. E., et al. (2005). Trastuzumab plus adjuvant chemotherapy for operable HER2-positive breast cancer. *N. Engl. J. Med.* 353, 1673–1684. doi: 10.1056/NEJMoa052122

Sacconi, L., Ferrantini, C., Lotti, J., Coppini, R., Yan, P., Loew, L. M., et al. (2012). Action potential propagation in transverse-axial tubular system is impaired in heart failure. *Proc. Natl. Acad. Sci. U.S.A.* 109, 5815–5819. doi: 10.1073/pnas.1120188109

Sag, C. M., Kohler, A. C., Anderson, M. E., Backs, J., and Maier, L. S. (2011). CaMKII-dependent SR Ca leak contributes to doxorubicin-induced impaired Ca handling in isolated cardiac myocytes. *J. Mol. Cell Cardiol.* 51, 749–759. doi: 10.1016/j.yjmcc.2011.07.016

Santoro, C., Arpino, G., Esposito, R., Lembo, M., Paciolla, I., Cardalesi, C., et al. (2017). 2D and 3D strain for detection of subclinical anthracycline cardiotoxicity in breast cancer patients: a balance with feasibility. *Eur. Heart J. Cardiovasc. Imaging* 18, 930–936. doi: 10.1093/ehjci/jex033

Sathish, V., Xu, A., Karmazyn, M., Sims, S. M., and Narayanan, N. (2006). Mechanistic basis of differences in Ca2+ -handling properties of sarcoplasmic reticulum in right and left ventricles of normal rat myocardium. *Am. J. Physiol. Heart Circ. Physiol.* 291, H88–H96. doi: 10.1152/ajpheart.01372.2005

Sawaya, H., Sebag, I. A., Plana, J. C., Januzzi, J. L., Ky, B., Tan, T. C., et al. (2012). Assessment of echocardiography and biomarkers for the extended prediction of cardiotoxicity in patients treated with anthracyclines, taxanes, and trastuzumab. *Circ. Cardiovasc. Imaging* 5, 596–603. doi: 10.1161/CIRCIMAGING.112.973321

Sawyer, D. B., Zuppinger, C., Miller, T. A., Eppenberger, H. M., and Suter, T. M. (2002). Modulation of anthracycline-induced myofibrillar disarray in rat ventricular myocytes by neuregulin-1beta and anti-erbB2: potential mechanism for trastuzumab-induced cardiotoxicity. *Circulation* 105, 1551–1554. doi: 10.1161/01.cir.0000013839.41224.1c

Schneider, C., Wallner, M., Kolesnik, E., Herbst, V., Machler, H., Pichler, M., et al. (2018). The anti-cancer multikinase inhibitor sorafenib impairs cardiac contractility by reducing phospholamban phosphorylation and sarcoplasmic calcium transients. *Sci. Rep.* 8:5295. doi: 10.1038/s41598-018-23630-w

Steinberg, J. S., Cohen, A. J., Wasserman, A. G., Cohen, P., and Ross, A. M. (1987). Acute arrhythmogenicity of doxorubicin administration. *Cancer* 60, 1213–1218. doi: 10.1002/1097-0142(19870915)60:6<1213::aid-cncr2820600609<3.0.co;2-v

Thavendiranathan, P., Grant, A. D., Negishi, T., Plana, J. C., Popovic, Z. B., and Marwick, T. H. (2013). Reproducibility of echocardiographic techniques for sequential assessment of left ventricular ejection fraction and volumes: application to patients undergoing cancer chemotherapy. *J. Am. Coll. Cardiol.* 61, 77–84. doi: 10.1016/j.jacc.2012.09.035

Tocchetti, C. G., Ragone, G., Coppola, C., Rea, D., Piscopo, G., Scala, S., et al. (2012). Detection, monitoring, and management of trastuzumab-induced left ventricular dysfunction: an actual challenge. *Eur. J. Heart Fail.* 14, 130–137. doi: 10.1093/eurjhf/hfr165

Wei, S., Guo, A., Chen, B., Kutschke, W., Xie, Y. P., Zimmerman, K., et al. (2010). T-tubule remodeling during transition from hypertrophy to heart failure. *Circ. Res.* 107, 520–531. doi: 10.1161/CIRCRESAHA.109.212324

Conflict of Interest: MF was employed by company Windtree Therapeutics Inc.

The remaining authors declare that the research was conducted in the absence of any commercial or financial relationships that could be construed as a potential conflict of interest.

IVYSPRING INTERNATIONAL PUBLISHER

Theranostics

2022; 12(11): 5237-5257. doi: 10.7150/thno.70884

Research Paper

Stress-induced premature senescence is associated with a prolonged QT interval and recapitulates features of cardiac aging

Edoardo Lazzarini[1#]; Alessandra Maria Lodrini[2,3#]; Martina Arici[2]; Sara Bolis[1,4]; Sara Vagni[2]; Stefano Panella[1]; Azucena Rendon-Angel[1,6]; Melissa Saibene[7]; Alessia Metallo[2]; Tiziano Torre[5]; Giuseppe Vassalli[4,6]; Pietro Ameri[8,9]; Claudia Altomare[1*]; Marcella Rocchetti[2✉*]; Lucio Barile[1,6,10✉*]

1. Cardiovascular Theranostics, Istituto Cardiocentro Ticino, Laboratories for Translational Research, Ente Ospedaliero Cantonale, Bellinzona, Switzerland.
2. Department of Biotechnology and Biosciences, Università degli Studi di Milano-Bicocca, Milano, Italy.
3. Department of Cell and Chemical Biology, Leiden University Medical Center, Leiden, Netherlands.
4. Cellular and Molecular Cardiology, Istituto Cardiocentro Ticino, Laboratories for Translational Research, Ente Ospedaliero Cantonale, Bellinzona, Switzerland.
5. Department of Cardiac Surgery Istituto Cardiocentro Ticino, Ente Ospedaliero Cantonale, Lugano, Switzerland.
6. Faculty of Biomedical Sciences, Università della Svizzera Italiana, Lugano, Switzerland.
7. Department of Earth and Environmental Sciences, Università degli Studi di Milano-Bicocca, Milano, Italy.
8. Cardiovascular Disease Unit, IRCCS Ospedale Policlinico, Genova, Italy.
9. Department of Internal Medicine, University of Genova, Genova, Italy.
10. Institute of Life Science, Scuola Superiore Sant'Anna, Pisa, Italy.

# The first two Authors contributed equally to the study, authors are listed in alphabetical order.

*These authors are senior authors

✉ Corresponding authors: Lucio Barile, PhD. Istituto Cardiocentro Ticino, Laboratories for Translational Research, EOC Via Chiesa 5, 6500 Bellinzona, Switzerland. +41 586667104 lucio.barile@eoc.ch; Marcella Rocchetti, PhD. University of Milano-Bicocca, Dept. of Biotechnology and Biosciences, P.za della Scienza 2, 20126 Milano, Italy. +39 0264483313 marcella.rocchetti@unimib.it.

Received: 2022.01.10; Accepted: 2022.06.11; Published: 2022.07.04

Abstract

Rationale: Aging in the heart is a gradual process, involving continuous changes in cardiovascular cells, including cardiomyocytes (CMs), namely cellular senescence. These changes finally lead to adverse organ remodeling and resulting in heart failure. This study exploits CMs from human induced pluripotent stem cells (iCMs) as a tool to model and characterize mechanisms involved in aging.

Methods and Results: Human somatic cells were reprogrammed into human induced pluripotent stem cells and subsequently differentiated in iCMs. A senescent-like phenotype (SenCMs) was induced by short exposure (3 hours) to doxorubicin (Dox) at the sub-lethal concentration of 0.2 μM. Dox treatment induced expression of cyclin-dependent kinase inhibitors p21 and p16, and increased positivity to senescence-associated beta-galactosidase when compared to untreated iCMs. SenCMs showed increased oxidative stress, alteration in mitochondrial morphology and depolarized mitochondrial membrane potential, which resulted in decreased ATP production. Functionally, when compared to iCMs, SenCMs showed, prolonged multicellular QTc and single cell APD, with increased APD variability and delayed afterdepolarizations (DADs) incidence, two well-known arrhythmogenic indexes. These effects were largely ascribable to augmented late sodium current (I_{NaL}) and reduced delayed rectifier potassium current (Ikr). Moreover sarcoplasmic reticulum (SR) Ca^{2+} content was reduced because of downregulated SERCA2 and increased RyR2-mediated Ca^{2+} leak. Electrical and intracellular Ca^{2+} alterations were mostly justified by increased CaMKII activity in SenCMs. Finally, SenCMs phenotype was furtherly confirmed by analyzing physiological aging in CMs isolated from old mice in comparison to young ones.

Conclusions: Overall, we showed that SenCMs recapitulate the phenotype of aged primary CMs in terms of senescence markers, electrical and Ca^{2+} handling properties and metabolic features. Thus,

Dox-induced SenCMs can be considered a novel *in vitro* platform to study aging mechanisms and to envision cardiac specific anti-aging approach in humans.

Key words: Induced pluripotent stem cell-derived cardiomyocytes; senescence; aging; heart

Introduction

It is estimated that by the year 2035, nearly one in four individuals will be 65 years of age or older, and this change in the world demographics will result in a large increase in the prevalence of age-related cardiovascular disabilities [1]. Primary drivers of tissue damage in aging, such as oxidative stress, DNA damage, mitochondrial dysfunction, and metabolic dysregulation, play a role in inducing cellular senescence. The latter represents a cellular response to such stimuli, thereby being defined as an "antagonistic" hallmark of aging [2]. The discovery that senescent cells aberrantly accumulate in aging tissues has substantiated the hypothesis that senescence itself can drive aging [2-4]. Indeed, accumulating senescent cells secrete pro-inflammatory molecules triggering the senescence-associated secretory phenotype (SASP), with deleterious effects on the tissue microenvironment leading to age-dependent functional impairment [5, 6]. Advanced age has been identified as one of the traditional risk factors for the development of aging-related cardiovascular disease (CVD) [7], increasing incidence of death, disability, and morbidity [8] with a high impact on the utilization of healthcare resources [9]. Cardiomyocytes (CMs) enduring exogenous cellular insult may develop a stress-induced premature senescence (SIPS) phenotype, which recapitulates many cellular and molecular features as those undergoing natural aging process [10, 11]. SIPS has emerged as possible link between long-term consequences of some pathological conditions such as sepsis [12] or anthracycline cardiotoxicity [13] and cardiovascular complications [14, 15]. Nowadays, cellular mechanisms behind such unexplained cardiac abnormalities regardless of age, are not completely understood.

It has been shown that aging alters the pattern of electrical activation in the heart of overtly healthy older subjects, resulting in prolonged myocardial repolarization [16], thus increasing the risk of malignant ventricular arrhythmias and sudden death [17]. Evidence in small animal model suggested that cardiac performance in aging heart is affected by electrical alterations at cellular level [18]. Increase in the late Na^+ current (I_{NaL}) in senescent mouse CMs prolongs the action potential (AP) and influences temporal kinetics of Ca^{2+} cycling [18]. However, whether this applies also for human cells is unknown. Therefore, studying the mechanisms underlying intracellular ionic balance in senescent human CMs, that constitute the vast majority of cardiac cell mass, [19] might pave the way for understanding the intricacies of age-related changes in the physiology of human heart [18, 20] and the increased susceptibility of the aged heart to injury [21].

Currently, the most used approaches to study cellular senescence are based on aging prone transgenic organisms [22]. However, the cardiovascular phenotype of transgenic animals only partially mimics the changes occurring in humans. CMs derived from human induced pluripotent stem cells (iCMs) offer an unprecedented platform that overcomes not only species-specific limitations but also the technical difficulties of accessing human primary CMs as well as their limited lifespan in culture. This study aimed to develop an *in vitro* tool for understanding human cardiac senescence's molecular basis that may affect age-related CVDs. Based on extensive published data showing that doxorubicin (Dox) can induce senescence in neonatal murine CMs [23], cardiac progenitor cells (CPCs) [24, 25] and vascular smooth muscle cells [26], we used sub-apoptotic doses of Dox as an inducer of SIPS in human iCMs. We explored phenotypic, functional and metabolic properties of human senescent CMs (SenCMs) in comparison to untreated controls (iCMs). Moreover, our model elucidated some basic aspects of SIPS, which is well known to impact diastolic and systolic function following stressors such as myocardial infarction and cancer therapy-induced cardiotoxicity [27, 28]. We compared our findings in human cells with electrophysiological changes occurring in CMs of naturally aged mice highlighting the importance of modelling senescence in human cells. By taking advantage of in-house biobank of human atrial appendage tissue specimens we correlated the expression of specific ion channels with age in heart tissue of small observational cohort of patients. Finally, some key markers of SIPS in CMs were validated by analyzing open-access heart-tissue transcriptomic data.

Methods and Materials

Data Source and Collection

Right cardiac atrial appendage tissue specimens were collected from patients who underwent surgical

repair of heart valves and had no concomitant coronary artery disease. Patients gave written informed consent. Protocols used in this study were approved by local Ethical Committee for Clinical Research (Comitato Etico Cantonale, Bellinzona, Switzerland; Rif. CE 2923), and study was performed in accordance with the Declaration of Helsinki. The observational study for the expression of KCNH2 gene was performed on atrial appendage tissue from 13 consecutive enrolled male patients between Feb 2018 and Nov 2019. Mean age was 68±8.7 (55-78). All experiments involving animals conformed to the guidelines for Animal Care endorsed by the University of Milano-Bicocca (project 29C09.N.5TB) and to the Directive 2010/63/EU of the European Parliament on the protection of animals used for scientific purpose.

Data for single nuclei transcriptomic analysis were obtained from Human Heart Atlas database (https://www.heartcellatlas.org/), a specific section of the Human Cell Atlas initiative (https://data.humancellatlas.org/) [29].

Generation and characterization of human Induced pluripotent stem (iPS) cells.

iPS cells were obtained by the reprogramming of adult stromal cardiac-specific mesenchymal cells (cMSC). Somatic cells were derived as cellular outgrowth from the explants using an *ex vivo* primary tissue culture technique, as previously described [30-32]. Briefly, atrial tissue was rinsed with phosphate buffer saline (PBS) and cut into small pieces that were placed into a 100-mm cell culture dish (Corning). To facilitate cell outgrowth, atrial tissue was treated with Trypsin/EDTA (SIGMA Life Science) for 2–3 min. Tissue pieces were plated on 0,02% gelatin and cultured in IMDM medium (Iscove's Modified Dulbecco's Medium) supplemented with 20% fetal bovine serum (FBS) and 1% penicillin/streptomycin (all from Life Technologies). The culture medium was changed twice a week. After 25–30 days of culture, cMSC were enzymatically detached using Trypsin/EDTA and transferred to a gelatin-coated 35-mm dish (Corning, 2.5×10^5 cells/dish). After additional 48 hours, cMSC were transduced with the integration-free Sendai virus cocktail hKOS:hc-Myc:hKlf4 at a MOI of 5:5:3 (CytoTune-iPS 2.0 Sendai Reprogramming Kit, Thermo Fisher Scientific), as per manufacturer's instructions. The virus was removed after 24 h and the medium was changed daily in the next 7 days. A week after transduction, medium was changed to StemFlex (Thermo Fisher Scientific). Individual colonies with embryonal stem cells (ESC)-like morphology typically appeared after 25-35 days and were transferred manually into 12-well plates coated with Matrigel (hESC Qualified Matrix, Corning) and expanded. Established human iPS cell lines were maintained in 33-mm Matrigel-coated plates (Falcon), passaged with TrypLe solution (TrypLE Express Enzyme 1x, Thermo Fisher Scientific) and cultured in StemFlex medium.

Directed differentiation of iPS cells into iCMs

Directed differentiation of human iPS cells into iCMs was performed via WNT signaling pathway modulation. Differentiation was initiated at 90% confluence in 12-well Matrigel-coated plates with a differentiation medium composed of RPMI 1640 supplemented with B-27 minus insulin (Thermo Fisher Scientific) with 4 μM CHIR99021 (Merck Millipore) for 48 h and subsequently 5 μM IWP4 (Merck Millipore) for 48 hours [33]. The medium was changed to a maintenance medium composed of RPMI 1640 with B-27 plus insulin (Thermo Fisher Scientific) at day 7. Metabolic selection of CMs was performed using a selection medium composed of RPMI 1640 without glucose (Thermo Fisher Scientific), 0.5 mg/ml human recombinant albumin, 0.2 mg/ml L-ascorbic acid 2-phosphate, and 4 mM lactate (Sigma-Aldrich) from days 10 to 17. Afterwards, iCMs were cultured in maintenance medium at least to day 30 for further maturation.

Mouse CMs isolation

Ventricular CMs were isolated from young (7 weeks) and old (18 months) mice (mCMs) as previously described with minor modifications [34]. Rod-shaped, Ca^{2+}-tolerant mCMs were used within 12 hours from dissociation.

Doxorubicin-induced CM senescence

Optimal conditions to obtain a Dox-induced senescent phenotype were empirically determined by dose response experiments, exposing iCMs to Dox at concentration ranging from 0.2 μM to 5 μM. Briefly, spontaneously beating iCMs were enzymatically dissociated (Multi Tissue Dissociation Kit 3, Miltenyi Biotec) and then plated in Synthemax II-SC Substrate (Corning)-coated wells (5×10^4 cells/cm^2). After 24-48 hours, part of the wells had medium replaced with Dox-containing maintenance medium to obtain senescent-like cardiomyocytes (SenCMs). After 3 hours from Dox administration, all cells were washed twice with PBS and placed back in fresh maintenance medium.

Senescence associated (SA)-β-gal staining

iCMs were stained for senescence-associated β-galactosidase (SA-β-gal) activity as previously described [35]. Briefly, cells were washed twice with PBS, fixed with 2% formaldehyde and 0.2%

glutaraldehyde in PBS, and washed twice in PBS. Cells were stained in X-gal staining solution (1 mg/ml X-gal, 40 mM/l citric acid/sodium phosphate, 5 mM/l potassium ferricyanide, 5 mmol/l potassium ferrocyanide, 150 mM/l NaCl, 2 mM/l $MgCl_2$, pH 6.0). After 6 hours, cells were washed twice with PBS. For a sensitive determination of the total cell number, cells were counterstained with 1 µg/ml Hoechst 33342 (Molecular Probes). Stained cells were examined using Lionheart FX Automated Microscope (BioTek Instruments Inc., Winooski, VT, USA) and analyzed with Gen 5.0 software (Biotek Instruments).

Cell viability

Cellular viability was assessed by double labeling of cells with 1 µM calcein-AM and 1.2 µM DRAQ7; total nuclei were stained with 1µg/ml Hoechst 33342 (Merck). Viable total and dead cells were counted using the Lionheart FX Automated Microscope (BioTek Instruments Inc., Winooski, VT, USA). Apoptosis was further evaluated by Terminal deoxynucleotidyl transferase dUTP nick end labeling (TUNEL) assay. CMs were treated and after 24hours fixed in 4%methanol-free Paraformaldehyde (PFA) for 15 min then processed with DEadEnd Fluorimetric TUNEL system (Promega) following manufacturer protocol. Total cells were stained with DAPI 1µg/ml (Merck).

Stained cells were acquired using Lionheart FX Automated Microscope (BioTek Instruments) and analyzed with Gen 5.0 software (BioTek Instruments).

Immunocytochemistry

After treatment, iCMs were washed twice with PBS and then fixed for 5 min at RT using a PFA-4%/sucrose-2% solution. Fixed cells were incubated for 10 min with glycine 0.1 M and then washed with PBS for 5 min. Cells were then permeabilized with 0.3% Triton X (Triton X detergent, Sigma-Aldrich) in PBS for 30 min, followed by a 5-min wash with PBS. Cells were then blocked with 2% bovine serum albumin (BSA) (Merck) for 1 h at RT. Subsequently, they were incubated with PBS containing 0.1% Tween, 1% BSA, and the primary antibody overnight at 4°C. To assess cardiac differentiation, cells were stained using antibodies against Sarcomeric Actin (α-S-Actin) (Abcam 9465), cardiac Troponin I (cTnI, AbCam 47003), cardiac Troponin T (cTnT) (13-11 Thermo Fisher Scientific), Myosin light chain 2 atrial (MLC2a, Synaptic System 311011), and Myosin light chain 2 ventricular (MLC2v, Proteintech 10906) to assess presence of DNA breaks, cells were stained using antibodies against γ-H2AX (9718 Cell Signaling), to assess cytotoxicity cells were stained with cleaved Caspase-3 Ab (Cell Signaling Technologies 9664). To assess senescence induction cells were stained with P16 and P21 (Proteintech 10355) Antibodies.

Nuclei were counterstained with DAPI 1µg/ml or Hoechst-33342 1µg/ml

EdU (1 µM) was supplied to the cells 24hours after Dox treatment. After further 48hours cells were fixed and EdU incorporation was revealed through Click-it kit (Thermo Fisher Scientific) following manufacturer protocol to measure active DNA synthesis. Stained cells were examined using Lionheart FX Automated Microscope (BioTek Instruments) and analyzed with Gen 5.0 software (BioTek Instruments).

Real time PCR analysis

iCMs were washed twice with PBS and RNA was extracted by adding 1 mL of TRI-Reagent (Sigma-Aldrich) as per manufacture instructions. For reverse transcription, 500ng of RNA was reverse-transcribed using GoScript Reverse Transcription System kit (Promega) as per manufacture instructions. To perform real-time PCR, the following mix was used: 2 µL DEPC water, 5 µL SsoAdvanced Universal SYBR Green Supermix 2x (BioRad), 2 µL of cDNA diluted 1:50 in DEPC water, 0.5 µL primers forward 10mM, and 0.5 µL primers reverse 10mM. Amplification and detection of specific products were performed in triplicate using a CFX Connect™ Real-Time PCR Detection System (Bio-Rad Labs). The threshold cycle (Ct) of each gene was automatically defined and normalized to the geometric mean control housekeeping genes GAPDH and RPL27(ΔCt value). To compare gene expression levels among different treatments, ΔΔCt values in treated CMs were calculated as the differences between the ΔCt value in these groups and the ΔCt value in untreated CMs following Livak method [36]. Primers sequences are shown in Supplementary Table 1.

Western blot analysis

Total proteins were extracted by lysing cells and then heated at 95 °C for 5 min (except for SERCA2 and PLN detection) with Laemmli SDS sample buffer 6× containing: 0.375 M Tris-HCl pH 6.8, 12% SDS, 60% glycerol, 0.6 M DTT, 20% (v/v) beta-mercaptoethanol, 70.2% (w/v) bromophenol blue (VWR International LCC). Proteins were separated on 4–20% Mini-PROTEAN® TGX™ Precast Gel (Bio-Rad) (or 4-12% Bis-Tris Criterion BIO-RAD gels for SERCA2 and PLN detection) and transferred onto a PVDF membrane with a semi-dry transfer system (Bio-Rad). The membranes were blocked for 1 h with Intercept (TBS) Blocking Buffer (Licor) or milk and incubated

with the primary Abs at 4 °C overnight (anti-p16, 1:1'000, Proteintech 10883; anti-p21, 1:1'000 eBiosciences 14-6715-81; anti-KCNH2, 1:200, Alomone APC-109; anti-P AMPK, 1:1'000, Cell Signaling 2537; anti-CAMKII, 1:2'000, Abcam 92332; anti-P CAMKII, 1:2'000, Abcam 171095; anti-SERCA2, 1:1000, N-19 Santa Cruz Biotechnology; anti-PLN 1:1000, 2D12, Abcam; anti-actin 1:5000, Merck). Membranes were then rinsed and incubated with appropriated fluorophore-conjugated secondary antibodies (Li-COR) at RT for 2 h. Subsequently, the membranes were rinsed then acquired and analyzed using the Odyssey CLx Detection System (LI-COR Biosciences).

ATP/AMP ratio

iCMs were lysed by incubation with an ultrapure water buffer containing perchloric acid 2.5% for 10 min, followed by a freeze (-20 °C)-thaw cycle. The lysate was then incubated with KH_2CO_3 for 5 min, resulting in precipitate and CO_2 formation. At the end of the reaction, the supernatant was centrifuged (18000 G for 15 min) to remove any precipitate. For ATP detection, the supernatant was incubated with an ultrapure water buffer containing (mM) 100 Tris, 50 glucose, 0.2 $NADP^+$, 5 $MgCl_2$, 0.27 Hexokinase/ Glucose-6-Phosphate dehydrogenase. The increase in absorbance over time indicated the reduction of NADPH and it correlated with the ATP levels in the supernatant. For AMP detection, the supernatant was incubated with an ultrapure water buffer containing (mM) 100 Tris, 0.15 NADH, 0.2 ATP, 1 Phospo-Enol-Pyruvate, 5 $MgCl_2$, 0.27 Pyruvate Kinase/Lactate dehydrogenase, 0.27 Adenilate Kinase. The decrease in absorbance over time indicated the oxidation of NADH and it correlated with the AMP levels in the supernatant.

Reactive oxygen species (ROS) detection assay

iCMs were seeded in 96-well/clear bottom plates for fluorescent measurements. Cells were washed twice with PBS and then incubated at 37°C in the dark with the ROS staining buffer containing dihydroethidium (5 μM) (Thermo Fisher Scientific). After 30 min of incubation, designated positive control wells were treated with TBHT (100 μM). After 30 additional minutes, iCMs were gently washed with PBS. The fluorescence was measured using the Infinite M-series fluorescent plate reader (TECAN) using an excitation wavelength of 480-520 nm and an emission wavelength of 580-600 nm. To exclude interference of Dox intrinsic fluorescence, fluorescent values were subtracted of baseline–cells treated with Dox but not incubated with dihydroethidium.

Mitochondrial Stress Test Assay

iCMs and SenCMs were harvested and seeded at 7.5×10^4 cells/well in a Seahorse XF miniplate (Agilent). After 48h the maintenance medium were chanced with Seahorse XF RMI supplemented 1 mM pyruvate, 2 mM glutamine, and 10 mM glucose with and cells were then analyzed for Oxygen Consumption Rate (OCR) with Seahorse XFp instruments, following Cell Mito Stress Test (Agilent) manufacturer protocol. OCR was measured every 7 minutes, inhibitors concentration was Oligomycin 1μM, FCCP 0.5μM, Rotenone/Antimycin A 1μM. Basal respiration was measured as OCR level previous to Oligomycin treatment minus minimum OCR level after Rotenone/Antimycin A injection. ATP linked production was measured as Maximum OCR level after Oligomycin injection minus Basal Respiration. Normalization for cell number was obtained with Sulforhodamine B assay. Briefly at the end of the experiment cells were fixed in 10% Trichloroacetic acid for 1h. Cells were washed and incubated with 0.057% SRB solution for 30 minutes. Cells were washed in acetic acid and air dried. Remaining cell-bind SRB were eluted in Tris pH10.5 and absorbance measured at 510nm wavelength in Tecan Infinite 2000 reader. Analysis was performed with Wave software (Agilent).

Transmission electron microscopy (TEM) acquisition and mitochondrial analysis

iCMs were cultured on glass coverslips, washed with PBS and incubated overnight in a fixative solution (2.5% glutaraldehyde in PBS) at 4°C. Cells were then washed with PBS and post-fixed in aqueous osmium tetroxide solution (1%). Next, cells were dehydrated in a series of ethanol solutions (50%-70%-90%-95%-100%), incubated in grated absolute ethanol/propylene oxide solutions and infiltrated in epoxy resin. Following removal of glass coverslip, ultrathin sections (50-70 nm) were stained with uranyl acetate and lead citrate solutions. Samples were observed with JEOL JEM-2100 Plus (JEOL, Italy) transmission electron microscope at 200 kV.

The images were analyzed using ImageJ to quantify the following morphological mitochondrial shape descriptors: mitochondria surface area, Feret's diameter (longest distance between any two points within a given mitochondrion), aspect ratio (major axis)/(minor axis) as the measure of the "length to width ratio".

JC10 assay

Designed positive control cells were incubated with maintenance medium containing CCCP (carbonyl cyanide m-chlorophenyl hydrazine) at 37 °C for 1 hour. All wells were then washed twice with PBS

and incubated with the JC10 dye (Abcam) as per manufacturer instructions. After 45 min of incubation, the fluorescence was measured using the Infinite M-series fluorescent plate reader (TECAN) using an excitation wavelength of 490 nm and emission wavelengths of 520-570 nm.

Microelectrode arrays (MEA)

Field potentials (extracellular recordings) of spontaneously beating clusters of iCMs were recorded at 37 °C using a 60MEA100/10iR-Ti-gr 64-electrode Microelectrode Arrays (MEA, Multi Channel Systems). iCMs were seeded in the Syntemax-coated MEA chambers (volume 500 µl) for at least 4 days before appropriate Dox treatment and recordings. The latter were performed in maintenance medium. For each time-point, measurements were taken 10 min after signals had reached a steady state value. The duration of field potentials (FPD), reflecting the electrical systole, was measured from the onset of the sharp positive deflection to the peak of the secondary slow deflection. This measurement is representative of the electrocardiographic QT interval. The rate corrected QT intervals (QTc) were calculated by applying Bazett's correction (QTc = QT/√RR). MEA data analysis was performed with MC Rack, MC Data Tool (both by Multi Channel Systems) and Clampfit 10.7 (Molecular Devices).

Patch clamp measurements

iCMs and mCMs were clamped in the whole-cell configuration. During measurements, myocytes were superfused at 2 ml/min with Tyrode's solution containing 154 mM NaCl, 4 mM KCl, 2 mM $CaCl_2$, 1 mM $MgCl_2$, 5 mM HEPES/NaOH, and 5.5 mM D-glucose, adjusted to pH 7.35. A thermostated manifold, allowing for fast (electronically timed) solution switch, was used for cell superfusion. All measurements were performed at 35 ± 0.5°C. The pipette solution contained (unless otherwise specified) 23 KCl, 110 KAsp, 0.4 $CaCl_2$, 3 $MgCl_2$, 5 HEPES-KOH, 1 EGTA-KOH, 0.4 NaGTP, 5 Na_2ATP, 5 Na_2PC, pH 7.3. Membrane capacitance (C_m) and series resistance were measured in every cell but left uncompensated. Signals were acquired with MultiClamp 700B amplifier (Molecular Devices) connected to Digidata 1550A (Molecular Devices) and analyzed via pClamp 10.6 (Molecular Devices).

Electrical activity

Action Potentials (APs) were acquired in iCMs and mCMs in I-clamp mode at specific stimulation rates. In particular, to overcome the low expression of the inward-rectifier potassium current (I_{K1}) in iCMs, *in silico* I_{K1} was injected through the Dynamic Clamp (DC) technique as previously reported [37]. Briefly, APs, recorded from iCMs, were acquired at a sampling rate of 10 kHz into the computer memory to drive the numerical I_{K1} according to the Nygren et al [38]. C_m and the estimated liquid junction potential (8 mV) were computed in generating numerical I_{K1}; I_{K1} maximal conductance was set to 0.7 nS/µF, as required to bring iCM diastolic potential (E_{diast}) near -80 mV, and kept constant for all experiments. The AP duration at 90% of the repolarization phase (APD_{90}) and the E_{diast} were quantified. Delayed afterdepolarizations (DADs) were defined as diastolic depolarizations with amplitude >1mV and their incidence was evaluated. Beat-to-beat variability of repolarization was expressed as the short-term variability (STV) of APD_{90} (i.e., the mean orthogonal deviation from the identity line [39, 40], calculated as follows: STV = ∑ ⟦(| ⟦APD⟧ _(n+1)- ⟦APD⟧ _n |/[n_(beats) x √2] ⟧) for 30 consecutive APs (nbeats) at steady-state level.

Membrane currents

The rapid delayed rectifier K^+ current (I_{Kr}) was recorded as E-4031 (3 µM)-sensitive current by applying depolarizing steps from -40 mV to +40 mV in the presence of I_{Ks} and I_{CaL} blockers HMR1556 (1 µM) and nifedipine (1 µM) respectively. I_{Kr} I/V relationships were obtained by measuring tail currents at -40 mV. The late component of the Na^+ current (I_{NaL}) was isolated as TTX (2 µM)-sensitive current (I_{TTX}) by applying slow voltage ramps (28 mV/s) from -100 mV to +40 mV. I_{TTX} at 0 mV was taken as representative of I_{NaL}, while peak I_{TTX} value, occurring at more negative potentials, was assumed to reflect the Na^+ 'window component' (I_{Naw}) as previously described [41]. Current densities (pA/pF) were obtained by normalizing current amplitudes to C_m.

Intracellular Ca^{2+} dynamics

Cytosolic Ca^{2+} and membrane current were simultaneously recorded in V-clamped iCMs loaded with Fluo4-AM (10 µM). iCMs were superfused at 2 ml/min with the Tyrode's solution added with 2 mM 4-aminopyridine and 1 mM $BaCl_2$ to block K^+ currents. In the pipette solution EGTA was decreased to 0.1 mM and 0.01 mM Fluo4-K^+ salt was added. Fluorescence at the holding potential (-80 mV) was used as reference (F_0) for signal normalization (F/F_0) after subtraction of background. Ca^{2+} transients (CaT) and I_{CaL} were recorded during 300 ms steps to 0 mV following 50 ms step to -35 mV to inactivate Na^+ channels. I_{CaL} was isolated as nifedipine (10 µM)-sensitive current; nmols of Ca^{2+} entering the cell (CaL influx) were quantified integrating I_{CaL} during the step. Sarcoplasmic reticulum (SR) Ca^{2+} content

(CaSR) was estimated by both integrating the Na^+/Ca^{2+} exchanger (NCX) current (I_{NCX}) and measuring CaT amplitude elicited by caffeine (10 mM) pulse, obtaining comparable results.

Ca^{2+} sparks

Spontaneous unitary Ca^{2+} release events (Ca^{2+} sparks) were recorded at room temperature in Fluo4-AM (10μM) loaded myocytes at resting condition. Tyrode bath solution contained 1 mM $CaCl_2$. Images were acquired at x60 magnification in line-scan mode (xt) at 0.5 kHz by confocal Nikon A1R microscope. Each cell was scanned along a longitudinal line and #10 xt frames (512 pxls x 512 pxls) were acquired. Non-cell fluorescence was acquired too to allow background fluorescence measurement. Confocal setting parameters were kept constant throughout experimental groups to permit group comparison analysis. Images were analysed by SparkMaster plugin (Fiji) software [42]. Automatic spark detection threshold (criteria) was imposed to 3.8. Only in focus Ca^{2+} sparks (amplitude > 0.3) were considered to quantify their characteristics. In particular, the following spark parameters were measured: frequency (N of events/s/100μm), amplitude (ΔF/F0), full width at half-maximal amplitude (FWHM, μm), full duration at half-maximal amplitude (FDHM, ms) and decay time constant (τ, ms). Spark mass (spark amplitude*1.206* $FWHM^3$) was also calculated as index of Ca^{2+} spark volume.

Expression analyses of significant genes associated with SenCM

Cardiomyocytes transcriptomic data from single-nucleus RNA sequencing (snRNA-seq) were obtained from public repository Human Cell Atlas https://www.humancellatlas.org). Data were referring to Litviňuková et al [29]. We used atrial- and ventricular-specific subset to derive expression profile of specific genes. Data were normalized and scaled through Serurat package for R environment (ver. 4.0.6). Analysis was performed with Seurat package and heatmaps of the expression levels of senescence-associated genes were visualized using ggplot2 package on R environment. Heatmaps display the average level of expression at single cell level (colour scale 0-1) and frequency of expression (dots dimensions) in the specific cell population. To minimize the influence of pathological unknown constituents, we did not included data from patients presenting Diabetes or Hypertension.

Statistical analysis

Data are expressed as the mean ± standard error of the mean (SEM) of independent experiments. The differences between groups were tested with unpaired t-test or one-way ANOVA analysis as appropriate. Post-hoc comparison between individual means was performed with Tukey test. A p-value < 0.05 was considered statistically significant. For the correlation between KCNH2 expression and age a linear regression analysis showing 95% confidence band of the best fit trend line, was performed.

Results

Sub-lethal concentrations of Dox induce cell cycle arrest in human iCMs accompanied by negligible cytotoxicity

We successfully generated three different cell lines of human iPS from cardiac somatic cells source that were reprogrammed to functional cardiomyocytes (iCMs) using a small molecules protocol as previously described [32, 43]. The differentiation protocol reached an efficiency of about 90% (Supplementary Figure S1A/B). Analysis of single cell electrical activity by patch-clamp recording showed that 70% of differentiated cells had ventricular-like phenotype with typical AP morphology with a sustained plateau phase. Those cells were distinct from iCMs with triangular AP shape mostly recapitulating atrial-like phenotype that account for about 30% of differentiated cells (Supplementary Figure S1C).

Premature senescence was induced in iCMs by a short-time exposure (3 hours) to sub-lethal concentrations of Dox followed by drug washout (Supplementary Figure S1D). Cells were analyzed for the expression of SA-β-gal and simultaneously monitored for cell death hallmarks. Cell death (DRAQ7 positive cells) remained negligible upon exposure to Dox at concentration ranging from 0.2 to 0.5 μM whereas at higher doses cell-viability decreased and apoptosis (number of iCMs positive for Tunel and expressing cleaved caspases-3) increased in a dose-dependent manner (Figure 1A-B; Supplementary Figure S2A). The concentration of 0.2 μM significantly increased the expression SA-β-gal by 25%. Such increase remains stable at 0.5 μM and decreased over higher doses in concomitance with augmented cell death (Figure 1C). Since chromogenic beta-gal substrate generates a far-red-shifted fluorescent signal [44], we further co-localized SA-β-gal expression with cardiac specific protein and visualized its intracellular distribution by immunofluorescence analysis (Figure 1D). The dose of 0.2 μM Dox was selected as critical for inducing onset of senescence phenotype with minimal cell death. Thus, iCMs treated with 0.2 μM Dox are hereinafter referred to as senescent-like CMs (SenCMs). Unless otherwise specified, measurements were performed 4 days after Dox treatment.

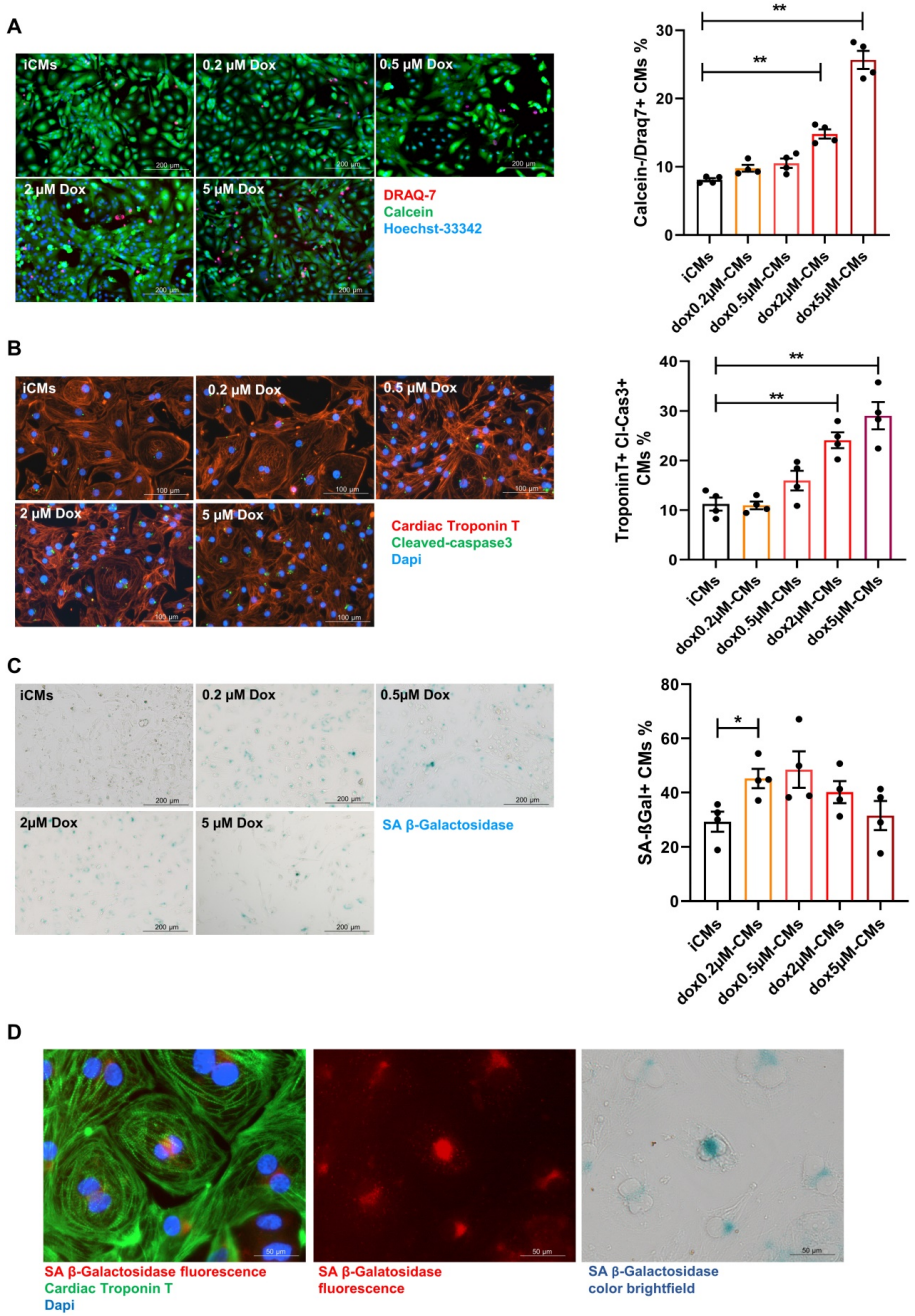

Figure 1: Response of human iPS-derived cardiomyocytes (iCMs) to doxorubicin (Dox). (A) Cell viability assay. Cells were labelled with Calcein-AM (green, viable cells) or DRAQ7 (red, dead cells) as described in methods section. Quantitative data (ratio of DRAQ7 positive and Calcein negative cells on the total number of cells) are shown in the bar graphs representing means of four independent experiments ± SEM. * P < 0.05, ** P < 0.01 *vs* iCMs. (B) Apoptosis was assessed by cleaved caspase-3 staining. Cleaved caspase was stained in green. Counterstaining of nuclei was performed with DAPI (blue). Cardiomyocytes were stained with cardiac Troponin T antibody (cTnT Red). Quantitative data (ratio of caspase positive cells on the total number of cTnT positive cells) are shown in the bar graphs representing means of four independent experiments ± SEM. * P < 0.05, ** P < 0.01 *vs* iCMs. (C) representative bright-field microscopy images of SA β-gal staining in iCMs and in Dox-treated cells at different concentration (0.2-5 µM). The percentages of SA β-gal-positive cells are shown in the bar graphs representing the mean of four independent experiments ± SEM. * P < 0.05 *vs* iCMs. (D) representative image showing SA β-gal-positive in SenCM upon excitation at 628 nm (far-red spectrum). Cardiac cTnT is shown in green, SA β-gal is shown in red correspondent bright-field microscopy images of SA β-gal staining is shown in the right panel.

SenCMs display senescence-associated pathways

We performed a series of experiments aiming to assess whether SenCMs exhibit typical features of SIPS [45, 46].

Neonatal and adult CMs possess residual capability of DNA synthesis leading to poly-nucleation accompanied by limited cell division. New DNA-synthesis is also a feature of differentiated iCM and incorporation thymidine analogue 5-ethynyl-2'-deoxyuridine (EdU) account for about 15% of total cells in basal condition (Figure 2A). The number of dividing cells (AURKB positive) in such condition is about 0.9% (Supplementary Figure S2B). Thus, suggesting that EdU incorporation very likely reflects CM karyokinesis (without cytokinesis) during binucleation process [47, 48]. In such context we assessed whether Dox affected the capability of iCMs to synthesize new DNA. We found that Dox treatment dramatically decreased the incorporation of EdU by 16-folds as compared to untreated iCMs (Figure 2A). In accordance with direct Dox-induced DNA damage, we observed a significant increase in the number of γ-H2AX-positive nuclear foci more than 5-fold in SenCMs compared to control iCMs (Figure 2B). Accumulation of γH2AX in SenCMs was associated with augmented expression of CDKN1A (hereafter $p21^{cip1/waf1}$) and CDKN2A (hereafter $p16^{INK4a}$) at both mRNA and protein levels (Figure 2C-E). Time-course RT-PCR experiments showed a pick of expression of $p21^{cip1/waf1}$ at 24hrs after exposure to Dox and a subsequent decreasing overtime from day one to seven. $p16^{INK4a}$ showed slight but constant increase overtime (Figure 2C). Most important $p21^{cip1/waf1}$ and $p16^{INK4a}$ were also increased at protein level as shown by WB and immunostaining at day 4 after exposure to Dox (Figure 2D-E). SenCMs were characterized by an increased expression of SASP-associated genes (Figure 3A). Transcripts of CXCL8, TGFB2, SERPINE1 and GDF15 genes were significantly overexpressed in SenCMs *vs* iCMs. Remarkably, levels of expression of CXCL8 and SERPINE-1 were 4-fold higher in SenCMs *vs* iCMs. Finally since aged hearts develop significant cardiac hypertrophy [49], we assessed whether this also occurs in our model. The expression of atrial natriuretic peptides (NPPA) and brain/B-type natriuretic peptides (NPPB), known to be predominantly expressed by the post-natal heart in response to stress-associated hypertrophy [50], were both significantly upregulated in SenCMs as compared to iCMs (Figure 3B). The occurred hypertrophy in Dox-treated CMs was also confirmed by measuring the cell membrane capacitance (C_m) which reflects cellular dimensions (Figure 3C) and was further confirmed by direct measurement of CM surface-area (Figure 3D).

Dox-induced senescence is associated with mitochondrial dysfunction and oxidative stress in SenCMs

Mitochondria are essential determinants of cellular homeostasis in CMs due to the high energetic demand of these cells. To gain insights into the Dox-induced mitochondrial impairment in SenCMs, we assessed key parameters of mitochondrial respiration by using a Seahorse extracellular flux analyzer.

SenCMs showed decreased OCR at basal respiration phases, with significant decrease in ATP-production linked respiration (Figure 4A-B). A loss in mitochondrial membrane potential in SenCMs was evaluated by JC-10 assay (Figure 4C). Membrane potential ($\Delta\Psi m$) of mitochondria became significantly depolarized in SenCMs (Figure 4C), suggesting a potential disruption in organelle integrity. At ultrastructural level SenCMs showed significant mitochondrial perturbations that were characterized by irregular architecture with loss of defined cristae and changes in general shape with significant decreased surface area, Feret's diameter and aspect ratio, indicating a longitudinal shortening (Figure 4D). Moreover, a clear mitochondrial intracellular clustering was observed in SenCMs, suggesting an altered mitochondrial relocation. Mitochondrial dysfunction occurring during senescence process is generally associated with increased production of ROS [51]. Indeed, SenCMs had significantly increased in ROS levels as compared to iCMs (Figure 4E) and generalized decline of metabolic capacity, as shown by the significant decrease in the cellular ATP/AMP ratio (Figure 4F). The imbalance in the energetic fluxes in SenCMs was associated with increased activity of the 5'-AMP-activated protein kinase (AMPK) as highlighted by the positive ratio between the Thr172 phosphorylated AMPK (pAMPK) and the total protein level (Figure 4G). However, the increased activity was not accompanied by concomitant increase in mRNA expression level (Figure 4H). This suggests that cytosolic AMP levels could intrinsically increase AMPK activity by inducing its allosteric activation [52].

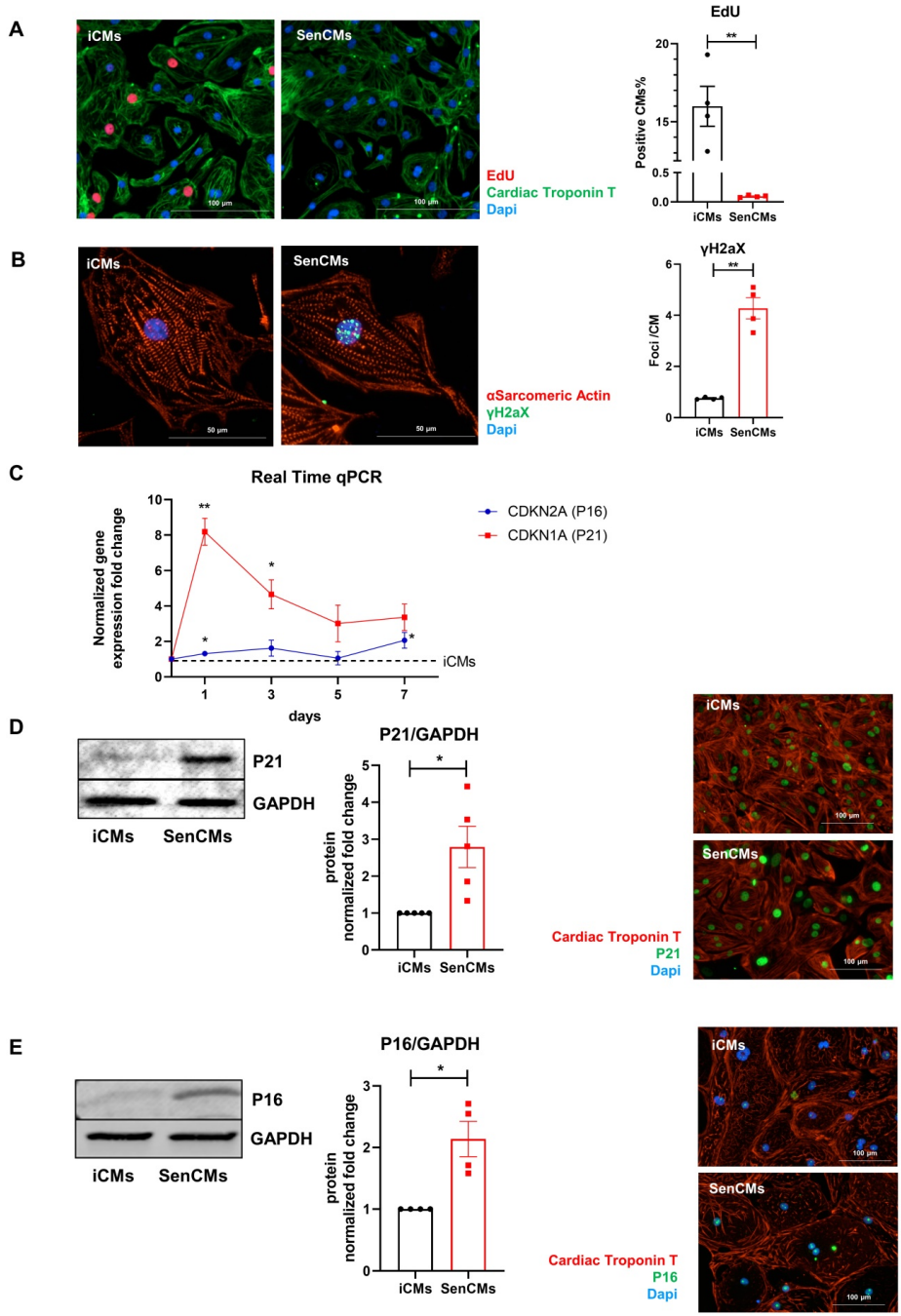

Figure 2: Expression of senescence markers in SenCMs. (A) EdU incorporation in iCM and SenCM. Cells were stained for cTnT followed by counterstaining with DAPI. Quantitative analysis of double-positive cells for EdU and cTnT is shown in the bar graphs representing four independent experiments ± SEM. * P < 0.05, ** P < 0.01 *vs* iCMs. (B) Representative images of immunofluorescence analysis of iCMs and SenCM using anti-γ-H2AX (green) and anti-sarcomeric α-actinin (red) antibodies. Cells nuclei were counterstained with DAPI. The number of γ-H2AX-positive foci per cell was calculated. Data are means of four independent experiments ± SEM. ** P < 0.01 *vs* iCMs. (C) Time-course for CDKN2A and CDKN1A mRNA relative expression in SenCMs versus iCMs (black dotted line). Data are means of four independent experiments ± SEM; * P < 0.05. (D) Western blotting analysis of p16 and p21 proteins in iCMs and SenCMs. Quantitative data are densitometry analysis of four independent experiments ± SEM; * P < 0.05. Images are showing nuclear expression of p16 and p21 (green) in iCMs and SenCMs stained for cardiac Troponin-T (red) and counterstained with DAPI.

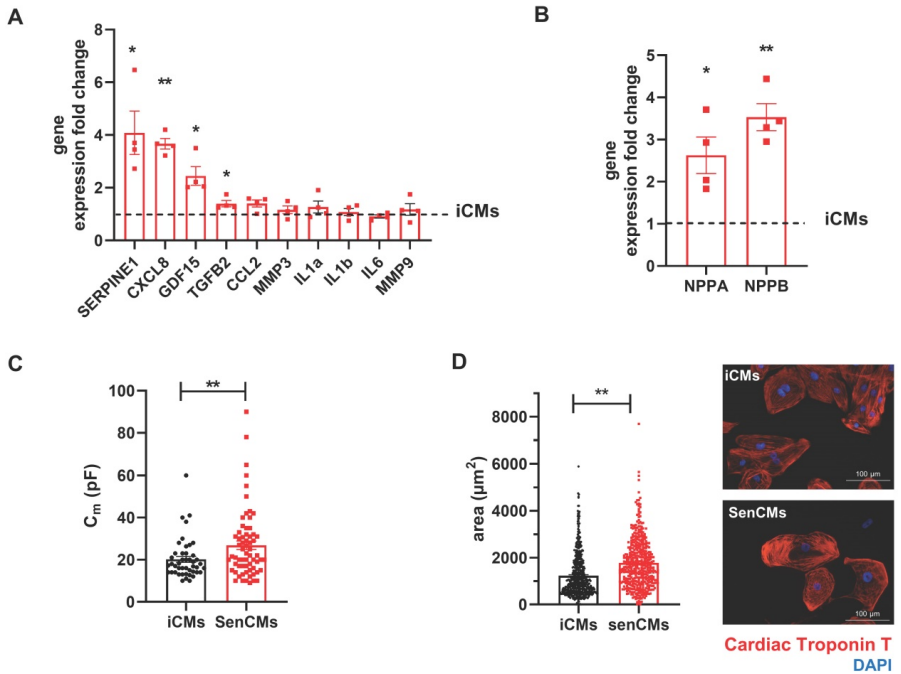

Figure 3: Expression of SASP and induction of hypertrophy in SenCMs (A) SASP-associated genes mRNA relative expression in SenCMs versus iCMs (black dotted line). Data are means of four independent experiments ± SEM. * P < 0.05, ** P < 0.01 *vs* iCMs. (B) NPPA and NPPB mRNA relative expression in SenCMs *versus* iCMs. Data are means of four independent experiments ± SEM. * P < 0.05, ** P < 0.01 *vs* iCMs. (C) Membrane capacitance (C_m) recorded by patch-clamp technique from SenCMs and iCMs. Data are means of 65 and 45 cells respectively, pooled from four independent experiment ± SEM. * P < 0.05. (D) Cell surface area in SenCMs and iCMs. Data are means of 577 and 459 cells respectively, pooled from four independent experiment ± SEM. * P < 0.05.

Dox-induced senescence affects electrical properties and intracellular Ca^{2+} dynamics of SenCMs

Aging is associated with an increased incidence of cardiac arrhythmias and heart failure. Indeed, the ability of SenCMs to respond to stressors is compromised by ionic remodelling, abnormalities in Ca^{2+} handling, and defective SR-mitochondria crosstalk [53, 54]. Dox is also known to cause arrhythmias in humans as well as animal models [55-57]. Using the MEA technology, we sought to explore whether Dox-induced senescence may affect FPD in spontaneously beating clusters. We found that electrophysiological properties of multicellular preparations of SenCMs were significantly altered as compared to iCMs, with a time-dependent increase of the corrected FPD (named QTcB) (Figure 5A). Notably, the prolongation of QTcB worsened over time and reached a steady-state value 5-7 days after single Dox exposure at day 0.

As the QT interval reflects the duration of the AP, we further investigated by patch-clamp analysis the specific contribution of inward and outward ionic currents that might explain the QT prolongation observed at multicellular level. As first attempt we measured at a single-cell level the electrical activity in terms of the duration of the AP, measured at 90% of repolarization (APD_{90}). Both iCMs and SenCMs well adapted in terms of APD shortenings as the stimulation frequency increased; however, at low stimulation rate (1Hz), SenCMs showed a huge APD prolongation in comparison to iCMs (Figure 5B). As the increase in APD_{90} is directly linked with the variability of repolarization phase, we assessed the rate-dependency of STV APD_{90}. As expected, STV resulted increased in SenCM at 1 Hz (Figure 5C) as a direct consequence of the prolongation of APD_{90}. Moreover, the linear correlation STV/APD_{90} was steeper in SenCMs than iCMs, suggesting that other Dox-induced effects in addition to APD_{90} prolongation can affect the variability of APD. Overall, these results indicate that SenCMs have a pronounced tendency to arrhythmogenesis in comparison to iCMs. This was further confirmed by the higher number of cells exhibiting DADs among the treated cells as respect to iCMs (Figure 5D).

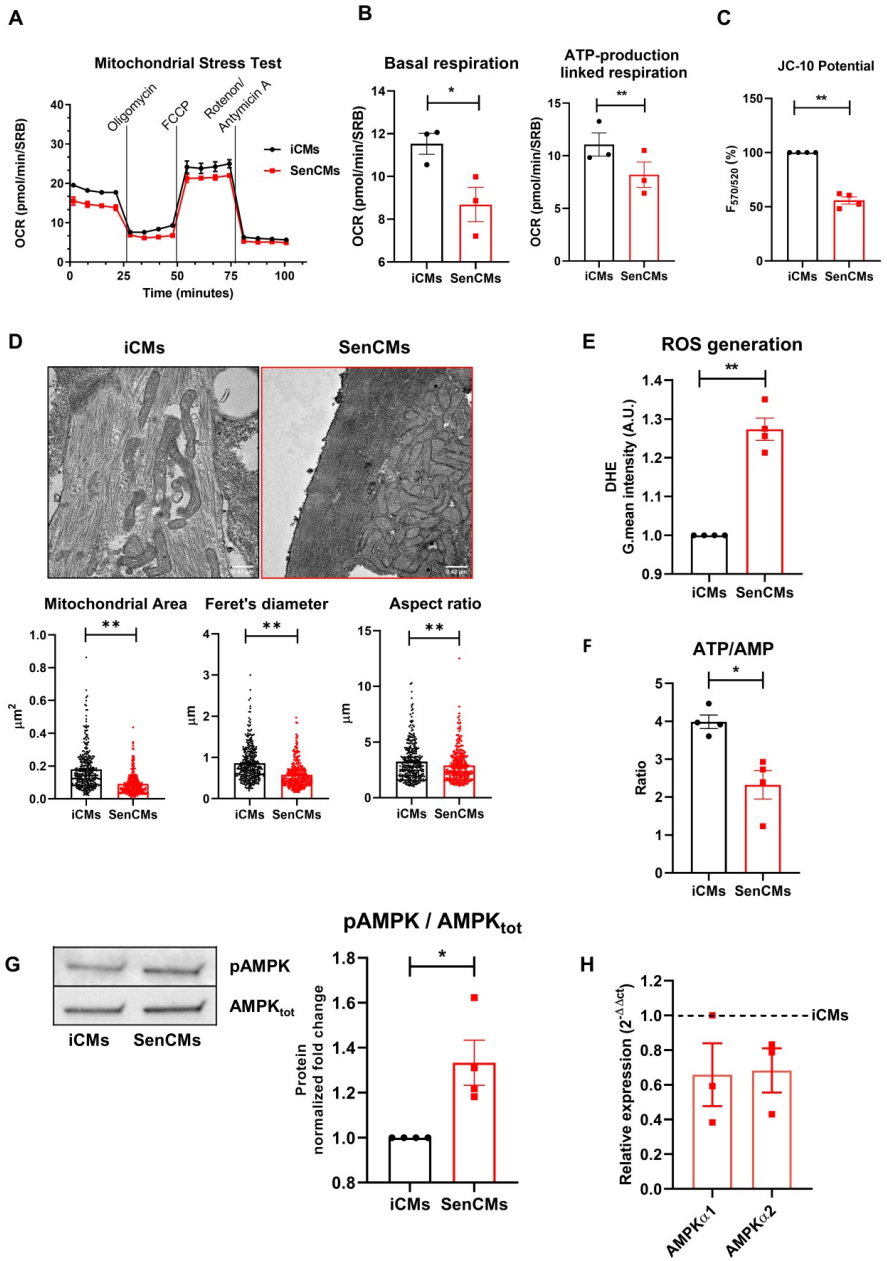

Figure 4: Induction of mitochondrial damage in SenCMs. (A) Measurement of oxygen consumption rate (OCR) by Seahorse-XF assay. Time-course of oxygen consumption rate (OCR) is shown in iCMs (black line) and SenCMs (red line). Timing for injection of Oligomycin 1μM, FCCP 0.5μM, Rotenone/Antimycin A 1μM OCR are indicated. (B) Basal respiration was measured as OCR level previous to Oligomycin treatment - minimum OCR level after Rotenone/Antimycin A injection. ATP linked production was measured as maximum OCR level after Oligomycin injection – Basal Respiration. Normalization for cell number was obtained with Sulforhodamine B assay. Data are means of three independent experiments ± SEM; * P < 0.05, ** P < 0.01 *vs* iCMs. (C) Mitochondrial membrane potential (ΔΨm) is evaluated by potential-sensitive dye JC-10. The graph represents the means of four independent experiments ± SEM ** P < 0.01 *vs* iCMs. (D) Representative TEM images and quantitative analysis (surface area, Feret's diameter and aspect ratio) of mitochondria morphology in SenCMs (N=136) *vs* iCMs (N=80). Data are pooled from three independent experiments ± SEM ** P < 0.01. (E) Reactive oxygen species were assessed in SenCMs *vs* iCMs using DHE assay. Cells were incubated with DHE for intracellular H_2O_2 detection as described in Methods and Materials. Quantitative data are shown in the bar graph as means of four independent experiments ± SEM; * P < 0.05, ** P < 0.01 *vs* iCMs. (F) ATP/AMP ratio was by measuring intracellular ATP and AMP levels as described in Methods and Materials. Data are means of four independent experiments ± SEM; * P < 0.05 vs iCMs (G) pThr172 AMPK:$AMPK_{tot}$ protein expression levels. Quantitative data of four independent experiments ± SEM (densitometric values for the proteins of interest normalized for GAPDH). (H) AMPKα1 and AMPKα2 mRNA relative expression in SenCMs versus iCMs. Data are means of three independent experiments ± SEM. * P < 0.05, ** P < 0.01 *vs* iCMs.

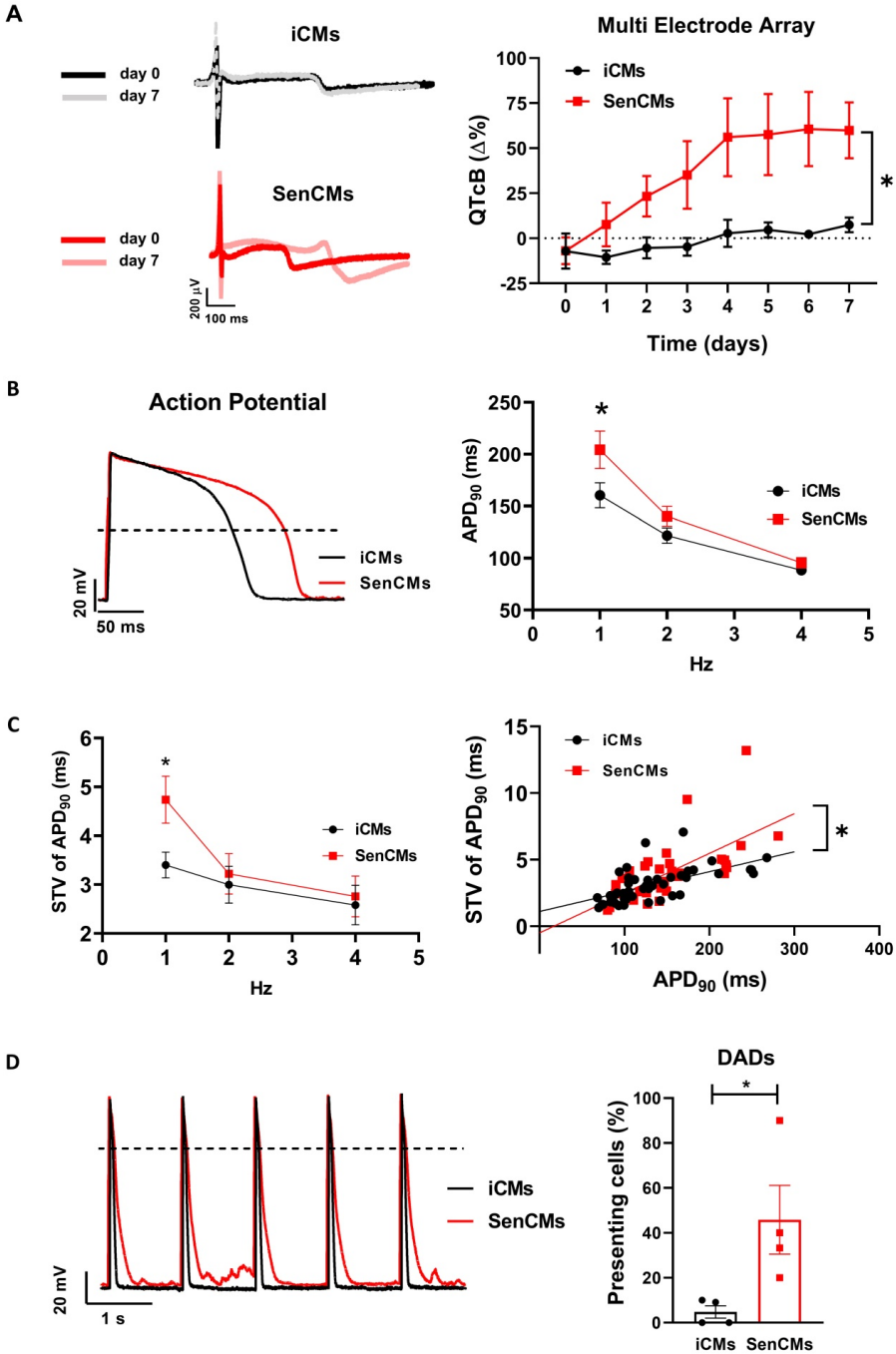

Figure 5: Alterations of electrical activity in SenCMs. (A) The electrical activity of spontaneously beating clusters of iCMs and SenCMs was recorded using MEA for 7 consecutive days after Dox treatment. Data are means of five independent experiments ± SEM; * P < 0.05 vs iCMs. QTcB: QT-interval corrected by Bazett's formula. Examples of field potentials in iCMs and SenCMs at day 1 and 7 are shown. (B) Rate-dependency of APD in isolated SenCMs (N=17) vs iCMs (N=22). Data are pooled from four indipendent experiments. ± SEM. * P < 0.05. Representative APs recorded at 1 Hz in each group are shown. Numerical I_{K1} (see Methods) was injected through Dynamic Clamp technique to compensate the low expression of native I_{K1} in iCMs. (C) Rate-dependency of short term variability (STV) of APD_{90} (left panel) and linear correlations between STV of APD_{90} and APD_{90} values (right panel) in each group; data from all stimulation rates were pooled. Data are means of at least 20 cells for every group, pooled from four independent experiments ± SEM. * P < 0.05. (D) DADs incidence in each group; recordings at 1Hz in each group are superimposed on the left to highlight DADs occurrence. *p<0.05 *vs* iCMs.

We investigated the rapid delayed rectifier K^+ current (I_{Kr}) I/V relationship, mediated by the HERG (also known as KCNH2) channel, as possible mechanism responsible for reduced repolarization reserve in SenCMs. SenCMs showed significant downregulation of I_{Kr} density in comparison to control iCMs (Figure 6A). Moreover, the protein expression level of the HERG channel at this time point was reduced in SenCMs *vs* iCMs (Figure 6B). As it was the first time that a decrease in expression of KCNH2 was associated with senescent CMs, we took advantage of our in-house biobank of human atrial appendage tissue specimens to verify a possible correlation between the protein levels and the age of the donors. Consistent with the *in vitro* data, we found a significant inverse correlation between KCNH2 expression and age of the patient (Supplementary Figure S3A).

A further cause of prolonged QT in CMs might be ascribable to an increased inward current during the plateau phase of the AP. Thus, we evaluated the Dox-induced modulation of the late component of Na^+ current (I_{NaL}), a good candidate accordingly to its sensitivity to the cellular redox state [58]. I_{NaL} I/V relationships were obtained by measuring TTX (2 μM)-sensitive current (I_{TTX}) during slow voltage ramps. Inward steady-state I_{TTX} might be representative of both Na^+ window current at negative potentials and I_{NaL} at more positive potentials [41]. While peak I_{TTX} at –39 mV (mostly representing I_{Naw}) was not significantly affected in SenCMs, I_{TTX} measured at 0 mV (mostly representing I_{NaL}) significantly increased in SenCMs compared to iCMs (Figure 6C). Accordingly, the proportion of CAMKII phosphorylated on the Thr286 of its alpha subunit (pCAMKII), a well-known modulator of I_{NaL} [59], increased in SenCMs (Figure 6D). Overall, the combination of I_{Kr} downregulation and I_{NaL} enhancement may largely justify the Dox-induced senescence-dependent electrical remodeling leading to QT/APD prolongation.

Next, to complete the characterization of SenCM phenotype, we studied the intracellular Ca^{2+} dynamics in FLUO-4 voltage clamped iCMs (Figure 6E). In comparison to controls, Ca^{2+} transient (CaT) amplitude and sarcoplasmic reticulum Ca^{2+} content (CaSR), evaluated through a caffeine (10 mM) pulse, were significantly reduced in SenCMs 5-7 days after treatment, leading to a similar fractional release (0.41±0.04 *vs* 0.44±0.04, ns). As expected, SR Ca^{2+} levels evaluated by measuring caffeine-induced CaT amplitude (Figure 6E) or caffeine-induced I_{NCX} (Supplementary Figure S4A) showed comparable results. Both Ca^{2+} influx through L-type Ca^{2+} channel and peak ICa_L density (-9.8±1.4 pA/pF *vs* -11.1±1.1 pA/pF, ns) at 0 mV were not significantly affected in SenCMs. SERCA2 protein levels were significantly reduced in SenCMs, while the protein levels of the physiological SERCA2 inhibitor phospholamban (PLN) in both the monomeric (m) and pentameric forms were not altered, leading to a SERCA2/PLN ratio reduction in SenCMs (Figure 6F), a finding previously reported in aged animal models[60]. To have a complete overview of SR function in SenCMs, potential alterations in SR Ca^{2+} release in addition to SR Ca^{2+} uptake, was evaluated in SenCMs by measuring Ca^{2+} sparks rate and characteristics. While Ca^{2+} sparks rate was not significantly altered in SenCMs in comparison to iCMs, analysis of Ca^{2+} sparks parameters underlined spatial and temporal Ca^{2+} spark duration enhancement in SenCMs, leading to a greater global volume of SR Ca^{2+} released by each Ca^{2+} release unit (namely spark mass) (Figure 6G and Supplementary Figure S4B). This finding well fits with the increased CaMKII activity in SenCMs, known to increase SR Ca^{2+} leak [61]. Moreover, accordingly to SERCA2 depression, Ca^{2+} sparks decay became slower (that is τ decay enhancement) in SenCMs (Figure 6G). Overall, these data suggest a huge alteration of intracellular Ca^{2+} dynamics that largely explain the proarrhythmic phenotype of SenCMs (i.e. DADs occurrency).

Model comparison with aging mice CMs

To exploit potential specie-specific differences with mouse CMs, key electrophysiological features were also evaluated in CMs isolated from young (y-mCMs) *vs* old mice (o-mCMs) (Figure 7). o-mCMs exhibited a depolarized E_{diast} at all stimulation rates (Figure 7B) and prolonged APD_{90} at 2 and 4 Hz (Figure 7C). Moreover, a significant number of o-mCMs failed to adapt at higher stimulation rates (7 Hz) (inset Figure 7C). Of note, as expected, the rate-dependency of APD_{90} in mice shows opposite trend as compared to human cells. In line with human model, in o-mCMs the STV of APD_{90} was significantly increased at low stimulation rates (Figure 7D) and the STV/APD_{90} correlation tended to be steeper in comparison to y-mCMs (Figure 7E). As observed in SenCMs, the APD prolongation in o-mCMs was largely dependent on enhanced I_{NaL} (Figure 7F) that contextually was ascribable to the increased proportion of CAMKII phosphorylated on Thr286 (Figure 7G).

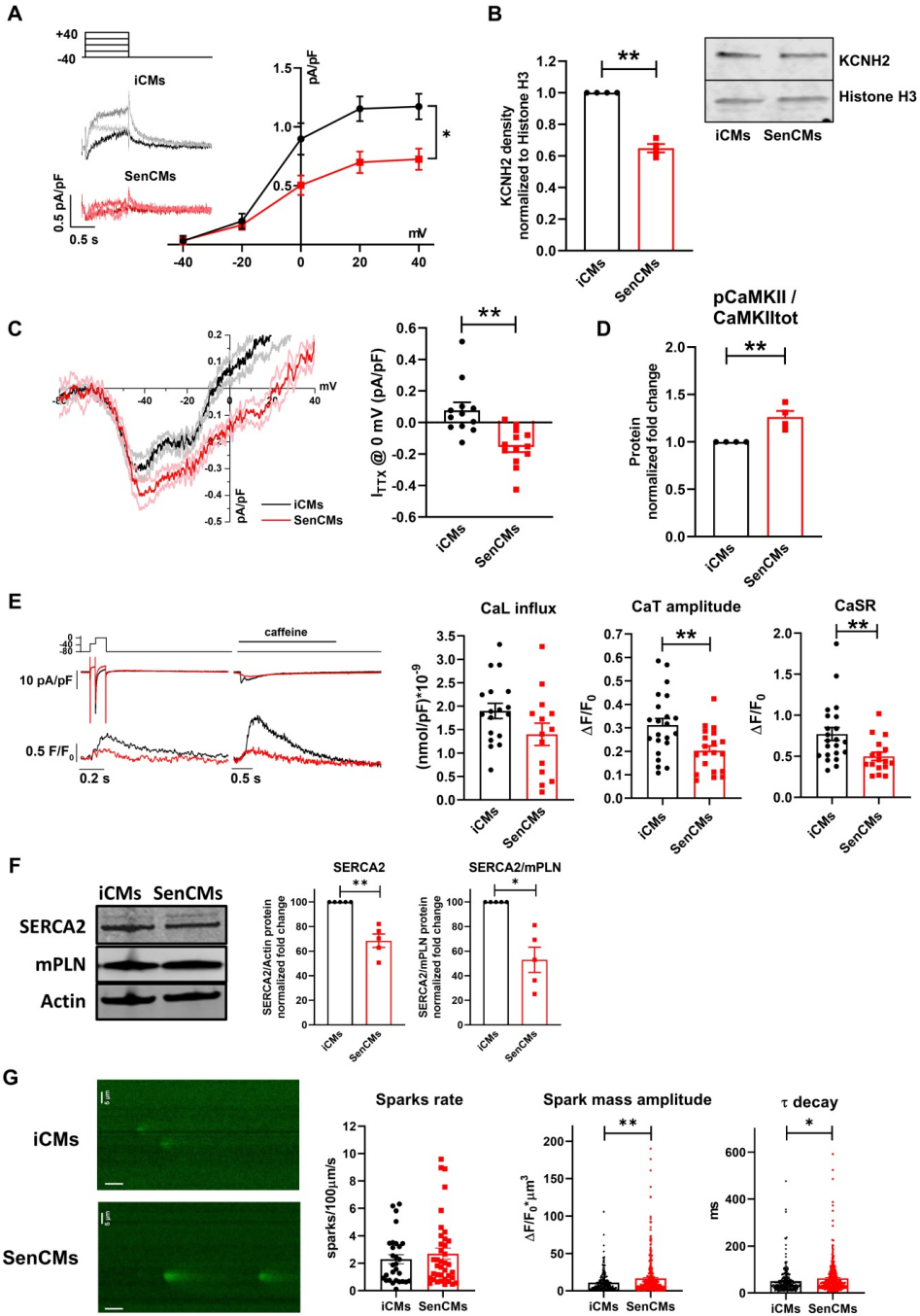

Figure 6: Alterations of I_{Kr}, I_{NaL} and Ca^{2+} handling in SenCMs. (A) E-4031 (3µM)-sensitive currents (I_{Kr}) activated according to the protocol shown on top and relative I/V relationships in iCMs (N = 21) and SenCMs (N = 26) 5-7 days after treatment. Data pooled from four independent experiments are presented as ± SEM. * P < 0.05, ** P < 0.01 *vs* iCMs. (B) HERG (KCNH2) protein expression levels in iCMs and SenCMs. Quantitative data of four independent experiments ± SEM (densitometric values for the protein of interest normalized for histone H3). ± SEM. * P < 0.05, ** P < 0.01 *vs* iCMs. (C) TTX (2 µM)-sensitive current (I_{TTX}) activated during slow voltage ramps (28 mV/sec) from a holding potential of -100 mV. Mean ± SEM I/V relationships for iCMs (N = 12) and SenCMs (N = 13) are shown. Data pooled from four independent experiments are presented as ± SEM. * P < 0.05, ** P < 0.01 *vs* iCMs. Statistics of I_{TTX} at 0 mV, representative of I_{NaL}, are reported on the right. (D) pThr286 CAMKII:CAMKII total protein expression levels in SenCMs versus iCMs. Quantitative data are from four independent experiments ± SEM (densitometric values for the proteins of interest normalized for GAPDH). * P < 0.05,

** P < 0.01 *vs* iCMs. (E) Membrane currents and Ca^{2+} transients (CaT) were recorded simultaneously according to the voltage clamp protocol shown on top in Fluo4-loaded iCMs. Examples (left panel) and statistics (right panel) of CaL influx, CaT amplitude and caffeine-induced CaT amplitude (estimating CaSR) in iCMs (N = 22) and SenCMs (N= 14) 5-7 days after Dox treatment. Data pooled from four independent experiments are presented as ± SEM. * P < 0.05, ** P < 0.01 *vs* iCMs. (F) SERCA2 and monomeric (m) PLN protein expression levels in iCMs and SenCMs. Quantitative data of five independent experiments ± SEM (densitometric values for the protein of interest normalized for actin). (G) Statistics of Ca^{2+} spark rate and characteristics in SenCMs (N=410) *vs* iCMs (N=266). Line scan (xt) images are shown on the left (time bar: 100 ms). * P < 0.05, ** P < 0.01 *vs* iCMs.

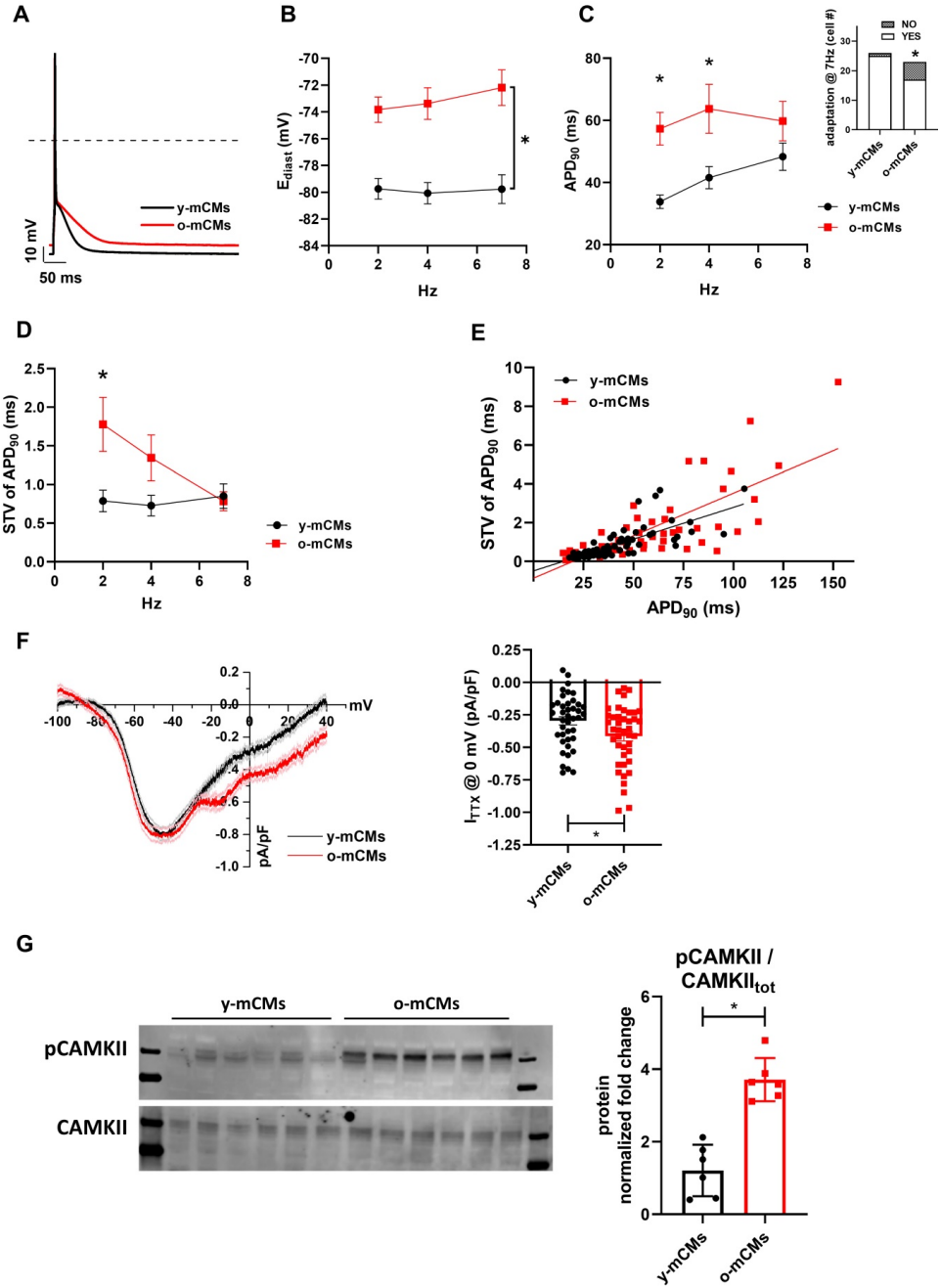

Figure 7: Validation of Dox-induced senescence through physiological senescence in mice. (A) APs recorded at 2 Hz in old (o-) *vs* young (y-) mCMs are superimposed. (B-C) Statistics of rate-dependency of E_{diast} and APD_{90} in y-mCMs (N=25-34) and o-mCMs (N=17-31). In comparison to y-mCMs, a significative portion of

o-mCMs failed to adapt at 7 Hz (statistics in the inset on the right). Data pooled from four independent experiments are presented as ± SEM; * P < 0.05, ** P < 0.01 *vs* iCMs. (D) Rate-dependency of short term variability (STV) of APD_{90}. (E) linear correlations between STV of APD_{90} and APD_{90} values in each group; data from all stimulation rates were pooled. Data pooled from four independent experiments are presented as ± SEM; * P < 0.05, ** P < 0.01 *vs* iCMs. (F) TTX (2 μM)-sensitive current (I_{TTX}) activated during slow voltage ramps (28 mV/sec) from a holding potential of -100 mV. Mean ± SEM I/V relationships for y-mCMs (N = 41) and o-mCMs (N = 42) (left panel) and statistics of I_{TTX} at 0 mV, representative of I_{NaL} (right panel). Data pooled from four independent experiments are presented as ± SEM; * P < 0.05, ** P < 0.01 *vs* iCMs. (G) pThr286 CAMKII:CAMKII total protein expression levels in o-mCMs in comparison to y-mCMs. Quantitative data are from six independent experiments ± SEM (densitometric values for the proteins of interest normalized for GAPDH).

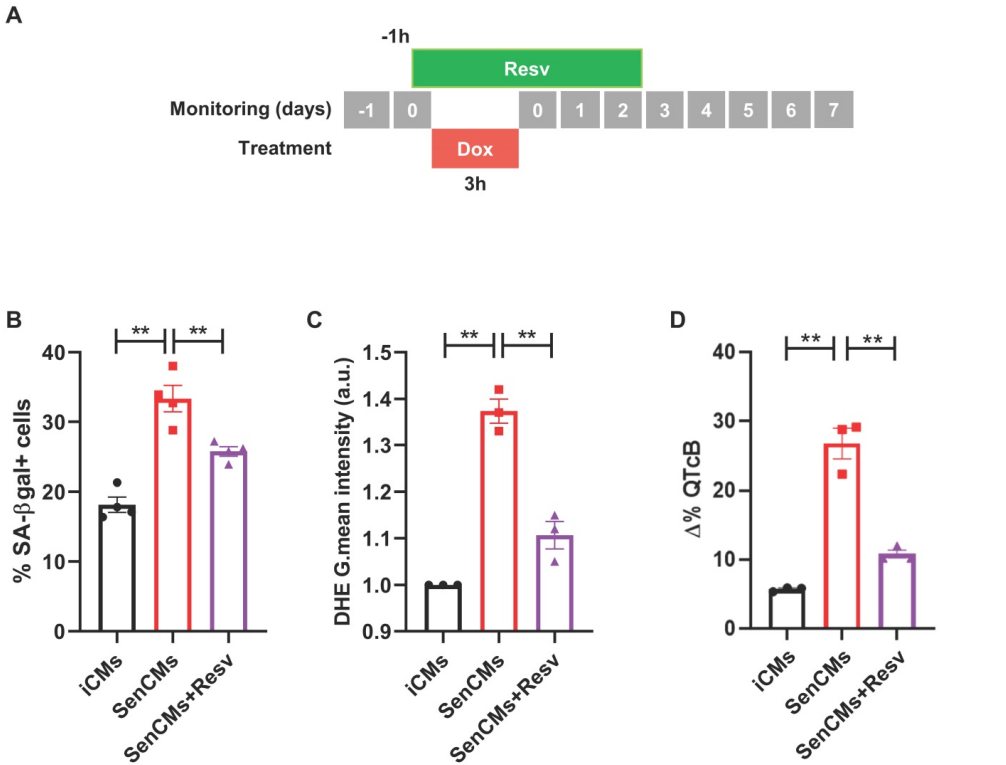

Figure 8: Prevention of most aging markers by resveratrol treatment. (A) Protocol outline. (B-D) Statistics of SA β-gal positive cells, ROS levels through DHE assay, and QTc prolongation in all experimental groups (iCMs, SenCMs and SenCms + Resv 25 μM). Quantitative data of three-four independent experiments ± SEM. * P < 0.05, ** P < 0.01 *vs* SenCMs.

Model validation using heart-tissue transcriptomic data

To put in scale our human-based in-vitro model of iCMs with naturally aging CMs, data from repository-available snRNA seq was used to validate age-related expression of key genes that were found up-regulated in SenCMs. In-line with our model, CDKN1A ($p21^{cip1/waf1}$) and CDKN2A ($p16^{INK4a}$) were significantly upregulated in aging heart with marked overexpression of the former. Similar trend was also found for GDF15, CCL2 and NPPA, NPPB in ventricular and atrial CMs respectively (Supplementary Figure S3B).

Model validation using pharmacological approach

To validate our model as drug testing platform [62, 63] we treated SenCMs with a well-known antioxidant and anti-aging compound: Resveratrol (Resv) (Figure 8). SenCMs treated with Resv showed significant reduction in SA-β-gal expression as well as in ROS production as compared to its counterpart. Notably at functional level, Resv was able to rescue prolongation of QTcB to basal level. All together, these data showed that our model is a reliable cardiac-specific platform for testing potential senolytic and/or senostatic agents.

Discussion

Stressors such as DNA-damaging agents [64], overexpression of oncogenic genes [65], and oxidants [66] can induce age-independent senescence. SIPS not only plays a role in the arrest of cell cycle and cell propagation in replicating tissues [67], but also impairs the functionality of organs with scarce

residual replicative capacity, as it is the heart. SIPS is considered a novel mechanism in the heart remodelling after acute myocardial infarction [27, 68], cancer therapy-induced cardiotoxicity [28] and long-term cardiovascular complications following sepsis [12]. Maejima et al. reported that murine neonatal CMs that undergo SIPS have common features of replicative-senescence, including upregulation of cell-cycle regulatory inhibitors, expression of SA-β-gal, and the attenuation of telomerase activity [23]. Here we extended existing data to human iCMs, overcoming potential specie-specific limitations, and exploring for the first time functional electrophysiological properties of aged human CMs. The present report showed that sub-toxic concentration of Dox induced expression of both $p21^{cip1/waf1}$ and $p16^{INK4a}$ in human CMs and caused cellular senescence. Senescent cells displayed components of DNA-damage response (DDR), such as γH2AX-positive foci. Possible consequence of this effect is that the residual CM renewal – which has been demonstrated occurring in humans by approximately 0.5% to 2% per year [69] and accounting for a stable turnover of CMs in the healthy adult heart [70], might be impaired by SIPS. In a broader view, here we showed evidence that underlying mechanisms of diminished cardiomyocyte turnover with aging [69, 71] are likely attributable to cardiomyocyte senescence. In fact, the synthesis of new DNA was dramatically abrogated in SenCMs. SenCMs well recapitulate features of senescence cells in terms of "non-canonical senescence-associated secretory phenotype" as shown by Anderson et al [72]. The latter may contribute to age-related cardiac dysfunction as SenCM-associated SASPs including GDF15 and TGFB2 have been associated with myofibroblast activation and CMs hypertrophy [72].

Finally, SenCMs showed mitochondrial damage in terms of a depolarized mitochondrial membrane potential, impaired energy production capability and ultrastructural disruption, that have been previously seen as effects of aging on mitochondria during the development of heart failure [73]. Moreover, a clear mitochondrial intracellular clustering was observed in SenCMs, suggesting an altered mitochondrial relocation. Such "clustering" of intracellular organelles is coupled with β-gal signal that was mostly distributed in the peri-nuclear area (Figure 1D), which is consistent with retrograde transport along the microtubule system of intracellular organelles, including lysosomes, that have been previously described in aging CMs [74]. A second possible explanation of mitochondrial accumulation is an occurring insufficient mitophagy in SenCMs. Under normal conditions, damaged mitochondria undergo asymmetrical fission where the dysfunctional mitochondrial fragments are then eliminated by mitophagy. Overall, the findings in this study support evidence in animal models, suggesting a defective clearance of damaged mitochondria [51].

Impairment of mitochondrial function has a direct consequence in increased level of ROS in SenCMs in line with evidences showing the involvement of ROS in cell senescence [75, 76]. Interventions against ROS production and improving mitochondrial function represent attractive strategies to reduce age-related cardiac remodelling [76, 77]. Consistent with this, iCMs treated with resveratrol prevented key aging hallmarks induced by Dox.

We provided evidence showing that senescence affects ionic currents in human CMs. We observed a reduction of the rapid delayed rectifier K^+ current (I_{Kr}) and enhancement of the late Na^+ current (I_{NaL}) in SenCMs *vs* control ones, resulting in a prolonged QTc interval. The latter constitutes a downright novel finding that supports at cellular level a recent population study by Rabkin and colleagues [78]. They applied a rigorous analytical method to compare six QTc formulae and clearly showed that older individuals have a greater QTc. A significant association between QTc and age was evident in both sexes and regardless of whether they considered a linear or non-linear relationship [78]. This finding was sustained by our data in human tissue showing a significant inverse relationship between age and KCNH2 expression. Although some aspects of the study from Rabkin and colleagues remain controversial as other investigators have reported no association between age and QTc [79, 80], our data supports the hypothesis that elderly patients are more vulnerable to situations and medications that might prolong the QTc, leading to increased propensity to arrhythmias.

The senescence-associated reduction of the repolarization reserve related to I_{NaL} enhancement in iCMs was well reproduced in old mouse CMs. The mechanisms underlying I_{NaL} enhancement can be related to changes in the cellular redox state and increased CAMKII activity [81] as we observed in both aging models. Accordingly to its rate-dependency, in both human and mouse models I_{NaL} enhancement affected APD especially at low rates, thus increasing temporal variability of repolarization, a well-known proarrhythmic condition [82]. Indeed, even though I_{NaL} enhancement with aging might represent an inotropic support for the aged heart, abnormal I_{NaL} can contribute to the pathogenesis of both electrical and contractile cardiac dysfunction. Accordingly, we found that SIPS affects the pro-arrhythmogenic susceptibility expressed in

terms of STV index; moreover, increased DADs incidence in SenCMs is symptomatic of a Ca^{2+} overload condition strictly dependent on intracellular Na^{+} and Ca^{2+} levels alterations. Although we confirmed the enhancement of the late Na^{+} current (I_{NaL}) in CMs from old mice as compared to their young counterpart, we could not assess the contribution of I_{Kr} as such component of the repolarizing current is not expressed in mice [83, 84]. Thus, highlighting the importance of having a "human-based" model to critical dissect specific mechanisms.

To analyse aging related functional changes in proteins involved in excitation-contraction (EC) coupling, Ca^{2+} handling measurements were performed in voltage clamped iCMs, thus, controlling membrane potential, any changes secondary to altered electrical activity were avoided. This approach was suitable to highlight in SenCMs SR Ca^{2+} content reduction, confirmed by a downregulated functionality of SERCA2 pumping activity. A similar finding has been reported in animal models [60] and can justify the diastolic relaxation impairment in the aged population [85].

Moreover, impairment of intracellular Ca^{2+} dynamics in SenCMs was underlined by measuring Ca^{2+} sparks characteristics and rate. SIPS induced increased Ca^{2+} spark mass, likely dependent on increased CAMKII activity [37]. Thus, both increased SR Ca^{2+} leak and reduced SR Ca^{2+} uptake by SERCA2 contributed to depress SR Ca^{2+} content in SenCMs. Overall, alterations in intracellular Ca^{2+} compartmentalization in SenCMs can be considered a general hallmark promoting aging-induced electrical activity alterations (i.e. DADs incidence) [86]. Ca^{2+} sparks characteristics reported in senescent cells from old mice and rats [87, 88] are not fully comparable to the present ones, probably because of species-specificity of the aging model. Thus, a "human-based" model of cardiac senescence is once again useful to better understand aging related mechanisms. We are aware that iCMs have some limitations. Important functional parameters such as the cells' resting membrane potential, the conduction velocities, and the amplitudes of the mechanical forces generated do not reach the same level of maturity as the adult CMs [89]. This early maturity state represents a general limitation in the iPS-derived CMs and nowadays there are no available protocols that may completely overcome such limitation. Ongoing efforts are aiming to ameliorate the field and generate more mature CMs by optimizing extracellular matrix composition, mechanical and electrical training [90, 91]. Nevertheless, our data sheds light on the significance of having a human *in vitro* platform for exploring cellular senescence in CMs in terms of pathogenic mechanisms and possible cardioprotective approach.

Supplementary Material

Supplementary figures and table.
https://www.thno.org/v12p5237s1.pdf

Acknowledgments

This study has been supported by Velux Shiftung Swiss Foundation (grant 1127). The study has been partially supported by the Swiss National Science Foundation_CRSII5_202302, Cardiocentro Ticino Institute (Lugano, Switzerland) and University of Milano-Bicocca (Milano, Italy) for administrative, technical support, and donations in kind (e.g., materials used for experiments).

Competing Interests

The authors have declared that no competing interest exists.

References

1. Zi H, He SH, Leng XY, Xu XF, Huang Q, Weng H, et al. Global, regional, and national burden of kidney, bladder, and prostate cancers and their attributable risk factors, 1990-2019. Mil Med Res. 2021; 8: 60.
2. McHugh D, Gil J. Senescence and aging: Causes, consequences, and therapeutic avenues. J Cell Biol. 2018; 217: 65-77.
3. Childs BG, Durik M, Baker DJ, van Deursen JM. Cellular senescence in aging and age-related disease: from mechanisms to therapy. Nat Med. 2015; 21: 1424-35.
4. Ogrodnik M, Salmonowicz H, Gladyshev VN. Integrating cellular senescence with the concept of damage accumulation in aging: Relevance for clearance of senescent cells. Aging Cell. 2019; 18: e12841.
5. Kuilman T, Michaloglou C, Mooi WJ, Peeper DS. The essence of senescence. Genes Dev. 2010; 24: 2463-79.
6. Wiley CD, Velarde MC, Lecot P, Liu S, Sarnoski EA, Freund A, et al. Mitochondrial Dysfunction Induces Senescence with a Distinct Secretory Phenotype. Cell Metab. 2016; 23: 303-14.
7. Dhingra R, Vasan RS. Age as a risk factor. Med Clin North Am. 2012; 96: 87-91.
8. Roth GA, Johnson C, Abajobir A, Abd-Allah F, Abera SF, Abyu G, et al. Global, Regional, and National Burden of Cardiovascular Diseases for 10 Causes, 1990 to 2015. J Am Coll Cardiol. 2017; 70: 1-25.
9. Steenman M, Lande G. Cardiac aging and heart disease in humans. Biophys Rev. 2017; 9: 131-7.
10. Shimizu I, Minamino T. Cellular senescence in cardiac diseases. J Cardiol. 2019; 74: 313-9.
11. Campisi J. Senescent cells, tumor suppression, and organismal aging: good citizens, bad neighbors. Cell. 2005; 120: 513-22.
12. Merdji H, Schini-Kerth V, Meziani F, Toti F. Long-term cardiovascular complications following sepsis: is senescence the missing link? Ann Intensive Care. 2021; 11: 166.
13. Abid S, Lipskaia L, Adnot S. Anthracycline cardiotoxicity: looking for new therapeutic approaches targeting cell senescence? Cardiovasc Res. 2018; 114: 1304-5.
14. Walaszczyk A, Dookun E, Redgrave R, Tual-Chalot S, Victorelli S, Spyridopoulos I, et al. Pharmacological clearance of senescent cells improves survival and recovery in aged mice following acute myocardial infarction. Aging Cell. 2019: e12945.
15. Dookun E, Walaszczyk A, Redgrave R, Palmowski P, Tual-Chalot S, Suwana A, et al. Clearance of senescent cells during cardiac ischemia-reperfusion injury improves recovery. Aging Cell. 2020; 19: e13249.
16. Reardon M, Malik M. QT interval change with age in an overtly healthy older population. Clin Cardiol. 1996; 19: 949-52.
17. O'Neal WT, Singleton MJ, Roberts JD, Tereshchenko LG, Sotoodehnia N, Chen LY, et al. Association Between QT-Interval Components and Sudden Cardiac Death: The ARIC Study (Atherosclerosis Risk in Communities). Circ Arrhythm Electrophysiol. 2017; 10.
18. Signore S, Sorrentino A, Borghetti G, Cannata A, Meo M, Zhou Y, et al. Late Na(+) current and protracted electrical recovery are critical determinants of the aging myopathy. Nat Commun. 2015; 6: 8803.
19. Pinto AR, Ilinykh A, Ivey MJ, Kuwabara JT, D'Antoni ML, Debuque R, et al. Revisiting Cardiac Cellular Composition. Circ Res. 2016; 118: 400-9.

20. Maeder MT, Kaye DM. Heart failure with normal left ventricular ejection fraction. J Am Coll Cardiol. 2009; 53: 905-18.
21. Jahangir A, Sagar S, Terzic A. Aging and cardioprotection. J Appl Physiol (1985). 2007; 103: 2120-8.
22. Reed AL, Tanaka A, Sorescu D, Liu H, Jeong EM, Sturdy M, et al. Diastolic dysfunction is associated with cardiac fibrosis in the senescence-accelerated mouse. Am J Physiol Heart Circ Physiol. 2011; 301: H824-31.
23. Maejima Y, Adachi S, Ito H, Hirao K, Isobe M. Induction of premature senescence in cardiomyocytes by doxorubicin as a novel mechanism of myocardial damage. Aging Cell. 2008; 7: 125-36.
24. Piegari E, De Angelis A, Cappetta D, Russo R, Esposito G, Costantino S, et al. Doxorubicin induces senescence and impairs function of human cardiac progenitor cells. Basic Res Cardiol. 2013; 108: 334.
25. Lazzarini E, Balbi C, Altieri P, Pfeffer U, Gambini E, Canepa M, et al. The human amniotic fluid stem cell secretome effectively counteracts doxorubicin-induced cardiotoxicity. Sci Rep. 2016; 6: 29994.
26. Bielak-Zmijewska A, Wnuk M, Przybylska D, Grabowska W, Lewinska A, Alster O, et al. A comparison of replicative senescence and doxorubicin-induced premature senescence of vascular smooth muscle cells isolated from human aorta. Biogerontology. 2014; 15: 47-64.
27. Cui S, Xue L, Yang F, Dai S, Han Z, Liu K, et al. Postinfarction Hearts Are Protected by Premature Senescent Cardiomyocytes Via GATA 4-Dependent CCN 1 Secretion. J Am Heart Assoc. 2018; 7: e009111.
28. Mitry MA, Laurent D, Keith BL, Sira E, Eisenberg CA, Eisenberg LM, et al. Accelerated cardiomyocyte senescence contributes to late-onset doxorubicin-induced cardiotoxicity. Am J Physiol Cell Physiol. 2020; 318: C380-C91.
29. Litvinukova M, Talavera-Lopez C, Maatz H, Reichart D, Worth CL, Lindberg EL, et al. Cells of the adult human heart. Nature. 2020; 588: 466-72.
30. Andriolo G, Provasi E, Brambilla A, Lo Cicero V, Soncin S, Barile L, et al. GMP-Grade Methods for Cardiac Progenitor Cells: Cell Bank Production and Quality Control. Methods Mol Biol. 2020.
31. Barile L, Gherghiceanu M, Popescu LM, Moccetti T, Vassalli G. Human cardiospheres as a source of multipotent stem and progenitor cells. Stem Cells Int. 2013: 916837.
32. Pianezzi E, Altomare C, Bolis S, Balbi C, Torre T, Rinaldi A, et al. Role of somatic cell sources in the maturation degree of human induced pluripotent stem cell-derived cardiomyocytes. Biochim Biophys Acta Mol Cell Res. 2020; 1867: 118538.
33. Lian X, Zhang J, Azarin SM, Zhu K, Hazeltine LB, Bao X, et al. Directed cardiomyocyte differentiation from human pluripotent stem cells by modulating Wnt/beta-catenin signaling under fully defined conditions. Nat Protoc. 2013; 8: 162-75.
34. Alemanni M, Rocchetti M, Re D, Zaza A. Role and mechanism of subcellular Ca2+ distribution in the action of two inotropic agents with different toxicity. J Mol Cell Cardiol. 2011; 50: 910-8.
35. Dimri GP, Lee X, Basile G, Acosta M, Scott G, Roskelley C, et al. A biomarker that identifies senescent human cells in culture and in aging skin *in vivo*. Proc Natl Acad Sci U S A. 1995; 92: 9363-7.
36. Livak KJ, Schmittgen TD. Analysis of relative gene expression data using real-time quantitative PCR and the 2(-Delta Delta C(T)) Method. Methods. 2001; 25: 402-8.
37. Rocchetti M, Sala L, Dreizehnter L, Crotti L, Sinnecker D, Mura M, et al. Elucidating arrhythmogenic mechanisms of long-QT syndrome CALM1-F142L mutation in patient-specific induced pluripotent stem cell-derived cardiomyocytes. Cardiovasc Res. 2017; 113: 531-41.
38. Nygren A, Fiset C, Firek L, Clark JW, Lindblad DS, Clark RB, et al. Mathematical model of an adult human atrial cell: the role of K+ currents in repolarization. Circ Res. 1998; 82: 63-81.
39. Heijman J, Zaza A, Johnson DM, Rudy Y, Peeters RL, Volders PG, et al. Determinants of beat-to-beat variability of repolarization duration in the canine ventricular myocyte: a computational analysis. PLoS Comput Biol. 2013; 9: e1003202.
40. Altomare C, Bartolucci C, Sala L, Bernardi J, Mostacciuolo G, Rocchetti M, et al. IKr Impact on Repolarization and Its Variability Assessed by Dynamic Clamp. Circ Arrhythm Electrophysiol. 2015; 8: 1265-75.
41. Rocchetti M, Sala L, Rizzetto R, Staszewsky LI, Alemanni M, Zambelli V, et al. Ranolazine prevents INaL enhancement and blunts myocardial remodelling in a model of pulmonary hypertension. Cardiovasc Res. 2014; 104: 37-48.
42. Picht E, Zima AV, Blatter LA, Bers DM. SparkMaster: automated calcium spark analysis with ImageJ. Am J Physiol Cell Physiol. 2007; 293: C1073-81.
43. Altomare C, Pianezzi E, Cervio E, Bolis S, Biemmi V, Benzoni P, et al. Human-induced pluripotent stem cell-derived cardiomyocytes from cardiac progenitor cells: effects of selective ion channel blockade. Europace. 2016; 18: iv67-iv76.
44. Levitsky KL, Toledo-Aral JJ, Lopez-Barneo J, Villadiego J. Direct confocal acquisition of fluorescence from X-gal staining on thick tissue sections. Sci Rep. 2013; 3: 2937.
45. Chandrasekaran A, Idelchik M, Melendez JA. Redox control of senescence and age-related disease. Redox Biol. 2017; 11: 91-102.
46. Watanabe S, Kawamoto S, Ohtani N, Hara E. Impact of senescence-associated secretory phenotype and its potential as a therapeutic target for senescence-associated diseases. Cancer Sci. 2017; 108: 563-9.
47. Engel FB, Schebesta M, Keating MT. Anillin localization defect in cardiomyocyte binucleation. J Mol Cell Cardiol. 2006; 41: 601-12.
48. Kadow ZA, Martin JF. Distinguishing Cardiomyocyte Division From Binucleation. Circ Res. 2018; 123: 1012-4.
49. Lee LE, Chandrasekar B, Yu P, Ma L. Quantification of myocardial fibrosis using noninvasive T2 -mapping magnetic resonance imaging: Preclinical models of aging and pressure overload. NMR Biomed. 2021: e4641.
50. Li X, Lan Y, Wang Y, Nie M, Lu Y, Zhao E. Telmisartan suppresses cardiac hypertrophy by inhibiting cardiomyocyte apoptosis via the NFAT/ANP/BNP signaling pathway. Mol Med Rep. 2017; 15: 2574-82.
51. Tocchi A, Quarles EK, Basisty N, Gitari L, Rabinovitch PS. Mitochondrial dysfunction in cardiac aging. Biochim Biophys Acta. 2015; 1847: 1424-33.
52. Kim J, Yang G, Kim Y, Kim J, Ha J. AMPK activators: mechanisms of action and physiological activities. Exp Mol Med. 2016; 48: e224.
53. Ruiz-Meana M, Minguet M, Bou-Teen D, Miro-Casas E, Castans C, Castellano J, et al. Ryanodine Receptor Glycation Favors Mitochondrial Damage in the Senescent Heart. Circulation. 2019; 139: 949-64.
54. Mirza M, Strunets A, Shen WK, Jahangir A. Mechanisms of arrhythmias and conduction disorders in older adults. Clin Geriatr Med. 2012; 28: 555-73.
55. Doherty KR, Talbert DR, Trusk PB, Moran DM, Shell SA, Bacus S. Structural and functional screening in human induced-pluripotent stem cell-derived cardiomyocytes accurately identifies cardiotoxicity of multiple drug types. Toxicol Appl Pharmacol. 2015; 285: 51-60.
56. Zhu W, Shou W, Payne RM, Caldwell R, Field LJ. A mouse model for juvenile doxorubicin-induced cardiac dysfunction. Pediatr Res. 2008; 64: 488-94.
57. Altomare C, Lodrini AM, Milano G, Biemmi V, Lazzarini E, Bolis S, et al. Structural and Electrophysiological Changes in a Model of Cardiotoxicity Induced by Anthracycline Combined With Trastuzumab. Front Physiol. 2021; 12: 658790.
58. Yang PC, Song Y, Giles WR, Horvath B, Chen-Izu Y, Belardinelli L, et al. A computational modelling approach combined with cellular electrophysiology data provides insights into the therapeutic benefit of targeting the late Na+ current. J Physiol. 2015; 593: 1429-42.
59. Hegyi B, Banyasz T, Izu LT, Belardinelli L, Bers DM, Chen-Izu Y. beta-adrenergic regulation of late Na(+) current during cardiac action potential is mediated by both PKA and CaMKII. J Mol Cell Cardiol. 2018; 123: 168-79.
60. Hamilton S, Terentyev D. Altered Intracellular Calcium Homeostasis and Arrhythmogenesis in the Aged Heart. Int J Mol Sci. 2019; 20.
61. Sag CM, Kohler AC, Anderson ME, Backs J, Maier LS. CaMKII-dependent SR Ca leak contributes to doxorubicin-induced impaired Ca handling in isolated cardiac myocytes. J Mol Cell Cardiol. 2011; 51: 749-59.
62. Breljak D, Micek V, Geric M, Gajski G, Oguic SK, Rasic D, et al. Long-term effects of melatonin and resveratrol on aging rats: A multi-biomarker approach. Mutat Res Genet Toxicol Environ Mutagen. 2022; 876-877: 503443.
63. He S, Zhou M, Zheng H, Wang Y, Wu S, Gao Y, et al. Resveratrol inhibits the progression of premature senescence partially by regulating v-rel avian reticuloendotheliosis viral oncogene homolog A (RELA) and sirtuin 1 (SIRT1). Ren Fail. 2022; 44: 171-83.
64. Wlaschek M, Hommel C, Wenk J, Brenneisen P, Ma W, Herrmann G, et al. Isolation and identification of psoralen plus ultraviolet A (PUVA)-induced genes in human dermal fibroblasts by polymerase chain reaction-based subtractive hybridization. J Invest Dermatol. 2000; 115: 909-13.
65. Spyridopoulos I, Isner JM, Losordo DW. Oncogenic ras induces premature senescence in endothelial cells: role of p21(Cip1/Waf1). Basic Res Cardiol. 2002; 97: 117-24.
66. Chen QM, Tu VC, Liu J. Measurements of hydrogen peroxide induced premature senescence: senescence-associated beta-galactosidase and DNA synthesis index in human diploid fibroblasts with down-regulated p53 or Rb. Biogerontology. 2000; 1: 335-9.
67. Wiley CD, Campisi J. From Ancient Pathways to Aging Cells-Connecting Metabolism and Cellular Senescence. Cell Metab. 2016; 23: 1013-21.
68. Lodrini AM, Goumans MJ. Cardiomyocytes Cellular Phenotypes After Myocardial Infarction. Front Cardiovasc Med. 2021; 8: 750510.
69. Bergmann O, Bhardwaj RD, Bernard S, Zdunek S, Barnabe-Heider F, Walsh S, et al. Evidence for cardiomyocyte renewal in humans. Science. 2009; 324: 98-102.
70. Eschenhagen T, Bolli R, Braun T, Field LJ, Fleischmann BK, Frisen J, et al. Cardiomyocyte Regeneration: A Consensus Statement. Circulation. 2017; 136: 680-6.
71. Richardson GD, Laval S, Owens WA. Cardiomyocyte Regeneration in the mdx Mouse Model of Nonischemic Cardiomyopathy. Stem Cells Dev. 2015; 24: 1672-9.
72. Anderson R, Lagnado A, Maggiorani D, Walaszczyk A, Dookun E, Chapman J, et al. Length-independent telomere damage drives post-mitotic cardiomyocyte senescence. EMBO J. 2019; 38.
73. Doenst T, Nguyen TD, Abel ED. Cardiac metabolism in heart failure: implications beyond ATP production. Circ Res. 2013; 113: 709-24.
74. Sanbe A, Osinska H, Saffitz JE, Glabe CG, Kayed R, Maloyan A, et al. Desmin-related cardiomyopathy in transgenic mice: a cardiac amyloidosis. Proc Natl Acad Sci U S A. 2004; 101: 10132-6.
75. Davalli P, Mitic T, Caporali A, Lauriola A, D'Arca D. ROS, Cell Senescence, and Novel Molecular Mechanisms in Aging and Age-Related Diseases. Oxid Med Cell Longev. 2016; 2016: 3565127.
76. Bayliak MM, Lushchak VI. Pleiotropic effects of alpha-ketoglutarate as a potential anti-ageing agent. Ageing Res Rev. 2021; 66: 101237.

77. Rizvi F, Preston CC, Emelyanova L, Yousufuddin M, Viqar M, Dakwar O, et al. Effects of Aging on Cardiac Oxidative Stress and Transcriptional Changes in Pathways of Reactive Oxygen Species Generation and Clearance. J Am Heart Assoc. 2021; 10: e019948.
78. Rabkin SW, Cheng XJ, Thompson DJ. Detailed analysis of the impact of age on the QT interval. J Geriatr Cardiol. 2016; 13: 740-8.
79. Tran H, White CM, Chow MS, Kluger J. An evaluation of the impact of gender and age on QT dispersion in healthy subjects. Ann Noninvasive Electrocardiol. 2001; 6: 129-33.
80. Huang JH, Lin YQ, Pan NH, Chen YJ. Aging modulates dispersion of ventricular repolarization in the very old of the geriatric population. Heart Vessels. 2010; 25: 500-8.
81. Erickson JR, He BJ, Grumbach IM, Anderson ME. CaMKII in the cardiovascular system: sensing redox states. Physiol Rev. 2011; 91: 889-915.
82. Zaza A, Belardinelli L, Shryock JC. Pathophysiology and pharmacology of the cardiac "late sodium current.". Pharmacol Ther. 2008; 119: 326-39.
83. Kaese S, Verheule S. Cardiac electrophysiology in mice: a matter of size. Front Physiol. 2012; 3: 345.
84. Schuttler D, Bapat A, Kaab S, Lee K, Tomsits P, Clauss S, et al. Animal Models of Atrial Fibrillation. Circ Res. 2020; 127: 91-110.
85. Kitzman DW. Diastolic dysfunction in the elderly. Genesis and diagnostic and therapeutic implications. Cardiol Clin. 2000; 18: 597-617, x.
86. Zaza A, Rocchetti M. Calcium store stability as an antiarrhythmic endpoint. Curr Pharm Des. 2015; 21: 1053-61.
87. Howlett SE, Grandy SA, Ferrier GR. Calcium spark properties in ventricular myocytes are altered in aged mice. Am J Physiol Heart Circ Physiol. 2006; 290: H1566-74.
88. Feridooni HA, Dibb KM, Howlett SE. How cardiomyocyte excitation, calcium release and contraction become altered with age. J Mol Cell Cardiol. 2015; 83: 62-72.
89. Goldfracht I, Protze S, Shiti A, Setter N, Gruber A, Shaheen N, et al. Generating ring-shaped engineered heart tissues from ventricular and atrial human pluripotent stem cell-derived cardiomyocytes. Nat Commun. 2020; 11: 75.
90. Shiti A, Goldfracht I, Shaheen N, Protze S, Gepstein L. Reply to 'Are atrial human pluripotent stem cell-derived cardiomyocytes ready to identify drugs that beat atrial fibrillation?'. Nat Commun. 2021; 12: 1729.
91. Christ T, Lemoine MD, Eschenhagen T. Are atrial human pluripotent stem cell-derived cardiomyocytes ready to identify drugs that beat atrial fibrillation? Nat Commun. 2021; 12: 1725.

Bioorganic Chemistry 109 (2021) 104739

Contents lists available at ScienceDirect

Bioorganic Chemistry

journal homepage: www.elsevier.com/locate/bioorg

Targeting GRP receptor: Design, synthesis and preliminary biological characterization of new non-peptide antagonists of bombesin

Alessandro Palmioli [a,b], Gabriella Nicolini [b,c], Farida Tripodi [a], Alexandre Orsato [a,d], Cecilia Ceresa [b,c], Elisabetta Donzelli [b,c], Martina Arici [a], Paola Coccetti [a], Marcella Rocchetti [a], Barbara La Ferla [a,*], Cristina Airoldi [a,b,*]

[a] Department of Biotechnology and Biosciences, University of Milano - Bicocca, P.zza della Scienza 2, 20126 Milan, Italy
[b] Milan Center for Neuroscience, University of Milano-Bicocca, P.zza dell'Ateneo Nuovo 1, 20126 Milano, Italy
[c] School of Medicine and Surgery, Experimental Neurology Unit, University of Milano - Bicocca, Via Cadore 48, 20900 Monza, MB, Italy
[d] Departamento de Química, CCE, Universidade Estadual de Londrina, CEP 86057-970 Londrina, Paraná, Brazil

ARTICLE INFO

Keywords:
Gastrin Releasing Peptide (GRP)
GRP receptors (GRP-R)
Bombesin (BN)
Circular dichroism
NMR-based structural and conformational analysis
MM and MD conformational studies
GRP-R antagonists
GRP-R ligands

ABSTRACT

We report the rational design, synthesis, and *in vitro* preliminary evaluation of a new small library of non-peptide ligands of Gastrin Releasing Peptide Receptor (GRP-R), able to antagonize its natural ligand bombesin (BN) in the nanomolar range of concentration.

GRP-R is a transmembrane G-protein coupled receptor promoting the stimulation of cancer cell proliferation. Being overexpressed on the surface of different human cancer cell lines, GRP-R is ideal for the selective delivery to tumor cells of both anticancer drug and diagnostic devices. What makes very challenging the design of non-peptide BN analogues is that the 3D structure of the GRP-R is not available, which is the case for many membrane-bound receptors. Thus, the design of GRP-R ligands has to be based on the structure of its natural ligands, BN and GRP.

We recently mapped the BN binding epitope by NMR and here we exploited the same spectroscopy, combined with MD, to define BN conformation in proximity of biological membranes, where the interaction with GRP-R takes place. The gained structural information was used to identify a rigid *C*-galactosidic scaffold able to support pharmacophore groups mimicking the BN key residues' side chains in a suitable manner for binding to GRP-R.

Our BN antagonists represent hit compounds for the rational design and synthesis of new ligands and modulators of GRP-R. The further optimization of the pharmacophore groups will allow to increase the biological activity. Due to their favorable chemical properties and stability, they could be employed for the active receptor-mediated targeting of GRP-R positive tumors.

1. Introduction

Peptide receptors have been shown to be over-expressed in several types of human neoplasia [1,2]. These observations have led to the development of diagnostic and radio-therapeutic applications, using radiolabeled peptides for *in vivo* receptor scintigraphy or peptide radiotherapy [3] in tumor patients. Furthermore, peptides linked to cytotoxic drugs [4] or stable peptide agonists or antagonists [5,6] have been used for long-term targeted chemotherapy in animal tumor models.

Bombesin (BN), a 14 amino acid (Pyr-QRLGNQWAVGHLM-NH_2) peptide isolated in amphibians, and its mammalian counterpart gastrin-releasing peptide (GRP) [7], a 27 amino acid peptide that shares the same C-terminal decapeptide with BN with the exception of one amino acid, are hormonally active peptides that function as autocrine or paracrine growth factors in a variety of cells. Their sequence homology accounts for an identical physiological action, triggered by the ability to interact with the same receptors.

BN/GRP receptors (GRP-R) are G-protein coupled receptors (GPCR) involved in several biological processes. The binding of BN/GRP to their cognate receptors leads to a rapid intracellular calcium mobilization from internal stores [8,9], as well as to the activation of multiple transduction pathways, which act synergistically to promote cell

* Corresponding authors at: Department of Biotechnology and Biosciences, University of Milano - Bicocca, P.zza della Scienza 2, 20126 Milan, Italy (C. Airoldi).
E-mail addresses: barbara.laferla@unimib.it (B. La Ferla), cristina.airoldi@unimib.it (C. Airoldi).

https://doi.org/10.1016/j.bioorg.2021.104739
Received 29 December 2020; Received in revised form 3 February 2021; Accepted 4 February 2021
Available online 17 February 2021

proliferation [8]. For this reason, these receptors play an important role in cancer development and are frequently over-expressed in many human tumors [1]. The involved growth mechanisms and the possible therapeutic potential have been well studied in the case of GRP-R, particularly in lung, prostate and head/neck cancer cells. This evidence suggests GRP-R as a very good marker of carcinogenesis and possible target for receptor-mediated tumor targeting [10].

By preventing the receptor activation, GRP-R antagonists could have a powerful application as potential anticancer compounds [11,12]. On the other hand, GRP-R agonists can be a powerful tool for the development of new tumor targeting strategies. In a mechanism that is typical for GPCR, the GRP-R is internalized by endocytosis after binding to agonists [13]. This feature can be exploited to promote the selective internalization of cytotoxic drugs by tumor cells over-expressing GRP-R, through the chemical conjugation of anticancer agents with GRP-R agonists. However, also receptor antagonists, when showing a high affinity for the target, can be exploited to deliver selectively cytotoxic drugs at the tumor site, providing therapeutic effects [14,15]. High affinity GRP-R ligands, independently of their putative agonistic/antagonistic activity, can also deliver diagnostic tools at the tumor site [16].

Notably, the use of GRP-R natural ligands GRP and BN as peptide carriers for tumor targeting and/or therapy is anyway a very limited strategy, because of their low metabolic stability [17–19]. Thus, the design of synthetic and chemically stable GRP/BN analogues presenting agonist/antagonist activities, and, possibly, also an increased affinity for the receptor is of paramount importance.

Both GRP-R agonists and antagonists have been reported [17–19], but these compounds are essentially peptide-pseudopeptide in nature, and, consequently, due to the presence of amide bonds, proteolytically unstable under physiological conditions. This evidence prompted the search for GRP-R non-peptide ligands. Nevertheless, the only non-peptide antagonist is the compound PD176252 and its derivatives; however, it has poor selectivity, due to its excessive conformational flexibility [20,21].

What makes very challenging the design of non-peptide BN analogues is that the three-dimensional structure of the GRP-R is not available, which is the case for many membrane-bound receptors. Thus, the design of GRP-R ligands must be based on the structure of its natural ligands, BN and GRP. For this reason, we recently exploited advanced Nuclear Magnetic Resonance (NMR) spectroscopy techniques to study the binding of BN to GRP-R, identifying the structural determinants of this interaction [22]. Saturation Transfer Difference (STD) NMR experiments acquired on samples containing BN and tumor cells expressing the receptor on their surface afforded high-quality spectra, allowing the identification of Trp and His belonging to the C-terminal fragment of the peptide among the most important for GRP-R recognition and binding [22].

Moreover, in this paper we combined Nuclear Overhauser Effect SpectroscopY (NOESY) experiments and molecular dynamic (MD) simulations verifying the propensity of BN to adopt an α-helix conformation in proximity of the cell membrane.

Hence, starting from the structural information gained, we designed a small library of GRP-R potential ligands.

To this end, we exploited a carbohydrate scaffold, already reported by our group [23], functionalizable at four different positions, with as many pharmacophore groups. The cyclic structure of carbohydrates, characterized by several hydroxyl groups presenting specific spatial orientations, can be indeed properly functionalized for the generation of libraries of compounds by the combinatorial decoration with different pharmacophores [24–26]. Moreover, at variance with peptides, compounds based on scaffolds from carbohydrate-derivatives, for example *C*-glycosides, have a high chemical and metabolic stability and a poor conformational flexibility, allowing to increase ligands' affinity and selectivity for the receptor.

The ability of the selected *C*-glycidic scaffold to bear the putative pharmacophores properly oriented in space for the interaction with GRP-R was assessed by molecular mechanics (MM) and molecular dynamics (MD) simulations.

After their synthesis, compounds were preliminary evaluated for their ability to act as agonists or antagonists of the receptor.

2. Results and discussion

2.1. Bombesin conformational analysis

BN conformation has been studied in various solvents, demonstrating that it adopts an unordered structure in aqueous media and in dimethyl sulfoxide [27], while a helical structure has been observed in aqueous solutions containing trifluoroethanol (TFE) [28] or membrane mimetics [29,30]. To deepen this point, we applied circular dichroism (CD) and NMR spectroscopy to characterize BN conformational behavior in presence of sodium dodecyl sulphate (SDS) micelles, a biological membrane mimetic [31] recently employed for the study of its effect on neuromedin C (NMC) conformation [32].

First, we performed a CD analysis of BN and BN (8-14), the minimal carboxyl fragment interacting with the receptor, acquired in absence or presence of SDS micelles (Supporting information - Figure S1). The CD spectra of BN and BN (8-14), acquired in an aqueous solution, indicate that in this condition the peptides are disordered, as evidenced by the minimum located at 197 nm (Supporting information - Figure S1, blue, red and green spectra) [33].

However, in both cases the addition of 150 mM SDS [32] induced a conformational change characterized by a notable increment of the α-helical content and a decrement of random coil regions, as indicated by the positive band around 190 nm and the increase of the negative ellipticities around 206 and 220 nm (Supporting information - Figure S1, violet, yellow, black spectra). This behavior was independent from temperature, as experiments collected at 10, 25 and 37 °C gave overlapping spectra. These results, in agreement with previous studies performed in presence of membrane mimetics, indicate that both peptides adopt a predominant α-helix conformation upon addition of SDS micelles, at all the three tested temperatures.

Accordingly, NMR spectroscopy also supported this conformational change. The direct comparison of ^{1}H NMR (Supporting information - Figure S2) and 2D-NOESY (Supporting information - Figure S3) spectra acquired in absence (A) or presence (B) of 150 mM d_{25}-SDS at pH 7.0, 25 °C, reveals dramatic differences. Analogous results were obtained when experiments were performed at 10 or 37 °C (data not shown). In fact, the inter-residual NOE connectivity in the fingerprint region of NOESY spectra (Supporting information - Figure S3) suggested an unordered (Supporting information - Figure S3-A) vs a folded (Supporting information - Figure S3-B) conformation of the peptide. The ^{1}H and ^{15}N NMR assignments (Supporting information - Table S1) were exploited to calculate the solution structures of BN in presence of SDS micelles. The secondary structure and RCI-S2 prediction window suggested the involvement of all BN residues in a α-helix secondary structure (Supporting information - Figure S4). NOEs intensities were used as geometrical restraints during the simulated annealing molecular dynamics (SA-MD) calculations performed through the CYANA software [34,35]. As reported in Fig. 1A, the corresponding BN structure obtained in presence of the membrane mimetic resembles an α-helix. The tridimensional structure is freely available as .pdb files on Mendeley Data repository [36].

The same conformational behavior was recently described for neuromedin C (NMC) [32], an endogenous decapeptide (GNHWAVGHLM-NH_2) highly conserved in mammals that exerts a variety of biological effects both on the central nervous system (CNS) and in the gastrointestinal tract [37], belonging to the bombesin-like peptide family. As confirmation, BN and NMC conformations obtained in presence of SDS micelles present a significant overlap (Fig. 1B) showing the same arrangement both of the backbone and of the side chains of the amino acids important for the binding to the receptor (Trp8, His12 and Leu13

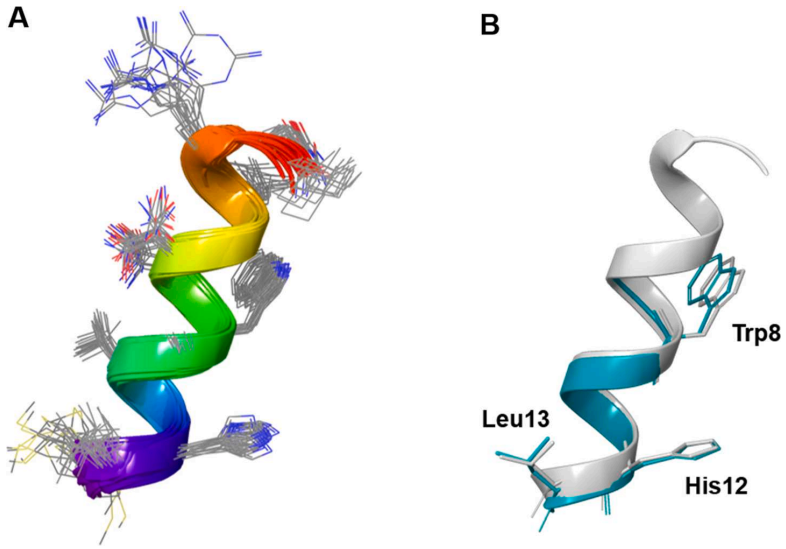

Fig. 1. **(A)** Bundle of the 10 best BN conformers calculated through CYANA from NOESY conformational restrains obtained in presence of SDS micelles. **(B)** Superimposition of BN and NMC structures [32] (one conformer for each) both calculated in presence of SDS micelles.

in BN) [22].

2.2. GRP-R ligands design and synthesis

The rational design of the non-peptidic BN-like compounds was based on the analysis of BN conformation in SDS micelles solution, supporting its α-helical conformation (Fig. 1A) in proximity of biological membranes, where the interaction with GRP-R takes places, and the BN binding epitope recently reported by our group [22], indicating the involvement of residues Trp8, His12, Leu13 and, with a lower extent, Met14 side chains in its molecular recognition of the receptor. These structural data were exploited to design BN analogues based on a rigid scaffold able to spatially orient, in an effective way, the potential pharmacophores, as putative mimetics of the side chains of BN amino-acids mainly involved in the binding to GRP-R.

To this end, we evaluated the use of different glycidic scaffolds deriving from natural sugars and their more stable derivatives (eg, *C*-glycosides) [38]. We selected the scaffold depicted in Fig. 2, presenting four different possible sites of functionalization and already described by our group [23]. This scaffold was used to design a small library of compounds, reported in Fig. 2, bearing the putative pharmacophores properly oriented in space.

The proper pharmacophores' orientation was supported by the conformational analysis made on compound **GRPR-L3** and carried out using molecular mechanics (MM) and molecular dynamics (MD) simulations. Calculations were performed by using AMBER* force field [39], as implemented in the MacroModel program (Schrödinger Suite) [40] (Supporting information - Figure S5A). Then the relative spatial arrangement of **GRPR-L3** pharmacophores was compared with that of Trp8, His12 and Leu13 side chains in BN structure as calculated in

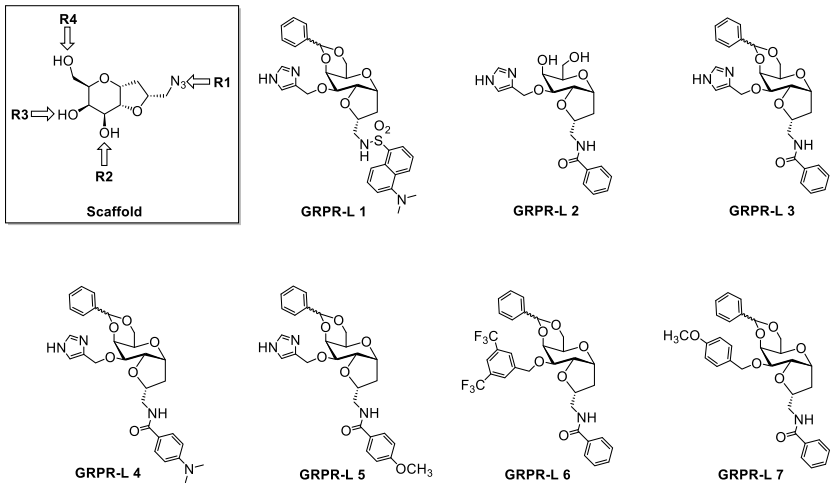

Fig. 2. Structures of the bicyclic *C*-galactosidic scaffold, with indication of the four (R1, R2, R3 and R4) and the putative GRPR ligands (**GRPR-L**) **1–7**.

presence of membrane mimetic (Fig. 1A and B). Fig. 3 reports the superimposition of the two structures and clearly shows that the imidazole ring inserted in **GRPR-L3** structure as R2 group overlaps with the side chain of BN His12, the aromatic entity introduced as R1 with the indole ring of Trp8, while benzylidene in position R3 and R4 is very closed to the side chains of Leu13, reproducing a hydrophobic environment suitably spaced from the other two groups of the BN binding epitope.

All the GRP-R ligands were prepared from the rigid bicyclic *C*-galactosidic scaffold bearing a furan ring fused to the C1-C2 bond of the sugar moiety, substituted with an azido-methylene group with an *(R)* configuration on C8 (compound **4*(R)***). The synthesis of **3**, as a mixture of diastereoisomers at C8, is easily achievable from commercially available methyl-α-D-galactopyranoside and has been previously reported [23]. The regioselective introduction of a benzylidene group on C4 and C6 hydroxyls allowed the separation of the two diastereoisomers affording the core structure, starting material for the synthesis of the GRPR ligands library (Scheme 1).

The synthesis of a first set of ligands (**GRPR-L1, 3, 4, 5**) containing two common pharmacophoric entities, the 4–6 *O*-benzylidene moiety and the imidazole group on C3-OH, and bearing different amide derivatives, is described in Scheme 2.

Intermediate **4*(R)*** was successfully alkylated at C3-OH with a trityl protected imidazole [41] (**5**, NaH, THF/DMF) with acceptable yields (77%, compound **6**), attempts with differently protected imidazole moieties such as BOC and Cbz did not lead to the desired alkylation product but instead basic reaction conditions lead to the transfer of the protective group from the imidazole to the sugar C3-OH. The azide was then selectively reduced through catalytic hydrogenation (H_2, Pd Lindlar), and the obtained amine **7** was acylated with different aromatic acyl-chlorides to afford the protected ligands compounds **8**, **9**, **10**, **11** in high yields. Removal of the trityl protection in mild acidic conditions (5% HCOOH in MeOH) afforded **GRPR-L1, 3, 4, 5.** Compound **9** was also deprotected from the benzylidene moiety (TFA 50%), in order to afford **GRPR-L2**, containing only two pharmacophoric groups.

The second set of GRP-R ligands (**GRPR-L6** and **7**) (Scheme 3) are analogues of **GRPR-L3** but carry a different pharmacophoric group on the C3-OH.

The groups were selected in order to verify the importance of the imidazole entity and to simultaneously explore the possibility to introduce detectable groups/elements that could be exploited by diagnostic techniques such as fluorinated groups (CF_3) that can be easily detected by NMR. Compound **4*(R)*** was alkylated at C3-OH with different benzyl halide derivatives (NaH, THF/DMF), affording compounds **12**–**14** with good yields. These were then converted to the final ligands **GRPR-L6** and **L7** through reduction of the azido group followed by reaction with benzoyl chloride.

2.3. Screening and biological evaluation of new GRP-R ligands.

Compounds presenting three pharmacophoric groups, and therefore

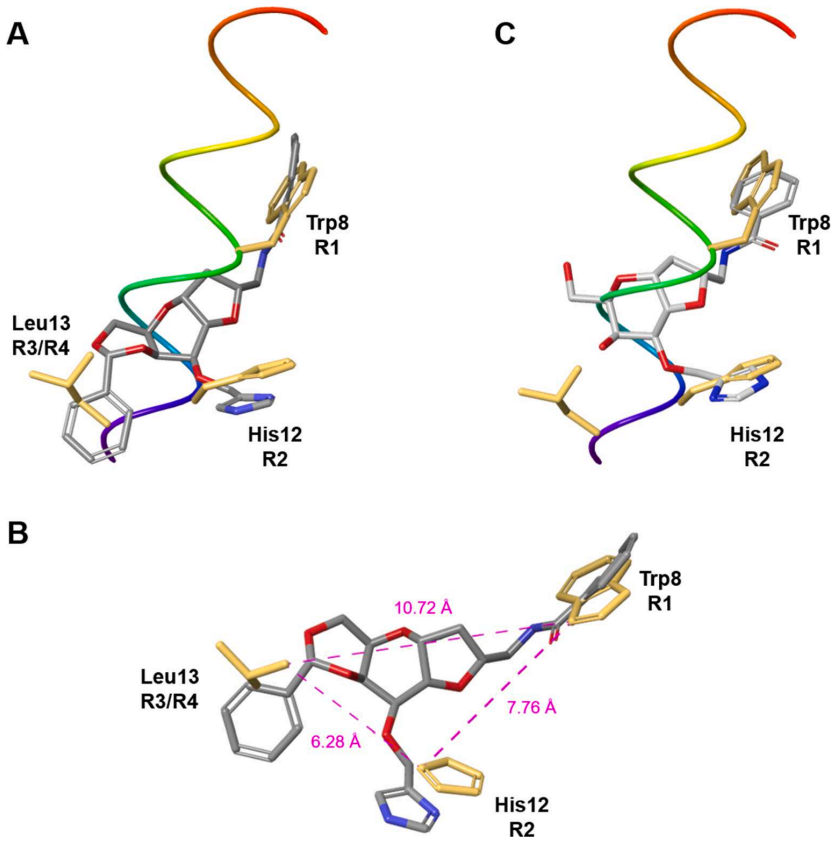

Fig. 3. **(A)** Superimposition of BN structure calculated in presence of SDS micelles and **GRPR-L3** structure obtained through MM and MD calculations; **(B)** Distances among BN Trp, His and Leu residues involved in GRP-R binding and their overlap with R1, R2 and R3/R4 putative pharmacophores in **GRPR-L3** structure; **C)** Superimposition of BN structure calculated in presence of SDS micelles and **GRPR-L2** structure obtained through MM and MD calculations.

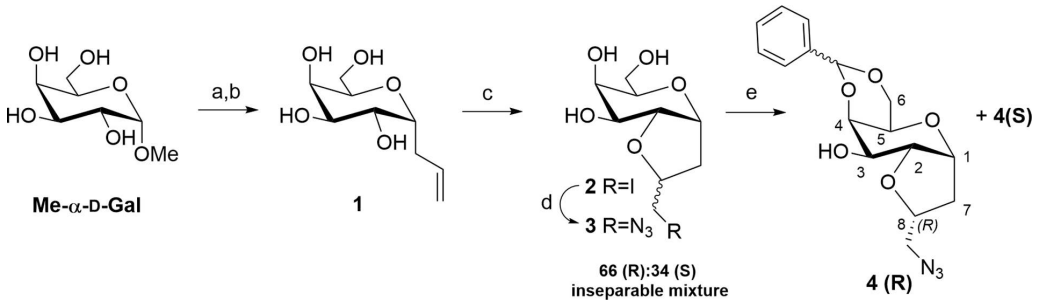

Scheme 1. Synthesis of intermediate **4(R)**, used as scaffold template: (a) BSTFA, MeCN dry, reflux, 1 h then (b) Allyl-TMS, TMSOTf rt, O.N. 74%; (c) NIS, DMF dry, 78%; (d) NaN3, DMF dry, quant %; (e) benzaldehyde dimethyl acetal, CSA, DMF dry, 70 °C, in vacuo, 75%, 48%(R) + 27% (S).

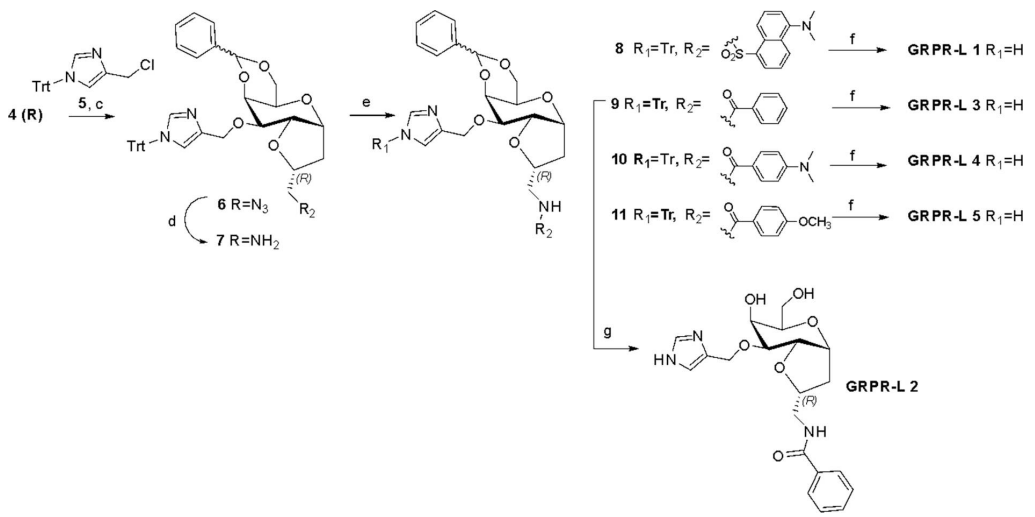

Scheme 2. Synthesis of **GRPR-L 1**–**5**: (c) NaH, THF/DMF dry O.N. rt, 77%; (d) H_2, Pd Lindlar, MeOH deg then e) Et_3N, DCM dry; Dansyl-Cl, 92% (**8**); BzCl, 98% (**9**); 4-(Dimethylamino)benzoyl chloride, 87% (**10**); 4-Methoxybenzoyl chloride, 88% (**11**) (f) HCOOH 5%, MeOH dry, 50 °C; 92% (**GRPR-L 1**); quant. yield % (**GRPR-L 3**); 92% (**GRPR-L4**); 83% (**GRPR-L5**); g) TFA 50% in MeOH dry, quant. Yield (**GRPR-L 2**).

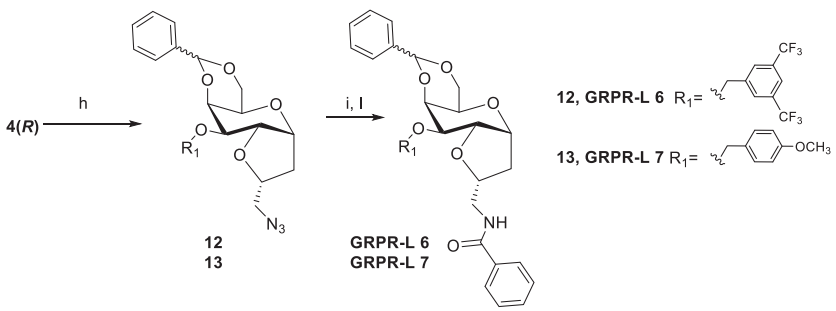

Scheme 3. Synthesis of **GRPR-L6, 7**: (h) NaH, THF/DMF dry O.N. rt; 3,5-Bis(trifluoromethyl)benzyl chloride, 73% (**12**); 4-Methoxybenzyl chloride, 87% (**13**); (i) H_2, Pd Lindlar, MeOH deg, then (l) BzCl, Et_3N, DCM dry, 89% (**GRPR-L6**); 87% (**GRPR-L7**).

more promising as potential ligands, were screened for their ability to agonize/antagonize BN activity in PC3 (Prostate Cancer) cells, chosen as experimental models because of their GRP-R overexpression [42,43]. We tested their ability to stimulate intracellular Ca^{2+} mobilization, as expected for BN agonist, or decrease BN-induced intracellular Ca^{2+} mobilization, as observed for antagonists. PC3 cells were loaded with the Ca^{2+} sensitive dye Fluo4-AM and intracellular Ca^{2+} mobilization was measured in the presence of each ligand. No compound showed significant agonist activity. However, our compounds showed, although with different efficacy, an antagonistic effect against BN-induced Ca^{2+}

mobilization. Fig. 4 reports the increase of Ca^{2+} levels induced by 200 nM BN with or without 30 min pre-treatment with 50 nM test compounds.

As BN binding to GRP-R stimulates cell proliferation, our molecules' ability to counteract this effect was assayed. PC3 cells were treated with 50 nM of the different compounds (GRPR-L) and then with BN to stimulate proliferation. **GRPR-L4-7** showed a very potent effect in preventing PC3 BN-induced proliferation (Fig. 5A).

Moreover, to validate the results we performed the same experiment in a second cell model represented by MCF-7 (Michigan Cancer Foundation-7), a breast cancer cell line also characterized by GRP-R overexpression whose proliferation is increased after treatment with BN [44]. Results depicted in Fig. 5B confirmed those observed on PC3 cells except for compound **GRPR-L7** whose activity, in this case, was not statistically significant. This evidence fits with the lack of inhibition of BN-induced Ca^{2+} mobilization (Fig. 4) and suggests a different molecular mechanism responsible for **GRPR-L7** inhibition of PC3 growth.

Collectively, these preliminary experiments performed to characterize GRPR-L's ability to prevent the BN-induced activation of GRP-R clearly demonstrated that compounds **GRPR-L4-6** are able to antagonize both the BN-induced Ca^{2+} mobilization and the BN-induced proliferation of PC-3 and MCF-7 cell lines in the nanomolar range of concentration. These bioactive compounds present three potential pharmacophore groups: a benzylidene moiety in position R3 and R4, an imidazole (**GRPR-L4** and **L5**) or a 3,5-bis-(trifluoromethyl) phenyl (**GRPR-L6**) group in R2 and a phenyl amide, with or without *para* substituents, in R1 (Fig. 2). These findings support our scaffold ability to orient the pharmacophore groups in an effective way to promote interaction with the receptor mimicking the 3D pharmacophore template of the natural ligands BN and NMC (Fig. 1B).

Moreover, due to the poor water solubility of **GRPR-L4-6**, we decided to also submit compound **GRPR-L2** to proliferation assays on PC3 and MCF-7 cell lines. **GRPR-L2** is a synthetic variant devoided of the benzylidene pharmacophore that therefore presents a good solubility in water. Very interestingly, **GRPR-L2** showed an ability to counteract the BN-induced cell proliferation comparable to the best inhibitors (Fig. 5). Notably, the superimposition of BN conformation obtained in presence of SDS micelles (Fig. 1) and **GRPR-L2** structure as calculated by MM and MD (Supporting information - Figure S5B) showed that also in this case the pharmacophores in R1 and R2 overlap with Trp8 and His12 side chains (Fig. 3C). This evidence suggested that the presence of two aromatic entities on the bicyclic scaffold, mimicking Trp indole and His imidazole rings and oriented in a suitable manner, could be enough to obtain a high affinity for the receptor and a considerable antagonistic activity.

The higher water solubility of compound **GRPR-L2**, together with the presence of two free hydroxyl groups exploitable for further chemical functionalization, makes also this GRP-R ligand an interesting hit compound for the development of a new library of GRP-R ligand and modulators.

3. Experimental section

3.1. General procedures and materials

BN and BN (8-14) were purchased as lyophilized powders from Bachem AG (Bubendorf, Switzerland). Chemicals were purchased from Sigma Aldrich (St. Louis, MO, US) and Thermo Fisher Scientific (Waltham, MA, US) and used without further purification, unless otherwise indicated. When anhydrous conditions were required, the reactions were performed in oven-dried glassware under argon atmosphere. Anhydrous solvents over molecular sieves were purchased from Acros Organics® (Thermo Fisher Scientific, Waltham, MA, US) with a content of water $\leq$ 50 ppm. Thin layer chromatography (TLC) was performed on silica gel $60F_{254}$ plates or RP-C18 Silica plates (Merck Darmstadt, Germany) and visualized with UV detection (254 nm and 365 nm) or using appropriate developing solutions. Flash column chromatography was performed on silica gel 230–400 mesh (Merck KGaA, Darmstadt, Germany), according to the procedure described in the literature. Automated flash chromatography was performed on a Biotage® Isolera™ Prime system (Biotage, Uppsala, Sweden). NMR experiments were recorded on a Varian 400 MHz or a Bruker Avance III 600 MHz equipped with a cryogenic probe instrument at 298 K. Chemical shifts (δ) are reported in ppm downfield from the residual solvent peak, whereas coupling constants (*J*) are stated in Hz. The ^{1}H and ^{13}C NMR resonances of compounds were assigned by means of COSY and HSQC experiments. NMR data processing was performed with MestReNova v14.1 software (Mestrelab Research, Santiago de Compostela, Spain). Mass spectra (ESI-MS) were recorded on a Sciex 3200 Qtrap®.

3.2. BN conformational studies

3.2.1. Circular dichroism (CD)

CD spectra of BN and BN(8–14) were obtained on a Jasco-815 spectropolarimeter equipped with a thermostated cell holder controlled by a Jasco Peltier element (Jasco Europe S.R.L., LC, Italy). Far-UV CD spectra were acquired from 260 to 185 nm at 10, 25 or 37 °C in a 1 mm pathlength quartz cuvette at a BN or BN(8-14) concentration of 75 μM in 10 mM phosphate buffer (pH 7.4) in absence or in presence of 150 mM SDS. The scan speed was 20 nm/min with a response time of

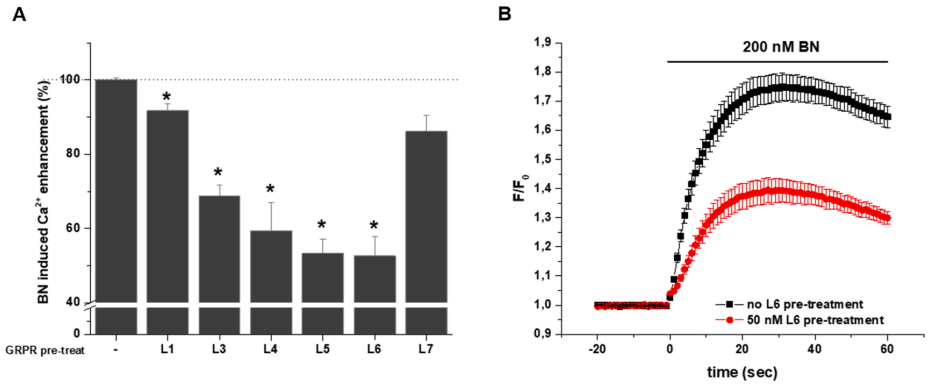

Fig. 4. (**A**) Intracellular Ca^{2+} mobilization in PC3 cells induced by 200 nM BN with or w/o pre-treatment with 50 nM GRPR-L. *$p < 0.05$ vs BN w/o GRPR-L pre-treatment (unpaired *t*-test) (two independent experiments with six replicates). (**B**) Time dependent changes of BN-induced Ca^{2+} enhancement with (red line) or w/o **GRPR-L6** pre-treatment (black line). (For interpretation of the references to colour in this figure legend, the reader is referred to the web version of this article.)

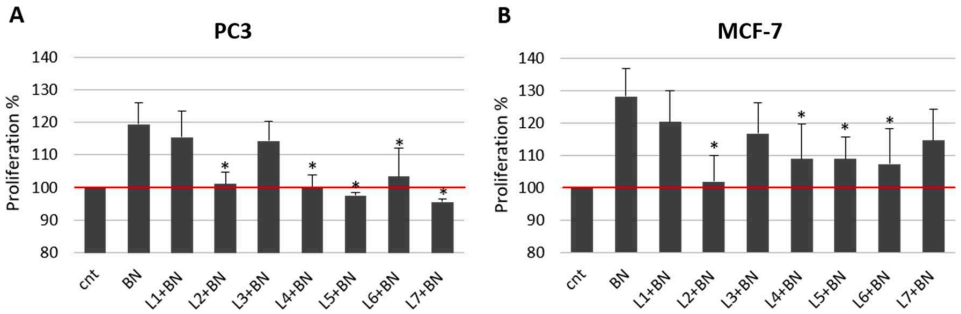

Fig. 5. PC3 and MCF-7 proliferation rate after treatment with BN in the absence or presence of 50 nM of test compounds (GRPR-L). Proliferation assay was performed after 24 h of treatments. *$p < 0.05$ relative to BN treatment.

2 s and a step resolution of 0.2 nm, whereas 3 scans were accumulated. Buffer spectra were subtracted for all spectra.

3.2.2. NMR spectroscopy and SA-MD

NMR experiments in presence of SDS micelles. Samples for the NMR-based conformational studies were prepared by dissolving the peptide in 500 μL of PB or d_{25}-SDS aqueous solution (9:1 H_2O:D_2O, PB buffer at pH 7.0) to make a final BN concentration of 0.7 mM and a SDS final concentration of 150 mM. The NMR spectra were recorded at 10, 25 or 37 °C with a Bruker Avance III 600 MHz NMR spectrometer equipped with a 5 mm QCI cryo-probe (Bruker Inc., Billerica, MA, US). 1- and 2D spectra were recorded suppressing water signal by excitation sculpting. For each of these experiments, 512 t1 increments were used. 32, 64 and 96 transients were collected for $^1H,^1H$ TOCSY, $^1H,^1H$ NOESY, $^1H,^{15}N$ HSQC experiments respectively. The TOCSY spectra were recorded using the DIPSI pulse sequence with mixing times (spin-lock) of 60–80 ms. The NOESY experiments were acquired with mixing times of 50–100 ms. For reference, NOESY experiments on BN dissolved in PB a NOE mixing time in the range 300–500 ms was used. Spectra were acquired and processed using the TopSpin™ (Bruker Inc, Billerica, MA, US) software. The peptide resonance assignments were obtained using standard strategies based on the 2D NMR experiments.

BN structure calculation. Interactive peak picking using the CARA software (http://cara.nmr-software.org/portal/) was exploited to generate the peak lists for NOESY spectra. The NOESY cross-peak volumes were determined using the automated CARA peak integration routine. Conversion of NOE peak intensities to distance restraints was done using automatic calibration as implemented in CYANA 3.98 [34,35]. Prediction of the peptide backbone torsion angles from chemical shifts obtained through TALOS+ [45]. The three-dimensional structures of BN in presence of SDS micelles were determined using the standard protocol of combined automated NOE (nuclear Overhauser effect) assignment and the structure calculation implemented in CYANA. Seven cycles of combined automated NOESY assignment and structure calculations were followed by a final structure calculation. The structure calculation started in each cycle from 200 randomized conformers and the standard simulated annealing schedule was used. The 20 conformers with the lowest final CYANA target function values were retained for analysis and passed to the next cycle.

The Maestro suite [46] as implemented in Schrödinger Release 2016-4 was used to visualize 3D structures.

3.3. Conformational studies on potential GRP-R ligands

Molecular mechanics and dynamics studies were conducted with MacroModel as implemented in Schrödinger Release 2016-4 [40], using AMBER* force field [39]. The starting coordinates for dynamics calculations were those obtained after energy minimization of the structures, followed by conformational search. A systematic variation of the torsional degrees of freedom of the molecules allowed different starting structures to be constructed that were further minimized to provide the corresponding local minima. For each compound, the conformer with the lowest energy was considered. Simulations were carried out over 5 ns at 298 K with a 0.25 fs time step and a 20 ps equilibration step; 100 structures were sampled and minimized for further analysis. The continuum GB/SA solvent model was employed and the general PRCG (Polak–Ribiere Conjugate Gradient) method for energy minimization was used. An extended cut-off was applied and the SHAKE procedure for bonds was not selected.

3.4. Chemical synthesis

Compounds **1**–**3** [23] and compound **5** [41] were synthetized according to slightly modified procedures described in literature. The synthesis and characterization, including NMR spectra, of all intermediates, compounds **1**–**14**, are fully reported in Supplementary materials.

Compound 4(R). To a stirred solution of **3** (1.3 g, 5.32 mmol) in anhydrous DMF (10 mL), benzaldehyde dimethyl acetal (927 μL, 6.38 mmol) and (±)-10-Camphorsulfonic acid (CSA) (494 mg, 2.13 mmol) were added under argon atmosphere and the resulting mixture was stirred at 70 °C under reduced pressure for 2 h. Then, the reaction was quenched by addition of Et_3N (333 μL, 2.39 mmol) and the solvent was removed under reduced pressure. The crude was purified by automated flash chromatography (Hex:AcOEt gradient elution) obtaining pure compound 4(R) as mixture of inseparable diastereoisomers (73:27) at benzylidene function (yellow oil, 830 mg, 44% yield, total recovery 75%). TLC RF = 0.47 (petroleum ether: AcOEt 1:1). ^1H NMR (400 MHz, Methanol-d_4) δ 7.58–7.45 (m, 2H, H17, H21), 7.41–7.31 (m, 3H, H18, H19, H20), 5.76 (s, H15 minor isomer), 5.58 (s, 1H, H15), 5.04 (dt, J = 7.5, 4.1 Hz, 1H, 2), 4.74 (d, J = 8.3 Hz, H2 minor isomer), 4.68–4.61 (m, minor isomer), 4.36 (bt, 1H, H3), 4.30 (m, minor isomer), 4.25 (d, J = 12.7 Hz, 1H, H13′), 4.19–4.13 (m, 1H, H13″), 4.08 (dt, J = 10.9, 5.4 Hz, 1H, H10), 4.03 (dd, J = 5.5, 2.1 Hz, H7 minor isomer), 4.00–3.95 (m, 1H, H7), 3.94 (m, H4, H10 minor isomer), 3.88–3.81 (m, 1H, H8), 3.71 (s, 1H, H4), 3.68–3.62 (m, minor isomer), 3.58 (dd, J = 13.2, 3.1 Hz, H12′ minor isomer), 3.44 (dd, J = 12.9, 3.4 Hz, 1H, H12′ and H12″ minor isomer), 3.33 (m, 1H, H12″ over solvent peak), 2.50 (dt, J = 15.1, 7.8 Hz, H11′ minor isomer), 2.31 (dt, J = 14.3, 7.3 Hz, 1H, H11′), 1.94–1.88 (m, H11″ minor isomer), 1.83 (ddd, J = 13.5, 6.9, 3.2 Hz, 1H, H11″). ^{13}C NMR: (100 MHz, Methanol-d_4) δ 139.77 (C16), 138.41 (C16 minor isomer), 130.67, 129.90, 129.17, 129.11, 128.42, 127.45 (Ph), 105.05(C15 minor isomer), 101.87 (C15), 85.10 (C7), 78.46 (C10), 78.33 (C10 minor isomer), 78.17 (C2), 76.73 (C3), 76.08(C7 minor isomer), 75.38 (C2 minor isomer), 74.52 (C8), 73.60 (minor isomer), 73.35 (C13), 73.18 (minor isomer), 70.58 (C4 minor isomer), 68.65 (C4), 62.79 (minor isomer), 61.53 (minor isomer), 55.41 (C12), 54.34 (C12 minor isomer), 37.72 (C11 minor isomer), 36.19 (C11). MS (ESI)

calculated for [$C_{16}H_{19}N_3O_5$] 333.13; found 334.2 [M + H]$^+$, 356.2 [M + Na]$^+$, 351.3 [M + H_2O + H]$^+$.

GRPR-L1. To a stirred solution of **8** (28.3 mg, 0.033 mmol) in anhydrous MeOH (1.7 mL), formic acid (87 μL) was slowly added at 0 °C and the resulting mixture was heated at 50 °C and stirred for 5 h under argon atmosphere. Then, reaction was quenched by addition of Et_3N (100 μL) and concentrated under reduced pressure. The crude was purified by automated flash chromatography (AcOEt:MeOH gradient elution) obtaining pure compound **GRPR-L1** (19 mg, 91% yield). TLC RF = 0.27 (AcOEt:MeOH 9:1). ^{1}H NMR (400 MHz, Chloroform-*d*) δ 8.49 (d, J = 8.5 Hz, 1H, Harom), 8.40 (d, J = 8.6 Hz, 1H, H14), 8.37 (d, J = 8.6 Hz, H14* minor isomer), 8.20 (ddd, J = 7.3, 2.8, 1.3 Hz, 1H, Harom), 8.15 (s, 1H, H13), 8.08 (s, minor isomer), 7.58–7.41 (m, 3H, Harom), 7.39–7.31 (m, 3H, CH Ph), 7.31–7.27 (m, 2H, CH Ph), 7.15–7.08 (m, 2H, H12, Harom), 6.98 (s, minor isomer), 5.67 (s, H15* minor isomer), 5.42 (s, 1H, H15), 5.05–4.93 (m, 1H, H1), 4.74 (d, J = 12.8 Hz, 1H, H10′), 4.66 (d, J = 12.5 Hz, 1H, H10″), 4.55 (d, J = 12.6 Hz, H10′* minor isomer), 4.50–4.41 (m, H10″* minor isomer), 4.38 (t, J = 2.5 Hz, 1H, H4), 4.23–4.07 (m, 3H, H2, H8, H6″), 3.95 (d, J = 12.2 Hz, 1H, H6′), 3.85 (dt, J = 5.4, 2.6 Hz, 1H, H3), 3.67 (dt, J = 8.6, 4.5 Hz, minor isomer), 3.59 (d, J = 5.9 Hz, 1H, H6′* minor isomer), 3.44 (bm, 1H, H5), 3.24 (dd, J = 14.2, 4.1 Hz, H9′* minor isomer), 3.08 (qt, J = 9.8, 5.4 Hz, 2H, H9), 2.84 (s, 6H, NMe), 2.30 (dt, J = 14.7, 7.4 Hz, H7′* minor isomer), 2.07 (td, J = 13.4, 12.6, 6.1 Hz, 1H, H7′), 2.00 (d, J = 13.6 Hz, H7″* minor isomer), 1.65–1.55 (m, 1H, H7″). ^{13}C NMR (100 MHz, $CDCl_3$) δ 151.95, 151.91 (Cq N), 137.76 (Cq S), 136.64 (Cq), 135.47 (C11), 135.30, 132.42, 131.50, 130.43, 130.29, 130.01, 129.94 (Cq), 129.72 (Cq), 129.68, 129.29, 129.23, 129.05, 128.83, 128.51, 128.42, 128.39, 127.88, 127.45, 126.41, 123.35, 119.42, 119.22, 118.50, 115.40, 115.34, 104.09, 100.81 (C15), 82.68 (C2), 80.17 (C3), 77.66 (C8), 76.54, 75.15, 74.54, 74.28, 72.87 (C4), 72.41 (C6), 72.31, 72.05, 69.98, 67.47, 67.05 (C5), 65.14, 63.64, 61.65 (C10), 47.39 (C9), 45.54 (NMe), 45.13, 36.40, 35.17 (C7). MS (ESI) calculated for [$C_{32}H_{36}N_4O_7S$] 620.23; found 621.5 [M + H]$^+$, 643.3 [M + Na]$^+$, 655.3 [M + K]$^+$.

GRPR-L2. To a stirred solution of **9** (32 mg, 0.044 mmol) in anhydrous MeOH (1 mL), TFA (1 mL) was slowly added at 0 °C and the resulting mixture was heated at 50 °C and stirred for 5 h under argon atmosphere. Then, reaction was quenched by addition of Et_3N (100 μL) and concentrated under reduced pressure. The crude was purified by automated flash chromatography (RP18, H_2O:MeOH gradient elution) obtaining pure compound **GRPR-L2** (17 mg, quant % yield). TLC RF = 0.10 (AcOEt:MeOH 7:3). ^{1}H NMR (400 MHz, Methanol-d_4) δ 8.87 (bs, 1H, H13), 7.87–7.79 (m, 2H, Harom), 7.58–7.50 (m, 2H, H12, H14), 7.50–7.40 (m, 3H, Harom), 4.78 (d, J = 2.2 Hz, 1H, H10), 4.58 (m, 1H, H1), 4.31–4.20 (m, 1H, H8), 4.17 (bt, 1H, H4), 4.01 (dd, J = 10.1, 5.3 Hz, 1H, H2), 3.91–3.76 (m, 2H, H5, H6″), 3.75–3.61 (m, 2H, H3, H6′), 3.57 (ddd, J = 21.6, 13.3, 5.2 Hz, 2H, H9), 2.30 (dq, J = 14.3, 7.3 Hz, 1H, H7″), 1.89 (m, 1H, H7′). ^{13}C NMR (101 MHz, Methanol-d_4) δ 170.47 (CO), 135.67 (Cq), 132.74, 132.69 (C12, C14), 132.133 (C11), 129.64, 129.58, 128.24 (Carom), 82.51 (C2), 81.47 (C3), 78.18 (C8), 78.05 (C5), 74.49 (C1), 67.31 (C4), 61.71 (C10), 60.88 (C6), 45.31 (C9), 35.42 (C7). MS (ESI) calculated for [$C_{20}H_{25}N_3O_6$] 403.17; found 404.1 [M + H]$^+$, 426.1 [M + Na]$^+$.

GRPR-L3. To a stirred solution of **9** (15 mg, 0.02 mmol) in anhydrous MeOH (1 mL), formic acid (54 μL) was slowly added at 0 °C and the resulting mixture was heated at 50 °C and stirred for 5 h under argon atmosphere. Then, reaction was quenched by addition of Et_3N (100 μL) and concentrated under reduced pressure. The crude was purified by automated flash chromatography (AcOEt:MeOH gradient elution) obtaining pure compound **GRPR-L3** (10 mg, quant % yield). TLC RF = 0.19 (AcOEt:MeOH 9:1). ^{1}H NMR (400 MHz, Methanol-d_4) δ 8.36 (s, 1H, H13), 7.90 (s, 1H, H14), 7.82 (m, 2H, Harom), 7.56–7.49 (m, 1H, Harom), 7.49–7.39 (m, 5H, Harom), 7.39–7.30 (m, 3H, Harom), 7.17 (s, 1H, H12), 7.09 (s, H12* minor isomer), 5.74 (s, H15* minor isomer), 5.54 (s, 1H, H15), 5.10 (ddd, J = 7.1, 4.5, 2.7 Hz, 1H, H1), 4.71 (dd, J = 12.8, 2.2 Hz, 2H, H10), 4.64 (dd, J = 8.4, 2.5 Hz, minor isomer), 4.51 (t, J = 2.6 Hz, 1H, H4), 4.42 (d, J = 5.3 Hz, H10* minor isomer), 4.26–4.21 (m, 1H, H6′), 4.22–4.16 (m, 1H, H8), 4.13 (dd, J = 12.6, 2.2 Hz, 1H, H6″), 4.11–4.05 (m, 1H, H2), 4.02–3.98 (m, minor isomer), 3.81 (dd, J = 5.5, 2.1 Hz, 1H, H3), 3.68–3.60 (m, 2H, H5, H9′), 3.54 (dd, J = 13.8, 4.2 Hz, 1H, H9″), 2.52 (dt, J = 14.9, 7.8 Hz, H7′* minor isomer), 2.38 (dt, J = 14.3, 7.4 Hz, 1H, H7′), 1.85 (ddd, J = 13.9, 6.2, 2.6 Hz, 1H, H7″). ^{13}C NMR (100 MHz, Methanol-d_4) δ 170.49 (CO), 139.67 (Cq), 135.81 (Cq), 134.57 (C11), 132.68, 129.97, 129.58, 129.55, 129.19, 129.14, 128.41, 128.38, 128.30, 127.45, 119.98 (C12), 105.09 (C15* minor isomer), 101.80 (C15), 84.33 (C2), 81.52 (C3), 78.60 (C1), 78.51 (C8), 74.05 (C4), 73.52 (C6), 68.79 (C5), 65.59 (C10* minor isomer), 63.57 (C10), 45.22 (C9), 36.76 (C7). MS (ESI) calculated for [$C_{27}H_{29}N_3O_6$] 491.20; found 492.2 [M + H]$^+$, 514.2 [M + Na]$^+$, 530.2 [M + K]$^+$.

GRPR-L4. To a stirred solution of **10** (26 mg, 0.033 mmol) in anhydrous MeOH (1.5 mL), formic acid (75 μL) was slowly added at 0 °C and the resulting mixture was heated at 50 °C and stirred for 5 h under argon atmosphere. Then, reaction was quenched by addition of Et_3N (150 μL) and concentrated under reduced pressure. The crude was purified by automated flash chromatography (AcOEt:MeOH gradient elution) obtaining pure compound **GRPR-L4** (16.4 mg, 92% yield). TLC RF = 0.15 (AcOEt:MeOH 9:1). ^{1}H NMR (400 MHz, Methanol-d_4) δ 8.34 (s, 1H, H14), 8.08 (s, 1H, H12), 7.78–7.65 (m, 2H, Harom), 7.55–7.49 (m, 1H, minor isomer), 7.48–7.40 (m, 2H, Harom), 7.35 (m, 4H, Harom), 6.80–6.63 (m, 2H, Harom), 5.74 (s, H15*minor isomer), 5.54 (s, 1H, H15), 5.17–4.99 (m, 1H, H1), 4.72 (s, 2H, H10), 4.54–4.49 (m, 1H, H4), 4.47–4.34 (m, H10* minor isomer), 4.29–4.21 (m, 1H, H6′), 4.15 (m, 2H, H6‘‘, H8), 4.08 (t, J = 4.5 Hz, 1H, H2), 4.03–3.90 (m, minor isomer), 3.80 (d, J = 5.4 Hz, 1H, H3), 3.67–3.63 (m, 1H, H5), 3.62–3.56 (m, 1H, H9″), 3.56–3.49 (m, 1H, H9′), 3.01 (s, 6H, NMe), 2.99 (s, NMe, minor isomer), 2.50 (dt, J = 14.8, 7.8 Hz, H7′* minor isomer), 2.43–2.29 (m, 1H, H7′), 1.84 (dd, J = 14.7, 10.2 Hz, 1H, H7″). ^{13}C NMR (100 MHz, CD_3OD) δ 170.66, 170.59 (CO), 154.27, 154.24, 139.66, 138.38, 130.70, 130.49, 129.98, 129.88, 129.76, 129.19, 129.15, 128.40, 127.45, 121.94, 121.69, 119.84, 112.18, 112.11, 112.07, 105.08, 101.81 (C15), 84.08 (C2), 81.64 (C3), 78.70 (C8), 78.57 (C1), 78.45, 75.84, 75.62, 74.04 (C4), 73.60, 73.48 (C6), 73.32, 70.77, 68.76 (C5), 68.73, 65.14, 63.13 (C10), 45.08 (C9), 43.34, 40.24, 40.23 (NMe), 38.13, 36.69 (C7). MS (ESI) calculated for [$C_{29}H_{34}N_4O_6$] 534.25; found 535.2 [M + H]$^+$, 557.2 [M + Na]$^+$.

GRPR-L5. To a stirred solution of **11** (26 mg, 0.33 mmol) in anhydrous MeOH (1.6 mL), formic acid (75 μL) was slowly added at 0 °C and the resulting mixture was heated at 50 °C and stirred for 5 h under argon atmosphere. Then, reaction was quenched by addition of Et_3N (100 μL) and concentrated under reduced pressure. The crude was purified by automated flash chromatography (AcOEt:MeOH gradient elution) obtaining pure compound **GRPR-L5** (13 mg, 83% yield). TLC RF = 0.16 (AcOEt:MeOH 9:1). ^{1}H NMR (400 MHz, Chloroform-d) δ 7.87–7.76 (m, 3H, Harom), 7.58–7.48 (m, 1H, H14), 7.45–7.29 (m, 5H, Harom), 7.01 (s, 1H, H12), 6.87 (m, 2H, Harom), 5.74 (s, minor isomer), 5.46 (s, 1H, H15), 5.13 (ddd, J = 6.7, 4.3, 2.1 Hz, 1H, H1), 4.71 (dd, J = 13.3, 9.2 Hz, 2H, H10), 4.66–4.56 (m, minor isomer), 4.50 (d, J = 12.4 Hz, minor isomer), 4.42–4.37 (m, 1H, H4), 4.31 (m, 2H, H8, H6′), 4.23 (dd, J = 8.3, 1.7 Hz, minor isomer), 4.13 (t, J = 4.9 Hz, 1H, H2), 4.05 (dd, J = 12.9, 2.2 Hz, 1H, H6″), 4.01–3.87 (m, minor isomer), 3.80 (s, 1H, minor isomer), 3.79 (s, 3H, OMe), 3.78–3.69 (m, 2H, H3, H9″), 3.63–3.55 (m, 1H, H9′), 3.53 (s, 1H, H5), 2.50 (dt, J = 15.1, 8.1 Hz, minor isomer), 2.37 (dq, J = 15.2, 7.6 Hz, 1H, H7″), 1.92–1.76 (m, 1H, H7′). ^{13}C NMR (100 MHz, $CDCl_3$) δ 167.92 (CO), 167.81, 162.42, 162.25 (Cq), 137.78 (Cq), 136.54 (C11), 130.09, 129.34, 129.13, 129.08, 128.56, 128.46, 127.45, 126.79 (Cq), 126.43, 126.37, 113.87, 113.79, 104.20, 100.84 (C15), 83.34 (C2), 79.59 (C3), 77.77 (C8), 77.51 (C1), 76.98, 74.76, 74.15, 72.97, 72.68 (C6), 72.28, 72.18, 69.95, 67.92, 67.54 (C5), 64.52, 61.92 (C10), 55.56, 55.54 (OMe), 44.02 (C9), 43.18, 37.72, 35.95 (C7). MS (ESI) calculated for [$C_{28}H_{31}N_3O_7$] 521.22; found 522.2 [M + H]$^+$, 544.3 [M + Na]$^+$.

GRPR-L6. To a stirred solution of **12** (30 mg, 0.053 mmol) in freshly degassed MeOH (2.7 mL), a catalytic amount of $Pd/CaCO_3$ (Lindlar's catalyst) was added, then the mixture was stirred under H_2 atmosphere at r.t. for 2 h. The crude was diluted with MeOH and the catalyst was filtered off through a celite pad. Removal of the solvent under reduced pressure afforded pure amine in a quantitative yield that was immediately used. Amine derivative was resuspended in anhydrous DCM (1.4 mL), benzoyl-chloride (12 μL, 0.106 mmol) and Et_3N (22 μL, 0.159 mmol) were added at 0 °C. The mixture was allowed to return to room temperature and stirred under argon atmosphere overnight. Then, the reaction was quenched with MeOH and concentrated under reduced pressure and the crude was purified by automated flash chromatography (Hex:AcOEt gradient elution) obtaining pure compound **GRPR-L6** (30 mg, 89% yield). TLC RF = 0.59 (EDP:AcOEt 1:1). ^{1}H NMR (400 MHz, Chloroform-d) δ 7.86 (s, 1H, Harom), 7.83–7.73 (m, 3H, Harom), 7.61–7.30 (m, 8H, Harom), 6.76 (t, J = 5.2 Hz, 1H, NH), 6.62–6.51 (m, minor isomer), 5.79 (s, minor isomer), 5.55 (s, 1H, H15), 5.19 (ddd, J = 6.5, 3.9, 1.8 Hz, 1H, H1), 4.90 (d, J = 13.1 Hz, 1H, H10′), 4.84–4.75 (m, 1H, H10″), 4.68 (dd, J = 8.2, 2.5 Hz, minor isomer), 4.65–4.54 (m, minor isomer), 4.51 (t, J = 2.6 Hz, 1H, H4), 4.38 (d, J = 12.7 Hz, 1H, H6′), 4.33 (dd, J = 8.2, 1.8 Hz, minor isomer), 4.27 (dtd, J = 8.7, 5.7, 3.0 Hz, 1H, H8), 4.17 (t, J = 4.4 Hz, 1H, H2), 4.12 (dd, J = 12.8, 2.2 Hz, 1H, H6″), 4.04 (ddt, J = 12.8, 7.1, 3.3 Hz, minor isomer), 4.00–3.90 (m, minor isomer), 3.83–3.67 (m, 2H, H3, H9″), 3.67–3.63 (m, minor isomer), 3.63–3.55 (m, 2H, H5, H9′), 3.50 (ddd, J = 13.7, 7.6, 4.5 Hz,), 2.60 (dt, J = 14.7, 7.6 Hz, minor isomer), 2.44 (ddd, J = 14.8, 8.4, 6.8 Hz, 1H, H7′), 1.87 (ddd, J = 14.5, 6.0, 2.0 Hz, 1H, H7″), 1.84–1.76 (m, minor isomer). ^{13}C NMR (100 MHz, $CDCl_3$) δ 168.03 (Cq), 167.70, 141.04, 140.92, 137.66, 136.49, 134.89, 134.29, 133.50, 131.84, 131.80, 131.75, 131.56, 131.51, 131.47, 130.16, 130.09, 129.32, 128.75, 128.69, 128.62, 128.56, 128.54, 128.52, 128.46, 127.61, 127.57, 127.43, 127.32, 127.08, 127.00, 126.24, 104.29, 100.68 (C15), 83.51 (C2), 81.14 (C3), 77.60 (C1), 77.29, 77.19 (C8), 74.80, 74.17, 72.79 (C4), 72.69 (C6), 72.23, 71.97, 71.95, 70.39, 69.58 (C10), 67.84, 67.69 (C5). MS (ESI) calculated for $[C_{32}H_{29}F_6NO_6]$ 637.19; found 638.28 $[M + H]^+$, 660.24 $[M + Na]^+$, 676.26 $[M + K]^+$.

GRPR-L7. To a stirred solution of **13** (26 mg, 0.057 mmol) in freshly degassed MeOH (2.9 mL), a catalytic amount of $Pd/CaCO_3$ (Lindlar's catalyst) was added, then the mixture was stirred under H_2 atmosphere at r.t. for 2 h. The crude was diluted with MeOH and the catalyst was filtered off through a celite pad. Removal of the solvent under reduced pressure afforded pure amine in a quantitative yield that was immediately used. Amine derivative was resuspended in anhydrous DCM (1.45 mL), benzoyl-chloride (13 μL, 0.114 mmol) and Et_3N (24 μL, 0.171 mmol) were added at 0 °C. The mixture was allowed to return to room temperature and stirred under argon atmosphere overnight. Then, the reaction was quenched with MeOH and concentrated under reduced pressure and the crude was purified by automated flash chromatography (Hex:AcOEt gradient elution) obtaining pure compound **GRPR-L7** (27 mg, 87% yield). TLC RF = 0.38 (EDP:AcOEt 4:6). ^{1}H NMR (400 MHz, Chloroform-d) δ 8.17–8.04 (m, minor isomer), 7.87–7.71 (m, 2H, Harom), 7.65–7.34 (m, 9H, Harom), 7.32 (qAB, J = 8.5 Hz, 1H, Harom), 7.22 (d, J = 8.5 Hz, minor isomer), 6.88–6.80 (qAB, 2H, Harom), 6.58 (t, J = 5.6 Hz, NH), 5.79 (s, H15* minor isomer), 5.49 (s, 1H, H15), 5.16 (ddd, J = 6.3, 4.0, 1.7 Hz, 1H, H1), 4.76 (d, J = 11.8 Hz, 1H, H10′), 4.64 (d, J = 12.0 Hz, 1H, H10″), 4.49 (d, J = 11.7 Hz, 10′* minor isomer), 4.40 (d, J = 11.8 Hz, 10″* minor isomer), 4.37 (t, J = 2.6 Hz, 1H, H4), 4.35–4.24 (m, 2H, H8, H6″), 4.16 (t, J = 4.3 Hz, 1H, H2), 4.05 (dd, J = 12.7, 2.1 Hz, 1H, H6′), 4.01–3.95 (m, minor isomer), 3.82 (dd, J = 5.4, 3.1 Hz, 1H, H9″), 3.79 (s, minor isomer), 3.75 (s, 3H, OMe), 3.63 (dt, J = 4.7, 2.4 Hz, 1H, H3), 3.60–3.51 (m, 1H, H9′), 3.49 (d, J = 3.7 Hz, 1H, H5), 2.55 (dt, J = 14.9, 7.7 Hz, H7′* minor isomer), 2.41 (ddd, J = 14.8, 8.5, 6.8 Hz, 1H, H7′), 1.86 (ddd, J = 14.3, 5.5, 1.8 Hz, 1H, H7″), 1.82–1.76 (m, H7″* minor isomer). ^{13}C NMR (100 MHz, $CDCl_3$) δ 167.87 (CO), 167.61(*), 159.25 (Cq), 159.14 (*), 137.71 (Cq), 136.54 (*), 134.85 (Cq), 134.23 (*), 133.44, 131.58, 131.34 (CHarom), 130.20 (Cq), 130.09, 129.87, 129.65, 129.56 (CHarom), 129.54 (*), 129.39, 129.33, 129.09, 128.99, 128.59, 128.53, 128.47, 128.41, 128.39, 128.25, 127.34, 126.98, 126.93, 126.90, 126.25 (CH arom), 113.75 (CH arom AB), 113.71 (*), 104.03 (*), 100.66 (C15), 83.75 (C2), 79.04 (C3), 77.44 (C1), 76.73 (C8), 74.85, 73.90, 73.17 (*), 73.03 (C4), 72.51 (C6), 72.10, 71.98, 70.45 (C10), 69.22 (*), 67.80, 67.54 (C5), 55.26, 55.23 (OMe), 43.93 (C9), 43.15 (*), 37.25 (*), 35.63 (C7). MS (ESI) calculated for $[C_{31}H_{33}NO_7]$ 531.22; found 532.14 $[M + H]^+$, 554.20 $[M + Na]^+$, 570.15 $[M + K]^+$.

3.5. Cell cultures

PC3 and MCF-7 cell lines were obtained from ATCC. PC-3 cells were cultured in RPMI 1640 w/Glutamine supplemented with 10% (v/v) fetal bovine serum (FBS), 100 U/mL penicillin, 100 μg/mL streptomycin (all from Euroclone SpA, Pero, Italy). MCF-7 cells were cultured in EMEM/NEAA supplemented with 10% (v/v) FBS, 2 mM L-glutamine, 100 U/mL penicillin, 100 μg/mL streptomycin (all from Euroclone SpA, Pero, Italy). Both cell lines were maintained at 37 °C in a humidified 5% CO_2 incubator.

3.6. Calcium mobilization assay

Calcium mobilization was evaluated using the FLUO-4 Calcium Assay kit (ThermoFisher Scientific, Waltham, MA, US, cat # F36206) according to manufacturer's instruction. The assay was performed using a BMG OmegaStar (LabTech, Sorisole, BG, Italy) multiplate reader equipped with a dual automatic injection system and fluorescence instrument settings appropriate for excitation at 494 nm and emission at 516 nm. The assay chamber was maintained at 37 °C for the whole experiment duration. Briefly, PC3 cells were plated $4x10^4$ cells/well in 96-well dark plates with transparent bottom. The next day, after removing the culture medium, 100 μL/well dye loading solution was added and incubated for 45 min at 37 °C in the dark. The plate was transferred into the multiplate reader assay chamber. Using the automatic injection system GRPR-L diluted in assay buffer was added to each well to obtain a final concentration of 50 nM; fluorescence (F) was acquired in each well every second for 20 s just prior to compound injection and for 60 s after injection. Mean fluorescence prior compound injection was used as reference (F_0) for signal normalization (F/F_0). After 30 min using the automatic injection system, BN dissolved in assay buffer was added (well concentration 200 nM) and fluorescence was acquired as described above to monitor intracellular Ca^{2+} mobilization. Samples not pre-treated with any GRPR-L and stimulated only with Bombesin 200 nM were also assayed. Cells treated with assay buffer only represented the negative control.

3.7. PC3 cell proliferation assays

To assess the effect of the different GRPR-L compounds on PC3 cell proliferation, the SRB (SulfoRhodamine B) assay was performed. PC3 cells were seeded 5000/well in 96-wells plate in complete medium, consisting of RPMI 1640 w/Glutamine supplemented with antibiotics and 10% Fetal Bovine Serum (FBS) (all from Euroclone). The day after, the complete medium was replaced with RPMI 1640 w/Glutamine supplemented with antibiotics without serum. After 36–48 h of serum starvation, cells were treated with 50 nM of GRPR-L compounds in complete medium for 1 h and subsequently BN was added to reach a final concentration of 200 nM; samples not treated with BN received the same amount of medium. Controls were treated with complete medium without any drug. A BN control (cells treated with BN only) was also performed. After 24 h of GRPR-L induction, 50 μL of 50% Trichloroacetic acid (TCA) was added to each well and the plate was incubated for 1 h at 4 °C. Plate was rinsed with tap water and allowed to dry at room temperature. SRB solution (0.4% SRB in TCA 1%) was added (50 μL/well) and incubated for 15 min. Excess dye was rinsed thoroughly with

TCA 1% and the plate was allowed to dry at room temperature. SRB was solubilized with Tris(Hydroxymethyl)aminomethane 10 mM 150 μL/well and optical density at 540 nm was measured using a multiplate reader (OmegaStar, BMG Labtech, Germany). To account for unspecific staining, wells without cells but containing medium for the entire experimental period were also assayed and the value obtained was subtracted as background. Proliferation was calculated as ratio versus control untreated cells. Three independent experiments were conducted, each with six replicates.

3.8. MCF-7 cell proliferation assays

The activity of the GRPR-L compounds on MCF-7 proliferation was measured by the 3-(4,5-dimethylthiazol-2-yl)-2,5-diphenyltetrazolium bromide (MTT) assay. 4000 cells/well were seeded in 96-well plates. The day after, the complete medium was replaced with EMEM-serum free medium containing 0.1% BSA (Merck KGaA, Darmstadt, Germany). After 24 h starvation, GRPR-L compounds were added at the indicated concentrations from 1000X stocks in 100% DMSO, in the presence or absence of 100 nM BN to stimulate proliferation; 0.1% DMSO was added in the solvent control wells. After 24 h treatment, the MTT solution (Merck, used at a final concentration of 0.5 mg/ml) was added and plates were incubated for 2 h at 37 °C. The purple formazan crystals were solubilized, and the plates were read on a Victor X3 Microplate Reader (Perkin Elmer inc., Waltham, MA, US) at 570 nm. Growth of each condition was referred to solvent control, which was set to 100%. All conditions were tested at least in three independent experiments, all in technical triplicates. Wells without cells but containing medium for the entire experimental period were also assayed and the value obtained was subtracted as background. Proliferation was calculated as ratio versus control untreated cells.

4. Conclusions

Here we combined CD, NMR and MM/MD-based conformational studies, organic synthesis and *in vitro* cellular assays to develop a new small library of GRP-R ligands based on a rigid bicyclic *C*-galactosidic scaffold.

Collectively, our results clearly indicate that we obtained new non-peptide GRP-R high affinity ligands, some of which show a significant BN antagonist activity. To the best of our knowledge, our compounds are the only example of a small library of non-peptide GRP-R antagonists active in the nM range of concentration, with the only exception of compound PD176252, that, as already mentioned, shows poor selectivity for GRP-R [20,21],

These molecules are hit compounds for the rational design and synthesis of new ligands and modulators of GRP-R. Due to their favorable chemical properties and stability, they can be used for the active receptor-mediated targeting of GRP-R positive tumors.

To give specific examples, the presence of free hydroxyl groups on compound **GRPR-L2** can be exploited to enable its chemical conjugation to radiolabeled compounds for selective anti-tumor radiotherapy and/or imaging, or well-characterized and potent anti-cancer agents, obtaining very efficient molecular devices for drug targeting of tumor tissues. Moreover, the bioactivity of compounds **GRPR-L6**, bearing a 3,5-bis-(trifluoromethyl) phenyl group, suggests the possibility to synthesize ^{18}F-labeled GRPR-L as potential PET agents for the imaging of GRP-R positive tumors.

These new strategies, assuming the development of specific synthetic approaches for the preparation of new derivatives and conjugates, will be explored by our group in the near future.

Declaration of Competing Interest

The authors declare that they have no known competing financial interests or personal relationships that could have appeared to influence the work reported in this paper.

Acknowledgments

The authors acknowledge AIRC for funding My First AIRC project 17030 - Targeting of Gastrin-Releasing Peptide receptor expressing tumors: NMR characterization of Bombesin/GRP-R interaction.

Authors thanks Prof. Antonino Natalello (Dept of Biotechnology and Biosciences, University of Milano – Bicocca) for helpful discussion of CD data.

Appendix A. Supplementary material

Supplementary data to this article can be found online at https://doi.org/10.1016/j.bioorg.2021.104739.

References

[1] D. Pooja, A. Gunukula, N. Gupta, D.J. Adams, H. Kulhari, Bombesin receptors as potential targets for anticancer drug delivery and imaging, Int. J. Biochem. Cell Biol. 114 (2019) 105567.
[2] T.W. Moody, Peptide receptors as cancer drug targets, Ann. N. Y. Acad. Sci. 1455 (1) (2019) 141–148.
[3] T.J. Stott Reynolds, C.J. Smith, M.R. Lewis, Peptide-based radiopharmaceuticals for molecular imaging of prostate cancer, in: H. Schatten (Ed.), Advances in Experimental Medicine and Biology, Springer International Publishing, 2018, pp. 135–158.
[4] A. Nagy, A.V. Schally, G. Halmos, P. Armatis, R.Z. Cai, V. Csernus, M. Kovács, M. Koppán, K. Szepesházi, Z. Kahán, Synthesis and biological evaluation of cytotoxic analogs of somatostatin containing doxorubicin or its intensely potent derivative, 2-pyrrolinodoxorubicin, PNAS 95 (4) (1998) 1794–1799.
[5] H. Zia, T. Hida, S. Jakowlew, M. Birrer, Y. Gozes, J.C. Reubi, M. Fridkin, I. Gozes, T.W. Moody, Breast cancer growth is inhibited by vasoactive intestinal peptide (VIP) hybrid, a synthetic VIP receptor antagonist, Cancer Res. 56 (15) (1996) 3486–3489.
[6] T.W. Moody, I. Ramos-Alvarez, R.T. Jensen, Neuropeptide G protein-coupled receptors as oncotargets, Front. Endocrinol. 9 (345) (2018).
[7] T.J. McDonald, H. Jörnvall, G. Nilsson, M. Vagne, M. Ghatei, S.R. Bloom, V. Mutt, Characterization of a gastrin releasing peptide from porcine non-antral gastric tissue, Biochem. Biophys. Res. Commun. 90 (1) (1979) 227–233.
[8] E. Rozengurt, Signal transduction pathways in the mitogenic response to G protein–coupled neuropeptide receptor agonists, J. Cell. Physiol. 177 (4) (1998) 507–517.
[9] A.G. Aprikian, K. Han, S. Chevalier, M. Bazinet, J. Viallet, Bombesin specifically induces intracellular calcium mobilization via gastrin-releasing peptide receptors in human prostate cancer cells, J. Mol. Endocrinol. 16 (3) (1996) 297.
[10] M. Pagé, Tumor targeting in cancer therapy, Springer Science & Business Media, 2002.
[11] J.C. Reubi, Peptide receptors as molecular targets for cancer diagnosis and therapy, Endocr. Rev. 24 (4) (2003) 389–427.
[12] S.M. Okarvi, Peptide-based radiopharmaceuticals and cytotoxic conjugates: Potential tools against cancer, Cancer Treat. Rev. 34 (1) (2008) 13–26.
[13] E.F. Grady, L.W. Slice, W.O. Brant, J.H. Walsh, D.G. Payan, N.W. Bunnett, Direct observation of endocytosis of gastrin releasing peptide and its receptor, J. Biol. Chem. 270 (9) (1995) 4603–4611.
[14] A. Accardo, R. Mansi, G. Salzano, A. Morisco, M. Aurilio, A. Parisi, F. Maione, C. Cicala, B. Ziaco, D. Tesauro, L. Aloj, G. De Rosa, G. Morelli, Bombesin peptide antagonist for target-selective delivery of liposomal doxorubicin on cancer cells, J. Drug Target. 21 (3) (2013) 240–249.
[15] R. Cescato, T. Maina, B. Nock, A. Nikolopoulou, D. Charalambidis, V. Piccand, J. C. Reubi, Bombesin receptor antagonists may be preferable to agonists for tumor targeting, J. Nucl. Med.: Off. Publ. Soc. Nucl. Med. 49 (2) (2008) 318–326.
[16] K. Abiraj, R. Mansi, M.L. Tamma, M. Fani, F. Forrer, G. Nicolas, R. Cescato, J. C. Reubi, H.R. Maecke, Bombesin antagonist-based radioligands for translational nuclear imaging of gastrin-releasing peptide receptor-positive tumors, J. Nucl. Med.: Off. Publ. Soc. Nucl. Med. 52 (12) (2011) 1970–1978.
[17] C. Kroll, R. Mansi, F. Braun, S. Dobitz, H.R. Maecke, H. Wennemers, Hybrid bombesin analogues: combining an agonist and an antagonist in defined distances for optimized tumor targeting, J. Am. Chem. Soc. 135 (45) (2013) 16793–16796.
[18] Z. Heidari, R. Sariri, M. Salouti, Gold nanorods-bombesin conjugate as a potential targeted imaging agent for detection of breast cancer, J. Photochem. Photobiol., B 130 (2014) 40–46.
[19] M. Pourghiasian, Z. Liu, J. Pan, Z. Zhang, N. Colpo, K.S. Lin, D.M. Perrin, F. Bénard, (18)F-AmBF3-MJ9: a novel radiofluorinated bombesin derivative for prostate cancer imaging, Bioorg. Med. Chem. 23 (7) (2015) 1500–1506.
[20] V. Ashwood, V. Brownhill, M. Higginbottom, D.C. Horwell, J. Hughes, R. A. Lewthwaite, A.T. McKnight, R.D. Pinnock, M.C. Pritchard, N. Suman-Chauhan, C. Webb, S.C. Williams, PD 176252–the first high affinity non-peptide gastrin-releasing peptide (BB2) receptor antagonist, Bioorg. Med. Chem. Lett. 8 (18) (1998) 2589–2594.

[21] E. Lacivita, E. Lucente, C. Kwizera, I.F. Antunes, M. Niso, P. De Giorgio, R. Perrone, N.A. Colabufo, P.H. Elsinga, M. Leopoldo, Structure-activity relationship study towards non-peptidic positron emission tomography (PET) radiotracer for gastrin releasing peptide receptors: Development of [(18)F] (S)-3-(1H-indol-3-yl)-N-[1-[5-(2-fluoroethoxy)pyridin-2-yl]cyclohexylmethyl]-2-methyl-2-[3-(4-nitrophenyl) ureido]propionamide, Bioorg. Med. Chem. 25 (1) (2017) 277–292.
[22] A. Palmioli, C. Ceresa, F. Tripodi, B. La Ferla, G. Nicolini, C. Airoldi, On-cell saturation transfer difference NMR study of Bombesin binding to GRP receptor, Bioorg. Chem. 99 (2020) 103861.
[23] S. Mari, F.J. Cañada, J. Jiménez-Barbero, A. Bernardi, G. Marcou, I. Motto, I. Velter, F. Nicotra, B. La Ferla, Synthesis and conformational analysis of galactose-derived bicyclic scaffolds, Eur. J. Org. Chem. 2006 (13) (2006) 2925–2933.
[24] U. Hunger, J. Ohnsmann, H. Kunz, Carbohydrate scaffolds for combinatorial syntheses that allow selective deprotection of all four positions independent of the sequence, Angew. Chem. Int. Ed. Engl. 43 (9) (2004) 1104–1107.
[25] F. Nicotra, L. Cipolla, B. La Ferla, C. Airoldi, C. Zona, A. Orsato, N. Shaikh, L. Russo, Carbohydrate scaffolds in chemical genetic studies, J. Biotechnol. 144 (3) (2009) 234–241.
[26] L. Cipolla, B. La Ferla, C. Airoldi, C. Zona, A. Orsato, N. Shaikh, L. Russo, F. Nicotra, Carbohydrate mimetics and scaffolds: sweet spots in medicinal chemistry, Future Med. Chem. 2 (4) (2010) 587–599.
[27] J.A. Carver, The conformation of bombesin in solution as determined by two-dimensional 1H-NMR techniques, Eur. J. Biochem. 168 (1) (1987) 193–199.
[28] M.D. Díaz, M. Fioroni, K. Burger, S. Berger, Evidence of complete hydrophobic coating of bombesin by trifluoroethanol in aqueous solution: an NMR spectroscopic and molecular dynamics study, Chem. – Eur. J. 8 (7) (2002) 1663–1669.
[29] P. Cavatorta, G. Farruggia, L. Masotti, G. Sartor, A.G. Szabo, Conformational flexibility of the hormonal peptide bombesin and its interaction with lipids, Biochem. Biophys. Res. Commun. 141 (1) (1986) 99–105.
[30] P. Cavatorta, A. Spisni, A.G. Szabo, G. Farruggia, L. Franzoni, L. Masotti, Conformation of bombesin in buffer and in the presence of lysolecithin micelles: Nmr, CD, and fluorescence studies, Biopolymers 28 (1) (1989) 441–463.
[31] D.E. Warschawski, A.A. Arnold, M. Beaugrand, A. Gravel, É. Chartrand, I. Marcotte, Choosing membrane mimetics for NMR structural studies of transmembrane proteins, Biochim. Biophys. Acta (BBA) – Biomembr. 1808 (8) (2011) 1957–1974.
[32] M. Adrover, P. Sanchis, B. Vilanova, K. Pauwels, G. Martorell, J.J. Pérez, Conformational ensembles of neuromedin C reveal a progressive coil-helix transition within a binding-induced folding mechanism, RSC Adv. 5 (101) (2015) 83074–83088.
[33] S.M. Kelly, N.C. Price, The application of circular dichroism to studies of protein folding and unfolding, Biochim. Biophys. Acta (BBA) - Protein Struct. Mol. Enzymol. 1338 (2) (1997) 161–185.
[34] P. Güntert, C. Mumenthaler, K. Wüthrich, Torsion angle dynamics for NMR structure calculation with the new program Dyana11Edited by P. E. Wright, J. Mol. Biol. 273 (1) (1997) 283–298.
[35] P. Güntert, Automated NMR structure calculation With CYANA, in: A.K. Downing (Ed.), Protein NMR Techniques, Humana Press, Totowa, NJ, 2004, pp. 353–378.
[36] A. Palmioli, C. Airoldi, Bombesin structure in presence of SDS micelles, Mendeley Data, v1 (2019), doi: 10.17632/sg5fcrnk9z.1.
[37] H. Ohki-Hamazaki, M. Iwabuchi, F. Maekawa, Development and function of bombesin-like peptides and their receptors, Int. J. Dev. Biol. 49 (2–3) (2005) 293–300.
[38] C. Airoldi, A. Palmioli, Synthesis of C- and S-glycosides, reference module in chemistry, Molecular Sciences and Chemical Engineering, Elsevier, 2020.
[39] J. Wang, R.M. Wolf, J.W. Caldwell, P.A. Kollman, D.A. Case, Development and testing of a general amber force field, J. Comput. Chem. 25 (9) (2004) 1157–1174.
[40] MacroModel, Schrödinger Release 2016-4, Schrödinger, LLC, New York, NY, Schrödinger Release 2016-4, Schrödinger, LLC, New York, NY, 2016.
[41] H. Peng, D. Carrico, V. Thai, M. Blaskovich, C. Bucher, E.E. Pusateri, S.M. Sebti, A. D. Hamilton, Synthesis and evaluation of potent, highly-selective, 3-aryl-piperazinone inhibitors of protein geranylgeranyltransferase-I, Org. Biomol. Chem. 4 (9) (2006) 1768–1784.
[42] W.J. Wasilenko, J. Cooper, A.J. Palad, K.D. Somers, P.F. Blackmore, J.S. Rhim, G. L. Wright Jr., P.F. Schellhammer, Calcium signaling in prostate cancer cells: evidence for multiple receptors and enhanced sensitivity to bombesin/GRP, Prostate 30 (3) (1997) 167–173.
[43] H. Reile, P.E. Armatis, A.V. Schally, Characterization of high-affinity receptors for bombesin/gastrin releasing peptide on the human prostate cancer cell lines PC-3 and DU-145: internalization of receptor bound 125I-(Tyr4) bombesin by tumor cells, Prostate 25 (1) (1994) 29–38.
[44] M. Gugger, J.C. Reubi, Gastrin-releasing peptide receptors in non-neoplastic and neoplastic human breast, Am. J. Pathol. 155 (6) (1999) 2067–2076.
[45] Y. Shen, F. Delaglio, G. Cornilescu, A. Bax, TALOS+: a hybrid method for predicting protein backbone torsion angles from NMR chemical shifts, J. Biomol. NMR 44 (4) (2009) 213–223.
[46] Maestro, Schrödinger Release 2016-4, Schrödinger, LLC, New York, NY, Schrödinger Release 2016-4, Schrödinger, LLC, New York, NY, 2016.

Cardiovascular Diabetology

ORIGINAL INVESTIGATION

Open Access

Liraglutide preserves CD34$^+$ stem cells from dysfunction Induced by high glucose exposure

Annalisa Sforza[1†], Vera Vigorelli[1†], Erica Rurali[1], Gianluca Lorenzo Perrucci[1], Elisa Gambini[1], Martina Arici[2], Alessia Metallo[2], Raffaella Rinaldi[1], Paolo Fiorina[3,4,5], Andrea Barbuti[6], Angela Raucci[7], Elena Sacco[2], Marcella Rocchetti[2], Giulio Pompilio[1,8], Stefano Genovese[9†] and Maria Cristina Vinci[1*†]

Abstract

Background: Glucagon like peptide-1 receptor agonists (GLP-1RAs) have shown to reduce mortality and cardiovascular events in patients with type 2 diabetes mellitus (T2DM). Since the impairment in number and function of vasculotrophic circulating CD34$^+$ hematopoietic stem progenitor cells (HSPCs) in T2D has been reported to increase cardiovascular (CV) risk, we hypothesized that one of the mechanisms whereby GLP-1 RAs exert CV protective effects may be related to the ability to improve CD34$^+$ HSPC function.

Methods: In cord blood (CB)-derived CD34$^+$ HSPC, the expression of GLP-1 receptor (GLP-1R) mRNA, receptor protein and intracellular signaling was evaluated by RT-qPCR and Western Blot respectively. CD34$^+$ HSPCs were exposed to high glucose (HG) condition and GLP-1RA liraglutide (LIRA) was added before as well as after functional impairment. Proliferation, CXCR4/SDF-1α axis activity and intracellular ROS production of CD34$^+$ HSPC were evaluated.

Results: CD34$^+$ HSPCs express GLP-1R at transcriptional and protein level. LIRA treatment prevented and rescued HSPC proliferation, CXCR4/SDF-1α axis activity and metabolic imbalance from HG-induced impairment. LIRA stimulation promoted intracellular cAMP accumulation as well as ERK1/2 and AKT signaling activation. The selective GLP-1R antagonist exendin (9–39) abrogated LIRA-dependent ERK1/2 and AKT phosphorylation along with the related protective effects.

Conclusion: We provided the first evidence that CD34$^+$ HSPC express GLP-1R and that LIRA can favorably impact on cell dysfunction due to HG exposure. These findings open new perspectives on the favorable CV effects of GLP-1 RAs in T2DM patients.

Keywords: GLP-1 receptor agonist, CD34$^+$ hematopoietic stem progenitor cells, Type 2 diabetes mellitus, Cardiovascular disease

Background

Type 2 diabetes mellitus (T2DM) has now attained the status of a global pandemic with over 400 million individuals affected worldwide [1]. Despite glucose lowering therapies, mortality from cardiovascular disease (CVD) remains high and extremely costly for health care systems both in terms of medical expenses and disability-adjusted life years [2]. For these reasons, the development of new

*Correspondence: cristina.vinci@ccfm.it
†Annalisa Sforza and Vera Vigorelli equally contributed as first author
†Stefano Genovese and Maria Cristina Vinci equally contributed as last author
[1] Unit of Vascular Biology and Regenerative Medicine, Centro Cardiologico Monzino IRCCS, Via C. Parea 4, 20138 Milan, Italy
Full list of author information is available at the end of the article

therapeutic strategies able to prevent CVD morbidity and mortality is crucial. Patients with T2DM are characterized by a significant decrease in circulating $CD34^+$ stem/progenitor cells. $CD34^+$ hematopoietic stem/progenitor cells (HSPCs) are known to possess vascular regenerative and proangiogenic capacity [3]. Their functional and numerical depletion is now considered a significant contributor to CV homeostasis impairment in diabetes. To this regard, Fadini et al. demonstrated that $CD34^+$ HSPCs are reduced of about 40% in T2DM [4], and that such impairment contributes to enhanced CV risk [5]. Notably, in patients with T2DM, the reduction of $CD34^+$ HSPCs number and function predicts adverse CV outcomes, defined as major CV events (MACE), and hospitalizations for CV causes [6, 7]. Recent large-scale trials have unequivocally demonstrated the ability of glucagon-like peptide 1 receptor agonists (GLP1-RAs) to reduce the risk of MACE in T2DM patients with established or at high risk of CVD [8–10]. GLP1-RAs are now recommended by guidelines as first-line agent for prevention of CVD in T2DM patients [11, 12]. Such pleiotropic CV benefit appears to be additional to glucose-lowering effects and the mechanisms whereby they exert such striking CV protective effects are still largely unknown. At cellular and molecular level, GLP1-RA effects are mediated by GLP1-R, a Gs coupled receptor family member, which is present in various human tissues [13]. To date, there are no data describing the effects of GLP1-RAs on $CD34^+$ HSPCs of T2DM patients. We hypothesized that at least part of the unknown mechanisms whereby GLP1-RAs exert CV protective effect are mediated by its ability to improve $CD34^+$ HSPC function. Here, by exploiting an in vitro model of diabetes, we show for the first time that $CD34^+$ HSPCs express GLP-1R and that its stimulation by liraglutide (LIRA), a GLP1-RA, prevents and recovers the dysfunction induced by hyperglycemia.

Methods

Experimental design

We recently established a stem cell culture model of diabetes based on the use of cord blood (CB)-derived $CD34^+$ HSPCs [14]. This method already provided a consistent and reproducible recapitulation of the major $CD34^+$ HSPC dysfunction hallmarks in diabetes [14]. To assess the ability of GLP-1 RA to prevent $CD34^+$ HSPC dysfunction induced by glucose overload the cells were expanded in high glucose (HG; 30 mM) conditions along with 50 nM or 100 nM LIRA treatment (Fig. 1A). In a different experimental setting, $CD34^+$ HSPCs were expanded in HG condition and then treated with LIRA only after loss of glucose tolerance (Fig. 1B). Afterwards, we assessed the ability of the drug to recover a compromised phenotype. $CD34^+$ HSPCs cultured in normoglycemic condition (NG; 30 mM mannitol) were used as control. At the end of both experiments, the main dysfunctional hallmarks of the cells, namely proliferation and CXCR4/SDF-1α axis impairment, were evaluated (Fig. 1).

Cell culture

Umbilical cord blood (UCB) was collected from the umbilical cord of full-term normal deliveries in collaboration with Milano Cord Blood Bank (IRCSS Ca' Granda Foundation – Ospedale Maggiore Policlinico). The mononuclear cell fraction was obtained by density gradient centrifugation using Ficoll-Paque (Lymphoprep, Sentinel Diagnostics) and $CD34^+$ HSPCs were immunomagnetically isolated using CD34 Microbead Kit (MiniMACS kit, Miltenyi Biotec). Flow-cytometric analysis allowed to assess the purity of sorted cell population, displaying 90% of $CD34^+$ HSPCs and negligible presence of $CD14^+$ (monocytes) and $CD3^+$ (lymphocytes) cells (Additional file 1: Figure S1). Isolated $CD34^+$ HSPCs were cultured in Stem Span medium (StemCell Technologies) supplemented with 20 ng/mL of interleukin (IL)-6 (PeproTech), 20 ng/mL of IL-3 (PeproTech), 50 ng/mL of fms-like tyrosine kinase 3 (FLT3, PeproTech), and 50 ng/mL of stem cell factor (SCF, PeproTech). Cells were cultured in HG (30 mM of glucose, Sigma-Aldrich) or NG (30 mM of mannitol, Sigma-Aldrich) conditions for up to 20 days and treated or not with increasing concentration of LIRA (50 nM and 100 nM; MedCHemExpress) ± selective GLP-1R antagonist exendin (9-39) (150 nM EXE; MedCHemExpress).

Capan-1 cells (HTB-79™), used as GLP-1R positive control, were purchased from ATCC and grown in RPMI medium supplemented with 20% FBS, as indicated by the supplier.

Isolation of $CD34^+$ HSPCs from patient bone marrow

$CD34^+$ HSPCs were isolated from sternal bone marrow (BM) biopsy of T2DM patients underwent bypass surgery. During surgical procedure, 2 mL of sternal BM blood were withdrawn by biopsy needle (15G × 25/90 mm; MDL) and suspended in saline buffer solution. BM-derived $CD34^+$ HSPCs were isolated as aforementioned and collected for GLP-1R mRNA analysis.

All experiments were carried out upon approval of local ethic committees (CCM 205–RE 3428) and informed written consent was obtained from all patients before BM harvesting.

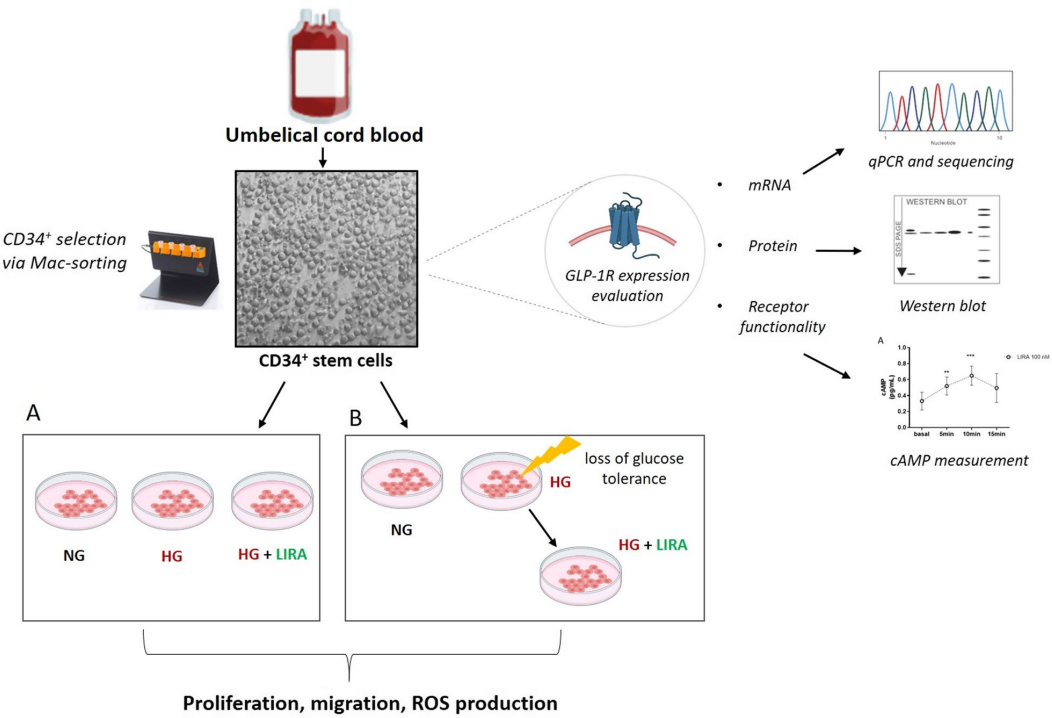

Fig. 1 Schematic representation of the study. CD34$^+$ HSPCs were isolated via Mac-sorting from cord blood and characterized for GLP-1R transcript and protein expression levels, and downstream signaling pathway activation. Then, CD34$^+$ HSPCs were expanded in HG condition with or without LIRA (**A**). In a different experimental setting the cells were treated with LIRA only after the loss of glucose tolerance (**B**). CD34$^+$ HSPCs cultured in NG (30 mM mannitol) condition were used as control (**A**, **B**). Proliferation, migration and oxidative stress were finally assessed at the end of experiments. GLP-1R = glucagone-like peptide 1 receptor; HG = high glucose; LIRA = liraglutide; NG = normal glucose

Cell proliferation assay

CD34$^+$ HSPCs were seeded at an initial density of 2.0×10^5 cells/well and cultured for up to 20 days in NG and HG ± LIRA conditions. Cells were counted on days 5, 10, 15 and 20. Doubling time was calculated with the following formula:

$$\text{Doubling time: } \frac{duration\ x\ \log\ (2)}{\log\ (final\ concentration) - \log\ (initial\ concentration)}$$

Migration assays

Cell migration was determined the use of Boyden modified chamber consisting of transwell culture inserts (5-µm pore membrane; Corning Incorporated, Corning, NY). In brief, 1×10^5 cells were seeded onto the upper chamber and allowed to migrate toward the lower chamber containing, or not, stromal cell-derived factor 1 (SDF-1α 50 ng/mL; PeproTech EC Ltd.). The transwells were incubated at 37 °C, 5% CO_2, for 4 h. Migrated cells in the lower chamber were counted and migration index were calculated with the following formula:

$$\text{Migration index: } \frac{migrated\ cells\ in\ presence\ of\ SDF - 1a}{migrated\ cells\ in\ absence\ of\ SDF - 1a}$$

Cyclic adenosine monophosphate (cAMP) quantification

Intracellular cAMP was quantified by cAMP ELISA kit (Enzo Life Science) according to manufacturer's instructions. Briefly, 5×10^5 CD34$^+$ HSPCs were stimulated with LIRA ± EXE and lysed in 0.1 M HCl and 0,1% Triton X-100. Sample absorbance was spectrophotometrically evaluated at 405 nm by Tecan (Infinite M200 Pro, TECAN).

Intracellular Ca^{2+} handling

The measurement of intracellular Ca^{2+} has been assessed through single cell and population analysis by means of confocal Nikon A1R microscope and FLUOstar Omega (BMG Labtech) multiplate reader respectively. $CD34^+$ HSPCs were starved for 2 h (with IMDM and albumin 0.1%) and incubated with the Ca^{2+-}sensitive dye Fluo-4 AM (ThermoFisher, 2 μM) in Tyrode's solution (containing in mM: 154 NaCl, 4 KCl, 2 CaCl2, 1 MgCl2, 5 HEPES/NaOH, and 5.5 d-glucose, adjusted to pH 7.35) for 1 h.

Confocal single cell analysis was performed by plating $CD34^+$ HSPCs on fibronectin/polylisin D coated glass coverslips; fluorescence (F) images (512*512 pxls) were acquired at × 60 magnification every 5 s in basal condition and following 100 nM LIRA addition at 37 °C and 5% CO2 thanks to Okolab incubator mounted on the microscope stage. Changes in single cell mean F during acquisition time were quantified through NIS-Elements analysis software following F backgroud subtraction. Population analysis was performed by plating cells in 96-well dark plates by means of the multiplate reader equipped with an automatic injection system to inject LIRA (100 nM). F was acquired in each well every 0.74 s for 20 s just prior to compound injection and for 100 s after injection. Mean F prior compound injection was used as reference (F0) for signal normalization (F/F0).

RNA extraction and RT-qPCR

Total RNA from both cord-blood and sternal $CD34^+$ HSPCs was isolated by using the Direct-zol RNA Kit (Zymo Research), following manufacturer's protocol. One μg of total RNA was converted to cDNA with the Superscript III kit (Life Technologies) and used to assess GLP-1R gene expression. qPCR reactions were performed with SYBR Green Supermix 2X (BIO-RAD Laboratories) on CFX96 Real–Time System PCR (BIO-RAD Laboratories). Specific GLP-1R primers (Fw: 5'-GTG TGGCGGCCAATTACTAC-3'; Rv: 5'-CTTGGCAAG TCTGCATTTGA-3') were appositely designed to evaluated mRNA expression by amplifying a region of 347 bp. The qPCR products were loaded on a 1% agarose gel with an appropriate molecular marker (PCR Marker Solution, Sigma-Aldrich). Then, the 347 bp bands were excised and purified with QIAquick Gel extraction kit (Qiagen) for subsequent Sanger sequencing analysis.

Sanger sequencing

The RT-qPCR products, appropriately purified from agarose, were sequenced with the help of an external service (Microsynth Biotech) by Sanger method with the use of GLP-1R Fw primer. Sequencing results were analysed by a Multiple sequence ClustalW alignment (BioEdit software) throughout the comparison of the published GLP-1R cDNA sequence (NCBI Reference sequence: NM_002062.5).

Western blot

$CD34^+$ HSPCs and Capan-1 cells were lysed in lysis buffer (50 mM TRIS-HCl, 150 mM NaCl, 1 mM EDTA, 1% Triton) added with protease inhibitors (1:10, Halt Protease Inhibitor Cocktail, Thermo Scientific). Protein lysate was then quantified by Pierce™ BCA Protein Assay Kit (ThermoFisher Scientific). Fourty μg and 20 μg of protein from $CD34^+$ stem cells and capan-1 cells respectively were resolved on 10% SDS-PAGE in denaturing conditions. Proteins were then transferred onto a polyvinylidene difluoride (PVDF) membrane (Millipore) at 400 mA, 4 °C for 90 min. To prevent aspecific binding, the membrane was blocked with 5% bovin serum albumin (BSA) in PBS + 0, 1% Tween-20 (PBST) for 1 h. The membranes were then incubated with the primary antibodies, appropriately diluted in 3% BSA-PBST, at 4 °C O/N and with the appropriate secondary antibody linked to horseradish peroxidase (HRP) the day after for 1 h. Specific information about antibodies and appropriate dilutions are reported in Table 1. The signal was detected by Enhanced chemiluminescence (ECL) system and quantified by Chemidoc MP Imaging System (BIO-RAD Laboratories). GLP-1R-mediated AKT and ERK1/2 pathway activation was evaluated by treating the cells with 100 nM LIRA ± 1 μM wortmannin (Sigma Aldrich; WT; inhibitor of phosphatidylinositol 3-kinase, PI3K), 100 μM PD 98059 (Sigma Aldrich; PD; a specific inhibitor of mitogen-activated protein kinase kinase 1/2, MEK1/2), or 150 nM EXE (selective GLP-1R antagonist) and with either no additions as control.

Table 1 List of Western blot antibodies

	Code (purchased from)	Source	Dilution
Primary antibody			
GLP-1R (D-6)	Sc-390774 (Santa Cruz Biotecnology)	Mouse	1:200
Phospho-p44/42 MAPK (ERK1/2) (Thr202/Tyr204)	#4370 (Cell signaling)	Rabbit	1:2000
p44/42 MAPK (ERK1/2)	#9102 (Cell signaling)	Rabbit	1:1000
Phospho-AKT (Ser473)	#9271 (Cell signaling)	Rabbit	1:1000
Secondary antibody			
ECL Anti-rabbit IgG	NA9340 (Amersham Biosciences)	donkey	1:10000
ECL Anti-mouse IgG	NA9310 (Amersham Biosciences)	sheep	1:5000

Flow cytometric assays

$CD34^+$ HSPCs were incubated for 30 min with allophycocyanin-conjugated monoclonal antihuman CXCR4 antibody (BD Biosciences) or with CellROX Green Flow Cytometry Assay Kit (Life Technologies) for the detection of CXCR4 and reactive oxygen species (ROS) respectively. The Gallios Flow Cytometer platform (Beckman Coulter Life Sciences) was used to analyze the samples after appropriate physical gating. At least 20^4 events in the indicated gates were acquired.

Immunocytochemistry

$CD34^+$ HSPCs were temporarily adhered to a glass coverslip surface by mixed fibronectin-polylysine D (1:1) coating solution. Immediately after adhesion, cells were incubated with Green CellROX (Life Technologies) for 20 min and then fixed with 2% paraformaldehyde solution. Before mounting, cells were counterstained with Hoechst for the nuclei (1:1000) and Wheat Germ Agglutinin for the cell membrane (WGA) (1:200). The images were acquired by ZEISS Apotome fluorescence microscope at 40X magnification.

Analysis of mitochondrial and glycolytic bioenergetic parameters

Bioenergetic parameters were analyzed by using Seahorse XFe96 Extracellular Flux analyzer (Agilent). Before the analysis, cells were collected and counted: 35×10^3 cells were suspended in 50 µL low buffered DMEM-based XF assay medium (103575-100 Agilent) supplemented with 10 mM glucose, 2 mM glutamine, 1 mM Na-pyruvate, and plated in a fibronectin-polylysine D coated 96-well XF plate (Agilent). The XF plate was centrifuged at 200 g (zero braking) for 1 min and incubated for 20 min at 37 °C in a no-CO_2 incubator. Before testing, 150 µL complete XF assay medium was added to each well and cells were furtherly incubated for 30 min at 37 °C.

Mitochondrial bioenergetic parameters were analyzed according to the Seahorse Mito Stress test kit protocol (Agilent) that include oxygen consumption rate (OCR; $pmolO_2$/min) measurements under basal condition and after the sequential injection of the ATP synthase inhibitor oligomycin A (1.5 µM), the ETC accelerator ionophore FCCP (carbonilcyanide p-triflouromethoxyphenylhydrazone, 2 µM), and the ETC inhibitors mixture rotenone (0.5 µM) + antimycin A (0.5 µM). The minimal doses of oligomycin A and FCCP causing the maximal response used in the Mito Stress test assay were determined for each experimental group in a preliminary Seahorse assay (Additional file 2: Figure S2).

Glycolytic bioenergetic parameters were analyzed by combining the Seahorse ATP rate and Glyco rate test kit protocols (Agilent) including extracellular acidification rate (ECAR; mpH/min) measurements under basal condition and after the sequential injection of 1.5 µM oligomycin A, 0.5 µM rotenone + 0.5 µM antimycin A mixture, and finally 50 mM 2-Deoxy-D-Glucose (2DG).

Seahorse parameters were normalized to cell number in each well. To this purpose, at the end of the Seahorse analysis, cell nuclei were marked with Hoechst 33342 (1 µg/mL) for about 15 min and acquired with Leica Thunder Imager microscope through a 10x objective. Cell number was quantified through ImageJ software. Samples were analyzed with at least 10 technical replicates from two independent experiments. Bioenergetic parameters were calculated from the Seahorse data using Wave2.6.1 (Agilent) software.

Respiratory parameters were calculated using the following formulas:

Basal Mitochondrial Respiration (Basal MR) = OCR under basal condition (OCR_{basal})–OCR following rotenone/antimycin A injection ($OCR_{rot/ant}$); Maximal MR (Max MR) = OCR following FCCP injection (OCR_{FCCP}) − $OCR_{rot/ant}$; Spare respiratory capacity = Max MR–Basal MR; Coupling efficiency = delta OCR following oligomycin A injection (OCR_{basal}-OCR_{oligo})/OCR_{basal}; Proton Leak = OCR_{oligo}-$OCR_{rot/ant}$.

Glycolytic parameters were calculated using the following formulas:

Proton Efflux rate (PER; $pmolesH^+$/min) was calculated from Extracellular Acidification Rate (ECAR) applying the Buffer Factor of the XF assay medium; Basal glycolysis = PER under basal condition (PER_{basal})–PER following 2DG injection (PER_{2DG}); Maximal glycolysis = PER following rotenone/antimycin A injection ($PER_{rot/ant}$)–PER_{2DG}.

ATP rate parameters were calculated using the following formulas:

ATP linked respiration (OCR_{ATP}) = OCR_{basal}–OCR_{oligo}; mitoATP production rate = OCR_{ATP} *2 * P/O (P/O = 2.75); mitoOCR = OCR_{basal}–$OCR_{rot/ant}$; mitoPER = mitoOCR * CO_2 Contribution Factor (CCF = 0.61); PER = ECAR * Buffer Factor * VolXF microchamber * Kvol (Kvol = 1.6); glycoATP production rate (glycoPER) = PER–mitoPER.

Statistical analysis

Results are given as mean ± SEM. All experiments were performed at least in triplicate, unless stated otherwise. The data were tested for the normality by using the Shapiro–Wilk normality test. Differences between data were evaluated by 1-way, 2-way repeated-measures ANOVA followed by the post-hoc Newman–Keuls or Tukey's multiple comparison test, as appropriate. A value of $P \leq 0.05$ was considered significant. All statistical analysis

was performed using GraphPad Prism software (GraphPad Software Inc.).

Results

CD34$^+$ HSPCs express GLP-1 receptor

We profiled the expression of GLP-1R in CD34$^+$ HSPCs at both mRNA and protein levels. In order to ensure cDNA amplification of the target mRNA and exclude PCR products from DNA contamination, we designed a couple of primers spanning exon-exon junction (Fig. 2A). Additionally, to confirm the correct amplification of the target template, the amplicon of 347 bp, characterized by a melting temperature of 83 °C, was resolved on 1% agarose gel. The bands were then excised and sequenced. The alignment of sequenced PCR end-point products with reference coding cDNA (NM_002062.5) showed 99% of identity (Fig. 2B, C and D). Additionally, in order to further support our hypothesis, GLP-1R mRNA expression was confirmed in CD34$^+$ HSPCs isolated from sternal BM biopsy of T2DM patients underwent bypass surgery (Additional file 3: Figure S3). Finally, total protein cell lysates obtained from 3 different samples of CD34$^+$ HSPCs were subjected to Western blot analysis. Protein cell lysate of capan-1 cells was used as positive control. As shown in Fig. 1E, GLP-1R antibody detected a unique, distinct protein band of the expected molecular weight (55 kDa) in all samples.

The administration of GLP-1 receptor agonist LIRA stimulates intracellular cAMP production

GLP-1Rs are known to be coupled to activation of Gαs proteins. In pancreatic β cells the receptor agonist engagement results in activation of adenylate cyclase with consequent production of 3′,5′-cyclic adenosine monophosphate (cAMP), intracellular Ca^{2+} increase and insulin release [15]. To determine whether CD34$^+$ HSPCs express a functional GLP-1R, we assessed intracellular cAMP production and Ca^{2+} mobilization after LIRA stimulation.

Consistent with activation of Gαs, the treatment of cells with LIRA elicited a significant accumulation of intracellular cAMP over basal level in a time- and dose dependent manner reaching the highest value after 10 min of stimulation at 100 nM (Fig. 3A and B). Notably, the addition of the selective GLP-1R antagonist exendin (9-39) (EXE) prevented intracellular cAMP accumulation at all tested LIRA concentrations, demonstrating a receptor-mediated effect (Fig. 3B). Interestingly, single cell analysis showed occurrence of spontaneous Ca^{2+} transients in CD34$^+$ HSPCs not significantly altered by 100 nM LIRA addition (Additional file 4: Figure S4A). Moreover, cell population analysis showed negligible increase in intracellular Ca^{2+} following LIRA addition (+4% over basal Ca^{2+} level, Additional file 4: Figure S4B). Thus, unlike pancreatic β-cells, acute GLP-1R stimulation in CD34$^+$ HSPCs did not significantly alter intracellular Ca^{2+}.

GLP-1R stimulation prevents CD34$^+$ HSPC dysfunction induced by chronic glucose overload

We recently published that metabolic stress induced by prolonged HG exposure results in loss of cell proliferation ability and CXCR4/SDF1-α axis impairment [14]. Herein, we tested whether LIRA, a GLP-1RA, was able to avert all these functional damages.

Despite the chronical exposure to HG concentration, LIRA dose-dependently (50 and 100 nM), prevented cell proliferation impairment. Noteworthy, the presence of 100 nM LIRA maintained cell proliferation rate to the control values (NG) (Fig. 4A and B). Similarly, LIRA treatment prevented CXCR4/SDF1-α axis defect promoted by HG exposure. Indeed, LIRA significantly maintained in dose dependent manner the migration ability of cells toward 50 ng/mL of SDF-1α (Fig. 4C) and CXCR4 expression (Fig. 4D and E).

LIRA reduces the oxidative state of CD34$^+$ HSPCs and metabolic imbalance promoted by HG exposure

We previously demonstrated that the loss of function promoted by HG-exposure was incident with mitochondrial ROS accumulation [14]. As shown in Fig. 5A and B, the maintenance of functional parameters despite HG presence was associated with a significant drug-induced reduction of cell oxidative state.

Moreover, HG-induced mitochondrial ROS accumulation was associated to oxidative metabolism dysfunction (Fig. 6). HG exposed CD34$^+$ HSPCs showed reduced maximal and spare MR, without significantly affecting basal MR. LIRA (100 nM) was able to restore maximal and spare MR to NG levels (Fig. 6A and Additional file 5: Figure S5A). Notably, neither HG-exposure nor LIRA treatment altered the percentage of the mitochondrial machinery used under basal conditions, as indicated by basal to maximal MR ratio, which remained constant

(See figure on next page.)

Fig. 2 GLP-1R expression in CD34$^+$ HSPCs. mRNA expression was assessed by RT-qPCR in 3 different CD34$^+$ HSPC biological replicates. An exon-exon spanning reverse primer was used to exclude any amplification of possible contaminating DNA; capan-1 cells were used as positive control (**A**). The identity of RT-qPCR products was determined by melting curve (**B**), agarose gel run (347 bp) (**C**) and finally by Sanger sequencing (**D**). CD34$^+$ HSPC lysates (40 µg) deriving from three biological replicates were immunoblotted in order to evaluate GLP-1R protein expression. Capan-1 cell lysate (20 µg) was used as positive control (**E**). S1, S2, S3 = samples 1, 2, 3

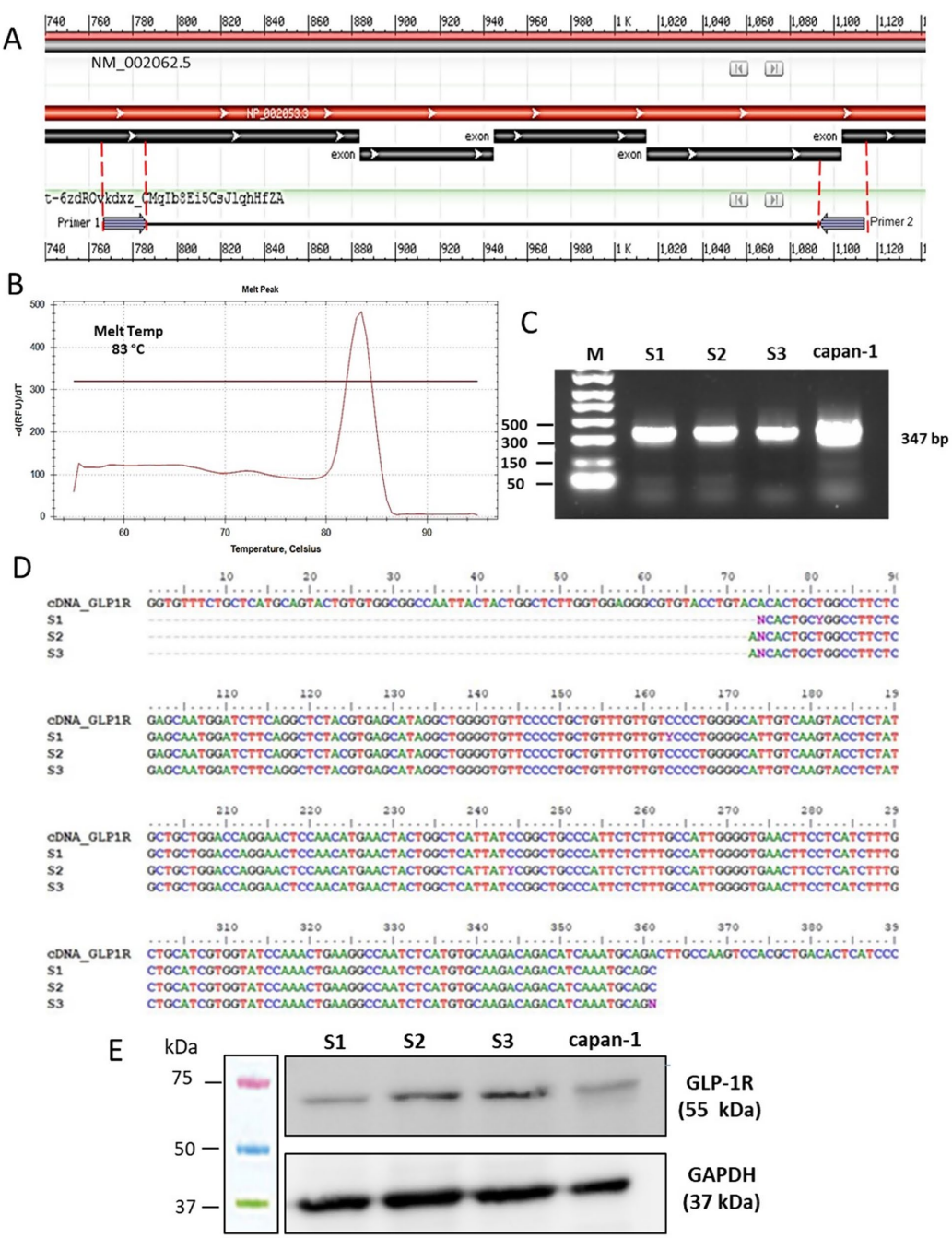

Fig. 2 (See legend on previous page.)

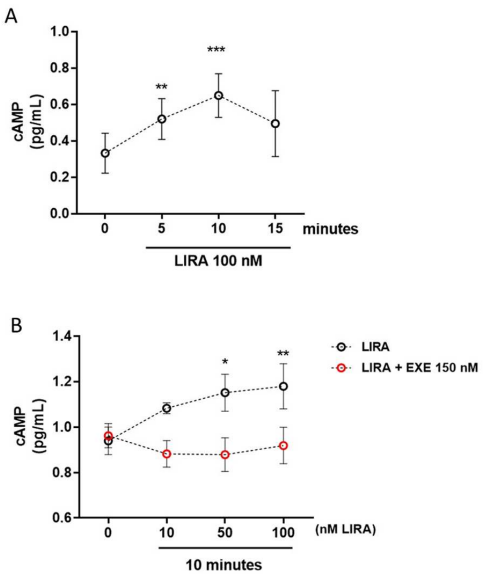

Fig. 3 GLP-1R downstream signaling pathway activation after stimulation by LIRA treatment. **A** $CD34^+$ HSPC stimulation with 100 nM LIRA determined a significant time-dependent accumulation of intracellular cAMP, with a maximum peak after 10 min of treatment (**p ≤ 0.01; ***p ≤ 0.001 *vs* basal; one-way ANOVA). **B** The addition of 150 nM EXE, a competitive antagonist of GLP-1R prevented the intracellular cAMP accumulation induced by increasing concentration of LIRA (10–100 nM) (*p ≤ 0.05, **p ≤ 0.01 *vs* basal two-way ANOVA). EXE = exendin 9–39, LIRA = liraglutide

in all groups. LIRA also restored the basal respiration devoted to ATP production (here reported as coupling efficiency, Fig. 6A). These effects of both HG and LIRA treatment were correlated to a trend in proton leak alteration (Additional file 5: Figure S5B). From the analysis of the glycolytic parameters, it emerged that HG-exposure increased the basal and maximal glycolysis and ATP produced via this metabolic route (Fig. 6B). Unlike the mitochondrial function, LIRA was unable to restore HG-induced glycolytic bioenergetic parameters changes to NG levels.

Overall, following HG exposure, LIRA treatment improved mitochondrial metabolism, stimulated ATP production via OXPHOS (Additional file 5: Figure S5C and S5D) and thereby increased the ATP rate index (Fig. 6).

GLP-1R stimulation promotes activation of ERK1/2 and PI3K signaling pathways

Stimulation of the GLP-1R is known to activate numerous pleiotropic signaling pathways in human pancreatic islet cells including PI3K and extracellular regulated kinases 1 and 2 (ERK1/2) [16, 17]. To determine whether the stimulation of endogenous GLP-1R expressed in $CD34^+$ HSPCs was also coupled to similar signal transduction pathways, we assessed the phosphorylation of ERK1/2 and AKT (a downstream effector of PI3K). As shown in Fig. 7A and C, stimulation of the cells with 100 nM LIRA elicited a time-dependent activation of both ERK1/2 and AKT kinases. LIRA-dependent kinase activation was abrogated by the addition of the two selective ERK1/2 and PI3K inhibitors: PD and WT, respectively (Fig. 7E and G).

These data indicate that $CD34^+$ HSPCs express a functional GLP-1R whose stimulation is coupled to additional signaling pathways other than adenylate cyclase.

Exendin (9–39) antagonizes LIRA effects against hyperglycemia

In order to confirm that LIRA-induced activation of diverse pro-survival signaling pathways was acting through GLP-1R activation, aforementioned experiments were carried out in the presence or absence of EXE antagonist (150 nM) [18]. As shown in Fig. 8A, EXE abrogated LIRA-dependent ERK1/2 and AKT phosphorylation as well as its protective effect on cell proliferation, measured as doubling time, (Fig. 8D) and CXCR4 membrane expression (Fig. 8E). Taken together, these findings support a GLP-1R-mediated effect of LIRA on intracellular pathways and functions of $CD34^+$ HSPCs.

LIRA partially recovers the functional damage induced by HG exposure in $CD34^+$ HSPCs

As we recently reported, a strong antioxidant machinery confers to $CD34^+$ HSPCs a particular resistance to HG-induced oxidative stress [14]. However, after antioxidant defense exhaustion, irreversible functional alterations take place. Here, in a different experimental setting (Fig. 1B), we aimed at investigating whether LIRA was also able to recover the compromised cell phenotype induced by HG exposure.

While 100 nM LIRA modestly improved HG-$CD34^+$ cell growth rate (Fig. 9A), we found that the same drug concentration significantly recovered CXCR4 membrane expression (Fig. 9B), and restored migration ability of the cells (Fig. 9C), although the latter less efficiently than when added concomitantly to HG. Again, these effects were associated with a significant drug-dependent reduction of intracellular ROS levels (Fig. 9D).

Discussion

CV complications remain the major cause of morbidity and mortality of patients with DM and first-generation glucose lowering agents have proved to be inadequate

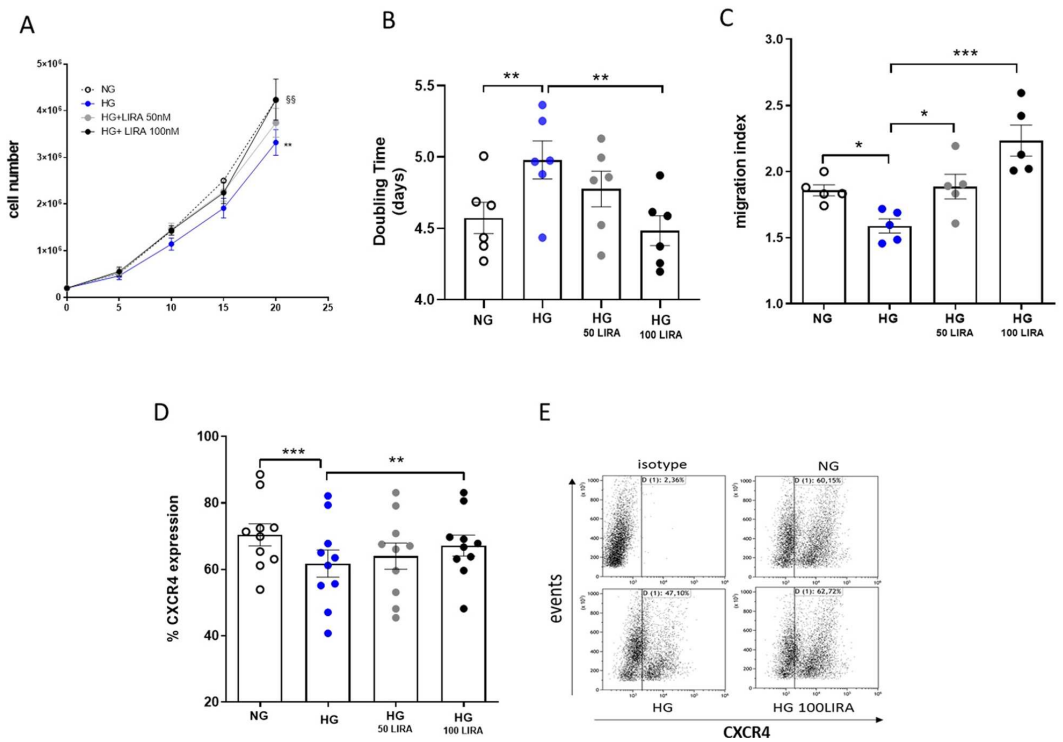

Fig. 4 LIRA treatment prevented CD34$^+$ HSPC proliferation, CXCR4/SDF-1α axis impairment and ROS accumulation caused by 20 days HG exposure. **A** Proliferation curve of CD34$^+$ HSPC amplified in NG, HG ± 50 nM and 100 nM LIRA conditions (**p ≤ 0.01 HG *vs* NG; §§ p ≤ 0.01 HG 100 LIRA *vs* HG; two-way ANOVA). **B** Doubling time of CD34$^+$ HSPCs cultured in NG, HG ± 50 nM and 100 nM LIRA (**p ≤ 0.01 HG *vs* NG; **p ≤ 0.01 HG 100 LIRA *vs* HG; one- way ANOVA). **C** CD34$^+$ HSPC migration towards SDF-1α (50 ng/mL) after NG, HG ± 50 nM and 100 nM LIRA treatment (*p ≤ 0.05 HG *vs* NG; *p ≤ 0.05 HG 50 LIRA *vs* HG; ***p ≤ 0.001 HG 100 LIRA *vs* HG; one-way ANOVA). **D** Analysis by flow cytometry of CXCR4 expression in NG, HG ± 50 nM and 100 nM LIRA treated CD34$^+$ HSPCs (***p ≤ 0.001 HG *vs* NG; ** p ≤ 0.01 HG 100 LIRA *vs* HG; one-way ANOVA). **E** Representative dot plot of CXCR4 cytofluorimetric analysis. HG = high glucose, LIRA = liraglutide, NG = normal glucose

[19] or only partially able to favorably impact CV prognosis [20]. Recently, large-scale trials unequivocally demonstrated the CV protective effects of two novel classes of glucose-lowering agents characterized by different dominant mechanism of action: sodium–glucose cotransporter-2 (SGLT2) inhibitors and GLP-1RAs. Both classes of drugs showed to significantly reduce the risk for MACE and all-cause mortality on top of standard of care in T2DM patients [8–10, 21, 22]. These CV benefits, independent from their glucose-lowering action, rely on the enrolment of different and not definitively understood mechanisms at multiple organ systems. Among the numerous pleiotropic actions of GLP-1RAs that favorably affect diabetes comorbidities, the metabolic changes of the patients are determinant. LIRA showed to improve beta cell function, especially in subjects treated with multiple daily insulin injection [23], and to ameliorate circulating metabolome, with particular regard to sphingolipids (e.g. ceramide) [24] and LDL metabolism, this latter by reduction of plasma PCSK9 level [25]. Collectively, these metabolic effects, along with a direct and complementary activity of the drugs at CV level, concur to the beneficial features of GLP-1RAs [26, 27]. Nevertheless, the existence of additional mechanisms has been postulated. CD34$^+$ HSPCs are known to play a central role in the maintenance of CV homeostasis by regulating vascular repair and regeneration [28–30]. The importance of CD34$^+$ HSPC biological functions on CV outcome [6] is supported by the common ontological origin of vascular and hematopoietic system [31]. Notably, Nandula and colleagues demonstrated that the amelioration of metabolic, CV and renal parameters of T2DM patients after canagliflozin therapy, a SGLT2 inhibitor, was associated with the improvement of CD34$^+$ HSPCs

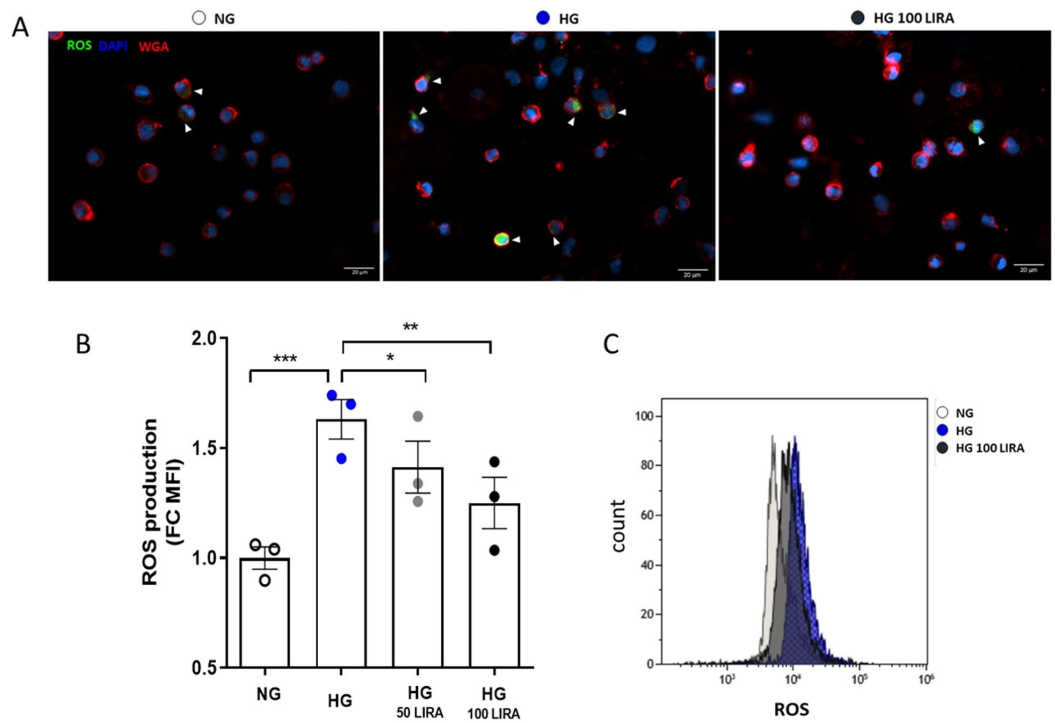

Fig. 5 Quantification of intracellular ROS level by immunocytochemistry (A) and flow cytometry (B) in NG, HG ± 50 nM and 100 nM LIRA treated cells (***p ≤ 0.001 HG *vs* NG; *p ≤ 0.05 HG 50 LIRA *vs* HG; ** p ≤ 0.01 HG 100 LIRA *vs* HG; one-way ANOVA). C) Representative flow cytometry histograms of intracellular ROS quantification. HG = high glucose, LIRA = liraglutide, NG = normal glucose

function [32]. Although different mechanisms of action are involved in CV protection of SGLT2 inhibitors, this study further supports the hypothesis that part of the mechanisms whereby GLP-1RAs improve CV outcome could rely on LIRA ability to reverse the functional impairment of $CD34^+$ HSPC provoked by HG.

$CD34^+$ HSPCs express a functional GLP-1R

We firstly provided unprecedented evidence that cord blood- and BM-derived $CD34^+$ HSPCs express GLP-1R (Fig. 2 and Additional file 3: Figure S3). The demonstration of GLP-1R expression by the identification of mRNA transcripts encoding for GLP-1R open reading frame and the use of validated antisera is often lacking and controversial in literature [33]. Therefore, to assess mRNA expression, we designed a couple of primers containing a reverse primer spanning an exon-exon junction. This granted the sole amplification of GLP-1R transcripts excluding any products deriving from possible DNA contamination, as we successfully confirmed by qPCR amplification of genomic DNA (data not shown). Afterwards, qPCR products were sequenced and aligned with the reference coding cDNA (NM_002062.5) confirming their identity. GLP-1R protein expression was finally detected by a top cited and validated antibody [34, 35], whose specificity was further proven in capan-1 cell lysate, a pancreatic cancer cell line expressing GLP-1R [36].

GLP-1R is a member of the secretin family or class B G protein-coupled receptors (GPCRs) [37]. Consistently with its canonical Gs mediated pathway activation, we showed that $CD34^+$ HSPCs express a functional GLP-1R. In fact, LIRA elicited a time- and dose-dependent accumulation of intracellular cAMP that was abrogated by the competitive receptor antagonist EXE (Fig. 3). Noteworthy, differently from what reported in pancreatic β-cells, we observed a weak intracellular intracellular Ca^{2+} mobilization, suggesting that, in $CD34^+$ HSPCs, Ca^{2+}-mediated signaling pathways may not be fundamental for the biological activity of the receptor [38] (Additional file 4: Figure S4).

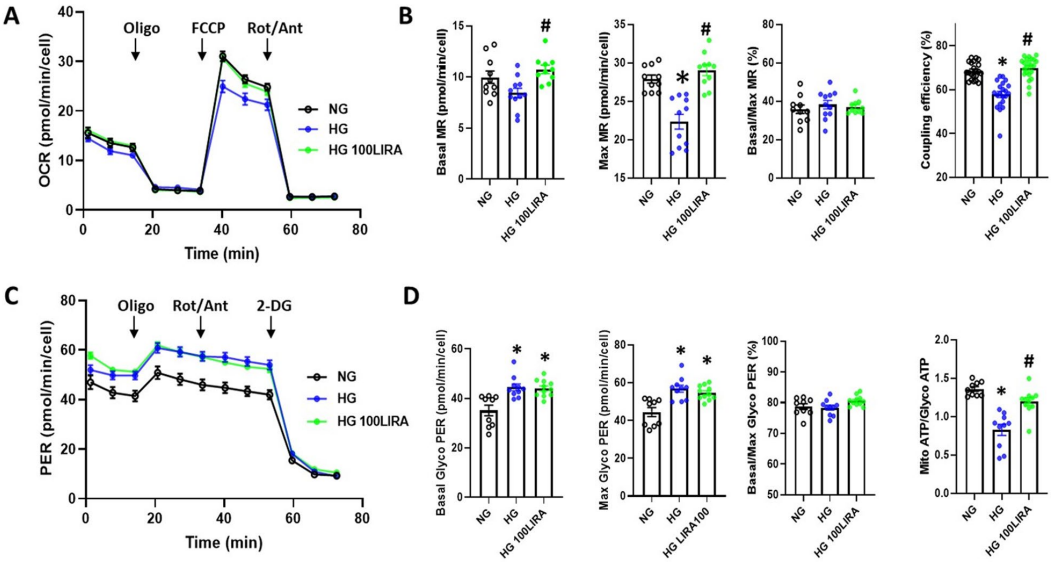

Fig. 6 LIRA recovered HG-damaged CD34$^+$ HSPC oxidative metabolism. Analysis of bioenergetics profiling with Seahorse in control (NG), after 20 days HG exposure alone (HG) or in the presence of 100 nM LIRA (HG 100LIRA). **A** Oxygen Consumption Rate (OCR) profiles of cells subjected to sequential injections of 1.5 µM oligomycin A, 2 µM FCCP and 0.5 µM rotenone + 0.5 µM antimycin A (XF Mito Stress Test protocol). OCR values were normalized to cell number by counting Hoechst-positive nuclei at the end of the experiment. **B** Statistics of mitochondrial parameters, including basal Mitochondrial Respiration (Basal MR), maximal Mitochondrial Respiration (Max MR), basal to maximal MR ratio and coupling efficiency. **C** Proton Efflux Rate (PER) profiles of cells subjected to sequential injections of 1.5 µM oligomycin A, 0.5 µM rotenone + 0.5 µM antimycin A and 50 mM 2-Deoxy-D-Glucose (combined XF ATP and Glyco rate protocols). **D** Statistics of glycolytic bioenergetic parameters, including basal Glycolysis (Basal GlycoPER), maximal Glycolysis (Max GlycoPER), basal to maximal GlycoPER ratio, ATP rate index (Mito ATP/Glyco ATP). *$p < 0.05$ vs NG, # $p < 0.05$ vs HG (one-way ANOVA plus Tukey's multiple comparison). Bioenergetic parameters were calculated from Seahorse data as described in Methods. Mean ± SEM from two individual experiments (n = 10–24 technical replicates). HG = high glucose, LIRA = liraglutide, NG = normal glucose

GLP-1R stimulation prevent HG-induced CD34$^+$ HSPC dysfunction and promotes mitochondrial metabolism

In the last years, a number of preclinical and clinical studies have demonstrated that native GLP-1 as well as GLP-1 RAs exert pleiotropic effects on different tissue subsets through both GLP-1R-dependent and independent mechanisms [27, 39]. At CV system level, they showed to improve endothelial function, reduce atherosclerosis, as well as oxidative stress and vascular and cardiac inflammation [27]. After GLP-1R expression in HSPC was confirmed, we were puzzled to evaluate its biological effects in a diabetic environment. We recently reported that the loss of glucose tolerance in CD34$^+$ HSPCs was associated with the reduction of proliferation rate, increase in mitochondrial ROS production and CXCR4/SDF-1α axis impairment [14]. These functional deficits are known to be primarily involved in the impairment of CD34$^+$ HSPC mobilization and migration capacity from the BM to sites of ischemia and endothelial injury in diabetic patients [40, 41]. Here we found that the concomitant administration of LIRA in HG setting was able to prevent HG-induced CD34$^+$ HSPC dysfunction and

(See figure on next page.)

Fig. 7 Intracellular pathway cross-talk after GLP-1R1 stimulation with 100 nM LIRA. **A** Representative immunoblots of ERK1/2 and **C** AKT phosphorylation in CD34$^+$ HSPCs treated with 100 nM LIRA for 5, 10 and 15 min and after the addition of MEK1/2 and PI3K selective pathway inhibitors, PD (**E**) and WT (**G**) respectively. GAPDH was used as loading control. **B**, **D**, **F**, **H** Immunoblotting quantification presented as arbitrary units after normalization to the GAPDH protein levels of three independent experiments. AKT = protein kinase B, ERK1/2 = extracellular signal-regulated kinases 1 and 2 GAPDH = Glyceraldehyde 3-phosphate dehydrogenase, LIRA = liraglutide, p-AKT = phospho-AKT, p-ERK1/2 = phospho-ERK1/2, PD = PD 98,059, WT = wortmannin

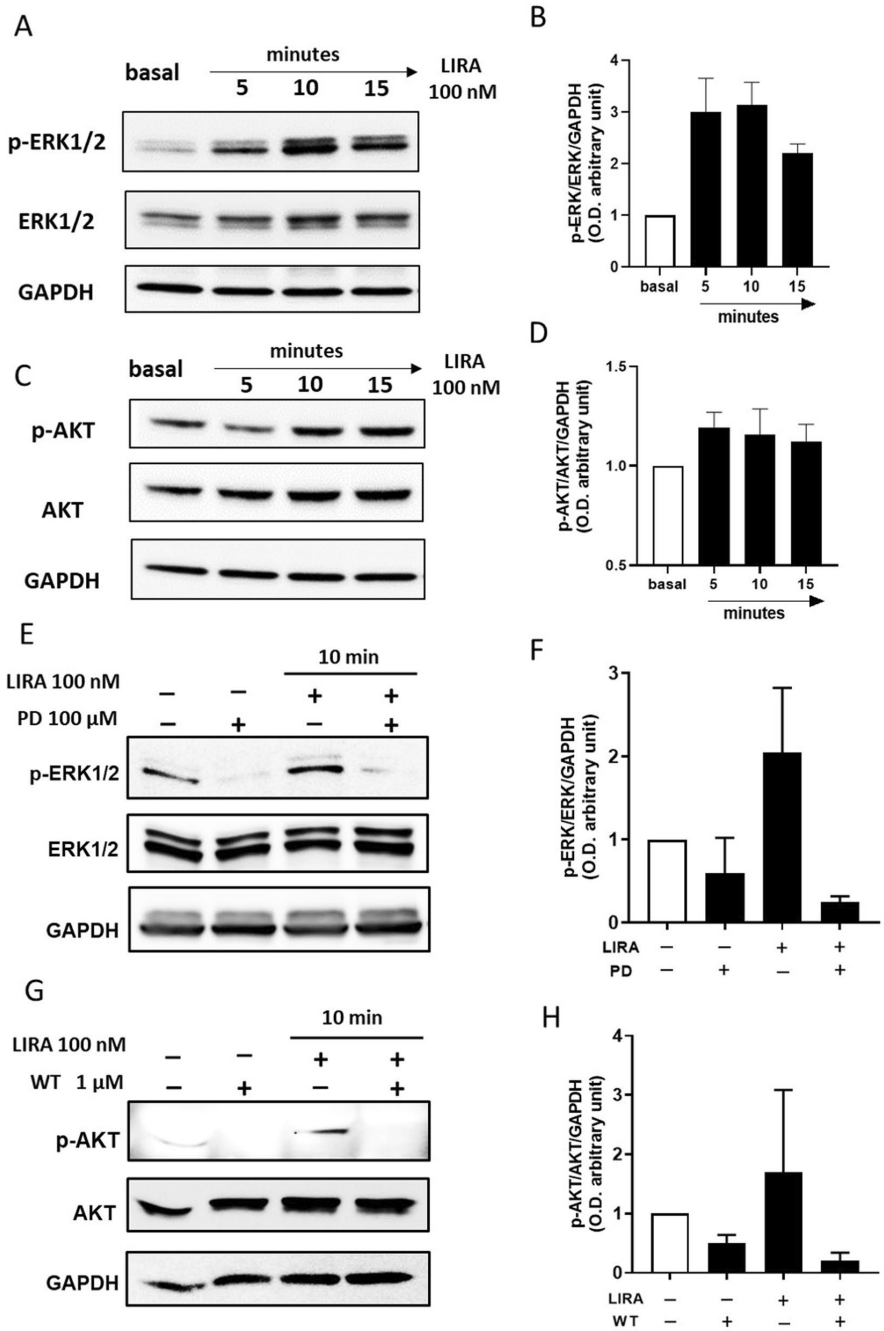

Fig. 7 (See legend on previous page.)

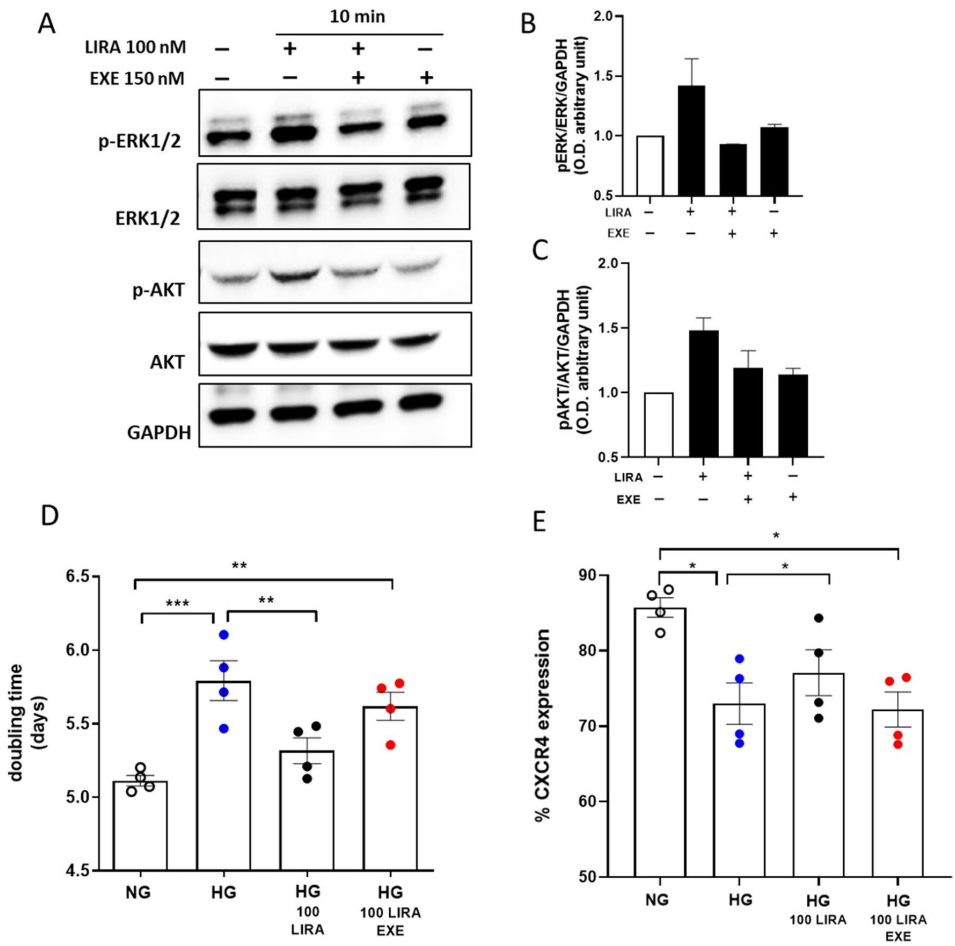

Fig. 8 The GLP-1R antagonist EXE abolished ERK1/2 and AKT phosphorylation as well as the protective effects promoted by LIRA treatment. **A** Representative immunoblot of ERK1/2 and AKT phosphorylation after stimulation with LIRA 100 nM ± EXE 150 nM for 10 min. GAPDH was used as loading control. **B**, **C** Immunoblotting results presented as arbitrary units after normalization to the GAPDH protein levels. **D** Doubling time of $CD34^+$ HSPCs cultured in NG, HG ± 50 nM and 100 nM ± EXE conditions (***$p \leq 0.001$ HG *vs* NG; ** $p \leq 0.01$ HG 100 LIRA *vs* HG; ** $p \leq 0.01$ HG 100 LIRA + EXE *vs* NG; one-way ANOVA. E) Analysis by flow cytometry of CXCR4 expression in NG, HG ± 50 nM and 100 nM ± EXE $CD34^+$ HSPCs (*$p \leq 0.05$ HG *vs* NG; *$p \leq 0.05$ HG 100 LIRA *vs* HG; *$p \leq 0.05$ HG 100 LIRA + EXE *vs* NG; one-way ANOVA). EXE = exendin 9–39, HG = high glucose, LIRA = liraglutide, NG = normal glucose

to improve their oxidative state (Figs. 4 and 5). It is well known that HG-induced overproduction of ROS can disrupt the mitochondrial membrane potential and damage mitochondrial function [42–45]. Seahorse analysis confirmed that exposure to HG of $CD34^+$ HSPCs induces a significant reduction of ATP produced by mitochondrial respiration (OXPHOS), as well as a reduced maximal and spare respiratory capacity. HG-exposed cells compensate for the impairment of mitochondrial function with an improvement of glycolytic ATP production, associated with increased basal and maximal glycolytic capacity. GLP-1R stimulation by LIRA affected cellular bioenergetics and restored mitochondrial function. These results further support the hypothesis that GLP-1RAs are able to reverse the functional impairment of $CD34^+$ HSPC provoked by HG.

Interestingly, in line with recent findings, the protective effects of LIRA persisted throughout the entire duration

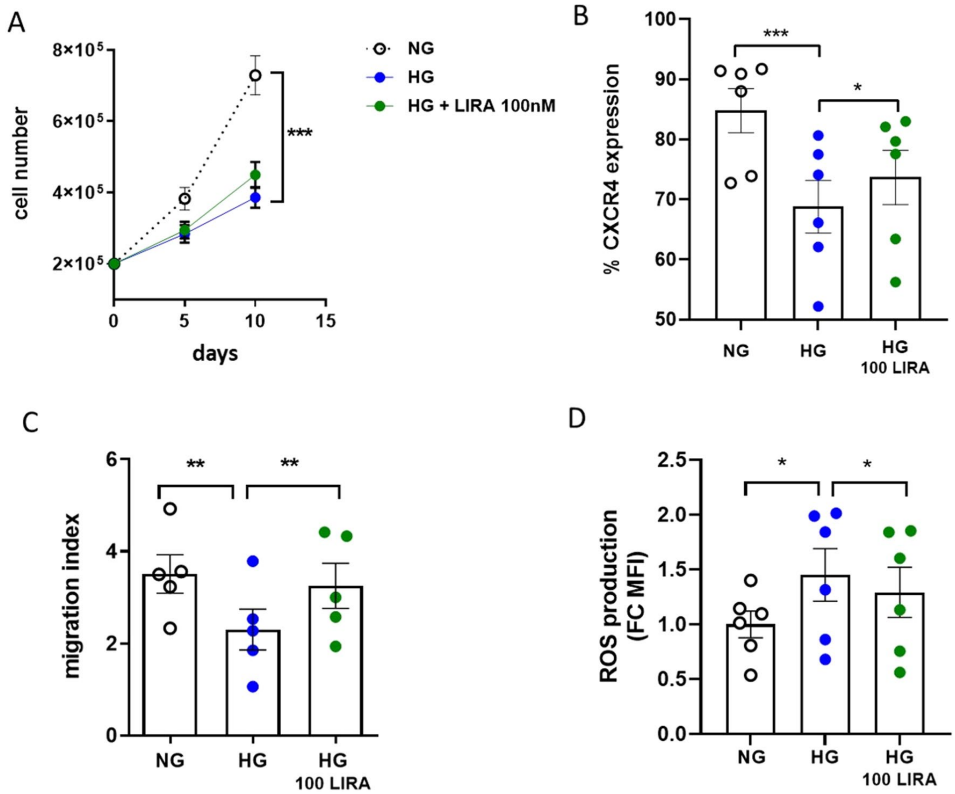

Fig. 9 LIRA partially recovered HG-damaged CD34$^+$ HSPC functions. **A** Proliferation curve of HG-damaged CD34$^+$ HSPCs after 10 days stimulation with 100 nM LIRA (***p ≤ 0.001 HG *vs* NG; two-way ANOVA). **B** Analysis by flow cytometry of CXCR4 expression level in HG-damaged CD34$^+$ HSPCs after 10 days of LIRA treatment (***p ≤ 0.001 HG *vs* NG; * p ≤ 0.05 HG 100 LIRA *vs* HG; one-way ANOVA). **C** Migration of HG-damaged CD34$^+$ HSPCs after 10 days of LIRA treatment (**p ≤ 0.01 HG *vs* NG; ** p ≤ 0.01 HG 100 LIRA *vs* HG; one-way ANOVA). **D** Quantification of intracellular ROS level by flow cytometry in HG-damaged CD34$^+$ HSPCs after 10 days of LIRA treatment (*p ≤ 0.05 HG *vs* NG; * p ≤ 0.05 HG 100 LIRA *vs* HG; one-way ANOVA). HG = high glucose, LIRA = liraglutide, NG = normal glucose

of the experiment, suggesting a sustained endosomal cyclic AMP generation induced by internalized activated receptor complex [46, 47].

GLP-1R stimulation promotes the activation of cytoprotective pathways

GLP-1R stimulation is known to promote transactivation of multiple intracellular pathways including PI3K, and ERK1/2. These pathways, which exert proliferative and cytoprotective functions [48], have been described in numerous extra glucose-lowering actions of incretins [39, 49]. In our hands, the treatment with 100 nM LIRA promoted in CD34$^+$ HSPCs a time dependent ERK1/2 and AKT phosphorylation that was completely abolished by the addition of PD 98059 and wortmannin, selective MEK1/2 and PI3K inhibitors respectively, and by the co-treatment with the GLP-1R antagonist EXE along with the related protective effects (Figs. 7 and 8). Albeit we are aware that we have not provided a full demonstration of the exact mechanism by which GLP-1R activation mediates ERK1/2 and AKT phosphorylation, we think we provided enough evidence that the protective effect of LIRA in CD34$^+$ HSPCs is mediated by GLP-1R, even if other mechanisms cannot be excluded.

According to guidelines, GLP1-RAs are now recommended to reduce the risk of CV events and mortality in T2DM patients. According to our hypothesis, this implies that LIRA cardiovascular protective effects are exerted after CD34$^+$ HSPC dysfunction has taken hold. To assess the ability of LIRA to recover a HG-related compromised

stem cell phenotype, the drug was given after the dysfunctional phenotype emerged. LIRA was able to recover $CD34^+$ HSPC function, even if less efficiently than early administration (Fig. 9). This observation corroborates accumulating evidence for supporting the use of GLP-1 RAs for CVD prevention in T2DM patients.

Conclusion

We provided first evidence that $CD34^+$ HSPCs express GLP-1R, and that the GLP-1RA LIRA prevents proliferation and migration impairment induced by chronic HG exposure. LIRA was also able to improve, even if less efficiently, $CD34^+$ HSPC function when previously exposed to HG conditions. Taken together these data suggest that the reported CV benefits of GLP-RAs can at least in part be related to cytoprotective effects on $CD34^+$ HSPCs.

Abbreviations

AKT/PKB: Protein kinase B; cAMP: Cyclic adenosine monophosphate; CB: Cord blood; CVD: Cardiovascular disease; ECAR: Extracellular acidification rate; ERK1/2: Extracellular signal-regulated kinases 1/2; EXE: Exendin fragment (9-39); FLT3: Fms-like tyrosine kinase 3; GLP-1: Glucagon-like peptide 1; GLP1-RAs: GLP-1 receptor agonists; HG: Hyperglycemic; IL: Interleukin; LIRA: Liraglutide; MACE: Major cardiovascular events; MEK1/2: Mitogen-activated protein kinase kinase; MR: Mitochondrial respiration; NG: Normoglycemic; OCR: Oxygen consumption rate; OXPHOS: Oxidative phosphorylation; PER: Proton efflux rate; PI3K: Phosphatidylinositol 3-kinase; PD: PD98059; PVDF: Polyvinylidene difluoride; ROS: Reactive oxygen species; SCF: Stem cell factor; SGLT2: Sodium–glucose cotransporter-2; T2DM: Type 2 diabetes mellitus; WT: Wortmannin.

Supplementary Information

The online version contains supplementary material available at https://doi.org/10.1186/s12933-022-01486-9.

Additional file 1: Figure S1 Flow-cytometric evaluation of sorted $CD34^+$ cell purity vs CD14 and CD3 cell contamination.

Additional file 2: Figure S2 A FCCP-uncoupled respiration (Maximal MR) and **B** coupling efficiency calculated from a Mito stress test assay performed on $CD34^+$ HSPC grown in NG, HG and HG 100 LIRA using different combinations of oligomycin A (0.5 and 1.5 μM) and FCCP (0.5, 1, 2 and 5 μM) to identify their minimal dose with the maximal response. Data were normalized to 0.5 μM oligomycin A + 0.5 μM FCCP to highlight differences. Mean ± SEM from one experiment (n = 4 technical replicates). Bars indicate statistical differences between groups (one-way ANOVA).

Additional file 3: Figure S3 GLP-1R expression in BM-derived $CD34^+$ HSPCs of T2DM patients. mRNA expression was assessed by RT-qPCR in 3 different biological replicates. The identity of RT-qPCR products was determined by agarose gel run (347 bp). M = marker; PZ1, PZ2, PZ3 = patient 1, 2, 3; B = blank.

Additional file 4: Figure S4 Intracellular Ca^{2+} mobilization in $CD34^+$ HSPCs w/wo GLP-1R stimulation. **A** Spontaneous Ca^{2+} transients elicited in single FLUO4 loaded cells before and during LIRA treatment. **B** Mean FLUO4 fluorescence before and after LIRA injection from a population of $CD34^+$ HSPCs (N = 8).

Additional file 5: Figure S5 Statistics of Spare Mitochondrial Respiration (**A**, Spare MR), Proton Leak (**B**), Mito ATP (**C**) and Glyco ATP (**D**) from ATP rate assay in all experimental groups. Mean ± SEM from two individual experiments (n = 10–24 technical replicates). *p < 0.05 vs NG, # p < 0.05 vs HG (one-way ANOVA plus Tukey's multiple comparison).

Acknowledgements

None.

Author contributions

AS and VV performed the experiments and were responsible for collection and compilation of data and in writing the manuscript. ER and GLP helped in performing Western Blot analysis, compilation of the data and in manuscript writing. EG helped in flow cytometry analysis. RR contributed in performing cellular experiments. MA, AB and MR performed intracellular calcium signaling analysis. AM and ES performed glucose metabolism analysis. PF, AR and GP revised the manuscript. SG designed and revised the manuscript. MCV designed, performed statistical analysis, supervised the study and revised the manuscript. All authors read and approved the final manuscript.

Funding

The study has been supported by Ricerca Corrente of Italian Ministry of Health (RC 2019 2764158 to Centro Cardiologico Monzino IRCCS) and 5 × 1000 Charity Fund.

Declarations

Ethics approval and consent to participate

Not applicable.

Consent for publications

Not applicable.

Competing interests

The authors declare that they have no competing interests.

Author details

[1]Unit of Vascular Biology and Regenerative Medicine, Centro Cardiologico Monzino IRCCS, Via C. Parea 4, 20138 Milan, Italy. [2]Department of Biotechnology and Biosciences, Università degli Studi di Milano-Bicocca, Milan, Italy. [3]Division of Endocrinology, ASST Fatebenefratelli-Sacco, Milan, Italy. [4]International Center for T1D, Pediatric Clinical Research Center Romeo ed Enrica Invernizzi, DIBIC, Università di Milano, Milan, Italy. [5]Nephrology Division, Boston Children's Hospital, Harvard Medical School, Boston, MA, USA. [6]Department of Biosciences, Università degli Studi di Milano, Milan, Italy. [7]Unit of Experimental Cardio-Oncology and Cardiovascular Aging, Centro Cardiologico Monzino IRCCS, Milan, Italy. [8]Department of Biomedical, Surgical and Dental Sciences, Università degli Studi di Milano, Milan, Italy. [9]Diabetes, Endocrine and Metabolic Diseases Unit, Centro Cardiologico Monzino IRCCS, Milan, Italy.

Received: 18 November 2021 Accepted: 2 March 2022
Published online: 09 April 2022

References

1. Saeedi P, Petersohn I, Salpea P, Malanda B, Karuranga S, Unwin N, Colagiuri S, Guariguata L, Motala AA, Ogurtsova K, et al. Global and regional diabetes prevalence estimates for 2019 and projections for 2030 and 2045: results from the International Diabetes Federation Diabetes Atlas, 9(th) edition. Diabetes Res Clin Pract. 2019;157:107843.
2. American Diabetes A. classification and diagnosis of diabetes: standards of medical care in diabetes-2018. Diabetes Care. 2018;41(Suppl 1):S13–27.
3. Pozzoli O, Vella P, Iaffaldano G, Parente V, Devanna P, Lacovich M, Lamia CL, Fascio U, Longoni D, Cotelli F, et al. Endothelial fate and angiogenic properties of human CD34+ progenitor cells in zebrafish. Arterioscler Thromb Vasc Biol. 2011;31(7):1589–97.
4. Fadini GP, Boscaro E, de Kreutzenberg S, Agostini C, Seeger F, Dimmeler S, Zeiher A, Tiengo A, Avogaro A. Time course and mechanisms of circulating progenitor cell reduction in the natural history of type 2 diabetes. Diabetes Care. 2010;33(5):1097–102.
5. Fadini GP. A reappraisal of the role of circulating (progenitor) cells in the pathobiology of diabetic complications. Diabetologia. 2014;57(1):4–15.

6. Fadini GP, Rigato M, Cappellari R, Bonora BM, Avogaro A. Long-term prediction of cardiovascular outcomes by circulating CD34+ and CD34+CD133+ stem cells in patients with type 2 diabetes. Diabetes Care. 2017;40(1):125–31.
7. Rigato M, Avogaro A, Fadini GP. Levels of circulating progenitor cells, cardiovascular outcomes and death: a meta-analysis of prospective observational studies. Circ Res. 2016;118(12):1930–9.
8. Marso SP, Daniels GH, Brown-Frandsen K, Kristensen P, Mann JF, Nauck MA, Nissen SE, Pocock S, Poulter NR, Ravn LS, et al. Liraglutide and cardiovascular outcomes in type 2 diabetes. N Engl J Med. 2016;375(4):311–22.
9. Marso SP, Bain SC, Consoli A, Eliaschewitz FG, Jodar E, Leiter LA, Lingvay I, Rosenstock J, Seufert J, Warren ML, et al. Semaglutide and cardiovascular outcomes in patients with type 2 diabetes. N Engl J Med. 2016;375(19):1834–44.
10. Gerstein HC, Colhoun HM, Dagenais GR, Diaz R, Lakshmanan M, Pais P, Probstfield J, Riesmeyer JS, Riddle MC, Ryden L, et al. Dulaglutide and cardiovascular outcomes in type 2 diabetes (REWIND): a double-blind, randomised placebo-controlled trial. Lancet. 2019;394(10193):121–30.
11. American Diabetes A. Cardiovascular disease and risk management: standards of medical care in diabetes-2021. Diabetes Care. 2021;44(Suppl 1):S125–50.
12. Cosentino F, Grant PJ, Aboyans V, Bailey CJ, Ceriello A, Delgado V, Federici M, Filippatos G, Grobbee DE, Hansen TB, et al. 2019 ESC guidelines on diabetes, pre-diabetes, and cardiovascular diseases developed in collaboration with the EASD. Eur Heart J. 2020;41(2):255–323.
13. Wei Y, Mojsov S. Tissue-specific expression of the human receptor for glucagon-like peptide-I: brain, heart and pancreatic forms have the same deduced amino acid sequences. FEBS Lett. 1995;358(3):219–24.
14. Vigorelli V, Resta J, Bianchessi V, Lauri A, Bassetti B, Agrifoglio M, Pesce M, Polvani G, Bonalumi G, Cavallotti L, et al. Abnormal DNA methylation induced by hyperglycemia reduces CXCR 4 gene expression in CD 34(+) stem cells. J Am Heart Assoc. 2019;8(9):e010012.
15. Drucker DJ, Philippe J, Mojsov S, Chick WL, Habener JF. Glucagon-like peptide I stimulates insulin gene expression and increases cyclic AMP levels in a rat islet cell line. Proc Natl Acad Sci USA. 1987;84(10):3434–8.
16. Trumper J, Ross D, Jahr H, Brendel MD, Goke R, Horsch D. The Rap-B-Raf signalling pathway is activated by glucose and glucagon-like peptide-1 in human islet cells. Diabetologia. 2005;48(8):1534–40.
17. Park S, Dong X, Fisher TL, Dunn S, Omer AK, Weir G, White MF. Exendin-4 uses Irs2 signaling to mediate pancreatic beta cell growth and function. J Biol Chem. 2006;281(2):1159–68.
18. Goke R, Fehmann HC, Linn T, Schmidt H, Krause M, Eng J, Goke B. Exendin-4 is a high potency agonist and truncated exendin-(9–39)-amide an antagonist at the glucagon-like peptide 1-(7–36)-amide receptor of insulin-secreting beta-cells. J Biol Chem. 1993;268(26):19650–5.
19. Zoungas S, Chalmers J, Neal B, Billot L, Li Q, Hirakawa Y, Arima H, Monaghan H, Joshi R, Colagiuri S, et al. Follow-up of blood-pressure lowering and glucose control in type 2 diabetes. N Engl J Med. 2014;371(15):1392–406.
20. Riddle MC. Modern sulfonylureas: dangerous or wrongly accused? Diabetes Care. 2017;40(5):629–31.
21. Rajagopalan S, Brook R. Canagliflozin and cardiovascular and renal events in type 2 diabetes. N Engl J Med. 2017;377(21):2098–9.
22. Zinman B, Wanner C, Lachin JM, Fitchett D, Bluhmki E, Hantel S, Mattheus M, Devins T, Johansen OE, Woerle HJ, et al. Empagliflozin, cardiovascular outcomes, and mortality in type 2 diabetes. N Engl J Med. 2015;373(22):2117–28.
23. Westman K, Imberg H, Wijkman MO, Hirsch IB, Tuomilehto J, Dahlqvist S, Lind M. Effect of liraglutide on markers of insulin production in persons with type 2 diabetes treated with multiple daily insulin injections. J Diabetes Complications. 2022;36(3):108110.
24. Jendle J, Hyotylainen T, Oresic M, Nystrom T. Pharmacometabolomic profiles in type 2 diabetic subjects treated with liraglutide or glimepiride. Cardiovasc Diabetol. 2021;20(1):237.
25. Verges B, Hassid J, Rouland A, Bouillet B, Simoneau I, Petit JM, Duvillard L. Liraglutide reduces plasma PCSK9 in patients with type 2 diabetes not treated with statins. Diabetes Metab. 2021;48(2):101284.
26. Sposito AC, Berwanger O, de Carvalho LSF, Saraiva JFK. GLP-1RAs in type 2 diabetes: mechanisms that underlie cardiovascular effects and overview of cardiovascular outcome data. Cardiovasc Diabetol. 2018;17(1):157.
27. Drucker DJ. The cardiovascular biology of glucagon-like peptide-1. Cell Metab. 2016;24(1):15–30.
28. Vinci MC, Bassetti B, Pompilio G. Endothelial progenitors: when confusion may give rise to new understanding. Int J Cardiol. 2020;318:121–2.
29. Sietsema WK, Kawamoto A, Takagi H, Losordo DW. Autologous CD34+ cell therapy for ischemic tissue repair. Circ J. 2019;83(7):1422–30.
30. Ballard VL, Edelberg JM. Stem cells and the regeneration of the aging cardiovascular system. Circ Res. 2007;100(8):1116–27.
31. Bertrand JY, Chi NC, Santoso B, Teng S, Stainier DY, Traver D. Haematopoietic stem cells derive directly from aortic endothelium during development. Nature. 2010;464(7285):108–11.
32. Nandula SR, Kundu N, Awal HB, Brichacek B, Fakhri M, Aimalla N, Elzarki A, Amdur RL, Sen S. Role of Canagliflozin on function of CD34+ve endothelial progenitor cells (EPC) in patients with type 2 diabetes. Cardiovasc Diabetol. 2021;20(1):44.
33. Drucker DJ. Incretin action in the pancreas: potential promise, possible perils, and pathological pitfalls. Diabetes. 2013;62(10):3316–23.
34. Katsurada K, Nandi SS, Sharma NM, Zheng H, Liu X, Patel KP. Does glucagon-like peptide-1 induce diuresis and natriuresis by modulating afferent renal nerve activity? Am J Physiol Renal Physiol. 2019;317(4):F1010–21.
35. Yu M, Agarwal D, Korutla L, May CL, Wang W, Griffith NN, Hering BJ, Kaestner KH, Velazquez OC, Markmann JF, et al. Islet transplantation in the subcutaneous space achieves long-term euglycaemia in preclinical models of type 1 diabetes. Nat Metab. 2020;2(10):1013–20.
36. Koehler JA, Drucker DJ. Activation of glucagon-like peptide-1 receptor signaling does not modify the growth or apoptosis of human pancreatic cancer cells. Diabetes. 2006;55(5):1369–79.
37. Mayo KE, Miller LJ, Bataille D, Dalle S, Goke B, Thorens B, Drucker DJ. International Union of Pharmacology. XXXV. The glucagon receptor family. Pharmacol Rev. 2003;55(1):167–94.
38. Yabe D, Seino Y. Two incretin hormones GLP-1 and GIP: comparison of their actions in insulin secretion and beta cell preservation. Prog Biophys Mol Biol. 2011;107(2):248–56.
39. Graaf C, Donnelly D, Wootten D, Lau J, Sexton PM, Miller LJ, Ahn JM, Liao J, Fletcher MM, Yang D, et al. Glucagon-like peptide-1 and its class B G protein-coupled receptors: a long march to therapeutic successes. Pharmacol Rev. 2016;68(4):954–1013.
40. Cencioni C, Capogrossi MC, Napolitano M. The SDF-1/CXCR4 axis in stem cell preconditioning. Cardiovasc Res. 2012;94(3):400–7.
41. Egan CG, Lavery R, Caporali F, Fondelli C, Laghi-Pasini F, Dotta F, Sorrentino V. Generalised reduction of putative endothelial progenitors and CXCR4-positive peripheral blood cells in type 2 diabetes. Diabetologia. 2008;51(7):1296–305.
42. Sivitz WI, Yorek MA. Mitochondrial dysfunction in diabetes: from molecular mechanisms to functional significance and therapeutic opportunities. Antioxid Redox Signal. 2010;12(4):537–77.
43. Sifuentes-Franco S, Pacheco-Moises FP, Rodriguez-Carrizalez AD, Miranda-Diaz AG. The role of oxidative stress, mitochondrial function, and autophagy in diabetic polyneuropathy. J Diabetes Res. 2017;2017:1673081.
44. Ni R, Zheng D, Xiong S, Hill DJ, Sun T, Gardiner RB, Fan GC, Lu Y, Abel ED, Greer PA, et al. Mitochondrial calpain-1 disrupts ATP synthase and induces superoxide generation in Type 1 diabetic hearts: a novel mechanism contributing to diabetic cardiomyopathy. Diabetes. 2016;65(1):255–68.
45. Kaludercic N, Di Lisa F. Mitochondrial ROS formation in the pathogenesis of diabetic cardiomyopathy. Front Cardiovasc Med. 2020;7:12.
46. Girada SB, Kuna RS, Bele S, Zhu Z, Chakravarthi NR, DiMarchi RD, Mitra P. Galphas regulates Glucagon-like peptide 1 receptor-mediated cyclic AMP generation at Rab5 endosomal compartment. Mol Metab. 2017;6(10):1173–85.
47. Jones B, Buenaventura T, Kanda N, Chabosseau P, Owen BM, Scott R, Goldin R, Angkathunyakul N, Correa IR Jr, Bosco D, et al. Targeting GLP-1 receptor trafficking to improve agonist efficacy. Nat Commun. 2018;9(1):1602.
48. Vinci MC, Visentin B, Cusinato F, Nardelli GB, Trevisi L, Luciani S. Effect of vascular endothelial growth factor and epidermal growth factor on iatrogenic apoptosis in human endothelial cells. Biochem Pharmacol. 2004;67(2):277–84.
49. Gupta V. Pleiotropic effects of incretins. Indian J Endocrinol Metab. 2012;16(Suppl 1):S47-56.

Publisher's Note

ESC European Society of Cardiology

Cardiovascular Research (2022) **118**, 1020–1032
doi:10.1093/cvr/cvab123

SERCA2a stimulation by istaroxime improves intracellular Ca^{2+} handling and diastolic dysfunction in a model of diabetic cardiomyopathy

Eleonora Torre [1], Martina Arici [1], Alessandra Maria Lodrini [1], Mara Ferrandi [2], Paolo Barassi[2], Shih-Che Hsu[3], Gwo-Jyh Chang [4], Elisabetta Boz[5], Emanuela Sala [1], Sara Vagni[1], Claudia Altomare [6], Gaspare Mostacciuolo[1], Claudio Bussadori [5], Patrizia Ferrari[2], Giuseppe Bianchi[2], and Marcella Rocchetti [1]*

[1]Department of Biotechnology and Biosciences, Università degli Studi di Milano-Bicocca, Milan, Italy; [2]Windtree Therapeutics Inc., Warrington, PA, USA; [3]CVie Therapeutics Limited, Taipei, Taiwan; [4]Graduate Institute of Clinical Medical Sciences, Chang Gung University, Tao-Yuan 33305, Taiwan; [5]Clinica Veterinaria Gran Sasso Via Donatello, 26, 20131 Milano, Italy; and [6]Fondazione Cardiocentro Ticino, via Tesserete 48, Lugano 6900, Switzerland

Received 12 November 2020; revised 20 January 2021; editorial decision 22 March 2021; accepted 31 March 2021; online publish-ahead-of-print 1 April 2021

Aims Diabetic cardiomyopathy is a multifactorial disease characterized by an early onset of diastolic dysfunction (DD) that precedes the development of systolic impairment. Mechanisms that can restore cardiac relaxation improving intracellular Ca^{2+} dynamics represent a promising therapeutic approach for cardiovascular diseases associated to DD. Istaroxime has the dual properties to accelerate Ca^{2+} uptake into sarcoplasmic reticulum (SR) through the SR Ca^{2+} pump (SERCA2a) stimulation and to inhibit Na^+/K^+ ATPase (NKA). This project aims to characterize istaroxime effects at a concentration (100 nmol/L) marginally affecting NKA, in order to highlight its effects dependent on the stimulation of SERCA2a in an animal model of mild diabetes.

Methods and results Streptozotocin (STZ) treated diabetic rats were studied at 9 weeks after STZ injection in comparison to controls (CTR). Istaroxime effects were evaluated *in vivo* and in left ventricular (LV) preparations. STZ animals showed (i) marked DD not associated to cardiac fibrosis, (ii) LV mass reduction associated to reduced LV cell dimension and T-tubules loss, (iii) reduced LV SERCA2 protein level and activity and (iv) slower SR Ca^{2+} uptake rate, (v) LV action potential (AP) prolongation and increased short-term variability (STV) of AP duration, (vi) increased diastolic Ca^{2+}, and (vii) unaltered SR Ca^{2+} content and stability in intact cells. Acute istaroxime infusion (0.11 mg/kg/min for 15 min) reduced DD in STZ rats. Accordingly, in STZ myocytes istaroxime (100 nmol/L) stimulated SERCA2a activity and blunted STZ-induced abnormalities in LV Ca^{2+} dynamics. In CTR myocytes, istaroxime increased diastolic Ca^{2+} level due to NKA blockade albeit minimal, while its effects on SERCA2a were almost absent.

Conclusions SERCA2a stimulation by istaroxime improved STZ-induced DD and intracellular Ca^{2+} handling anomalies. Thus, SERCA2a stimulation can be considered a promising therapeutic approach for DD treatment.

*Corresponding author. Tel: +39 0264483313; fax: +39 0264483565, E-mail: marcella.rocchetti@unimib.it

Graphical Abstract

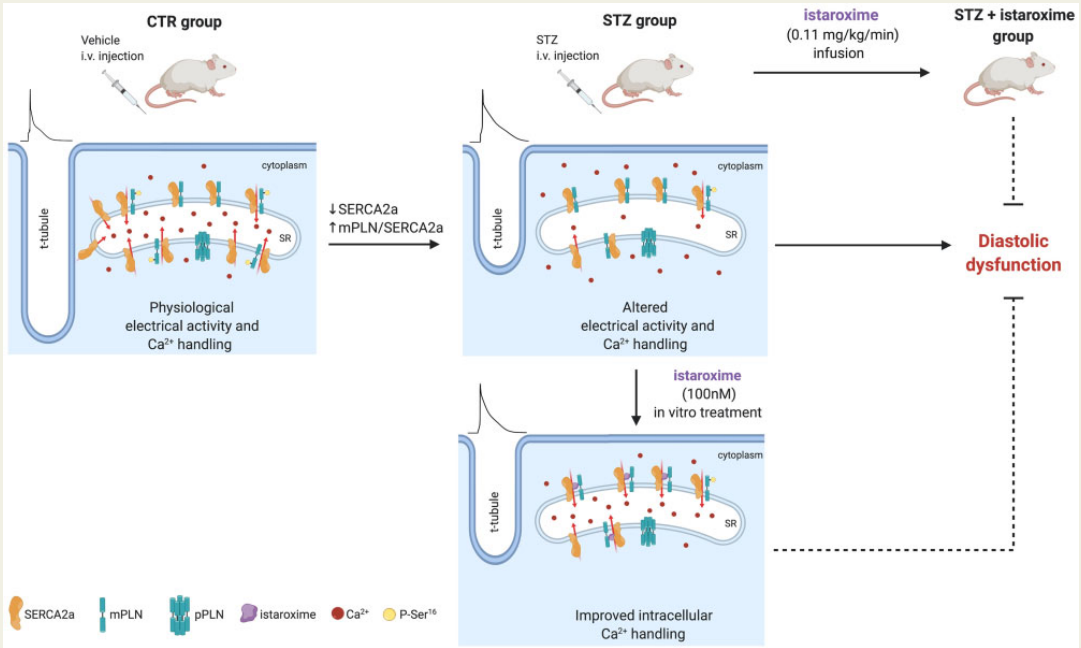

Keywords SERCA • Istaroxime • Diastolic dysfunction • Streptozotocin • Calcium handling

1. Introduction

Diabetes affects more than 300 million people globally and type 1 diabetes (T1D) accounts for up to 10% of cases.[1] Heart failure (HF) is the predominant cardiovascular complication of diabetes and represents the leading cause of morbidity and mortality. Diabetic cardiomyopathy (DCM) is a complex and multifactorial disease characterized by an early onset of diastolic dysfunction (DD), which precedes the development of systolic impairment.[2–5]

The molecular and pathophysiological mechanisms underlying diabetes include abnormalities in the regulation of Ca^{2+} homeostasis in cardiomyocytes and the consequent alteration of ventricular excitation–contraction coupling. In the diabetic heart, a dysregulation of Ca^{2+} cycling includes a reduction of SERCA2 activity, which may be accompanied by a decreased SERCA2 protein expression (mostly SERCA2a isoform).[6,7] A key role in the regulation of SERCA2a activity is played by phospholamban (PLN), a protein that behaves like its endogenous inhibitor when it is in its non-phosphorylated state.[8] In most diabetic models, PLN expression level appears increased while its phosphorylation state is reduced, thus, contributing to the inhibition of SERCA2a function.[6–8] This defect generates an impairment of sarcoplasmic reticulum (SR) Ca^{2+} refilling that results in slow diastolic relaxation. An abnormal Ca^{2+} distribution may facilitate cardiac arrhythmias appearance and myocyte apoptosis.[9,10]

Therefore, SERCA2a may represent a molecular target for a pharmacological intervention aimed at increasing the mechanical function and the energetic efficiency of the diabetic heart characterized by a defective SR Ca^{2+} loading. To date, the current medications have shown a limited efficacy in preventing the progression to HF in patients with DCM and diabetic complications.[10–12] New hypotheses have been recently proposed in HF aimed at improving cardiac contractility,[13–19] however, all these attempts are still far from being considered as beneficial treatment options available for clinicians and the treatment of HF and DCM remains an open field of research. The development of a small molecule as SERCA2a activator represents a promising strategy for HF and DCM treatment. Along this line, istaroxime is the first-in-class original luso-inotropic agent, shown to be highly effective and safe in patients.[20] Istaroxime is endowed of a double mechanism of action that consists in the ability to inhibit Na^+/K^+ ATPase (NKA) and enhance SERCA2a ATPase activity,[21] this last obtained through the relief of PLN inhibitory effect on SERCA2a,[22] without inducing spontaneous Ca^{2+} release (SCR) from SR.[21,23] In healthy and failing animal models and in patients with acute HF syndrome, istaroxime improves systolic and diastolic performance[20,24–28] and efficiency of cardiac contraction with a low oxygen consumption,[26] minimizing the risk of arrhythmias or ischaemia, without affecting other cardiovascular functions.[29–32]

In this study, we characterized the streptozotocin (STZ) model on different levels of biological organization, such as: (i) *in vivo*, to evaluate

STZ-induced DD, (ii) in isolated left ventricular (LV) cardiomyocytes, to evaluate structure, intracellular Ca^{2+} ($Ca^{2+}{}_i$) dynamics, electrical activity, and (iii) in LV and renal preparations (cell-free systems) to assess SERCA2a and NKA activity. We tested whether SERCA2a stimulation by a small molecule can improve the altered $Ca^{2+}{}_i$ handling responsible for the DD in STZ-treated rats. To this end, istaroxime was tested (i) *in vivo* after iv infusion in STZ rats, (ii) in LV myocytes at a concentration marginally affecting NKA to highlight its effects mostly dependent on SERCA2a stimulation, and (iii) in the cell-free systems.

2. Methods

All experiments involving animals (methods detailed in the online Supplementary material) conformed to the guidelines for Animal Care endorsed by the University of Milano-Bicocca and to the Directive 2010/63/EU of the European Parliament on the protection of animals used for scientific purposes. Male Sprague Dawley rats (150–175 gr) were used to generate a STZ-induced T1D cardiomyopathy model according to the Health Minister of Italy permission.

2.1 STZ rat model

T1D was induced through a single STZ (Sigma-Aldrich, 50 mg/kg) injection into a rat-tail vein; littermate control (CTR) rats received only citrate buffer (vehicle). Overnight fasting or non-fasting glycaemia was measured after 1 week by Contour XT system (Bayer). Animals were considered diabetic with fasting glycaemia values >290 mg/dL.

2.2 Echocardiography

Eight weeks after vehicle/STZ injection, rats were submitted to a transthoracic echocardiographic and Tissue Doppler evaluation, performed under urethane anaesthesia (1.25 g/kg i.p.) (M9 Mindray Echographer equipped with a 10 MHz probe, P10-4s Transducer, Mindray, China). Systolic and diastolic parameters were measured in CTR and diabetic (STZ) animals by a blinded investigator. Details are shown in the online Supplementary material.

A group of STZ rats was subjected to istaroxime infusion at 0.11 mg/kg/min for 15 min accordingly to a previous study.[25] Drug was infused through a polyethylene 50 cannula inserted into a jugular vein under urethane anaesthesia. Echocardiographic and Tissue Doppler parameters were measured under basal condition (before) and following 15 min istaroxime administration.

2.3 Morphometric parameters

Rats were euthanized by cervical dislocation under anaesthesia with ketamine-xylazine (130–7.5 mg/kg i.p) 9 weeks after STZ injection. Body weight (BW), heart weight (HW), LV weight (LVW), and kidney weight (KW) were measured. Body weight gain (BW gain) was obtained by subtracting the initial BW from the BW at sacrifice. HW and KW were normalized to tibia length (TL) to assess respectively cardiac and kidney indexes in CTR and STZ groups.

2.4 Myocyte dimensions and T-tubules (TT) analysis

Sarcolemmal membranes were stained by incubating isolated LV myocytes with 20 μmol/L di-3-ANEPPDHQ[33] (Life Technologies, Carlsbad, United States) to measure cell dimensions and TT organization/periodicity by a method based on Fast Fourier Transform.[34]

2.5 SERCA2a and Na^+/K^+ pump (NKA) activity measurement

SERCA2a activity was measured *in vitro* as ^{32}P-ATP hydrolysis at different Ca^{2+} concentrations (100–3000 nmol/L) in heart homogenates as previously described.[25] Ca^{2+} concentration–response curves were fitted by using a logistic function to estimate SERCA2a Ca^{2+} affinity (K_d Ca^{2+}) and V_{max}.

NKA activity was assayed *in vitro* by measuring the release of ^{32}P-ATP, as previously described.[35] The concentration of compound causing 50% inhibition of the NKA activity (IC_{50}) was calculated by using a logistic function.

2.6 Intracellular Na^+ and Ca^{2+} dynamics

Intracellular Na^+ ($Na^+{}_i$) and Ca^{2+} ($Ca^{2+}{}_i$) dynamics were evaluated by incubating LV myocytes with the membrane-permeant form of the dyes Ion NaTRIUM Green-2 AM (5 μmol/L) and Fluo4-AM (10 μmol/L), respectively.

$Na^+{}_i$ dynamics were monitored in I-clamp under physiological condition (Tyrode's solution) and in V-clamp under modified Tyrode's solution suitable to measure NKA current (I_{NKA}) at the same time.

$Ca^{2+}{}_i$ dynamics were analysed in field stimulated (2 Hz) and in patch-clamped myocytes. In field stimulated cells, SR Ca^{2+} loading and stability were evaluated through a post-rest potentiation protocol (Supplementary material online, *Figure S1*). Ca^{2+} transient (Ca_T) parameters and SR Ca^{2+} content (Ca_{SR}) were estimated at steady state (2 Hz) and following caffeine (10 mmol/L) superfusion, respectively. Moreover, incidence of SCR events was evaluated in each group during resting pauses and diastole.

To better highlight changes in $Ca^{2+}{}_i$handling not affected by modifications on electrical activity, $Ca^{2+}{}_i$ dynamic was also evaluated in voltage-clamped cells. Firstly, action potential (AP) clamp experiments were performed to verify whether Ca_T amplitude and Ca_{SR} were dependent on AP durations (APDs). To this end, two AP waveforms were used to dynamic voltage clamp STZ myocytes: a 'short AP' and a 'long AP' representative of the CTR and STZ group in terms of AP characteristics, respectively. $Ca^{2+}{}_i$ dynamics were then evaluated in voltage-clamped cells by standard V-clamp protocols.

Finally, to estimate SR uptake function in the absence of Na^+/Ca^{2+} exchanger (NCX) and NKA function, SR reloading protocol was applied in V-clamped cells by removing Na^+ from both sides of the sarcolemma (Supplementary material online, *Figure S2*).[21] Kinetics of SR Ca^{2+} reloading was evaluated; in particular, we considered the time constant of Ca_T decay (τ_{decay}) reflecting in this setting Ca^{2+} transport rate across the SR membrane, a functional index of SERCA2a activity.

2.7 Ca^{2+} sparks rate and characteristics

Spontaneous unitary Ca^{2+} release events (Ca^{2+} sparks) were recorded at room temperature in Fluo 4-AM (10 μmol/L) loaded myocytes at resting condition. Tyrode's bath solution contained 1 mmol/L $CaCl_2$.

2.8 AP rate-dependency and variability

APs were recorded in I-clamp condition by pacing myocytes at 1, 2, 4, and 7 Hz under Tyrode superfusion. Rate-dependency of APD at 50% (APD_{50}) and 90% (APD_{90}) of repolarization and diastolic potential (E_{diast}) were evaluated at steady state. Moreover, at each rate, a minimum of 30 APs were recorded at steady state to evaluate the short-term variability (STV) of APD_{90}, a well-known pro-arrhythmic index,[36] according to Eq. (1):

$$STV = \sum(|APD_{(n+1)} - APD_n|)/[n_{beats} \times \sqrt{2}] \quad (1)$$

Incidence of delayed afterdepolarizations (DADs) was evaluated.

2.9 Statistical analysis

Normal distribution of the results was checked by using the Shapiro–Wilk test. Paired or unpaired Student's *t*-test, one-way or two-way ANOVA were applied as appropriate test for significance between means. *Post hoc* comparison between individual means was performed by Tukey or Sidak multiple comparison tests. χ^2 test was used for comparison of categorical variables. Results are expressed as mean ± SEM. A value of $P < 0.05$ was considered significant.

Except when specified, *in vitro* istaroxime effects were analysed by incubating cells with the drug for at least 30 min, thus group comparison analysis was performed. Number of animals (*N*) and cells (*n*) are shown in each figure legend.

3. Results

3.1 Morphometric parameters

Diabetic rats were obtained by a single injection of STZ (50 mg/kg) into a tail vein and were compared to CTR rats receiving only vehicle. Fasting and non-fasting glycaemia increased significantly 1 week after STZ administration (*Table 1*).

At the time of STZ administration, BW was comparable among CTR and STZ groups (data not shown), while 9 weeks after STZ infusion, BW gain was largely different among groups because of a BW significantly lower in STZ than in CTR. TL was also measured as a rat growth index and resulted slightly reduced in STZ compared to CTR. HW was significantly lower in STZ than in CTR, even when HW was normalized to TL. Analogously, LVW normalized to HW, was significantly reduced in STZ in comparison to CTR. Likewise, LV cell length, volume, cross-sectional area (CSA), and cell membrane capacitance (C_m), a further index of cell dimension, were significantly reduced in STZ in comparison to CTR. Conversely, KW did not differ between the two groups, but KW/TL ratio resulted modestly increased in STZ rats vs. CTR, suggesting STZ-induced kidney hypertrophy (*Table 1*).

Table 1 Glycaemia values, morphometric parameters, and LV cell dimensions

	CTR	STZ	*P* vs. CTR
Fasting glycaemia (mg/dL)	94±2	390±14	*
Non-fasting glycaemia (mg/dL)	126±4	560±8	*
BW (g)	400±7	202±6	*
BW gain (g)	230±14	26±8	*
HW (g)	1.65±0.08	1.03±0.03	*
TL (cm)	4.3±0.02	3.63±0.03	*
HW/BW (g/kg)	4.11±0.17	5.16±0.11	*
HW/TL (g/cm)	0.40±0.03	0.28±0.009	*
LVW/HW (%)	67.9±1.0	63.4±0.7	*
KW (g)	2.23±0.05	2.19±0.07	NS
KW/TL (g/cm)	0.52±0.01	0.6±0.02	*
LV cell length (μm)	136±2.8	120±2.1	*
LV cell volume (10^3 μm^3)	65±1.9	37±1.03	*
LV CSA (um^2)	482±13.8	309±7.5	*
LV C_m (pF)	179±6	136±4	*

BW, Body weight; HW, heart weight; KW, kidney weight; LVW, left ventricular weight; TL, tibia length.
Morphometric parameters: CTR *N* =15–21, STZ *N* =23–34. Cell dimensions (length, volume, and CSA): CTR *N* =4 (*n* =58), STZ *N* =6 (*n* =108). Cell membrane capacitance (C_m): CTR *N* =12 (*n* =75), STZ *N* =13 (*n* =83).
*P<0.05 vs. CTR (unpaired *t*-test).

It was further investigated whether the decrease of cardiac weight/mass observed in STZ rats might be associated with cardiac fibrosis deposition. To this end, a western blot analysis for collagen type 1 and matrix metallopeptidase 9 (MMP-9) protein expression level was conducted on LV homogenates from CTR and STZ rats (Supplementary material online, *Figure S3*). The results indicate that any significant difference of collagen type 1 and MMP-9 protein content could be detected between the two rat groups.

3.2 STZ induces DD, reverted by acute istaroxime infusion

The echocardiographic parameters were measured in CTR and STZ rats 8 weeks after STZ injection (*Table 2*). Wall thickness for the interventricular septum (IVST) and posterior wall (PWT) both in diastole and systole did not differ between CTR and STZ rats. Analogously, LV end-diastolic and systolic diameter (LVEDD, LVESD) remained unchanged. The calculated fractional shortening (FS) did not differ while the TDI contraction velocity (s') was reduced in STZ animals when compared to CTR, thus suggesting an overall systolic function only partially compromised in STZ rats at this stage (*Table 2*).

The transmitral Doppler parameters were altered in STZ rats indicating an impairment of diastolic function. In particular, in STZ rats, while early (E) peak diastolic velocity was unchanged, E wave deceleration time (DT) was prolonged, thus, the mitral deceleration index (DT/E) and the deceleration slope (E/DT) tended respectively to increase and decrease; late peak diastolic velocity (A) was significantly increased and thus, E/A ratio resulted significantly reduced. Tissue Doppler examination showed in STZ rats a significant reduction of early diastolic myocardial velocity (e') and a significant increase of late diastolic myocardial velocity (a'), similarly to A wave. Thus, a significant reduction of e'/a' ratio and increase of the E/e' ratio was observed in STZ rats in comparison to CTR (*Table 2*).

The overall cardiac function indicated that stroke volume (SV), ejection fraction (EF), and cardiac output (CO) were not significantly affected in STZ rats although heart rate (HR) was reduced. Echocardiographic data mostly indicate that, at this time point, STZ induced a DCM characterized by DD and mostly preserved systolic function. Furthermore, the diastolic impairment observed in STZ rats at this early stage was not associated with cardiac fibrosis (Supplementary material online, *Figure S3*).

To analyse early *in vivo* effects of istaroxime in reducing STZ-induced DD, istaroxime was infused in STZ rats at 0.11 mg/kg/min[25] and echocardiographic parameters were collected 15 min later. The results (*Table 2*) showed that the compound was able to revert the DD documented in STZ rats with a significant reduction of DT and DT/E and an increase of E/DT and e'. No effect on CO, SV, and HR was observed following istaroxime infusion at this early time point (*Table 2*). Moreover, to exclude changes due to time dependent effects of urethane, echocardiographic parameters were collected every 5 min in a set of animals not treated with the drug. Up to 20 min in urethane anaesthesia, diastolic and systolic parameters remained constant (Supplementary material online, *Figure S4*). It should be noted that in a parallel study, we estimated istaroxime

Table 2 Echocardiographic and tissue Doppler parameters

	CTR	STZ basal	STZ + istaroxime
IVSTd (mm)	1.9±0.09	1.81±0.12	1.88±0.12
PWTd (mm)	1.71±0.17	1.45±0.08	1.47±0.07
LVEDD (mm)	6.6±0.35	7.08±0.32	7.27±0.23
IVSTs (mm)	2.6±0.22	2.54±0.18	2.57±0.19
PWTs (mm)	2.71±0.2	2.52±0.1	2.55±0.21
LVESD (mm)	3.07±0.39	3.11±0.28	3.1±0.34
FS (%)	53.8±5.66	56.2±2.4	57.7±3.7
E (m/s)	0.88±0.03	0.89±0.05	0.95±0.05
A (m/s)	0.52±0.07	0.7±0.03*	0.81±0.05**
E/A	1.82±0.21	1.26±0.03*	1.18±0.05
DT (ms)	53.5±1.55	61±2.17*	48.4±3.8**
DT/E (10^{-3} s^2/m)	61.3±1.43	69.3±4.5	52.2±5.6**
E/DT (10^3 m/s^2)	16.3±0.35	14.7±0.9	20.8±2.8**
s' (mm/s)	33.2±1.18	24.8±1.19*	25.2±1.11
e' (mm/s)	26.7±1.73	21.2±0.63*	24.5±1.46**
a' (mm/s)	20.7±1.61	27.8±1.99*	31.1±2
e'/a'	1.31±0.063	0.77±0.03*	0.79±0.02
E/e'	33.2±1.56	42.3±2.43*	39.1±1.57
HR (bpm)	303±9.5	233±10*	240±13
SV (mL)	0.59±0.1	0.73±0.08	0.78±0.05
CO (mL/min)	179.8±30.3	170.2±17	186.9±15
EF (%)	83.6±3.2	89.9±1.6	90.2±2.3
N	7	7	7

Average values in CTR and STZ animals before (basal) and after infusion with istaroxime at 0.11 mg/kg/min for 15 min.
A, a', late diastolic peak velocity; CO, cardiac output; DT, deceleration time; E, e', early diastolic peak velocity; EF, ejection fraction; FS, fractional shortening; HR, heart rate; IVSTd, telediastolic interventricular septum thickness; IVSTs, telesystolic interventricular septum thickness; LVEDD, left ventricular early-diastolic diameter; LVESD, left ventricular early-systolic diameter; PWTd, telediastolic posterior wall thickness; PWTs, telesystolic posterior wall thickness; s', systolic peak velocity; SV, stroke volume.
*P<0.05 vs. CTR (unpaired t-test),
**P<0.05 vs. STZ basal (paired t-test). CTR N=7, STZ N=7.

plasma level in male rats after 1 hour infusion at 0.11 mg/kg/min, resulting 780 nmol/L (N = 3, unpublished data); this suggests that drug concentration at 15 min infusion should be reasonably around 200 nmol/L.

3.3 Istaroxime affinity for rat NKA

To identify the *in vitro* istaroxime concentration suitable to limit its effects dependent on NKA inhibition, I_{NKA} was isolated in CTR rat LV myocytes and the concentration–response curve for istaroxime was evaluated as previously shown for guinea-pig[30] and mouse myocytes.[23] A saturating concentration of ouabain (1 mmol/L) was used (Supplementary material online, *Figure S5*) to evaluate the I_{NKA} inhibition by istaroxime as percentage of the ouabain-induced change. Moreover, a subgroup of cells was incubated with Ion NaTRIUM Green-2 to monitor Na^+_i changes under istaroxime or ouabain superfusion. The estimated IC_{50} for I_{NKA} inhibition by istaroxime was 32 ± 4 µmol/L (*Figure 1A*); a similar value was detected in cardiac (84 ± 20 µmol/L) (inset *Figure 1A*) and renal preparations (55 ± 19 µmol/L, Supplementary material online, *Figure S6*). Moreover, while NKA inhibition by 100 nmol/L istaroxime was detectable by measuring I_{NKA} in isolated myocytes (-6.9 ± 1.2%, P < 0.05, N = 14), istaroxime effects on NKA were not detectable up to 1 µmol/L in cardiac and renal preparations.

In isolated rat ventricular myocytes Na^+_i increased slightly under cumulative istaroxime concentrations (20 µmol/L istaroxime +2.2 ± 0.7%, P < 0.05, N = 5), while it was evident under saturating ouabain concentration (+8 6 ± 1.4%, P < 0.05, N = 5) (*Figure 1A*).

Consistently with the aim of the study, istaroxime effects on STZ-induced changes were evaluated by testing the compound at concentrations marginally affecting NKA (100 or 500 nmol/L).

3.4 STZ induces SERCA2a down-regulation and TT loss

LV homogenates from CTR and STZ rats were used to measure SERCA2a and PLN protein level by western blot analysis. Representative western blots from CTR and STZ samples and the relative densitometric analysis indicized for actin content are shown in *Figure 1B*. SERCA2a protein expression resulted significantly reduced in STZ vs. CTR samples (-45%, P < 0.001); while monomeric (m) PLN levels were unchanged, pentameric (p) PLN levels were slightly increased (+22%, P < 0.05). As a consequence, both mPLN/SERCA2a and pPLN/SERCA2a ratio were significantly increased (+89% and +128%, respectively, P < 0.001), suggesting higher SERCA2a inhibitory activity by PLN in STZ group. Moreover, in STZ samples, while the fraction of phosphorylated Thr^{17}-mPLN ($pThr^{17}$-mPLN/mPLN) resulted unchanged, the fraction of phosphorylated Ser^{16}-mPLN ($pSer^{16}$-mPLN/mPLN) was reduced (-42%, P < 0.05), thus highlighting reduced PKA-dependent SERCA2a modulation in STZ. Most of these measurements were also performed in isolated LV myocytes showing comparable results as those shown in LV homogenates (Supplementary material online, *Figure S7*).

SERCA2a activity was measured in cardiac SR homogenates from CTR and STZ rats as ^{32}P-ATP hydrolysis assay (*Figure 1C*). In comparison to CTR preparations, SERCA2a V_{max} was significantly decreased (-25%, P < 0.05) in STZ, while the K_d Ca^{2+} did not differ (Supplementary material online, *Figure S8*). Overall, SERCA2a protein level and activity were reduced in STZ preparations, a result in line with echocardiographic parameters showing STZ-induced DD.

Disarray of the TT system has been described in several failure models and was generally characterized by loss of the transverse component. A sharp pattern of transverse striations was observed in CTR myocytes (*Figure 1D*); accordingly, in these myocytes, pixel variance was largely represented by the periodic component, whose period was consistent with transverse TT arrangement. LV disarray of the transverse TT was visually obvious in STZ myocytes, a result confirmed by the quantitative analysis of the power of the periodic component (*Figure 1D*).

3.5 Istaroxime effects on STZ-induced changes in Ca^{2+} dynamics

Istaroxime (500 nmol/L) stimulated SERCA2a activity in cardiac SR homogenates from STZ diabetic rats by increasing SERCA2a V_{max} (+25%, P < 0.01) to a value similar to CTR rats (*Figure 1C*) without affecting the K_d Ca^{2+} affinity (575 ± 98 nmol/L vs. 450 ± 51 nmol/L, NS, Supplementary material online, *Figure S8*). Conversely, in CTR rat preparations, V_{max} (*Figure 1C*) and K_d Ca^{2+}(Supplementary material online, *Figure S8*) parameters were unchanged in the presence of istaroxime.

Istaroxime effects on STZ-induced DD were then evaluated at the cellular level by measuring the SR ability to accumulate resting Ca^{2+} through a post-rest potentiation protocol in field stimulated myocytes. As shown in *Figure 2A*, following increasing resting pauses, the amplitude of the first

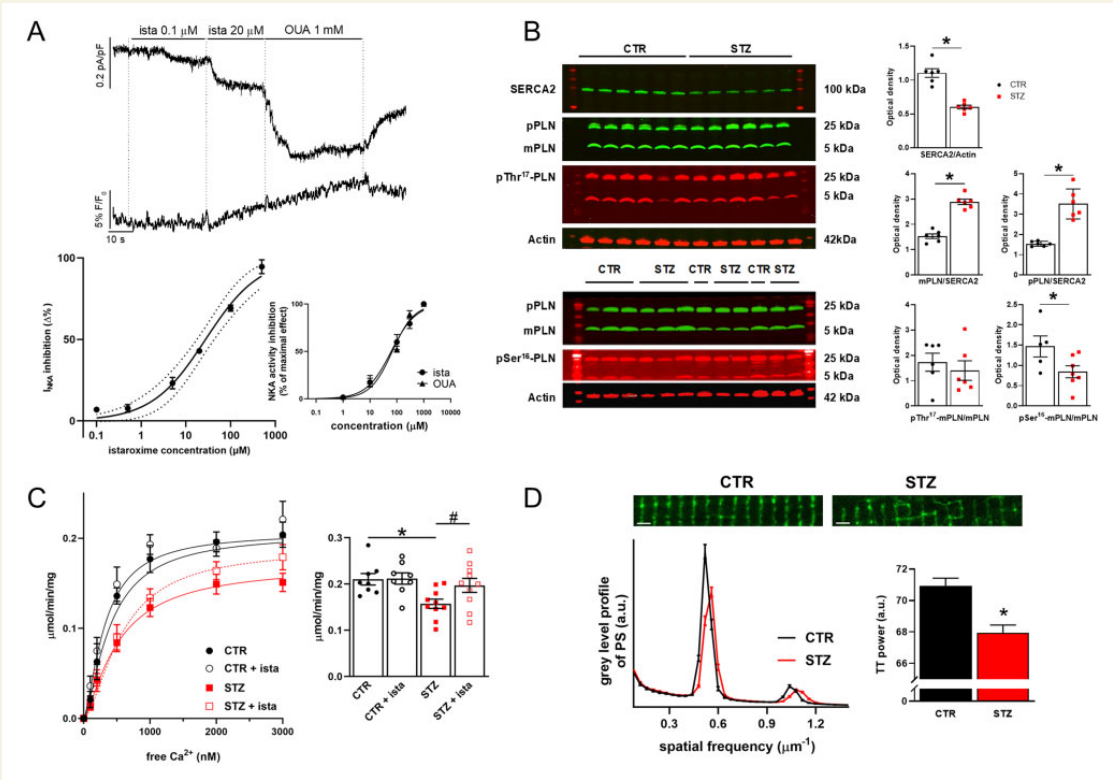

Figure 1 Istaroxime affinity for rat NKA. Changes in SERCA2, PLN levels, and TT expression in STZ vs. CTR rats. (*A*) Top: recordings of NKA current (I_{NKA}) and Ion NaTRIUM Green-2 fluorescence (Hp -40 mV) during exposure to increasing concentrations of istaroxime and, finally, to 1 mmol/L ouabain (OUA). Bottom: concentration-dependent I_{NKA} inhibition by istaroxime in isolated CTR LV myocytes (the best logistic fit and confidence intervals are shown, $N = 5$, $n = 6–27$). Concentration-dependent NKA activity inhibition by istaroxime and OUA in cardiac preparations is shown in the inset ($N = 5$). (*B*) Left: western blot for SERCA2, monomeric (m) and pentameric (p) PLN, pSer^{16}-PLN and pThr^{17}-PLN in STZ ($N = 6,7$) and CTR ($N = 5,6$) cardiac homogenates. Right: densitometric analysis; values are expressed as optical density in arbitrary units. *P<0.05 vs. CTR (unpaired t-test). (*C*) Left: Ca^{2+} activation curves of SERCA2a activity measured as cyclopiazonic acid sensitive component in cardiac SR homogenates from CTR ($N = 8$) and STZ ($N = 10$) rats with or w/o 500 nmol/L istaroxime. Right: statistics of the maximum velocity (V_{max}) of the Ca^{2+} activation curves estimated by sigmoidal fitting. *P<0.05 vs. CTR (unpaired t-test), #P<0.05 vs. STZ (paired t-test). (D) Top: confocal images of di-3-ANEPPDHQ (20 μmol/L) loaded CTR and STZ myocytes (horizontal bars 2 μm). Bottom: mean power spectrum profile of TT in CTR ($N = 5$, $n = 114$) and STZ ($N = 9$, $n = 181$) group; average results of the power of the periodic component on the right. *P<0.05 vs. CTR (unpaired t-test).

Ca_T increased progressively in CTR myocytes; according to STZ-induced SERCA2a down-regulation, post-rest potentiation was reduced in STZ myocytes at all resting intervals. Istaroxime at 100 nmol/L failed to affect post-rest potentiation in CTR myocytes, while it improved the ability of SR to accumulate Ca^{2+} especially at long resting pauses in STZ myocytes, in agreement with its stimulatory action on SERCA2a.

At steady-state, STZ increased diastolic Ca^{2+} (Ca_D) and CaT decay time ($t_{0.5}$), while leaving unchanged Ca_T amplitude and Ca_{SR} (*Figure 2B and C*). Istaroxime (100 nmol/L) significantly increased Ca_D in CTR myocytes, while blunted STZ-induced Ca_D enhancement in STZ myocytes. This was furtherly appreciable monitoring the time course of Ca_D enhancement during the SR reloading process following caffeine superfusion (*Figure 2D*). On the other hand, Ca_T amplitude, decay kinetics, and Ca_{SR} were not significantly affected by istaroxime in both CTR and STZ myocytes. Overall, STZ-induced SERCA2a down-regulation resulted in cytosolic Ca_D enhancement probably due to a reduced ability of SR to compartmentalize Ca^{2+} into the SR; however, SR Ca^{2+} content was preserved. In parallel, the effect of istaroxime on Ca_D in CTR myocytes was likely attributable to a partial NKA blockade, that was blunted in STZ myocytes by the simultaneous action on SERCA2a.

SCR events were evaluated in CTR and STZ cells. SCR events were absent in CTR while a not significant number of events occurred in STZ myocytes; istaroxime not affected their incidence in both CTR and STZ myocytes.

3.6 STZ induces changes in electrical activity affecting Ca^{2+}_i dynamics. Analysis of istaroxime effects

Potential changes in electrical activity in STZ myocytes might mask expected changes directly resulting from SERCA2a down-regulation (e.g. changes in Ca_{SR}).

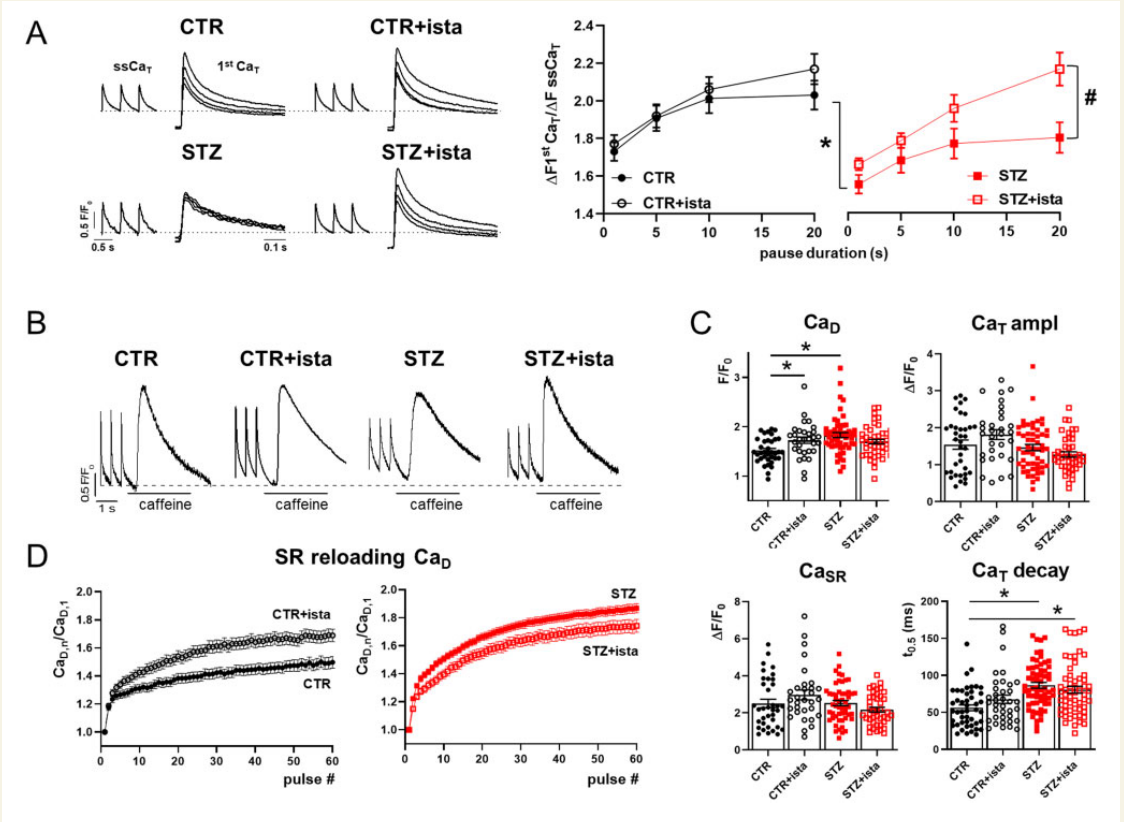

Figure 2 STZ-induced changes in Ca_i^{2+} dynamics in field stimulated myocytes. Analysis of istaroxime effects. (*A*) Left: post-rest potentiation protocol in Fluo4 field stimulated (2 Hz) myocytes; steady state Ca^{2+} transients ($ssCa_T$) and superimposed first Ca^{2+} transients (1^{st} Ca_T) following increasing resting pauses (1–5–10–20 s) are reported in CTR and STZ myocytes, with or w/o 100 nmol/L istaroxime. Traces were normalized to own diastolic Ca^{2+} (Ca_D) level (dotted lines). Right: analysis of the 1^{st} Ca_T amplitude normalized to the amplitude of the pre-pause $ssCa_T$ and its pause-dependency. CTR N = 5 (w/o istaroxime n = 44, with istaroxime n = 34), STZ N = 3 (w/o istaroxime n = 35, with istaroxime n = 23). *P<0.05 vs. CTR w/o istaroxime; #P<0.05 vs. STZ w/o istaroxime (two-way ANOVA plus *post hoc* Sidak's multiple comparisons). (*B*) $ssCa_T$ and caffeine-induced Ca_T evocated in field stimulated CTR and STZ myocytes with or w/o 100 nmol/L istaroxime (the dotted line indicates the Ca_D in CTR w/o istaroxime). (*C*) Statistics for $ssCa_D$, $ssCa_T$ amplitude, caffeine-induced Ca_T (named Ca_{SR}), and $ssCa_T$ half decay time ($t_{0.5}$). CTR N = 5 (n = 36 w/o istaroxime, n = 31 with istaroxime), STZ N = 7 (n = 52 w/o istaroxime, n = 42 with istaroxime). *P<0.05 vs. CTR w/o istaroxime (one-way ANOVA plus *post hoc* Tukey's multiple comparisons). (*D*) Changes in Ca_D during the reloading process after caffeine-induced SR depletion. Ca_D values ($Ca_{D,n}$) were normalized to the 1^{st} pulse Ca_D ($Ca_{D,1}$). CTR N = 5 (n = 36 w/o istaroxime, n = 29 with istaroxime), STZ N = 7 (n = 49 w/o istaroxime, n = 43 with istaroxime).

Thus, to verify STZ-induced changes in electrical activity, AP rate-dependency was evaluated in STZ myocytes in comparison to CTR. STZ induced a significant APD prolongation at all stimulation rates (*Figure 3A*), accordingly to voltage-dependent K^+ channels down-regulation.[37,38] Moreover, rate-dependency of E_{diast} observed in CTR myocytes was absent in STZ myocytes, probably due to STZ-induced NKA down-regulation.[39] In both CTR and STZ myocytes, istaroxime at 100 nmol/L not affected APD, while slightly depolarized E_{diast} especially in STZ myocytes (*Figure 3A*).

All these measurements were done following istaroxime incubation for at least 30 min to allow drug accumulation inside the cell and stimulate SERCA2a. On the other hand, to better understand drug effects on E_{diast}, likely attributable to NKA inhibition, a group of CTR myocytes were loaded with Ion NaTRIUM Green-2 and membrane potential plus Na^+_i were simultaneously recorded at 7 Hz (to highlight the contribution of NKA to E_{diast}) under basal condition and following istaroxime (100 nmol/L) superfusion; ouabain at saturating concentration was also tested as reference compound inhibiting NKA (*Figure 3B*). Istaroxime at 100 nmol/L slightly depolarized E_{diast} (Δ-0.58 ± 0.1 mV, n = 8, P < 0.05) in comparison to ouabain superfusion (Δ-13.5 ± 1.2 mV, n = 13, P < 0.05); in parallel, a significant Na^+_i enhancement was detectable during ouabain only (+3 ± 0.5% n = 13, P < 0.05).

Overall, as expected, STZ treatment largely affects ion channels and pumps resulting in AP shape changes; istaroxime at 100 nmol/L substantially leaved unchanged STZ-induced AP changes and further slightly depolarized E_{diast}, resulting from a minimal (about -7%) NKA inhibition.

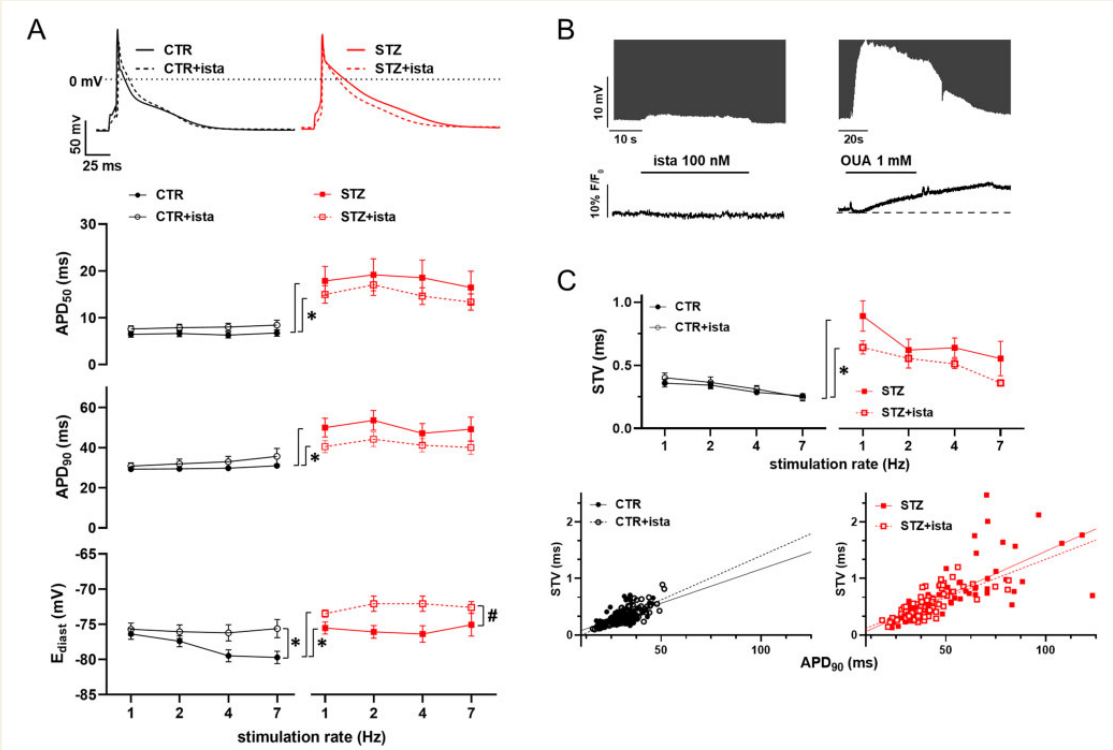

Figure 3 STZ-induced changes in electrical activity. Analysis of istaroxime effects. (*A*) Top: representative AP recorded at 1 Hz in CTR and STZ myocytes with or w/o 100 nmol/L istaroxime. Bottom: rate-dependency of AP parameters (APD_{50}, APD_{90}, E_{diast}) in CTR and STZ myocytes with or w/o 100 nM istaroxime. CTR $N = 4$ ($n = 29$ w/o istaroxime, $n = 25$ with istaroxime), STZ $N = 3$ ($n = 24$ w/o istaroxime, $n = 19$ with istaroxime). *P<0.05 vs. CTR w/o istaroxime, #P<0.05 vs. STZ w/o istaroxime (two-way ANOVA plus *post hoc* Sidak's multiple comparisons). (*B*) Effects of 100 nmol/L istaroxime superfusion on E_{diast} (top, AP *y* axis zoomed to highlight changes) and Na_i^+ (bottom) in comparison to the effect of 1 mmol/L OUA in CTR myocytes loaded with Ion Natrium Green-2 and stimulated at 7 Hz. (*C*) Top: rate-dependency of APD_{90} STV in each experimental group. CTR $N = 4$ ($n = 27$ w/o istaroxime, $n = 21$ with istaroxime), STZ $N = 3$ ($n = 24$ w/o istaroxime, $n = 20$ with istaroxime). *P<0.05 vs. CTR w/o istaroxime (two-way ANOVA plus *post hoc* Sidak's multiple comparisons). Bottom: linear correlation between STV of APD_{90} and APD_{90} values in CTR and STZ groups; data from all stimulation rates were pooled.

The STV of APD was evaluated in all groups, as a well-known pro-arrhythmic index. In comparison to CTR, STZ increased STV of APD at all pacing rates (*Figure 3C*); in both CTR and STZ myocytes, STV was not significantly affected by istaroxime, even though tended to be reduced in STZ myocytes. As expected, STV was directly correlated to APD_{90} in all groups; the slope of this correlation tended to increase in STZ group without reaching statistical significance (0.016 vs. 0.012, NS) and it was not significantly affected by istaroxime in both groups. These results suggest the absence of major mechanisms other than APD prolongation significantly affecting STV in all groups.[37]

Likewise to SCR incidence, DADs were completely absent in CTR myocytes and were present only in few cells in STZ groups (data not shown).

Given the STZ-induced APD prolongation, we verified if APD could effectively affect $Ca^{2+}{}_i$ handling in STZ myocytes. To this end, AP-clamp measurements were performed (*Figure 4A*). Ca_T were evocated in the same cell by using as voltage commands waveforms named 'short' AP (CTR AP) and 'long' AP (STZ AP) (see Section 2). In comparison to the short AP waveform, the long AP one caused a huge increase in Ca_T amplitude (+66 ± 9.4%, $P < 0.05$) and Ca_{SR} (+36 ± 9.8%, $P < 0.05$), confirming the hypothesis that the prolonged AP in STZ myocytes affected $Ca^{2+}{}_i$ handling.

3.7 STZ-induced $Ca^{2+}{}_i$ handling changes under control of membrane potential are reverted by istaroxime SERCA2a stimulation

To clarify direct effects of SERCA2a down-regulation and its stimulation by istaroxime on $Ca^{2+}{}_i$ handling, analysis on voltage-clamped myocytes was performed (*Figure 4B*) through a standard V-clamp protocol. Cells were superfused with Tyrode's solution to allow evaluation of both SR and NCX function. As shown in *Figure 4B*, STZ induced Ca_T and Ca_{SR} amplitude reduction, leaving unchanged fractional release. Influx through L-

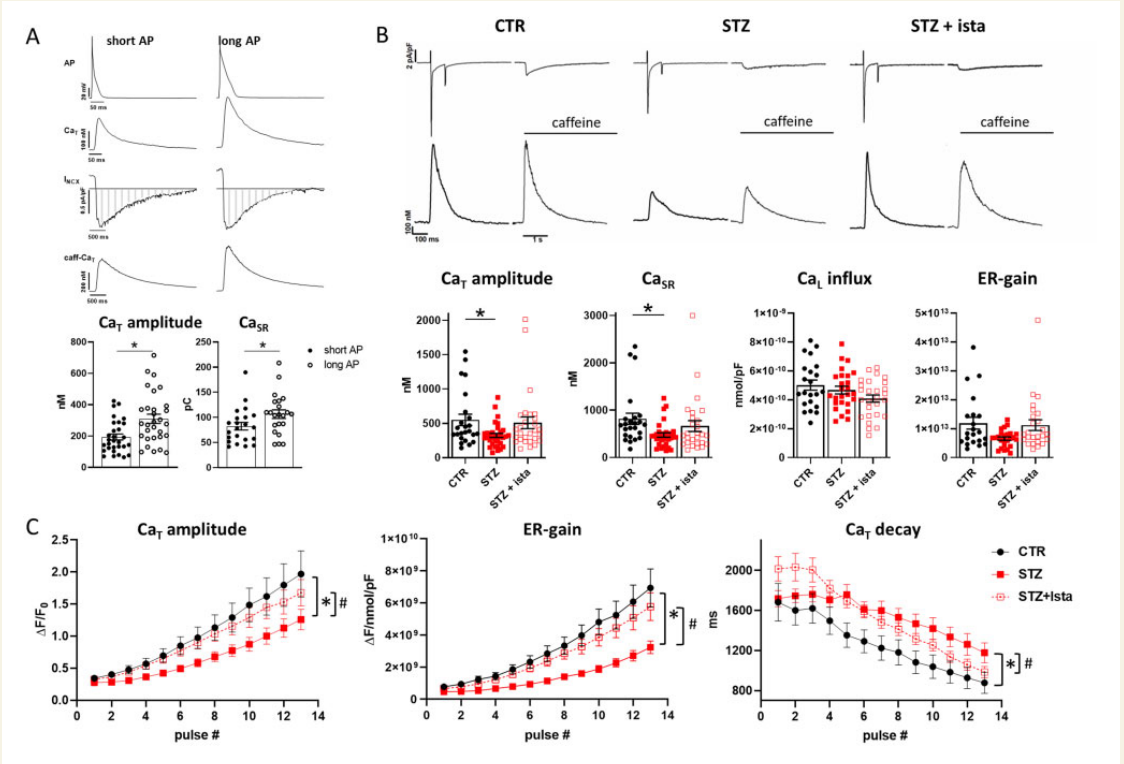

Figure 4 STZ-induced Ca_i^{2+} handling changes under control of membrane potential. Analysis of istaroxime effects. (*A*) Top: APs waveforms (CTR and STZ APs named short and long APs, respectively) and corresponding Ca_T evocated in V-clamped STZ myocyte through AP-clamp experiments (2 Hz). Caffeine-induced Ca_T (caff-Ca_T) and the corresponding NCX current (I_{NCX}) were recorded at -80 mV following steady state stimulation with short and long AP to estimate changes in SR Ca^{2+} content (Ca_{SR}). Bottom: statistics of Ca_T amplitude (N = 5, n = 30) and Ca_{SR} (integral of inward I_{NCX}, marked as striped area) (N = 5, n = 22) under short and long AP stimulation. Fluorescence signals were converted to free Ca^{2+} estimating F_{max} in each cell. *P<0.05 vs. short AP (paired t-test). (*B*) Top: transmembrane currents and Ca_T simultaneously recorded in voltage-clamped cells (Hp -35 mV) from CTR and STZ myocytes with or w/o 100 nmol/L istaroxime. Bottom: statistics of Ca_T amplitude, Ca_{SR}, Ca^{2+} influx through L-type Ca^{2+} channel (Ca_L influx), and ER gain. CTR N = 3 (n = 22–24), STZ N = 5 (w/o istaroxime n = 26–33, with istaroxime n = 28). Fluorescence signals were converted to free Ca^{2+} estimating F_{max} in each cell. *P<0.05 vs. CTR (one-way ANOVA plus Tukey's multiple comparison). (*C*) Statistics of Ca_T parameters (CaT amplitude, ER-gain, and CaT decay time constant) measured during each pulse after SR depletion under NCX blockade (see Supplementary material online, *Figure S2*) in CTR and STZ myocytes with or w/o 100 nmol/L istaroxime. *P<0.05 vs. CTR; #P<0.05 vs. STZ w/o istaroxime (two-way ANOVA); CTR N = 5 (n = 13–21), STZ N = 4 (w/o istaroxime n = 13–28, with istaroxime n = 19–24).

type Ca^{2+} channels (Ca_L influx) was not affected in STZ group, leading to an excitation–release (ER) gain that tended to be reduced in comparison to CTR. Moreover, in STZ myocytes, I_{CaL} peak density at 0 mV was significantly reduced, but the current decay tended to be slower; in particular, the fast decay time constant (τ_{fast}), reflecting Ca^{2+}-dependent inactivation, tended to increase in comparison to CTR myocytes (Supplementary material online, *Figure S9*). Thus, all I_{CaL} changes justify a global unaltered Ca^{2+} influx in STZ myocytes under these settings. Finally, the slope of the linear correlation between NCX current (I_{NCX}) and the Ca_{SR} (ΔI_{NCX}/ΔCa_{SR}) was similar in CTR and STZ myocytes (Supplementary material online, *Figure S10*), suggesting that SERCA2a down-regulation was not associated to changes in NCX activity in STZ myocytes. Treatment of STZ myocytes with istaroxime blunted differences between CTR and STZ.

Lastly, to estimate SR Ca^{2+} uptake function in the absence of NCX and NKA function, SR reloading protocol was applied in V-clamped cells by removing Na^+ from both sides of the sarcolemma as previously described.[21] As shown in *Figure 4C*, after SR depletion by caffeine superfusion, in comparison to CTR myocytes, the SR reloading process was slower in STZ myocytes, clearly confirming the SERCA2a down-regulation. In particular, in STZ myocytes, the rate of Ca_T increment was reduced and this was associated with a slower enhancement of the ER-gain. Moreover, the decay time constant, mostly representing SR Ca^{2+} uptake function, increased at each pulse, accordingly to a reduced SERCA2a function in STZ myocytes. Stimulation of SERCA2a by istaroxime caused faster SR reloading and all parameters were restored to CTR condition.

3.8 SERCA2a activity affects Ca^{2+} sparks characteristics

As shown before, both DADs and SCR events were detected only in few STZ myocytes, suggesting that SR stability is mostly preserved in this DCM model. To further analyse this point, Ca^{2+} sparks rate and characteristics were evaluated in all groups (*Figure 5*). Compared to CTR, STZ myocytes showed Ca^{2+} sparks with reduced amplitude, width, duration, and spark mass (*Figure 5B*), in agreement with a reduced SR Ca^{2+} content at resting. Istaroxime, by stimulating SERCA2a, partially restored Ca^{2+} sparks characteristics in STZ myocytes. In particular, istaroxime-induced SERCA2a stimulation emerged also by the analysis of Ca^{2+} sparks decay that significantly became faster in the presence of the compound. Sparks rate was not significantly affected by STZ and istaroxime.

4. Discussion

Aim of this study was to assess the effect of SERCA2a stimulation mediated by istaroxime in improving $Ca^{2+}{}_i$ dynamics in a diabetic rat model characterized by impaired diastolic function.

Several therapeutic approaches that increase SERCA2a function have been recently investigated.[18,40–43] However, despite of the intense research in discovering small molecules or gene therapy aimed at selectively activating SERCA2a, no promising clinical outcomes have been reached so far.

Istaroxime is the first-in-class original luso-inotropic agent targeting SERCA2a in addition to NKA inhibition, that has shown efficacy and safety in clinical trials on patients with acute HF syndrome.[20,28] In the past, *in vitro* istaroxime effects were largely characterized at concentrations showing dual mechanism of action.[21,23,27,29,30] In this study, lusitropic SERCA2a-dependent istaroxime effects were evaluated by testing istaroxime both *in vitro* and *in vivo* at concentrations marginally affecting NKA. Estimated drug plasma level at 15 min infusion and drug concentrations adopted for *in vitro* assays were largely comparable.

To our knowledge, no other small molecules active on SERCA2a at submicromolar concentration are available.

4.1 STZ-induced DCM. DD is associated to down-regulated SERCA2a expression and activity and is improved by istaroxime infusion

STZ rats showed a clear DD highlighted by changes in mitral inflow, in line with published results, reporting that DCM often manifests first as DD (*Table 2*). Our echo measurements evidenced marked alterations on DD indexes in STZ rats. In particular, we showed a significant transmitral Doppler flow enhancement of E wave DT and reduced E/A ratio in STZ rats. Analogously, TDI parameters, relatively unaffected by load, indicated a significant reduction of early diastolic myocardial velocity (e') and e'/a' with an increase of E/e' ratio in STZ rats. Systolic function appeared almost unaffected in STZ as compared to CTR rats, as indicated by FS and CO values. Moreover, we observed a marked

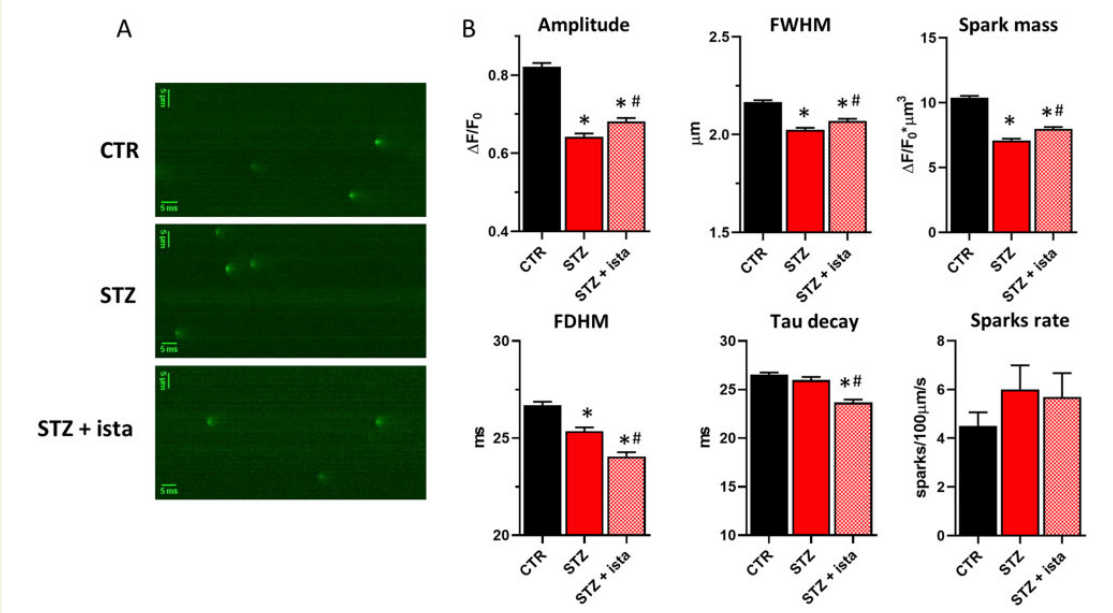

Figure 5 STZ-induced changes in Ca^{2+} sparks rate and characteristics. Analysis of istaroxime effects. (*A*) Representative xt images showing Ca^{2+} sparks at resting in CTR and STZ myocytes with or w/o 100 nmol/L istaroxime. (*B*) Statistics of Ca^{2+} sparks characteristics and rate for each group. *P<0.05 vs. CTR; #P<0.05 vs. STZ w/o istarpoxime (one-way ANOVA plus Tukey's multiple comparison); CTR N = 7 (n = 62, sparks # = 2789), STZ N = 5 (w/o istaroxime n = 53, sparks # = 2019, with istaroxime n = 47, sparks # = 1940). FWHM, full width at half maximum; FDHM, full duration at half maximum. Spark mass (spark amplitude*1.206* $FWHM^3$).

bradycardia, consistent with the impaired autonomic function and down-regulation of the expression of the pacemaker channel HCN4.[44]

Consistently with STZ-induced DD, in heart preparations and in cardiomyocytes from STZ rats, we observed a clear reduction of SERCA2 protein expression level, an increase of mPLN/SERCA2 ratio and a reduction of Ser^{16} phosphorylated mPLN (*Figure 1* and Supplementary material online, *Figure S7*). Conversely, CaMKII-dependent Thr^{17} phosphorylation of mPLN was similar between STZ and CTR rats (*Figure 1*). These biochemical alterations were associated with the reduction of SERCA2a ATPase activity observed in heart preparations from STZ compared to CTR rats (*Figure 1*) and indicate that these may translate into the impairment of diastolic function seen by the echocardiographic examination.

DCM is reported to be associated with cardiac fibrosis, which is responsible for increased LV stiffness and decreased ventricular wall compliance resulting in systolic and, in particular, DD.[45] However, in this study, no change of collagen type 1 and MMP-9 protein expression has been observed in LV from CTR and STZ rats, indicating that 8 weeks after STZ injection may be a time not long enough to develop this alteration. Moreover, several indexes indicated the absence of a concrete LV hypertrophy in STZ rats, because the increase in HW/BW was strictly dependent on BW loss. Otherwise, we observed reduced HW/TL and LV/HW ratios, results confirmed at the cellular level with reduced C_m, CSA, cell volume, and TT organization. These results are supported by a recent study showing reduced sinoatrial C_m in STZ-treated mice.[44] Loss of viable cardiomyocytes in STZ rats is also a possibility as previously shown.[46]

Collectively, these results indicate that STZ-induced DCM is characterized by impaired diastolic function associated with the down-regulation of SERCA2a expression and activity. This model is therefore suitable for testing the cardiac effects of SERCA2a stimulation by istaroxime. Istaroxime infused at 0.11 mg/kg/min for 15 min in STZ rats reverted the DD, inducing a significant reduction of DT and DT/E and an increase of e' (*Table 2*). The favourable mechanistic profile of istaroxime action is once again corroborated by our results in ameliorating DD in a DCM model.

4.2 STZ-induced changes in Ca^{2+}_i dynamics and electrical activity. Istaroxime effects at a concentration marginally affecting NKA

Consequences of STZ-induced SERCA2a down-regulation were functionally analysed in isolated LV myocytes. In particular, the post-rest potentiation protocol clearly highlighted the reduced ability of SR to accumulate Ca^{2+} at resting in STZ myocytes in comparison to CTR ones. This resulted in Ca_D enhancement when pacing cells at 2 Hz (*Figure 2*); in spite of this, Ca_{SR} left unchanged, probably as a consequence of STZ-induced changes in electrical activity. Indeed, STZ induced marked APD prolongation at all stimulation rates (*Figure 3A*), according to voltage-dependent K^+ channels down-regulation.[37] Moreover, the lack of E_{diast} rate dependent hyperpolarization in STZ myocytes is in agreement with STZ-induced NKA down-regulation.[39]

AP-clamp experiments clearly demonstrated the relevance of AP waveform in controlling Ca^{2+}_i dynamics (*Figure 4A*). Indeed, AP prolongation caused a sharp Ca^{2+}_i loading. Thus, STZ-induced changes in electrical activity might indirectly affect Ca^{2+}_i dynamics. In agreement with this, following the control of membrane potential (*Figure 4B*), direct effects of STZ-induced SERCA2a down-regulation were detected on Ca^{2+}_i handling. In particular, by clamping myocytes at -35 mV, STZ induced Ca_{SR} and Ca_T amplitude reduction, effects that were unseen in intact field stimulated cells. Moreover, incubating myocytes in extracellular and intracellular Na^+_i free solutions to remove NCX and NKA contribution (*Figure 4C*), SR Ca^{2+} uptake reloading kinetic following caffeine-induced SR depletion was clearly depressed in STZ myocytes.

Istaroxime stimulated SERCA2a in cardiac preparations from STZ rats by re-establishing the STZ-induced reduction of its maximal activity (V_{max}) without affecting its affinity for Ca^{2+} (K_d). Moreover, no effects on SERCA2a activity were detected in CTR heart preparation (*Figure 1*), indicating that the stimulatory action on SERCA2a is more remarkable when a pathological alteration (i.e. STZ-induced SERCA2a down-regulation) is present. Analogously, in dog cardiac SR vesicles, the stimulatory effect of istaroxime prevailed in the failing vs. healthy dog.[22] However, in healthy guinea pig cardiac microsomes, istaroxime stimulated SERCA2a by reducing the K_d Ca^{2+}.[21] The different effect of the compound on SERCA2a kinetic parameters in rat and dog (V_{max} enhancement) vs. guinea pig (K_d Ca^{2+} reduction) may not exclude species-specific differences in SERCA2a-PLN functional complex formation along the heart preparation, affecting istaroxime interaction. Furthermore, these kinetic changes across species might depend on how the compound interferes with species-specific SERCA2a-PLN complex domains. Although Ferrandi *et al.*[22] has already shown that istaroxime stimulates SERCA2a activity through a direct interaction with SERCA2a/PLN complex, favouring a partial dissociation of PLN from SERCA2a, further structural studies are still necessary to full understand istaroxime molecular mechanism of action.

At the cellular level, istaroxime stimulated SR Ca^{2+} uptake as clearly shown by applying the post-rest potentiation protocol to STZ myocytes (*Figure 2*). Moreover, as explain above, SERCA2a stimulation by the drug was fully remarkable by controlling membrane potential changes in voltage-clamped myocytes (*Figure 4*). Indeed, istaroxime, by stimulating SERCA2a, mostly restored STZ-induced changes in Ca_{SR} and Ca_T amplitude and it accelerated the SR uptake function, effects all compatible with a sharp enhancement of Ca^{2+} uptake by the SR, as expected from stimulation of SERCA2a activity.

STZ-induced Ca_D enhancement was blunted by istaroxime in paced STZ myocytes; by contrast, Ca_D was significantly increased by the drug in CTR myocytes. Moreover, istaroxime slightly depolarized E_{diast} in both CTR and STZ myocytes, as a result of a partial NKA blockade. Overall, the modulation of Ca_D by 100 nmol/L istaroxime might be the consequence of the balance between effects depending on SERCA2a stimulation and NKA inhibition, although negligible.

Abnormalities of the SR uptake function can be due to reduced SERCA2a activity or to increased Ca^{2+} leak through ryanodine receptor (RyR) channels. While functional and structural SERCA2a down-regulation (increased inhibition by PLN and reduced SERCA2a protein level) was observed, RyR open probability was not significantly changed in STZ myocytes. Indeed, Ca^{2+} sparks frequency (*Figure 5*), the incidence of Ca^{2+} waves and the related DADs were not significantly increased in STZ myocytes, thus suggesting the absence of a sharp SR instability at this stage of STZ-induced DCM. These findings lead to limit the detection of potential anti-arrhythmic effect of istaroxime as a direct consequence of SERCA2a stimulation.

Moreover, STZ-induced changes in Ca^{2+} sparks characteristics are a mirror image of the reduced SR Ca^{2+} content in STZ myocytes (*Figure 5*). Indeed, in comparison to CTR myocytes, Ca^{2+} sparks became smaller in amplitude, spatial and time duration, resulting in a smaller spark mass. Istaroxime, by stimulating SERCA2a, blunted these changes and even markedly accelerated Ca^{2+} sparks decay. The last event is

relevant for the potential anti-arrhythmic efficacy of istaroxime because of a faster Ca^{2+} release unit switch off, that can limit Ca^{2+} waves genesis. Moreover, the acceleration of Ca^{2+} spark decay induced by istaroxime seems independent on STZ-induced changes; thus, we cannot exclude direct effects of the drug on Ca^{2+} spark termination mechanisms.

Temporal dispersion of repolarization, quantified as STV of APD, is a well-known pro-arrhythmic index because plays an important role in the initiation of ventricular arrhythmias like *torsade de point*.[47] STV was significantly increased in STZ myocytes and this was mainly associated to APD prolongation (*Figure 3C*); istaroxime did not significantly affect STV.

4.3 Study limitation

The aim of the study was to test the effect of SERCA2a stimulation on DD in a DCM model. The study spreads from *in vivo* to *in vitro* effects of istaroxime at a concentration marginally affecting NKA. We would like to stress that even though effects dependent on NKA inhibition were detected, the general findings of the study are largely dependent on SERCA2a stimulation by the drug.

5. Conclusions and clinical implications

SERCA2a stimulation by istaroxime improves DD in diabetic rats, by controlling $Ca^{2+}{}_i$ compartmentalization. Thus, SERCA2a stimulation can be considered a promising therapeutic approach for DCM treatment. Even though the translation of drug effects from animal models to patients must take into account differences in the pathophysiological mechanisms/picture between animals and patients, STZ model was useful for studying the cardiac mechanical improvement produced by a drug endowed with a SERCA2a stimulatory activity. Accordingly, a recent phase II randomized clinical study in patients hospitalized for acute HF[28] showed that a 24 h infusion of istaroxime at 0.5 and 1 μg/kg/min improved cardiac function without major cardiac adverse effects. This is a proof-of-concept that SERCA2a stimulation is a novel and valid target for the treatment of high risk patients with reduced LVEF. Therefore, the development of small molecules active on SERCA2a only ('pure SERCA2a activators') might be clinically relevant to treat targeted patients with unfavourable cardiovascular outcomes with traditional therapies.

Supplementary material

Supplementary material is available at *Cardiovascular Research* online.

Authors' contributions

E.T. performed electrophysiological studies and drafted the manuscript; M.A. performed Ca^{2+} handling experiments; A.M.L. analysed data; E.S. and S.V. measured TT distribution and cell dimensions; M.F. and P.B. performed biochemical measurements; S.-C.H. and G.-J.C. performed *in vivo* measurements; E.B. and C.B. contributed to echocardiographic evaluations; C.A. analysed Ca^{2+} sparks; G.M. contributed with high-level technical assistance; P.F. and G.B. critically supervised the study; M.R. coordinated the study and wrote the manuscript.

Funding

This work was supported by CVie Therapeutics Limited (Taipei, Taiwan), Windtree Therapeutics (Warrington, USA), and FAR2019 of the University of Milano-Bicocca.

Conflict of interest: M.F. and P.B. are Windtree employees, P.F. and G.B. are Windtree consultants, S.-C.H. is employee of CVie Therapeutics Limited.

Data availability

The data underlying this article will be shared on reasonable request to the corresponding author.

References

1. Sherwin R, Jastreboff AM. Year in diabetes 2012: the diabetes tsunami. *J Clin Endocrinol Metab* 2012;**97**:4293–4301.
2. Schannwell CM, Schneppenheim M, Perings S, Plehn G, Strauer BE. Left ventricular diastolic dysfunction as an early manifestation of diabetic cardiomyopathy. *Cardiology* 2002;**98**:33–39.
3. Belke DD, Dillmann WH. Altered cardiac calcium handling in diabetes. *Curr Hypertens Rep* 2004;**6**:424–429.
4. Boudina S, Abel ED. Diabetic cardiomyopathy revisited. *Circulation* 2007;**115**:3213–3223.
5. Lebeche D, Davidoff AJ, Hajjar RJ. Interplay between impaired calcium regulation and insulin signaling abnormalities in diabetic cardiomyopathy. *Nat Clin Pract Cardiovasc Med* 2008;**5**:715–724.
6. Choi KM, Zhong Y, Hoit BD, Grupp IL, Hahn H, Dilly KW, Guatimosim S, Jonathan Lederer W, Matlib MA. Defective intracellular Ca^{2+} signaling contributes to cardiomyopathy in type 1 diabetic rats. *Am J Physiol Heart Circ Physiol* 2002;**283**:H1398–H1408.
7. Vasanji Z, Dhalla NS, Netticadan T. Increased inhibition of SERCA2 by phospholamban in the type I diabetic heart. *Mol Cell Biochem* 2004;**261**:245–249.
8. Kranias EG, Hajjar RJ. Modulation of cardiac contractility by the phopholamban/SERCA2a regulatome. *Circ Res* 2012;**110**:1646–1660.
9. Zaza A, Rocchetti M. Calcium store stability as an antiarrhythmic endpoint. *Curr Pharm Des* 2015;**21**:1053–1061.
10. Malek V, Gaikwad AB. Telmisartan and thiorphan combination treatment attenuates fibrosis and apoptosis in preventing diabetic cardiomyopathy. *Cardiovasc Res* 2019;**115**:373–384.
11. Dobrin JS, Lebeche D. Diabetic cardiomyopathy: signaling defects and therapeutic approaches. *Expert Rev Cardiovasc Ther* 2010;**8**:373–391.
12. Ng HH, Leo CH, Parry LJ, Ritchie RH. Relaxin as a therapeutic target for the cardiovascular complications of diabetes. *Front Pharmacol* 2018;**9**:501.
13. Jaski BE, Jessup ML, Mancini DM, Cappola TP, Pauly DF, Greenberg B, Borow K, Dittrich H, Zsebo KM, Hajjar RJ. Calcium upregulation by percutaneous administration of gene therapy in cardiac disease (CUPID Trial), a first-in-human phase 1/2 clinical trial. *J Card Fail* 2009;**15**:171–181.
14. Clark RJ, McDonough PM, Swanson E, Trost SU, Suzuki M, Fukuda M, Dillmann WH. Diabetes and the accompanying hyperglycemia impairs cardiomyocyte calcium cycling through increased nuclear O-GlcNAcylation. *J Biol Chem* 2003;**278**:44230–44237.
15. Shao CH, Capek HL, Patel KP, Wang M, Tang K, DeSouza C, Nagai R, Mayhan W, Periasamy M, Bidasee KR. Carbonylation contributes to SERCA2a activity loss and diastolic dysfunction in a rat model of type 1 diabetes. *Diabetes* 2011;**60**:947–959.
16. Kho C, Lee A, Jeong D, Oh JG, Gorski PA, Fish K, Sanchez R, Devita RJ, Christensen G, Dahl R, Hajjar RJ. Small-molecule activation of SERCA2a SUMOylation for the treatment of heart failure. *Nat Commun* 2015;**6**:7229.
17. Peng BY, Dubey NK, Mishra VK, Tsai FC, Dubey R, Deng WP, Wei HJ. Addressing stem cell therapeutic approaches in pathobiology of diabetes and its complications. *J Diabetes Res* 2018;**2018**:7806435.
18. Kaneko M, Yamamoto H, Sakai H, Kamada Y, Tanaka T, Fujiwara S, Yamamoto S, Takahagi H, Igawa H, Kasai S, Noda M, Inui M, Nishimoto T. A pyridone derivative activates SERCA2a by attenuating the inhibitory effect of phospholamban. *Eur J Pharmacol* 2017;**814**:1–8.
19. Bidasee KR, Zhang Y, Shao CH, Wang M, Patel KP, Dincer ÜD, Besch HR. Diabetes increases formation of advanced glycation end products on sarco(endo)plasmic reticulum Ca^{2+}-ATPase. *Diabetes* 2004;**53**:463–473.
20. Shah SJ, Blair JEA, Filippatos GS, MacArie C, Ruzyllo W, Korewicki J, Bubenek-Turconi SI, Ceracchi M, Bianchetti M, Carminati P, Kremastinos D, Grzybowski J, Valentini G, Sabbah HN, Gheorghiade M. Effects of istaroxime on diastolic stiffness in acute heart failure syndromes: results from the Hemodynamic, Echocardiographic, and Neurohormonal Effects of Istaroxime, a Novel Intravenous Inotropic and Lusitropic Agent: a Randomized Controlled Trial in Patients Hospitalized with Heart Failure (HORIZON-HF) trial. *Am Heart J* 2009;**157**:1035–1041.

21. Rocchetti M, Besana A, Mostacciuolo G, Micheletti R, Ferrari P, Sarkozi S, Szegedi C, Jona I, Zaza A. Modulation of sarcoplasmic reticulum function by Na+/K + pump inhibitors with different toxicity: digoxin and PST2744 [(E,Z)-3-((2-aminoethoxy)imino)androstane-6,17-dione hydrochloride]. *J Pharmacol Exp Ther* 2005;**313**:207–215.
22. Ferrandi M, Barassi P, Tadini-Buoninsegni F, Bartolommei G, Molinari I, Tripodi MG, Reina C, Moncelli MR, Bianchi G, Ferrari P. Istaroxime stimulates SERCA2a and accelerates calcium cycling in heart failure by relieving phospholamban inhibition. *Br J Pharmacol* 2013;**169**:1849–1861.
23. Alemanni M, Rocchetti M, Re D, Zaza A. Role and mechanism of subcellular Ca^{2+} distribution in the action of two inotropic agents with different toxicity. *J Mol Cell Cardiol* 2011;**50**:910–918.
24. Adamson PB, Vanoli E, Mattera GG, Germany R, Gagnol JP, Carminati P, Schwartz PJ. Hemodynamic effects of a new inotropic compound, PST-2744, in dogs with chronic ischemic heart failure. *J Cardiovasc Pharmacol* 2003;**42**:169–173.
25. Micheletti R, Palazzo F, Barassi P, Giacalone G, Ferrandi M, Schiavone A, Moro B, Parodi O, Ferrari P, Bianchi G. Istaroxime, a stimulator of sarcoplasmic reticulum calcium adenosine triphosphatase isoform 2a activity, as a novel therapeutic approach to heart failure. *Am J Cardiol* 2007;**99**:24A–32A.
26. Sabbah HN, Imai M, Cowart D, Amato A, Carminati P, Gheorghiade M. Hemodynamic properties of a new-generation positive luso-inotropic agent for the acute treatment of advanced heart failure. *Am J Cardiol* 2007;**99**:41A–46A.
27. Rocchetti M, Alemanni M, Mostacciuolo G, Barassi P, Altomare C, Chisci R, Micheletti R, Ferrari P, Zaza A. Modulation of sarcoplasmic reticulum function by PST2744 [Istaroxime; (E,Z)-3-((2-aminoethoxy)imino) androstane-6,17-dione hydrochloride] in a pressure-overload heart failure model. *J Pharmacol Exp Ther* 2008;**326**: 957–965.
28. Carubelli V, Zhang Y, Metra M, Lombardi C, Felker GM, Filippatos G, O'Connor CM, Teerlink JR, Simmons P, Segal R, Malfatto G, La Rovere MT, Li D, Han X, Yuan Z, Yao Y, Li B, Lau LF, Bianchi G, Zhang J, Istaroxime ADHF Trial Group. Treatment with 24 hour istaroxime infusion in patients hospitalised for acute heart failure: a randomised, placebo-controlled trial. *Eur J Heart Fail* 2020;**22**:1684–1693.
29. Micheletti R, Mattera GG, Rocchetti M, Schiavone A, Loi MF, Zaza A, Gagnol RJP, De Munari S, Melloni P, Carminati P, Bianchi G, Ferrari P. Pharmacological profile of the novel inotropic agent (E,Z)-3-((2-aminoethoxy)imino)androstane-6,17-dione hydrochloride (PST2744). *J Pharmacol Exp Ther* 2002;**303**:592–600.
30. Rocchetti M, Besana A, Mostacciuolo G, Ferrari P, Micheletti R, Zaza A. Diverse toxicity associated with cardiac Na+/K+ pump inhibition: evaluation of electrophysiological mechanisms. *J Pharmacol Exp Ther* 2003;**305**:765–771.
31. Gheorghiade M, Ambrosy AP, Ferrandi M, Ferrari P. Combining SERCA2a activation and Na-K ATPase inhibition: a promising new approach to managing acute heart failure syndromes with low cardiac output. *Discov Med* 2011;**12**:141–151.
32. Bossu A, Kostense A, Beekman HDM, Houtman MJC, van der Heyden MAG, Vos MA. Istaroxime, a positive inotropic agent devoid of proarrhythmic properties in sensitive chronic atrioventricular block dogs. *Pharmacol Res* 2018;**133**:132–140.
33. Rocchetti M, Sala L, Rizzetto R, Irene Staszewsky L, Alemanni M, Zambelli V, Russo I, Barile L, Cornaghi L, Altomare C, Ronchi C, Mostacciuolo G, Lucchetti J, Gobbi M, Latini R, Zaza A. Ranolazine prevents INaL enhancement and blunts myocardial remodelling in a model of pulmonary hypertension. *Cardiovasc Res* 2014;**104**:37–48.
34. Pasqualin C, Gannier F, Malécot CO, Bredeloux P, Maupoil V. Automatic quantitative analysis of t-tubule organization in cardiac myocytes using ImageJ. *Am J Physiol Cell Physiol* 2015;**308**:C237–C245.
35. Ferrandi M, Tripodi G, Salardi S, Florio M, Modica R, Barassi P, Parenti P, Shainskaya A, Karlish S, Bianchi G, Ferrari P. Renal Na,K-ATPase in genetic hypertension. *Hypertension* 1996;**28**:1018–1025.
36. Altomare C, Bartolucci C, Sala L, Bernardi J, Mostacciuolo G, Rocchetti M, Severi S, Zaza A. IKr impact on repolarization and its variability assessed by dynamic clamp. *Circ Arrhythm Electrophysiol* 2015;**8**:1265–1275.
37. Meo M, Meste O, Signore S, Sorrentino A, Cannata A, Zhou Y, Matsuda A, Luciani M, Kannappan R, Goichberg P, Leri A, Anversa P, Rota M. Reduction in Kv current enhances the temporal dispersion of the action potential in diabetic myocytes: insights from a novel repolarization algorithm. *J Am Heart Assoc* 2016;**5**:e003078.
38. Howarth FC, Jacobson M, Qureshi MA, Shafiullah M, Hameed RS, Zilahi E, Al Haj A, Nowotny N, Adeghate E. Altered gene expression may underlie prolonged duration of the QT interval and ventricular action potential in streptozotocin-induced diabetic rat heart. *Mol Cell Biochem* 2009;**328**:57–65.
39. Ku DD, Sellers BM. Effects of streptozotocin diabetes and insulin treatment on myocardial sodium pump and contractility of the rat heart. *J Pharmacol Exp Ther* 1982; **222**:395–400.
40. Hoshijima M, Ikeda Y, Iwanaga Y, Minamisawa S, Date MO, Gu Y, Iwatate M, Li M, Wang L, Wilson JM, Wang Y, Ross J, Chien KR. Chronic suppression of heart-failure progression by a pseudophosphorylated mutant of phospholamban via in vivo cardiac rAAV gene delivery. *Nat Med* 2002;**8**:864–871.
41. Suckau L, Fechner H, Chemaly E, Krohn S, Hadri L, Kockskamper J, Westermann D, Bisping E, Ly H, Wang X, Kawase Y, Chen J, Liang L, Sipo I, Vetter R, Weger S, Kurreck J, Erdmann V, Tschope C, Pieske B, Lebeche D, Schultheiss HP, Hajjar RJ, Poller WC. Long-term cardiac-targeted RNA interference for the treatment of heart failure restores cardiac function and reduces pathological hypertrophy. *Circulation* 2009;**119**:1241–1252.
42. Watanabe A, Arai M, Yamazaki M, Koitabashi N, Wuytack F, Kurabayashi M. Phospholamban ablation by RNA interference increases Ca^{2+}uptake into rat cardiac myocyte sarcoplasmic reticulum. *J Mol Cell Cardiol* 2004;**37**:691–698.
43. Suzuki T, Wang JH. Stimulation of bovine cardiac sarcoplasmic reticulum Ca^{2+} pump and blocking of phospholamban phosphorylation and dephosphorylation by a phospholamban monoclonal antibody. *J Biol Chem* 1986;**261**:7018–7023.
44. Zhang Y, Wang Y, Yanni J, Qureshi MA, Logantha SJRJ, Kassab S, Boyett MR, Gardiner NJ, Sun H, Howarth FC, Dobrzynski H. Electrical conduction system remodeling in streptozotocin-induced diabetes mellitus rat heart. *Front Physiol* 2019;**10**:1–15.
45. Mihm MJ, Seifert JL, Coyle CM, Bauer JA. Diabetes related cardiomyopathy time dependent echocardiographic evaluation in an experimental rat model. *Life Sci* 2001;**69**: 527–542.
46. Wu W, Liu X, Han L. Apoptosis of cardiomyocytes in diabetic cardiomyopathy involves overexpression of glycogen synthase kinase-3β. *Biosci Rep* 2019;**39**:BSR20171307.
47. Smoczynska A, Beekman HDM, Vos MA. The increment of short-term variability of repolarisation determines the severity of the imminent arrhythmic outcome. *Arrhythm Electrophysiol Rev* 2019;**8**:166–172.

Translational perspective

Deficient SR Ca^{2+} uptake has been identified in cardiomyocytes from failing human hearts with impaired diastolic relaxation (e.g. diabetic hearts) and has been associated with a decreased SERCA2a expression and activity and/or with a higher SERCA2a inhibition by PLN. Thus, SERCA2a may represent a pharmacological target for interventions aimed at improving cytosolic Ca^{2+} compartmentalization into the SR to limit diastolic dysfunction pathologies. In this context, istaroxime is the first-in-class luso-inotropic agent targeting SERCA2a that has already demonstrated its efficacy in clinical trials and may be useful to clarify the relevance of SERCA2a stimulation in controlling cytosolic Ca^{2+} level.

A dynamic clamping approach using *in silico* I_{K1} current for discrimination of chamber-specific hiPSC-derived cardiomyocytes

Claudia Altomare[1,2]; Chiara Bartolucci[3]; Luca Sala[4]; Carolina Balbi[2,5,6]; Jacopo Burrello[1,7]; Nicole Pietrogiovanna[1]; Alessio Burrello[8]; Sara Bolis[1,2,5]; Stefano Panella[1,2]; Martina Arici[9]; Rolf Krause[10]; Marcella Rocchetti[9]; Stefano Severi*[3]; Lucio Barile*[1,2,10,11]

[1]Cardiovascular Theranostics, Istituto Cardiocentro Ticino, Ente Ospedaliero Cantonale, Lugano, Switzerland. [2]Laboratories for Translational Research, Ente Ospedaliero Cantonale, Bellinzona, Switzerland. [3]Department of Electrical, Electronic and Information Engineering 'Guglielmo Marconi', University of Bologna, Italy. [4]Istituto Auxologico Italiano IRCCS, Center for Cardiac Arrhythmias of Genetic Origin and Laboratory of Cardiovascular Genetics, Milan, Italy. [5] Cellular and Molecular Cardiology, Istituto Cardiocentro Ticino, Ente Ospedaliero Cantonale, Lugano, Switzerland. [6]Center for Molecular Cardiology, University of Zurich, Zurich Switzerland. [7]Division of Internal Medicine 4 and Hypertension Unit, Department of Medical Sciences, University of Turin, Italy. [8]Department of Electrical, Electronic and Information Engineering (DEI), University of Bologna, Italy. [9]Department of Biotechnology and Biosciences, Università degli Studi di Milano-Bicocca, Milano, Italy. [10]Faculty of Informatics, Università Svizzera Italiana, Lugano, Switzerland.[11]Faculty of Biomedical Sciences, Università Svizzera Italiana, Lugano, Switzerland.[12]Institute of Life Science, Scuola Superiore Sant'Anna, Pisa, Italy.

*Corresponding Authors

Addresses for correspondence:

Lucio Barile, PhD
Cardiocentro Ticino Institute
Ente Ospedaliero Cantonale
Via Tesserete 48
6900 Lugano, Switzerland
+41 918053384
lucio.barile@eoc.ch

Stefano Severi, PhD
University of Bologna
Via Guglielmo Marconi, 10,
40122 Bologna BO, Italy
stefano.severi@unibo.it

ABSTRACT

Human induced pluripotent stem cell (hiPSC)-derived cardiomyocytes (CM) constitute a mixed population of ventricular-, atrial-, nodal-like cells, limiting the reliability for studying chamber-specific disease mechanisms. Previous studies characterised CM phenotype based on action potential (AP) morphology but the classification criteria were still undefined . Our aim was to use in-silico models to develop an automated approach for discriminating the electrophysiological differences between hiPSC-CM. We propose dynamic clamp (DC) technique under injection of a specific I_{K1} current as a tool for deriving nine electrical biomarkers and blindly classifying differentiated CM. An unsupervised learning algorithm was applied to discriminate CM phenotypes and principal component analysis was used to visualise cell clustering. Pharmacological validation was performed by specific ion channel blockers and receptor agonists. The proposed algorithm improves the translational relevance of the hiPSC model for studying mechanisms underlying inherited or acquired atrial arrhythmias in human CM, and for screening anti-arrhythmic agents.

INTRODUCTION

To date, there is no specific *in vitro* protocol to induce differentiation of pluripotent stem cells toward a phenotype that recapitulates the complexity of the cardiovascular system during embryogenesis. Cardiomyocytes (CM) derived from human induced pluripotent stem cells (hiPSCs) are mainly characterised by a heterogeneous mixture of immature ventricular-, atrial- and nodal-like CM phenotypes whose proportion depends on the differentiation time and protocol [1]. This aspect affects the identification and characterisation of electrical properties of hiPSC-CM subtypes, which is crucial in studies investigating chamber-specific disease mechanisms [2]. Moroever, most antiarrhythmic drugs act through action potential (AP) shortening or prolonging effects, and the assessment of atrial- and ventricular-specific APs in human CM becomes critical. Attempts to determine the existence of distinct subpopulations of atrial, ventricular, and nodal CM mainly rely on qualitative morphological analyses of AP properties [2]. However, the discrimination of different immature AP morphologies in standard hiPSC-CM culture is difficult and largely debated [3-6].

A valid and effective approach to overcome immature characteristics of hiPSC-CM is the injection of *in silico* inward rectifier K^+ current (I_{K1}) in loop with recorded cellular membrane potential in a real-time [7-9] mode (dynamic clamp (DC) technique [10]. This technology allows the hyperpolarization of diastolic membrane potential (E_{diast}) to values suitable to generate a mature AP waveform. However, applying a generic I_{K1} formulation on heterogeneous hiPSC-CM populations may result in a misleading interpretation of the cellular electrical response due to differences in the biophysical properties of ventricular *vs* atrial I_{K1}; for instance, I_{K1} density and rectification are higher in human ventricles than in atria, thus leading to a different contribution to AP waveform [5,11].

Here, we sought to empirically unravel hiPSC-CM chamber specification by using a machine learning approach to combine several electrical biomarkers recorded in DC mode based on state-of-the-art *in silico* I_{K1}. We tested two I_{K1} formulations: the one from O'Hara-Rudy (ORd) model of human ventricular AP [12], which has been shown to perform well for induction of ventricular AP in hiPSC-CM [7,13] but has never been validated on cells differentiated toward atrial phenotype; the one from the Koivumäki's computational model of human atrial AP [14], which has never been applied to hiPSC-CM *in vitro*. Electrical biomarkers obtained in DC mode recordings were used to run an unsupervised learning algorithm to blindly classify the recorded CM. The

specificity of the algorithm was pharmacologically validated testing the effect of 4-aminopyridine (4-AP) on AP, in that it's the specific blocker of the atrial ultrarapid delayed rectifier potassium current (I_{Kur}). The approach was then used to evaluate the differentiation efficiency of two protocols known to enrich for either atrial- or ventricular-like CM. Finally, we assessed the use of a Koivumäki I_{K1} formulation on different cell types to determine how it impacts the interpretation of arrythmogenicity at the cellular level.

RESULTS

Assessment of ventricular vs atrial markers

Multiple differentiation protocols were applied to enrich for the functional subtypes, ventricular- *vs* atrial-like CM, to be used for validating DC models as discriminating (Supplemental Figure 1a). To this end, a previously validated standard protocol (Std), known to enrich the culture with ventricular-like CM [15], was modified by including RA treatment to induce atrial specification [16]. The presence of atrial-like CM was primarily confirmed at the mRNA level for the orphan nuclear transcription factors I and II (COUP-TF I/II), known to be the most significantly upregulated genes following RA treatment [17,18]. RA induced 16.81±4.7 ($p<0.004$)- and 10.4±3.1 ($p<0.008$)-fold increases in expression levels as compared to the Std protocol for COUP-TFI and COUP-TFII, respectively (Supplemental Figure 1b). Similarly, mRNA levels of KCNA5 and KCNJ3 genes, encoding for atrial-specific potassium channels ($K_V1.5$ and $K_{ir}3.1$, respectively) downstream of COUP-TFs [16], were upregulated following RA treatment (Figure 1a). Moreover, immunofluorescence staining showed an increase in the proportion of hiPS-CM expressing atrial myosin light chain 2 (MLC2a+) protein and a decrease in the proportion of cells expressing the ventricular isoform MLC2v, upon treatment with RA (Figure 1a). Analysis of the spontaneous activity confirmed differential specification of Std *vs* RA protocol: the increase in the beating rate in RA-treated cells was consistent with MEA and mechanical activity recordings (Figure 1b). Such increase in the beating rate matched the reduction in the FPDc in atrial-like cells. Example of mechanical activity simultaneously evaluated in MEA preparations with MUSCLEMOTION is shown in Figure 1c. All parameters, including contraction duration (Figure 1b), time to peak, relaxation time, relaxation time at 90% and 50% of the amplitude (RT_{90} and RT_{50}, respectively), showed a significant reduction in RA

hiPSC-CM (Supplemental Figure 1c**,** Supplemental Table 1). We also tested the ability of differentiated cells to elicit acetylcholine (ACh)-induced current mediated by the KCNJ3 channel gene (Figure 1d**)**, responsible for the specific parasympathetic modulation of atrial tissue. The superfusion of high ACh concentration (10 μM) increased the percentage of I_{KACh}-presenting CM from 47.8% in Std to 88% in RA conditions. Furthermore, the well known short-term desensitisation process of the I_{KACh} [19] well emerged in RA CMs only. Taken together, these data clearly show that RA treatment triggered the specification of CM towards an atrial-like phenotype.

O'Hara-Rudy vs Koivumäki I_{K1} formulation

To overcome the limitation of the low I_{K1} expression in immature hiPSC-CM, we applied two state-of-the-art I_{K1} *in silico* currents in DC mode and switched between models: the I_{K1} formulation from the O'Hara-Rudy computational model of human ventricular AP (hereby referred to as I_{K1_Ventr}) [12], and the I_{K1} formulation from the Koivumäki computational model of human atrial AP (hereby referred to as I_{K1_Atr}) [14,20]; differences in I_{K1} I/V relationships are shown in Figure 2a.

Examples of AP recordings following DC I_{K1} injection with the two alternative formulations are shown in Figure 2b. I_{K1_Atr} injection resulted in AP profiles that consistently recapitulate those of atrial or ventricular electrical activities (53/53 cells, red traces in Figure 2b), characterised by a fast phase-1 repolarisation in the former and a phase-2 plateau in the latter. Conversely, the injection of I_{K1_Ventr} current often failed to hyperpolarise cells to a physiological E_{diast} (17/53 cells, 32%; blue traces in Figure 2b).

Optimisation of the critical I_{K1} conductance value

Having shown that I_{K1_Atr} outperformed I_{K1_Ventr} in most cells, we sought to verify whether such a model might be used to discriminate cell subtypes. To this end, we first optimised the minimum amount of injected current needed for polarising the cell to a physiological E_{diast}. By progressively increasing the conductance (G_{K1}) of 0.05 nS/μF per step (Figure 3b), we set the value of 0.7 nS/μF as the "critical conductance" to stabilise E_{diast} and APD_{90} in both atrial and ventricular AP profiles (Figure 3, a and b, Supplemental Table 2). We pooled all data since the optimization resulted comparable in atrial and ventricular phenotypes.

hiPSC-CM phenotype classification

To test the power of I_{K1_Atr} in discriminating the phenotype of differentiated cells, we applied an unsupervised learning algorithm to classify the recorded cells deriving from the two differentiation protocols (46 cells from 3 independent Std and RA cultures) in two clusters on the exclusive basis of nine electrical biomarkers (see Methods). Principal component analysis was used to reduce the multidimensional parameter space in a two-dimensional plot and visualise cell clustering (Figure 4a). The two cell clusters (Cls) had similar cell capacitance while, upon I_{K1_Atr} injection, they resulted in significant differences in all the considered biomarkers (Figure 4b, Supplemental Table 3; $p<0.05$ for all comparisons). Cls 1 displayed an electrical pattern consistently attributable to the atrial phenotype. Indeed, E_{diast} + DC was less polarised and APD was shorter, with lower amplitude, and more triangular (as shown by lower APD_{20}/APD_{90} ratio). On the contrary, cells assigned to cls 2 were most likely recapitulating a ventricular phenotype. Moreover, we performed a ROC analysis to define a cut-off value that could allow discrimination of cells from cls 1 *vs* cls 2 (and hence atrial-*vs* ventricular-like cells) for each electrical biomarker. The best discriminants were APD_{20} (AUC=1.000 sensitivity and 100% specificity; cut-off 42.5 ms), APD_{20}/APD_{90} (AUC=0.996; 100% sensitivity and 96.4% specificity; cut-off 0.44 ms/ms), APD_{50} (AUC=0.984; 100% sensitivity and 92.9% specificity; cut-off 72.9 ms), and APD_{90} (AUC=0.960; 100% sensitivity and 85.7% specificity; cut-off 92.1 ms). Among these biomarkers, we selected APD_{20}/APD_{90} as the one to be used to define the cut-off since it represents the normalised APD_{20} parameter that resulted in higher sensitivity and specificity (Supplemental Table 4). Furthermore, it successfully distinguishes two different AP profiles in working CM characterised by a typical triangulation for atrial shape and a long plateau for ventricular shape [21].

Pharmacological validation

The APD_{20}/APD_{90} cut-off (0.44) defined through unsupervised learning as depicted above was validated pharmacologically in a distinct subset of cells by exploiting the sensitivity of atrial I_{Kur} to a specific dose of 4-AP (50 μM). As expected 4-AP superfusion caused the prolongation of AP in atrial-like cells (4-AP sensitive cells) whereas it did not affect ventricular-like cells (4-AP non-sensitive cells; Figure 5a). The percentages of 4-AP sensitive cells were 82% in cells displaying an $APD_{20}/APD_{90} < 0.44$ (thus classified as atrial-like by our

model) and 18% in those with an $APD_{20}/APD_{90} \geq 0.44$ (thus classified as ventricular–like by our model). Overall, the accuracy at experimental validation was about 78.9 % (Figure 5b). Analysis of 4-AP effects in APD changes showed that the highest prolongation was detected in the APD_{20} phase, where the I_{Kur} mostly contributed during the electrical activity of atrial CM (delta % of 56.8 ± 20.2, n=10, Supplemental Table 5).

Evaluation of RA efficiency

To determine whether the use of the I_{K1_Atr} model is a viable tool for discriminating between atrial and ventricular cells in a mixed population of differentiated CM, we compared the two differentiation protocols to evaluate their relative efficiency in enriching the two subtypes. A clonally-derived iPSC line was divided in two and subjected to Std and RA differentiation procedures. By applying a previously validated cut-off, 30% of recorded cells in the Std protocol were classified as atrial-like CM. The proportion of atrial–like cells doubled with RA (Figure 5c).

***I_{K1_Ventr}* vs *I_{K1_Atr}* application**

We quantified the impact of applying a generic I_{K1} formulation on heterogeneous hiPSC-CM populations. However, since this might result in misleading interpretations of the electrical and pharmacological responses, we assessed the beat-to-beat variability of repolarisation of APD_{90}, either in atrial- or in ventricular-like CM, under the injection of both models. An illustrative series of 30 APs recorded in atrial- and ventricular-like CM, during I_{K1_Ventr} and I_{K1_Atr} injection switching, are shown in Figure 6, a and b. Firstly, in the presence of I_{K1_Ventr} injection we observed a high percentage of atrial-like CM that gave rise to an irregular AP plateau (13/23, 56%; blue trace in Figure 6a, left panel), while ventricular-like CM elicited a longer AP plateau (23/30, 76.6%; blue trace in Figure 6b, right panel). In atrial APs, the I_{K1_Ventr} increased the STV of APD_{90} as detected both in AP recordings and in Poincaré plots; this agrees with the known intrinsic correlation between APD and STV [22]. In particular, the APD_{90}/STV correlation was fitted in a linear function, resulting in similar positive slopes in all conditions, except for the steeper dependence of STV on atrial-like APD_{90} cells injected with I_{K1_Ventr} model.

DISCUSSION

Faced with the difficulty of developing a protocol that can guarantee a pure selection of chamber-specific hiPSC-CMs, it is imperative to develop objective tools that can overcome conventional subjective criteria for phenotype classification. The aim of the current work was to develop an unsupervised learning algorithm that could discriminate the phenotype of differentiated CM based on several electrical biomarkers.

We first determined that the injection of an atrial *in silico* model of I_{K1} (I_{K1_Atr}) was best suited to uncover physiological electrical features in a mixed pool of cells including both atrial- and ventricular-like AP profiles (Figure 2b). Subsequently, we optimised the I_{K1_Atr} conductance value to define the minimum amount of injected current (0.7 nS/μF) required to obtain physiological E_{diast} and to stabilise APD_{90} [23]. We have shown that DC with I_{K1_Atr} allows distinction of atrial- from ventricular-like hiPSC-CMs. Of note, by taking advantage of DC, we could switch between I_{K1_Atr} and I_{K1_Ventr} models during single-cell analysis and dissect how they differently affect the AP profile within the same CM.

Chamber-specific *in silico* I_{K1} formulations from the O'Hara–Rudy (I_{K1_Ventr}) and the Koivumäki (I_{K1_Atr}) models were tested [20]. I_{K1_Ventr} is the more established model of human ventricular AP, and more recent models also inherit its formulation [24,25]. Moreover, it has been previously applied to study underlying mechanisms of long QT syndrome in hiPSC-CM [13]. The I/V relationship of I_{K1_Ventr} is characterised by a stronger rectification and higher maximal conductance while, although with lower maximal conductance, the I_{K1_Atr} model has a voltage dependence that evidences a greater current density at more depolarised potential values. To our knowledge, such specific behaviour may reflect a specific propensity of the I_{K1_Ventr} and I_{K1_Atr} models to mimic properties of the endogenous I_{K1} in adult ventricular and atrial CM, respectively [8,11,26]. The injection of I_{K1_Atr} was in all cases associated with a more hyperpolarised E_{diast} that led to distinct AP profiles whose waveforms' morphologies ranged from a triangular AP shape with no sustained plateau to a long AP with a spike-and-dome shape, mostly recapitulating either atrial or ventricular human APs.[21] Conversely, I_{K1_Ventr} generated APs characterised by an abnormal "chair-like" plateau when injected in atrial-like cells (Figure 2). Notably, by using $I_{K1\_Ventr,}$ 32% of analysed cells failed to hyperpolarise and trigger a physiological AP. The latter is consistent with the fact that the voltage-dependence of I_{K1_Ventr} only allowed the physiological

hyperpolarisation of the most mature cells, characterized by their already more hyperpolarized E_{diast}. Once optimised, the I_{K1_Atr} model was used as a tool to blindly derive cut-offs of nine biomarkers, which are well-known electrical phenotype indices, to potentially cluster cells within a heterogeneous population of hiPSC-CM. To the best of our knowledge, this is the first time that CM chamber-specificity could be distinguished and classified using DC. A spectral grouping-based algorithm has been used to separate the population of CM dissected from human embryoid bodies into distinct groups based on the similarity of their AP shapes but without the use of DC to make AP more physiological [27]. Meanwhile, despite Bett *et al.* used DC technology to derive APD_{30} and APD_{30}/APD_{90} as discriminants between cell types [9], the cut-off values used to distinguish the two different cell clusters based on these biomarkers were not uniquely defined [5,28].

The unsupervised analysis gave rise to two distinct cell clusters that were significantly different in all values except for the membrane capacitance. Among those biomarkers, the ADP_{20}/APD_{90} ratio reached an AUC of 0.996, with a sensitivity and specificity of 100% and 96.4%, respectively. This was not surprising as the ADP_{20}/APD_{90} ratio is known to discriminate between the fast ripolarizing phase of AP (typical of atrial CM) and AP with a long sustained plateau (typical of ventricular CM) [29,30]. About 80% of hiPSC-CM with $ADP_{20}/APD_{90} < 0.44$ were sensitive to 4-AP, thus indicating the presence of atrial ionic contributors in these cells. Conversely, cells with $ADP_{20}/APD_{90} > 0.44$ responded poorly or did not respond. Using this specific cut-off as a critical value to discriminate between atrial- and ventricular-like CM, we confirmed that RA treatment could double the presence of atrial-like hiPSC-CM in culture as compared to Std treatment applied to matched differentiations (73.5±5.1% *vs* 34±6.3%). This is in line with previous work that used immunostaining as a molecular approach to distinguish cell types following fixation [31].

Our findings were supported by perfusing cells with ACh which induced an ACh-sensitive current in 88% of RA-treated CM. Treatment led to a prototypical fast cholinergic response that was characterised by a slow decay due to receptor desensitisation, mirroring parasympathetic stimulation in nodal/atrial mature CM [32]. On the contrary, ACh-responsive cells that were a product of the Std differentiation protocol (~47%) showed atypical I_{KACh} kinetics which lacked the fast activation phase, suggesting the presence of a lower affinity ACh-dependent signalling (Figure 1d). Such pharmacological validation further highlighted the importance of using

chamber-specific CM to test drug effects and detect the direct interaction of drugs with specific receptor features [33].

Finally, the slope of the linear correlation between STV and APD_{90} was significantly increased when I_{K1_Ventr} was injected in atrial-like CM under basal conditions, suggesting a misleading association of such electrical instability to a pro-arrhythmic phenotype. This observation further points out the importance of combining chamber-specific differentiation protocols with an appropriate chamber-specific human *in silico* I_{K1} model to obtain a more mature electrophysiological phenotype (i.e., E_{diast}). Recent published data that supports this hypothesis show that in the absence of properly hyperpolarised E_{diast}, atrial hiPSC-CM differ from human atrium with respect to their repolarisation reserve.[34,35] Indeed, an "atrial specific" drug (i.e., vernakalant), known to induce prolongation of APD_{90} in atrial hiPSC-CMs,[36] failed to recapitulate such effects in human atrium.[36,37] This discrepancy might be ascribed to immature phenotype of atrial hiPSC-CMs and to a consequent differential ion channel contribution to AP. Using the model described here, drug testing in hiPSC-CM with a proper E_{diast} might closely reproduce the physiological drug effect [35,36,38] Such complex effects are not evident when using drugs on immature atrial hiPSC-CM where the voltage range hampers the physiological ion channel's contribution, but these effects are more clearly defined using the model described here. Our model was validated using one hiPSC line and the most used differentiation protocol towards the atrial lineage; however, given the phenotypic variability among hiPSC-CM from different hiPSC lines, cut-offs and conductance values might require hiPSC-line specific fine-tuning before being universally applicable to multiple hiPSC lines and protocols. Future works will be focussed to empirically determine such critical values.

METHODS

Generation of hiPSC-CMs

Cell isolation

iPSCs were obtained by reprogramming adult human dermal fibroblasts (HDFs) male healthy volunteer. Primary cell lines were derived from a biobank established within previous studies at Cardiocentro Ticino Institute Ente Ospedaliero Cantonale [15,39]. All studies were approved by the local Ethics Committee (Comitato Etico Cantonale, Bellinzona, Switzerland; Ref. CE 2923) and performed according to the Declaration of

Helsinki. HDFs were derived as the cellular outgrowth from sternum skin biopsy tissue explants using an *ex vivo* primary tissue culture technique, as described previously [40]. Briefly, tissue was rinsed with phosphate buffer saline (PBS) and cut into small pieces that were placed into a 100 mm cell culture dish (Corning). To facilitate cell outgrowth, skin tissue was treated with TrypLE™/EDTA (SIGMA Life Science) for 2–3 min. Tissue pieces were then transferred into a 100 mm dish coated with 1% gelatin and cultured in Iscove's modified Dulbecco's medium supplemented with 10% foetal bovine serum (FBS) and 1% penicillin-streptomycin (all from Life Technologies). Culture medium was changed twice a week. After 25–30 days of culture, HDFs were enzymatically detached using TrypLE (4 mL) at 37°C, which was subsequently blocked with culture medium containing 20% FBS. Cells were then centrifuged at 300 g for 5 min, resuspended, and plated onto a gelatin-coated 24 mm dish (Corning; 2.5×10^5 cells per dish). After 48 h, HDFs were reprogrammed into iPSCs.

Cellular reprogramming and cardiac differentiation

Two 35 mm dishes of HDFs were used for cellular reprogramming. One dish was used for cell counting and the other was used for infection with Sendai virus carrying OCT3/4, SOX2, KLF4, and MYC (CytoTune™-iPS 2.0 Sendai Reprogramming Kit; Thermo Fisher Scientific), as per manufacturer's instructions. Medium was changed 24 h later, and then every other day for 1 week. Subsequently, 90% of total cells were transferred into a 60 mm dish coated with Matrigel (hESC Qualified Matrix; Corning), and 10% of total cells were transferred into a second similar dish. Twenty-four hours later, the medium was switched to StemFlex Medium (Miltenyi). The first embryonic stem cell-like colonies appeared 20 to 40 days postinfection, then transferred onto 12-well plates coated with Matrigel (hESC Qualified Matrix; Corning) and expanded.

Cardiac differentiation was induced using Gibco™ PSC Cardiomyocyte Differentiation Kit (Miltenyi). Two clonally-derived hiPSC lines at passage P8-P10 were split in two and induced to differentiate into cardiomyocytes in feeder-free conditions using a “standard” protocol (Std) via modulation of canonical Wnt signalling or applying retinoic acid (RA) to induce atrial differentiation [16,41]. The latter included the addition of 1 μM RA at stages d4-d8 of the differentiation protocol. Both protocols included a cardiac-specific metabolic selection step by replacing glucose with lactate from d11 to d13 (Supplementalm Figure 1a).[31]

Spontaneously beating cells were maintained in RPMI (Gibco) supplemented with B27 (Gibco) at 37°C. Medium was changed every second day.

Molecular characterisation

Immunofluorescence

Cells were fixed with 4% paraformaldehyde and stained with primary antibody overnight (MLC2v; Proteintec 10906-1-AP and MLC2a; Synaptic System 311011). Alexa Fluor secondary antibody (Thermo Fisher Scientific) was used for detection. Immunostained cell culture images were acquired with a Lionheart FX automatic microscopy at 10× magnification and analysed with Gen5 software (Biotek).

RNA extraction, reverse transcription, and real-time PCR

hiPSC-CMs were lysed with TRI Reagent (Sigma) as per manufacturer's instructions. The pellet was air-dried, resuspended in DEPC water, and RNA was quantified with a NanoDrop™ 2000c (Thermo Fisher Scientific). RNA (500 ng) was reverse-transcribed using GoScript™ Reverse Transcription System (Promega). Real-time analysis was performed on a CFX connect Real-time PCR detection system (Bio-Rad). Data are shown as $2^{-\Delta\Delta Ct}$ values. Coupled primers were as follows: *COUP-TFI forward: AAGCCATCGTGCTGTTCAC, Reverse: GCTCCTCAGGTACTCCTCCA; COUP-TFII forward: CCGAGTACAGCTGCCTCAA, Reverse: TTTTCCTGCAAGCTTTCCAC; KCNA5 forward: CGAGGATGAGGGCTTCATTA, Reverse: CTGAACTCAGGCAGGGTCTC; KCNJ3 forward: AAAAACGATGACCCCAAAGA, Reverse: TGTCGTCATCCTAGAAGGCA; GAPDH forward: TGCACCACCAACTGCTTAGC, Reverse: GGCATGGACTGTGGTCATGAG.*

Electrophysiology

Multielectrode array (MEA) recordings

Extracellular field potentials (FPs) were recorded from microdissected, spontaneously beating cell clusters, at d30 of differentiation. MEA dishes were coated with 10 µg/ml Synthemax (Corning) and 0.02% gelatin and incubated for 2 h at 37°C. Clumps (200-300 µm) of beating cells were microdissected using surgical scissors and positioned on the electrodes of standard 60 electrode MEAs at high spatial (200 µm) resolution (60MEA-

200/30iR-Ti, Multi Channel Systems, Reutlingen, Germany). FPs were recorded after at least 72 h after plating to allow for cell attachment. During recordings, the temperature was maintained at 37°C. FP duration was analysed offline by Clampfit (Molecular Devices), as reported [42]. Corrected FP duration (FPDc) was calculated using the standard Bazett's formula.

Contractility measurements

Contractility was assessed in spontaneously beating cell clusters seeded on MEAs as previously described [43,44]. Briefly, beating clusters of both Std- and RA-hiPSC-CM were microdissected and seeded on standard 60 electrode MEAs (Multi Channel Systems). Movies of beating clusters were acquired with a Thorlabs DCC3240M CMOS camera at 120 fps together with MEA FP recordings. The movies were converted to raw AVI using *ffmpeg* (www.ffmpeg.org) and the contractile properties were quantified using the MUSCLEMOTION ImageJ macro [43]. FP and contraction traces were plotted as synchronised.

APs measurements

Dissociated hiPSC-CMs at ≥d30 of differentiation were plated onto 35 mm dishes at very low density and electrophysiologically analysed after 3 days. APs were acquired with MultiClamp 700B amplifier (Molecular Devices) connected to Digidata 1550A (Molecular Devices) and filtered at 1 kHz via pClamp 10.6 (Molecular Devices). APs were stimulated at 1 Hz during superfusion of Tyrode's solution: 154 mM NaCl, 4 mM KCl, 2 mM $CaCl_2$, 1 mM $MgCl_2$, 5.5 mM D-glucose, and 5 mM HEPES-NaOH (pH 7.35). Experiments were carried out in whole cell configuration at 35°C; the pipette solution contained: 23 mM KCl, 110 mM KAsp, 0.4 mM $CaCl_2$, 3 mM $MgCl_2$, 5 mM HEPES-KOH, 1 mM EGTA-KOH, mM 0.4 NaGTP, 5 mM Na_2ATP, and 5 mM Na_2PC.

Nine biomarkers were measured from AP recordings: cell membrane capacitance (C_m), E_{diast}, E_{diast} with DC, AP duration measured at 90%, 50%, and 20% of the repolarisation phase (APD_{90}, APD_{50}, and APD_{20}, respectively), APD_{20}/APD_{90} ratio, maximal AP phase 0 depolarisation velocity (dV/dt_{max}), and AP amplitude (APA). To evaluate the contribution of I_{Kur} to AP, 4-AP (Sigma-Aldrich) was added to the Tyrode's solution at 50 μM [45].

Beat-to-beat variability of repolarisation duration was expressed as the short-term variability (STV) of APD_{90} (i.e., the mean orthogonal deviation from the identity line in the APDn *vs* APDn+1 Poincaré plot [46,47]), and calculated as follows:

$$STV = \sum 〚(|〚APD〛_{(n+1)} - 〚APD〛_n |/[n_{(beats)} \times \sqrt{2}] 〛$$

for 30 consecutive APs (nbeats) at steady-state.

DC recordings

APs, recorded from the hiPSC-CMs, were acquired at a sampling rate of 5 kHz to drive the numerical I_{K1} model in DC. Modelled I_{K1} was calculated in real-time (within one sampling interval) and injected into the myocyte during continued AP recording. To implement DC, the Multiclamp 700B amplifier (Axon Instruments) was connected to a data acquisition board (DAQ, 6024E PCI, National Instruments) on a personal computer (Intel Celeron 3.20 GHz). The open-source Real-Time Experiment Interface (RTXI) was used[48]: it is a fast and versatile real-time biological experimentation system based on Real-Time Linux. System features and custom user code were implemented as modules written in C++.

In silico I_{K1}

We considered two I_{K1} formulations from two of the most recent human AP models). For the ventricular I_{K1} the equation was taken from the ORd model [12] (eq.1; I_{K1_Ventr}), while for the atrial I_{K1} the equation was from Koivumäki *et al*. [20] (eq.2; I_{K1_Atr}), which has inherited the expression from the parent model of Nygren *et al*. [14]:

$$x_{K1,\infty} = \frac{1}{1 + e^{\left(-\frac{V+2.5538\cdot[K^+]_o+144.59}{1.5692\cdot[K^+]_o+3.8115}\right)}}$$

$$\tau_{x,K1} = \frac{122.2}{e^{\left(\frac{-(V+127.2)}{20.36}\right)} + e^{\left(\frac{V+236.8)}{69.33}\right)}}$$

$$\frac{dx_{K1}}{dt} = \frac{x_{K1,\infty} - x_{K1}}{\tau_{x,K1}}$$

$$R_{K1} = \frac{1}{1 + e^{\left(\frac{V+105.8-2.6\cdot[K^+]_o}{9.493}\right)}}$$

$$\underline{G_{K1}} = 0.1908 * scaling_{DC}\ \frac{mS}{\mu F}$$

$$I_{K1\_Ventr} = \underline{G_{K1}} \cdot \sqrt{[K^+]_o} \cdot x_{K1} \cdot R_{K1} \cdot (V - E_K) \quad (1)$$

$$\underline{G_{K1}} = 0.07 * scaling_{DC}\ \frac{nS}{pF}$$

$$I_{K1\_Atr} = \frac{\underline{G_{K1}} \cdot [K^+]_o^{0.4457} \cdot (V - E_K)}{\left(1 + e^{\left(1.5\cdot(V-E_K+3.6)*\frac{F}{\frac{R}{T}}\right)}\right)} \quad (2)$$

where V and E_K denote the membrane potential and K^+ equilibrium potential (in mV) respectively; E_K was set to –94.7 mV based on K^+ concentration in exte rnal bath ($[K^+]_o$) and pipette solutions (see *APs measurements*); $\underline{G_{K1}}$ is the maximal conductance which has been varied using the scaling factor, $scaling_{DC}$, from 0.2 to 1 with a 0.05 step. The DC implementation, based on "modules" architecture, allows the user to switch in real-time the I_{K1} formulation to be injected into the cell and to analyse its response in terms of AP waveform changes.

Statistics

Data are expressed as the mean ± standard error of mean (SEM). The differences between groups were tested with paired or unpaired *t*-test analysis as appropriate. Post-hoc comparison between individual means was performed with the Bonferroni test. A p-value < 0.05 was considered statistically significant. For the correlation between STV and APD_{90}, a linear regression analysis that showed a 95% confidence band of the best fit trend line was performed.

AP parameters distribution was assessed by the Kolmogorov-Smirnov test. Non-normally distributed data was expressed as median and interquartile range (25^{th}, 50^{th}, and 75^{th} percentiles) and analysed by the Mann-Whitney U test. Diagnostic performance of single electrical biomarkers was evaluated by analysis of receiver operating characteristic (ROC) curves; the area under the curve was reported together with the 95% confidence interval. The cut-off correspondent to the maximum accuracy was derived by the Youden Index (J = Sensitivity + Specificity-1). Cell clusterisation was obtained by unsupervised learning algorithms. A K-means classification algorithm was used to discriminate cells in clusters according to AP parameters values. Principal component analysis was used to reduce high-dimensional data into a two-dimensional plot and visualise cell clustering according to an electrical pattern.

Acknowledgments

Cardiocentro Ticino Institute for administrative, technical support, and donations in kind (e.g., materials used for experiments).

Author contributions

LB, SS, CA conceived and designed the study. CA, CB, LS, SS identified and prioritized in silico variables for model. AC, CB, LC, CB, JB, NP, AB, SB, SP, MA performed experiments, collected and analyzed data. CA, LB, assembled figures and tables. LB, CA, SS, MR, RK wrote and revised the manuscript. LB secured funding for the study. All authors approved the manuscript.

The authors have declared that no conflict of interest exists

References

1 Lodrini, A. M., Barile, L., Rocchetti, M. & Altomare, C. Human Induced Pluripotent Stem Cells Derived from a Cardiac Somatic Source: Insights for an In-Vitro Cardiomyocyte Platform. *Int J Mol Sci* **21**, doi:10.3390/ijms21020507 (2020).

2 Kane, C. & Terracciano, C. M. N. Concise Review: Criteria for Chamber-Specific Categorization of Human Cardiac Myocytes Derived from Pluripotent Stem Cells. *Stem Cells* **35**, 1881-1897, doi:10.1002/stem.2649 (2017).

3 Moretti, A. *et al.* Patient-specific induced pluripotent stem-cell models for long-QT syndrome. *N Engl J Med* **363**, 1397-1409, doi:10.1056/NEJMoa0908679 (2010).

4 Ben-Ari, M. *et al.* Developmental changes in electrophysiological characteristics of human-induced pluripotent stem cell-derived cardiomyocytes. *Heart Rhythm* **13**, 2379-2387, doi:10.1016/j.hrthm.2016.08.045 (2016).

5 Kane, C., Du, D. T., Hellen, N. & Terracciano, C. M. The Fallacy of Assigning Chamber Specificity to iPSC Cardiac Myocytes from Action Potential Morphology. *Biophys J* **110**, 281-283, doi:10.1016/j.bpj.2015.08.052 (2016).

6 Giles, W. R. & Noble, D. Rigorous Phenotyping of Cardiac iPSC Preparations Requires Knowledge of Their Resting Potential(s). *Biophys J* **110**, 278-280, doi:10.1016/j.bpj.2015.06.070 (2016).

7 Meijer van Putten, R. M. *et al.* Ion channelopathies in human induced pluripotent stem cell derived cardiomyocytes: a dynamic clamp study with virtual IK1. *Front Physiol* **6**, 7, doi:10.3389/fphys.2015.00007 (2015).

8 Verkerk, A. O. *et al.* Patch-Clamp Recording from Human Induced Pluripotent Stem Cell-Derived Cardiomyocytes: Improving Action Potential Characteristics through Dynamic Clamp. *Int J Mol Sci* **18**, doi:10.3390/ijms18091873 (2017).

9 Bett, G. C. *et al.* Electronic "expression" of the inward rectifier in cardiocytes derived from human-induced pluripotent stem cells. *Heart Rhythm* **10**, 1903-1910, doi:10.1016/j.hrthm.2013.09.061 (2013).

10 Ravagli, E. *et al.* Cell-specific Dynamic Clamp analysis of the role of funny If current in cardiac pacemaking. *Prog Biophys Mol Biol* **120**, 50-66, doi:10.1016/j.pbiomolbio.2015.12.004 (2016).

11 Wang, Z., Yue, L., White, M., Pelletier, G. & Nattel, S. Differential distribution of inward rectifier potassium channel transcripts in human atrium versus ventricle. *Circulation* **98**, 2422-2428, doi:10.1161/01.cir.98.22.2422 (1998).

12 O'Hara, T., Virag, L., Varro, A. & Rudy, Y. Simulation of the undiseased human cardiac ventricular action potential: model formulation and experimental validation. *PLoS Comput Biol* **7**, e1002061, doi:10.1371/journal.pcbi.1002061 (2011).

13 Rocchetti, M. *et al.* Elucidating arrhythmogenic mechanisms of long-QT syndrome CALM1-F142L mutation in patient-specific induced pluripotent stem cell-derived cardiomyocytes. *Cardiovasc Res* **113**, 531-541, doi:10.1093/cvr/cvx006 (2017).

14 Nygren, A. *et al.* Mathematical model of an adult human atrial cell: the role of K+ currents in repolarization. *Circ Res* **82**, 63-81, doi:10.1161/01.res.82.1.63 (1998).

15 Pianezzi, E. *et al.* Role of somatic cell sources in the maturation degree of human induced pluripotent stem cell-derived cardiomyocytes. *Biochim Biophys Acta Mol Cell Res* **1867**, 118538, doi:10.1016/j.bbamcr.2019.118538 (2020).

16 Devalla, H. D. *et al.* Atrial-like cardiomyocytes from human pluripotent stem cells are a robust preclinical model for assessing atrial-selective pharmacology. *EMBO Mol Med* **7**, 394-410, doi:10.15252/emmm.201404757 (2015).

17 Jonk, L. J., de Jonge, M. E., Vervaart, J. M., Wissink, S. & Kruijer, W. Isolation and developmental expression of retinoic-acid-induced genes. *Dev Biol* **161**, 604-614, doi:10.1006/dbio.1994.1056 (1994).

18 van der Wees, J. *et al.* Developmental expression and differential regulation by retinoic acid of Xenopus COUP-TF-A and COUP-TF-B. *Mech Dev* **54**, 173-184, doi:10.1016/0925-4773(95)00471-8 (1996).
19 Murakami, S., Inanobe, A. & Kurachi, Y. Short-term desensitization of muscarinic K+ current in the heart. *Biophys J* **105**, 1515-1525, doi:10.1016/j.bpj.2013.08.009 (2013).
20 Koivumaki, J. T., Korhonen, T. & Tavi, P. Impact of sarcoplasmic reticulum calcium release on calcium dynamics and action potential morphology in human atrial myocytes: a computational study. *PLoS Comput Biol* **7**, e1001067, doi:10.1371/journal.pcbi.1001067 (2011).
21 Dawodu, A. A. *et al.* The shape of human atrial action potential accounts for different frequency-related changes in vitro. *Int J Cardiol* **54**, 237-249, doi:10.1016/0167-5273(96)02605-8 (1996).
22 Zareba, W., Piotrowicz, K., McNitt, S., Moss, A. J. & Investigators, M. I. Implantable cardioverter-defibrillator efficacy in patients with heart failure and left ventricular dysfunction (from the MADIT II population). *Am J Cardiol* **95**, 1487-1491, doi:10.1016/j.amjcard.2005.02.021 (2005).
23 Fabbri, A., Goversen, B., Vos, M. A., van Veen, T. A. B. & de Boer, T. P. Required GK1 to Suppress Automaticity of iPSC-CMs Depends Strongly on IK1 Model Structure. *Biophys J* **117**, 2303-2315, doi:10.1016/j.bpj.2019.08.040 (2019).
24 Dutta, S. *et al.* Optimization of an In silico Cardiac Cell Model for Proarrhythmia Risk Assessment. *Front Physiol* **8**, 616, doi:10.3389/fphys.2017.00616 (2017).
25 Bartolucci, C., Passini, E., Hyttinen, J., Paci, M. & Severi, S. Simulation of the Effects of Extracellular Calcium Changes Leads to a Novel Computational Model of Human Ventricular Action Potential With a Revised Calcium Handling. *Front Physiol* **11**, 314, doi:10.3389/fphys.2020.00314 (2020).
26 Koumi, S., Backer, C. L. & Arentzen, C. E. Characterization of inwardly rectifying K+ channel in human cardiac myocytes. Alterations in channel behavior in myocytes isolated from patients with idiopathic dilated cardiomyopathy. *Circulation* **92**, 164-174, doi:10.1161/01.cir.92.2.164 (1995).
27 Gorospe, G. *et al.* Automated grouping of action potentials of human embryonic stem cell-derived cardiomyocytes. *IEEE Trans Biomed Eng* **61**, 2389-2395, doi:10.1109/TBME.2014.2311387 (2014).
28 Du, D. T., Hellen, N., Kane, C. & Terracciano, C. M. Action potential morphology of human induced pluripotent stem cell-derived cardiomyocytes does not predict cardiac chamber specificity and is dependent on cell density. *Biophys J* **108**, 1-4, doi:10.1016/j.bpj.2014.11.008 (2015).
29 Verkerk, A. O. *et al.* Patch-Clamp Recordings of Action Potentials From Human Atrial Myocytes: Optimization Through Dynamic Clamp. *Front Pharmacol* **12**, 649414, doi:10.3389/fphar.2021.649414 (2021).
30 Verkerk, A. O. & Wilders, R. Dynamic Clamp in Electrophysiological Studies on Stem Cell-Derived Cardiomyocytes-Why and How? *J Cardiovasc Pharmacol* **77**, 267-279, doi:10.1097/FJC.0000000000000955 (2021).
31 Cyganek, L. *et al.* Deep phenotyping of human induced pluripotent stem cell-derived atrial and ventricular cardiomyocytes. *JCI Insight* **3**, doi:10.1172/jci.insight.99941 (2018).
32 Wang, Y. G., Samarel, A. M. & Lipsius, S. L. Laminin acts via beta 1 integrin signalling to alter cholinergic regulation of L-type Ca(2+) current in cat atrial myocytes. *J Physiol* **526 Pt 1**, 57-68, doi:10.1111/j.1469-7793.2000.t01-1-00057.x (2000).
33 Dick, E., Rajamohan, D., Ronksley, J. & Denning, C. Evaluating the utility of cardiomyocytes from human pluripotent stem cells for drug screening. *Biochem Soc Trans* **38**, 1037-1045, doi:10.1042/BST0381037 (2010).
34 Lemoine, M. D. *et al.* Human Induced Pluripotent Stem Cell-Derived Engineered Heart Tissue as a Sensitive Test System for QT Prolongation and Arrhythmic Triggers. *Circ Arrhythm Electrophysiol* **11**, e006035, doi:10.1161/CIRCEP.117.006035 (2018).
35 Christ, T., Lemoine, M. D. & Eschenhagen, T. Are atrial human pluripotent stem cell-derived cardiomyocytes ready to identify drugs that beat atrial fibrillation? *Nat Commun* **12**, 1725, doi:10.1038/s41467-021-21949-z (2021).

36 Goldfracht, I. *et al.* Generating ring-shaped engineered heart tissues from ventricular and atrial human pluripotent stem cell-derived cardiomyocytes. *Nat Commun* **11**, 75, doi:10.1038/s41467-019-13868-x (2020).
37 Wettwer, E. *et al.* The new antiarrhythmic drug vernakalant: ex vivo study of human atrial tissue from sinus rhythm and chronic atrial fibrillation. *Cardiovasc Res* **98**, 145-154, doi:10.1093/cvr/cvt006 (2013).
38 Wettwer, E. *et al.* Role of IKur in controlling action potential shape and contractility in the human atrium: influence of chronic atrial fibrillation. *Circulation* **110**, 2299-2306, doi:10.1161/01.CIR.0000145155.60288.71 (2004).
39 Altomare, C. *et al.* Human-induced pluripotent stem cell-derived cardiomyocytes from cardiac progenitor cells: effects of selective ion channel blockade. *Europace* **18**, iv67-iv76, doi:10.1093/europace/euw352 (2016).
40 Barile, L. *et al.* Extracellular vesicles from human cardiac progenitor cells inhibit cardiomyocyte apoptosis and improve cardiac function after myocardial infarction. *Cardiovasc Res* **103**, 530-541, doi:10.1093/cvr/cvu167 (2014).
41 Argenziano, M. *et al.* Electrophysiologic Characterization of Calcium Handling in Human Induced Pluripotent Stem Cell-Derived Atrial Cardiomyocytes. *Stem Cell Reports* **10**, 1867-1878, doi:10.1016/j.stemcr.2018.04.005 (2018).
42 Sala, L., Ward-van Oostwaard, D., Tertoolen, L. G. J., Mummery, C. L. & Bellin, M. Electrophysiological Analysis of human Pluripotent Stem Cell-derived Cardiomyocytes (hPSC-CMs) Using Multi-electrode Arrays (MEAs). *J Vis Exp*, doi:10.3791/55587 (2017).
43 van Meer, B. J. *et al.* Quantification of Muscle Contraction In Vitro and In Vivo Using MUSCLEMOTION Software: From Stem Cell-Derived Cardiomyocytes to Zebrafish and Human Hearts. *Curr Protoc Hum Genet* **99**, e67, doi:10.1002/cphg.67 (2018).
44 Sala, L. *et al.* MUSCLEMOTION: A Versatile Open Software Tool to Quantify Cardiomyocyte and Cardiac Muscle Contraction In Vitro and In Vivo. *Circ Res* **122**, e5-e16, doi:10.1161/CIRCRESAHA.117.312067 (2018).
45 Hilderink, S., Devalla, H. D., Bosch, L., Wilders, R. & Verkerk, A. O. Ultrarapid Delayed Rectifier K(+) Channelopathies in Human Induced Pluripotent Stem Cell-Derived Cardiomyocytes. *Front Cell Dev Biol* **8**, 536, doi:10.3389/fcell.2020.00536 (2020).
46 Heijman, J. *et al.* Determinants of beat-to-beat variability of repolarization duration in the canine ventricular myocyte: a computational analysis. *PLoS Comput Biol* **9**, e1003202, doi:10.1371/journal.pcbi.1003202 (2013).
47 Altomare, C. *et al.* IKr Impact on Repolarization and Its Variability Assessed by Dynamic Clamp. *Circ Arrhythm Electrophysiol* **8**, 1265-1275, doi:10.1161/CIRCEP.114.002572 (2015).
48 Patel, Y. A. *et al.* Hard real-time closed-loop electrophysiology with the Real-Time eXperiment Interface (RTXI). *PLoS Comput Biol* **13**, e1005430, doi:10.1371/journal.pcbi.1005430 (2017).

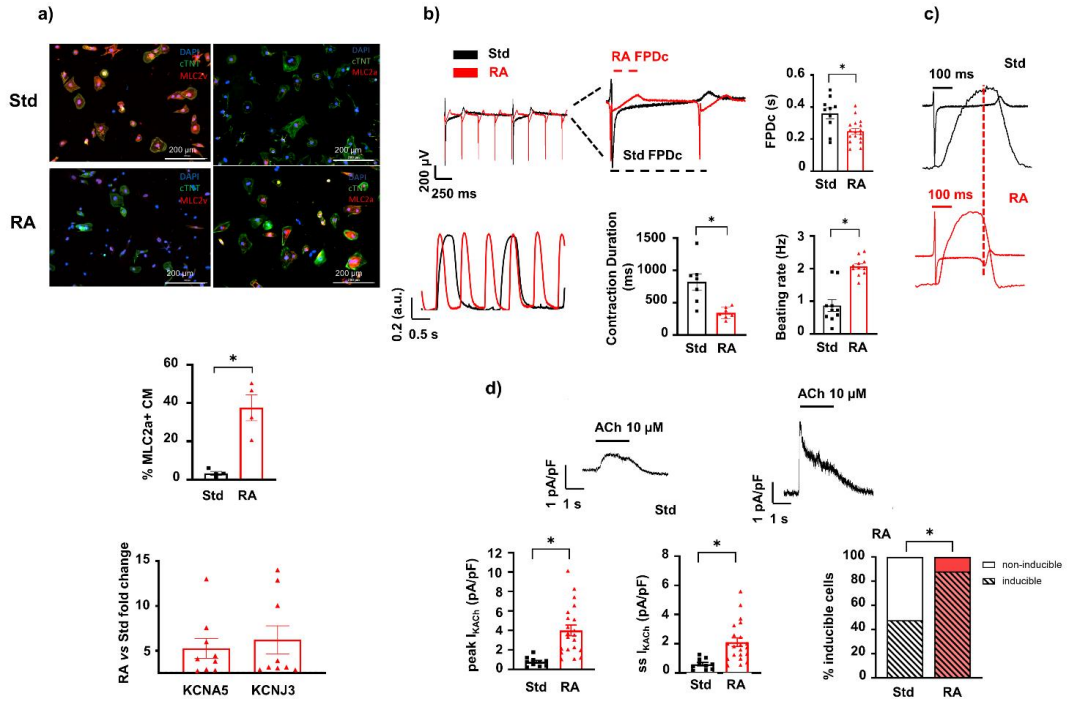

Figure 1. **Molecular and functional assessment of atrial-like hiPSC-CMs at 30 days of differentiation**. (**a**) The percentage of atrial cardiomyocytes (CM) was evaluated by immunostaining for myosin light chain 2 (MLC2v and MLCVa, for ventricular and atrial respectively isoform) in positive cardiac troponin T (TnT) cells. The molecular investigation of repolarising K^+ channel genes (KCNA5 and KCNJ3 genes) was expressed as RA/Std fold change. (**b**) Functional evaluations by MEA (upper panel) and contractility (with MUSCLEMOTION, bottom panel) were indicative of a higher electrical and mechanical beating rate of RA-treated CMs (n=11) compared to Std treatment (n=10). Shorter FPDc in electrical and contraction duration in mechanical RA events were analysed. (**c**) Overlapped recordings highlight different kinetic properties of excitation-contraction (EC) coupling in both conditions. (**d**) Examples of ACh-elicited current recordings in Std and RA CM and analysis of peak, steady-state, and Peak/steady-state ratio of induced currents in Std- and RA-treated CM (n=10 and n=21, respectively). **(e)** Percentage of inducible (red) and not-inducible CM (black) are quantified using both differentiation protocols. Data shown are mean ± SEM. (Std, standard protocol; RA, retinoic acid; FPDc, corrected field potential duration; Contr. Duration, contraction duration; ACh, acetylcholine; I_{KACh}, ACh-induced current).

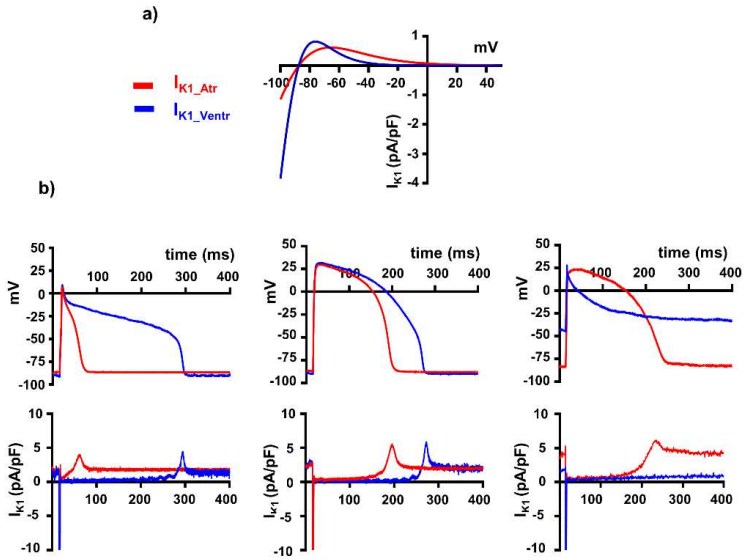

Figure 2. I_{K1_Atr} *vs* I_{K1_Ventr} formulation effect on action potential (AP) profile. (**a**) I_{K1_Atr} and I_{K1_Ventr} computational model I/V relationships. (**b**) AP profiles (upper panels) recorded in three hiPSC-CM following the alternative injection of I_{K1_Ventr} (blue) and I_{K1_Atr} (red) computational models (bottom panels). I_{K1_Atr}, the Koivumäki computational model of human atrial AP; I_{K1_Ventr}, the O'Hara-Rudy (ORd) computational model of human ventricular AP. (I_{K1_Ventr}, ventricular I_{K1} equation; I_{K1_Atr}, atrial I_{K1} equation)

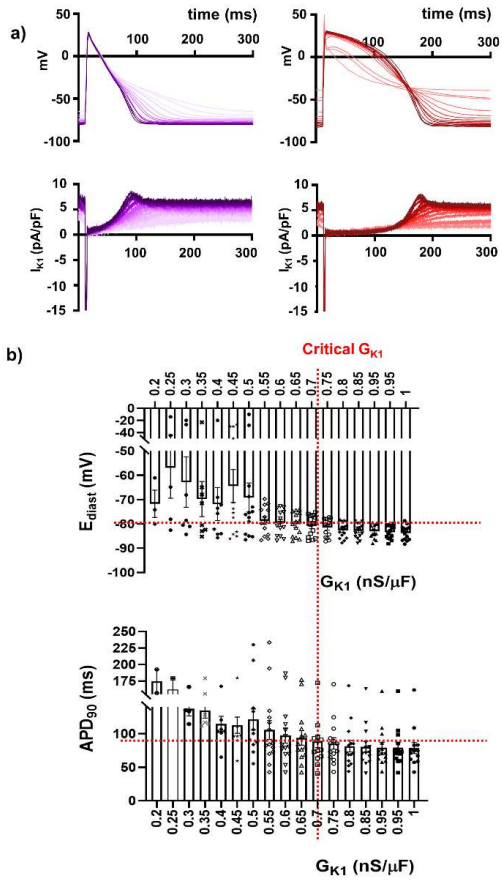

Figure 3. G_{K1} parameter setting of I_{K1_Atr} model. (**a**) Examples of evoked shorter (atrial-like) and longer (ventricular-like) AP profiles following progressive increase of G_{K1} ranging from 0.2 to 1 nS/µF (0.05 nS/µF step). Light colour code for low G_{K1} values and dark colours code for high G_{K1} values. (**b**) E_{diast} and APD_{90} changes yielded from all cardiomyocytes (n=3-14 cells, depending on the cell stability at lower G_{K1}) are represented against G_{K1} values. Red dashed line identifies the critical G_{K1} value to reach stable AP parameters. (APD_{90}, AP duration measured at 90% of the repolarisation phase; E_{diast}, diastolic membrane potential; G_{K1}, I_{K1} conductance).

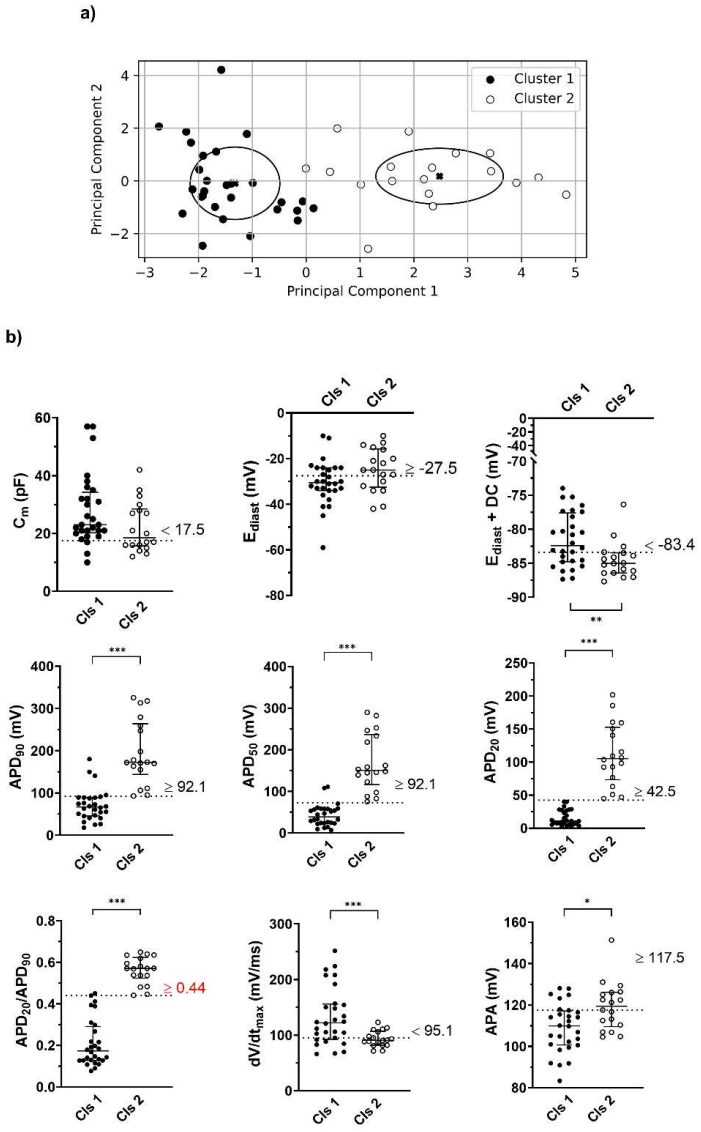

Figure 4. hiPSC-CMs AP phenotype cell classification by unsupervised learning algorithm. (**a**) A K-means classification algorithm was applied to clusterize cells according to 9 electrical parameters (cluster 1 *vs.* cluster 2). (**b**) C_m, E_{diast}, E_{diast} + DC, APD_{90}, APD_{50}, APD_{20}, APD_{20}/APD_{90}, dV/dt_{max}, APA in cluster 1 vs. cluster 2. The best cut-off discriminating cluster 1 *vs.* cluster 2 was defined by ROC curve analysis (see also Table S4) and indicated with a dashed line. Data shown are median interquartile range (25^{th}, 50^{th}, 75^{th} percentiles and analysed by the Mann-Whitney U test. (C_m, cell membrane capacitance, E_{diast}, diastolic membrance potential; E_{diast} with DC, diastolic membrance potential with dynamic clamp; APD_{90}, APD_{50}, and APD_{20}, action potential duration measured at 90%, 50%, and 20% of the repolarisation phase, respectively; APD_{20}/APD_{90}, ratio between APD_{20} and APD_{90}; dV/dt_{max}, maximal AP phase 0 depolarisation velocity, APA, AP amplitude).

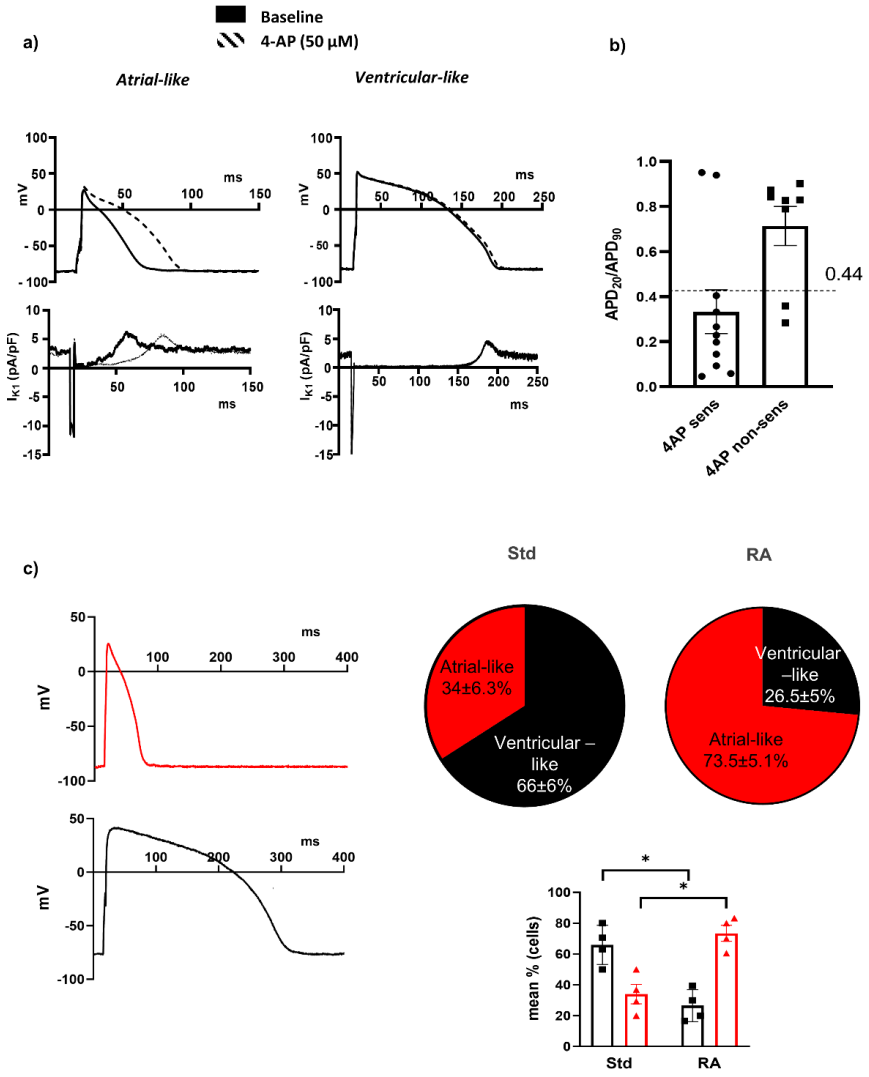

Figure 5. Based-model pharmacological validation and RA efficiency evaluation. (**a**) Example of cut-off-based atrial- and ventricular-like APs recorded during the baseline condition and the superfusion of I_{Kur}-specific blocker 4-aminopyridine (4-AP, 50 µM). (**b**) Distribution of APD_{20}/APD_{90} values of 4-AP-sensitive and 4-AP non-sensitive CMs, with respect to the critical cut-off value (0.44). (**d**) Atrial- and ventricular-like AP phenotypes represented in the panel and their quantitative change (%) with either the Std- or RA-treated cellular platform (n=4 parallel differentiation). (Std, standard protocol; RA, retinoic acid; APD_{20}/APD_{90}, ratio between APD_{20} and APD_{90}).

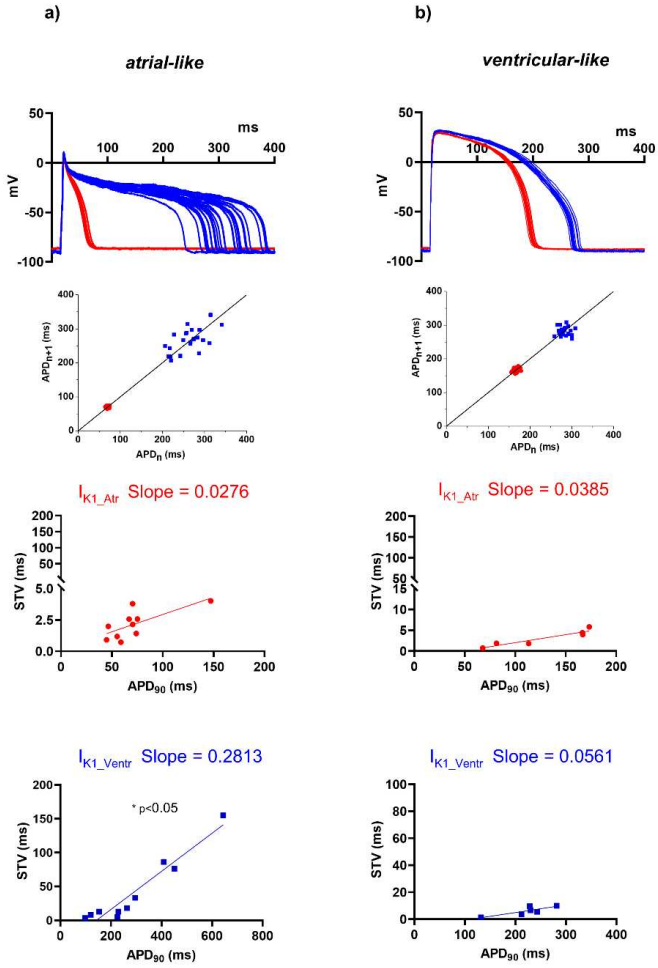

Figure 6. I_{K1_Ventr} *vs* I_{K1_Atr} application and repolarization stability. A series of 30 APs recorded under the injection of I_{K1_Atr} or I_{K1_Ventr} computational model either in (**a**) atrial- or (**b**) ventricular-like CMs. In parallel, the dispersion of relative APD_{90} values is plotted around the identity line in Poincaré plots (upper panels). Linear STV/APD_{90} correlations in each condition (bottom panels), resulting significantly higher with I_{K1_Ventr} *vs* I_{K1_Atr} model in atrial- and ventricular-like CMs (n=10 and n=5 respectively). (APD_{90}, AP duration measured at 90% of the repolarisation phase; I_{K1_Ventr}, ventricular I_{K1} equation; I_{K1_Atr}, atrial I_{K1} equation; STV, short-term variability).